

Women in chemistry 2023

Edited by

Maria Rosaria Plutino, Brigida Boicchio, Claudia Espro,
Noelia Faginas Lago, Elizabeth Flórez, Junko Habasaki,
Maria Manuel Marques, Christiana Mitsopoulou, Annie Ng,
Laura De Luca and Daniela Iannazzo

Published in

Frontiers in Chemistry
Frontiers in Materials



FRONTIERS EBOOK COPYRIGHT STATEMENT

The copyright in the text of individual articles in this ebook is the property of their respective authors or their respective institutions or funders. The copyright in graphics and images within each article may be subject to copyright of other parties. In both cases this is subject to a license granted to Frontiers.

The compilation of articles constituting this ebook is the property of Frontiers.

Each article within this ebook, and the ebook itself, are published under the most recent version of the Creative Commons CC-BY licence. The version current at the date of publication of this ebook is CC-BY 4.0. If the CC-BY licence is updated, the licence granted by Frontiers is automatically updated to the new version.

When exercising any right under the CC-BY licence, Frontiers must be attributed as the original publisher of the article or ebook, as applicable.

Authors have the responsibility of ensuring that any graphics or other materials which are the property of others may be included in the CC-BY licence, but this should be checked before relying on the CC-BY licence to reproduce those materials. Any copyright notices relating to those materials must be complied with.

Copyright and source acknowledgement notices may not be removed and must be displayed in any copy, derivative work or partial copy which includes the elements in question.

All copyright, and all rights therein, are protected by national and international copyright laws. The above represents a summary only. For further information please read Frontiers' Conditions for Website Use and Copyright Statement, and the applicable CC-BY licence.

ISSN 1664-8714
ISBN 978-2-8325-5669-6
DOI 10.3389/978-2-8325-5669-6

About Frontiers

Frontiers is more than just an open access publisher of scholarly articles: it is a pioneering approach to the world of academia, radically improving the way scholarly research is managed. The grand vision of Frontiers is a world where all people have an equal opportunity to seek, share and generate knowledge. Frontiers provides immediate and permanent online open access to all its publications, but this alone is not enough to realize our grand goals.

Frontiers journal series

The Frontiers journal series is a multi-tier and interdisciplinary set of open-access, online journals, promising a paradigm shift from the current review, selection and dissemination processes in academic publishing. All Frontiers journals are driven by researchers for researchers; therefore, they constitute a service to the scholarly community. At the same time, the *Frontiers journal series* operates on a revolutionary invention, the tiered publishing system, initially addressing specific communities of scholars, and gradually climbing up to broader public understanding, thus serving the interests of the lay society, too.

Dedication to quality

Each Frontiers article is a landmark of the highest quality, thanks to genuinely collaborative interactions between authors and review editors, who include some of the world's best academicians. Research must be certified by peers before entering a stream of knowledge that may eventually reach the public - and shape society; therefore, Frontiers only applies the most rigorous and unbiased reviews. Frontiers revolutionizes research publishing by freely delivering the most outstanding research, evaluated with no bias from both the academic and social point of view. By applying the most advanced information technologies, Frontiers is catapulting scholarly publishing into a new generation.

What are Frontiers Research Topics?

Frontiers Research Topics are very popular trademarks of the *Frontiers journals series*: they are collections of at least ten articles, all centered on a particular subject. With their unique mix of varied contributions from Original Research to Review Articles, Frontiers Research Topics unify the most influential researchers, the latest key findings and historical advances in a hot research area.

Find out more on how to host your own Frontiers Research Topic or contribute to one as an author by contacting the Frontiers editorial office: frontiersin.org/about/contact

Women in chemistry 2023

Topic editors

Maria Rosaria Plutino — Institute for the Study of Nanostructured Materials, National Research Council (CNR), Italy

Brigida Bochicchio — University of Basilicata, Italy

Claudia Espro — University of Messina, Italy

Noelia Faginas Lago — University of Perugia, Italy

Elizabeth Flórez — Universidad de Medellín, Colombia

Junko Habasaki — Retired, Setagaya, Japan

Maria Manuel Marques — Universidade Nova de Lisboa, Portugal

Christiana Mitsopoulou — National and Kapodistrian University of Athens, Greece

Annie Ng — Nazarbayev University, Kazakhstan

Laura De Luca — University of Messina, Italy

Daniela Iannazzo — University of Messina, Italy

Citation

Plutino, M. R., Bochicchio, B., Espro, C., Lago, N. F., Flórez, E., Habasaki, J., Marques, M. M., Mitsopoulou, C., Ng, A., De Luca, L., Iannazzo, D., eds. (2024). *Women in chemistry 2023*. Lausanne: Frontiers Media SA.
doi: 10.3389/978-2-8325-5669-6

Table of contents

05	Editorial: Women in chemistry 2023 Maria Rosaria Plutino
07	Highly efficient morpholine-based organocatalysts for the 1,4-addition reaction between aldehydes and nitroolefins: an unexploited class of catalysts Francesco Vaghi, Giorgio Facchetti, Isabella Rimoldi, Matteo Bottiglieri, Alessandro Contini, Maria Luisa Gelmi and Raffaella Bucci
19	Matrices for radioactive waste immobilization: a review Ritu Kumari Pilania and Charu Lata Dube
32	Theoretical and computational study of benzenium and toluenium isomers Falcone C. Moumbogno Tchodimo and Walter C. Ermler
40	Governing the emissive properties of 4-aminobiphenyl-2-pyrimidine push–pull systems via the restricted torsion of N,N-disubstituted amino groups Alejandro Cortés-Villena, Iván Soriano-Díaz, Moisés Domínguez, Matías Vidal, Pablo Rojas, Carolina Aliaga, Angelo Giussani, Antonio Doménech-Carbó, Enrique Ortí, Raquel E. Galian and Julia Pérez-Prieto
54	Decoding the secrets: how conformational and structural regulators inhibit the human 20S proteasome Pedro M. P. Fernandes, Romina A. Guedes, Bruno L. Victor, Jorge A. R. Salvador and Rita C. Guedes
71	Exploring the behavior of <i>Candida antarctica</i> lipase B in aqueous mixtures of an imidazolium ionic liquid and its surfactant analogue Paola R. Campodónico, Cristian Calderón, Jackson J. Alcázar, Belén Olivares, Limberg Jaldin and Cristian Suárez-Rozas
82	Syntheses, reactivity, and biological applications of coumarins Andrea Citarella, Serena Vittorio, Christian Dank and Laura Ielo
110	Structure-reactivity analysis of novel hypervalent iodine reagents in S-vinylation of thiols Sayad Doobary, Ester Maria Di Tommaso, Alexandru Postole, A. Ken Inge and Berit Olofsson

- 120 **Practical applications of copper-based enzymes: synthesis of sulfonated polyaniline through laccase-catalyzed oxidation**
Fabrizia Fabrizi de Biani, Maddalena Corsini, Rebecca Pogni and Maria Camilla Baratto
- 128 **Structural insights of an LCP protein–LytR—from *Streptococcus dysgalactiae subs. dysgalactiae* through biophysical and *in silico* methods**
João Paquete-Ferreira, Filipe Freire, Henrique S. Fernandes, Jayaraman Muthukumaran, João Ramos, Joana Bryton, Alejandro Panjkovich, Dmitri Svergun, Marino F. A. Santos, Márcia A. S. Correia, Alexandra R. Fernandes, Maria João Romão, Sérgio F. Sousa and Teresa Santos-Silva



OPEN ACCESS

EDITED AND REVIEWED BY

Luis D. Carlos,
University of Aveiro, Portugal

*CORRESPONDENCE

Maria Rosaria Plutino,
✉ mariarosaria.plutino@cnr.it

RECEIVED 21 October 2024

ACCEPTED 23 October 2024

PUBLISHED 30 October 2024

CITATION

Plutino MR (2024) Editorial: Women in chemistry 2023.

Front. Chem. 12:1514782.

doi: 10.3389/fchem.2024.1514782

COPYRIGHT

© 2024 Plutino. This is an open-access article distributed under the terms of the [Creative Commons Attribution License \(CC BY\)](#). The use, distribution or reproduction in other forums is permitted, provided the original author(s) and the copyright owner(s) are credited and that the original publication in this journal is cited, in accordance with accepted academic practice. No use, distribution or reproduction is permitted which does not comply with these terms.

Editorial: Women in chemistry 2023

Maria Rosaria Plutino*

Institute for the Study of Nanostructured Materials, National Research Council (ISMN-CNR), Third party Research Unit of Messina, Messina, Italy

KEYWORDS

organocatalysis, micelles, nanocomposites, waste management, theoretical calculations

Editorial on the Research Topic Women in chemistry 2023

Chemical Sciences and Technologies has grown and improved dramatically in both the industrial and academic sectors over the last several decades, with a paradigm shift from conventional synthetic approach toward a creative and multidisciplinary methodology that is taking advantage of green methodology, and AI and machine learning facilities.

Following the celebration of International Women's Day 2023 and the UNESCO International Day of Women and Girls in Science, Frontiers in Chemistry has offered its platform to promote the work of women working in different fields of Chemistry.

Women have made significant contributions to the chemical sciences since the beginnings, but most of their work went unnoticed and unheard. Currently, fewer than 30% of researchers globally are women. Long-standing prejudices and gender stereotypes still discourage women and girls from pursuing science-related careers, particularly STEM and Chemistry research. UNESCO, on the other hand, emphasizes the importance of science and gender equality in ensuring sustainable development. To shift conventional ideas, gender equality must be promoted, prejudices dismantled, and girls and women encouraged to seek Chemical fields.

The Research Topic "Women in Chemistry 2023" aims to highlight the achievements of female researchers in all fields of chemistry.

With ten contributions from Original Research to Review Articles, 60 authors, most of them women, from universities and research institutions contributed to the success of this Research Topic by conducting research and providing expertise on: the restriction of raw materials and resources led the organic chemists to change their mindset and design chemical processes based on:

- organocatalysis (Vaghi et al.; Citarella et al.; Fabrizi de Biani et al.);
- development of nanocomposite to entrap high-level waste (Pilania and Dube);
- theoretical calculation and computation chemistry (Cortés-Villena et al.; Tchodimo and Ermler; Fernandes et al.; Paquete-Ferreira et al.);
- enzymatic processes and micellar aggregates (Campodónico et al.);
- medicinal chemistry (Doobary et al.).

As follows, a summary of the scientific contributions is given.

The synthesis of novel organocatalysts from the family of β -morpholine amino acids were performed, which were investigated in a model reaction, namely, the 1,4-addition reaction of aldehydes to nitroolefins, beginning with commercially accessible amino acids and

epichlorohydrin. Computational studies did reveal the reaction's transition state, which explains why, despite the morpholine ring's limitations for enamine catalysis, the best obtained catalyst works efficiently, producing condensation products with excellent yields, diastereoselection, and good-to-excellent enantioselectivity (Vaghi et al.).

The proper disposal of nuclear waste is critical to ensuring the long-term usage of nuclear energy. Radioactive waste must be immobilized before ultimate disposal to allow for intermediate storage and transportation, on glass, ceramics, and glass-ceramics matrices for immobilizing high-level waste, focusing on the synthetic processes, leaching behavior, and radiation resistance of matrices (Pilania and Dube).

Four computational quantum chemistry approaches are utilized to investigate hyperconjugation in protonated aromatic compounds. Benzene, benzenium, toluene, and four isomeric forms of toluenium are investigated at the self-consistent field level, followed by configuration interaction, coupled cluster calculations, and density functional theory. The computed results are consistent with earlier computational research and experimental evidence (Tchodimo and Ermler).

Candida antarctica lipase B (CALB) performance was evaluated in 1-butyl-3-methylimidazolium tetrafluoroborate (BMIMBF₄)/water mixtures in a wide range of molar fractions (χ BMIMBF₄) with and without 1-dodecyl-3-methylimidazolium tetrafluoroborate (C12-MIMBF₄), a surfactant derived from BMIMBF₄, to emphasize the superactivity phenomena caused by the reaction medium and micelle interaction (Campodónico et al.).

Donor-acceptor-substituted biphenyl derivatives are especially intriguing model compounds because of the degree of charge transfer between both substituents. The addition of a 4-[1,1'-biphenyl]-4-yl-2-pyrimidinyl moiety to various disubstituted amino groups at the biphenyl terminal might result in push-pull compounds with varied photophysical characteristics, influenced by the torsion angle of the disubstituted amino group (Cortés-Villena et al.).

Targeted therapy highlights the necessity of developing novel methods for predicting drug binding and possible resistance owing to specific protein alterations. A comprehensive computational analysis is used to determine the consequences of specific mutations (Ala49Thr, Ala50Val, and Cys52Phe) in the active region of the human proteasome (Fernandes et al.).

A thorough analysis spanning 2021–2023 delves into the varied chemical and pharmacological potential of coumarins, highlighting their importance as adaptable natural derivatives in medicinal chemistry. Innovative methodologies have been used to enhance coumarin production and functionalization, useful in a wide range of potential uses in medicinal chemistry (Citarella et al.).

Many novel types of hypervalent iodine vinylation reagents, including vinylbenziodazolones, vinylbenziodoxolonimine, and vinyliodoxathiole dioxide have been obtained; their synthetic, structural, and electrical characteristics are explained and connected with S-vinylation results, giving light on several intriguing aspects of these chemicals (Doobary et al.).

The LytR-CpsA-Psr (LCP) protein family, which facilitates the insertion of cell wall glycopolymers (CWGPs) such as teichoic acids into peptidoglycan, has emerged as an attractive target for antibiotic development. The structural and functional properties of the LytR's LCP domain from *Streptococcus dysgalactiae* subsp were investigated by Small-angle X-ray scattering (SAXS), and by docking and molecular dynamics (MD) simulations (Paquete-Ferreira et al.).

Sulfonated PANI (SPANI) was developed to overcome solubility issues, making it more practical. UV-vis spectroscopy was used to monitor the *Trametes versicolor* laccase-induced oxidation of 3-ABSa, indicating SPANI production. NMR and spectroelectrochemistry validate the green production of SPANI via laccase (Fabrizi de Biani et al.).

To summarize, the contributions in this Research Topic show the current broad interest in different Chemical industrial, academic and research sectors, with the challenge to involve more women in Chemistry, and with an eye on Sustainability and Innovation.

Author contributions

MP: Conceptualization, Writing–original draft, Writing–review and editing.

Funding

The author(s) declare that no financial support was received for the research, authorship, and/or publication of this article.

Acknowledgments

I am grateful to all of the authors who contributed to this Research Topic. I also thank the referees for evaluating the articles. Reviewers' professionalism and knowledge contributed to the improved quality and effect of all submitted articles. Finally, I sincerely thank all the co-editors, Brigida Bochicchio, Claudia Espro, Noelia Faginas Lago, Elizabeth Flórez, Junko Habasaki, Maria Manuel Marques, Christiana Mitsopoulou, Annie Ng, Laura De Luca, Daniela Iannazzo, and all the editorial staff of *Frontiers in Chemistry*, for their support during the development and publication of this Research Topic.

Conflict of interest

The author declares that the research was conducted in the absence of any commercial or financial relationships that could be construed as a potential conflict of interest.

Generative AI statement

The author(s) declare that no Generative AI was used in the creation of this manuscript.

Publisher's note

All claims expressed in this article are solely those of the authors and do not necessarily represent those of their affiliated organizations, or those of the publisher, the editors and the reviewers. Any product that may be evaluated in this article, or claim that may be made by its manufacturer, is not guaranteed or endorsed by the publisher.



OPEN ACCESS

EDITED BY

Maria Manuel Marques,
Universidade Nova de Lisboa, Portugal

REVIEWED BY

Rajendra Rohokale,
University of Florida, United States
Albert Moyano,
University of Barcelona, Spain

*CORRESPONDENCE

Raffaella Bucci,
✉ raffaella.bucci@unimi.it

[†]These authors have contributed equally
to this work

RECEIVED 01 June 2023

ACCEPTED 24 July 2023

PUBLISHED 11 August 2023

CITATION

Vaghi F, Facchetti G, Rimoldi I,
Bottiglieri M, Contini A, Gelmi ML and
Bucci R (2023), Highly efficient
morpholine-based organocatalysts for
the 1,4-addition reaction between
aldehydes and nitroolefins: an
unexploited class of catalysts.
Front. Chem. 11:1233097.
doi: 10.3389/fchem.2023.1233097

COPYRIGHT

© 2023 Vaghi, Facchetti, Rimoldi,
Bottiglieri, Contini, Gelmi and Bucci. This
is an open-access article distributed
under the terms of the [Creative
Commons Attribution License \(CC BY\)](#).
The use, distribution or reproduction in
other forums is permitted, provided the
original author(s) and the copyright
owner(s) are credited and that the original
publication in this journal is cited, in
accordance with accepted academic
practice. No use, distribution or
reproduction is permitted which does not
comply with these terms.

Highly efficient morpholine-based organocatalysts for the 1,4-addition reaction between aldehydes and nitroolefins: an unexploited class of catalysts

Francesco Vaghi[†], Giorgio Facchetti[†], Isabella Rimoldi,
Matteo Bottiglieri, Alessandro Contini, Maria Luisa Gelmi and
Raffaella Bucci*

Dipartimento di Scienze Farmaceutiche, DISFARM, Sezione Chimica Generale e Organica "A. Marchesini",
Università degli Studi di Milano, Milan, Italy

Many studies have demonstrated how the pyrrolidine nucleus is more efficient than the corresponding piperidine or morpholine as organocatalysts in the condensation of aldehydes with electrophiles *via* enamine. Focussing on morpholine–enamines, their low reactivity is ascribed to the presence of oxygen on the ring and to the pronounced pyramidalisation of nitrogen, decreasing the nucleophilicity of the enamine. Thus, the selection of efficient morpholine organocatalysts appears to be a difficult challenge. Herein, we reported on the synthesis of new organocatalysts belonging to the class of β -morpholine amino acids that were tested in a model reaction, *i.e.*, the 1,4-addition reaction of aldehydes to nitroolefins. Starting from commercially available amino acids and epichlorohydrin, we designed an efficient synthesis for the aforementioned catalysts, controlling the configuration and the substitution pattern. Computational studies indeed disclosed the transition state of the reaction, explaining why, despite all the limitations of the morpholine ring for enamine catalysis, our best catalyst works efficiently, affording condensation products with excellent yields, diastereoselection and good-to-exquisite enantioselectivity.

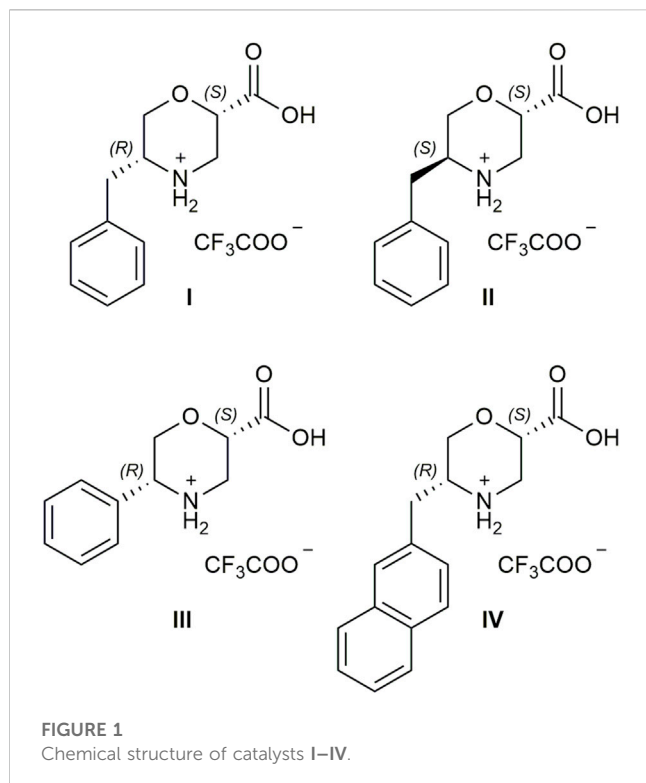
KEYWORDS

non-coded amino acids, β -amino acids, organocatalysis, morpholine, Michael addition, enamine catalysis

Introduction

The restriction of raw materials and resources led the organic chemists to change their mindset and design chemical processes based on the “Sustainable Development” concept. Inspired by Nature, since the late 1990s, scientists have laid the groundwork for asymmetric organocatalysis (Ahrendt *et al.*, 2000; List *et al.*, 2000), allowing a green and direct access to highly functionalised chiral products, including important key intermediates in the total syntheses of bioactive compounds (Xiang and Tan, 2020; Han *et al.*, 2021).

At the dawn of organocatalysis, (S)-Proline (Pro) was identified as “the simplest enzyme” because of its ability to promote enantioselectivity in different reactions (List *et al.*, 2000; 2001; Movassaghi and Jacobsen, 2002). Since then, plenty of analogues were designed to bypass the Pro limitations as an organocatalyst, such as its poor solubility in organic solvents



(Obregón-Zúñiga et al., 2017). Moreover, the introduction of sterically hindered groups allowed the formation of more rigid transition states, leading to better stereo-induction within the studied reaction (Seebach et al., 1985; Seebach et al., 2013; Liu and Wang, 2017). As an example, MacMillan (Ahrendt et al., 2000) and Hayashi-Jorgensen (Hayashi et al., 2007; Reyes et al., 2007) catalysts are at present commercially available compounds for routine enantioselective syntheses. Due to the increasing demand of chiral compounds, the research of new organocatalysts continues to be a hot topic of research.

Recently, our research group reported on the synthesis of non-natural β -amino acids (β -AA) with a constrained heterocyclic core (Oliva et al., 2019), mostly focussing on morpholine β -amino acids (β -Morph-AAs) for different applications (Penso et al., 2012; Bucci et al., 2019; Bucci et al., 2020; Bucci et al., 2021; Vaghi et al., 2020), i.e., from the synthesis of photoluminescent nucleopeptides (Bucci et al., 2020) to their use as inducers of the polyproline helix when inserted in the model's peptides (Bucci et al., 2019; Bucci et al., 2021; Vaghi et al., 2020).

Being inspired by the use of nitrogen-containing heterocycles in asymmetric synthesis *via* enamine, here, we studied the use of new β -Morph-AAs as very challenging and stimulating organocatalysts. It has already been reported that in comparison to enamines with a pyrrolidine and piperidine core, the morpholine cores are orders of magnitude less reactive. Pyrrolidine enamines are the most reactive due to the higher p-character of the nitrogen lone pair in their five-membered ring, indicating higher nucleophilicity compared to the six-membered piperidine ring. The presence of oxygen in morpholine-enamines further increases the ionisation potential and consequently reduces nucleophilicity compared to piperidine cores (Kempf et al., 2003). Moreover, the most pronounced

pyramidalisation of morpholine-enamines, resulting in poor reactivity, should be another limitation of the proposed catalysts (Brown et al., 1978; Schnitzer et al., 2020b).

To test our catalysts, we focussed on a model Michael addition reaction between aldehydes and nitrostyrenes, which is usually promoted by pyrrolidine-based organocatalysts. As the main drawback, except for few examples (Lombardo et al., 2009; Borges-González et al., 2019; Schnitzer et al., 2020a; Schnitzer et al., 2020b), their use requires a 10–20 mol% of the catalyst and an excess of the carbonyl compound (List et al., 2001; Sakthivel et al., 2001; Hayashi et al., 2005; Choudary et al., 2007; Ni et al., 2007; Llopis et al., 2018).

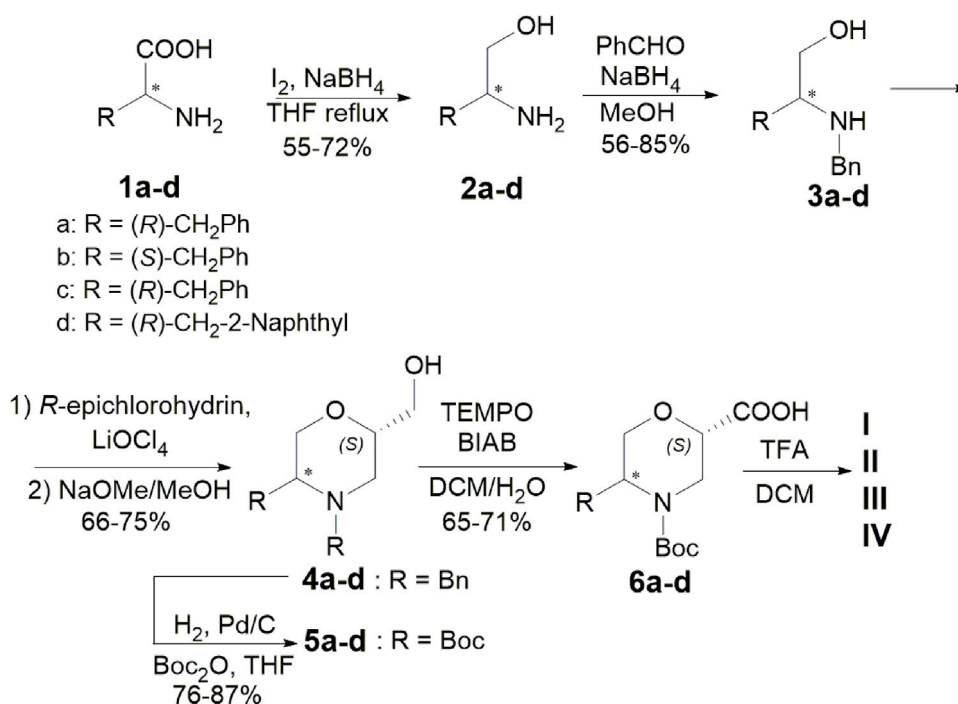
It has to be underlined that some base research on morpholine-enamine to understand the topological rule for C,C-bond-forming processes between prochiral centres was conducted by Seebach and Goliński (1981). On the other hand, the use of morpholine catalysts is, in general, very limited, mostly in terms of reagent conversion. Moreover, to the best of our knowledge, only few examples of chiral morpholine organocatalysts were tested for this reaction, yielding poor diastereo- and enantioselectivity (Mossé et al., 2006; Laars et al., 2009; Laars et al., 2010).

Starting from inexpensive commercially available *a*-AAs and chiral epichlorohydrin, we designed a straightforward enantioselective synthesis of β -Morph-AAs I–IV (Figure 1) with a different sterically hindered group at C-5, which is derived from the *a*-AA side chain, and a carboxylic function at C-2, which is crucial for the success of this reaction. By playing with different stereochemistries of the two starting materials, it is possible to modulate the formation of *cis* or *trans* isomers of the two substituents and their absolute configuration that will reflect on the stereochemistry of the final compound.

The efficacy of the hindered group, together with the best steric relationship between C-2 and C-5 substituents of morpholine ring, was investigated. Both experimental and computational data confirmed that catalyst I has a remarkable ability to control the diastereo- and enantioselectivity of the 1,4-addition reaction between aldehydes and nitroolefins. Despite the already explained limitations of morpholine catalysts with enamine mode of action, different from the majority of the reported organocatalysts, only 1 mol% of I and 1.1 eq. of aldehyde are required to reach a quantitative conversion of the reagents. We also proved the crucial role of the carboxylic group; i.e., in the presence of I capped as methyl ester under standard conditions, no condensation products were observed after 48 h. Furthermore, excellent diastereoselection was detected (90%–99% *d. e.*), along with the enantioselection ranging from 70% to 99% *e. e.*, depending on the reagents.

Results and discussion

5-Substituted β -Morph-AAs were synthesised from commercially available (*R*) or (*S*) *a*-AAs and (*R*)-epichlorohydrin (Scheme 1). AAs 1 were treated with NaBH₄ (2.5 eq.) and I₂ (1 eq.) in refluxing THF, yielding the corresponding amino alcohol 2 (55%–72%). Subsequent reductive amination of 2 with benzaldehyde (1.3 eq.) and NaBH₄ (3 eq.) in MeOH at r. t. afforded compounds 3 (56%–85%). According to a one-pot procedure reported in the work of Breuning et al. (2007), Morph-derivatives 4 (66%–75%) were obtained by the treatment of 3, first with *R*-epichlorohydrin (1.3 eq.) in the presence of LiClO₄



SCHEME 1
 Synthesis of catalysts I-IV.

(1.3 eq.) in toluene (60°C) and then with MeONa in MeOH. Using H₂ and Pd/C (10% loading) in the presence of Boc₂O (1.05 eq.) in THF, **4** was transformed into the Boc-protected amino alcohol **5** (76%–87%). Oxidation with TEMPO (0.2 eq.) and BIAB (2 eq.) in CH₂Cl₂/H₂O (2:1) provided the desired β-Morph-AAs **6** (65%–71%) and then deprotected yielding catalysts **I-IV**, as CF₃CO₂H salts, characterised by different stereochemistry and substitution patterns.

In order to demonstrate the potential of our Morph-catalysts, the reaction between butyraldehyde (**7a**, 1 eq.) and trans-β-nitrostyrene (**8a**, 1.5 eq.) was chosen as the model. In principle, it can provide two diastereoisomers as a couple of enantiomers, *i.e.*, (2*R**,3*S**)- and (2*S**,3*S**)-2-ethyl-4-nitro-3-phenylbutanals (**9**). To control the diastereo- and enantioselection, several reaction conditions (solvent, temperature, and reaction time) were tested using 1% of catalysts **I-IV** (Table 1) in the presence of *N*-methylmorpholine (NMM, 1 mol%) as the base, in order to obtain the free amino group of the catalyst.

Catalyst **I** was selected as the first catalyst to predominantly yield the *syn* (2*R*,3*S*)-adduct **9**. Different solvents were screened (40°C, 12 h; entries 1–5, Table 1). Mixtures with fluorinated alcohols were also tested for their peculiar features, being known as efficient additives in Michael additions with proline as the catalyst (Pellissier, 2021).

In general, an excellent conversion of the reagents was achieved, revealing the use of alcoholic solvents or co-solvent beneficial for diastereoselection. These solvents were, thus, selected, and additional studies were performed, decreasing the temperature (0°C, 12 h, entries 6–8; –10°C, 24 h, entries 9–11; Table 1). *i*PrOH was found to be the best solvent at –10°C (entry 11, Table 1), giving the expected product **9** with quantitative conversion and higher

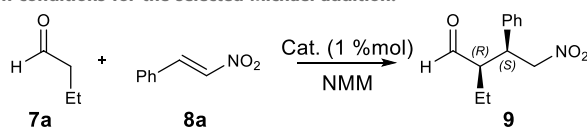
diastereo- (96% *d. e.*) and enantioselectivity (90% *e. e.*). This result agrees with the computational analysis that predicted the importance of protic solvents for the stabilisation of the transition state (see the following sections).

Catalyst **II**, having the opposite configuration at C-5, was then tested (entries 12–15, Table 1), which resulted to be less efficient; *i.e.*, the reaction reached a quantitative conversion but only at 40°C, giving lower *d. e.* and *e. e.* (entries 12–14, Table 1). Operating in *i*PrOH at –10°C, 85% *d. e.*, and 86% *e. e.* was indeed found but with a modest conversion (entry 15, Table 1). Interestingly, the inversion of the configuration at C-5 of **II** with respect to **I** allows the obtainment of *syn* (2*S*,3*R*)-adduct as the main enantiomer (entries 12–15, Table 1).

Since the (2*S*,5*R*)-stereochemistry of **I** resulted to be the most efficient, we chose to evaluate the effect of the group at C-5 by selecting phenyl and CH₂-2-naphthyl groups, considering their limited freedom and increased bulkiness, respectively. The phenyl group in **III** at 40°C caused a loss in the conversion rate and stereocontrol (entries 16–18, Table 1). Moreover, operating in *i*PrOH at –10°C, only traces of the desired compound were detected (entry 19, Table 1). On the other hand, operating at –10°C for 24 h and using the more hindered catalyst **IV** (entries 20–21, Table 1), 60% conversion, high level of diastereoselection (99% *d. e.*), and satisfactory enantioselection (73% *e. e.*) were reached. By increasing the reaction time, the conversion was slightly increased but with the loss of enantioselectivity (entry 21, Table 1).

In summary, the C-5 benzyl group of **I**, *cis* with respect to the C-2 carboxylic function, induces an excellent diastereo- and enantioselectivity operating in *i*PrOH at –10°C. Thus, with only 1% of the catalyst and only 1:1.5 ratio of **7a:8a**, excellent conversion was observed. By using the aforementioned best conditions and

TABLE 1 Screening of catalysts and reaction conditions for the selected Michael addition.



Entry	Cat. (1%)	Solvent	T (°C)	Conv (%) ^a	Time (h)	d.e. (%) ^b	e.e. (%) ^c
1	I	CHCl ₃ /TFE (1/1)	40	>99	12	31	49
2	I	ACN/HFIP (1/1)	40	>99	12	65	67
3	I	iPrOH	40	>99	12	64	55
4	I	ACN	40	>99	12	49	31
5	I	Toluene	40	>99	12	69	32
6	I	CHCl ₃ /TFE (1/1)	0	86	12	86	65
7	I	ACN/HFIP (1/1)	0	91	12	92	72
8	I	iPrOH	0	>99	12	87	80
9	I	CHCl ₃ /TFE (1/1)	−10	88	24	89	60
10	I	ACN/HFIP (1/1)	−10	93	24	93	75
11	I	iPrOH	−10	>99	24	96	90
12	II	CHCl ₃ /TFE (1/1)	40	>99	12	62	58 ^d
13	II	ACN/HFIP (1/1)	40	>99	12	70	59 ^d
14	II	ACN	40	72	12	56	48 ^d
15	II	iPrOH	−10	65	24	85	86 ^d
16	III	CHCl ₃ /TFE (1/1)	40	84	12	72	21
17	III	ACN/HFIP (1/1)	40	83	12	70	24
18	III	ACN	40	81	12	70	10
19	III	iPrOH	−10	5	24	99	39
20	IV	iPrOH	−10	60	24	99	73
21	IV	iPrOH	−10	70	48	99	67

Reaction condition: **7a** (1.0 eq.)/**8a** (1.5 eq.)/NMM (1 mol%)/Cat (1 mol%).

^aConversion was determined by ¹H NMR on the crude mixture.

^bd.e. was determined by ¹H NMR on the crude mixture since the diastereoisomers are hardly separable by flash chromatography.

^ce.e. was determined by chiral HPLC analysis in comparison with the authentic racemic material.

^d(2*S*,3*R*)-**9** was formed as the main isomer. TFE, trifluoroethanol; HFIP, 1,1,1,3,3,3-hexafluoro 2-propanol.

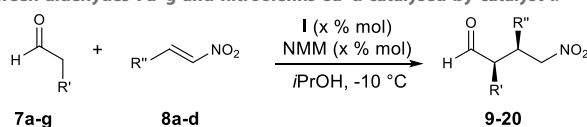
catalysts, a series of aldehydes **7b–g** and nitroolefins **8b–d** were screened to expand the scope of the reaction (Table 2). To reach the right balance between conversion, *d. e.* and *e. e.*, different attempts were carried out, using different amounts of catalyst, reaction times, and temperatures. The best results are summarised in Table 2 (additional results are described in SI, including two examples with aliphatic nitroolefins that gave poor results in terms of *d. e.* and *e. e.*).

Elongating the alkyl chain of the aldehyde, a decrease in conversion was observed, while a growth of *e. e.* was obtained with excellent *d. e.* (up to 99%, entries 1–4, Table 2).

On the other hand, compound **13** (entry 5, Table 2) was obtained with an *e. e.* slightly lower than 90% probably because of the multi-degree of freedom arising from the alkyl chain of the hexanal. To obtain compound **14** from phenylpropionaldehyde

(**7f**) with satisfactory conversion, the amount of the catalyst was increased to 5% (comparing entries 6 and 7, Table 2). With the hindered cyclopentylaldehyde (**7g**), a similar amount of catalysts was needed, but operating at 40°C. A low conversion along with a moderate enantioselectivity was observed (entry 8, Table 2). Finally, we focussed on the reactivity of nitrostyrenes **8** containing an electron-rich (*i.e.*, 4-MeOPh, thiophenyl; entries 9–11, Table 2) or electron-poor (*i.e.*, 4-ClPh; entries 12–13, Table 2) aromatic moiety that were matched with **7b** and **7c**. With an exception (entry 10, Table 2), the reaction works with 1% of the catalyst. As a general trend, the more electron rich the aryl substituent in compounds **8** is, the higher is the conversion (comparing entries 9 with 12 and entries 10 with 13, Table 2), and in all cases, high *d. e.* and satisfactory *e. e.* were detected (*d.e.* > 89% and *e. e.* 67%–80%).

TABLE 2 Conjugate addition reactions between aldehydes 7a–g and nitroolefins 8a–d catalysed by catalyst I.



Entry	Product	Aldehyde 7	Nitroolefin 8	Catalyst % conv (%) ^a	Time (h)	Yield (%) ^b	d.e. (%) ^c	e.e. (%) ^d
1	9	a: R' = Et	a: R'' = Ph	1	24	92	96	90
				>99				
2	10	b: R' = Me	a: R'' = Ph	0.5 ^e	24	95	94	73
				>99				
3	11	c: R' = nPr	a: R'' = Ph	1	48	86	99	99
				90				
4	12	d: R' = iPr	a: R'' = Ph	1	48	58	99	95
				68				
5	13	e: R' = nBu	a: R'' = Ph	1	48	52	99	87
				60				
6	14	f: R' = CH ₂ Ph	a: R'' = Ph	1	48	38	99	88
				40				
7	14	f: R' = CH ₂ Ph	a: R'' = Ph	5	48	72	89	82
				80				
8	15	7g: cyclopentylaldehyde	a: R'' = Ph	5	48 ^f	50	-	35
				53				
9	16	b: R' = Me	b: R'' = pOMe-Ph	1	48	87	91	80
				>99				
10	17	c: R' = nPr	b: R'' = pOMe-Ph	5	48	70	98	70
				74				
11	18	b: R' = Me	c: R'' = tiophenyl	1	48	82	89	67
				>99				
12	19	b: R' = Me	d: R'' = pCl-Ph	1	48	87	93	77
				90				
13	20	c: R' = nPr	d: R'' = pCl-Ph	1	48	55	94	74
				60				

Reaction condition: aldehyde 7 (1.0 eq.)/nitrostyrene 8 (1.5 eq.)/catalyst I/NMM (x mol%, according to the amount of catalyst) and iPrOH, −10°C.

^aConversion was determined by ¹H NMR on the crude mixture.

^bThe yield was calculated after flash chromatography.

^cd.e. was determined by ¹H NMR on crude since the diastereoisomers are hardly separable by flash chromatography.

^de.e. were determined by chiral HPLC analysis in comparison with the authentic racemic material.

^eThe same results were obtained with 1% of the catalyst.

^fThe reaction was performed at 40°C.

Computational analysis of the reaction mechanism

The mechanism for the addition of aldehydes to nitroalkenes through enamine catalysis was previously analysed both theoretically and experimentally (Sahoo et al., 2012; Földes et al.,

2017). Two main hypotheses were carried out for the addition: the first implies the formation of a zwitterion (**Int1-ZW**-like, Figure 2) derived from the addition of the enamine to the β-carbon of the nitroalkene. The second one suggests cycloaddition, leading to dihydrooxazine oxide (**Int1-OX**-like, Figure 2) in equilibrium with a cyclobutane species (**Int1-CB**-like, Figure 2). The

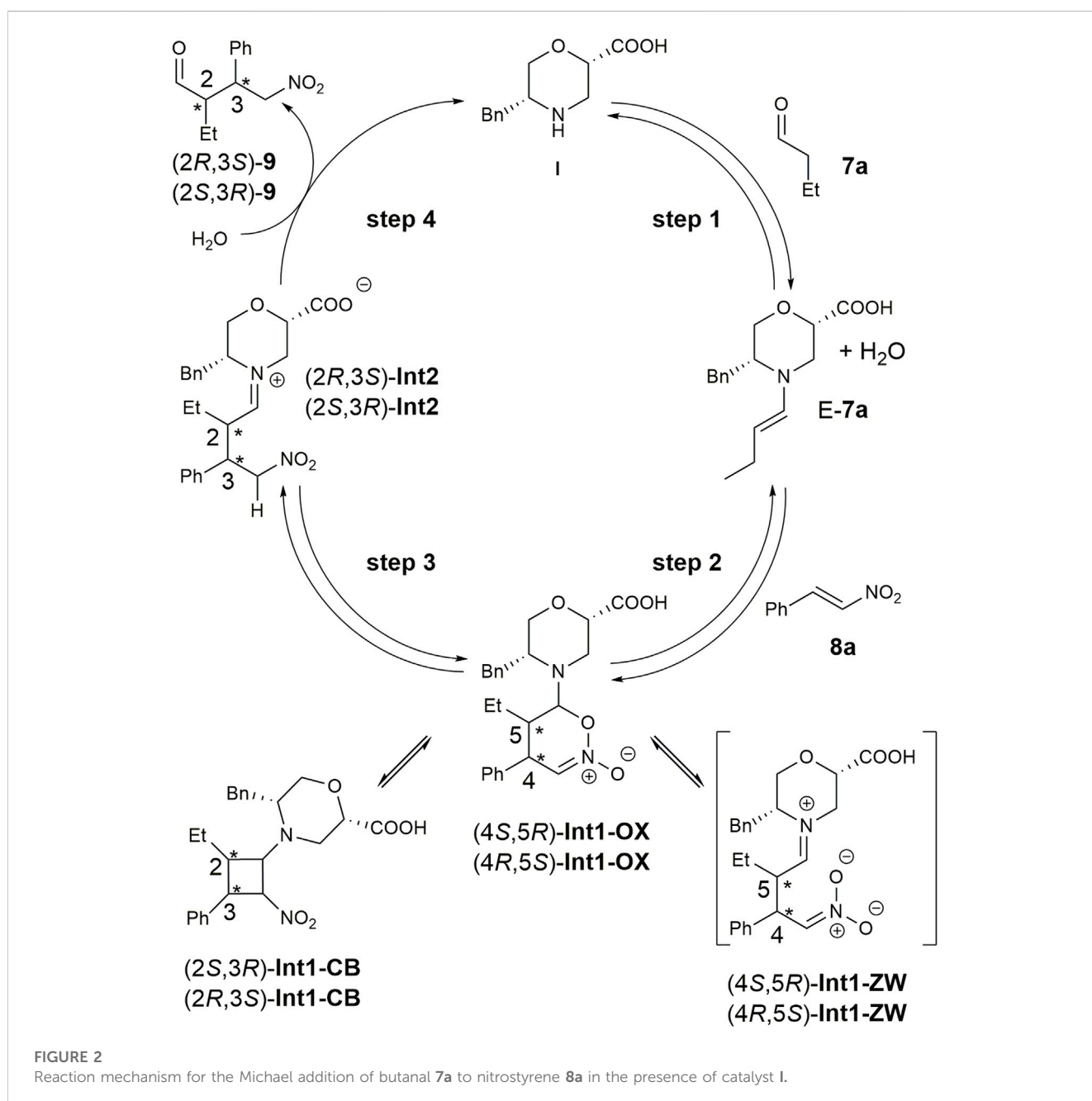
dihydrooxazine oxide intermediate can be protonated at the α -carbon with respect to the nitro group and evolve to the imino intermediate (Int2-like, Figure 2) that is hydrolysed to the final product.

To elucidate the possible role of our catalyst, we decided to model the equilibrium steps described in Figure 2 by using consolidated density functional theory (DFT) methods (Gassa et al., 2010; Grimme et al., 2010; Sahoo et al., 2012; Giofrè et al., 2021).

We initially performed a conformational search on the hypothesised zwitterion Int1-ZW at the molecular mechanic level, considering both diastereoisomers. All conformations within 3.0 kcal/mol were optimised at the DFT level, but all simulations either failed or converged into the Int1-OX intermediate (Figure 2) for both (4*R*,5*S*) and (4*S*,5*R*) stereoisomers. These results, together with the

lack of experimental evidence of the zwitterion intermediate, suggested that the reaction can directly proceed with a cycloaddition-like mechanism.

Consequently, we modelled both the Int1-OX and Int1-CB intermediates, considering both the 4*S*,5*R*/4*R*,5*S* or 2*S*,3*R*/2*R*,3*S* stereoisomers, respectively (Figure 2), that were subjected to a conformation search using molecular mechanics. Considering that a transient stereocentre is formed at the C-bearing morpholine group, both configurations were evaluated, and the most stable stereoisomer was further considered. All conformations within a range of 3 kcal/mol were optimised by DFT, and energy was calculated by considering *i*PrOH solvent effects and empirical correction for dispersive interactions (Grimme et al., 2010).



For both stereoisomers, the most stable conformation of the **Int1-OX** intermediate was used to model the transition state (TS1) for the attack of the enamine **E-7a** to the nitrostyrene **8a**. The lowest-energy transition states (TSs) are shown in Figure 3.

The geometries of the two TS1 stereoisomers indicate that the reaction formally occurs as a [4 + 2] cycloaddition directly leading to the **Int1-OX** intermediates. This has been confirmed by intrinsic reaction coordinate (IRC) calculations that showed TS1 connecting the activated complex between **E-7a** and nitrostyrene **8a** to **Int1-OX** (Supplementary Figures S1, S2, SI). A TS directly leading to **Int1-CB** was not located, even if experimental evidence shows that **Int1-CB** is often the dominant species (Burés et al., 2011; Sahoo et al., 2012). We hypothesised that the equilibrium between **Int1-OX** and **Int1-CB** occurs through a concerted ring opening/closure, according to Scheme 2. Despite several attempts, a unique TS for this equilibrium reaction was not found. However, since **Int1-CB** can be considered a dead end in the reaction mechanism (Sahoo et al., 2012), we focussed on identifying TSs that are relevant to step 3 (Figure 2).

Thus, TS2 was modelled by starting from the lowest-energy structure of **Int1-OX**. It was shown that the protonation step triggering the ring opening in step 3 was the reaction rate determining step (rds) (Sahoo et al., 2012). We, thus, hypothesised that the carboxylic group of catalyst **I** might play a key role in controlling the enantioselectivity observed in this study, as confirmed by experimental data (mentioned previously). We also hypothesised that *i*PrOH, used as a solvent, might bridge the H-transfer between the carboxylic group of the morpholine moiety and Ca-NO₂. Thus, one molecule of *i*PrOH was explicitly considered in TS2 geometries for both stereoisomers. Several conformations were evaluated for each TS2, and both the *E* and *Z* configurations were considered for the imino group of **Int2**. IRC calculations were conducted to confirm that TS2 connects **Int1** to **Int2** (Supplementary Figures S1, S2, SI). To compute that activation barriers and reaction energies are comparable with those reported in previous computational studies (Sahoo et al., 2012), all the selected stationary points were reoptimised using the ωB97X-D functional and 6-311G (d,p) basis set, including the solvent effect for *i*PrOH. More accurate single-point energies were then computed at the same level of theory by using 6-311++G (3df,3pd), as suggested by Sahoo et al. (2012). The obtained free energies were then used to draw the reaction path represented in Figure 4. The most stable geometries for (2*R*,3*S*)- and (2*S*,3*R*)-TS2 are shown in Figure 5. We can observe that the energy path relative to the formation of the (2*S*,3*R*)-**9** enantiomer is characterised by higher activation free energy barriers (ΔΔ*G*[‡]) for both TS1 and TS2, compared to the favoured (2*R*,3*S*)-**9** enantiomer. Among the two energy paths, the greatest difference in ΔΔ*G*[‡] is observed for TS2, where the protonation step occurs concerted to the ring opening (Figures 4, 5). This step is then confirmed as the r.d.s and the path leading to the isolated (2*R*,3*S*)-**9** as the kinetically favoured path. Interestingly, the **Int1** intermediate results as the global minimum on both the free energy (Figure 4) and enthalpy path (Supplementary Figure S3, SI), suggesting that the hydrolysis of the **Int2** intermediate is the non-equilibrium step that drives the reaction towards the final product.

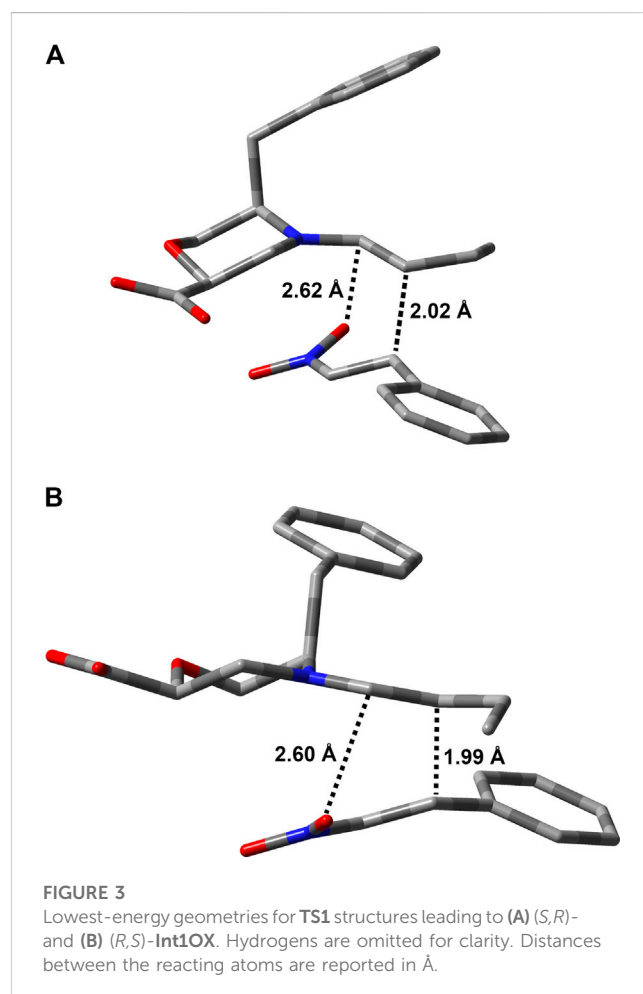
TS2 geometries (Figure 5) evidenced the role of the β-Morph carboxylic acid in self-catalysing the proton transfer from *i*PrOH to Ca-NO₂. This role was also confirmed experimentally; i.e., the reaction between **7a** and **8a** catalysed by the methyl ester of **I**

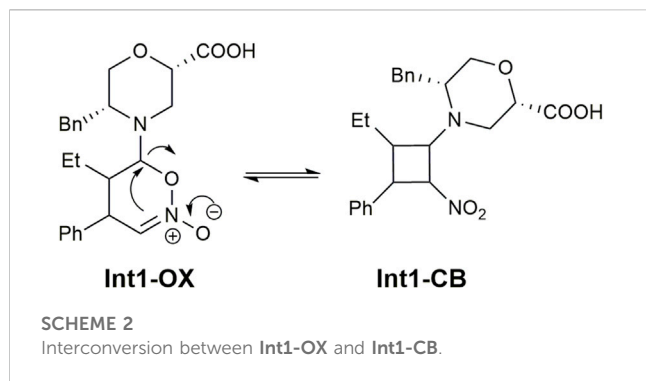
was performed under standard conditions, but no condensation products were observed after 48 h.

Interestingly, both TS2 structures share similar geometrical parameters related to the H-transfer (see distances in Figure 5). However, the most relevant difference that could be associated to the greater stability of (2*R*,3*S*)-TS2, as compared to (2*S*,3*R*)-TS2, is the configuration at the imino group of the forming **Int2** product (Supplementary Figure S1, SI). Indeed, the opening of the dihydrooxazine oxide ring led to the *E*-configuration for (2*R*,3*S*)-TS2, while the more hindered *Z*-configuration is obtained from (2*S*,3*R*)-TS2 (Schnitzer et al., 2020a). To confirm this finding, the corresponding *Z* and *E*-TSs were also located for (2*R*,3*S*)-TS2 and (2*S*,3*R*)-TS2, but higher energies were obtained in both cases (Supplementary Figure S4, SI).

Conclusion

In conclusion, we presented here a new class of β-AAs with a morpholine core prepared by a straightforward synthesis, from commercially available α-AAs and chiral epichlorohydrin, that can control the configuration of substituent patterns. Despite the known limitations of the morpholine ring during enamine catalysis, our results provided the first evidence on the actual effectiveness of this chiral catalyst that works efficiently in the selected 1,4-addition





model reaction between aldehydes and nitroolefins, thanks to the presence of a carboxylic moiety in position β to the amine. Experimental data have proven that the reaction goes with excellent conversion and diastereoselection and satisfactory to excellent enantioselection, depending on the substitution pattern of the two reagents. It is to be noted that only 1% of the catalyst and a 1/1.5 ratio of **7/8** is needed, *i*PrOH being the key solvent. These results were supported by a theoretical study on the best catalyst, evidencing the role of the β -Morph carboxylic group in self-catalysing the protonation of the dihydrooxazine oxide intermediate, which is generally considered the rate limiting step of this class of reactions. Experiments confirmed this observation, laying the groundwork for further optimisation of the catalyst and opening its general use for a plethora of asymmetric syntheses.

Experimental

Computational methods

The structures of the enamine **E-7a** and the dihydrooxazine oxide intermediates (4*S*,5*R*)- and (4*R*,5*S*)-**Int1** were initially

constructed using MOE 2020.0901 software (Molecular Operating Environment, 2023). Geometries were minimised and then subjected to a conformational search using the MMFF94x force field (Halgren, 1996) and the Born solvation model for water, since no Born implicit solvent model was observed for *i*PrOH in MOE (Molecular Operating Environment, 2023). All geometries within the 3 kcal/mol interval were successively optimised by DFT using the method described hereafter. Only the lowest-energy structures were further considered. **TS1** structures were originally obtained by modifying the corresponding dihydrooxazine oxide. All structures of reactants, TSs, and products were initially optimised at the mPW1B95/6-31G* level (Zhao and Truhlar, 2004). Frequency calculations were then performed at the same level to confirm the stationary points as minima (0 imaginary frequencies) or TSs (1 imaginary frequency corresponding to the vibration of the forming/breaking bonds). Single-point energy calculations were then performed at the mPW1B95/6-311+G** level, including the GD3 empirical correction for dispersive interactions (Grimme et al., 2010) and the solvent effects for *i*PrOH with the CPCM solvation model (Cossi et al., 2003). Several alternative geometries were constructed and optimised for each TS, and only the lowest-energy structures were further considered. IRC analyses were conducted starting from each TS and following the reaction path in both the “forward” and “reverse” direction. Fifty points on the reaction path were requested for each IRC calculation that was conducted at the same level of theory used for geometry optimisation.

To compute a more reliable activation and reaction energies, as well as to provide a direct comparison with the energies computed for similar reactions previously (Sahoo et al., 2012), all the selected stationary points were reoptimised using the range-separated ω B97X-D functional that includes empirical atom–atom dispersion corrections (Chai and Head-Gordon, 2008). The triple-split valence 6-311G (d,p) basis sets were adopted in geometry optimisations and frequency calculations, while single-

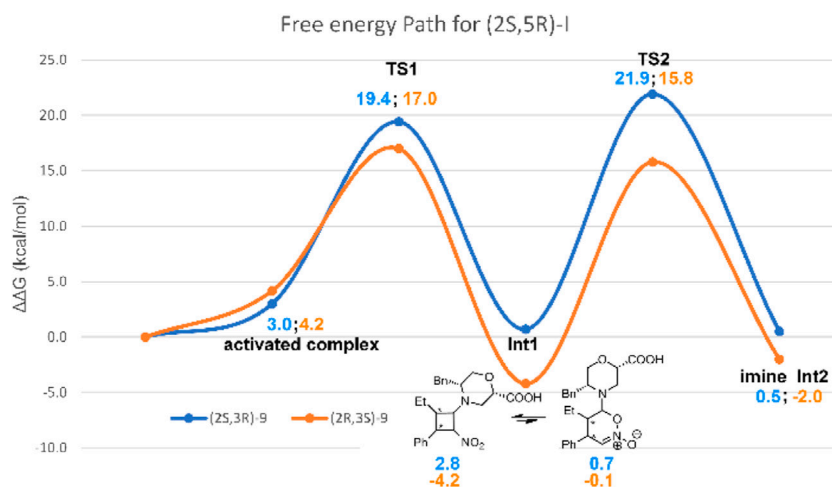
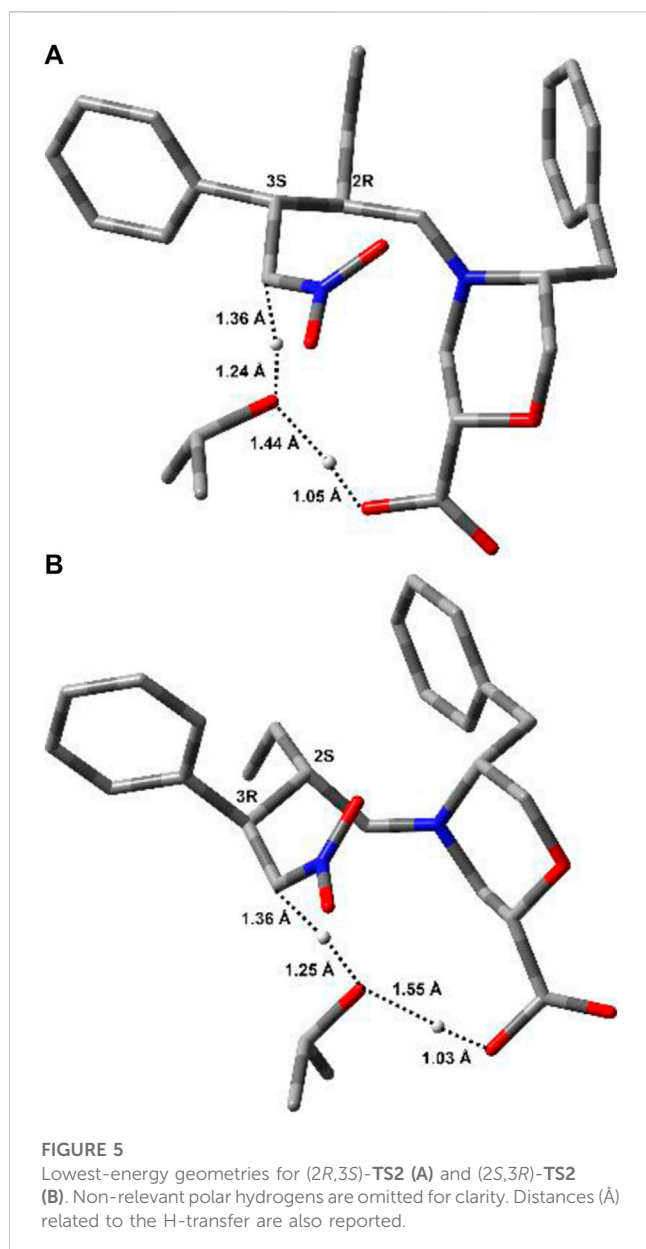


FIGURE 4

Free-energy path for the reaction of **7a** and **8a** in the presence of catalyst **I**. Relative solution-phase Gibbs free energies (kcal/mol) with respect to reactants are reported.



point energies were computed on the optimised structure using the 6-311++G (3df, 3pd) basis set. The CPCM solvent model for *i*PrOH was used both in optimisations and frequency calculations and in the single-point calculations. Gaussian16 software was used for all calculations (Frisch et al., 2016).

General information

Chemicals were purchased from Sigma-Aldrich and were used without further purification. Mass spectra were recorded on an LCQESI MS and LCQ Advantage spectrometer from Thermo Finnigan and an LCQ Fleet spectrometer from Thermo Scientific. The NMR spectroscopic experiments were carried out either on Varian MercuryPlus 300 MHz (300 and 75 MHz for ^1H and ^{13}C , respectively) or Bruker Avance I

400 MHz spectrometers (400 and 101 MHz for ^1H and ^{13}C , respectively). Optical rotations were measured on a Perkin-Elmer 343 polarimeter at 20°C (concentration in g/100 mL). Chemical shifts (δ) are given in ppm relative to the CHCl_3 internal standard, and the coupling constants J are reported in Hertz (Hz).

Enantiomeric excess was monitored by HPLC with a Merck Hitachi L-7100 HPLC System equipped with a UV6000LP detector and Chiral column (Chiralcel AD, OD-H, and IC). Spectroscopic analyses for each compound are reported in SI.

General procedure for amino alcohols 2a–d synthesis

A three-neck round-bottom flask was fitted with a magnetic stirring bar and a reflux condenser. The remaining neck was sealed with a septum and nitrogen line attached. The flask was charged with sodium borohydride (1146.3 mg, 30.3 mmol) in THF (0.2 M). Amino acid **1** (12.1 mmol) was added in one portion, and the flask was cooled to 0°C in an ice bath. A solution of iodine (3071.1 mg, 12.1 mmol) dissolved in THF (80 mL, 0.15 M) was slowly dropped over 30 min. After the addition of iodine was completed and gas evolution ceased, the flask was heated to reflux for 18 h. The reaction was cooled to r. t., and MeOH (30 mL) was added cautiously until the mixture became clear. After stirring (30 min), the solvent was removed, yielding a white paste, and then dissolved in aqueous KOH (20%, 24 mL). The solution was stirred for 4 h and extracted CH_2Cl_2 (3 \times 15 mL). The organic layers were dried over Na_2SO_4 and concentrated under reduced pressure, yielding a white semisolid. The crude material was crystallised from toluene to yield the final amino alcohol **2** as colourless crystals.

General procedure for benzyl-amino alcohols 3a–d synthesis

A solution of amino alcohol **2** (6.5 mmol) and benzaldehyde (902.0 mg, 8.5 mmol) in absolute MeOH (0.3 M, 30 mL) was stirred at 20°C for 2 h, NaBH_4 (741.5 mg, 19.6 mmol) was added at 0°C, and the reaction mixture was left stirred for 1 h CH_2Cl_2 (20 mL) and saturated aq. NH_4Cl (30 mL) was added, and the layers were separated. The aqueous layer was extracted with CH_2Cl_2 . The combined organic layers were washed with brine and dried with Na_2SO_4 , and the solvent was removed under reduced pressure. The crude material was purified by flash column chromatography (*n*hexane/ AcOEt , from 0% to 100%), yielding pure compound **3** as a white solid.

General procedure for benzyl-morpholine amino alcohols 4a–d synthesis

A solution of the amino alcohol **3** (4.0 mmol) in absolute toluene (0.3 M, 13.4 mL) was treated with (*R*)-epichlorohydrin (490.3 mg, 5.3 mmol) and LiClO_4 (563.9 mg, 5.3 mmol). After 24 h at 60°C, MeONa (545.6 mg, 10.1 mmol) in MeOH (25%v/v) was added and

stirring was continued for 24 h. The reaction mixture was quenched with a saturated aq. NH_4Cl (12 mL), and the aqueous layer was extracted with AcOEt (3×10 mL). The combined organic layers were washed with brine and dried with Na_2SO_4 , and the solvent was removed under reduced pressure. Chromatographic purification (silica gel; Et_2O /hexanes, 1:1) gave compound **4** as a colourless oil.

General procedure for Boc-morpholine amino alcohols **5a–d** synthesis

Operating in a round-bottom flask equipped with a magnetic stirrer, compound **4** (1 eq., 1.7 mmol) was dissolved in THF (0.1 M, 17 mL). Boc_2O (401.6 mg, 1.84 mmol) and Pd/C (931 mg, 10% loading) were added to the solution. The suspension was stirred under H_2 (1 atmosphere) at 25°C . After 24 h, the mixture was filtered on the Celite pad. The solvent was evaporated, and the yellow oil was dissolved in CH_2Cl_2 (5 mL) and washed with a solution of KHSO_4 (5%, 5 mL) and a saturated solution of NaCl (6 mL). The organic layer was dried over Na_2SO_4 , filtered, and concentrated in vacuum. The purification of the crude by flash chromatography (*n*hexane/ AcOEt , 1:1) yielded product **5a–d** as a colourless oil.

General procedure for Boc-morpholine amino acids **6** synthesis

To a vigorously stirred solution of Boc-morpholine amino alcohol **5** (0.33 mmol) in $\text{CH}_2\text{Cl}_2/\text{H}_2\text{O}$ (2:1; 0.15 M, 2 mL), TEMPO (11.0 mg, 0.07 mmol) and BIAB [(diacetoxyiodo)benzene, 225.4 mg, 0.7 mmol] were added at 0°C . After 6 h, the reaction was quenched with MeOH (2 mL), and the mixture was evaporated to dryness. Silica gel column chromatography ($\text{CH}_2\text{Cl}_2/\text{MeOH}$, 20:1) yielded Boc-morpholine amino acid **6** as a colourless oil.

General procedure of morpholine β -amino acids **I–IV** synthesis

To a round-bottom flask equipped with a magnetic stirring bar was added Boc-Morph-AA **6** (0.2 mmol) and dissolved in CH_2Cl_2 (0.1 M). The solution was cooled to 0°C and TFA (1 mL TFA for 25 mg reagent) was slowly added dropwise, and then, the mixture was stirred for 3 h. The crude mixture was concentrated *in vacuo*, yielding products **I–IV** in the quantitative yield as white solids.

Synthesis γ -nitroaldehydes **9–20**

Catalyst (1–5 mol%; see Table 2) was added to a solution of *N*-methylmorpholine (1–5 mol%), nitroolefin **8** (0.17 mmol), and aldehyde **7** (0.11 mmol) in *i*PrOH (0.380 mL). The reaction mixture was stirred at -10°C for 24–48 h (Table 2). The solvent was removed under reduced pressure, and the crude mixture was subjected to flash chromatography (silica gel; 5% \rightarrow 20% EtOAc in hexane) to

yield γ -nitroaldehyde **9–20** (Table 2). The diastereomeric ratio was determined by the ^1H NMR spectroscopic analysis of the isolated product by comparison of the aldehyde R-CHO signals. The enantiomeric excess was determined by chiral stationary phase HPLC.

Further details and spectroscopic analyses for each compound are reported in SI.

Data availability statement

The original contributions presented in the study are included in the article/Supplementary Material, further inquiries can be directed to the corresponding author.

Author contributions

RB, GF, and MG conceptualised the research; FV and MB synthesised the catalysts **I–IV**; RB, FV, and MB performed the screening of the catalysts and expanded the scope of the reaction; FV and GF conducted HPLC analysis; AC performed the computational analysis; RB, IR, MG, and AC interpreted the data; RB, AC, and MG wrote the manuscript. All authors contributed to the article and approved the submitted version.

Acknowledgments

The authors gratefully acknowledge Ministero dell'Università e della Ricerca (PRIN 2020; project no. 2020833Y75) for financial support.

Conflict of interest

The authors declare that the research was conducted in the absence of any commercial or financial relationships that could be construed as a potential conflict of interest.

Publisher's note

All claims expressed in this article are solely those of the authors and do not necessarily represent those of their affiliated organizations, or those of the publisher, the editors, and the reviewers. Any product that may be evaluated in this article, or claim that may be made by its manufacturer, is not guaranteed or endorsed by the publisher.

Supplementary material

The Supplementary Material for this article can be found online at: <https://www.frontiersin.org/articles/10.3389/fchem.2023.1233097/full#supplementary-material>

References

- Ahrendt, K. A., Borths, C. J., and MacMillan, D. W. C. (2000). New strategies for organic catalysis: The first highly enantioselective organocatalytic Diels–Alder reaction. *J. Am. Chem. Soc.* 122, 4243–4244. doi:10.1021/ja000092s
- Borges-González, J., García-Monzón, I., and Martín, T. (2019). Conformational control of tetrahydropyran-based hybrid dipeptide catalysts improves activity and stereoselectivity. *Adv. Synth. Catal.* 361, 2141–2147. doi:10.1002/adsc.201900247
- Breuning, M., Winnacker, M., and Steiner, M. (2007). Efficient one-pot synthesis of enantiomerically pure 2-(hydroxymethyl)morpholines. *Eur. J. Org. Chem.* 2007, 2100–2106. doi:10.1002/ejoc.200601006
- Brown, K. L., Damm, L., Dunitz, J. D., Eschenmoser, A., Hobi, R., and Kratky, C. (1978). Structural studies of crystalline enamines. *Helv. Chim. Acta* 61, 3108–3135. doi:10.1002/hlca.19780610839
- Bucci, R., Bossi, A., Erba, E., Vaghi, F., Saha, A., Yuran, S., et al. (2020). Nucleobase morpholino β amino acids as molecular chimeras for the preparation of photoluminescent materials from ribonucleosides. *Sci. Rep.* 10, 19331. doi:10.1038/s41598-020-76297-7
- Bucci, R., Contini, A., Clerici, F., Pellegrino, S., and Gelmi, M. L. (2019). From glucose to enantiopure morpholino β -amino acid: A new tool for stabilizing γ -turns in peptides. *Org. Chem. Front.* 6, 972–982. doi:10.1039/C8QO01116H
- Bucci, R., Foschi, F., Loro, C., Erba, E., Gelmi, M. L., and Pellegrino, S. (2021). Fishing in the toolbox of cyclic turn mimics: A literature overview of the last decade. *Eur. J. Org. Chem.* 2021, 2887–2900. doi:10.1002/ejoc.202100244
- Burés, J., Armstrong, A., and Blackmond, D. G. (2011). Mechanistic rationalization of organocatalyzed conjugate addition of linear aldehydes to nitro-olefins. *J. Am. Chem. Soc.* 133, 8822–8825. doi:10.1021/ja203660r
- Chai, J.-D., and Head-Gordon, M. (2008). Long-range corrected hybrid density functionals with damped atom–atom dispersion corrections. *Phys. Chem. Chem. Phys.* 10, 6615–6620. doi:10.1039/B810189B
- Choudary, B. M., Rajasekhar, Ch. V., Gopi Krishna, G., and Rajender Reddy, K. (2007). L-Proline-Catalyzed Michael addition of aldehydes and unmodified ketones to nitro olefins accelerated by Et₃N. *Synth. Commun.* 37, 91–98. doi:10.1080/00397910600978218
- Cossi, M., Rega, N., Scalmani, G., and Barone, V. (2003). Energies, structures, and electronic properties of molecules in solution with the C-PCM solvation model. *J. Comput. Chem.* 24, 669–681. doi:10.1002/jcc.10189
- Facchetti, G., Bucci, R., Fusè, M., Erba, E., Gandolfi, R., Pellegrino, S., et al. (2021). Alternative strategy to obtain artificial imine reductase by exploiting vancomycin/D-ala-D-ala interactions with an iridium metal complex. *Inorg. Chem.* 60, 2976–2982. doi:10.1021/acs.inorgchem.0c02969
- Facchetti, G., Bucci, R., Fusè, M., and Rimoldi, I. (2018). Asymmetric hydrogenation vs transfer hydrogenation in the reduction of cyclic imines. *ChemistrySelect* 3, 8797–8800. doi:10.1002/slct.201802223
- Facchetti, G., Pellegrino, S., Bucci, R., Nava, D., Gandolfi, R., Christodoulou, M. S., et al. (2019). Vancomycin-iridium (III) interaction: An unexplored route for enantioselective imine reduction. *Molecules* 24, 2771–2779. doi:10.3390/molecules24152771
- Földes, T., Madarász, Á., Révész, Á., Dobi, Z., Varga, S., Hamza, A., et al. (2017). Stereocontrol in diphenylprolinol silyl ether catalyzed Michael additions: Steric shielding or Curtin–Hammett scenario? *J. Am. Chem. Soc.* 139, 17052–17063. doi:10.1021/jacs.7b07097
- Frisch, M. J., Trucks, G. W., Schlegel, H. B., Scuseria, G. E., Robb, M., Cheeseman, J. R., et al. (2016). *Gaussian 16, revision A 03*. Wallingford CT, 3.
- Gassa, F., Contini, A., Fontana, G., Pellegrino, S., and Gelmi, M. L. (2010). A highly diastereoselective synthesis of α -hydroxy- β -amino acid derivatives via a Lewis acid catalyzed three-component condensation reaction. *J. Org. Chem.* 75, 7099–7106. doi:10.1021/jo1011762
- Giofrè, S., Loro, C., Molteni, L., Castellano, C., Contini, A., Nava, D., et al. (2021). Copper(II)-Catalyzed aminohalogenation of alkynyl carbamates. *Eur. J. Org. Chem.* 2021, 1750–1757. doi:10.1002/ejoc.202100202
- Grimme, S., Antony, J., Ehrlich, S., and Krieg, H. (2010). A consistent and accurate *ab initio* parametrization of density functional dispersion correction (DFT-D) for the 94 elements H–Pu. *J. Chem. Phys.* 132, 154104. doi:10.1063/1.3382344
- Halgren, T. A. (1996). Merck molecular force field. I. Basis, form, scope, parameterization, and performance of MMFF94. *J. Comput. Chem.* 17, 490–519. doi:10.1002/(SICI)1096-987X(199604)17:5<490::AID-JCC1>3.0.CO;2-P
- Han, B., He, X.-H., Liu, Y.-Q., He, G., Peng, C., and Li, J.-L. (2021). Asymmetric organocatalysis: An enabling technology for medicinal chemistry. *Chem. Soc. Rev.* 50, 1522–1586. doi:10.1039/D0CS00196A
- Hayashi, Y., Gotoh, H., Hayashi, T., and Shoji, M. (2005). Diphenylprolinol silyl ethers as efficient organocatalysts for the asymmetric Michael reaction of aldehydes and nitroalkenes. *Angew. Chem. Int. Ed.* 44, 4212–4215. doi:10.1002/anie.200500599
- Hayashi, Y., Okano, T., Aratake, S., and Hazeld, D. (2007). Diphenylprolinol silyl ether as a catalyst in an enantioselective, catalytic, tandem Michael/Henry reaction for the control of four stereocenters. *Angew. Chem.* 119, 5010–5013. doi:10.1002/anie.200700909
- Kempf, B., Hampel, N., Ofial, A. R., and Mayr, H. (2003). Structure–nucleophilicity relationships for enamines. *Chem. – A Eur. J.* 9, 2209–2218. doi:10.1002/chem.200204666
- Laars, M., Ausmees, K., Uudsemaa, M., Tamm, T., Kanger, T., and Lopp, M. (2009). Enantioselective organocatalytic Michael addition of aldehydes to β -nitrostyrenes. *J. Org. Chem.* 74, 3772–3775. doi:10.1021/jo900322h
- Laars, M., Raska, H., Lopp, M., and Kanger, T. (2010). Cyclic amino acid salts as catalysts for the asymmetric Michael reaction. *Tetrahedron Asymmetry* 21, 562–565. doi:10.1016/j.tetasy.2010.02.025
- List, B., Lerner, R. A., and Barbas, C. F. (2000). Proline-catalyzed direct asymmetric aldol reactions. *J. Am. Chem. Soc.* 122, 2395–2396. doi:10.1021/ja994280y
- List, B., Pojarliev, P., and Martin, H. J. (2001). Efficient proline-catalyzed Michael additions of unmodified ketones to nitro olefins. *Org. Lett.* 3, 2423–2425. doi:10.1021/ol015799d
- Liu, J., and Wang, L. (2017). Recent advances in asymmetric reactions catalyzed by proline and its derivatives. *Synth. Ger.* 49, 960–972. doi:10.1055/s-0036-1588901
- Llopis, S., García, T., Cantín, Á., Velly, A., Díaz, U., and Corma, A. (2018). Chiral hybrid materials based on pyrrolidine building units to perform asymmetric Michael additions with high stereocontrol. *Catal. Sci. Technol.* 8, 5835–5847. doi:10.1039/C8CY01650J
- Lombardo, M., Chiarucci, M., Quintavalla, A., and Trombini, C. (2009). Highly efficient ion-tagged catalyst for the enantioselective Michael addition of aldehydes to nitroalkenes. *Adv. Synth. Catal.* 351, 2801–2806. doi:10.1002/adsc.200900599
- Molecular Operating Environment (MOE) (2023). 2022.02 Chemical Computing Group ULC. Montreal, QC, Canada.
- Mossé, S., Laars, M., Kriis, K., Kanger, T., and Alexakis, A. (2006). 3,3'-Bimorpholine derivatives as a new class of organocatalysts for asymmetric Michael addition. *Org. Lett.* 8, 2559–2562. doi:10.1021/ol0607490
- Movassaghi, M., and Jacobsen, N. E. (2002). The simplest “enzyme”. *Science* 298, 1904–1905. (1979). doi:10.1126/science.1076547
- Ni, B., Zhang, Q., and Headley, A. D. (2007). Functionalized chiral ionic liquid as recyclable organocatalyst for asymmetric Michael addition to nitrostyrenes. *Green Chem.* 9, 737. doi:10.1039/B702081C
- Obregón-Zúñiga, A., Milán, M., and Juaristi, E. (2017). Improving the catalytic performance of (S)-Proline as organocatalyst in asymmetric aldol reactions in the presence of solvate ionic liquids: Involvement of a supramolecular aggregate. *Org. Lett.* 19, 1108–1111. doi:10.1021/acs.orglett.7b00129
- Oliva, F., Bucci, R., Tamborini, L., Pieraccini, S., Pinto, A., and Pellegrino, S. (2019). Bicyclic pyrrolidine-isoxazoline γ amino acid: A constrained scaffold for stabilizing α -turn conformation in isolated peptides. *Front. Chem.* 7, 133. doi:10.3389/fchem.2019.00133
- Pellegrino, S., Facchetti, G., Contini, A., Gelmi, M. L., Erba, E., Gandolfi, R., et al. (2016). Ctr-1 Mets7 motif inspiring new peptide ligands for Cu(I)-catalyzed asymmetric Henry reactions under green conditions. *RSC Adv.* 6, 71529–71533. doi:10.1039/c6ra16255j
- Pellissier, H. (2021). Organocatalytic total synthesis of bioactive compounds based on one-pot methodologies. *Phys. Sci. Rev.* 411, 411–428. doi:10.1515/psr-2021-0025
- Penso, M., Foschi, F., Pellegrino, S., Testa, A., and Gelmi, M. L. (2012). Diastereoselective protocols for the synthesis of 2,3-trans- and 2,3-cis-6-Methoxymorpholine-2-carboxylic acid derivatives. *J. Org. Chem.* 77, 3454–3461. doi:10.1021/jo300221y
- Reyes, E., Jiang, H., Milelli, A., Elsner, P., Hazell, R. G., and Jørgensen, K. A. (2007). How to make five contiguous stereocenters in one reaction: Asymmetric organocatalytic synthesis of pentasubstituted cyclohexanes. *Angew. Chem.* 119, 9202–9205. doi:10.1002/anie.200704454
- Sahoo, G., Rahaman, H., Madarász, Á., Pápai, I., Melarto, M., Valkonen, A., et al. (2012). Dihydrooxazine oxides as key intermediates in organocatalytic Michael additions of aldehydes to nitroalkenes. *Angew. Chem. Int. Ed.* 51, 13144–13148. doi:10.1002/anie.201204833
- Sakthivel, K., Notz, W., Bui, T., and Barbas, C. F. (2001). Amino acid catalyzed direct asymmetric aldol reactions: A bioorganic approach to catalytic asymmetric Carbon–Carbon bond-forming reactions. *J. Am. Chem. Soc.* 123, 5260–5267. doi:10.1021/ja010037z
- Schnitzer, T., Budinská, A., and Wennemers, H. (2020a). Organocatalyzed conjugate addition reactions of aldehydes to nitroolefins with anti selectivity. *Nat. Catal.* 3, 143–147. doi:10.1038/s41929-019-0406-4

Schnitzer, T., Möhler, J. S., and Wennemers, H. (2020b). Effect of the enamine pyramidalization direction on the reactivity of secondary amine organocatalysts. *Chem. Sci.* 11, 1943–1947. doi:10.1039/C9SC05410C

Seebach, D., Beck, A. K., Goliński, J., Hay, J. N., and Laube, T. (1985). Über den sterischen Verlauf der Umsetzung von Enaminen aus offenkettigen Aldehyden und Ketonen mit Nitroolefinen zu 2,3-disubstituierten 4-Nitroketonen. *Helv. Chim. Acta* 68, 162–172. doi:10.1002/hlca.19850680120

Seebach, D., and Goliński, J. (1981). Synthesis of Open-Chain 2,3-Disubstituted 4-nitroketones by Diastereoselective Michael-addition of (E)-Enamines to (E)-Nitroolefins. A topological rule for C, C-bond forming processes between prochiral centres. Preliminary communication. *Helv. Chim. Acta* 64, 1413–1423. doi:10.1002/hlca.19810640518

Seebach, D., Sun, X., Ebert, M.-O., Schweizer, W. B., Purkayastha, N., Beck, A. K., et al. (2013). Stoichiometric reactions of enamines derived from

diphenylprolinol silyl ethers with nitro olefins and lessons for the corresponding organocatalytic conversions – A survey. *Helv. Chim. Acta* 96, 799–852. doi:10.1002/hlca.201300079

Vaghi, F., Bucci, R., Clerici, F., Contini, A., and Gelmi, M. L. (2020). Non-natural 3-Arylmorpholino- β -amino acid as a PPII helix inducer. *Org. Lett.* 22, 6197–6202. doi:10.1021/acs.orglett.0c02331

Xiang, S.-H., and Tan, B. (2020). Advances in asymmetric organocatalysis over the last 10 years. *Nat. Commun.* 11, 3786. doi:10.1038/s41467-020-17580-z

Zhao, Y., and Truhlar, D. G. (2004). Hybrid meta density functional theory methods for thermochemistry, thermochemical kinetics, and noncovalent interactions: The MPW1B95 and MPWB1K models and comparative assessments for hydrogen bonding and van der Waals interactions. *J. Phys. Chem. A* 108, 6908–6918. doi:10.1021/jp048147q



OPEN ACCESS

EDITED BY

Claudia Espro,
University of Messina, Italy

REVIEWED BY

Grant Henderson,
University of Toronto, Canada
Amey Rajendra Khanolkar,
Idaho National Laboratory (DOE),
United States

*CORRESPONDENCE

Charu Lata Dube,
✉ charulata.dube@cug.ac.in

RECEIVED 08 June 2023

ACCEPTED 15 September 2023

PUBLISHED 28 September 2023

CITATION

Pilania RK and Dube CL (2023), Matrices for radioactive waste immobilization: a review.

Front. Mater. 10:1236470.

doi: 10.3389/fmats.2023.1236470

COPYRIGHT

© 2023 Pilania and Dube. This is an open-access article distributed under the terms of the [Creative Commons Attribution License \(CC BY\)](#). The use, distribution or reproduction in other forums is permitted, provided the original author(s) and the copyright owner(s) are credited and that the original publication in this journal is cited, in accordance with accepted academic practice. No use, distribution or reproduction is permitted which does not comply with these terms.

Matrices for radioactive waste immobilization: a review

Ritu Kumari Pilania and Charu Lata Dube*

School of Nano Sciences, Central University of Gujarat, Sector-30, Gandhinagar, Gujarat, India

Nuclear energy is considered a clean, reliable, and an inexhaustible energy source for power generation. Nuclear power is harnessed from nuclear fission reactions in a dedicated power plant. The by-products (produced in the nuclear power plant) are radioactive and pose a threat to the environment. The safe disposal of nuclear waste is vital to ensure the sustainable use of the nuclear energy. The immobilization of radioactive waste before final disposal is essential for the interim storage and transportation. This review summarizes the recent work on glass, ceramics, and glass–ceramics matrices to immobilize high-level waste. The synthesis methods, leaching behavior, and radiation resistance of matrices are discussed briefly.

KEYWORDS

glass, glass–ceramics, leaching, nuclear waste, radiation stability

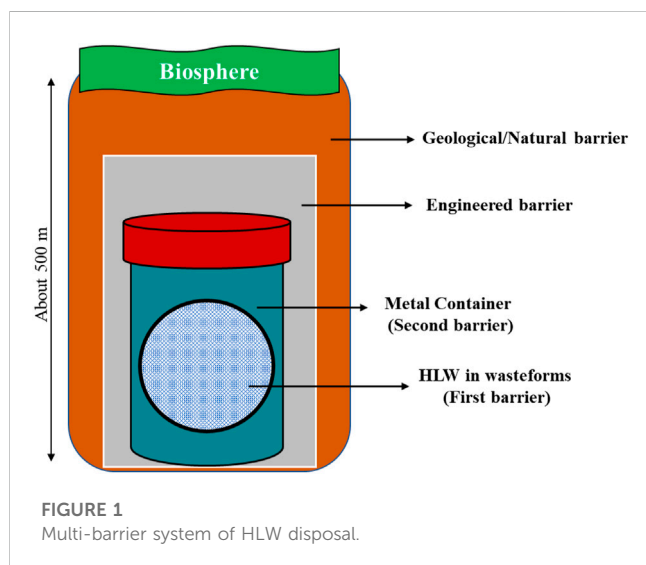
1 Introduction

Primarily, nuclear energy is used in power generation, producing nearly 15% of electricity. Nuclear reactors (437 operational reactors in 2021 worldwide) produce more than 10% of all the energy consumed globally. Nuclear energy can fulfill the increasing demand of energy and contribute to reducing the consumption of fossil fuels and emission of greenhouse gases. Moreover, energy consumption in the future will rise, so the demand for building new nuclear power reactors to meet energy requirements will increase. Consequently, the generation of radioactive waste will be enhanced, owing to the increased use of fuel (uranium and plutonium oxide) to run the reactors (Englert et al., 2012). Radioactive waste is generated from chemical sludges, fission products, reactor decommissioning, and spent nuclear fuel; the radioactive waste or nuclear waste is generally categorized, based on its radioactivity level, as low-level waste (LLW), intermediate-level waste (ILW), and high-level waste (HLW), as summarized in Table 1 (IAEA Safety Standards, 2009).

The total radioactive waste comprises LLW, ILW, and HLW. HLW has the lowest volume in total radioactive waste and generates extensive heat due to radioactive decay. The reprocessed nuclear fuel constitutes the bulk of “high-level waste” (HLW), as defined by the International Atomic Energy Agency (IAEA) (McCloy and Goel, 2017). In order to reduce the amount of radionuclides in the spent nuclear fuel, efforts are being made to extract Pu and U using the PUREX process. The PUREX process is a liquid–liquid separation process that utilizes tri-n-butyl phosphate (TBP). In addition, normal paraffinic hydrocarbon (NPH) and numerous solvents are used (Baumgärtner and Ertel, 1980; Herbst et al., 2011). TBP is used for selective extraction of Pu and U from spent nuclear fuel. The modern PUREX processes include more than two cycles of extraction, scrubbing, and stripping the fuel (Kumari et al., 2020). The extracted Pu and U from the spent nuclear fuel can be reused after enrichment and conditioning. Later, the resulting waste obtained after reprocessing the spent fuel can be immobilized in a matrix, followed by final disposal in the deep geological

TABLE 1 Classification of radioactive waste and their sources.

Nuclear waste type	Volume in total waste (in %)	Radioactivity percentage of total nuclear waste (in %)	Source
LLW	90	1	Paper, clothing, tools, and rags from industries, hospitals, and nuclear fuel cycles
ILW	7	4	Contaminated materials from reactor decommissioning, resins, chemical sludges, and metal fuel cladding
HLW	3	95	Fission products, transuranic elements, and minor actinides from burning of uranium fuel in the nuclear reactor and from hospitals



repository. Invariably, the radioactive waste generated from nuclear power plants is chemically complex and contains a wide range of fission products (Lee et al., 2006; Lee et al., 2013a; Jantzen et al., 2013). In addition to the spent nuclear fuel, legacy waste (generated during the Second World War and decommissioning of a nuclear site or reactor) comes under the category of HLW (Zorpete, 1996; Rao, 2001; Beckitt, 2012).

Depending upon the category of radioactive waste, the disposal of wastes can be carried out in landfill disposal, shallow-level disposal, and deep geological repositories (Darda et al., 2021). HLW is further categorized as i) long-lived radionuclides and ii) short-lived radionuclides. The half-life time of long-lived radionuclides, such as ^{239}Pu , ^{129}I , ^{99}Tc , and ^{93}Zr , is of the order of millions of years. On the other hand, the half-life time of short-lived radionuclides, such as ^{90}Sr , ^{137}Cs , ^{60}Co , and ^{192}Ir , is hundreds to thousands of years (IAEA, 2017; Ojovan et al., 2019; Ojovan, 2023). Long-lived radionuclides containing HLW are proposed to be disposed using the concept of a multi-barrier system (as shown in Figure 1). The multi-barrier system has different layers of barriers. The first barrier is wasteform; the second barrier is the HLW container; the third barrier is an engineered barrier; and the fourth is a geological barrier (Lee et al., 2006; Jantzen and Ojovan, 2019).

HLW is immobilized in a suitable wasteform before disposal in the multi-barrier system. Immobilization is the process where the

waste is made immovable in the form of wasteforms through various routes, such as containment, solidification, and vitrification (Jantzen et al., 2013; Li et al., 2021; Jo et al., 2022). The containment process includes pumping, capping, and installation of slurry walls. The solidification process involves the transformation of waste into a stable and immovable form for storage or disposal, such as cementation. The vitrification process transforms hazardous waste into a chemically stable wasteform, such as glass, glass-ceramic, and ceramics (Meegoda et al., 2003).

The chemical durability and radiation stability of matrix/wasteforms of any chosen wasteform should be good for immobilizing waste radionuclides (Lee et al., 2006). The wasteforms for immobilization of HLW are primarily of three types i) glass, ii) ceramic, and iii) glass-ceramic wasteforms. A potential wasteform/matrix should have the following features (Wang and Liang, 2012; Lee et al., 2013a; Ojovan and Lee, 2014; Hyatt and Ojovan, 2019; Jantzen and Ojovan, 2019).

- 1) The loading capacity (ability to accommodate waste inside the matrix) should be high. In addition, the wasteform should be able to incorporate daughter products as well.
- 2) The wasteforms should have good durability under aqueous conditions. The waste must always be isolated from the biosphere until the radionuclide becomes non-radioactive (10 half-lives) (Khan et al., 2010). The porosity of the matrix should be negligible as minimal porosity will help avoid permeability and hence leachability under aqueous conditions.
- 3) The matrix should be highly radiation-tolerant to sustain under the α - and β -decays of radionuclides against any phase changes, owing to the heat generated during the decay processes inside the matrix.
- 4) The volume of wasteforms should be as small as possible. It should have good mechanical properties, which will be helpful in avoiding fracture or crack during transportation and handling.
- 5) The composition of wasteforms should be close to natural analogs. However, there is no true natural analog for borosilicate glass wasteform as it includes a high content of boron and radionuclides. However, natural basaltic glass can be considered a natural analog of borosilicate glass because of its chemically durable properties (Techer et al., 2001; Crovisier et al., 2003).

The different types of wasteforms are discussed in the following subsection.

2 Types of wasteforms

2.1 Non-crystalline wasteforms

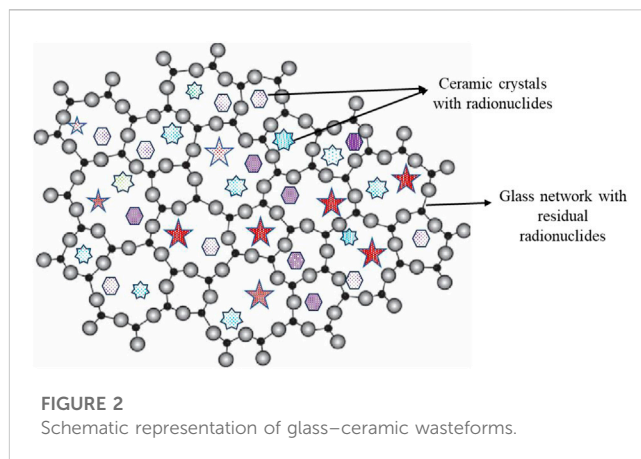
Glass is an inorganic solid prepared by quenching from the melt while preventing the crystallization. The typical glass structure has mainly three constituents, namely, 1) network formers, 2) intermediates, and 3) network modifiers (Lee et al., 2006; Lee et al., 2013b; Hyatt and Ojovan, 2019). The open and random structure of glass is primarily responsible for achieving high waste loading and chemical durability (Jantzen, 2011). The radionuclides in glass are immobilized by primary or/and secondary bonding within the glass network. The glass has a random structure with specific characteristics as per the model proposed by Zachariasen (Varshneya and Mauro, 2019; Shelby, 2020). The characteristics are i) no oxygen atom may be linked to more than two cations; ii) the cation coordination number should be 3 or 4; iii) the oxygen polyhedra should share corners only (not edges or faces); and iv) for a 3D network, at least three corners must be shared. Glass has been considered for immobilizing matrix due to its structural flexibility, simple synthesis route, high waste loading capacity, and inexpensive raw materials. The glass wasteforms have good radiation stability. The high chemical durability enables the glass to remain stable in corrosive environments for thousands of years (Kavaz et al., 2020).

2.2 Crystalline wasteforms

The ceramic wasteforms have widely been divided into a) single-phase ceramics, such as zircon, to accommodate a limited range of active species, such as Pu; and b) multi-phase systems, such as Synroc (composed of hollandite ($\text{BaAl}_2\text{Ti}_6\text{O}_{16}$), zirconolite ($\text{CaZrTi}_2\text{O}_7$), and perovskite (CaTiO_3)), to accommodate a wide range of active species (Ringwood et al., 1979; Ojovan et al., 2019; Orlova et al., 2019). However, Synroc has its own disadvantages, such as being thermodynamically unstable (Nesbitt et al., 1981). Synroc is not being used for immobilization of HLW by any country to the best of our knowledge. Furthermore, the pyrochlore-structured titanate/zirconate ceramics, such as $\text{Gd}_2\text{Zr}_2\text{O}_7$ and $\text{Er}_2\text{Zr}_2\text{O}_7$, are potential ceramic wasteforms (Maddrell, 2001; Ewing et al., 2004; Sattonnay et al., 2008). Zirconolite is mainly used to immobilize the long-lived radionuclides (Pu), while the perovskite phase is primarily suitable for the short-lived radionuclides (Sr and Ba). The hollandite phase is a potential candidate to immobilizing Cs, K, Rb, and Ba radionuclides (Ringwood, 1978; Xu and Wang, 2000). The major disadvantage of crystalline wasteforms is their inability to accommodate a wide range of radionuclides (Wang and Liang, 2012).

2.3 Glass–ceramic wasteforms

Recently, the glass–ceramic materials (GCMs) with mineral-like phases are reported for the immobilization of complex waste (Ojovan et al., 2021). The major component of GCM may be either the crystalline phases with the glass acting as a binding agent or the vitreous phase with the crystalline particles dispersed in the glass matrix (Ojovan et al., 2008; Donald, 2010; Ojovan et al., 2021). The most exciting feature of GCMs is that both the long-lived and short-



lived radionuclides can be immobilized. The long-lived radionuclides can be immobilized in stable and durable crystals, whereas the short-lived radionuclides can be immobilized in the vitreous phase. The advantages of immobilizing complex HLW in GCMs are as follows: a) GCMs have nearly zero porosity and hence lead to minimal leaching. It can be synthesized on a mass scale by existing glass-forming techniques; b) the desired glass and ceramic can be incorporated in a single matrix (Zanotto, 2010).

Glass–ceramic wasteforms possess higher durability, high thermal stability, and superior mechanical properties than glass and ceramic wasteforms (Davis and Zanotto, 2017). The ceramic crystals are embedded in a glass network of the glass–ceramic matrix, as shown in Figure 2.

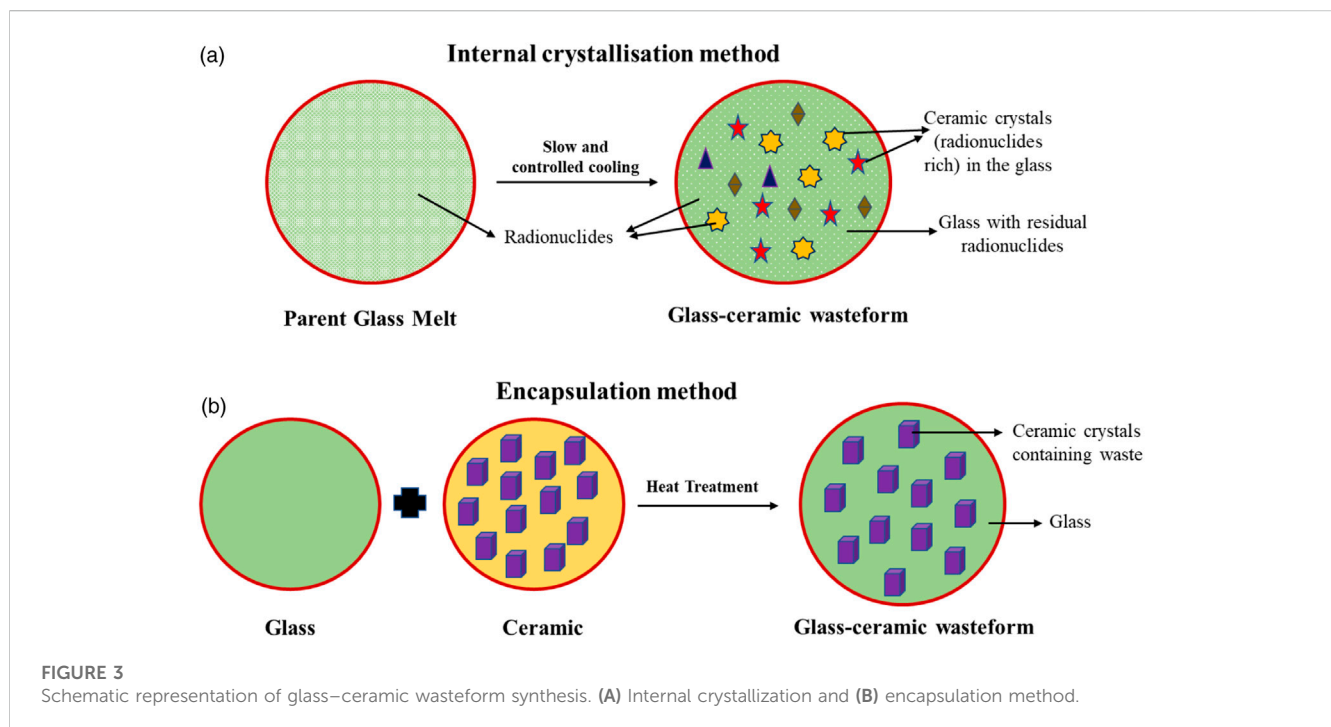
The leaching of radionuclides will be initially hindered by the glass phase surrounding the ceramic phase. Hence, the glass is another barrier to the outgoing movement of radionuclides from the ceramic phase. The highly durable crystals homogeneously dispersed in the bulk of the glass matrix will form an enhanced containment barrier for radionuclides. There is a potential risk that conventional glass wasteforms partially crystallize during cooling or because of radiation effects over long periods, especially in HLWs (Mahmoudysephehr and Marghussian, 2009). The glass–ceramic wasteforms are chemically more flexible and less expensive to prepare than pure ceramics, and in addition, they offer higher chemical durability than conventional glass and ceramic wasteforms. The different wasteforms, their suitability, and composition are tabulated in Table 2.

3 Synthesis of wasteforms

Wasteforms can be synthesized by different methods, rendering different properties. The wasteforms are invariably synthesized by employing the melt-quench, solid-state sintering, hot pressing, microwave sintering (Wei et al., 2020), self-propagating high-temperature synthesis (SHS) (Barinova et al., 2008), and spark plasma sintering (SPS) methods (Aldean et al., 2022). The synthesis method should be simple, cost-effective, and capable of avoiding the production of secondary radioactive waste. The synthesis temperature should be low so that evaporation of volatile radionuclides (such as I, Cs, and Ru) can be minimized. The viscosity of the molten glass should be optimum so that

TABLE 2 Different types of wasteforms and their composition.

Wasteform	Composition	Country	Waste type	Reference
Magnox	47.2SiO ₂ -16.9B ₂ O ₃ -4.8Al ₂ O ₃ -5.3MgO-8.4Na ₂ O-17.4Others	UK	HLW	Backhouse et al. (2019)
R7T7	45.5SiO ₂ -14B ₂ O ₃ -4.9Al ₂ O ₃ -9.9Na ₂ O-2.9Fe ₂ O ₃ -22.8Others	France	HLW	Gin et al. (2011)
K26	48.2SiO ₂ -7.5B ₂ O ₃ -2.5Al ₂ O ₃ -16.1Na ₂ O-15.5CaO-10.2Others	Russia	LILW	Ojovan et al. (2005)
CCM	52P ₂ O ₅ -19Al ₂ O ₃ -21Na ₂ O-7.8Others	Russia	HLW	Ojovan and Batyukhnova (2019)
DWPF	50SiO ₂ -8B ₂ O ₃ -4Al ₂ O ₃ -8.7Na ₂ O-1.4 MgO-27.9Others	United States	HLW	Ojovan and Batyukhnova (2019)
PAMELA	52.7SiO ₂ -13.2B ₂ O ₃ -2.7Al ₂ O ₃ -5.9Na ₂ O-4.6CaO-20.9Others	Germany–Belgium	HLW	Ojovan and Batyukhnova (2019)



homogenization and pouring can be achieved. The following subsections briefly describe a few selected conventional and modern methods for the synthesis of wasteforms.

3.1 Melt-quench method

In this method, oxide/carbonates/nitrates of parent materials are mixed and heated in a crucible to a desired temperature to get a molten liquid (melt). To get homogeneity, the melt is continuously stirred. When the melt is quenched (non-equilibrium cooling), it produces a glass structure. The traditional method is preferred because it is simple and efficient even at the mass-scale production.

3.2 Internal crystallization and encapsulation method

The glass–ceramic can be synthesized under slow and controlled molten liquid cooling conditions by employing the internal

crystallization method. Under controlled cooling, nucleation occurs, and growth of crystals takes place in the glass matrix. The method results in the formation of crystals inside the glass structure (Rawlings et al., 2006; Zhang et al., 2022). The thermal stability of these glass–ceramic wasteforms is relatively high compared to the glass and ceramic wasteforms (McCloy and Goel, 2017).

In the encapsulation method, the ceramic phase is added directly to the glass charge. The powder-containing glass charge and ceramic are invariably maintained at the melting temperature of the glass. Subsequently, the homogeneous melt is quenched, and the glass–ceramic wasteform is obtained. The schematic representation of both the methods for the synthesis of glass–ceramic wasteforms is shown in Figure 3.

3.3 Sintering Methods

The ceramic wasteforms can be synthesized using conventional solid-state sintering, hot pressing, and the most recent microwave

sintering methods. In recent days, the wasteform synthesis through microwave energy is a novel concept. The microwave (MW) heating method can be employed to synthesize different wasteforms to minimize melting time/temperature and thereby power consumption. MW heating is rapid and volumetric in nature (Knox and Copley, 1997). The heating of materials under microwaves depends upon materials' dielectric and magnetic properties. Most of the oxide precursors are poor microwave absorbers at room temperature. Nevertheless, above a critical temperature, oxides start absorbing microwaves (Mandal and Sen, 2015). In a non-absorbing system, initially, oxides are raised to a critical temperature with the help of a microwave susceptor (SiC) (Mandal and Sen, 2017).

4 Immobilization mechanism

The wasteforms discussed in the previous section can be utilized for immobilization of HLW mainly using two concepts (Donald et al., 1997; Ojovan and Lee, 2014):

- (A) Waste dissolution: the waste can be incorporated into the glass or crystalline (single or multiphase) phase. The radionuclides are immobilized at a microscopic scale in the wasteforms (National Research Council, 2011).
- (B) Waste encapsulation: the wasteforms can be envisaged, where a high loading of radionuclides can be encapsulated in a durable glass/ceramic/glass–ceramic phase. This method mainly immobilizes radionuclides at a microscopic scale. If the resultant matrix (obtained after incorporating radionuclides) exhibits good chemical durability, the matrix can be considered a secondary barrier against dissolution through water (Donald et al., 1997). The inclusion of foreign atoms in the random glass network can improve the stability and durability of the matrix. The foreign atoms may settle into interstitial/substitutional sites of the crystal structure of ceramic wasteforms. In a glass–ceramic wasteform, foreign atoms may settle either in the random glass network or at interstitial/substitutional sites in the ceramic phase. The chemical durability and radiation stability of the wasteform play important roles in the selection of wasteforms. The chemical durability and radiation stability of different kinds of wasteforms are discussed in the following subsections.

5 Chemical durability of wasteforms

The chemical durability of the matrix defines the long-term structural integrity and the elemental release from the matrix (Ojovan and Lee, 2014; Clark et al., 2021). The standard protocols are employed to study the leaching behavior of the immobilizing matrix. The frequently used protocols are described as follows (Strachan et al., 1982; Thorpe et al., 2021):

- i) Material characterization center (MCC-1): the leach test setup is static in nature, and the test is performed at temperatures <100°C. The reference temperatures are taken as 40°C, 70°C, and 90°C. The glass monolith is immersed in de-ionized water (DI) water/

reference groundwater at the reference temperatures. The sample surface area to water volume (SA/V) ratio is usually maintained as low as $\sim 10 \text{ m}^{-1}$. The test duration is generally 28 days, but it can vary. The test is used to measure the initial rate and residual rates, and to understand the mechanism of alteration layer formation.

- ii) Material characterization center (MCC-2): the static leach test is performed in the temperature range 100°C–200°C. The reference temperatures are taken as 100°C, 150°C, and 190°C. The glass monolith is immersed in DI water/reference groundwater for a duration of 28 days. The test is used for the analysis of the residual rate and alteration layer.
- iii) Material characterization center (MCC-3): this test is performed on powdered specimens. The powdered specimens are kept under a constant agitation condition. The sample surface area to water volume (SA/V) ratio is maintained as high as 2000 m^{-1} . The test temperature and duration are similar to the MCC-2 test. This test gives information related to the residual rate of leaching.
- iv) Material characterization center (MCC-4): the additional parameter of the leachant flow is introduced in the test. The reference flow rates used are between 0.1 and $0.001 \text{ mL min}^{-1}$. The glass monolith is used for the test and performed at temperatures <100 °C for 28 days. This test is suitable to measure the initial rate of leaching.
- v) Material characterization center (MCC-5): the glass monolith is kept in the flowing leachant. The leaching solution is DI water, and the test temperature ranges between 35°C and 300°C. The test is used to measure the initial rate of leaching in distilled water only.
- vi) Product consistency test (PCT-A): this is a static leach test and performed at 90°C. The powdered sample (74–149 μm) is kept in DI water for 7 days. The sample surface area to water volume (SA/V) ratio is maintained as high as $2,000 \text{ m}^{-1}$. The test is performed to measure the initial rate of leaching.
- vii) Product consistency test (PCT-B): this test is similar to PCT-A. The sample powder is kept at temperatures <100°C. The test is used to measure the initial rate and residual rates of leaching.
- viii) Vapor hydration test (VHT): the leach test is performed with a glass monolith sample in the temperature ranges 5°C–300°C. This test is static in nature and performed under steam for 24 days. The residual rate and alteration layer thickness are measured.
- ix) Single-pass flow-through test (SPFT): the test is performed with glass powder or monoliths at temperatures <100°C. This is a dynamic test, and the forward rate of leaching/dissolution is generally measured.

6 Leaching mechanism of the wasteforms

The leaching of the matrix generally happens in three stages:

Stage (1): **hydrolysis of network**: in this process, ion exchange reactions take place between the matrix (glass, ceramic, or glass–ceramic type network) and the aqueous media; as a result, the ion exchange reactions (hydrolysis of the matrix) occur (Bunker et al., 1984; Abrajano et al., 1986; Clark et al., 1992).

Stage (2): **network dissolution**: in this process, breakage of bridging bonds occurs and secondary phases (possible phases: analcime, phillipsite, sepiolite, and tobermorite) get precipitated. In this process, dissolution can decrease or increase depending on the type of phases on the matrix surface (Pierce et al., 2010; Corkhill et al., 2013).

Stage (3): **formation of the hydrated gel layer**: the dissolution rate is related to the formation of a gel layer/alteration products (zeolites and calcium silicates). The amorphous gel layer's composition and thickness depend upon the matrix composition, temperature, and pH of the aqueous media. The alteration products are crystalline, sandwiched between the hydrated gel layer and the aqueous media. This process plays a crucial role in the leaching of the matrix as it will alter the thickness of the hydrated gel layer (Ma et al., 2017; Hopf et al., 2018; Wilkinson et al., 2019; Gin et al., 2020; Stone-Weiss et al., 2020; Zubekhina et al., 2020).

The normalized leach rate ($\text{g}\cdot\text{m}^{-2}\cdot\text{day}^{-1}$) of nuclide i from the matrix can be calculated using the following expression (Ojovan et al., 2019):

$$NR_i = \frac{C_i}{f_i \cdot (SA/V) \cdot t} \quad (1)$$

Here, C_i : concentration of element “ i ” in the solution ($\text{g}\cdot\text{L}^{-1}$);

f_i : mass fraction of element “ i ” in the samples (unitless);

SA: surface area of the sample (m^2);

V: leachant volume (L) and t is the leaching time.

6.1 Chemical durability of glass wasteforms

In order to investigate the chemical durability of wasteforms, the United Kingdom HLW glass was synthesized with 25 wt% of simulated high-level waste (Corkhill et al., 2013). The chemical durability of glass was studied at pH 12.7 in a saturated $\text{Ca}(\text{OH})_2$ solution and alkaline water at pH 9.8. The dissolution of elements was explained in three regimes that were named as the i) initial incubation phase, ii) intermediate phase, and iii) residual phase. The normalized dissolution rates of glass powder (S/V : $10,000\text{ m}^{-1}$) for elements B, Li, Na, and Si were found to be 1.9×10^{-5} , 1.7×10^{-5} , 4.5×10^{-5} , and $4.2 \times 10^{-7}\text{ g m}^{-2}\cdot\text{day}^{-1}$ after 168 days, respectively, in alkaline water, which was nearly an order lower than obtained rates of 28 days. The normalized dissolution rates of glass powder in a saturated calcium hydroxide solution of B, Li, Na, and Si were found to be of the order of $10^{-5}\text{ g m}^{-2}\cdot\text{day}^{-1}$ after 168 days, respectively; C–S–H ($\text{CaO-SiO}_2\text{-H}_2\text{O}$) phase formation was observed in the initial incubation phase, which led to the reduction in dissolution rates. The normalized dissolution rates of glass monolith samples (S/V : 10 m^{-1}) in the saturated $\text{Ca}(\text{OH})_2$ solution of B, Li, and Na were obtained as 5.4×10^{-5} , 1.8×10^{-4} , and $3.6 \times 10^{-4}\text{ g m}^{-2}\cdot\text{day}^{-1}$ after 70 days, respectively. The leaching of Si was not observed throughout the period in glass monolith samples. The same group investigated the long-term leaching behavior of International Simple Glass (ISG) in acidic to hyper alkaline conditions using PCT and MCC-1 leaching tests for 120 and 720 days, respectively (Backhouse et al., 2018). The B, Na, and Si dissolution rates were comparable to others (Inagaki et al., 2013; Neeway et al., 2018). The localized preferential attack and cracks in

the high pH conditions were seen in the ISG samples. The leaching behavior of the ISG samples was also tested as per MCC-1 protocol at 50°C . The formation of C–S–H alteration products during the initial incubation phase led to passivate the dissolution of ISG glass.

The aluminoborosilicate glass was synthesized using the conventional method, and it investigated the roles of Mg and Ca in structure and chemical durability using the PCT-B test (Backhouse et al., 2019). The Na and B leaching rates were obtained in the order of $10^{-3}\text{ g m}^{-2}\cdot\text{day}^{-1}$ after 112 days. A novel matrix of nanoporous aluminoborosilicate was developed for cesium removal from liquid radioactive waste and its stable immobilization (Abbasi et al., 2020). The matrix showed the maximum Cs sorption (removal of a compound from solution by solid-phase constituents) capacity. The leaching test results of heat-treated samples at $1,100^\circ\text{C}$ have shown the effective stabilization of Cs in the alumina–borosilicate matrix. The effect of cerium doping in borosilicate glass was investigated (Zhu et al., 2019). Ce doping led to an increase in the breakage of B–O–B bonds in $[\text{BO}_3]$ units. According to the product consistency test (PCT) results, normalized leaching rates of the main elements (B and Si) and actinide surrogate Ce in the glass were very low.

The stability of aluminoborate glass was studied in the acid, basic, and neutral solutions. The hygroscopic nature of B_2O_3 deteriorates the chemical durability of glass. To avoid this condition, Mascaraque et al. (2019) designed a glass in which the modifier ion content was not more than 25 mol% and the aluminum to boron ratio varied. The increased aluminum content in the glass results in improved chemical durability in the neutral and acidic media, but it is constant in the basic media. It can be concluded that B_2O_3 is highly susceptible to nucleophilic OH^- attack.

Furthermore, durability studies have been found on pharmaceutical glass that contains a mixture of modifier ions in the glass structure. A borosilicate glass was designed with the substitution of CaO with MgO, and the effect of the increased MgO concentration in the glass was observed; furthermore, aqueous stability was tested at 80°C for 40 days (Yang et al., 2021). The borosilicate glass undergoes the whole dissolution mechanism that initiates from the ion exchange process forward to forming a silica-rich layer at the surface of the glass. The increased concentration of MgO led to the deterioration of the chemical durability of glass. The selective leaching of phase-separated iron-containing sodium borosilicate glass was studied (Konon et al., 2022). The chemical durability was affected by Fe^{+3} cations. The acidic treatment on glass led to formation of porous glass (PG), and increasing the time led to an increased pore volume in glass.

The effect of the glass composition and SA/V ratio on the initial and residual rates of leaching was investigated (Gin et al., 2013a). The tests were performed at 90°C after 5 years and compared with SON68 (French inactive R7/T7-type glass). It was found that, with the increase in the SA/V ratio, the normalized leaching rates of Si were decreased. The leaching studies were performed on the SON68 glass under a dynamic test with a higher SA/V ratio ($\sim 14,000\text{ m}^{-1}$) at 90°C . The normalized leaching rate was found in the order of $10^{-4}\text{ g m}^{-2}\cdot\text{day}^{-1}$ at pH 10.5 after 200 days (Neeway et al., 2011). In another study, the leaching behavior of glass was investigated by using ISG as a reference and the leaching mechanism was found (Gin et al., 2013b).

6.2 Chemical durability of ceramic wasteforms

The waste is immobilized into ceramics such as perovskite (CaTiO_3), hollandite ($\text{BaAl}_2\text{Ti}_6\text{O}_{16}$), and zirconolite ($\text{CaZrTi}_2\text{O}_7$) (Barinova et al., 2008). The perovskite/zirconolite matrix can accommodate a wide range of the elements present in HLW. The hollandite–perovskite composite ceramic matrix was synthesized using the solid-state reaction method (Ma et al., 2021). The hollandite and perovskite phases were chosen to immobilize Cs and Sr radionuclides. The chemical durability of the ceramic matrix was tested with the MCC-1 protocol. The normalized leach rate of Sr and Cs was found in the order of 10^{-5} and $10^{-3} \text{ g m}^{-2}\text{day}^{-1}$ after 42 days, respectively, with the matrix of composition (75% of hollandite and 25% of perovskite). The iodine and cesium radionuclide loading was proposed to be immobilized in the defect perovskite structure named $\text{Cs}_3\text{Bi}_2\text{I}_9$ (Yang et al., 2020). The chemical durability was tested in the form of a silica–ceramic composite matrix (30% silica and 70% perovskite) and a core-shell matrix (80% silica as shell and 20% perovskite as core) with a semi-dynamic leaching experiment for 14 days. The BiOI passivating layer was formed in the silica–ceramic composite matrix, whereas the silica shell prevents the migration of elements in the aqueous media in the case of the silica–perovskite (core-shell structure) matrix. The normalized leach rate of iodine was found to be $30 \text{ mg m}^{-2}\text{day}^{-1}$ for the silica–ceramic composite matrix and $5.0 \times 10^{-3} \text{ g m}^{-2}\text{day}^{-1}$ for the core-shell matrix at 90°C .

The powellite ceramic is a potential candidate for immobilizing Mo and minor actinides. A series of ceramics ($\text{Ca}_{1-x}\text{Li}_x/2\text{Gd}_x/2\text{MoO}_4$) was synthesized using a solid-state reaction method, and the sintering temperature was maintained between 525°C and 950°C (Fillet et al., 2004; Frugi et al., 2008; Roessler et al., 2015; Claparede et al., 2017; Meng et al., 2020). The Gd^{+3} ion was taken as a surrogate of minor actinide Cm^{+3} . The normalized mass losses of gadolinium and molybdenum were 1.4×10^{-4} and $2.2 \times 10^{-4} \text{ g m}^{-2}$ after 28 days, respectively.

The rare earth phosphates, such as $\text{Gd}_{1-x}\text{Yb}_x\text{PO}_4$ (where $x = 0, 0.1, 0.2, \dots, 1$), were synthesized using a solid-state reaction method and sintered at different temperatures ranging from 600°C to $1,600^\circ\text{C}$ (Li et al., 2018). Phase transformation was observed as ytterbium ions replaced gadolinium ions at the lattice site of the ceramic phase. The phase transformation led to distortion in the PO_4 tetrahedra, resulting in decreased elemental leaching. The normalized mass loss of gadolinium and ytterbium was obtained as 2.0×10^{-7} and $2.3 \times 10^{-7} \text{ g m}^{-2}$, respectively, with $\text{Gd}_{0.9}\text{Yb}_{0.1}\text{PO}_4$ composition after 28 days. $\text{Gd}_2\text{Zr}_2\text{O}_7$ was synthesized using the SPS method at a sintering temperature of $1,800^\circ\text{C}$. The phase was loaded with 45 mol% simulated waste (Wei et al., 2022). The phase transformation occurred from fluorite to pyrochlore after the inclusion of waste. The normalized leach rate of Gd was obtained as $3.5 \times 10^{-8} \text{ g m}^{-2}\text{day}^{-1}$ after 42 days with 45 mol% loading of waste. The zirconolite ceramic matrix was synthesized using the solid-state method. Nd (up to 15 at% stabilized) was added as the surrogate of actinides in the matrix (Cai et al., 2016). The leaching study was performed at different pH values (5, 7, and 9) at 90°C . The normalized leach rate of Ca was high at $\text{pH} = 5$ and was obtained as $5.6 \times 10^{-3} \text{ g m}^{-2}\text{day}^{-1}$ after 42 days. The normalized leaching rate of Nd was almost the same (in the order of $\sim 10^{-5} \text{ g m}^{-2}\text{day}^{-1}$) at all the

pH values. Therefore, the zirconolite matrix was found suitable for immobilizing the Nd radionuclide at different pH values. In addition, the yttrium iron garnet [$\text{Y}_{3-x}\text{Ce}_x\text{Fe}_5\text{O}_{12}$ ($0 \leq x \leq 1$)] was found to be a potential host for the immobilization of HLW (Luo et al., 2021). The normalized leaching rates of Ce and Y were obtained in the order of 10^{-4} and $10^{-5} \text{ g m}^{-2}\text{day}^{-1}$ after 42 days, respectively.

6.3 Chemical durability of glass–ceramic wasteforms

The glass–ceramic matrix has gained attention widely due to its ability to immobilize a wide range of actinides. The addition of cerium (Ce) and neodymium (Nd) in the borosilicate glass–ceramic wasteforms (crystalline phase: zirconolite) was investigated, and an aqueous chemical durability test was performed (Zhu et al., 2020a). Nd is invariably used as a nonradioactive or nonactive surrogate of plutonium (Pu) and minor actinides. The aqueous chemical durability was performed through PCT-B and MCC-1 methods at 90°C for 28 days. The normalized leach rates of elements (Si, Ca and Nd) were obtained as 4.5×10^{-3} , 2.5×10^{-3} , and $1.2 \times 10^{-4} \text{ g m}^{-2}\text{day}^{-1}$ with the MCC-1 method, respectively (with 20 wt % of $\text{CeO}_2 + 20 \text{ wt\% Nd}_2\text{O}_3$), and the concentration of Ce in leachate was found negligible. It was also reported that with an increase in the loading % from 15 to 40 of Nd and Ce (in equal amount), an oxyapatite phase appeared in the glass–ceramics, and the appeared phase did not significantly influence the chemical durability of glass–ceramics.

A glass–ceramic wasteform containing calcium neodymium cerium oxide silicate [$\text{Ca}_2\text{Nd}_{8-x}\text{Ce}_x(\text{SiO}_4)_6\text{O}_2$] as the ceramic phase was synthesized to immobilize the rare-earth ions in wastes generated by pyro-processing (Kim and Heo, 2015). The normalized leach rate values of Nd and Ce were obtained as 2.2×10^{-6} and $2.6 \times 10^{-6} \text{ g m}^{-2}\text{day}^{-1}$, respectively, from the PCT test, and the leach rate values were found to be <0.1 ppb from the MCC-1 test performed at 90°C for 35 days. The normalized leach rates of elements were lower in glass–ceramic compared to the glass matrix. The zirconolite–sodium borosilicate glass–ceramic wasteforms were prepared using the one-step slow cooling method (Zhu et al., 2020b). The normalized leach rates of Si, Ca, and Ce were found to be minimal even after 56 days. The zirconolite–borosilicate glass–ceramic matrix had shown good aqueous durability and was found suitable for immobilizing HLW. The barium borosilicate glass–ceramic containing CTZ (Molar ratio of CaO , TiO_2 , and ZrSiO_4 —2:2:1) was prepared with the addition of 0, 45, and 55 wt% CTZ in the glass (Li et al., 2015). The CTZ45 glass–ceramic matrix (annealed at 950°C) showed lower normalized leaching rates. The normalized leaching rates of Na, B, and Nd were obtained as 7.7×10^{-3} , 8.8×10^{-3} , and $7.5 \times 10^{-6} \text{ g m}^{-2}\text{day}^{-1}$, respectively after 28 days. However, glass (CTZ0 matrix) was not chemically durable. The CTZ55 glass–ceramic matrix had multiple crystalline phases, resulting in decreased network formers and poor chemical durability. Therefore, the CTZ45 glass–ceramic matrix was found to be the most chemically durable.

The barium borosilicate glass–ceramics were synthesized with neodymium oxide (0–12 wt%) (Wu et al., 2016). The loading of

Nd_2O_3 in the range of 2–6 wt% results in mainly zirconolite and titanate phases, whereas increasing the content of Nd_2O_3 up to 8 wt% led to the formation of the titanate phase only. The normalized leach rate of the glass–ceramics with 6 wt% loading of Nd_2O_3 was low compared to 8 wt% loading in the glass–ceramic matrix. The normalized leach rates of Nd, Ca, and B were 4.4×10^{-6} , 1.6×10^{-3} , and $6.8 \times 10^{-3} \text{ g m}^{-2} \text{ day}^{-1}$, respectively, with a loading of 6 wt% Nd_2O_3 glass–ceramics after 42 days. Furthermore, the zirconolite barium borosilicate glass–ceramics with simulated sulfate containing liquid waste (0, 16, 20, 30 wt%) was synthesized (Wu et al., 2018). The zirconolite phase and some minor baddeleyite phases were present at 16 wt% liquid waste loading. In contrast, increasing the content of liquid waste (20–30 wt%) led to the perovskite phase formation. The normalized leaching rates of Si, B, Na, and La were obtained as 8.1×10^{-4} , 1.6×10^{-3} , 7.2×10^{-3} , and $1.2 \times 10^{-3} \text{ g m}^{-2} \text{ day}^{-1}$, respectively, after 28 days with 16 wt% liquid waste content. The zirconolite barium borosilicate glass–ceramic matrices were prepared with the loading of the SO_3 content (0, 2, 6, and 8 wt%) (Wang et al., 2017). The matrix with 4 wt% of SO_3 content led to a new barite phase. The normalized leach rates of Si, B, and Ba were found in the order of 10^{-3} , 10^{-3} , and $10^{-4} \text{ g m}^{-2} \text{ day}^{-1}$ after 14 days, respectively. The 8 wt% SO_3 -loaded glass–ceramic matrix had shown higher leaching rates because it had pores and an unstable nardite phase, leading to poor chemical durability.

The pyrochlore-based borosilicate glass–ceramics were synthesized at $1,300^\circ\text{C}$ and cooled to $1,050^\circ\text{C}$ at the rate of $10^\circ\text{C min}^{-1}$ using the one-step heat treatment method with a uniform distribution of the crystalline phase (Wu et al., 2020). The normalized leach rates of Na, B, Al, Si, Nd, Ti, and Nb were obtained as 6.8×10^{-3} , 3.7×10^{-4} , 1.5×10^{-2} , 2.2×10^{-3} , 3.0×10^{-5} , 5.1×10^{-5} , and $5.5 \times 10^{-6} \text{ g m}^{-2} \text{ day}^{-1}$ after 28 days, respectively. The borosilicate glass–ceramics were synthesized with the loading of the strontium oxide content in the range of 10–25 mol% (Pilania et al., 2023). The normalized leach rates of Si, B, and Sr were obtained as 1.2×10^{-8} , 3.7×10^{-9} , and $1 \times 10^{-8} \text{ g m}^{-2} \text{ day}^{-1}$ after 30 days, respectively.

7 Radiation stability of wasteforms

In addition to chemical durability, the radiation stability of the wasteforms/matrices plays a major role in selecting a matrix. The actinides in the radioactive waste emit alpha particles and recoil nuclei (Weber et al., 1998). The recoil nucleus undergoes several cascade collisions within the matrix. These primary and secondary collisions lead to defect generation within the matrix. The radiation stability of different types of matrices is reviewed in the following section.

7.1 Radiation stability of glass wasteforms

In order to obtain radiation-resistant wasteforms, efforts are being made to explore a matrix with moderate radiation resistance. The radiation stability of borosilicate glass was investigated by electron paramagnetic resonance and ultraviolet-visible spectroscopy (Wang et al., 2020). The glass samples were exposed to ^{60}Co gamma radiation with a dose rate of

$5,560 \text{ Gy h}^{-1}$, and we observed an increase in non-bridging oxygen (NBO) ions, formation of peroxy radical, etc., which were detrimental for the structural integrity of the matrix. The gamma irradiation effect on the Fe- and Eu-doped Trombay nuclear waste glass was investigated through electron spin resonance and photoluminescence spectroscopy (Mohapatra et al., 2014). The ^{60}Co gamma source was irradiated at doses 1 kGy h^{-1} and 8 kGy h^{-1} . Europium (Eu^{+3}) was used as a surrogate for plutonium (Pu^{+3}) in the glass matrix. The PL results showed the stability of trivalent species in the matrix. The formation of the Eu^{+2} oxidation state was not observed in the glass, but Eu sites were more disordered after gamma irradiation (de Bonfils et al., 2007). The effects of beta irradiation on the 30 mol% Fe_2O_3 –70 mol% P_2O_5 polyphosphate glass were studied. The glass was irradiated with a beta emitter $^{90}\text{Sr}/^{90}\text{Y}$ source (varying dose from 5.4 to 22 kGy) (Gaj et al., 2019). The glass structure led to the breakage of P–O–P bonding upon irradiation, and the broken bonds might form the P–O–H bridges, which can decrease the chemical durability. The knocking out process of phosphorous can create the P–O–O–P linkage, which also relaxes in the form of P–O–P bridges and O_2 (oxygen bubbles). The Fe–O–P bridges were radiation-tolerant, as compared to P–O–P bridges. In another study on iron phosphate glass (IPG: 45 Fe_2O_3 –55 P_2O_5 in mol%) using electron beam irradiation, an increase in electron dose from 1×10^{26} to $4.8 \times 10^{26} \text{ e m}^{-2}$ led to the formation of Fe-rich and P-rich nanophases along with phase separation (Sun et al., 2003). Self-heating and charging were anticipated factors that led to the structural changes in IPG. In order to investigate the effect of the ^{137}Cs radionuclide on the radiation stability of sodium aluminophosphate glass, Ba was taken as a surrogate of Cs (Stefanovsky et al., 2019). The Ba replacement for Cs exhibited a slight modification in the glass network but no substantial effects on the hydrolytic durability of the phosphate glass. There was no change observed in the Fe^{3+} to Fe^{2+} ratio.

The samples become radioactive after irradiation in existing gamma and beta sources; therefore, induced activity inhibits detailed investigation of irradiated samples. In addition, the availability of irradiation sources and energy is limited. To overcome the activity of irradiated samples, the ion irradiation method can be used as a surrogate method with the added advantage of desired fluence and energy. The ion-irradiated samples do not get activated and can be tested in the existing laboratory setup. Similar conditions can be simulated with high-energy ion beams, and radiation stability can be performed (Dube et al., 2015). The radiation stability of iron phosphate glass was studied by (Dube et al., 2020), in which cerium was used as a surrogate of actinides. The pure and cerium-doped iron phosphate glass (IPG) was irradiated with a gold source of energy 750 keV at a fluence of $2 \times 10^{15} \text{ ion cm}^{-2}$ to mimic ballistic damage due to the cascade of recoil atoms during the decay of actinides. The Raman spectra confirmed the incorporation of cerium as a modifier in the glass. A significant reduction of iron was observed after gold ion irradiation. The iron reduction might lead to the formation of crystals, so poor chemical durability of cerium-doped glass was anticipated. Swift heavy ion irradiation using 14.4 MeV Si ions at a fluence of $1 \times 10^7 \text{ ions cm}^{-2}$ on zinc phosphate glass showed the formation of ion tracks and reduced the number of bridging O atoms (Awazu et al., 2003). The heavy ion irradiation using 4 MeV O^+ ions from 5×10^{13} to $5 \times 10^{16} \text{ ion cm}^{-2}$

on IPG leads to the formation of nanocrystals with different phases, such as $\text{Fe}_4(\text{P}_2\text{O}_7)_3$ and $\text{Fe}(\text{PO}_3)_3$. The ion track was formed upon irradiation, owing to stress in the matrix, which results in considerable deformation (shear bands). The shear bands led to the formation of nanocrystals (Jegadeesan et al., 2015).

7.2 Radiation stability studies on ceramic wasteforms

The ceramic wasteforms exhibit long-term stability, radiation tolerance, and leaching resistance, and most of the actinides and fission products can be incorporated into polycrystalline phases (Weber et al., 1998). A synroc is a widely known ceramic for the immobilization of minor actinides, which are generated from the nuclear fuel cycle and reprocessing of fuel. The synroc consists of hollandite, perovskite, and zirconolite phases. Among these phases, zirconolite has a better radiation stability, aqueous corrosion resistance, and thermal stability (Rossell, 1992). Several attempts have been made to study the radiation-induced modification in the zirconolite matrix. The radiation stability of zirconolite ceramics was investigated using a surrogate method of ion irradiation. The matrix was bombarded with He^+ ions (30 keV) at fluence ranging from 1×10^{17} to 1×10^{21} ions cm^{-2} (Gupta et al., 2016). The XRD results of irradiated samples revealed the damage at fluence 1×10^{20} ions cm^{-2} , and the decrease in intensity of the XRD peaks with the increase in fluence was attributed to the radiation-induced defects in the matrix. However, the monoclinic structure was intact even at the maximum fluence used for the study. Nd-doped zirconolite and perovskite (Nd as Pu surrogate) were irradiated with Kr^+ ions of energy 2 MeV at a fluence of 5×10^{15} ions cm^{-2} (Davoisine et al., 2011). The micro-diffraction patterns revealed radiation-induced structural changes in the Nd-doped perovskite matrix, which indicated the symmetry change (from orthorhombic to cubic) along with matrix amorphization.

Nd-doped zirconolite pellets were irradiated with He^+ ions (30 keV) to observe the irradiation-induced effects in the matrix (Gupta et al., 2020). A decrease in intensity and an increase in the width of the peaks at the fluence of 1×10^{17} ions cm^{-2} in XRD peaks were observed without loss of significant crystallinity. It was anticipated that an increase in the fluence of He^+ ions can lead to the formation of helium bubbles in the matrix. Consequently, the radiation stability property of the matrix might get deteriorated. The same group further studied the effects of Au (120 MeV) ion irradiation on the Nd-doped zirconolite to simulate the α -decay events at a fluence of 3×10^{13} ions cm^{-2} (Gupta et al., 2019). The broadening and reduction in the intensity of the XRD peaks confirmed the induced defects and vacancies at the fluence of 3×10^{13} ions cm^{-2} . The heavy ion irradiation-induced amorphous track formation was observed in the matrix. The irradiation effect on the pyrochlore ceramic matrix ($\text{A}_2\text{Ti}_2\text{O}_7$; where A: Y, Sm, Gd, Er, and Yb) was investigated with ^{197}Au ions (2.2 GeV) (Shamblin et al., 2016). The amorphous nature and track formation were observed in all compositions. The $\text{Y}_2\text{Ti}_2\text{O}_7$ ceramic was more amorphous resistant than other compositions, whereas $\text{Gd}_2\text{Ti}_2\text{O}_7$ was prone to amorphization.

The Nd-doped zirconolite ($(\text{Ca}_{0.8}\text{Nd}_{0.2})\text{Zr}(\text{Ti}_{1.8}\text{Al}_{0.2})\text{O}_7$) ceramic was irradiated with i) Kr^+ ions (2 MeV) at a fluence of

1×10^{14} and 5×10^{15} ions cm^{-2} and ii) He^+ ions (200 keV) at a fluence of 1×10^{14} , 5×10^{15} and 1×10^{17} ions cm^{-2} (Gilbert et al., 2011). There was no significant damage at a lower fluence of both the ions; however, at a higher fluence (5×10^{15} ions cm^{-2}) of Kr^+ ions, zirconolite got completely amorphized, whereas helium accumulation or helium bubbles were observed at a high fluence of He^+ ions. The radiation-induced modifications in the single-crystal yttria-stabilized zirconolite (YSZ) ceramic using He^+ ions (100 keV) have been studied (Yang et al., 2012). An effort was made to investigate the damage evolution process in three fluence regimes: i) at a low fluence in the range of 1×10^{16} to 4×10^{16} ions cm^{-2} , formation of point defects was seen; ii) at an intermediate fluence in the range of 8×10^{16} to 1×10^{17} ions cm^{-2} , volume defect clusters were seen; iii) at a fluence of 2×10^{17} and 4×10^{17} ions cm^{-2} , ribbon-like He bubbles and cracks were observed, which cause the blistering on the surface. A similar study was performed on polycrystalline yttria-stabilized zirconolite ceramics, which were irradiated with He^+ ions (70 keV). The single crystal and polycrystalline samples of YSZ had shown similar behavior (spherical and ribbon-like helium bubbles of different shapes under irradiation) (Yang et al., 2015a).

The decay of ^{90}Sr emits beta particles of energy in the range of 0.546–2.28 MeV. The interaction of beta particles and generated recoil nuclei in ceramic wasteforms led to the deterioration in the physical properties of the matrix (Aubin-Chevaldonnet et al., 2006). Therefore, ceramic wasteforms are desired to be stable under the beta decay of Sr. In order to simulate the effect of energetic beta particles on the radiation stability of ceramic wasteforms, strontium titanate was irradiated with an electron beam of energy 1.8 MeV with a flux of 1.5×10^{13} electrons/ $\text{cm}^2 \cdot \text{s}^{-1}$ (Yang et al., 2015b). The energetic electrons can produce atomic displacements by depositing energy to the matrix, which may induce phase separation, chemical disordering, or amorphization in irradiated materials (Kinsho et al., 2003). The perovskite structure did not change after electron irradiation, as revealed from the Raman spectrum of SrTiO_3 . The electron microscopic images revealed a dense microstructure, which was advantageous to avoid radioactive nuclide leaking into the environment. The CaZrO_3 perovskite was irradiated with the Au^+ ions (940 MeV) at a fluence of 1.5×10^{13} ions cm^{-2} (Lang et al., 2012). Perovskite got completely amorphized, and amorphous tracks of size 6 ± 0.6 nm were seen.

The polycrystalline pyrochlore ($\text{Lu}_2\text{Ti}_2\text{O}_7$) was irradiated with the beam of He^+ ions (200 keV) in a fluence ranging 2×10^{15} – 2×10^{17} ions cm^{-2} (Zhang et al., 2015). Micro-swelling was observed at the fluence of more than 2×10^{16} ions cm^{-2} ; on further increase in the fluence, the matrix turned into a completely disordered structure. The pristine pyrochlore phase was intact up to a fluence of 5×10^{16} ions cm^{-2} , and at higher fluence, order to disorder transformation was seen. The amorphization of pyrochlore was not observed even at a fluence of 2×10^{17} ions cm^{-2} . The radiation stability of $\text{Gd}_2\text{Zr}_2\text{O}_7$ pyrochlore with Au^{+3} ions (7 MeV) at a fluence of 2.2×10^{15} ions cm^{-2} was investigated (Taylor et al., 2016). The samples irradiated with Au^{+3} ions underwent pyrochlore-to-defect fluorite structure transformation, and swelling was also seen. Subsequently, the irradiated samples were bombarded with He^+ ions at a fluence of 2×10^{15} and 2×10^{16} ions cm^{-2} ; furthermore, an increase in lattice swelling was seen. The lattice swelling was decreased at a higher fluence of 2×10^{17} ions cm^{-2} (Debelle et al., 2010).

7.3 Radiation stability studies on glass–ceramic wasteforms

In order to determine the radiation stability of glass–ceramic matrices, the borosilicate glass–ceramic matrices incorporating Cs/Sr (CS), lanthanide (LN), and transition metal (TM)) were investigated under different irradiation conditions (Tang et al., 2014). The samples were irradiated with a high-energy (5 MeV) alpha ion beam at a fluence of 1×10^{21} ions m^{-2} and a low-energy (600 keV) Kr heavy-ion beam at a fluence of 2.5×10^{19} ions m^{-2} to observe self-irradiation effects in the matrix. The light-ion beam (alpha ion) did not induce structural changes in the matrix, whereas the heavy-ion beam (Kr ion) led to a change from crystalline phases into an amorphous phase. The electron irradiation study was performed at a dose of 10^{13} Gy (equivalent to 1,000 years of Cs/Sr-loaded wasteform irradiation dose (Weber et al., 2009)) to observe the changes in the ceramic phase. The studies show that the matrix was radiation-tolerant under β - and γ -beam irradiation. The radiation stability of the zirconolite-based aluminosilicate glass–ceramic matrix was investigated (Mir et al., 2021). The matrix was irradiated with a He ion beam at different energies and fluence. The 10-keV He ions at a fluence of 8×10^{16} He cm^{-2} h led to the formation of He bubbles in the ceramic phase and oxygen bubbles in the glass phase. Helium bubble formation was not observed in the glass phase, which may be due to a large He diffusion coefficient. The amorphization of the zirconolite phase was observed with 20-keV He ion irradiation at a fluence of 1.2×10^{17} He cm^{-2} at 143 k temperature.

8 Summary

The review uncovers broader aspects of matrices for radioactive waste immobilization. An introduction to wasteforms and types of wasteforms for radioactive waste immobilization are discussed. The glass, ceramic, and glass–ceramic wasteforms are introduced and reviewed in detail. The glass–ceramic wasteforms revolutionized have given a new perspective for the immobilization of radionuclides. However, glass–ceramics are still under exploration. Glass–ceramics can be potential wasteforms for the immobilization of waste generated from next-generation nuclear reactors.

References

- Abbasi, A., Davarkhah, R., Avanes, A., Yadollahi, A., Ghannadi-Maragheh, M., and Sepehrian, H. (2020). Development of nanoporous alumino-borosilicate as a novel matrix for the sorption and stable immobilization of cesium ions. *J. Inorg. Organomet. Polym. Mater.* 30, 369–378. doi:10.1007/s10904-019-01195-z
- Abrajano, T. A., Bates, J. K., and Byers, C. D. (1986). Aqueous corrosion of natural and nuclear waste glasses I. Comparative rates of hydration in liquid and vapor environments at elevated temperatures. *J. Non Cryst. Solids.* 84 (1-3), 251–257. doi:10.1016/0022-3093(86)90783-0
- Aldean, I., Sun, S. K., Wilkins, M. C. D., Gardner, L. J., Mason, A. R., Stennett, M. C., et al. (2022). Synthesis and characterisation of Ce-doped zirconolite $\text{Ca}_{0.80}\text{Ce}_{0.20}\text{ZrTi}_{1.60}\text{Mg}_{0.40}\text{O}_7$ (M = Fe, Al) formed by reactive spark plasma sintering (RSPS). *MRS Adv.* 7, 75–80. doi:10.1557/S43580-022-00221-6
- Aubin-Chevaldonnet, V., Gourier, D., Caurant, D., Esnouf, S., Charpentier, T., and Costantini, J. M. (2006). Paramagnetic defects induced by electron irradiation in barium hollandite ceramics for caesium storage. *J. Phys. Condens. Matter.* 18, 4007–4027. doi:10.1088/0953-8984/18/16/009
- Awazu, K., Roorda, S., Brebner, J. L., Ishii, S., and Shima, K. (2003). Structure of latent tracks created by swift heavy ions in amorphous SiO_2 and zinc phosphate glass. *Jpn. J. Appl. Phys.* 42, 3950–3957. doi:10.1143/JJAP.42.3950
- Backhouse, D. J., Corkhill, C. L., Hyatt, N. C., and Hand, R. J. (2019). Investigation of the role of Mg and Ca in the structure and durability of aluminoborosilicate glass. *J. Non Cryst. Solids.* 512, 41–52. doi:10.1016/j.jnoncrysol.2019.03.003
- Backhouse, D. J., Fisher, A. J., Neway, J. J., Corkhill, C. L., Hyatt, N. C., and Hand, R. J. (2018). Corrosion of the international simple glass under acidic to hyperalkaline conditions. *npj Mater. Degrad.* 2, 29. doi:10.1038/s41529-018-0050-5
- Barinova, T. V., Borovinskaya, I. P., Ratnikov, V. I., and Ignat'eva, T. I. (2008). Self-propagating high-temperature synthesis for immobilization of high-level waste in mineral-like ceramics: 1. Synthesis and study of titanate ceramics based on perovskite and zirconolite. *Radiochemistry* 50, 316–320. doi:10.1134/S1066362208030181
- Baumgärtner, F., and Ertel, D. (1980). The modern purex process and its analytical requirements. *J. Radioanal.* 58, 11–28. doi:10.1007/BF02533770
- Beckitt, S. (2012). *Decommissioning of legacy nuclear waste sites: Dounreay, UK, nuclear decommissioning planning, execution and international experience.* Cambridge: Woodhead Publishing, 701–744. doi:10.1533/9780857095336.3.701
- Bunker, B. C., Arnold, G. W., and Wilder, J. A. (1984). Phosphate glass dissolution in aqueous solutions. *J. Non Cryst. Solids.* 64 (3), 291–316. doi:10.1016/0022-3093(84)90184-4
- The immobilization of spent metallic fuels generated from next-generation nuclear reactors needs to be addressed. The reprocessing of used fuel to recover uranium reduces the wastage of uranium and plutonium. Long-lived actinides are being reprocessed to be converted into short-lived actinides. Short-lived actinides along with traces of long-lived actinides can be immobilized in suitable glass–ceramic wasteforms. In addition, spreading awareness about storage among the public should be considered. At proposed storage/disposal sites, a series of awareness campaigns should be conducted to educate the public.

Author contributions

RP contributed to the literature review and writing of the manuscript. CD presented the idea to conceptualize the article, and gave critical comments and suggestions to improve the manuscript.

Acknowledgments

The authors received the financial assistance from UGC and infrastructure from CUG, Gandhinagar, for the work.

Conflict of interest

The authors declare that the research was conducted in the absence of any commercial or financial relationships that could be construed as a potential conflict of interest.

Publisher's note

All claims expressed in this article are solely those of the authors and do not necessarily represent those of their affiliated organizations, or those of the publisher, the editors, and the reviewers. Any product that may be evaluated in this article, or claim that may be made by its manufacturer, is not guaranteed or endorsed by the publisher.

- Cai, X., Teng, Y., Wu, L., Zhang, K., and Huang, Y. (2016). The synthesis and chemical durability of Nd-doped single-phase zirconolite solid solutions. *J. Nucl. Mater.* 479, 455–460. doi:10.1016/j.jnucmat.2016.07.042
- Claparede, L., Guigue, M., Jouan, G., Nadah, N., Dacheux, N., and Moisy, P. (2017). Long-term behavior of refractory thorium-plutonium dioxide solid solutions. *J. Nucl. Mater.* 483, 158–166. doi:10.1016/j.jnucmat.2016.11.007
- Clark, B. M., Tumurugoti, P., Sundaram, S. K., Amoroso, J. W., and Marra, J. C. (2021). Preparation and characterization of multiphase ceramic designer waste forms. *Sci. Rep.* 11, 4512. doi:10.1038/s41598-021-84014-1
- Clark, D. E., and Zito, B. K. (1992). *Corrosion of glass, ceramics and ceramic superconductors: Principles, testing, characterization and applications*. United States: Noyes Publications.
- Corkhill, C. L., Cassingham, N. J., Heath, Paul G., and Hyatt, N. C. (2013). Dissolution of UK high-level waste glass under simulated hyperalkaline conditions of a collocated geological disposal facility. *Int. J. Appl. Glass Sci.* 4, 341–356. doi:10.1111/ijag.12042
- Crovisier, J.-L., Advocat, T., and Dussossoy, J.-L. (2003). Nature and role of natural alteration gels formed on the surface of ancient volcanic glasses (Natural analogs of waste containment glasses). *J. Nucl. Mater.* 321 (1), 91–109. doi:10.1016/S0022-3115(03)00206-X
- Darda, S. A., Gabbar, H. A., Damideh, V., Aboughaly, M., and Hassen, I. (2021). A comprehensive review on radioactive waste cycle from generation to disposal. *J. Radioanal. Nucl. Chem.* 329, 15–31. doi:10.1007/S10967-021-07764-2
- Davis, M. J., and Zanotto, E. D. (2017). Glass-ceramics and realization of the unobtainable: property combinations that push the envelope. *MRS Bull.* 42, 195–199. doi:10.1557/MRS.2017.27
- Davoisne, C., Stennett, M. C., Hyatt, N. C., Peng, N., Jeynes, C., and Lee, W. E. (2011). Krypton irradiation damage in Nd-doped zirconolite and perovskite. *J. Nucl. Mater.* 415, 67–73. doi:10.1016/j.jnucmat.2011.05.043
- de Bonfils, J., Panczer, G., de Ligny, D., Peugeot, S., and Champagnon, B. (2007). Behaviour of simplified nuclear waste glasses under gold ions implantation: A microluminescence study. *J. Nucl. Mater.* 362, 480–484. doi:10.1016/j.jnucmat.2007.01.101
- Debelle, A., and Declémy, A. (2010). XRD investigation of the strain/stress state of ion-irradiated crystals. *Nucl. Instrum. Methods Phys. Res. B* 268, 1460–1465. doi:10.1016/j.nimb.2010.01.009
- Donald, I. W., Metcalfe, B. L., and Taylor, R. N. J. (1997). The immobilization of high-level radioactive wastes using ceramics and glasses. *J. Mater. Sci.* 32, 5851–5887. doi:10.1023/A:1018646507438
- Donald, I. W. (2010). *Waste immobilization in glass and ceramic based hosts: Radioactive, toxic and hazardous wastes*. doi:10.1002/9781444319354
- Dube, C. L., Kulriya, P. K., Dutta, D., Pujari, P. K., Patil, Y., Mehta, M., et al. (2015). Positron annihilation lifetime measurement and X-ray analysis on 120 MeV Au⁺ irradiated polycrystalline tungsten. *J. Nucl. Mater.* 467, 406–412. doi:10.1016/j.jnucmat.2015.05.029
- Dube, C. L., Stennett, M. C., Ananthanarayanan, A., David, C., Shah, J. G., and Hyatt, N. C. (2020). Radiation stability study on cerium loaded iron phosphate glasses by ion irradiation method. *J. Radioanal. Nucl. Chem.* 323, 1381–1386. doi:10.1007/s10967-020-07012-z
- Englert, M., Krall, L., and Ewing, R. C. (2012). Is nuclear fission a sustainable source of energy? *MRS Bull.* 37, 417–424. doi:10.1557/MRS.2012.6
- Ewing, R. C., Weber, W. J., and Lian, J. (2004). Nuclear waste disposal—pyrochlore (A₂B₂O₇): nuclear waste form for the immobilization of plutonium and “minor” actinides. *J. Appl. Phys.* 95 (11), 5949–5971. doi:10.1063/1.1707213
- Fillet, C., Advocat, T., Bart, F., Leturcq, G., and Rabiller, H. (2004). Titanate-based ceramics for separated long-lived radionuclides. *Comptes Rendus. Chim.* 7, 1165–1172. doi:10.1016/J.CRCI.2004.02.018
- Frugier, P., Gin, S., Minet, Y., Chave, T., Bonin, B., Godon, N., et al. (2008). SON68 nuclear glass dissolution kinetics: current state of knowledge and basis of the new GRAAL model. *J. Nucl. Mater.* 380, 8–21. doi:10.1016/J.JNUCMAT.2008.06.044
- Gilbert, M., Davoisne, C., Stennett, M., Hyatt, N., Peng, N., Jeynes, C., et al. (2011). Krypton and helium irradiation damage in neodymium–zirconolite. *J. Nucl. Mater.* 416, 221–224. doi:10.1016/j.jnucmat.2010.11.089
- Gin, S., Abdelouas, A., Criscenti, L. J., Ebert, W. L., Ferrand, K., Geisler, T., et al. (2013b). An international initiative on long-term behavior of high-level nuclear waste glass. *Mater. Today* 16, 243–248. doi:10.1016/J.MATTOD.2013.06.008
- Gin, S., Frugier, P., Jollivet, P., Bruguier, F., and Curti, E. (2013a). New insight into the residual rate of borosilicate glasses: effect of S/V and glass composition. *Int. J. Appl. Glass Sci.* 4 (4), 371–382. doi:10.1111/IJAG.12048
- Gin, S., Guittouneau, C., Godon, N., Neff, D., Rebiscoul, D., Cabé, M., et al. (2011). Nuclear glass durability: new insight into alteration layer properties. *J. Phys. Chem. C* 115, 18696–18706. doi:10.1021/JP205477Q
- Gin, S., Mir, A. H., Jan, A., Delaye, J. M., Chauvet, E., De Puydt, Y., et al. (2020). A general mechanism for gel layer formation on borosilicate glass under aqueous corrosion. *J. Phys. Chem. C* 124 (9), 5132–5144. doi:10.1021/ACS.JPC.9B10491
- Goj, P., Jelen, P., Marczevska, B., and Stoch, P. (2019). Effect of β -Irradiation on the structure of iron polyphosphate glass. *J. Nucl. Mater.* 523, 198–205. doi:10.1016/j.jnucmat.2019.06.014
- Gupta, M., Kulriya, P. K., Kumar, R., and Ghumman, S. S. (2020). Structural investigation of Nd-zirconolite irradiated with He⁺ ions. *J. Radioanal. Nucl. Chem.* 323, 1413–1418. doi:10.1007/s10967-019-06873-3
- Gupta, M., Kulriya, P. K., Meena, R. C., Neumeier, S., and Ghumman, S. S. (2019). Probing swift heavy ion irradiation damage in Nd-doped zirconolite. *Nucl. Instrum. Methods Phys. Res. B* 453, 22–27. doi:10.1016/j.nimb.2019.06.002
- Gupta, M., Kulriya, P. K., Shukla, R., Dhaka, R. S., Kumar, R., and Ghumman, S. S. (2016). Reduction and structural modification of zirconolite on He⁺ ion irradiation. *Nucl. Instrum. Methods Phys. Res. B* 379, 119–125. doi:10.1016/j.nimb.2016.04.020
- Herbst, R. S., Baron, P., and Nilsson, M. (2011). *Standard and advanced separation: PUREX processes for nuclear fuel reprocessing, advanced separation techniques for nuclear fuel reprocessing and radioactive waste treatment*. Cambridge: Woodhead Publishing, 141–175. doi:10.1533/9780857092724.2.141
- Hopf, J., Eskelsen, J. R., Chiu, M., Levlev, A. V., Ovchinnikova, O. S., Leonard, D., et al. (2018). Toward an understanding of surface layer formation, growth, and transformation at the glass–fluid interface. *Geochim. Cosmochim. Acta* 229, 65–84. doi:10.1016/j.gca.2018.01.035
- Hyatt, N. C., and Ojovan, M. I. (2019). Special issue: materials for nuclear waste immobilization. *Materials* 12 (21), 3611. doi:10.3390/ma12213611
- IAEA Safety Standards (2009). Classification of radioactive waste for protecting people and the environment No. GSG-1 general safety guide. Available at: <http://www-ns.iaea.org/standards>.
- IAEA (2017). *Selection of technical solutions for the management of radioactive waste*. Vienna, Austria: IAEA TECDOC SERIES.
- Inagaki, Y., Kikunaga, T., Idemitsu, K., and Arima, T. (2013). Initial dissolution rate of the international simple glass as a function of pH and temperature measured using microchannel flow-through test method. *Int. J. Appl. Glass Sci.* 4, 317–327. doi:10.1111/IJAG.12043
- Jantzen, C. M. (2011). “Development of glass matrices for high level radioactive wastes,” in *Handbook of advanced radioactive waste conditioning technologies* (Cambridge: Woodhead Publishing), 230–292. doi:10.1533/9780857090959.2.230
- Jantzen, C. M., Lee, W. E., and Ojovan, M. I. (2013). “Radioactive waste (RAW) conditioning, immobilization, and encapsulation processes and technologies: overview and advances,” in *Radioactive waste management and contaminated site clean-up: Processes, technologies and international experience* (Cambridge: Woodhead Publishing), 171–272. doi:10.1533/9780857097446.1.171
- Jantzen, C. M., and Ojovan, M. I. (2019). On selection of matrix (wasteform) material for higher activity nuclear waste immobilization (review). *Russ. J. Inorg. Chem.* 64, 1611–1624. doi:10.1134/S0036023619130047
- Jegadeesan, P., Amirthapandian, S., Joseph, K., David, C., Panigrahi, B. K., and Kutty, K. V. G. (2015). Ion irradiation induced crystallization in iron phosphate glass – TEM investigations. *Adv. Mater. Lett.* 6, 224–227. doi:10.5185/amlett.2015.5725
- Jo, Y., Garbev, K., Çevirir-Papaioannou, N., Blanco, O. D., de Blochouse, B., Altmaier, M., et al. (2022). Solubility of niobium(V) in cementitious systems relevant for nuclear waste disposal: characterization of the solubility-controlling solid phases. *J. Hazard. Mater.* 440, 129810. doi:10.1016/J.JHAZMAT.2022.129810
- Kavaz, E., El Agawany, F. I., Tekin, H. O., Perişanoğlu, U., and Rammah, Y. S. (2020). Nuclear radiation shielding using barium borosilicate glass ceramics. *J. Phys. Chem. Solids* 142, 109437. doi:10.1016/j.jpcs.2020.109437
- Khan, S., Syed, A. T., Ahmad, R., Rather, T. A., Ajad, M., and Jan, F. A. (2010). Radioactive waste management in a hospital. *Int. J. Health Sci.* 4 (1), 39–46.
- Kim, M., and Heo, J. (2015). Calcium-borosilicate glass-ceramics wasteforms to immobilize rare-earth oxide wastes from pyro-processing. *J. Nucl. Mater.* 467, 224–228. doi:10.1016/j.jnucmat.2015.09.040
- Kinsho, M., Saito, Y., Nishizawa, D., and Michizono, S. (2003). 2.5 MeV electron irradiation effect of alumina ceramics. *J. Nucl. Mater.* 318, 307–312. doi:10.1016/S0022-3115(03)00018-7
- Knox, M., and Copley, G. (1997). Use of microwave radiation for the processing of glass. *Glass Technol.* 38, 91–96.
- Konon, M., Antropova, T., Zolotov, N., Simonenko, T., Simonenko, N., Brazovskaya, E., et al. (2022). Chemical durability of the iron-containing sodium borosilicate glasses. *J. Non Cryst. Solids* 584, 121519. doi:10.1016/j.jnoncrysol.2022.121519
- Kumari, I., Kumar, B. V. R., and Khanna, A. (2020). A review on UREX processes for nuclear spent fuel reprocessing. *Nucl. Eng. Des.* 358, 110410. doi:10.1016/J.NUCENGDES.2019.110410
- Lang, M., Zhang, F., Li, W., Severin, D., Bender, M., Klamünzer, S., et al. (2012). Swift heavy ion-induced amorphization of CaZrO₃ perovskite. *Nucl. Instrum. Methods Phys. Res. B* 286, 271–276. doi:10.1016/j.nimb.2011.12.028
- Lee, W. E., Ojovan, M. I., Stennett, M. C., and Hyatt, N. C. (2006). Immobilisation of radioactive waste in glasses, glass composite materials and ceramics. *Adv. Appl. Ceram.* 105, 3–12. doi:10.1179/174367606X81669

- Lee, W. E., Ojovan, M. I., and Jantzen, C. M. (2013b). *Radioactive waste management and contaminated site clean-up processes, technologies and international experience*. Amsterdam, Netherlands: Elsevier.
- Lee, W. E., Ojovan, M. I., and Jantzen, C. M. (2013a). *Radioactive waste management and contaminated site clean-up: Processes, technologies and international experience*. Cambridge: Woodhead Publishing.
- Li, H., Wu, L., Xu, D., Wang, X., Teng, Y., and Li, Y. (2015). Structure and chemical durability of barium borosilicate glass-ceramics containing zirconolite and titanite crystalline phases. *J. Nucl. Mater.* 466, 484–490. doi:10.1016/j.jnucmat.2015.08.031
- Li, J., Xu, D., Wang, X., Liu, K., Mao, Y., Wang, M., et al. (2021). Encapsulation of cesium with a solid waste-derived sulfoaluminate matrix: A circular economy approach of treating nuclear wastes with solid wastes. *J. Hazard. Mater.* 416, 126156. doi:10.1016/j.jhazmat.2021.126156
- Li, W., Ding, X., Meng, C., Ren, C., Wu, H., and Yang, H. (2018). Phase structure evolution and chemical durability studies of Gd_{1-x}Yb_xPO₄ ceramics for immobilization of minor actinides. *J. Mater. Sci.* 53, 6366–6377. doi:10.1007/S10853-018-2031-Z
- Luo, S., Xu, Z., Liu, J., Xu, B., Ji, S., Ding, Y., et al. (2021). The solubility, microstructure, and chemical durability of Ce-doped YIG ceramics designed as actinide waste forms. *Int. J. Energy Res.* 45, 19883–19894. doi:10.1002/ER.7058
- Ma, J., Fang, Z., Yang, X., Wang, B., Luo, F., Zhao, X., et al. (2021). Investigating hollandite-perovskite composite ceramics as a potential waste form for immobilization of radioactive cesium and strontium. *J. Mater. Sci.* 56, 9644–9654. doi:10.1007/S10853-021-05886-2
- Ma, L., Brow, R. K., and Schlesinger, M. E. (2017). Dissolution behavior of Na₂O–FeO–Fe₂O₃–P₂O₅ glasses. *J. Non Cryst. Solids.* 463, 90–101. doi:10.1016/j.jnncryst.2017.02.022
- Maddrell, E. R. (2001). Generalized titanate ceramic waste form for advanced purex reprocessing. *J. Am. Ceram. Soc.* 84, 1187–1189. doi:10.1111/j.1151-2916.2001.tb00814.x
- Mahmoudyseppehr, M., and Marghussian, V. K. (2009). SiO₂–PbO–CaO–ZrO₂–TiO₂–(B₂O₃–K₂O), A new zirconolite glass–ceramic system: crystallization behavior and microstructure evaluation. *J. Am. Ceram. Soc.* 92, 1540–1546. doi:10.1111/j.1551-2916.2009.03095.X
- Mandal, A. K., and Sen, R. (2017). An overview on microwave processing of material: A special emphasis on glass melting. *Mater. Manuf. Process.* 32, 1–20. doi:10.1080/10426914.2016.1151046
- Mandal, A., and Sen, R. (2015). Microwave absorption of barium borosilicate, zinc borate, Fe-doped aluminophosphate glasses and its raw materials. *Technol. (Basel)* 3, 111–125. doi:10.3390/technologies3020111
- Mascarque, N., Januchta, K., Frederiksen, K. F., Youngman, R. E., Bauchy, M., and Smedskjaer, M. M. (2019). Structural dependence of chemical durability in modified aluminoborate glasses. *J. Am. Ceram. Soc.* 102, 1157–1168. doi:10.1111/jace.15969
- McCloy, J. S., and Goel, A. (2017). Glass-ceramics for nuclear-waste immobilization. *MRS Bull.* 42 (3), 233–240. doi:10.1557/MRS.2017.8
- Meegoda, J. N., Ezeldin, A. S., Fang, H. Y., and Inyang, H. I. (2003). Waste immobilization technologies. *Pract. Periodical Hazard. Toxic, Radioact. Waste Manag.* 7, 46–58. doi:10.1061/(ASCE)1090-025X(2003)7:1(46)
- Meng, C., Li, W., Ren, C., and Zhao, J. (2020). Structure and chemical durability studies of powellite ceramics Ca_{1-x}Lix/2Gdx/2MoO₄ (0 ≤ x ≤ 1) for radioactive waste storage. *J. Mater. Sci.* 55, 2741–2749. doi:10.1007/S10853-019-04223-Y
- Mir, A. H., Hyatt, N. C., and Donnelly, S. E. (2021). An *in-situ* TEM study into the role of disorder, temperature and ballistic collisions on the accumulation of helium bubbles and voids in glass-ceramic composites. *J. Nucl. Mater.* 548, 152836. doi:10.1016/j.jnucmat.2021.152836
- Mohapatra, M., Mishra, R. K., Kaushik, C. P., and Tomar, B. S. (2014). Investigation of radiation damage in Trombay nuclear waste glasses by ESR and photoluminescence techniques. *Procedia Mater. Sci.* 7, 247–251. doi:10.1016/j.mspro.2014.10.032
- National Research Council (2011). *Waste forms technology and performance: Final report*. Washington, DC: The National Academies Press. doi:10.17226/13100
- Neeway, J., Abdelouas, A., Grambow, B., and Schumacher, S. (2011). Dissolution mechanism of the SON68 reference nuclear waste glass: new data in dynamic system in silica saturation conditions. *J. Nucl. Mater.* 415, 31–37. doi:10.1016/j.jnucmat.2011.05.027
- Neeway, J. J., Rieke, P. C., Parruzot, B. P., Ryan, J. V., and Asmussen, R. M. (2018). The dissolution behavior of borosilicate glasses in far-from equilibrium conditions. *Geochim. Cosmochim. Acta.* 226, 132–148. doi:10.1016/j.gca.2018.02.001
- Nesbitt, H. W., Bancroft, G. M., Fyfe, W. S., Karkhanis, S. N., Nishijima, A., and Shin, S. (1981). Thermodynamic stability and kinetics of perovskite dissolution. *Nature* 289, 358–362. doi:10.1038/289358A0
- Ojovan, M. I., and Batyukhnova, O. G. (2019). *Glasses for nuclear waste immobilization*. Tucson, AZ: WM'07 Conference.
- Ojovan, M. I., Hand, R. J., Ojovan, N. V., and Lee, W. E. (2005). Corrosion of alkali-borosilicate waste glass K-26 in non-saturated conditions. *J. Nucl. Mater.* 340, 12–24. doi:10.1016/j.jnucmat.2004.10.095
- Ojovan, M. I., Juoi, J. M., Boccaccini, A. R., and Lee, W. E. (2008). *Glass composite materials for nuclear and hazardous waste immobilisation*. Cambridge, UK: Cambridge University Press. doi:10.1557/PROC-1107-245
- Ojovan, M. I., and Lee, W. E. (2014). *Immobilisation of radioactive wastes in glass, an introduction to nuclear waste immobilisation*, 245–282. doi:10.1016/B978-0-08-099392-8.00017-6
- Ojovan, M. I., Lee, W. E., and Kalmykov, S. N. (2019). *An introduction to nuclear waste immobilisation*. Amsterdam, Netherlands: Elsevier.
- Ojovan, M. I. (2023). Nuclear waste disposal. *Nucl. waste Dispos. Encycl.* 3 (2), 419–429. doi:10.3390/encyclopedia3020028
- Ojovan, M. I., Petrov, V., and Yudinsev, S. V. (2021). Glass crystalline materials as advanced nuclear wasteforms. *Sustainability* 13 (8), 4117. doi:10.3390/su13084117
- Orlova, A. I., and Ojovan, M. I. (2019). Ceramic mineral waste-forms for nuclear waste immobilization. *Mater. (Basel)* 12 (16), 2638. doi:10.3390/ma12162638
- Pierce, E. M., Reed, L. R., Shaw, W. J., McGrail, B. P., Icenhower, J. P., Windisch, C. F., et al. (2010). Experimental determination of the effect of the ratio of B/Al on glass dissolution along the nepheline (NaAlSiO₄)–malinkoite (NaBSiO₄) join. *Geochim. Cosmochim. Acta.* 74 (9), 2634–2654. doi:10.1016/j.gca.2009.09.006
- Pilania, R. K., Pathak, N., Saini, M., Sooraj, K. P., Ranjan, M., and Dube, C. L. (2023). Synthesis of the chemically durable glass-ceramic matrix for radioactive waste immobilisation. *Ceram. Int.* 49, 15931–15938. doi:10.1016/j.ceramint.2023.01.188
- Rao, K. R. (2001). Radioactive waste: the problem and its management. *Curr. Sci. Assoc.* 81 (12), 1534–1546.
- Rawlings, R. D., Wu, J. P., and Boccaccini, A. R. (2006). Glass-ceramics: their production from wastes-A review. *J. Mater. Sci.* 41, 733–761. doi:10.1007/S10853-006-6554-3
- Ringwood, A. E., Kesson, S. E., Ware, N. G., Hiberson, W., and Major, A. (1979). Immobilisation of high-level nuclear reactor wastes in SYNROC. *Nature* 278, 219–223. doi:10.1038/278219a0
- Ringwood, A. E. (1978). *Safe disposal of high-level nuclear reactor wastes: A new strategy*. RG Menzies: Australian National University Press.
- Roessler, J. G., Townsend, T. G., and Ferraro, C. C. (2015). Use of leaching tests to quantify trace element release from waste to energy bottom ash amended pavements. *J. Hazard. Mater.* 300, 830–837. doi:10.1016/j.jhazmat.2015.08.028
- Rossell, H. J. (1992). Solid solution of metal oxides in the zirconolite phase CaZrTi₃O₇. II: the ternary phase CaZr_xTi_{3-x}O₇. *J. solid state Chem.* 99, 52–57. doi:10.1016/0022-4596(92)90287-6
- Sattonnag, G., Moll, S., Herbst-Ghysel, M., Legros, C., Costantini, J.-M., and Thomé, L. (2008). Mechanical stresses induced in ceramic oxides by ion irradiation. *Nucl. Instrum. Methods Phys. Res. B* 266 (12–13), 3052–3056. doi:10.1016/j.nimb.2008.03.162
- Shamblin, J., Tracy, C. L., Ewing, R. C., Zhang, F., Li, W., Trautmann, C., et al. (2016). Structural response of titanate pyrochlores to swift heavy ion irradiation. *Acta Mater* 117, 207–215. doi:10.1016/j.actamat.2016.07.017
- Shelby, J. E. (2020). *Introduction to glass science and technology*. London, UK: Royal Society of Chemistry. doi:10.1039/9781839169229
- Stefanovsky, S. v., Stefanovsky, O. I., Prusakov, I. L., Kadyko, M. I., Nikonov, B. S., and Glazkova, I. S. (2019). Simulation of radioactive decay by barium substitution for cesium in sodium aluminum-iron phosphate glass. *J. Radioanal. Nucl. Chem.* 319, 817–826. doi:10.1007/s10967-018-6365-4
- Stone-Weiss, N., Youngman, R. E., Thorpe, R., Smith, N. J., Pierce, E. M., and Goel, A. (2020). An insight into the corrosion of alkali aluminoborosilicate glasses in acidic environments. *Phys. Chem. Chem. Phys.* 22, 1881–1896. doi:10.1039/C9CP06064B
- Strachan, D. M., Turcotte, R. P., and Barnes, B. O. (1982). MCC-1: A standard leach test for nuclear waste forms. *Nucl. Technol.* 56 (2), 306–312. doi:10.1318/NT82-A32859
- Sun, K., Ding, T., Wang, L. M., and Ewing, R. C. (2003). Radiation-induced nanostructures in an iron phosphate glass. *MRS Proc.* 792, R3.21. doi:10.1557/PROC-792-R3.21
- Tang, M., Kossov, A., Jarvinen, G., Crum, J., Turo, L., Riley, B., et al. (2014). Radiation stability test on multiphase glass ceramic and crystalline ceramic waste forms. *Nucl. Instrum. Methods Phys. Res. B* 326, 293–297. doi:10.1016/j.nimb.2013.10.092
- Taylor, C. A., Patel, M. K., Aguiar, J. A., Zhang, Y., Crespillo, M. L., Wen, J., et al. (2016). Bubble formation and lattice parameter changes resulting from He irradiation of defect-fluorite Gd₂Zr₂O₇. *Acta Mater* 115, 115–122. doi:10.1016/j.actamat.2016.05.045
- Techer, I., Advocat, T., Lancelot, J., and Liotard, J.-M. (2001). Dissolution kinetics of basaltic glasses: control by solution chemistry and protective effect of the alteration film. *Chem. Geol.* 176 (1–4), 235–263. doi:10.1016/S0009-2541(00)00400-9
- Thorpe, C. L., Neeway, J. J., Pearce, C. I., Hand, R. J., Fisher, A. J., Walling, S. A., et al. (2021). Forty years of durability assessment of nuclear waste glass by standard methods. *Npj Mater. Degrad.* 5 (1), 61–28. doi:10.1038/s41529-021-00210-4
- Varshneya, A. K., and Mauro, J. C. (2019). *Fundamentals of inorganic glasses, fundamentals of inorganic glasses*. Amsterdam, Netherlands: Elsevier, 1–735. doi:10.1016/C2017-0-04281-7
- Wang, L., and Liang, T. (2012). Ceramics for high level radioactive waste solidification. *J. Adv. Ceram.* 1, 194–203. doi:10.1007/s40145-012-0019-8
- Wang, T. T., Zhang, X. Y., Sun, M. L., Du, X., Guan, M., Peng, H. B., et al. (2020). γ-Irradiation effects in borosilicate glass studied by EPR and UV–Vis spectroscopies. *Nucl. Instrum. Methods Phys. Res. B* 464, 106–110. doi:10.1016/j.nimb.2019.12.007

- Wang, X., Wu, L., Li, H., Xiao, J., Cai, X., and Teng, Y. (2017). Preparation and characterization of SO_3 -doped barium borosilicate glass-ceramics containing zirconolite and barite phases. *Ceram. Int.* 43, 534–539. doi:10.1016/j.ceramint.2016.09.190
- Weber, W. J., Ewing, R. C., Catlow, C. R. A., de la Rubia, T. D., Hobbs, L. W., Kinoshita, C., et al. (1998). Radiation effects in crystalline ceramics for the immobilization of high-level nuclear waste and plutonium. *J. Mater. Res.* 13, 1434–1484. doi:10.1557/JMR.1998.0205
- Weber, W. J., Navrotsky, A., Stefanovsky, S., Vance, E. R., and Vernaz, E. (2009). Materials science of high-level nuclear waste immobilization. *MRS Bull.* 34, 46–53. doi:10.1557/mrs2009.12
- Wei, G., Shu, X., Wen, M., Lu, Y., Duan, T., Chen, S., et al. (2022). Immobilization mechanism of $\text{Gd}_2\text{Zr}_2\text{O}_7$ ceramic for nuclear waste treatment. *Ceram. Int.* 48, 37164–37173. doi:10.1016/j.ceramint.2022.08.292
- Wei, Z. J., Blackburn, L. R., Gardner, L. J., Tan, S. H., Sun, S. K., Guo, W. M., et al. (2020). Rapid synthesis of zirconolite ceramic wasteform by microwave sintering for disposition of plutonium. *J. Nucl. Mater.* 539, 152332. doi:10.1016/j.jnucmat.2020.152332
- Wilkinson, C. J., Doss, K., Hahn, S. H., Keilbart, N., Potter, A. R., Smith, N. J., et al. (2019). Topological control of water reactivity on glass surfaces: evidence of a chemically stable intermediate phase. *J. Phys. Chem. Lett.* 10, 3955–3960. doi:10.1021/acs.jpclett.9b01275
- Wu, K., Wang, F., Liao, Q., Zhu, H., Liu, D., and Zhu, Y. (2020). Synthesis of pyrochlore-borosilicate glass-ceramics for immobilization of high-level nuclear waste. *Ceram. Int.* 46, 6085–6094. doi:10.1016/j.ceramint.2019.11.071
- Wu, L., Li, H., Wang, X., Xiao, J., Teng, Y., Li, Y., et al. (2016). Effects of Nd content on structure and chemical durability of zirconolite–barium borosilicate glass-ceramics. *J. Am. Ceram. Soc.* 99, 4093–4099. doi:10.1111/JACE.14440
- Wu, L., Xiao, J., Wang, X., Teng, Y., Li, Y., and Liao, Q. (2018). Crystalline phase, microstructure, and aqueous stability of zirconolite–barium borosilicate glass-ceramics for immobilization of simulated sulfate bearing high-level liquid waste. *J. Nucl. Mater.* 488, 241–248. doi:10.1016/j.jnucmat.2017.10.031
- Xu, H., and Wang, Y. (2000). Crystallization sequence and microstructure evolution of Synroc samples crystallized from $\text{CaZrTi}_2\text{O}_7$ melts. *J. Nucl. Mater.* 279, 100–106. doi:10.1016/S0022-3115(99)00272-X
- Yang, K., Zhu, W., Scott, S., Wang, Y., Wang, J., Riley, B. J., et al. (2020). Immobilization of cesium and iodine into $\text{Cs}_3\text{Bi}_2\text{I}_9$ perovskite-silica composites and core-shell waste forms with high waste loadings and chemical durability. *J. Hazard. Mater.* 401, 123279. doi:10.1016/j.jhazmat.2020.123279
- Yang, R., Liu, H., Ding, Z., Zheng, J., Mauro, J. C., Kim, S. H., et al. (2021). Chemical durability of borosilicate pharmaceutical glasses: mixed alkaline earth effect with varying $[\text{MgO}]/[\text{CaO}]$ ratio. *J. Am. Ceram. Soc.* 104, 3973–3981. doi:10.1111/jace.17850
- Yang, T., Huang, X., Gao, Y., Wang, C., Zhang, Y., Xue, J., et al. (2012). Damage evolution of yttria-stabilized zirconia induced by He irradiation. *J. Nucl. Mater.* 420, 430–436. doi:10.1016/j.jnucmat.2011.10.033
- Yang, T., Taylor, C. A., Wang, C., Zhang, Y., Weber, W. J., Xiao, J., et al. (2015a). Effects of He irradiation on yttria-stabilized zirconia ceramics. *J. Am. Ceram. Soc.* 98, 1314–1322. doi:10.1111/jace.13423
- Yang, Y., Luo, S., Dong, F., Chen, Q., and Yang, M. (2015b). Response of strontium titanate to electron irradiation for the immobilization of strontium. *J. Radioanal. Nucl. Chem.* 303, 341–345. doi:10.1007/s10967-014-3356-y
- Zanotto, E. D. (2010). A bright future for glass-ceramics. *Am. Ceram. Soc. Bull.* 89, 19–27.
- Zhang, J., Wang, Y. Q., Tang, M., Sun, C., Yin, D. M., and Li, N. (2015). Helium irradiation induced micro-swelling and phase separation in pyrochlore $\text{Lu}_2\text{Ti}_2\text{O}_7$. *Nucl. Instrum. Methods Phys. Res. B* 342, 179–183. doi:10.1016/j.nimb.2014.09.036
- Zhang, Y., Kong, L., Ionescu, M., and Gregg, D. J. (2022). Current advances on titanate glass-ceramic composite materials as waste forms for actinide immobilization: A technical review. *J. Eur. Ceram. Soc.* 42 (5), 1852–1876. doi:10.1016/j.jeurceramsoc.2021.12.077
- Zhu, H., Wang, F., Liao, Q., Liu, D., and Zhu, Y. (2019). Structure features, crystallization kinetics and water resistance of borosilicate glasses doped with CeO_2 . *J. Non Cryst. Solids* 518, 57–65. doi:10.1016/j.jnoncrsol.2019.04.044
- Zhu, H., Wang, F., Liao, Q., Wang, Y., and Zhu, Y. (2020a). Effect of CeO_2 and Nd_2O_3 on phases, microstructure and aqueous chemical durability of borosilicate glass-ceramics for nuclear waste immobilization. *Mater. Chem. Phys.* 249, 122936. doi:10.1016/j.MATCHEMPHYS.2020.122936
- Zhu, H., Wang, F., Liao, Q., and Zhu, Y. (2020b). Synthesis and characterization of zirconolite-sodium borosilicate glass-ceramics for nuclear waste immobilization. *J. Nucl. Mater.* 532, 152026. doi:10.1016/j.jnucmat.2020.152026
- Zorpette, G. (1996). Hanford's nuclear wasteland. *Hanford's Nucl. Wastel. Sci. Am.* 274 (5), 88–97. doi:10.1038/scientificamerican0596-88
- Zubekhina, B. Y., Burakov, B. E., and Ojovan, M. I. (2020). Surface alteration of borosilicate and phosphate nuclear waste glasses by hydration and irradiation. *Challenges* 11 (2), 14. doi:10.3390/challe11020014



OPEN ACCESS

EDITED BY

Sam P. De Visser,
The University of Manchester,
United Kingdom

REVIEWED BY

Slavko Radenković,
University of Kragujevac, Serbia
Grant Hill,
The University of Sheffield,
United Kingdom

*CORRESPONDENCE

Walter C. Ermler,
✉ Walter.Ermler@utsa.edu

RECEIVED 05 July 2023

ACCEPTED 19 September 2023

PUBLISHED 01 November 2023

CITATION

Tchodimo FCM and Ermler WC (2023),
Theoretical and computational study of
benzenium and toluenium isomers.
Front. Chem. 11:1253599.
doi: 10.3389/fchem.2023.1253599

COPYRIGHT

© 2023 Tchodimo and Ermler. This is an
open-access article distributed under the
terms of the [Creative Commons
Attribution License \(CC BY\)](#). The use,
distribution or reproduction in other
forums is permitted, provided the original
author(s) and the copyright owner(s) are
credited and that the original publication
in this journal is cited, in accordance with
accepted academic practice. No use,
distribution or reproduction is permitted
which does not comply with these terms.

Theoretical and computational study of benzenium and toluenium isomers

Falonne C. Moumbogno Tchodimo and Walter C. Ermler*

Department of Chemistry, The University of Texas at San Antonio, San Antonio, TX, United States

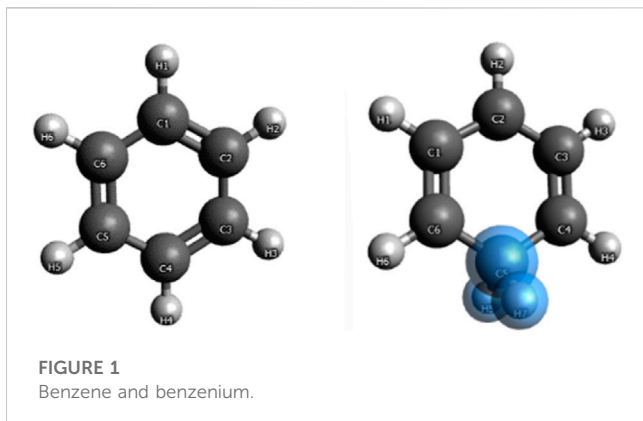
Four methods of computational quantum chemistry are used in a study of hyperconjugation in protonated aromatic molecules. Benzene, benzenium, toluene, and four isomeric forms of toluenium are examined using the self-consistent field level of theory followed by configuration interaction and coupled cluster calculations, as well as density functional theory. Results for proton affinities, geometric parameters, atomic populations, dipole moments, and polarizabilities are reported. The calculated results are in good agreement with previous computational studies and with experimental data. The presence of hyperconjugation is evident from the shortened carbon–carbon bond lengths in the aromatic ring and concomitant changes in dipole moments and polarizabilities. The proton affinities of benzene and toluene compare well with experimental values. The examination of all of the toluenium isomers reveals that the position of the methyl group has a minor impact on the strength of hyperconjugation, although the most stable isomer is found to be the para form. Mulliken population analyses indicate that the addition of a proton contributes to aromatic hyperconjugation and increases the strength of π -bonds at the expense of σ -bonds.

KEYWORDS

benzenium, toluenium, proton affinity, hyperconjugation, DFT

1 Introduction

The Baker–Nathan effect was discussed initially in 1935 (Baker and Nathan, 1935). It is rooted in the presence of additional resonance structures in certain molecules and, in general, is described as an electron density delocalization from a σ -bond to a p-orbital or a π -bond. In a series of seminal articles, Mulliken extended and generalized the Baker–Nathan concept and coined the term *hyperconjugation* (hereafter denoted as HC) (Mulliken, 1939; Rieke et al., 1941). The importance of delocalizing interactions involving σ -bonds has been examined theoretically and computationally (Reed et al., 1988). It has been reported that HC can influence conformational equilibria (Romers et al., 1969; Zefirov and Schechtman, 1971), modify reactivity (Baddeley, 1973; Chang et al., 1987), and determine selectivity (Beckwith and Duggan, 1998). Furthermore, it is has been established that the presence of HC is mainly responsible for the stability of the more highly substituted alkenes (Fox and Whitesell, 2004). The anomeric effect in the reactivity of α -haloglycine esters with various nucleophiles has been attributed to HC, leading to enhanced halogen nucleofugality which facilitates halogen abstraction by hydrogen-bond donor catalysts (Samanta and Stéphane, 2019). For example, the presence of HC has been attributed to improved catalysis in a pyridoxal 5'-phosphate-dependent enzyme (Dajnowicz et al., 2018), as well as being an important factor in stabilizing certain excited, radical, and ionic species (Muller and Mulliken, 1958; Lambert et al., 1987; Raabe et al., 1996). Davies maintained that HC activation in the presence of Sn–C bonds can accelerate a



reaction rate by more than a factor of 10^{14} (Davies, 1999). In organometallic compounds, the hyperconjugative β -proton coupling of an H-C σ -bond in a cyclic radical can be enhanced or decreased according to the symmetry of the π -orbital with which it hyperconjugates according to the so-called Whiffen effect (Davies, 1999). Ermler et al. (1976) carried out accurate *ab initio* self-consistent field (SCF) calculations to examine the role of HC in the benzenium and p-toluenium cations (Ermler and Mulliken, 1978). A recent study that examines the phenomenon of HC in aromatic systems is consistent with their conclusions (Xiaojuan et al., 2020).

2 Calculations

Benzene and benzenium are shown in Figure 1, and toluene and the four isomeric forms of toluenium are shown in Figure 2. The goal of the present study is to identify and codify the presence of HC in these molecules through a set of high-level calculations of energies, bond lengths, bond angles, electric dipole polarizabilities, and Mulliken populations.

The calculations reported in this study were accomplished using the Gaussian software suite (Frisch et al., 2016). SCF calculations were carried out followed by single plus double excitation configuration interaction (CISD) and coupled cluster with single and double and perturbative triple excitation (CCSD(T)) calculations. All were conducted using 6-311G** basis sets of contracted Gaussian-type

functions (Frisch et al., 2016). In addition, density functional theory (DFT) calculations using B3LYP exchange correlation functionals and 6-311G** basis sets were carried out. At each level of theory, a full geometry optimization was accomplished. The proton affinities of benzene and each toluene isomers were calculated at each level of theory. At each level of theory the proton affinity is defined as the difference between the total energy of the neutral species at its calculated equilibrium geometry less than that of the protonated species at its calculated equilibrium geometry. Finally, dipole moments, defined as expectation values of the dipole moment operator, and dipole polarizabilities, defined as the change in the dipole moment of a molecule when in a static electric field, are reported at all levels of theory (Frisch et al., 2016).

Initially, single-point energy SCF calculations were carried out to determine total energies, molecular orbital (MO) energies, Mulliken populations, and electric dipole polarizabilities. Results for the benzene systems and the toluene systems are compared to those obtained by Ermler et al. (1976) and Ermler and Mulliken (1978), respectively. These preliminary SCF calculations were followed by CISD and CCSD(T) calculations for each of these molecules, and the aforementioned properties were calculated. Additionally, the ortho, meta, and ipso forms of toluenium were also studied at the stated levels of theory. Figure 2 shows the position of the methyl group in the four isomers of protonated toluene. Datasets for the ortho, meta, para, and ipso forms of the toluenium molecules were constructed, and geometry optimizations were completed yielding equilibrium bond lengths and bond angles and the corresponding proton affinities. These structures were then used to calculate electric dipole polarizabilities and populations of each molecule.

3 Results and discussion

Table 1 compares the present results for benzene and benzenium with those of [17]. The results for toluene and toluenium are compared with those of [18] in Table 2.

The calculated results are in good agreement with those cited in both earlier studies, with differences attributable to the use of the somewhat smaller 6-311G** basis set in the current calculations compared to the σ/π -optimized polarized double zeta basis sets used in the work of Ermler et al. (1976) and Ermler and Mulliken (1978). The main differences in total energies are due to a more rigorous

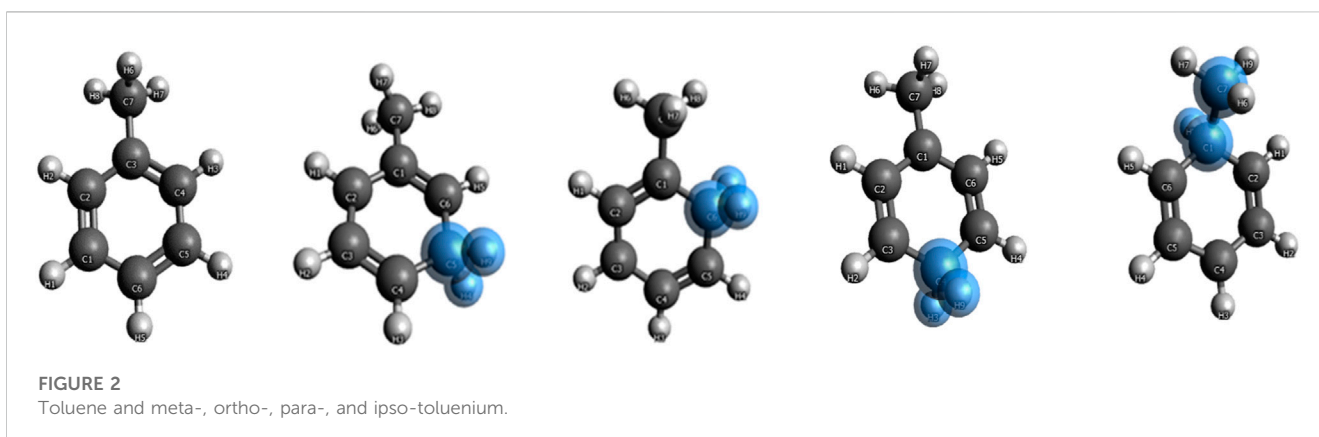
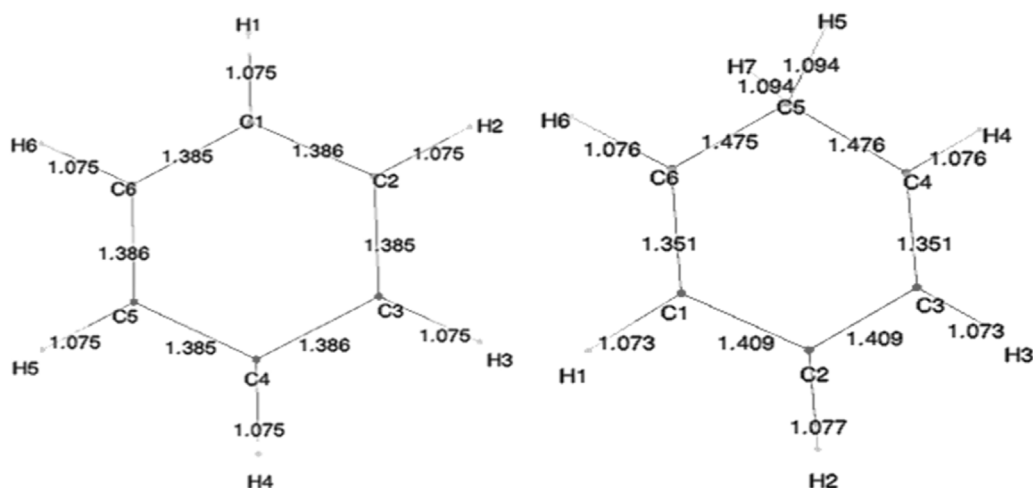


TABLE 1 Calculated total SCF energy, HOMO energy, and proton affinity for benzene and benzenium compared to the work of Ermler et al. (1976) (a.u.).

Source	Benzene		Benzenium	
	Ermler et al.	Calculated	Ermler et al.	Calculated
Total energy (a.u.)	−230.7771	−230.7540	−231.0784	−231.0635
HOMO energy (a.u.)	−0.337	−0.336	−0.546	−0.561
Proton affinity (kcal/mol)	189.1	194.2	-	-

TABLE 2 Calculated total SCF energy, HOMO energy, and proton affinity for toluene and p-toluenium compared to the work of Ermler and Mulliken (1978) (a.u.).

Source	Toluene		p-Toluenium	
	Ermler et al.	Calculated	Ermler et al.	Calculated
Total energy (a.u.)	−269.8245	−269.8000	−270.1399	−270.1243
HOMO energy (a.u.)	−0.323	−0.324	−0.612	−0.554
Dipole moment (D)	−0.328	−0.336	-	
Proton affinity (kcal/mol)	197.9	203.5	-	-

**FIGURE 3**
SCF-optimized bond lengths of benzene and benzenium (Å).**TABLE 3** CISD and CCSD(T) results for benzene and benzenium.

Energy (a.u.)	Benzene	Benzenium
CISD	−231.4517	−231.7553
CCSD(T)	−231.5824	−231.8831
Proton affinity (kcal/mol) observed	178.4	-
CISD	190.5	-
CCSD(T)	188.7	-

representation of the carbon 1s core electrons by 9 s-type GTOs *versus* the standard Gaussian 6 s-type GTOs in the 6-31G** basis sets. These core energy differences do not appreciably impact the quality of the MOs that describe the C valence electrons. The calculated highest occupied molecular orbital (HOMO) energy values in Table 1 and Table 2 are in excellent agreement with the work of Ermler et al. (1976) and Ermler and Mulliken (1978). Results for HOMO energies (from natural orbitals) and for proton affinities for the CISD calculations using the same 6-311G** basis set are shown in Table 3. It is noteworthy that the

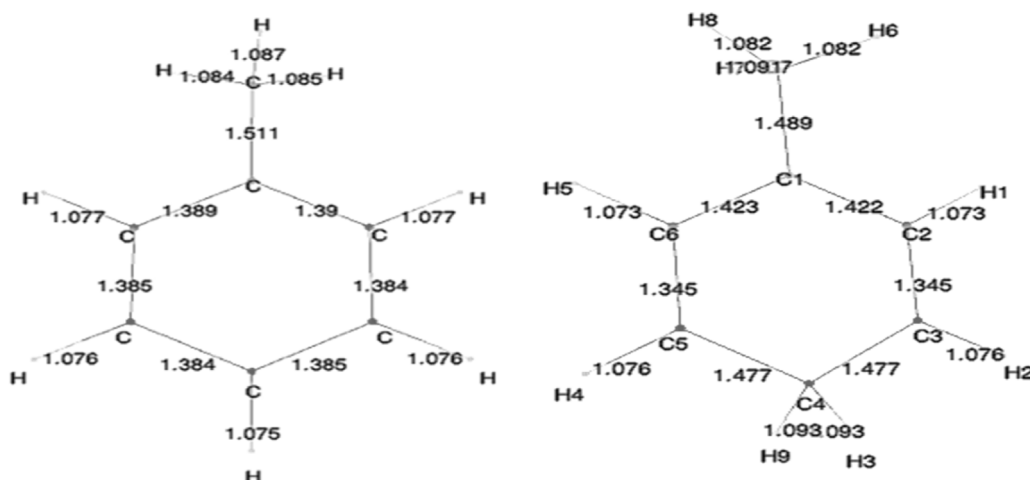


FIGURE 4
SCF-optimized bond lengths of toluene and p-toluenium (Å).

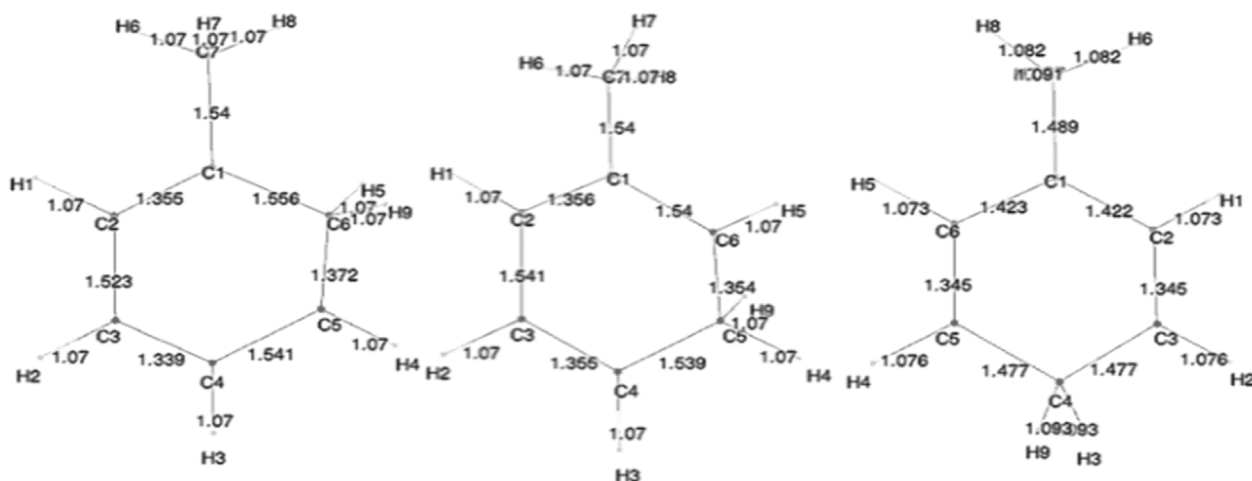


FIGURE 5
SCF-optimized bond lengths of o-, m-, and p-toluenium (Å).

CISD values for the proton affinities for benzenium and toluenium from the present calculations are in close agreement with the work of Ermler et al. (1976) and Ermler and Mulliken (1978) and with the experimentally determined (NIST Chemistry WebBook) values of 178.4 and 187.0 kcal/mol, respectively. The calculated dipole moment of toluene agrees well with the experimentally determined (NIST Chemistry WebBook) value of 0.36 D.

Geometry optimization calculations for each of the molecules were carried out at each of the levels of theory. As expected, in the presence of HC, the bond lengths of certain carbon-carbon bonds in the aromatic ring are expected to be impacted. Figure 3 shows the calculated bond lengths for benzene and benzenium, and Figure 4 shows those for toluene and toluenium.

The optimum benzene geometric parameters are in close agreement with the experiment. In the presence of HC, the bond

lengths of the C1-C6 and C3-C4 bonds are shortened whereas C1-C2, C5-C6, C5-C4, and C3-C2 are lengthened. As seen in Figure 4, which shows the bond lengths in benzenium, all of the carbon-carbon bonds are near 1.39 Å, somewhat shorter than the values of the standard value for an aromatic carbon-carbon bond length (1.47 Å). Additionally, all of the carbon-carbon bond lengths lie near the standard aromatic bond length of 1.39 Å in the toluene molecule as shown in Figure 4, indicative of the presence of HC.

In addition, the aliphatic carbon-carbon bond length (C7-C1, of 1.511 Å in toluene, shorter than the standard value of 1.54 Å) indicates the presence of HC. Furthermore, the C7-C1 bond length in toluene is calculated as 1.511 Å, but shortens to 1.489 Å in toluenium. Energies of the toluenium isomers and their respective proton affinities are reported in Table 4.

TABLE 4 Total energies, HOMOs, LUMOs, and proton affinities for toluene and the toluenium isomers.

	Toluene	o-Toluenium	m-Toluenium	p-Toluenium	ipso-Toluenium
Energy (a.u.)					
SCF	−269.8000	−270.1214	−270.1135	−270.1243	−270.1099
HOMO	−0.3235	−0.541	−0.542	−0.554	−0.553
LUMO	0.1362	−0.166	−0.173	−0.160	−0.174
CISD	−270.5619	−270.9219	−270.9149	−270.9245	−270.9109
DFT	−271.6063	−271.9496	−271.9425	−271.9516	−271.9371
CCSD(T)	−270.8216	−271.0991	−271.0928	−271.1018	−271.0886
Proton affinity of toluene Kcal/mol					
SCF	-	201.7	196.37	203.5	194.5
CISD	-	225.9	221.5	227.5	219.0
DFT	-	215.4	211.0	216.7	207.6
CCSD(T)	-	174.1	170.2	175.8	167.5

TABLE 5 Average bond lengths (Å), polarizabilities (a.u.), and HCH angles of benzene and benzenium at different levels of theory. Experimental values are shown in parentheses.

Benzene	DFT	CISD	SCF	CCSD(T)
RCH	1.08	1.08	1.08	1.09 (1.08)
RCC	1.39	1.39	1.39	1.4 (1.39)
Polarizability	59.957	57.944	58.455	57.593
Benzenium				
RCH	1.08	1.08	1.07	1.08 (1.08)
RCC	1.37	1.36	1.35	1.37 (1.36)
Polarizability	59.111	57.853	57.411	58.892
∠(HCH)	100°	103°	103°	102°

Calculations of electric dipole polarizabilities of benzene, benzenium, toluene, and all toluenium isomers at the optimized geometries were carried out at different levels of theory [SCF, DFT (B3LYP), CISD, and CCSD(T)]. As is shown, the SCF polarizability of benzene is calculated to be 58.45 a.u. compared to that of benzenium, which is smaller by 1.04 a.u. Also shown are the electric dipole polarizabilities calculated at the CISD level of theory, with the benzenium value smaller by 0.8 a.u. The electric dipole polarizability of toluene is 70.36 a.u., compared to that of toluenium, which is smaller by 0.48 a.u. As shown, the calculated values for both benzene and toluenium are all lower than the experimentally determined values (NIST Chemistry WebBook). Furthermore, the differences in polarizabilities between the neutral and protonated molecules indicate a tightening of the electron clouds for the latter, with the effect more pronounced for toluene.

The different structural isomers of toluenium were examined following geometry optimization calculations on each of the isomers. Examination of the methyl group at different positions (ortho, meta, para, or ipso [Figure 2](#)) is important because in

TABLE 6 Average bond lengths (Å), polarizabilities (a.u.), and HCH angles of toluene and toluenium isomers at different levels of theory. Experimental values are shown in parentheses.

Toluene	DFT	CISD	SCF	CCSD(T)
RCH	1.08	1.08	1.08	1.09 (1.08)
RCC	1.39	1.39	1.38	1.4 (1.39)
Polarizability	73.232	69.750	70.358	69.442
m-Toluenium	DFT	CISD	SCF	CCSD(T)
RCH	1.08	1.08	1.08	1.09
RCC	1.37	1.36	1.35	1.37
Polarizability	70.502	67.873	67.858	65.598
o-Toluenium	DFT	CISD	SCF	CCSD(T)
RCH	1.08	1.08	1.07	1.08
RCC	1.36	1.35	1.34	1.37
Polarizability	72.970	70.421	69.681	72.106
p-Toluenium	DFT	CISD	SCF	CCSD(T)
RCH	1.08	1.08	1.07	1.07
RCC	1.36	1.35	1.35	1.36
Polarizability	71.798	69.036	68.590	70.257
ipso-Toluenium	DFT	CISD	SCF	CCSD(T)
RCH	1.08	1.08	1.07	1.08
RCC	1.37	1.36	1.34	1.36
Polarizability	70.024	67.392	67.154	68.658

determining how the position of the methyl group affects HC. The results are presented in [Table 5](#) and [Table 6](#).

As can be seen in [Table 4](#), the protonation energies are relatively close to one another. That is, there are no major

TABLE 7 Comparison of Mulliken populations analyses as net charges for benzene, benzenium, toluene, and p-toluenium at the SCF and CISD levels of theory.

	Benzene	Benzenium	Toluene	p-Toluenium
SCF	C -0.099	C3 -0.113	C3 -0.076	C3 0.002
	C -0.099	C4 0.076	C1 -0.106	C1 -0.096
	C -0.099	C5 -0.113	C2 -0.114	C2 -0.014
	C -0.099	C2 -0.011	C6 -0.110	C6 -0.152
	C -0.099	C1 -0.163	C5 -0.076	C5 -0.014
	C -0.099	C6 -0.011	C4 -0.113	C4 -0.096
	H 0.099	H3 0.167	H1 0.096	H1 0.151
	H 0.099	H4 0.196	H2 0.086	H2 0.182
	H 0.099	H5 0.167	H3 0.086	H3 0.204
	H 0.099	H2 0.190	H5 0.097	H5 0.182
	H 0.099	H1 0.213	H4 0.095	H4 0.151
	H 0.099	H6 0.190	C7 -0.173	C7 -0.193
		H7 0.213	H6 0.112	H6 0.154
			H7 0.099	H7 0.181
			H8 0.096	H8 0.155
				H9 0.204
CISD	C -0.100	C3 -0.072	C3 -0.082	C3 -0.026
	C -0.100	C4 0.034	C1 -0.097	C1 -0.058
	C -0.100	C5 -0.072	C2 -0.107	C2 -0.029
	C -0.100	C2 -0.027	C6 -0.097	C6 -0.178
	C -0.100	C1 -0.190	C5 -0.082	C5 -0.029
	C -0.100	C6 -0.027	C4 -0.106	C4 -0.058
	H 0.100	H3 0.168	H1 0.095	H1 0.152
	H 0.100	H4 0.193	H2 0.085	H2 0.181
	H 0.100	H5 0.168	H3 0.085	H3 0.214
	H 0.100	H2 0.188	H5 0.095	H5 0.181
	H 0.100	H1 0.224	H4 0.094	H4 0.152
	H 0.100	H6 0.188	C7 -0.210	C7 -0.224
		H7 0.224	H6 0.119	H7 0.160
			H7 0.104	H6 0.187
			H8 0.104	H8 0.160
				H9 0.214

differences between the total energies, HOMOs, and LUMOs of o-, m-, and p-toluenium. This indicates that the methyl group position in the toluenium ion has a small impact on the strength of HC.

Figure 5 shows the bond lengths in the isomers of toluenium. The bond lengths in each molecule are similar to one other with the

TABLE 8 Overlap populations for benzene and benzenium.

	Benzene	Benzenium
C1-C2	0.514	0.391
C1-C6	0.515	0.589
C6-C5	0.514	0.389
C1-H1	0.434	0.434
C6-H5	0.038	0.030
C2-H2	0.434	0.425
C5-H7	0.038	0.395

TABLE 9 Overlap populations for toluene and toluenium isomers.

	Toluene	o-TH ⁺	m-TH ⁺	p-TH ⁺	ipso-TH ⁺
C1-C2	0.585	0.519	0.576	0.386	0.251
C2-C3	0.436	0.417	0.421	0.573	0.409
C3-C4	0.594	0.577	0.528	0.370	0.526
C4-C5	0.427	0.352	0.464	0.370	0.372
C5-C6	0.599	0.338	0.388	0.549	0.571
C6-C1	0.419	0.421	0.351	0.385	0.279
C3-C7	0.431	0.025	0.029	0.025	0.027
C7-H7	0.0003	0.0001	0.00001	0.0001	0.0004
C2-H1	0.037	0.434	0.439	0.446	0.423
C3-H2	0.039	0.431	0.426	0.424	0.431
C4-H3	0.005	0.432	0.435	0.401	0.421
C5-H9	-	0.266	-	-	-
C6-H5	0.004	0.428	0.389	0.446	0.429
C6-H9	-	-	0.274	-	-
C4-H9	-	-	-	0.398	-
C1-H9	-	-	-	-	0.037

p-toluenium showing slightly shorter bond lengths, indicating that the most stable isomer is the para form.

The mass spectrometric study of Kuck et al. (1985) on benzenium and toluenium syntheses revealed all of the structures shown in Figure 1 and Figure 2. Their results are consistent with the present calculated ones. Table 7 shows the Mulliken population analyses for benzene, benzenium, toluenium, and p-toluenium. Table 8 reports overlap populations for benzene, and Table 9 shows overlap populations for toluene and the four toluenium isomers.

The data revealed that, as the proton is added to the benzene ring, the overlap population decreases in that bond. For instance, all of the bond lengths in benzene are equal with overlap populations consistently 0.514–0.515. These are in contrast to the values of 0.389–0.391 in benzenium. This indicates that the addition of a proton contributes to the aromatic conjugation. In addition, HC affects the overlap

population by increasing the strength of the π -bond and decreasing that of the σ -bond. It is well known that HC is present in benzenium and absent in benzene. With that fact, looking at Table 9, it is seen that the π -bonds in benzene are stronger compared to the σ -bonds in benzenium. That is, the C1–C2 π -bond in benzene is 0.514, in contrast to the σ -bond in benzenium, which is 0.391. While it is expected that σ -bonds should be stronger than π -bonds, due to the presence of HC, this is reversed as seen in benzene and benzenium. The same trend is seen for toluene and toluenium isomers in terms of overlap populations (the results in Table 9 are defined with reference to Figure 2 with the exception that in toluene, C1 is C3 and C4 is C6.). In this instance, it is seen that the presence of HC bonding range is estimated to be 0.370–0.398.

As Mulliken and Ermler noted out in their analyses of other *ab initio* studies of six-membered ring molecules, all indicate that the structures have the proton attached to one carbon atom to form a CH₂ group perpendicular to the plane of the ring (Mulliken and Ermler, 1981). These earlier studies, all at the SCF level of theory, consistently predict proton affinities near 190 kcal/mol, within 10 kcal/mol of experimental values. The present correlated calculations are consistent with these SCF values, in keeping with the fact that all of the neutral and protonated molecules have the same numbers of electrons and the expectation that, in general, electron correlation does strongly impact proton affinities (Chandra and Goursot, 1996).

The Mulliken population analysis procedure was chosen to further analyze all of the SCF, CISD, CCSD(T), and DFT computational results beyond the energetics and other properties. Although it is implemented in Gaussian (Frisch et al., 2016) and nearly all currently available quantum chemistry software suites, Mulliken's method has well-known shortcomings, especially revealed in his so-called one-half overlap assignment (Mulliken and Ermler, 1977). As was carried out in our earlier calculations on benzenium (Ermler et al., 1976) and p-toluenium (Ermler and Mulliken, 1978), this work compares the results of population analyses described with the same GTO basis set and within the same level of theory, thereby providing a means by which changes in gross and overlap populations from one molecule or isomer to another can be compared in the same context.

The Mulliken population analysis method has been revisited by a host of researchers who have refined it to address its embedded constraints. Noteworthy are the development of natural bond orbitals (NBOs) by (Reed et al. (1985); Reed et al. (1988)), the atoms in molecules (AIMs) approach of Politzer et al. (1970) and Bader (1985), Roby's method based on electron density operators and projection operators (Roby, 1974), and the one based on electron localization functions (ELFs) (Silvi and Savin, 1994). In terms of the concept of hyperconjugation, the NBO method is especially compelling and can now be implemented in the context of existing software suites (Glendening et al., 2021).

There are also a number of the methods that do not deal with populations, but interpret electronic structure calculations through analyses of the molecular energy and total wave function. Two examples are the energy decomposition analysis (EDA) method (Mo et al., 2000) and a definition of aromaticity indices (Jug et al., 1991). While the analysis of molecular electronic structure calculations reported herein is based on geometric changes, protonation energies, polarizabilities, and Mulliken populations, future work that incorporates one or more of the aforementioned approaches can possibly provide additional insight into the nature of aromatic hyperconjugation.

4 Conclusion

This investigation into the effects of aromatic hyperconjugation in benzene, benzenium, toluene, and its isomers through high-level quantum chemical calculations shows good agreement with the available experimental data. The presence of HC in these molecules is evident from the observed shortening of carbon–carbon bond lengths in the aromatic ring and the diminishing of polarizabilities in the protonated forms. This phenomenon contributes to the stabilization of these molecules and can play a crucial role in determining their structural and electronic properties. The proton affinities of benzene and toluene calculated in this study are in close agreement with experimental values, further supporting the accuracy of the calculations and the role of HC in these systems.

Additionally, the investigation of all of the toluenium isomers reveals that the position of the methyl group has a minor impact on overall strength of the HC. However, the most stable isomer was found to be the para form, consistent with the influence of HC on the molecular stability and structure. The analysis of Mulliken population data further substantiates the presence of HC in the molecules, showing that the addition of a proton contributes to aromatic conjugation and strengthens π -bonds while weakening σ -bonds. This emphasizes the important role of HC in modifying electronic distributions and bonding patterns within these aromatic systems.

Overall, this investigation shed some light on the significance of hyperconjugation in aromatic molecules, highlighting its influence on structural stability, reactivity, and electronic properties. The implications of these results can be extended to various areas, including catalysis, reaction mechanisms, and the stability of aromatic species.

Data availability statement

The datasets presented in this article are not readily available. Requests to access the datasets should be directed to walter.ermler@utsa.edu.

Author contributions

FT and WE: writing – original draft.

Funding

This research was supported in part by the National Science Foundation under grant CHE-1853477. This work received computational resources from the University of Texas at San Antonio's HPC cluster operated by the Office of Information Technology and the Texas Advanced Computing Center (TACC) at the University of Texas at Austin.

Conflict of interest

The authors declare that the research was conducted in the absence of any commercial or financial relationships that could be construed as a potential conflict of interest.

Publisher's note

All claims expressed in this article are solely those of the authors and do not necessarily represent those of their affiliated

organizations, or those of the publisher, the editors, and the reviewers. Any product that may be evaluated in this article, or claim that may be made by its manufacturer, is not guaranteed or endorsed by the publisher.

References

- Baddeley, G. (1973). Delocalisation into antibond orbitals. *Tetrahedron Lett.* 14, 1645–1648. doi:10.1016/s0040-4039(01)96018-6
- Bader, R. F. W. (1985). Atoms in molecules. *Acc. Chem. Res.* 18, 9–15. doi:10.1021/ar00109a003
- Baker, J. W., and Nathan, W. S. (1935). The mechanism of aromatic side-chain reactions with special reference to the polar effects of substituents. *J. Chem. Soc.*, 1844–1847. doi:10.1039/jr9350001844
- Beckwith, A. L. J., and Duggan, P. J. (1998). The quasi-HOMO-anomeric interaction in substituted tetrahydropyranyl radicals: diastereoselectivity. *Tetrahedron* 54, 6919–6928. doi:10.1016/s0040-4020(98)00373-1
- Chandra, A. K., and Goursot, A. (1996). Calculation of proton affinities using density functional procedures: a critical study. *J. Phys. Chem.* 100, 11596–11599. doi:10.1021/jp9603750
- Chang, J. W. A., Taira, K., Urano, S., and Sorenstein, D. G. (1987). Stereoelectronic effects on the nucleophilic addition of phosphite to the carbonyl double bond. *ab initio* molecular orbital calculations on reaction surfaces and the σ -effect. *Tetrahedron* 43, 3863–3874. doi:10.1016/s0040-4020(01)81668-9
- Dajnowicz, S., Parks, J. M. P., Hu, X., Johnston, R. C., Kovalesky, A. Y., and Mueser, T. C. (2018). Hyperconjugation promotes catalysis in a pyridoxal 5'-phosphate-dependent enzyme. *ACS Catal.* 8 (7), 6733–6737. doi:10.1021/acscatal.8b01911
- Davies, A. G. (1999). The Whiffen effect of symmetry-enhanced and symmetry-forbidden hyperconjugation in spin-paired molecules. *J. Chem. Soc. Perkin Trans.*, 2461–2467. doi:10.1039/a905970i
- Ermler, W. C., and Mulliken, R. S. (1978). *Ab initio* SCF computations on toluene and the toluenium ion using a large contracted Gaussian basis set. *J. Am. Chem. Soc.* 100, 1647–1653. doi:10.1021/ja00474a001
- Ermler, W. C., Mulliken, R. S., and Clementi, E. (1976). *Ab initio* SCF computations on benzene and the benzenium ion using a large contracted Gaussian basis set. *J. Am. Chem. Soc.* 98, 388–394. doi:10.1021/ja00418a011
- Fox, M. A., and Whitesell, J. K. (2004). *Organic chemistry*. 3rd ed. Sudbury, MA, Burlington, MA: Jones and Bartlett Publishers.
- Frisch, M. J., Trucks, G. W., Schlegel, H. B., Scuseria, G. E., Robb, M. A., Cheeseman, J. R., et al. (2016). *Gaussian 16, revision C.01*. Wallingford, CT: Gaussian, Inc.
- Glendenning, E., Clark, L., and Weinhold, F. (2021). *Natural bond orbital 7.0 homepage*. Available at: <https://nbo6.chem.wisc.edu/index.htm>.
- Jug, K., and Köster, A. M. (1991). Aromaticity as a multi-dimensional phenomenon. *J. Phys. Org. Chem.* 4, 163–169. doi:10.1002/poc.610040307
- Kuck, D., Schneider, J., and Grutzmacher, H.-F. (1985). A study of gaseous benzenium and toluenium ions generated from 1,4-dihydro- and 1-methyl-1,4-dihydro-benzoic acids. *J. Chem. Soc. Perkin Trans. II*, 689–696. doi:10.1039/p29850000689
- Lambert, J. B., Wang, G.-T., Finzel, R. B., and Teramura, D. H. (1987). Stabilization of positive charge by β -silicon. *J. Am. Chem. Soc.* 109, 7838–7845. doi:10.1021/ja00259a036
- Mo, Y., Gao, J., and Peyerimhoff, S. D. (2000). Energy decomposition analysis of intermolecular interactions using a block-localized wave function approach. *J. Chem. Phys.* 112, 5530–5538. doi:10.1063/1.481185
- Muller, N., and Mulliken, R. S. (1958). Strong or isovalent hyperconjugation in some alkyl radicals and their positive ions. *J. Am. Chem. Soc.* 80, 3489–3497. doi:10.1021/ja01547a001
- Mulliken, R. S., and Ermler, W. C. (1977). *Diatom molecules: results of ab initio calculations*. Amsterdam: Elsevier. (reprinted 2012), Chap. II.
- Mulliken, R. S., and Ermler, W. C. (1981). *Polyatomic molecules: results of ab initio calculations*. Amsterdam: Elsevier. (reprinted 2012), Chap. XI.
- Mulliken, R. S. (1939). Intensities of electronic transitions in molecular spectra. IV. Cyclic dienes and hyperconjugation. *J. Chem. Phys.* 7, 339–352. doi:10.1063/1.1750446
- Politzer, P., and Harris, R. R. (1970). Properties of atoms in molecules. I. Proposed definition of the charge on an atom in a molecule. *J. Am. Chem. Soc.* 92, 6451–6454. doi:10.1021/ja00725a011
- Raabe, G., Gais, H. J., and Fleischhauer, J. (1996). *Ab initio* study of the effect of fluorination upon the structure and configurational stability of σ -sulfonyl carbanions: the role of negative hyperconjugation. *J. Am. Chem. Soc.* 118, 4622–4630. doi:10.1021/ja953034t
- Reed, A. B., Weinstock, R. B., and Weinhold, F. (1985). Natural population analysis. *J. Chem. Phys.* 83, 735–746. doi:10.1063/1.449486
- Reed, A. E., Curtiss, L. A., and Weinhold, F. (1988). Intermolecular interactions from a natural bond orbital, donor-acceptor viewpoint. *Chem. Rev.* 88, 899–926. doi:10.1021/cr00088a005
- Rieke, C. A., Brown, W. G., and Mulliken, R. S. (1941). Hyperconjugation. *J. Am. Chem. Soc.* 63, 41–56. doi:10.1021/ja01846a008
- Roby, K. R. (1974). Quantum theory of chemical valence concepts I. Definition of the charge on an atom in a molecule and of occupation numbers for electron density shared between atoms. *Mol. Phys.* 27, 81–104. doi:10.1080/00268977400100071
- Romers, C., Altona, C., Buys, H. R., and Havinga, E. (1969). Geometry and conformational properties of some five- and six membered heterocyclic compounds containing oxygen or sulfur. *Top. Stereochem.* 4, 39–97. doi:10.1002/9780470147139.ch2
- Samanta, S. S., and Stéphane, P. R. (2019). Synthesis and reactivity of α -haloglycine esters: hyperconjugation in action. *Eur. J. Org. Chem.* 2019 (39), 6597–6605. doi:10.1002/ejoc.201901033
- Silvi, B., and Savin, A. (1994). Classification of chemical bonds based on topological analysis of electron localization functions. *Nature* 371, 683–686. doi:10.1038/371683a0
- Xiaojuan, N., Yinong, Z., Gurjot, S., and Liu, F. (2020). π -Orbital Yin–Yang Kagome bands in anilato-based metal–organic frameworks. *Phys. Chem. Chem. Phys.* 44, 25827–25832. doi:10.1039/D0CP03941A
- Zefirov, N. S., and Schechtman, N. M. (1971). Anomeric effect. *Usp. Khim.* 40, 593–624.



OPEN ACCESS

EDITED BY

Claudia Espro,
University of Messina, Italy

REVIEWED BY

Kenkera Rayappa Naveen,
Julius Maximilian University of Würzburg,
Germany
Aneta Słodek,
University of Silesia in Katowice, Poland

*CORRESPONDENCE

Carolina Aliaga,
✉ carolina.aliaga@usach.cl
Enrique Orti,
✉ enrique.orti@uv.es
Raquel E. Galian,
✉ raquel.galian@uv.es
Julia Pérez-Prieto,
✉ julia.perez@uv.es

RECEIVED 11 September 2023

ACCEPTED 23 October 2023

PUBLISHED 10 November 2023

CITATION

Cortés-Villena A, Soriano-Díaz I,
Domínguez M, Vidal M, Rojas P, Aliaga C,
Giussani A, Doménech-Carbó A, Orti E,
Galian RE and Pérez-Prieto J (2023),
Governing the emissive properties of 4-
aminobiphenyl-2-pyrimidine push-pull
systems via the restricted torsion of N,N-
disubstituted amino groups.
Front. Chem. 11:1292541.
doi: 10.3389/fchem.2023.1292541

COPYRIGHT

© 2023 Cortés-Villena, Soriano-Díaz,
Domínguez, Vidal, Rojas, Aliaga, Giussani,
Doménech-Carbó, Orti, Galian and
Pérez-Prieto. This is an open-access
article distributed under the terms of the
[Creative Commons Attribution License](#)
(CC BY). The use, distribution or
reproduction in other forums is
permitted, provided the original author(s)
and the copyright owner(s) are credited
and that the original publication in this
journal is cited, in accordance with
accepted academic practice. No use,
distribution or reproduction is permitted
which does not comply with these terms.

Governing the emissive properties of 4-aminobiphenyl-2-pyrimidine push-pull systems via the restricted torsion of N,N-disubstituted amino groups

Alejandro Cortés-Villena¹, Iván Soriano-Díaz¹,
Moisés Domínguez², Matías Vidal², Pablo Rojas²,
Carolina Aliaga^{2,3*}, Angelo Giussani¹, Antonio Doménech-Carbó⁴,
Enrique Orti^{1*}, Raquel E. Galian^{1*} and Julia Pérez-Prieto^{1*}

¹Instituto de Ciencia Molecular, Universidad de Valencia, Valencia, Spain, ²Facultad de Química y Biología, Universidad de Santiago de Chile, Santiago, Chile, ³Centro para el Desarrollo de la Nanociencia y la Nanotecnología (CEDENNA), Universidad de Santiago de Chile, Santiago, Chile, ⁴Departamento de Química Analítica, Universidad de Valencia, Valencia, Spain

Donor-acceptor-substituted biphenyl derivatives are particularly interesting model compounds, which exhibit intramolecular charge transfer because of the extent of charge transfer between both substituents. The connection of a 4-[1,1'-biphenyl]-4-yl-2-pyrimidinyl moiety to differently disubstituted amino groups at the biphenyl terminal can offer push-pull compounds with distinctive photophysical properties. Herein, we report a comprehensive study of the influence of the torsion angle of the disubstituted amino group on the emissive properties of two pull-push systems: 4-[4-(4-N,N-dimethylaminophenyl)phenyl]-2,6-diphenylpyrimidine (**D1**) and 4-[4-(4-N,N-diphenylaminophenyl)phenyl]-2,6-diphenylpyrimidine (**D2**). The torsion angle of the disubstituted amino group, either N,N-dimethyl-amine or N,N-diphenyl-amine, at the biphenyl end governs their emissive properties. A drastic fluorescence quenching occurs in **D1** as the solvent polarity increases, whereas **D2** maintains its emission independently of the solvent polarity. Theoretical calculations on **D1** support the presence of a twisted geometry for the lowest energy, charge-transfer excited state ($S_{1,90}$), which corresponds to the minimum energy structure in polar solvents and presents a small energy barrier to move from the excited to the ground state, thereby favoring the non-radiative pathway and reducing the fluorescence efficiency. In contrast, this twisted structure is absent in **D2** due to the steric hindrance of the phenyl groups attached to the amine group, making the non-radiative decay less favorable. Our findings provide insights into the crucial role of the substituent in the donor moiety of donor-acceptor systems on both the singlet excited state and the intramolecular charge-transfer process.

KEYWORDS

intramolecular charge transfer, donor-acceptor systems, fluorosolvatochromism, photophysical properties, theoretical calculations

Introduction

Push–pull structures are conjugated organic molecules integrated by electron-donating and electron-withdrawing moieties separated by a π -system, which broadens the charge distribution across the molecule, endowing it with exotic optical and electronic properties (Bureš, 2014). This class of materials has been extensively used as sensitizers in dye-sensitized solar cells (DSSCs) (Verbitskiy et al., 2014; Verbitskiy et al., 2015; Tan et al., 2016; Kozlov et al., 2017; Sun et al., 2018; Verbitskiy et al., 2021b) and hole-transporting materials in perovskite-based solar cells (Maddala et al., 2021; Bouihi et al., 2022; Manda et al., 2022) owing to their high molar absorption coefficient and efficient hole mobility, respectively. Moreover, they can be integrated into organic light-emitting diodes (OLEDs) (Wong et al., 2002; Wu et al., 2002; Nakao et al., 2017; Ryutaro et al., 2018; Verbitskiy et al., 2021a) because of their high fluorescence quantum yields (Φ_F).

Pyrimidine derivatives have been used as the electron-withdrawing group in push–pull systems due to the significant π -deficient character of diazine rings (Bureš, 2014; Achelle et al., 2023). This character of the pyrimidine ring can be further increased by protonation, complexation, or alkylation of the nitrogen electron lone pair. Pyrimidine derivatives substituted with electron-donating fragments through π -conjugated linkers are highly fluorescent and sensitive to external stimuli (Achelle et al., 2023).

In general, push–pull organic chromophores play a strategic role in the development of new and sophisticated applications in photonics (Verbitskiy et al., 2021b). The optimization of the organic structure with the appropriate design of a π -electron structure has made it possible to bring these systems closer to the market. Thus, it is possible to exploit the unique properties of push–pull benzenoid derivatives and heterocyclic rings to obtain novel systems that can efficiently convert the emission of a cheap, easily available IR laser into that of a more technological valuable visible laser. Exploiting substituent effects and properly adjusting the π -electron structure can not only modulate the emission frequency, so that a whole range of laser wavelengths is accessible, but also improve upconversion efficiencies to meet market requirements (Fecková et al., 2020).

Particularly, push–pull organic systems exhibit strong fluorosolvatochromism as a consequence of the large dipole moment in the excited state (Hadad et al., 2011; Verbitskiy et al., 2014; Liu et al., 2022), thus making them interesting candidates for their application as chemical and biochemical environmental probes (Qin et al., 2021). The large Stokes shift observed upon increasing solvent polarity stems from an intramolecular relaxation process in an electronic excited state, which sometimes leads to a new energetic minimum far below the former structure in the excited state. This relaxation process typically accompanies not only changes in bond lengths and bond angles but also structural changes due to rotation around a single bond (Haberhauer, 2017).

The importance of electron-donor and acceptor groups, conjugation in the excited state, and the nature of π -bridges (particularly thiophene) has been investigated in the literature for indolo [2,3-b]quinoxaline-based dyes, aryl-substituted indolo [2,3-a]carbazole derivatives synthesized and indeno [1,2-b]indole donor derivatives (Venkateswararao et al., 2014; Yang et al., 2015; Qian et al., 2017). The solvent polarity effect has also been reported for a

large number of organic fluorophores, such as tetrazole-substituted pyrene and carbazole-substituted quinoline dyes (Slodek et al., 2019; Zych et al., 2019). Complex systems based on the D–D– π –A architecture such as new indolo [3,2,1-jk]carbazole derivatives have also been reported by Schab-Balcerzak, E. et al. for dye-sensitized solar cells. A phenothiazine unit and an acetylene linkage containing either an aldehyde or cyanoacrylic acid as electron-withdrawing groups were used, and a significant solvent effect was only observed for the cyanoacrylic acid, demonstrating the high sensitivity of the ICT state to the electronic properties of the linkage group (Gnida et al., 2022). Another D– π –D– π –A architecture reported by Schab-Balcerzak, E. et al. using a phenothiazine-based cyanoacrylic acid containing an imidazole ring substituted with the alkyl group with different chain lengths was employed. Time-resolved fluorescence studies were performed using different solvent polarities, indicating the presence of an ICT state more stabilized in polar solvents such as DMF (Zimosz et al., 2022).

The structure–fluorosolvatochromism relationship of pyrimidine-based chromophores has already been reported from an experimental point of view and using Taguchi methodology (Denneval et al., 2014; Achelle and Robin-le Guen, 2017). As a benchmark molecule that undergoes such a process, 4-(dimethylamino)benzonitrile (DMABN) has been widely used to disentangle empirical findings from a theoretical perspective. Yet, several models have been proposed for the explanation of the lower energy band exhibited by this relatively simple molecule; however, they are still under debate (Grabowski et al., 1979; Zachariasse et al., 1996; Gómez et al., 2021). First, the twisted intramolecular charge-transfer (TICT) model was proposed by Grabowski et al. to elucidate the dual fluorescence (from locally excited and intramolecular charge-transfer states) observed for DMABN in polar solvents (Grabowski et al., 1979; Grabowski et al., 2003; Sasaki et al., 2016). This model states that after the electronic excitation of DMABN in polar solvents, a charge transfer concomitantly with a ca. 90° twist of the single bond occurs, thereby electronically disconnecting the donor and acceptor moieties in the excited state. The resulting charge-transfer state is more stable than the preceding localized state (Galván et al., 2010; Segarra-Martí and Coto, 2014). The driving force for this sort of stabilization emerges from the minimization of the Coulomb interaction of the two unpaired electrons. Since the rotation leads to π -orbital decoupling, the fluorescence associated with a TICT process is typically weakened and redshifted (Haberhauer, 2017). On the other hand, Zachariasse et al. proposed the planarized intramolecular charge-transfer (PLICT) model to explain the opposite effect in which a rotation of ca. 90° leads to planarization of the donor and acceptor moieties in the excited state instead (Zachariasse et al., 1996; Zachariasse et al., 1997; Il'ichev et al., 1998). A key difference compared to the TICT process is that the fluorescence from a PLICT state to the ground state is now allowed, and thus high quantum yields are expected (Haberhauer et al., 2016).

Consequently, given the vast amount of the literature on DMABN as a model molecule that is still under discussion, we were motivated to shed light on the mechanism underlying fluorosolvatochromism that occurs in biphenylpyrimidine derivatives. The impact of the donor substituent on the optical and excited state properties of two π -extended biphenylpyrimidines

TABLE 1 Optical data (absorption and fluorescence maxima, Stokes shift, and absolute fluorescence quantum yield (Φ_F)) of **D1** and **D2** systems in solvents with a decreasing dielectric constant (ϵ) under anaerobic conditions. Fluorescence and Φ_F measurements were recorded upon excitation at 365 nm.

Sample	Solvent, dielectric constant (ϵ)	Abs. max., λ_{abs} (nm)	Fluor. max., λ_{em} (nm)	Stokes shift, $\Delta\lambda$ (nm)	Φ_F (%)	Nature of the solvent
D1	Dimethylsulfoxide (DMSO, $\epsilon = 46.7$)	265 and 376	410, 436, and 609	233	16	Polar aprotic
	Acetonitrile (ACN, $\epsilon = 37.5$)	260 and 349	418 and 593	244	19	
	Dimethylformamide (DMF, $\epsilon = 36.7$)	265 and 373	410, 438, and 588	215	29	
	Methanol (MeOH, $\epsilon = 32.7$)	260 and 361	410, 445, and 608	247	2	Polar protic
	Ethanol (EtOH, $\epsilon = 24.5$)	261 and 364	410 and 595	231	7	
	Dichloromethane (DCM, $\epsilon = 8.9$)	261 and 369	525	156	82	Medium polar
	Ethyl acetate (AcOEt, $\epsilon = 6.0$)	261 and 362	514	152	54	
	Chloroform (CHCl ₃ , $\epsilon = 4.8$)	262 and 365	497	132	41	
	Toluene (Tol, $\epsilon = 2.4$)	286 and 365	452	87	87	Non-polar
	Benzene (Bz, $\epsilon = 2.3$)	278 and 365	455	90	96	
	Hexane (Hx, $\epsilon = 1.9$)	259 and 354	403, 425, and 454	49	87	
D2	Dimethylsulfoxide (DMSO, $\epsilon = 46.7$)	287, 307, and 374	411 and 574	200	79	Polar aprotic
	Acetonitrile (ACN, $\epsilon = 37.5$)	265, 303, and 365	411 and 574	209	78	
	Dimethylformamide (DMF, $\epsilon = 36.7$)	279, 306, and 372	411 and 559	187	87	
	Methanol (MeOH, $\epsilon = 32.7$)	265, 304, and 365	411, 447, and 600	235	3	Polar protic
	Ethanol (EtOH, $\epsilon = 24.5$)	268, 305, and 367	411 and 571	204	31	
	Dichloromethane (DCM, $\epsilon = 8.9$)	269, 307, and 371	520	149	91	Medium polar
	Ethyl acetate (AcOEt, $\epsilon = 6.0$)	257, 304, and 366	493	127	82	
	Chloroform (CHCl ₃ , $\epsilon = 4.8$)	266, 308, and 372	493	121	84	
	Toluene (Tol, $\epsilon = 2.4$)	286, 306, and 373	444	71	96	Non-polar
	Benzene (Bz, $\epsilon = 2.3$)	287, 307, and 371	445	74	69	
	Hexane (Hx, $\epsilon = 1.9$)	267, 303, and 366	411, 434, and 465	45	75	

was studied. Particularly, push–pull systems which comprise a dialkylamino or diarylamino and a pyrimidine as electron-donor and -acceptor moieties, respectively, were studied by steady-state and time-resolved fluorescence techniques combined with theoretical calculations that significantly contribute to support the experimental findings.

This research contributes to expanding knowledge about the photochemical behavior and properties of simple push–pull systems and understanding of the relationship between the molecular structure of the amino donor, the solvent environment, and the fluorescence properties. This analysis can help select the right conditions for various applications in chemistry and materials science, such as sensing, imaging, and optoelectronic devices.

Materials and methods

Materials

The synthesis and characterization of the respective 2,4,6-triarylpyrimidine derivatives, 4-[4-(4-*N,N*-dimethylaminophenyl)

phenyl]-2,6-diphenylpyrimidine (**D1**) and 4-[4-(4-*N,N*-diphenylaminophenyl)phenyl]-2,6-diphenylpyrimidine (**D2**), by Rodríguez Aguilar and coworkers were reported elsewhere (Rodríguez-Aguilar et al., 2018). In brief, a microwave vial (10 mL) was charged with bromophenyl-4-pyrimidines (0.7 mmol), Pd(PPh₃)₄ (41 mg, 0.035 mmol, and 5 mol%), K₂CO₃ (97 mg and 0.7 mmol), *N,N*-dimethylformamide (5 mL), and 4-(*N,N*-dimethyl)phenylboronic acid (139 mg and 0.84 mmol) for **D1** or the 4-(*N,N*-diphenyl)phenylboronic acid (243 mg and 0.84 mmol) for **D2**. The resulting reaction mixture was heated for 1 h at 100°C. Upon the end of the reaction (as observed on TLC, *n*-hexanes/EtOAc, 5:1), the crude was diluted with water (25 mL) and extracted with EtOAc (3 × 15 mL). The combined organic extracts were dried over Na₂SO₄, and all the volatile components were removed by rotary evaporation. The respective products were purified by column chromatography (*n*-hexane: EtOAc, 20:1 → 5:1).

All commercially available solvents used for the spectroscopy investigation were purchased from Alfa Aesar and used as received without further purification. The short names of the solvents are included in Table 1.

Sample purging

A measure of 3 mL contained of optically matched **D1** or **D2** solutions at 0.1 OD at an excitation wavelength (365 nm) was purged with nitrogen directly from the cylinder (to degas air from the sample) for 5 min by placing a syringe needle through the septum into the bottom and another into the air space above the sample as a vent with a flow rate of dry nitrogen so that bubbles are observable in the sample, unless specified. In case, the solvent was evaporated upon bubbling, the cuvettes were refilled with extra purged solvent. Immediately after this procedure, samples were placed in the instrument for measurement. Cuvettes of 1 cm optical path length were used for spectroscopy studies.

Steady-state UV-vis–NIR absorption spectroscopy

Steady-state UV-vis absorption spectra were recorded on a UV/Vis/NIR PerkinElmer LAMBDA 1050 spectrophotometer equipped with deuterium and tungsten halogen light sources and Peltier-controlled InGaAs and PbS detectors covering from 175 to 3,300 nm. The absorption spectra were collected in the range of 250–700 nm.

Steady-state photoluminescence spectroscopy

Stationary fluorescence spectra were recorded on a FLS1000 photoluminescence spectrometer (Edinburgh Instruments) equipped with a 450 W ozone-free continuous xenon arc lamp and a photomultiplier (PMT-980) detector in a cooled housing with an extended spectral range of 185–980 nm. A 365 nm excitation wavelength was used in all measurements. The emission range was registered between 380 and 800 nm.

Photoluminescence quantum yield

Absolute fluorescence quantum yields (Φ_F) were recorded on a FLS1000 photoluminescence spectrometer equipped with an integrating sphere system with a reflectance higher than 99% in the range of 400–1,500 nm. Sample solutions with optical density (OD) of 0.1 at a 365 nm excitation wavelength were used to minimize re-absorption effects. For reference, the neat solvent with the same volume was used.

Time-resolved photoluminescence spectroscopy

Time-resolved fluorescence measurements were recorded on a FLS1000 photoluminescence spectrometer through the time-correlated single-photon counting (TCSPC) technique coupled with a 375 nm ps pulsed diode laser (EPL-375, pulse width: 75 ps, peak power: 140 mW, and repetition rate: 10 MHz, Edinburgh Instruments) and a microchannel plate (MCP-900) detector in a

cooled housing with a spectral range of 200–850 nm in the nanosecond domain. A Ludox solution (0.1 OD at an excitation wavelength) was used as an instrument response function (IRF). The IRF was approximately 110 ps in our setup. All spectra were recorded using a 1-cm-path-length quartz cuvette at room temperature.

Electrochemical measurements

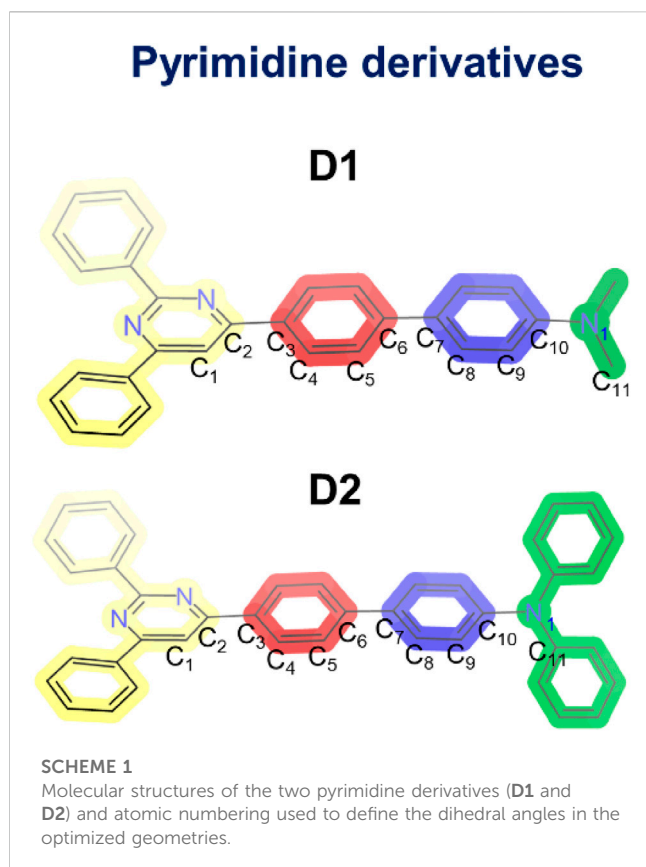
The characterization of redox properties was performed on an Autolab potentiostat (Autolab 128N potentiostat/galvanostat) using a three-electrode system. Cyclic voltammetry (CV) experiments were carried out in 0.1 M tetrabutylammonium tetrafluoroborate (TBABF₄) solution in dried acetonitrile (ACN) using Pt as a working electrode, Pt wire as an auxiliary electrode, and Ag/AgCl as a reference electrode separated from the tested solution by means of a Luggin capillary. The measurements were performed at room temperature (298 ± 1 K) partially deaerating the electrolyte solution by bubbling nitrogen for 2 min. Partially oxygenated solutions were optionally used to facilitate the use of the O₂/O₂^{•−} couple as the internal standard for electrode potential measurements. The concentration of the compounds was approximately 0.2 mM in dried acetonitrile. Experiments were performed under air conditions, with a scan rate of 100 mV/s. To evaluate the electrochemical bandgaps, potentials were referred to the Fc/Fc⁺ couple using 0.2 mM ferrocene solutions in 0.1 M TBABF₄/ACN.

Thermal measurements

The thermal properties of **D1** and **D2** were examined under a nitrogen atmosphere, with a heating rate of 10°C/min up to 950°C.

Computational details

The singlet ground state (S_0) was optimized using density functional theory (DFT) calculations. The first excited singlet state (S_1) was also optimized at the time-dependent DFT (TD-DFT) level of theory. All the calculations were performed based on the exchange-correlation Becke's three-parameter (B3LYP) functional (Lee et al., 1988; Becke, 1993) and the split-valence triple-zeta 6-311G** basis set (Francl et al., 1982), without imposing any symmetry restriction. Calculations were carried out using Gaussian 16 software (Rev. A.03) (Frisch et al., 2016). Solvent effects (hexane, toluene, ACN, and DMSO) were implicitly considered by employing the polarizable continuum model (PCM) method (Tomasi and Persico, 1994). For this reason, all the excited state geometries were obtained at the LR-PCM TD-DFT level of theory. Nevertheless, solvent effects on the photophysical processes (absorption and emission) can be inadequately reproduced using LR-PCM (Chibani et al., 2014). To solve this problem, single vertical point calculations were employed, at the optimized LR-TD-DFT geometries, using the corrected linear response (CLR-PCM) method (Improta et al., 2006; Improta et al., 2007). This approach allows to relax the interaction between the solvent and the solute molecule in the excited-state

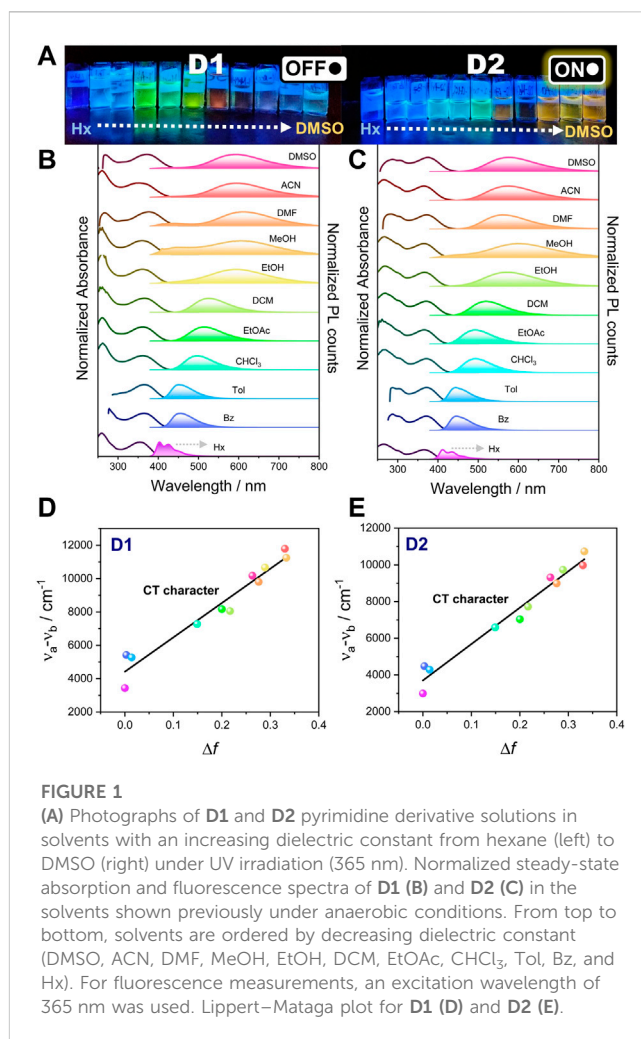


minima, thus improving the description of the excited states from an energetical point of view. All the energies discussed in the main text refer to PCM-CLR TD-DFT energies. The optimizations must be carried out at the LR-PCM TD-DFT level of theory because CLR-PCM TD-DFT is only implemented for single-point calculations. The ORCA 5.0.1 code was additionally used (Neese, 2022), employing the same computational approach (B3LYP/6-311G**) and simulating the solvent effects with CPCM methodology (Cammi et al., 2000) to characterize the minimum energy paths (MEPs) connecting two singlet excited-state minima belonging to the same potential energy surface (PES). This was accomplished by employing the climbing image nudged elastic band (CI-NEB) method (Henkelman et al., 2000). The energy of the so-obtained MEPs was then re-computed using Gaussian 16 as described previously. The computation of natural transition orbitals (NTOs) and the Mulliken population analysis were performed as implemented in Gaussian 16 (Martin, 2003; Soriano-Díaz et al., 2023).

Results and discussion

Optical and electrochemical properties

4-[4-(4-*N,N*-dimethylaminophenyl)phenyl]-2,6-diphenylpyrimidine (**D1**) and 4-[4-(4-*N,N*-diphenylaminophenyl)phenyl]-2,6-diphenylpyrimidine (**D2**) (Scheme 1) were synthesized using previously reported procedures (Rodríguez-Aguilar et al., 2018), and their procedure can be found in the Materials and Methods section. Their optical and



photophysical properties were investigated in a battery of solvents with different polarities.

The optical properties (steady-state absorption and photoluminescence) of compounds **D1** and **D2** were measured in diluted solutions of 0.1 OD at the excitation wavelength in solvents with an increasing dielectric constant at room temperature and under anaerobic conditions. The recorded absorption and emission spectra are shown in Figure 1, and the relevant optical data are summarized in Table 1. It is evident that these systems exhibit slight differences in the ground-state absorption features, which involve two major absorption bands, namely, 260–285 nm and 355–380 nm for high- and low-energy bands, respectively, and a small shoulder at approximately 303–307 nm for **D2**. The shape and energy of the absorption bands were proved to be weakly dependent on the solvent polarity (Figure 1B).

The shape and energy of the high-energy absorption band in both systems are nearly independent of the solvent polarity, whereas the low-energy band is shown to be weakly dependent on the solvent polarity, being redshifted in DMSO compared to Hx ($\Delta\lambda$ is 22 and 18 nm for **D1** and **D2**, respectively), which suggests a low molecular dipole moment in the ground state. However, the observation of a blueshift in polar protic solvents, particularly more intensified in MeOH, is attributed to the hydrogen-bond formation ability (α) of alcohol with the molecule in the ground state, which stabilizes this

state and leads to an increase in the energy gap as noted previously (Al-Ahmed et al., 2021). Interestingly, in the case of ACN, which is a highly polar solvent, there is also a significant blueshift in the low-energy absorption band compared to DMF, for which the dielectric constant is slightly lower. Then, the observed blueshift is justified by the better hydrogen-bond formation ability of ACN ($\alpha = 19$) than DMF ($\alpha = 0$).

In contrast to the absorption spectra, the fluorescence spectra under a 365 nm excitation wavelength show a strong dependence on the solvent polarity and a remarkable positive solvatochromism upon increasing the solvent dielectric constant. This fluorosolvatochromism suggests a potential intramolecular charge transfer between the donor and acceptor units in the emitting excited state, indicating that the excited state has a larger dipole moment than the ground state. The digital photographs of dye-containing solutions exhibited a wide range of colors, from deep blue to orange. In hexane, the fluorescence spectra of both compounds show that the fingerprint shape were associated with a structured emission as a result of the small solute-solvent interaction (Subuddhi et al., 2006). As the polarity of the solvent increases, the fluorescence spectrum loses its vibrational fine structure, and a broadening and bathochromic shift is observed when moving from hexane to DMSO (Table 1), thus supporting a charge-transfer character of the emitting excited state that explains the large Stokes shift observed (50–250 nm). It is worth mentioning that in polar solvents (from ethanol to DMSO), we observed the appearance of two emission bands, the higher-energy band being more pronounced in **D1** than in **D2** (Figure 1C). The coexistence of two emission bands (small contribution of the higher-energy band) can be rationally understood by the presence of two emitting species as previously observed on the vast number of push-pull systems found in the literature (Fecková et al., 2021). The higher-energy band may be ascribed to the locally excited (LE) state because of the negligible redshift as compared to the fluorescence in hexane. In contrast, the redshifted, higher-intensity emission band is attributed to the charge-transfer emitting state, which proves the large Stokes shift.

To further evaluate this, analysis using the Lippert–Mataga equation was employed in which the Stokes shift ($\Delta\nu$) is plotted as a function of the orientation polarizability (Δf) of the solvents (Equations 1, 2) (Lippert, 1955; Mataga et al., 1955):

$$\Delta\nu = \nu_a - \nu_b = \frac{2\Delta f}{hc} \frac{(\mu_E - \mu_G)^2}{a^3} + \text{constant}, \quad (1)$$

where ν_a and ν_b are the wavenumbers (cm^{-1}) of absorption and fluorescence peaks, respectively, h is the Planck's constant, c is the speed of light in vacuum, μ_E and μ_G are dipole moments in the excited and ground states, respectively, a is the radius of the Onsager cavity, and Δf is the orientation polarizability of the solvent given in the following equation:

$$\Delta f = \frac{\varepsilon - 1}{2\varepsilon + 1} - \frac{n^2 - 1}{2n^2 + 1}, \quad (2)$$

where ε and n are the dielectric constant and refractive index of the solvent, respectively. The clear linear trend in both compounds (except for hexane) indicates the increase in dipole moment in the excited state compared to the ground state and supports the ICT nature of the excited state (Figures 1D,E). The deviation of the

linearity in hexane in both compounds supports the existence of partial contribution of the LE state. A higher slope for **D1** than for **D2** suggests that it exhibits a more pronounced charge-transfer process.

Regarding the emission efficiency, both compounds exhibited high emission Φ_F in non-polar solvents such as hexane (Hx), toluene (Tol), and benzene (Bz). However, Φ_F of **D1** was significantly reduced in polar solvents such as dimethylformamide (DMF), acetonitrile (ACN), and dimethylsulfoxide (DMSO), whereas **D2** approximately maintains the high Φ_F observed in non-polar solvents (see photographs in Figure 1A and values in Table 1).

The solvent-dependent emissive properties shown in Table 1 can be classified according to the dielectric constants as follows: 1) non-polar; 2) medium polar; 3) protic polar; and 4) aprotic polar solvents (Table 1). In non-polar solvents, the fluorescence quantum yield is high because of the negligible non-radiative constants obtained for both **D1** and **D2**. In the case of solvents with intermediate polarity, the solvent polarizability (π^*) and dielectric constant (ε), could help understand the solvent-dependent photophysical behavior. For example, chloroform and ethyl acetate have π^* values of 0.58 and 0.55, respectively, i.e., a π^* value similar to toluene (0.54); however, they present an intermediate dielectric constant that deactivates **D1** in a non-radiative pathway, reducing the fluorescence quantum yield. However, DCM with higher ε in the block showed a high fluorescence quantum yield for both compounds, which can be attributed to the higher polarizability (0.82) of the solvent (Marcus, 1993).

It has been shown that the α values of chloroform and DCM play a key role in the aggregation of molecules in crystal structures and the ability to form H-bonds (Mansoor and Shafi, 2015). Chloroform and DCM present α values of 0.44 and 0.30, respectively, confirming the higher H-bond formation ability of chloroform, which consequently reduces the ICT character (Marcus, 1993). For chlorinated solvents with intermediate polarity values, the PL quantum yield could also be affected by π^* . The higher π^* for DCM (0.82) compared to chloroform (0.58) facilitates a larger ICT character, increasing the fluorescence quantum yield up to 82%. A similar behavior was observed for the D- π -D- π -A architecture where the greater the stabilized ICT state, the higher the fluorescence quantum yield (Zimosz et al., 2022).

In the polar protic solvent, the H-bond ability of alcohols and thus the α value play a key role in the ICT character and, consequently, the emissive properties (Marcus, 1993). Both molecules displayed low fluorescence Φ_F in polar protic solvents such as ethanol (EtOH) and methanol (MeOH), as previously observed for related aminopyrimidines (Herbich et al., 1992; Herbich and Waluk, 1994). Hence, Φ_F is strongly influenced by the polarity and hydrogen-bonding ability of solvents used (Pannipara et al., 2014; Kalyagin et al., 2022). Furthermore, MeOH and EtOH present the values of 0.98 and 0.86, respectively, indicating a higher hydrogen-bond formation ability for MeOH, which reduces the donor character of the substituted-amine group and, consequently, decreases the fluorescence quantum yield (2%–3%) for both systems (Anderson et al., 2019). However, a quantum yield of 31% is observed in EtOH for **D2**, suggesting a less-effective interaction of EtOH with the electron pair of the amine nitrogen due to the steric hindrance introduced by the phenyl substituents compared with the methyl groups in **D1** (7%) (Kinoshita et al., 2000).

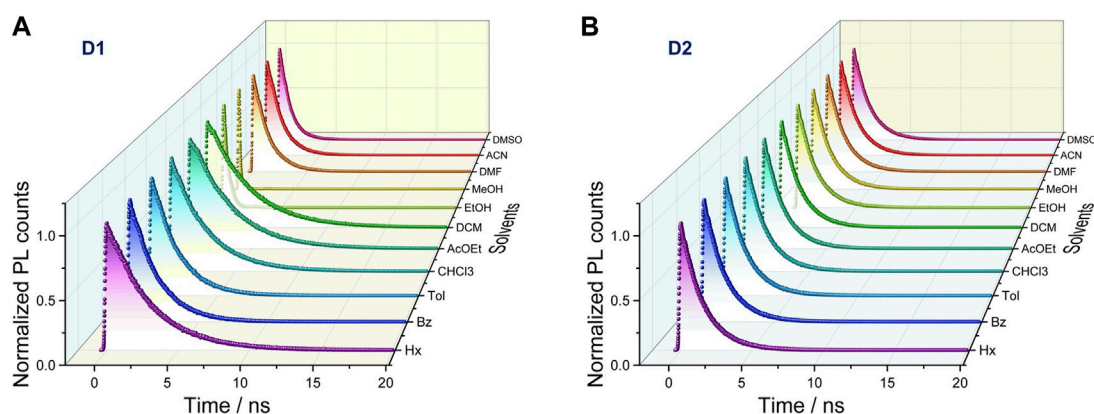


FIGURE 2

Time-resolved fluorescence spectra recorded in their maxima in different solvents under anaerobic conditions as a function of the dielectric constant for **D1** (A) and **D2** (B). An excitation wavelength of 375 nm was employed using a pulsed laser (10 MHz).

The significant redshift (35 nm) of the emission maximum in **D1** compared to **D2** in polar aprotic solvents such as DMSO could be rationalized due to a larger molecule planarization and better stabilization of the polar excited state by the solvent molecules of **D1**. Similar behavior has been observed in other systems such as *N,N'*-disubstituted dihydrodibenzo[*a,c*]phenazines (Chen et al., 2017).

Time-resolved fluorescence measurements were performed to analyze the dependence of the emissive properties of **D1** and **D2** on the dielectric constant of the solvent. The fluorescence decay profiles were recorded in all the aforementioned solvents (Figure 2 and Supplementary Table S1). Fluorescence decay traces showed a correlation of the lifetime parameter with solvent polarity only for **D2**, with lifetimes spanning from 1.51 ns to 4.64 ns from hexane to ACN. Nearly all the decays displayed a clear mono-exponential fitting, except for **D1** in DMF, ACN, and DMSO, which showed a biexponential behavior. It is worth noting that the fluorescence lifetime is drastically reduced in polar protic solvents for both compounds, and as a consequence, Φ_F decreases below 10% for **D1** (EtOH and MeOH) and to 31% and 3% for **D2** in EtOH and MeOH, respectively (Liu et al., 2022). Kinetic parameters (radiative and non-radiative rate constants) of both **D1** and **D2** systems were extracted from Φ_F and time-resolved measurements. As shown in Supplementary Table S2, the radiative rate constant (k_r) decreased as the solvent polarity increased for **D1**, whereas the non-radiative rate constant (k_{nr}) increased considerably, thus leading to a lower Φ_F . In contrast, both the radiative and non-radiative pathways decreased upon increasing the solvent polarity for **D2** (Supplementary Table S2 and Supplementary Figure S1), thus resulting in a high Φ_F even in polar solvents. These data agree with the high dependence of the emissive properties on the nature of the *N*-donor substituent of the biphenylpyrimidine push-pull systems.

The electrochemical properties of **D1** and **D2** were then characterized through cyclic voltammetry (CV) measurements, and the energies of the highest occupied (HOMO) and lowest unoccupied molecular orbital (LUMO) were estimated using the energy level of ferrocene (Fc, 4.8 eV) as an external standard and calibrated by comparing with the $E_{1/2}(\text{Fc}/\text{Fc}^+)$ half-wave electrode potential. The reduction potential of triarylpyrimidines has been

reported to be dependent on the nature of the aryl groups. The introduction of electron-donor groups would increase the reduction potential to some extent (Itami et al., 2004). Supplementary Figure S2 shows the comparison of the cyclic voltametric responses of **D1** and **D2** in partially deaerated ACN solutions. The voltammograms showed an essentially reversible couple near -0.65 V vs. Ag/AgCl, corresponding to the well-known one-electron reduction of dissolved oxygen, accompanied by an apparently irreversible cathodic signal at approximately -2.1 and -2.1 V and an apparently irreversible anodic wave at approximately 1 and 0.9 V for **D1** and **D2**, respectively. The value recorded for the reduction potential is close to that previously reported and is attributed to the introduction of one electron into the pyrimidine ring, whereas the oxidation potential arises from the strong electron-donating ability of the dimethyl/phenylamino group (Itami et al., 2004; Qiao et al., 2020).

To estimate the electrochemical bandgaps of **D1** and **D2**, we employed the following widely used equations:

$$E_{\text{HOMO}} = - \left[E_{1/2}^{\text{ox}} - E_{1/2} \left(\frac{\text{Fc}}{\text{Fc}^+} \right) + 4.8 \right] (\text{eV}), \quad (3)$$

$$E_{\text{LUMO}} = - \left[E_{1/2}^{\text{red}} - E_{1/2} \left(\frac{\text{Fc}}{\text{Fc}^+} \right) + 4.8 \right] (\text{eV}), \quad (4)$$

where E_{HOMO} and E_{LUMO} represent the energies in the vacuum scale of HOMO and LUMO, respectively; E_{ox} and E_{red} are the half-peak electrode potentials corresponding to the oxidation and reduction of the tested compounds, respectively, and the $E_{1/2}(\text{Fc}/\text{Fc}^+)$ half-wave electrode potential of the Fc/Fc⁺ couple is ca. 0.5 V under these conditions; all potentials relative to the reference electrode were used for voltametric measurements. Then, the electrochemical bandgap (ΔE^{CV}) was calculated using Eq. (5):

$$\Delta E^{\text{CV}} = E_{\text{LUMO}} - E_{\text{HOMO}}. \quad (5)$$

Since the oxidation and reduction of **D1** and **D2** are not electrochemically reversible processes, the half-wave potentials at 100 mV/s were used as approximate estimates of E_{ox} and E_{red} . The corresponding values led to the bandgaps of 3.1 ± 0.1 and 3.0 ± 0.1 eV for **D1** and **D2**, respectively. These values are consistent with the respective optical bandgaps (ΔE^{Opt}) determined for **D1** and **D2**

TABLE 2 Electrochemical data, HOMO and LUMO energies, and energy gaps obtained by cyclic voltammetry and optical measurements.

Sample	E_{ox} (V) irreversible	E_{red} (V) irreversible	E_{HOMO} (eV)	E_{LUMO} (eV)	ΔE^{CV} (eV)	ΔE^{Opt} (eV)
D1	1.0	−2.1	−5.3	−2.2	3.1	2.9
D2	0.9	−2.1	−5.2	−2.2	3.0	2.8

(2.9 and 2.8 eV) derived from the absorption onset. The energy levels obtained by CV for **D1** and **D2** are very close to each other, with the HOMO level of **D1** slightly more stabilized than that of **D2**. Table 2 summarizes the electrochemical data.

According to thermal properties (Supplementary Figure S3), both **D1** and **D2** compounds present good thermal stability at the usual annealing temperature (>100°C) required for optical device preparation, as demonstrated by thermogravimetric (TGA) and differential scanning calorimetry (DSC) analyses. The higher decomposition temperature observed for **D2** agrees with the presence of the phenyl groups in the amine-donor moiety.

Theoretical calculations

In order to explain the different optical behavior observed for **D1** and **D2**, the excited-state properties of these two molecules were theoretically investigated using DFT calculations for the ground state and TD-DFT calculations for the excited states. The geometry of the two systems was optimized, both in the ground electronic state (S_0) and in the lowest singlet excited state (S_1) at the DFT B3LYP/6-311G** and TD-DFT B3LYP/6-311G** levels of theory, respectively. Four solvents were chosen (hexane and toluene to describe the non-polar environments and ACN and DMSO to describe the polar solvents) to interpret the photophysical properties of **D1** and **D2**.

Supplementary Figure S4 shows the optimized geometries calculated for the electronic ground state (S_0) of the two molecules in the four different solvents. The $C_1C_2C_3C_4$, $C_5C_6C_7C_8$, and $C_9C_{10}N_1C_{11}$ dihedral angles, which account for the internal twisting of the pyrimidine ring, the central biphenyl unit, and the amino group, respectively, and define the deviations from molecular planarity, are used for characterizing the obtained minima (Scheme 1 shows the atomic numbering). Independent of the solvent, the $C_1C_2C_3C_4$ and $C_5C_6C_7C_8$ angles present similar values for both **D1** and **D2** (approximately 20° and 35°, respectively), whereas the $C_9C_{10}N_1C_{11}$ angle shows significantly different values of approximately 8° and 35° for **D1** and **D2**, respectively. This difference is most probably the result of the steric hindrance introduced by the phenyl groups borne by the terminal amine group in **D2**. The conjugated core of molecules **D1** and **D2** therefore presents a maximum deviation of 35° from planarity.

To disentangle the absorption spectra, the electronic $S_0 \rightarrow S_n$ transitions were calculated at the S_0 minimum-energy geometry using TD-DFT calculations. Independent of the solvent, the low- and high-energy bands experimentally observed at approximately 370 and 270 nm were assigned to transitions to the S_1 and S_4 singlet excited states, respectively. The nature of the S_1 state for the four solvents considered in our calculations (hexane, toluene, ACN, and DMSO) is mainly of a charge-transfer character for both **D1** and **D2**. The state is mainly described by a one-electron excitation from HOMO to LUMO, which are respectively localized over the amine,

with a large contribution of the biphenyl linker, and the pyrimidine part of the molecule (Figure 3 and Supplementary Figures S5, S6). The charge transfer upon excitation is supported by the localization of HOMO and LUMO orbitals over the four fragments defined in Scheme 1 that has been evaluated performing a Mulliken population analysis (Supplementary Table S3).

The charge-transfer nature of the S_1 state is reflected in the value calculated for the dipole moment, equal to 36 and 32 D for **D1** and **D2**, respectively, which is considerably larger than that computed for the S_0 state (6 and 3 D, respectively). The nature of the S_4 state of **D1** for the four solvents considered is of a $\pi-\pi^*$ state localized on the pyrimidine part of the molecule, being described by a one-electron promotion from HOMO-1 to LUMO orbitals (Supplementary Figure S5 and Supplementary Table S4). In contrast, the S_4 state of **D2** shows a charge-transfer character (similar to S_1) and mainly results from the HOMO \rightarrow LUMO+2 excitation (Supplementary Figure S6 and Supplementary Table S5). The nature of the S_1 and S_4 states of **D1** and **D2** is confirmed by computing the corresponding natural transition orbitals (NTOs), both at the ground-state minimum-energy geometry and at the S_1 minima (Supplementary Figures S7, S8). The topology of NTOs closely resembles the topology characterizing the MOs involved in the respective electronic transition.

The absorption maxima of **D1**, computed as the vertical energy to the S_1/S_4 states at the optimized S_0 minimum, are calculated at 447/315, 462/316, 483/316, and 492/316 nm (2.77/3.94, 2.68/3.92, 2.57/3.92, and 2.52/3.92 eV) in hexane, toluene, ACN, and DMSO, respectively. For **D2**, these values are 467/333, 480/336, 489/340, and 498/341 nm (2.66/3.72, 2.58/3.69, 2.54/3.65, and 2.49/3.64 eV), respectively. Then, theoretical calculations accurately predict that both absorptions weakly depend on the solvent polarity, being slightly redshifted passing from **D1** to **D2**. As previously suggested, this agrees with the small dipole moment calculated in S_0 for **D2** (3 D) and the slightly larger value obtained for **D1** (6 D). Compared with the experimental results (Table 1), the theoretical data were redshifted for all the solvents considered. The reported redshifted trend in the theoretical energies is not surprising, considering the charge-transfer character of the excited states and the well-documented underestimation that B3LYP gives in such cases (Dreuw and Head-Gordon, 2004).

To gain insights into the changes in the fluorescence properties that **D1** and **D2** undergo with the solvent, the geometry of both molecules in the emitting S_1 state was optimized at the TD-DFT 6-311G** level in the four solvents selected. The geometry optimization of S_1 evolves differently for **D1** and **D2**. For **D1**, two minima were found for S_1 (Supplementary Figure S9). In the first minimum, hereafter $S_{1,0}$, the amine group is placed in the same plane of the adjacent phenyl ring, displaying a $C_9C_{10}N_1C_{11}$ dihedral angle at approximately 0°. In the second minimum, hereafter $S_{1,90}$, the amine group is instead perpendicular to the plane of the adjacent

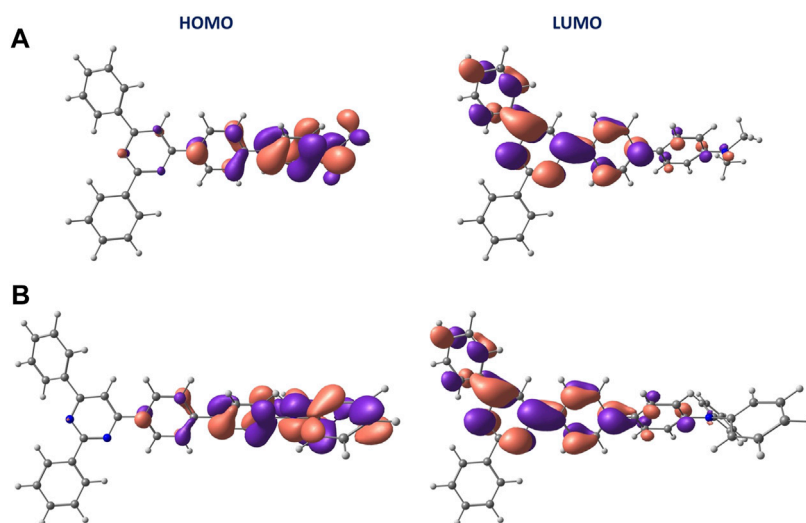


FIGURE 3
Isosurface contour plots (± 0.03 a. u.) calculated at the B3LYP/6-311G**(PCM) level for the HOMO and LUMO orbitals in ACN of **D1** (A) and **D2** (B).

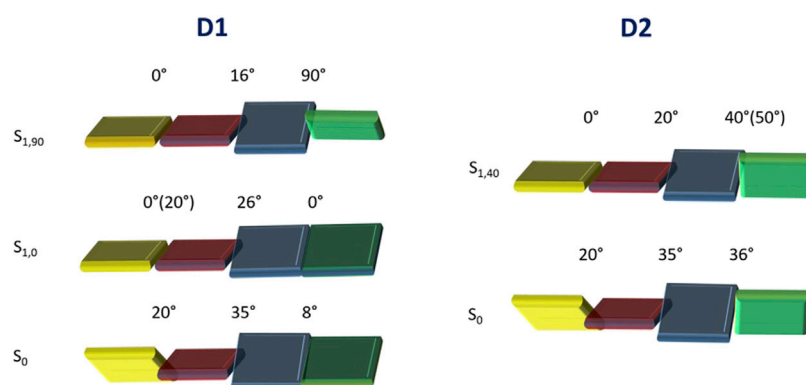


FIGURE 4
Schematic representation showing the twisting of the different molecular fragments constituting compounds **D1** and **D2**. Averaged values of the $C_1C_2C_3C_4$, $C_5C_6C_7C_8$, and $C_9C_{10}N_1C_{11}$ dihedral angles are given for the optimized S_0 and S_1 geometries of **D1** and **D2**. When the dihedral angle in non-polar solvents differs significantly, the value is reported in parenthesis. In order to better identify the dihedral angles, the same color code presented in [Scheme 1](#) was adopted.

phenyl ring, displaying a $C_9C_{10}N_1C_{11}$ dihedral angle close to 90° . Regarding the $C_5C_6C_7C_8$ twisting angle of the central biphenyl unit, its value decreases with respect to the S_0 minimum by approximately 8° and 16° in the $S_{1,0}$ and $S_{1,90}$ minima, respectively, independent of the polarity of the solvent.

On the other hand, the $C_1C_2C_3C_4$ angle defining the twisting of the pyrimidine environment decreases to almost zero in all cases, except for the $S_{1,0}$ minima in non-polar solvents, where it only decreases by a few degrees. The charge transfer between the amine and pyrimidine environments associated with the $S_0 \rightarrow S_1$ transition therefore determines that the conjugated skeleton of **D1** is, in general, more planar in S_1 than in S_0 . For **D2**, only one minimum was obtained, hereafter $S_{1,40}$, in which the amine group is significantly rotated ($C_9C_{10}N_1C_{11}$ dihedral angle equal to approximately 50° in hexane and toluene and at approximately

40° in ACN and DMSO), but it is not perpendicular to the phenyl ring. The non-planarity of such a structure is compatible with the steric hindrance offered by the phenyl rings in **D2**. All attempts to obtain a $S_{1,90}$ structure for **D2** were unsuccessful. Regarding the $C_1C_2C_3C_4$ and $C_5C_6C_7C_8$ angles, the former decreases to almost zero, and the latter is reduced by approximately 15° under both polar and non-polar conditions. The variation in the three aforementioned dihedral angles passing from S_0 to S_1 is schematically summarized in [Figure 4](#). The specific values of these dihedral angles shed light on the crucial role of the molecular geometry in their optical and electronic properties, including intramolecular charge transfer. According to the values obtained, the biphenyl spacer has a minimal impact on the connection with the acceptor triphenylpyrimidine moiety, thus facilitating ICT, but has a relevant impact on the conformation

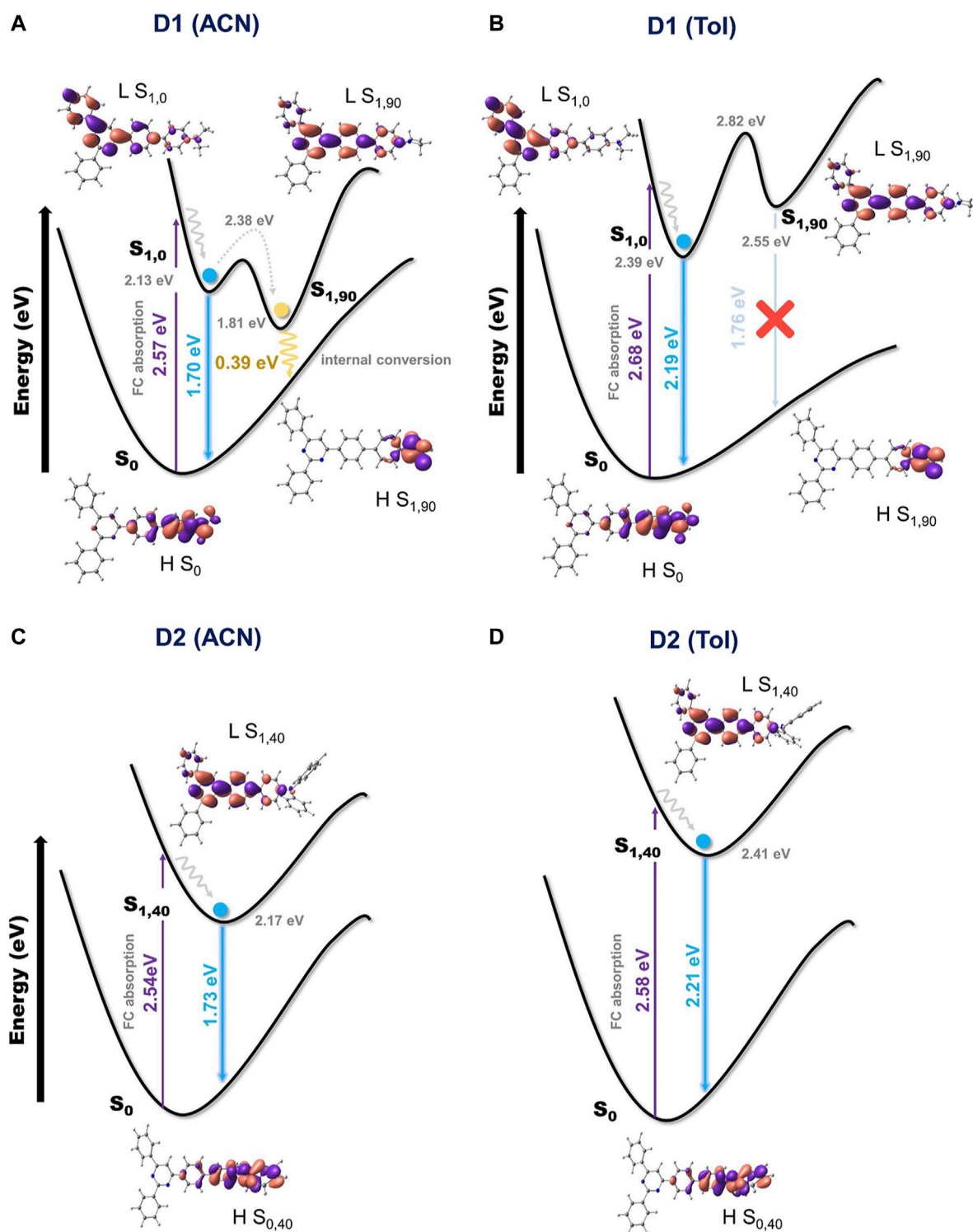


FIGURE 5

Schematic representation of the S_0 and S_1 PESs of **D1** (A, B) and **D2** (C, D) in polar (ACN) and non-polar (toluene) solvents.

adopted by the amine-donor group passing from S_0 to S_1 , depending on the substituent donor nature. For **D1**, a fully twisted 90° conformation is achieved upon excitation to the charge-transfer S_1 state ($S_{1,90}$), whereas only an intermediate twisting is possible for **D2** ($S_{1,40}$).

From the characterized S_1 minima, the vertical energy differences with respect to the ground state were computed and compared with the recorded fluorescence emission. For **D1**, the emission energies calculated from the $S_{1,0}$ minima are equal to 541, 566, 729, and 725 nm (2.29, 2.19, 1.70, and 1.71 eV)

in hexane, toluene, ACN, and DMSO, respectively. Despite the fact that these theoretical energies are considerably lower than the experimental energies, they correctly describe the experimentally recorded redshifting in the emission energy passing from non-polar to polar solvents. For example, the experimental data register a redshift of the emission in ACN with respect to toluene of approximately 0.6 eV, a value that agrees with the 0.5 eV difference based on the computational results. It is known that the functional used here tends to lower the energy to CT-type states (Cammi et al., 2000). Therefore, theoretical results predict the energetic minima of the CT character for all solvents, which are indeed in agreement with the experimental emission spectra in all solvent except hexane. Regarding the $S_{1,90}$ minima of **D1**, they appear to be non-emissive, with the computed oscillator strength for the transition to the ground state being equal to zero. This is a consequence of the 90° rotation of the amine group, making the overlap between HOMO and LUMO insignificant (Supplementary Figure S10). For **D2** (Supplementary Figure S11), the emission energies computed from $S_{1,40}$ are equal to 545, 561, 715, and 710 nm (2.27, 2.21, 1.73, and 1.75 eV) in hexane, toluene, ACN, and DMSO, respectively. Again, the absolute values predicted for the emission energies are too low compared to the experimental values but correctly described the redshifting of the emission from non-polar to polar solvents.

Employing the same example as that of **D1**, for **D2**, the experimental data found a redshift of 0.6 eV from toluene to ACN, a value that agrees with the 0.5 eV difference based on the computational results.

The drastic decrease observed experimentally for the value of Φ_F of **D1** in polar solvents can be rationalized by the presence of the $S_{1,90}$ structure, which is instead absent in **D2**. The $S_{1,90}$ minimum corresponds, in polar solvents, to the lowest S_1 minimum-energy structure (i.e., lower than the $S_{1,0}$ structure), and consequently, it will be the geometry toward which the S_1 population will evolve (Supplementary Table S6 for **D1** and Supplementary Table S7 for **D2**). Considering the geometrical similarities between the S_0 and $S_{1,0}$ structures (Supplementary Figures S4, S9, S12), it is, however, plausible to assume that the molecule will initially decay to the $S_{1,0}$ minimum. The energy barrier that separates the $S_{1,0}$ and $S_{1,90}$ structures was evaluated by computing the corresponding minimum energy path (MEP, Figure 5). From $S_{1,0}$, an energy barrier of 0.25 and 0.24 eV was computed to reach $S_{1,90}$ in ACN and DMSO, respectively. These relatively small values confirm the ability of the system to attain the $S_{1,90}$ structure. Even more relevant is the fact that the $S_{1,90}$ structure is separated from the ground state by a small energy gap of only 0.39 eV in polar solvents like ACN (0.40 eV in DMSO), which consequently favors the non-radiative decay back to the ground state (Figure 5A). The $S_{1,90}$ structure is then able to promote the non-radiative decay of **D1** in polar solvents, thus explaining the experimentally recorded low Φ_F values for such environments. In non-polar solvents instead, $S_{1,0}$ is the lowest S_1 minimum (Supplementary Table S6) to which consequently the system will tend to evolve. The barrier from the $S_{1,0}$ to $S_{1,90}$ minima in non-polar solvents was computed to have values of 0.44 and 0.43 eV for hexane and toluene, respectively. The population of $S_{1,90}$ in non-polar solvents is then much less probable than in polar solvents for two reasons: first, $S_{1,90}$ is not the lowest S_1 minimum;

second, it requires to surmount a significantly higher energy barrier. Moreover, in non-polar solvents, the energy gap with the ground state at the $S_{1,90}$ structure is of 1.94 and 1.76 eV in hexane and toluene, respectively, and will not allow a non-radiative decay (Figure 5B). This, together with the impossibility to emit fluorescence due to the small overlap between HOMO and LUMO orbitals, makes the contribution of the $S_{1,90}$ structure to the photophysics of the **D1** molecule in non-polar environments of marginal relevance. These theoretical findings support the high Φ_F values experimentally observed for **D1** in non-polar solvents.

Finally, the absence of an $S_{1,90}$ structure for **D2** explains why for such a system high Φ_F values are recorded in both non-polar and polar solvents (Figure 1; Table 1). The influence of the solvent polarity on the fluorescence properties of the **D2** molecule is thus reduced to a redshift of the emission passing from non-polar to polar solvents (Figures 5C,D).

Conclusion

A large fluorosolvatochromism is observed for biphenylpyrimidine-based push-pull systems bearing dimethylamino (**D1**) or diphenylamino (**D2**) as donor groups, where the *N,N*-substituent (dimethyl or diphenyl) determines their emissive properties according to the polarity of the solvent. Theoretical calculations have demonstrated to be a key tool to explain this effect. In the case of **D1**, the presence of a twisted geometry for the lowest-energy, charge-transfer excited state ($S_{1,90}$) was found to promote the non-radiative decay in polar solvents due to the lower energy of this structure and its energy proximity to the ground S_0 state. In contrast, in non-polar solvents, the $S_{1,90}$ structure is higher in energy and less attainable, making the non-radiative decay less likely. In the case of **D2**, the $S_{1,90}$ structure is not a minimum due to the steric hindrance between the phenyl rings of the amine group, and consequently, the fluorescence quantum yield is maintained independently of the polarity of the solvent. These systems are of high interest as possible hole transporters in electroluminescent devices based on semiconductor materials such as perovskites, due to their stunning emissive and electronic properties.

Data availability statement

The original contributions presented in the study are included in the article/Supplementary Material; further inquiries can be directed to the corresponding authors.

Author contributions

AC-V: formal analysis, investigation, and writing—original draft. IS-D: formal analysis, software, and writing—original draft. MD: methodology, supervision, and writing—review and editing. MV: methodology and writing—review and editing. PR: methodology and writing—review and editing. CA: methodology, supervision, and writing—review and editing. AG: formal analysis, software, and writing—original draft. AD-C: formal analysis and writing—review

and editing. EO: conceptualization, software, supervision, and writing-review and editing. RG: conceptualization, project administration, supervision, and writing-review and editing. JP: conceptualization, funding acquisition, project administration, supervision, and writing-review and editing.

Funding

The author(s) declare that financial support was received for the research, authorship, and/or publication of this article. Financial support by the MCIN/AEI of Spain (projects PID 2020-115710GB-I00, PID 2021-128569NB-I00, and CEX 2019-000919-M, funded by MCIN/AEI/10.13039/501100011033 and by “ERDF A way of making Europe”) and the Generalitat Valenciana (IDIFEDER/2018/064, IDIFEDER/2021/064, CIPROM/2022/57, PROMETEO/2020/077, MFA/2022/017, and MFA/2022/051) are acknowledged. The MFA/2022/017 and MFA/2022/051 projects form part of the Advanced Materials programme supported by MCIN with funding from European Union NextGenerationEU (PRTR-C17.I1) and by the Generalitat Valenciana. The study was also supported by CEDENNA AFB180001 and FONDECYT 1200192/1200116 projects.

Acknowledgments

AC-V thanks the “Maria de Maeztu” Programme for Units of Excellence in R&D (CEX 2019-000919-M) for a predoctoral fellowship (PRE2018-084294) funded by MCIN/AEI/10.13039/

501100011033 and ESF Investing in your future. IS-D also thanks the Generalitat Valenciana for their predoctoral grant CIACIF/2021/438. AG is indebted to MCIN/AEI for granting the Juan de la Cierva (IJC2018-035123-I) fellowship funded by MCIN/AEI/10.13039/501100011033 and by “European Union NextGenerationEU/PRTR.”

Conflict of interest

The authors declare that the research was conducted in the absence of any commercial or financial relationships that could be construed as a potential conflict of interest.

Publisher's note

All claims expressed in this article are solely those of the authors and do not necessarily represent those of their affiliated organizations, or those of the publisher, the editors, and the reviewers. Any product that may be evaluated in this article, or claim that may be made by its manufacturer, is not guaranteed or endorsed by the publisher.

Supplementary material

The Supplementary Material for this article can be found online at: <https://www.frontiersin.org/articles/10.3389/fchem.2023.1292541/full#supplementary-material>

References

- Achelle, S., and Robin-Le Guen, F. (2017). Emission properties of diazines chromophores: structure-properties relationship. *J. Photochem. Photobiol. A Chem.* 348, 281–286. doi:10.1016/j.jphotochem.2017.08.060
- Achelle, S., Rodríguez-López, J., and Robin-Le Guen, F. (2023). The arylvinylpyrimidine scaffold: a tunable platform for luminescent and optical materials. *Org. Biomol. Chem.* 21, 39–52. doi:10.1039/D2OB01841A
- Al-Ahmed, Z. A., Habib, I. H. I., Khattab, R. R., Abdelhameed, R. M., El-Naggar, M., Abu Bieh, M. H., et al. (2021). Synthesis, spectrophotometric, voltammetric, and density functional theory studies of tetrahydro[3,2-b]indolocarbazoles for sensing small molecules. *J. Heterocycl. Chem.* 58, 127–136. doi:10.1002/jhet.4153
- Anderson, R. S., Nagiramadugu, N. V., and Abelt, C. J. (2019). Fluorescence quenching of carbonyl-twisted 5-Acyl-1-dimethylaminonaphthalenes by alcohols. *ACS Omega* 4, 14067–14073. doi:10.1021/acsomega.9b01905
- Becke, A. D. (1993). Density-functional thermochemistry. III. The role of exact exchange. *J. Chem. Phys.* 98, 5648–5652. doi:10.1063/1.464913
- Bouhri, F., Schmaltz, B., Mathevet, F., Kreher, D., Faure-Vincent, J., Yildirim, C., et al. (2022). D- π -A-Type pyrazolo[1,5-a]pyrimidine-based hole-transporting materials for perovskite solar cells: effect of the functionalization position. *Materials* 15, 7992. doi:10.3390/ma15227992
- Bureš, F. (2014). Fundamental aspects of property tuning in push-pull molecules. *RSC Adv.* 4, 58826–58851. doi:10.1039/C4RA11264D
- Cammi, R., Mennucci, B., and Tomasi, J. (2000). Fast evaluation of geometries and properties of excited molecules in solution: a tamm-dancoff model with application to 4-dimethylaminobenzonitrile. *J. Phys. Chem. A* 104, 5631–5637. doi:10.1021/jp000156l
- Chen, W., Chen, C.-L., Zhang, Z., Chen, Y.-A., Chao, W.-C., Su, J., et al. (2017). Snapshotting the excited-state planarization of chemically locked N,N'-Disubstituted dihydrodibenzo[a,c]phenazines. *J. Am. Chem. Soc.* 139, 1636–1644. doi:10.1021/jacs.6b11789
- Chibani, S., Laurent, A. D., Blondel, A., Mennucci, B., and Jacquemin, D. (2014). Excited-state geometries of solvated molecules: going beyond the linear-response polarizable continuum model. *J. Chem. Theory Comput.* 10, 1848–1851. doi:10.1021/ct5001507
- Denneval, C., Achelle, S., Baudequin, C., and Robin-Le Guen, F. (2014). Prediction of photophysical properties of pyrimidine chromophores using Taguchi method. *Dyes Pigments* 110, 49–55. doi:10.1016/j.dyepig.2014.05.030
- Dreuw, A., and Head-Gordon, M. (2004). Failure of time-dependent density functional theory for long-range charge-transfer excited states: the Zinobacteriochlorin-Bacteriochlorin and Bacteriochlorophyll-Spheroidene complexes. *J. Am. Chem. Soc.* 126, 4007–4016. doi:10.1021/ja039556n
- Fecková, M., Kalis, I. K., Roisnel, T., Le Poul, P., Pytela, O., Klikar, M., et al. (2021). Photophysics of 9,9-dimethylacridan-substituted phenylstyrylpyrimidines exhibiting long-lived intramolecular charge-transfer fluorescence and aggregation-induced emission characteristics. *Chem. – A Eur. J.* 27, 1145–1159. doi:10.1002/chem.202004328
- Fecková, M., Le Poul, P., Bureš, F., Robin-Le Guen, F., and Achelle, S. (2020). Nonlinear optical properties of pyrimidine chromophores. *Dyes Pigments* 182, 108659. doi:10.1016/j.dyepig.2020.108659
- Franci, M. M., Pietro, W. J., Hehre, W. J., Binkley, J. S., Gordon, M. S., Defrees, D. J., et al. (1982). Self-consistent molecular orbital methods. XXIII. A polarization-type basis set for second-row elements. *J. Chem. Phys.* 77, 3654–3665. doi:10.1063/1.444267
- Frisch, M. J., Trucks, G. W., Schlegel, H. B., Scuseria, G. E., Robb, M. A., Cheeseman, J. R., et al. (2016). *Gaussian 16*. Wallingford, CT: Rev. C.01.
- Galván, I. F., Martín, M. E., and Aguilar, M. A. (2010). Theoretical study of the dual fluorescence of 4-(N,N-Dimethylamino)benzonitrile in solution. *J. Chem. Theory Comput.* 6, 2445–2454. doi:10.1021/ct9006713
- Gnida, P., Slodek, A., Chulkin, P., Vasylieva, M., Pająk, A. K., Seweryn, A., et al. (2022). Impact of blocking layer on DSSC performance based on new dye -indolo[3,2,1-jk]carbazole derivative and N719. *Dyes Pigments* 200, 110166. doi:10.1016/j.dyepig.2022.110166
- Gómez, S., Soysal, E. N., and Worth, G. A. (2021). Micro-solvated DMABN: excited state quantum dynamics and dual fluorescence spectra. *Molecules* 26, 7247. doi:10.3390/molecules26237247
- Grabowski, Z. R., Rotkiewicz, K., and Rettig, W. (2003). Structural changes accompanying intramolecular electron transfer: focus on twisted intramolecular charge-transfer states and structures. *Chem. Rev.* 103, 3899–4032. doi:10.1021/cr940745l

- Grabowski, Z. R., Rotkiewicz, K., and Siemiarz, A. (1979). Dual fluorescence of donor-acceptor molecules and the twisted intramolecular charge transfer (TICT) states. *J. Luminescence* 18–19, 420–424. doi:10.1016/0022-2313(79)90153-4
- Haberhauer, G. (2017). Planarized and twisted intramolecular charge transfer: a concept for fluorophores showing two independent rotations in excited state. *Chem. – A Eur. J.* 23, 9288–9296. doi:10.1002/chem.201700566
- Haberhauer, G., Gleiter, R., and Burkhart, C. (2016). Planarized intramolecular charge transfer: a concept for fluorophores with both large Stokes shifts and high fluorescence quantum yields. *Chem. – A Eur. J.* 22, 971–978. doi:10.1002/chem.201503927
- Hadad, C., Achelle, S., García-Martínez, J. C., and Rodríguez-López, J. (2011). 4-Arylvinyl-2,6-di(pyridin-2-yl)pyrimidines: synthesis and optical properties. *J. Org. Chem.* 76, 3837–3845. doi:10.1021/jo200204u
- Henkelman, G., Uberuaga, B. P., and Jónsson, H. (2000). A climbing image nudged elastic band method for finding saddle points and minimum energy paths. *J. Chem. Phys.* 113, 9901–9904. doi:10.1063/1.1329672
- Herbich, J., Karpiuk, J., Grabowski, Z. R., Tamai, N., and Yoshihara, K. (1992). Modification of the intramolecular electron transfer by hydrogen bonding: 4-(dialkylamino) pyrimidines. *J. Luminescence* 54, 165–175. doi:10.1016/0022-2313(92)90005-T
- Herbich, J., and Waluk, J. (1994). Excited charge transfer states in 4-aminopyrimidines, 4-(dimethylamino)pyrimidine and 4-(dimethylamino)pyridine. *Chem. Phys.* 188, 247–265. doi:10.1016/0301-0104(94)00256-8
- Il'ichev, Y. V., Kühnle, W., and Zachariasse, K. A. (1998). Intramolecular charge transfer in dual fluorescent 4-(dialkylamino)benzonitriles. Reaction efficiency enhancement by increasing the size of the amino and benzonitrile subunits by alkyl substituents. *J. Phys. Chem. A* 102, 5670–5680. doi:10.1021/jp980426o
- Improta, R., Barone, V., Scalmani, G., and Frisch, M. J. (2006). A state-specific polarizable continuum model time dependent density functional theory method for excited state calculations in solution. *J. Chem. Phys.* 125, 054103. doi:10.1063/1.2222364
- Improta, R., Scalmani, G., Frisch, M. J., and Barone, V. (2007). Toward effective and reliable fluorescence energies in solution by a new state specific polarizable continuum model time dependent density functional theory approach. *J. Chem. Phys.* 127, 074504. doi:10.1063/1.2757168
- Itami, K., Yamazaki, D., and Yoshida, J.-I. (2004). Pyrimidine-core extended π -systems: general synthesis and interesting fluorescent properties. *J. Am. Chem. Soc.* 126, 15396–15397. doi:10.1021/ja044923w
- Kalyagin, A., Antina, L., Ksenofontov, A., Antina, E., and Berezin, M. (2022). Solvent-dependent fluorescence properties of CH₂-bis(BODIPY)s. *Int. J. Mol. Sci.* 23, 14402. doi:10.3390/ijms232214402
- Kinoshita, M., Okamoto, Y., and Hirata, F. (2000). Peptide conformations in alcohol and water: analyses by the reference interaction site model theory. *J. Am. Chem. Soc.* 122, 2773–2779. doi:10.1021/ja993939x
- Kozlov, O. V., Liu, X., Luponosov, Y. N., Solodukhin, A. N., Toropynina, V. Y., Min, J., et al. (2017). Triphenylamine-based push-pull molecule for photovoltaic applications: from synthesis to ultrafast device photophysics. *J. Phys. Chem. C* 121, 6424–6435. doi:10.1021/acs.jpcc.6b12068
- Lee, C., Yang, W., and Parr, R. G. (1988). Development of the Colle-Salvetti correlation-energy formula into a functional of the electron density. *Phys. Rev. B* 37, 785–789. doi:10.1103/PhysRevB.37.785
- Lippert, E. (1955). Dipolmoment und Elektronenstruktur von angeregten Molekülen. *Z. für Naturforsch.* A 10, 541–545. doi:10.1515/zna-1955-0707
- Liu, J., Chen, C., and Fang, C. (2022). Polarity-dependent twisted intramolecular charge transfer in diethylamino coumarin revealed by ultrafast spectroscopy. *Chemosensors* 10, 411. doi:10.3390/chemosensors10100411
- Maddala, G., Gade, R., Ahmed, J., Kalvapalli, S., Simhachalam, N. B., Chetti, P., et al. (2021). Efficient, dopant free phenazine based hole transporting materials for high performance perovskite solar cells. *Sol. Energy* 226, 501–512. doi:10.1016/j.solener.2021.08.055
- Manda, K., Kore, R., Ambapuram, M., Chetti, P., Roy, S., Jadhav, V. D., et al. (2022). Benzodithiophene-based, donor-acceptor-pi-donor-acceptor systems as hole transporting materials for efficient perovskite solar cells. *Chemphotochem* 6, e202200062. doi:10.1002/cptc.202200062
- Mansoor, S. S., and Shafi, S. S. (2015). Oxidation of methionine by tetraethylammonium chlorochromate in non-aqueous media – a kinetic and mechanistic study. *Arabian J. Chem.* 8, 480–486. doi:10.1016/j.arabjc.2011.01.031
- Marcus, Y. (1993). The properties of organic liquids that are relevant to their use as solvating solvents. *Chem. Soc. Rev.* 22, 409–416. doi:10.1039/CS9932200409
- Martin, R. L. (2003). Natural transition orbitals. *J. Chem. Phys.* 118, 4775–4777. doi:10.1063/1.1558471
- Mataga, N., Kaifu, Y., and Koizumi, M. (1955). The solvent effect on fluorescence spectrum, change of solute-solvent interaction during the lifetime of excited solute molecule. *Bull. Chem. Soc. Jpn.* 28, 690–691. doi:10.1246/bcsj.28.690
- Nakao, K., Sasabe, H., Komatsu, R., Hayasaka, Y., Ohsawa, T., and Kido, J. (2017). Significant enhancement of blue OLED performances through molecular engineering of pyrimidine-based emitter. *Adv. Opt. Mater.* 5, 1600843. doi:10.1002/adom.201600843
- Neese, F. (2022). Software update: the ORCA program system—version 5.0. *WIREs Comput. Mol. Sci.* 12, e1606. doi:10.1002/wcms.1606
- Pannipara, M., Asiri, A. M., Alamry, K. A., Arshad, M. N., and El-Daly, S. A. (2014). Spectroscopic investigation, effect of solvent polarity and fluorescence quenching of a new D- π -A type chalcone derivative. *J. Fluoresc.* 24, 1629–1638. doi:10.1007/s10895-014-1449-1
- Qian, X., Yan, R., Hang, Y., Lv, Y., Zheng, L., Xu, C., et al. (2017). Indeno[1,2-b] indole-based organic dyes with different acceptor groups for dye-sensitized solar cells. *Dyes Pigments* 139, 274–282. doi:10.1016/j.dyepig.2016.12.028
- Qiao, W., Duan, G., Wang, J., Dong, J., Pan, B., and Mu, X. (2020). Photoinduced charge transfer in push/pull systems of two-photon absorption. *ACS Omega* 5, 17275–17286. doi:10.1021/acsomega.0c01482
- Qin, X., Yang, X., Du, L., and Li, M. (2021). Polarity-based fluorescence probes: properties and applications. *RSC Med. Chem.* 12, 1826–1838. doi:10.1039/D1MD00170A
- Rodríguez-Aguilar, J., Vidal, M., Pastenes, C., Aliaga, C., Rezende, M. C., and Domínguez, M. (2018). The solvatofluorochromism of 2,4,6-triarylpyrimidine derivatives. *Photochem. Photobiol.* 94, 1100–1108. doi:10.1111/php.12982
- Ryutaro, K., Hisahiro, S., and Junji, K. (2018). Recent progress of pyrimidine derivatives for high-performance organic light-emitting devices. *J. Photonics Energy*, 032108. doi:10.1117/1.JPE.8.032108
- Sasaki, S., Drummen, G. P. C., and Konishi, G.-I. (2016). Recent advances in twisted intramolecular charge transfer (TICT) fluorescence and related phenomena in materials chemistry. *J. Mater. Chem. C* 4, 2731–2743. doi:10.1039/C5TC03933A
- Segarra-Martí, J., and Coto, P. B. (2014). A theoretical study of the intramolecular charge transfer in 4-(dimethylamino)benzethyne. *Phys. Chem. Chem. Phys.* 16, 25642–25648. doi:10.1039/C4CP03436H
- Slodek, A., Zych, D., Maroń, A., Malecki, J. G., Golba, S., Szafraniec-Gorol, G., et al. (2019). Does the length matter? - synthesis, photophysical, and theoretical study of novel quinolines based on carbazoles with different length of alkyl chain. *Dyes Pigments* 160, 604–613. doi:10.1016/j.dyepig.2018.08.048
- Soriano-Díaz, I., Ortí, E., and Giussani, A. (2023). On the importance of equatorial metal-centered excited states in the photophysics of cyclometallated Ir(III) complexes. *Dalton Trans.* 52, 10437–10447. doi:10.1039/D3DT01404E
- Subuddhi, U., Halder, S., Sankararaman, S., and Mishra, A. K. (2006). Photophysical behaviour of 1-(4-N,N-dimethylaminophenylethynyl)pyrene (DMAPEPy) in homogeneous media. *Photochem. Photobiological Sci.* 5, 459–466. doi:10.1039/B600009F
- Sun, H., Liu, D., Wang, T., Li, P. A., Bridgman, C. N., Li, W., et al. (2018). Charge-separated sensitizers with enhanced intramolecular charge transfer for dye-sensitized solar cells: insight from structure-performance relationship. *Org. Electron.* 61, 35–45. doi:10.1016/j.orgel.2018.06.045
- Tan, C.-J., Yang, C.-S., Sheng, Y.-C., Amini, H. W., and Tsai, H.-H. G. (2016). Spacer effects of donor- π spacer-acceptor sensitizers on photophysical properties in dye-sensitized solar cells. *J. Phys. Chem. C* 120, 21272–21284. doi:10.1021/acs.jpcc.6b07032
- Tomasi, J., and Persico, M. (1994). Molecular interactions in solution: an overview of methods based on continuous distributions of the solvent. *Chem. Rev.* 94, 2027–2094. doi:10.1021/cr00031a013
- Venkateswararao, A., Tyagi, P., Justin Thomas, K. R., Chen, P.-W., and Ho, K.-C. (2014). Organic dyes containing indolo[2,3-b]quinoxaline as a donor: synthesis, optical and photovoltaic properties. *Tetrahedron* 70, 6318–6327. doi:10.1016/j.tet.2014.04.009
- Verbitskiy, E. V., Cheprakova, E. M., Subbotina, J. O., Schepochkin, A. V., Lepukhin, P. A., Rusinov, G. L., et al. (2014). Synthesis, photophysical and electrochemical properties of pyrimidine-containing dyes as photosensitizers for dye-sensitized solar cells. *Dyes Pigments* 100, 201–214. doi:10.1016/j.dyepig.2013.09.006
- Verbitskiy, E. V., Kvashnin, Y. A., Bogdanov, P. I., Medvedeva, M. V., Svalova, T. S., Kozitsina, A. N., et al. (2021a). The effect of molecular structure on the efficiency of 1,4-diazine-based D-(π)-A push-pull systems for non-doped OLED applications. *Dyes Pigments* 187, 109124. doi:10.1016/j.dyepig.2020.109124
- Verbitskiy, E. V., Schepochkin, A. V., Makarova, N. I., Dorogan, I. V., Metelitsa, A. V., Minkin, V. I., et al. (2015). Synthesis, photophysical and redox properties of the D- π -A type pyrimidine dyes bearing the 9-phenyl-9H-carbazole moiety. *J. Fluoresc.* 25, 763–775. doi:10.1007/s10895-015-1565-6
- Verbitskiy, E. V., Steparuk, A. S., Zhilina, E. F., Emets, V. V., Grinberg, V. A., Krivogina, E. V., et al. (2021b). Pyrimidine-based push-pull systems with a new anchoring amide group for dye-sensitized solar cells. *Electron. Mater.* 2, 142–153. doi:10.3390/electronicmat2020012
- Wong, K.-T., Hung, T. S., Lin, Y., Wu, C.-C., Lee, G.-H., Peng, S.-M., et al. (2002). Suzuki coupling approach for the synthesis of Phenylene-Pyrimidine alternating oligomers for blue light-emitting material. *Org. Lett.* 4, 513–516. doi:10.1021/ol017066z

- Wu, C. C., Lin, Y. T., Chiang, H. H., Cho, T. Y., Chen, C. W., Wong, K. T., et al. (2002). Highly bright blue organic light-emitting devices using spirobifluorene-cored conjugated compounds. *Appl. Phys. Lett.* 81, 577–579. doi:10.1063/1.1493669
- Yang, S., Guan, D., Yang, M., Tian, J., Chu, W., and Sun, Z. (2015). Synthesis and characterization of novel butterfly-shaped aryl-substituted indolo[2,3-a]carbazole derivatives. *Tetrahedron Lett.* 56, 2223–2227. doi:10.1016/j.tetlet.2015.03.058
- Zachariasse, K. A., Grobys, M., Von Der Haar, T., Hebecker, A., Il'ichev, Y. V., Jiang, Y. B., et al. (1996). Intramolecular charge transfer in the excited state. Kinetics and configurational changes. *J. Photochem. Photobiol. A Chem.* 102, 59–70. doi:10.1016/S1010-6030(96)04368-7
- Zachariasse, K. A., Grobys, M., Von Der Haar, T., Hebecker, A., Il'ichev, Y. V., Morawski, O., et al. (1997). Photoinduced intramolecular charge transfer and internal conversion in molecules with a small energy gap between S1 and S2. Dynamics and structure. *J. Photochem. Photobiol. A Chem.* 105, 373–383. doi:10.1016/S1010-6030(96)04601-1
- Zimosz, S., Slodek, A., Gnida, P., Glinka, A., Ziólek, M., Zych, D., et al. (2022). New D– π –D– π –A systems based on phenothiazine derivatives with imidazole structures for photovoltaics. *J. Phys. Chem. C* 126, 8986–8999. doi:10.1021/acs.jpcc.2c01697
- Zych, D., Slodek, A., and Frankowska, A. (2019). Is it worthwhile to deal with 1,3-disubstituted pyrene derivatives? – Photophysical, optical and theoretical study of substitution position effect of pyrenes containing tetrazole groups. *Comput. Mater. Sci.* 165, 101–113. doi:10.1016/j.commatsci.2019.04.041



OPEN ACCESS

EDITED BY

Laura De Luca,
University of Messina, Italy

REVIEWED BY

Francesca Vasile,
University of Milano, Italy
Nicola Micale,
University of Messina, Italy

*CORRESPONDENCE

Jorge A. R. Salvador,
✉ salvador@ci.uc.pt
Rita C. Guedes,
✉ rguedes@ff.ulisboa.pt

RECEIVED 16 October 2023

ACCEPTED 15 December 2023

PUBLISHED 08 January 2024

CITATION

Fernandes PMP, Guedes RA, Victor BL,
Salvador JAR and Guedes RC (2024),
Decoding the secrets: how
conformational and structural regulators
inhibit the human 20S proteasome.
Front. Chem. 11:1322628.
doi: 10.3389/fchem.2023.1322628

COPYRIGHT

© 2024 Fernandes, Guedes, Victor,
Salvador and Guedes. This is an open-
access article distributed under the terms
of the [Creative Commons Attribution
License \(CC BY\)](#). The use, distribution or
reproduction in other forums is
permitted, provided the original author(s)
and the copyright owner(s) are credited
and that the original publication in this
journal is cited, in accordance with
accepted academic practice. No use,
distribution or reproduction is permitted
which does not comply with these terms.

Decoding the secrets: how conformational and structural regulators inhibit the human 20S proteasome

Pedro M. P. Fernandes^{1,2,3}, Romina A. Guedes^{1,2,3}, Bruno L. Victor⁴,
Jorge A. R. Salvador^{1,2*} and Rita C. Guedes^{3*}

¹Laboratory of Pharmaceutical Chemistry, Faculty of Pharmacy, University of Coimbra, Coimbra, Portugal, ²Center for Innovative Biomedicine and Biotechnology (CIBB), Center for Neuroscience and Cell Biology (CNC), University of Coimbra, Coimbra, Portugal, ³Research Institute for Medicines (iMed.U LISBOA), Faculdade de Farmácia, Universidade de Lisboa, Lisboa, Portugal, ⁴BiolSI-Biosystems & Integrative Sciences Institute, Faculty of Sciences, Universidade de Lisboa, Lisboa, Portugal

Acquired resistance to drugs that modulate specific protein functions, such as the human proteasome, presents a significant challenge in targeted therapies. This underscores the importance of devising new methodologies to predict drug binding and potential resistance due to specific protein mutations. In this work, we conducted an extensive computational analysis to ascertain the effects of selected mutations (Ala49Thr, Ala50Val, and Cys52Phe) within the active site of the human proteasome. Specifically, we sought to understand how these mutations might disrupt protein function either by altering protein stability or by impeding interactions with a clinical administered drug. Leveraging molecular dynamics simulations and molecular docking calculations, we assessed the effect of these mutations on protein stability and ligand affinity. Notably, our results indicate that the Cys52Phe mutation critically impacts protein-ligand binding, providing valuable insights into potential proteasome inhibitor resistance.

KEYWORDS

20S proteasome inhibitors, drug resistance, mutations, molecular dynamics, molecular docking

1 Introduction

Cellular homeostasis is a tightly controlled process balancing protein synthesis and degradation mechanisms (Chondrogianni et al., 2015). In eukaryotic cells, intracellular protein degradation primarily occurs through two pathways: lysosomes and the Ubiquitin-Proteasome Pathway (UPP), also known as the Ubiquitin-Proteasome System (UPS). The UPS is crucial in ATP-dependent protein degradation within the cytoplasm and nucleus, affecting cell cycle control, apoptosis, DNA repair, transcription, immune response, and signaling processes by degrading key cellular players like cyclins and tumor suppressors (Hochstrasser, 1995; Ciechanover, 2007). Dysfunctions in these pathways are linked to diseases like cancer and neurodegeneration (Kisselev et al., 2003; Da Fonseca and Morris, 2008; Da Fonseca et al., 2012; Schweitzer et al., 2016). Central to the UPS is the 20S core particle (or 20S proteasome) (Figure 1), responsible for degrading unnecessary or damaged proteins, facilitated by its catalytic subunits (Ciechanover, 2007; Finley, 2009; Blackburn et al., 2010; Verbrugge et al., 2015). Structurally, the 20S proteasome consists of a cylindrical assembly of approximately 160 Å in length and 120 Å in diameter, formed by four

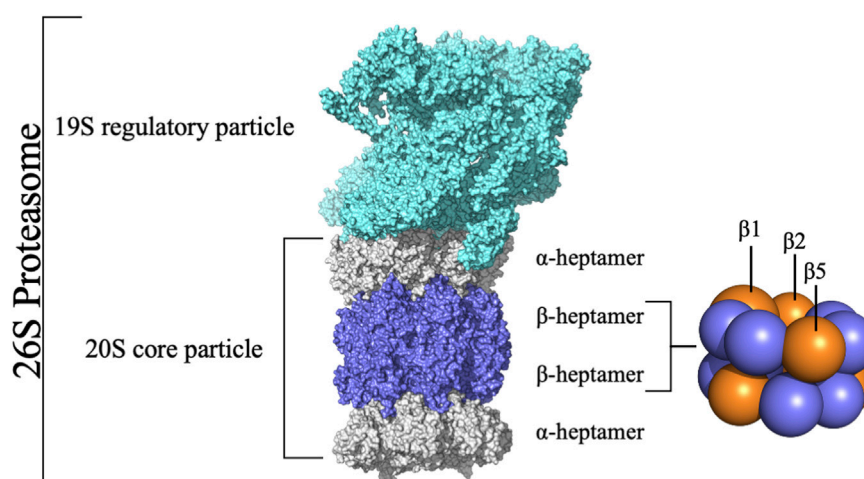


FIGURE 1

Structure of the 26S Proteasome. The 26S proteasome comprises the 20S core particle capped by the 19S regulatory particle. The 20S core particle comprises 28 subunits grouped in four rings stacked into a α - β - β - α pattern.

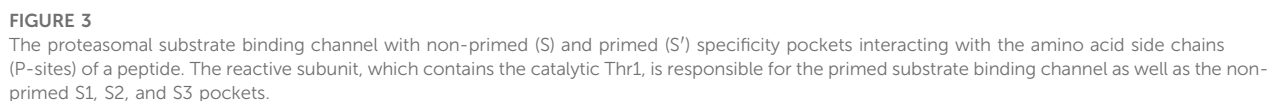
heptameric rings (two α -rings and two β -rings in an α - β - β - α arrangement) (de Bettignies and Coux, 2010; Jung and Grune, 2012).

The 20S proteasome's multiple catalytic sites, $\beta 1$, $\beta 2$, and $\beta 5$, each with unique specificities, enable efficient degradation of cellular proteins. While inhibiting $\beta 1$ or $\beta 2$ does not significantly impact protein degradation, targeting $\beta 5$ dramatically reduces it. Each of these sites features an N-terminal threonine (Kisselev et al., 2006) which, through its γ -hydroxyl moiety, acts as a nucleophile in peptide bonds hydrolysis (Zhu et al., 2009; Diez-Rivero et al., 2010; Beck et al., 2012). The substrate-binding sites share a topology where the S1 region is buried in the subunit adjacent to the threonine, S2 is exposed, and both the catalytic unit and its neighbor contribute to the S3 position (Groll and Huber, 2003). These subunits demonstrate distinct cleavage preferences: $\beta 1$ shows "caspase-like" (C-L) or "post acidic" (PA) activity, $\beta 2$ has "trypsin-like" (T-L) activity, and $\beta 5$ exhibits "chymotrypsin-like" (CT-L) activity (Nussbaum et al., 1998; Groll et al., 1999; Kisselev et al., 1999; Borissenko and Groll, 2007; Basse et al., 2010; Beck et al., 2012; Huber et al., 2012). Although catalytic activity occurs only at $\beta 1$, $\beta 2$, and $\beta 5$ subunits, the contribution of adjacent subunits significantly impacts the definition of the catalytic pockets, substrate stabilization, and positioning (Loizidou and Zeinalipour-Yazdi, 2014). Key amino acids at these sites, especially threonine 1 (Thr1), aspartate 17 (Asp17), lysine 33 (Lys33), serine 129 (Ser129), aspartate 166 (Asp166), and serine 169 (Ser169) (Figure 2), play pivotal roles in both catalysis and maintaining the structural activity of the active site (Unno et al., 2002; Borissenko and Groll, 2007; Huber et al., 2012). Despite the protonation of Thr1 N-Terminal (Thr1N) under physiological conditions, which makes it unlikely initial nucleophile (Trivella et al., 2014), its O γ atom is considered the general nucleophile in proteasome interactions. The other residues (Ser129, Asp166, and Ser169) contribute not only to catalysis but also to the structural integrity of the active site (Figure 2) (Unno et al., 2002; Borissenko and Groll, 2007; Huber et al., 2012). The substrate binding channels of the proteasome exhibit distinct primed and non-primed

specificity pockets, facilitating the binding of target polypeptides in a C- to N-terminal direction (Figure 3). The primed sites, characterized by shallow profiles, likely facilitate the early release of the C-terminal cleavage product within the reaction cycle. In contrast, the pronounced non-primed pockets enable tight interactions with the N-terminal polypeptide segment, thereby substantially influencing cleavage specificity (Groll et al., 1997). The scissile peptide bond, positioned between primed and non-primed sites, undergoes cleavage catalyzed by the active site Thr1 residue (Figure 3), thereby classifying the proteasome as an N-terminal nucleophile hydrolase. Harshbarger et al. (Harshbarger et al., 2015) described that the substrate selectivity for each active site is determined by the interaction of the P1 side chain of the substrate with the S1 specificity pocket of the active site. Residue 45 at the base of the S1 pocket is essential to determine the three different cleavage preferences; in the CT-L active site, the $\beta 5$ subunit amino acids of the S1 pocket responsible for the CT-L activity are Ala20, Met45, Ala49, and Cys52. Met45 protrudes from the pocket, allowing it to accommodate hydrophobic residues such as alanine, valine, or tyrosine (Figure 3) (Harshbarger et al., 2015). The mutation of these residues, especially in the S1 pocket, impacts drug binding and thus resistance mechanisms, highlighting the need for understanding their structural and functional roles for developing efficient proteasome inhibitors.

1.1 Proteasome inhibitors and drug resistance

The development of 20S proteasome inhibitors (PIs) has been a pivotal strategy in treating diseases associated with the UPS. Various PIs, including peptide aldehydes, boronates, α',β' -epoxyketones, and others, have been identified (Kisselev et al., 2012; Micale et al., 2014). Bortezomib (2003), carfilzomib (2012), and ixazomib (2015) are FDA-approved PIs (Figure 4) for treating refractory multiple myeloma (MM) and mantle cell lymphoma



Resistance to PIs, both innate and acquired, is a significant challenge in therapy, as underscored by [Leonardo-Sousa et al. \(2022\)](#). Efforts to tackle this issue have largely focused on the covalent reversible inhibitor bortezomib ([Kale and Moore, 2012](#); [Petrucci et al., 2013](#); [Schmitt et al., 2014](#)). While bortezomib initially elicits favorable responses in many patients, resistance often develops, leading to treatment failure or relapse ([Lü et al.,](#)

The development of resistance to PIs is often linked to mutations in target proteins, a well-established phenomenon in cancer drug resistance. Studies by [Kale and Moore \(2012\)](#) and [Niewerth et al. \(2015\)](#) highlight the strong association between acquired resistance to PIs and point mutations in PSMB5. These mutations, occurring either near or distal to the PSMB5 binding site, can alter drug affinity by either preventing compound binding or inducing allosteric inhibition. Several other groups ([Lü et al., 2008a](#); [Lü et al., 2008b](#); [Lü et al., 2009](#); [Franke et al., 2012](#); [Lichter et al., 2012](#); [Manasanch and Orłowski, 2017](#)) have found that continued *in vitro* exposure of cell lines related to hematological cancers (e.g., RPMI8226, CCRF-CEM, and Jurkat

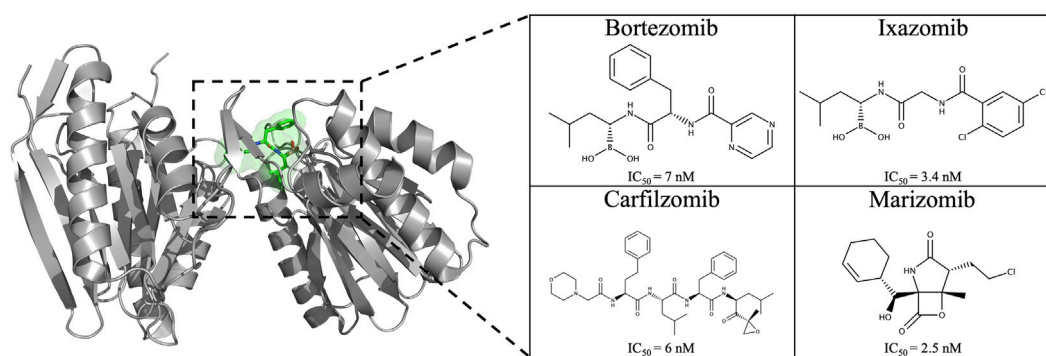


FIGURE 4

Chemical structure of the four proteasome inhibitors currently on the market and/or approved. IC₅₀ values of PIs on the CT-L active site: bortezomib (Demo et al., 2007), carfilzomib (Demo et al., 2007), ixazomib (Kupperman et al., 2010), and marizomib (Chauhan et al., 2005).

cells) to the proteasome inhibitor bortezomib may lead to mutations in the PMSB5 gene (which encodes the $\beta 5$ subunit of the 20S proteasome), causing different point mutations, e.g., Ala49Thr, Ala50Val, Thr21Ala, Met45Val, and Cys52Phe. Franke et al. (2012) even mention the existence of a “mutation cluster region”, describing that most mutations occur around the highly conserved S1 pocket of the $\beta 5$ subunit (Figure 3) (Lü et al., 2008a; Lü et al., 2008b; Lü et al., 2009; Oerlemans et al., 2008; Ri et al., 2010; Franke et al., 2012; Verbrugge et al., 2012). These mutations, including Ala49Thr and Cys52Phe, often cluster around the S1 pocket of the $\beta 5$ subunit, affecting bortezomib binding and catalytic activity by altering hydrogen bond formation and causing steric hindrance. This mutation-induced alteration in the proteasome’s structure, particularly in the S1 pocket, underscores the complexity of overcoming resistance in therapeutic approaches targeting the proteasome (Figure 3) (Groll et al., 2006; Franke et al., 2012; Huber et al., 2012).

Considering the primary targeting of the $\beta 5$ subunit by PIs, and the occurrence of mutations in this subunit, understanding their role in resistance mechanisms is crucial for developing effective inhibitors (Kale and Moore, 2012; Niewerth et al., 2015).

This study focuses on the significant mutations in the $\beta 5$ subunit, investigating how these alterations impact proteasome structure and interaction with inhibitors. Utilizing molecular dynamics and docking methods (Guedes et al., 2016; Guedes et al., 2023), we conducted a detailed analysis of various point mutations near the binding site. Our goal is to comprehend how these mutations influence resistance to bortezomib, comparing mutated proteasome structures with their wild type (WT) counterparts. The insights from this research will inform strategies for designing drugs that can effectively target these mutations, enhancing the fight against drug resistance (Guedes et al., 2019; Guedes et al., 2023).

2 Methods section

2.1 System setup

In this work, we performed molecular dynamics (MD) simulations for the two β -rings (each composed of $\beta 1$ -7

subunits) of the 20S proteasome core particle. Four systems were simulated: native WT, Ala49Thr, Ala50Val, and Cys52Phe mutants. The initial coordinates for 20S proteasome simulations were obtained from the X-ray structure with PDB code 5LE5 (Schrader et al., 2016) and were prepared by stripping out any water molecules, ions, and ligands.

2.2 Modeling of mutants

Three mutants (Ala49Thr, Ala50Val, and Cys52Phe) were prepared from the native WT (PDB code: 5LE5), using the mutagenesis wizard module of PyMOL software (Schrödinger, 2023) and applied to both $\beta 5$ subunits (one in each β -ring).

2.3 Molecular dynamics simulations

All simulations were performed using the GROMACS 2016.3 (Berendsen et al., 1995; Lindahl et al., 2001; Van Der Spoel et al., 2005; Hess et al., 2008; Pronk et al., 2013; Abraham et al., 2015; Páll et al., 2015) software package and the GROMOS 54a7 (Schmid et al., 2011) force field together with the SPC water model (Berendsen et al., 1981). The protonation states of the titratable protein residues were set using the GROMACS pdb2gm tool, taking into account their dominant form at pH 7.4. The N- and C-terminals from all subunits were set to their charged form. The Thr1 residue at the binding site was protonated in agreement with the observations in the X-ray diffraction study performed by Schrader et al. (2016). In each simulated system, the protein (in its WT and mutant forms) was solvated in a dodecahedron simulation box and then neutralized by adding 14 Na⁺ ions. Each system was first minimized with 1,000 steps of steepest descent, followed by 1,000 steps of conjugated gradient. After minimization, the system was equilibrated by performing 1 ns in the canonical (NVT) ensemble using the V-rescale weak-coupling method (Bussi et al., 2007) followed by 1 ns in the NPT ensemble with the Parrinello-Rahman barostat (pressure 1 bar) (Parrinello, 1981; Nosé and Klein, 1983). During this process, the heavy atoms of

the protein were restrained using a constant force of 1,000 kJ/mol/nm². After the equilibration process, we performed three replicate simulations for each simulated system, each one 100 ns long. In these production runs, the conformational space was sampled according to the NPT ensemble with the pressure set to 1 bar with a coupling constant of 2 ps (Parrinello-Rahman barostat) and a temperature set at 300 K using a coupling constant of 0.1 ps (V-rescale weak coupling). An isotropic pressure coupling with compressibility of 4.5×10^{-5} bar⁻¹ was used. The long-range electrostatics were calculated with the particle mesh Ewald (Darden et al., 1993; Essmann et al., 1995) method, with a real space cutoff of 1.0 nm and a Fourier grid spacing of 0.12 nm. Van der Waals interactions were truncated above 1.0 nm. All protein bonds were constrained using the LINCS algorithm while SETTLE was used to constrain the water molecules. The equations of motion were integrated every 2 fs with an update of the neighbor's list done every 10 steps.

2.4 MD simulation analyses

All MD simulations were analyzed using rms, gyrate, hbond, and distance tools implemented in the GROMACS software package (Van Der Spoel et al., 2005). These utilities allowed us to obtain the root-mean-square deviation (RMSD), the radius of gyration (Rg), the number of hydrogen bonds (H-bonds), and the distance between residues, respectively. The open-source POVME (Durrant et al., 2011; 2014; Wagner et al., 2017) binding pocket analysis software was used to calculate the catalytic pocket volume of the $\beta 5$ subunit, which maps the flexibility of the binding pocket employing a voxel/grid-based 3D pocket representation.

All the molecular graphical presentations were created using PyMOL (Schrödinger, 2023) and all plots were generated using Gnuplot (Williams et al., 2019).

2.5 Molecular docking

Covalent docking calculations of the proteasome inhibitor bortezomib were performed using GOLD 2020.1 (Jones et al., 1997). Bortezomib protonation states were initially determined at pH = 7.4 and 300 K. Partial atomic charges were assigned using the Amber10:EHT force field implemented in the Molecular Operating Environment (MOE) 2019.0102 software package (Chemical Computing group ULC, 2023). After parameterization, all compounds were energy-minimized. The genetic algorithm implemented in GOLD was used to generate different ligand interaction binding poses. The generated solutions were then ranked using the CHEMPLP (Korb et al., 2009) scoring function.

The docking calculations were performed using the human proteasome crystal structure available on PDB (PDB code: 5LF3) and on four different MD-derived structures of the WT, the Ala49Thr, Ala50Val, and Cys52Phe mutants ($\beta 5$ subunit). The structures represent the central conformation of the equilibrated region of all MD replicate simulations. The human proteasome 3D structure (PDB code: 5LF3 – 20S proteasome complexed with bortezomib (Schrader et al., 2016)) was prepared using MOE

2019.0102 (Chemical Computing group ULC, 2023). All calculations were performed on the CT-L binding site of the $\beta 5$ -subunit. Hydrogen atoms were added, and the protonation states of the side chains of the protein residues were the same as previously used in MD simulations. The AMBER10:EHT force field was then used to assign atom types and charges to each atom in the receptor. The Thr1 residue at the binding site was protonated in agreement with the observations in the X-ray diffraction study performed by Schrader et al. (Schrader et al., 2016). The “searching space” in all docking calculations was centered at the Thr1Oy with a radius of 15 Å. Covalent docking calculations were performed according to the following settings: CHEMPLP scoring function, 500 genetic algorithm (GA) runs, and 100% search efficiency. The boron atom of bortezomib was set as the link atom to covalently bind to the hydroxyl group oxygen of Thr1. Finally, the scores were ranked, and the results were visually analyzed. We selected the best 10 docking solutions based on the scoring function.

2.6 Key interaction determination

Protein and ligand were saved in PDB format with the MOE 2019.0102 software. The Python source code of the Protein-Ligand Interaction Profiler (PLIP) web server (Adasme et al., 2021) was installed locally, and ligand interactions were determined. A heatmap was generated with Seaborn (Waskom, 2021) and Matplotlib (for visualization with Python) (Hunter, 2007). The data analysis workflow was assembled using the Jupyter Notebook platform (Kluyver et al., 2016).

3 Results and discussion

Although in the available crystallographic structures of the 20S proteasome, the entire 20S core particle is available, in this work, we only simulated the two β -rings (Figure 1). In these two rings, one can find the region of interest of this work (the $\beta 5$ subunit, namely, the CT-L pocket), guaranteeing at the same time the structural integrity of the protein core and a low computational cost of the simulations. As stated above, we focused our analysis on the stability of the $\beta 5$ subunit in its WT form and three different mutants (Ala49Thr, Ala50Val, and Cys52Phe) due to their link to acquired resistance to various proteasome inhibitors. As seen in Figure 5, our mutational studies focused on the CT-L binding site region and are expected to influence inhibitor binding. However, the extent of structural changes associated with these mutants is still not fully understood and, with this study, we aim to gather more structural information on their impact, before evaluating the influence in the binding of bortezomib. According to structural modeling analysis, the mutant residues in this study, Ala49, and Ala50 are placed at the top of α -helix 1 (Figures 5, 6) suggesting their structural involvement in the enclosing of the CT-L active site. Regarding Cys52, one can see that this residue is placed in the middle of the same α -helix 1. Although it is not directly on the surface of the pocket, the mutation to a residue with different chemical properties is expected to impact the α -helix 1 stability, with consequent implications on the shape of the catalytic pocket.

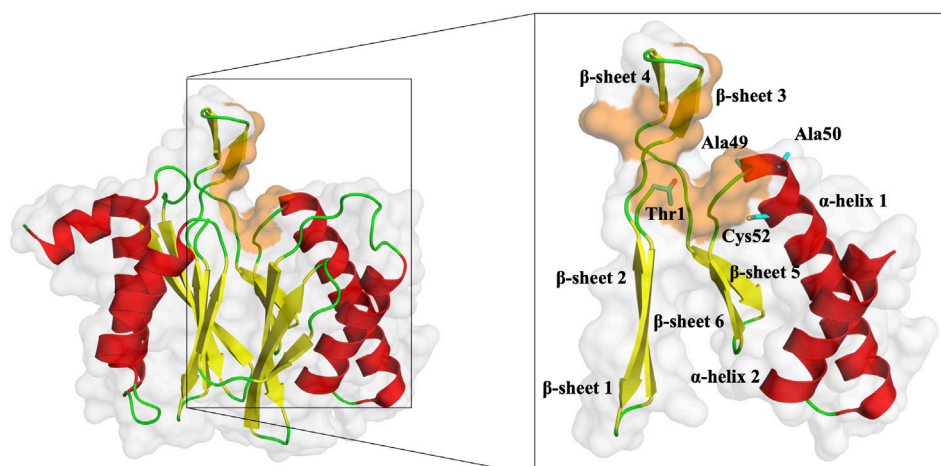


FIGURE 5

Representation of the $\beta 5$ subunit, with emphasis on the catalytic pocket in orange. Part of the $\beta 5$ subunit is represented by its secondary structure: β -sheet 1 (from residue 1–9), β -sheet 2 (from residue 10–18), β -sheet 3 (from residue 19–23), β -sheet 4 (from residue 24–29), β -sheet 5 (from residue 34–38), β -sheet 6 (from residue 39–47), α -helix 1 (from residue 49–70) and α -helix 2 (from residue 76–88). In sticks, we have also represented the N-terminal of the protein (Thr1), where typically 20S proteasome inhibitors covalently bind, Ala49, Ala50, and Cys52 (placed at the end of the β -sheet 3 and beginning of α -helix 1, respectively). This figure was built using PyMOL software (Schrodinger, 2023).

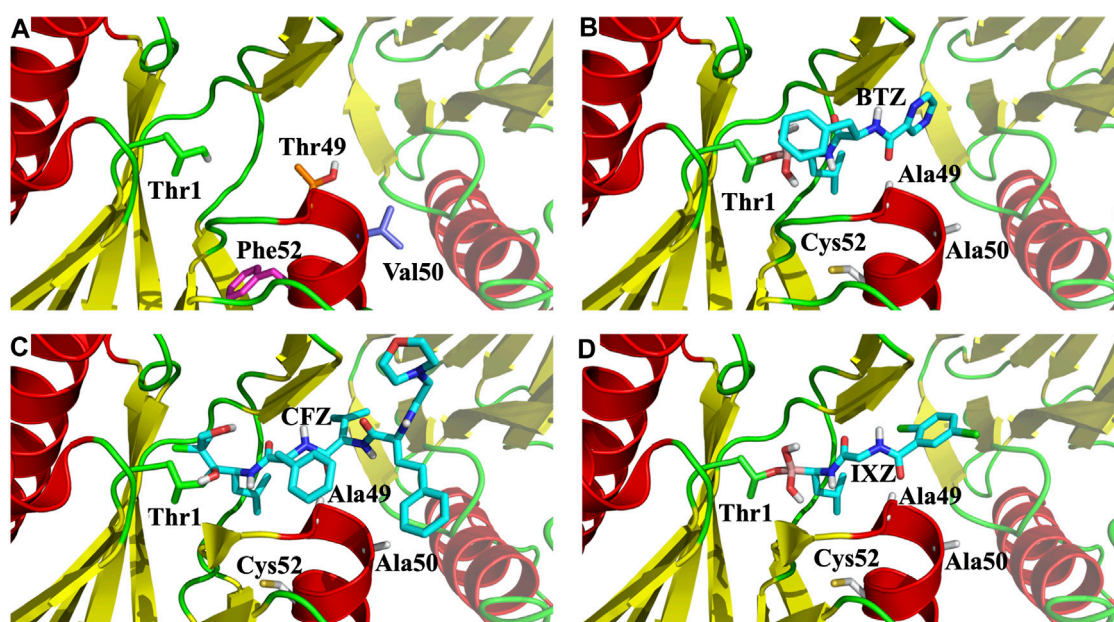


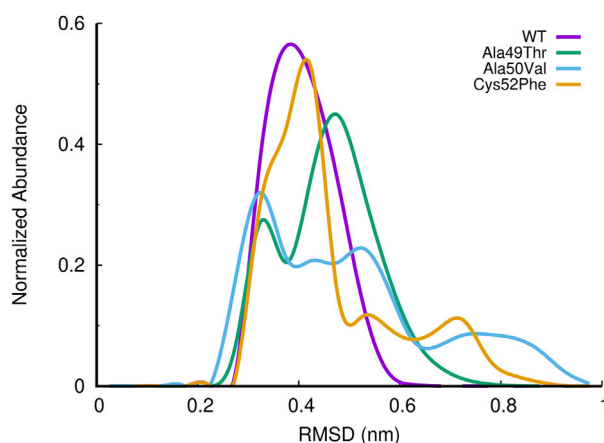
FIGURE 6

Zoom of the CT-L catalytic site of 20S proteasome. (A) Side chains of the three mutated residues and the N-terminal Thr1 are marked with sticks; (B), (C), and (D), X-ray binding pocket positions of bortezomib (BTZ), carfilzomib (CFZ) and ixazomib (IXA), respectively. All figures show the $\beta 5$ and $\beta 6$ subunits as cartoon, with $\beta 6$ being faded out.

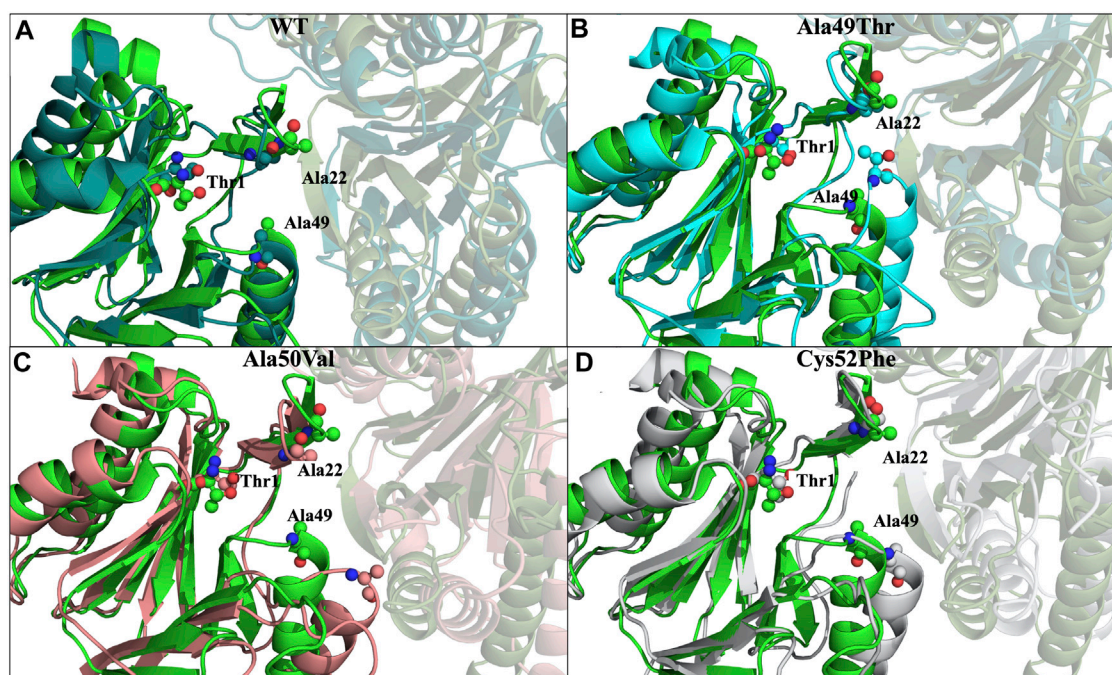
3.1 Conformational analysis of the stability of the $\beta 5$ subunit

To evaluate the impact of the three mutations on the dynamics of the 20S proteasome $\beta 5$ subunit, we started by analyzing the root-mean-square deviation (RMSD) of the β -rings from the $\beta 5$ subunits for the WT and studied mutants, using all replicate MD simulations.

In Figure 7, we have represented the RMSD distribution collected from the equilibrated parts of the different simulation systems in the form of the abundance of normalized RMSD histograms (Figure 7). The RMSD distribution of the WT system shows a profile resembling a perfect sigmoid, with a peak at around 0.4 nm of RMSD. On the other hand, all mutated systems show distinct and simultaneously, different profiles concerning the WT system, while visiting higher RMSD conformational states. A more

**FIGURE 7**

Histogram of the normalized abundance of the distribution of the RMSD of the c-alpha atoms of the $\beta 5$ subunits for the WT, Ala49Thr, Ala50Val and Cys52Phe simulations. RMSD values were calculated taking as reference, the initial conformation of the system of the first replicate for each simulated system (only equilibrated regions of the simulations were considered).

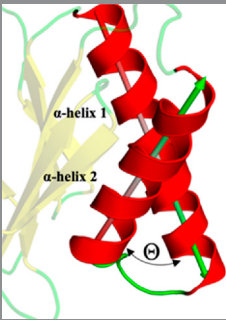
**FIGURE 8**

Most representative conformations of the different simulated systems. In light green we have represented the crystallographic structure (PDB code: 5LE5) of the $\beta 5$ subunit, while the $\beta 6$ subunit is represented as a faded cartoon. (A) In dark green we have represented the most populated conformation found in the simulations of the WT system, with a RMSD of 0.4 nm in respect to the crystallographic structure; (B) In cyan we have represented the most populated conformation found in the simulations of the Ala49Thr mutant, with a RMSD of 0.5 nm; (C) In light pink we have represented the most populated conformation found in the simulations of the Ala50Val mutant, with a RMSD of 0.3 nm; (D) In grey we have represented the most populated conformation found in the simulations of the Cys52Phe mutant, with a RMSD of 0.4 nm. RMSD values were calculated taking as reference, the initial conformation of the system of the first replicate for each simulated system.

detailed analysis of Ala49Thr mutant RMSD results revealed two major population sets of conformations found at around 0.3, (in a low degree) and 0.5 nm of RMSD (most populated conformation). Regarding Ala50Val simulations we can observe that this mutated simulated system visited a spread of conformations, ranging from

0.3 to 1 nm of RMSD concerning the reference stated, with clear peaks of conformational populations at 0.3 (most populated), 0.5, and 0.8. For simulations of the Cys52Phe mutant, we can observe a similar abundance profile of RMSD when compared to the WT system, with a major conformational peak observed around 0.4 nm

TABLE 1 Angle between α -helix 1 and α -helix 2 of $\beta 5$ subunit.

Angle between α -helix 1 and α -helix 2				
				
X-ray	WT	Ala49Thr	Ala50Val	Cys52Phe
129.45°	133.14°	130.09°	131.25°	125.23°

of RMSD. However, this simulated system visits additional conformational states, up to values of around 0.9 RMSD, concerning the reference structure. All the mutated systems compared to the WT visited a higher conformational state, which can be related to changes in structural aspects of the binding pocket of the $\beta 5$ subunit.

If we analyze in detail the extracted representative conformations for the most populated peaks in each simulated system (Figure 8), we can structurally understand in detail which conformational changes were responsible for the observed differences.

Comparing the conformation of the $\beta 5$ subunit in the crystal structure with the most populated conformation identified in the replicate MD simulations of the WT form of the proteasome, we observe a high general similarity between them, with the main differences arising from small loop movements and amino acid side-chain arrangements (Figure 8A).

Regarding the conformation extracted from Ala49Thr simulations with an RMSD around 0.5 nm (Figure 8B), the substitution of an alanine by a threonine appears to push α -helix 1 (Table 1) towards the $\beta 6$ subunit, leading to a different structural arrangement that affects the shape of the CT-L binding pocket.

In what concerned the results obtained from the simulations of the Ala50Val mutant, several changes can be identified in the $\beta 5$ subunit. In the conformation extracted with a RMSD value of around 0.3 nm (Figure 8C), one can find a high resemblance with the conformation observed in the crystal structure of the WT protein. The main difference lies at the top of α -helix 1, where the mutation was placed, where a clear reduction in the helix length is observed. Moreover, the β -sheet 6 before this helix (Figure 5) also becomes shorter, losing most of its secondary structure towards a more unstructured arrangement. These conformational changes carry consequences at the bottom of the CT-L binding pocket, influencing its shape.

With respect to the results obtained for the Cys52Phe mutation we identify the most populated conformation around 0.4 nm (Figure 8D) of RMSD. Our observations indicate that in this representative conformation, this mutation leads to an increase in the occupied volume in an enclosed region of the $\beta 5$ subunit, promoting a rotation of the phenylalanine residue into the

catalytic pocket, and pushing α -helix 1 away from the Thr1 residue (Table 1). As shown in Figure 8D, the Phe52 residue turns towards the $\beta 6$ subunit, with an associated unfolding of residues 48 to 52 (top of α -helix 1), affecting the shape of the binding pocket of the CT-L catalytic site. The less populated conformations obtained during the simulations are available in the (Supplementary Figure S1).

The secondary structure calculated using the dictionary of secondary structure (DSSP) (Kabsch and Sander, 1983; Touw et al., 2015) for the WT $\beta 5$ subunit shows an average of 0.27 of β -sheet, 0.33 of α -helix, and 0.2 of coil. Overall, all the remaining analyzed mutant systems show very similar secondary structure variation profiles, indicating that despite the observed RMSD profiles, no significant structural variations affecting the secondary structure of these systems are observed.

To evaluate the compactness of the $\beta 5$ subunit, we can evaluate simultaneously the number of hydrogen bonds (H-bonds) and the radius of gyration (Rg) of each simulated system. As shown in Figure 9A, the different mutations evaluated do not significantly impact the number of H-bonds established within the $\beta 5$ subunit. However, when we analyze the radius of gyration, we notice that despite both Ala49Thr and Ala50Val systems showing a very similar profile to that observed in the WT protein, the Cys52Phe mutant shows (Figure 9B) distinct compactness of the sampled conformational distribution. In the simulation of the former mutated system, it seems that the structure fluctuates between two conformational clusters, one with a more compact (with a radius of gyration around 1.68 nm), and another one with a less compact conformation (with higher values of the radius of gyration around 1.72 nm).

3.2 Chymotrypsin-like binding pocket ($\beta 5$ subunits) of the 20S proteasome

Focusing our analysis on the catalytic pocket of the $\beta 5$ subunit, we can see that this pocket is mainly shaped by three regions in the $\beta 5$ subunits: the terminus of β -sheet 1 and 2, respectively; the region below β -sheet 3; the beginning of α -helix 1 and the beginning and

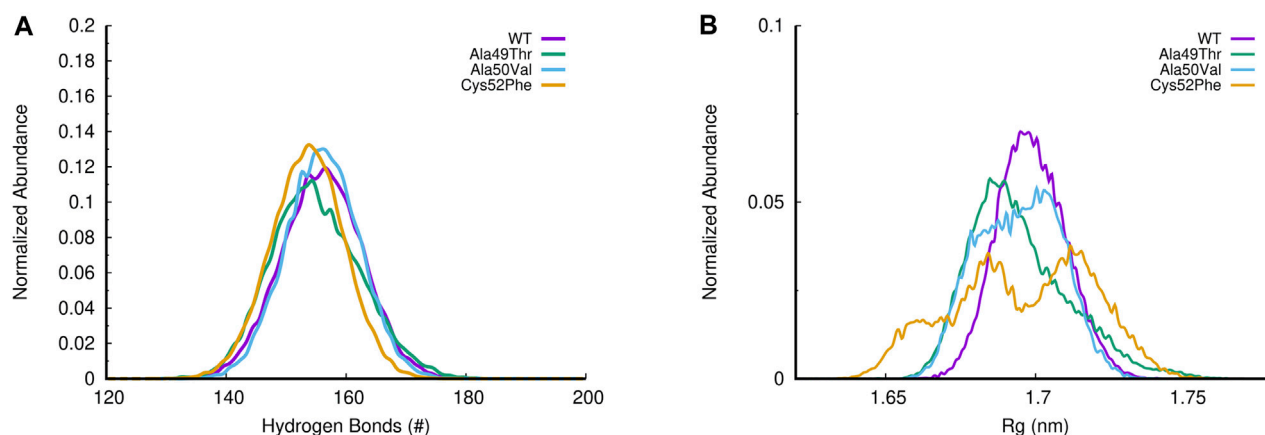


FIGURE 9

(A) Histogram of H-bonds distribution for all simulated systems; (B) Evaluation of the radius of gyration (R_g) in all $\beta 5$ subunit simulations.

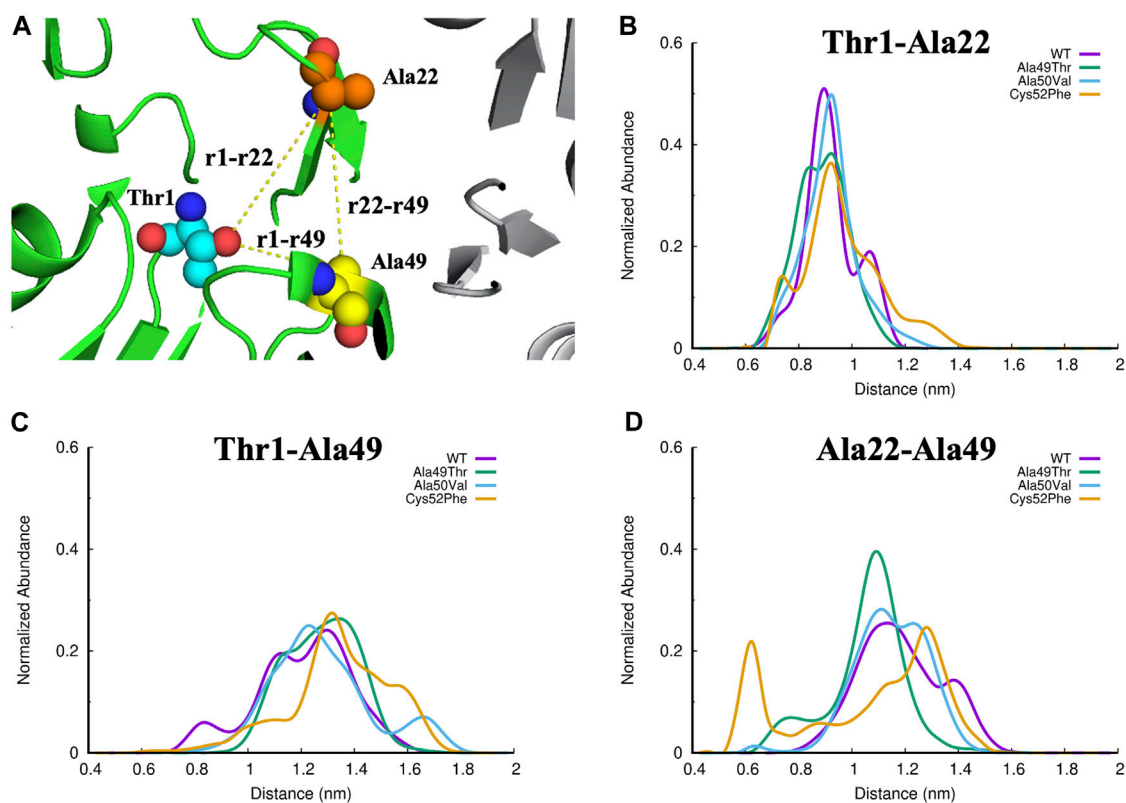


FIGURE 10

(A) Identification of the three regions of interest in the CT-L active site of the proteasome. The Thr1, Ala22 and Ala49 atoms are represented as small spheres, and the yellow lines represent the distances evaluated: (B) Thr1-Ala22, (C) Thr1-Ala49, and (D) Ala22-Ala49.

end of the β -sheet 5 and 6, respectively. The cleft resulting from these boundary regions makes the concavity of the conformation of the 20S proteasome perfect to accommodate stable protein-ligand interactions. To evaluate the effect of the studied mutations on the CT-L binding region of the $\beta 5$ subunit of the 20S proteasome we have analyzed the distance between the three

key residues in this region, which delimits the entire binding pocket: Thr1, which is the N-terminal where the covalent proteasome inhibitors bind to the protein; Ala22, a residue placed in the middle of the loop between β -sheet 3 and β -sheet 4 (Figure 5 for details); and, finally, Ala49, which is one of the mutated residues, and found on top of the α -helix 1.

TABLE 2 Volume of the catalytic pocket of $\beta 5$ subunit (20S proteasome). Volumes were calculated using POVME software considering only the most populated conformations of each set of simulations reported in **Figure 7**.

System	RMSD (nm)	Volume (\AA^3)	Ratio
X-ray		531	
WT	0.4	775	1
Ala49Thr	0.5	920	1.19
Ala50Val	0.3	742	0.96
Cys52Phe	0.4	672	0.87

An accurate analysis of the abundance of the different distances calculated in the equilibrated parts of the simulations of each system (**Figure 10**) indicates that the distances Thr1-Ala49 and Ala22-Ala49

show significant changes when compared with the distances between Thr1-Ala22. This suggests that the region where Ala49 is located is more susceptible to changes in its conformation in all the evaluated systems. As can be seen in **Figures 10C,D**, the Cys52Phe mutant is the most disruptive mutant of the ones tested since the abundance of the distance Ala22-Ala49 shows a much different profile when compared to all other simulated systems, suggesting in a first analysis, that this mutant promotes the greatest conformational changes from the evaluated systems, in the configuration of the CT-L binding site. As mentioned above, the inclusion of a more hydrophobic and larger residue (a cysteine is mutated by phenylalanine) forces significant structural changes in this region of the protein, changing both the shape and volume of the pocket.

Comparing the volume of the catalytic pocket in the most populated conformations obtained from the MD simulations for

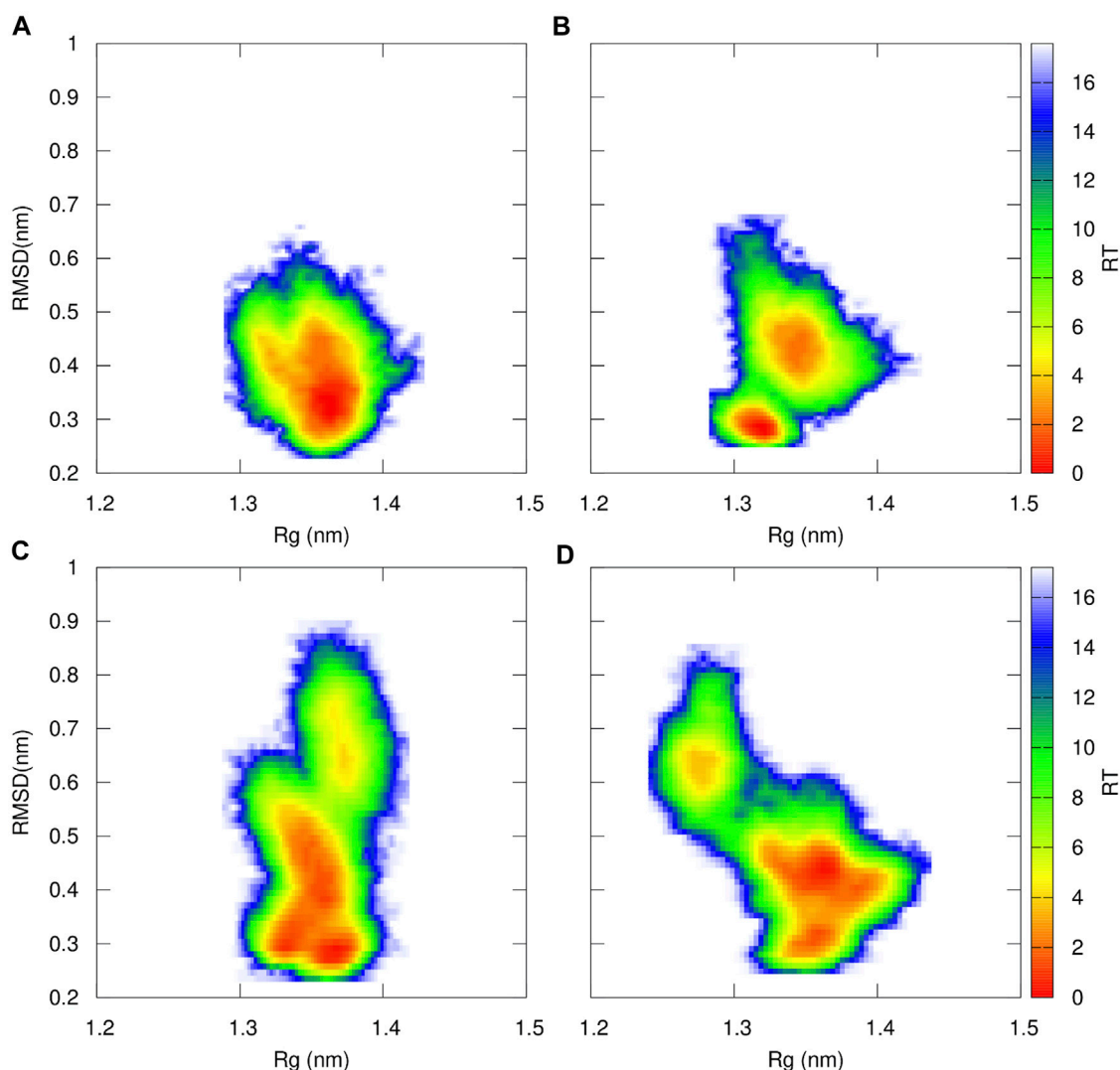


FIGURE 11

Free Energy Profiles for WT (**A**), Ala49Thr (**B**), Ala50Val (**C**) and Cys52Phe (**D**) of the catalytic region of the $\beta 5$ subunit of the 20S proteasome that delimits the catalytic pocket (residues 1 to 60—**Figure 5** for structural details) using RMSD and R_g as structural coordinates. Both RMSD and R_g were calculated using GROMACS software tools.

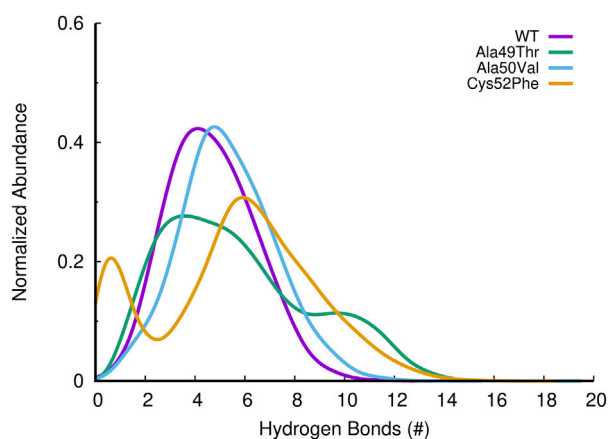


FIGURE 12

Histogram of the abundance of hydrogen bonds found between $\beta 5$ and $\beta 6$ subunits of the 20S proteasome, for the different simulated systems.

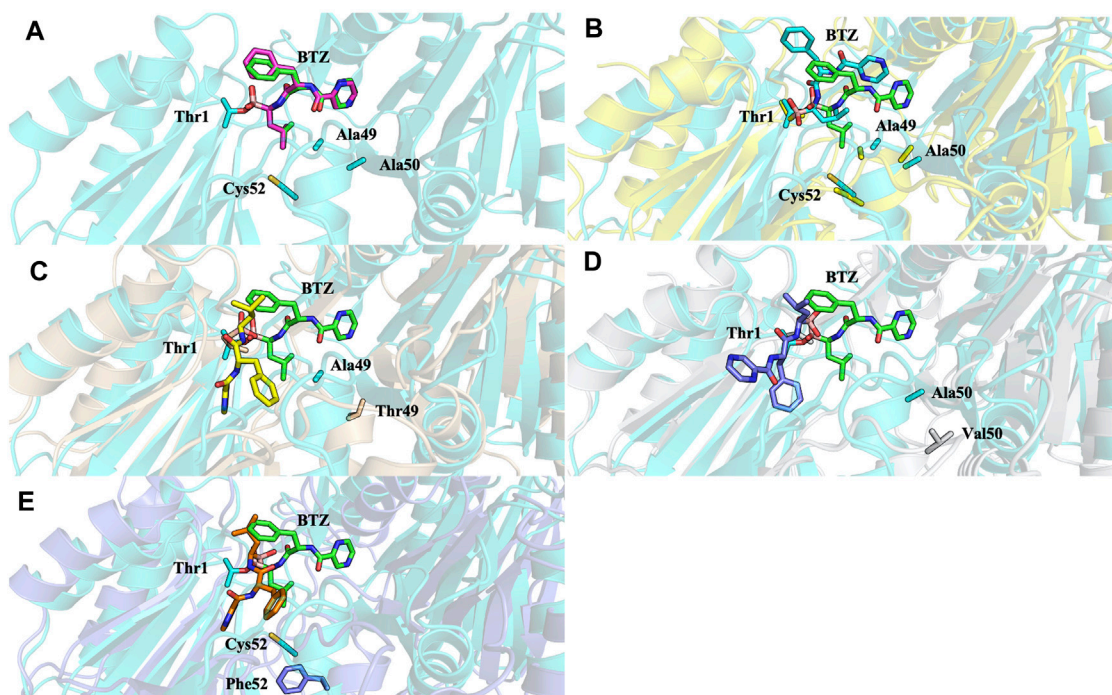


FIGURE 13

Superposition of the bortezomib docking poses of X-ray WT with docking results for: (A) bortezomib in docking validation, (B) WT, (C) Ala49Thr, (D) Ala50Val, and (E) Cys52Phe mutations with crystal structure 5LF3 (the crystallographic bortezomib is represented in green).

each set of simulations, we can see a wide range of volume. As seen in Table 2, concerning the crystal structure, we can see that a slightly higher volume of the catalytic pocket of $\beta 5$ subunit was determined in the representative conformation of the WT simulation, when compared to the WT crystallographic structure (775 Å³ compared to 531 Å³). The observed difference is expected since in the MD simulations there is no inhibitor to constrain the volume of the pocket, and the observed results occur due to a structural relaxation of this region of the protein, leading to changes affecting its shape

and volume. In the mutated system Ala49Thr the determined volume of the catalytic pocket of the representative conformation analyzed was 920 Å³, the highest pocket value identified in all systems under study. Regarding the representative conformation Ala50Val, the determined pocket volume was 742 Å³, which is a value very similar to the one determined for the WT system. Finally, for the representative conformation of the Cys52Phe system, the determined volume of the catalytic pocket was the lowest of all systems, indicating that the mutation of Cys52 to a larger

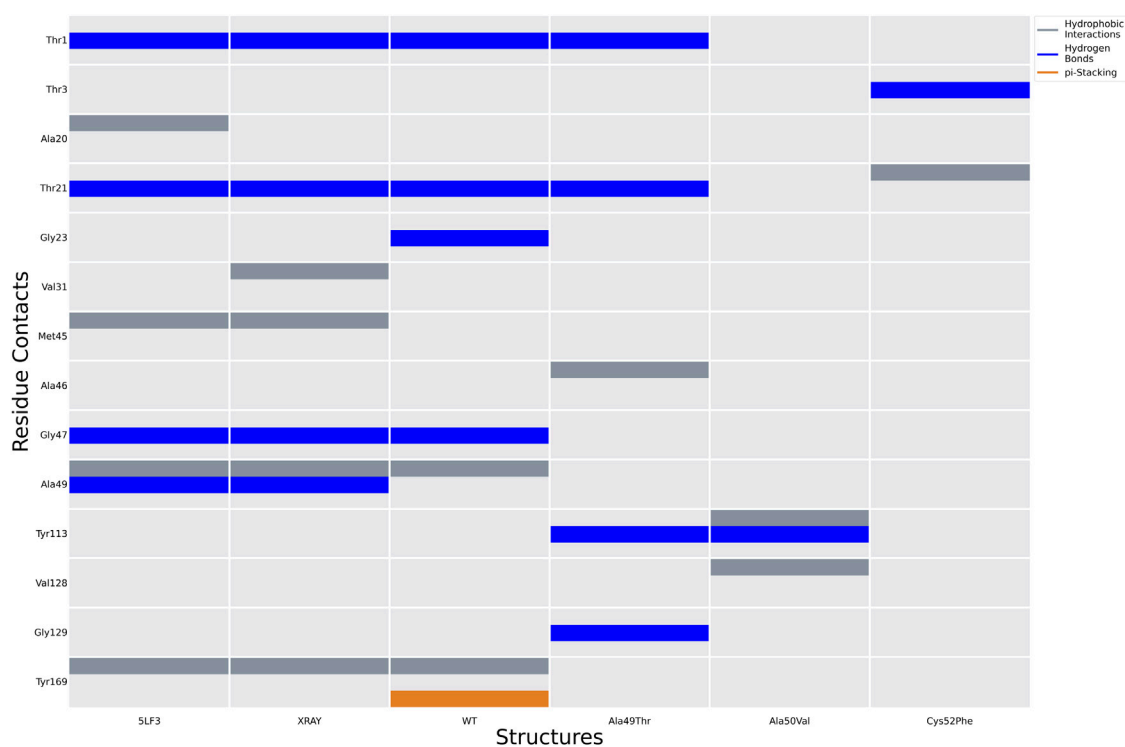


FIGURE 14

Ligand interactions established between bortezomib with the proteasome in the crystal structure 5LF3 and docking calculations performed using selected snapshots extracted from MD simulations of the WT and Ala49Thr, Ala50Val, and Cys52Phe mutants.

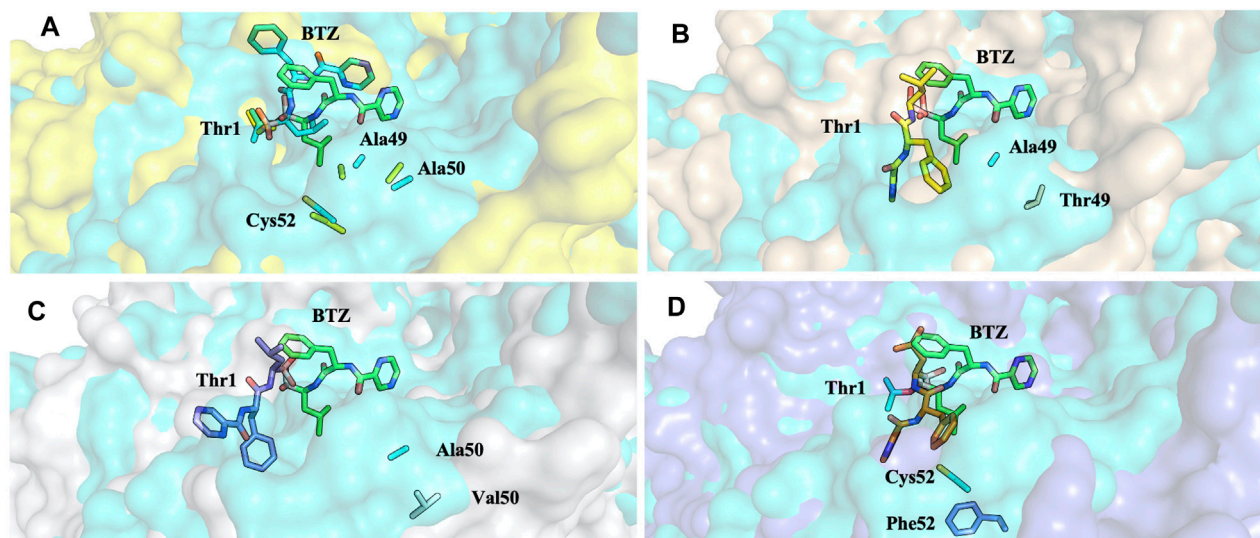


FIGURE 15

Superposition of the bortezomib docking poses of WT (A), Ala49Thr (B), Ala50Val (C), and Cys52Phe (D) mutations with crystal structure 5LF3 (the X-ray BTZ is represented in green). β 5- β 6 respective protein's surfaces.

hydrophobic residue significantly decreased the size of the pocket, up to a level that could indicate its collapse. The results focused on the analysis of the pocket volumes for each one of the simulated

systems can be correlated with the previously described results focused on the analysis of the distances between key residues (Figure 10). From the analysis of both properties, we can

conclude that the mutation Cys52Phe has a consistently higher impact on the structure stability and dynamics of the binding pocket.

To further characterize the proteasome's binding pocket configurations of the $\beta 5$ subunit, we calculated the Free Energy conformational profile for the WT, Ala49Thr, Ala50Val, and Cys52Phe based on the RMSD and Rg of the residues delimiting the catalytic pocket (residues 1–60) (Figure 11). In the WT simulations, one major conformational region is prevalent, as previously concluded from the histograms shown in Figure 7. However, this type of conformational profile is not observed in any of the mutant systems. If we focus on the results of Ala49Thr, despite the free energy profile being similar to the one observed for the WT system, we can identify two main basins, representing two distinct sets: one at around 0.3 nm of RMSD with a more “closed” conformation and another at 0.5 nm with a more “open” conformation (with a higher volume—table SM 1). Regarding the results obtained for the Ala50Val system, we can identify that a broader conformational space is populated with respect to the WT system, with three main conformational regions found at 0.3, 0.5, and 0.8 nm values of RMSD, each one with small differences on the observed Rg values. These small, but significant distances in the Rg, indicate the existence of open and closed configurations, consistent with the determined volumes shown in Table SM 1. The analysis of the Free energy profiles of the Cys52Phe mutant simulations, clearly indicates that this system is the one with a more dispersed configurational profile when compared to all the other simulated systems. From Figure 11D, we can identify two major configurational regions: one comprising two conformational results (RMSD 0.4 and 0.5 nm) with a more open configuration and, therefore, with higher volumes (Table 2), and a second one with higher RMSD values but with a more closed configuration (lower value of Rg) and therefore with a lower volume (Table 2). These results indicate that a good correlation between Rg and volumes of pockets is obtained.

3.3 Impact of mutations on $\beta 5$ – $\beta 6$ interactions

The $\beta 6$ subunit of the 20S proteasome contributes to the structure integrity and stability of the catalytic pocket present in the $\beta 5$ subunit. Analyzing the interactions between these two subunits can further help us understanding the influence of the mutations on the binding pocket. To evaluate the effect of the different mutations on the interaction between the $\beta 5$ and $\beta 6$ subunits of the 20S proteasome, we assessed the number of hydrogen bonds established between these two subunits during the simulations. As can be seen in Figure 12, the number of hydrogen bonds established between the two subunits in the Ala50Val mutation simulations is very similar when compared to the results obtained from the WT simulations. However, Ala49Thr mutation appears to promote some structural changes that significantly affect the interactions between $\beta 5$ and $\beta 6$ subunits. As shown in Figure 12, two major conformations are predominant: one in which the average number of hydrogen bonds is around 4–6 and another configuration with approximately 9–12 H-bonds. When

analyzed together with the results discussed in the previous sections, we can conclude about the existence in the Ala49Thr system of a higher packing/interaction between the two subunits, most probably related to an approximation of α -helix 1 of the $\beta 5$ subunit to the $\beta 6$ subunit. Regarding the Cys52Phe system, we can observe a higher variance in the number of hydrogen bonds. These results are consistent with the Rg vs. RMSD plots of the $\beta 5$ subunit previously analyzed, where it is possible to identify high conformational variability in the Cys52Phe simulations. Similarly, to what could be observed in the previous sections, this mutation seems to affect the shape of the binding pocket, influencing the interaction of the $\beta 5$ and $\beta 6$ subunits.

3.4 $\beta 5$ molecular docking

After studying the impact of these mutations on the structural stability and dynamics of the binding pocket of the $\beta 5$ subunit, we aim to understand how these mutations can affect the binding interactions between the $\beta 5$ subunit and a known proteasome inhibitor, bortezomib. The extensive research on bortezomib over the years offers a solid foundation for further investigation. The understanding of its mechanism of action is relatively more comprehensive compared to newer drugs, providing a clearer starting point for studying the effects of point mutations on drug binding and efficacy. Investigating bortezomib can provide insights that are potentially applicable to newer proteasome inhibitors.

Analysis of molecular docking calculations of the binding mode of bortezomib at the CT-L active site, when compared with the 5LF3 crystal structure, allows the observation of significant changes in the binding poses at the mutated structures and, consequently, in the protein-ligand (non-covalent) interactions that are formed (Figures 13–15). Our molecular docking protocol was initially used to try to reproduce the binding pose of bortezomib determined at the X-ray structure. As can be seen in Figure 13A, we were able to almost reproduce the binding of this compound exactly at the evaluated binding site. By analyzing the complex determined at the crystallographic structure, we could identify several interactions between bortezomib and Thr1 (H-bond), Ala20 (hydrophobic interaction), Thr21 (H-bond), Met45 (hydrophobic interaction), Gly47 (H-bond), Ala49 (H-bond and hydrophobic interactions), and Tyr169 (hydrophobic interaction) from the proteasome. Comparing the pose determined in the crystallographic structure and the ones obtained from our docking protocol we can observe the rotation of single bonds upon the docking of bortezomib in the WT structure (Figure 13B), driving a decrease in the interactions established with the protein (we can highlight the interaction with Thr1, Thr21, and Ala50).

Molecular docking calculations of bortezomib in the three mutant structures—Ala49Thr, Ala50Val, and Cys52Phe (Figures 13C–E, respectively)—strongly suggest that the presence of these single mutations alters bortezomib pose in the CT-L active site, impairing interactions with the S1 pocket, and hindering catalytic activity. Steric hindrance (due to bulkier side chains in the mutant residues) leads to substantial torsions resulting in

significant changes in the binding poses (e.g., in Ala50Val mutation, the pyrazine ring of bortezomib is about 12 Å from its position in the crystal structure) and consequently, a decrease in the number of key interactions of the ligand: the Ala49Thr mutation still allows the interaction of bortezomib with Thr1 (H-bond) and Thr21 (H-bond). However, in the Ala50Val mutation, bortezomib fails to interact with any residue usually enrolled for catalytic activity. In the Cys52Phe mutant, only the interaction with Thr21 is maintained, although switching from an H-bond to a hydrophobic interaction.

Mutation of the non-polar Ala49 to the polar threonine causes a steric clash with the bortezomib inhibitor and additionally with the proteasome's $\beta 6$ subunit, suggesting that the compounds failed to access the modified pocket preventing the binding.

4 Conclusion

Clinical resistance to proteasome inhibitors is a complex and challenging issue, influenced by multifactorial mechanisms such as mutations. To elucidate these resistance mechanisms and understand the structural changes that occur in $\beta 5$ subunit due to the emergence of mutations, here we report a computational study, using MD simulations and molecular docking, focused exclusively on three single mutations (Ala49Thr, Ala50Val, and Cys52Phe) which are involved in the binding of proteasome inhibitors (e.g., bortezomib) to the CT-L active site. Ala49 and Ala50 mutations were selected given their crucial location and potential impact on shaping and enclosing the active site. Cys52 is located in the middle of α -helix 1 in the N-terminal and, although not directly on the pocket surface, its mutation to a more hydrophobic and bulkier residue (Phe) has implications for the stability of α -helix 1 and hence the conformation of the binding pocket. The mutations were analyzed for their impact on proteasome conformation, functionality, and binding.

Trajectories obtained from the MD simulations were analyzed considering the RMSD, distances, H-bond contacts, binding pocket volume, and $\beta 5$ - $\beta 6$ interactions for the WT and the three mutant variants. In addition to comparing the stability of the $\beta 5$ variants, this study also explored the factors that may contribute to their stability and binding to inhibitors. Volume and “druggability/affinity” of mutants binding pockets by using bortezomib binding as an illustrative example were investigated. All mutant systems exhibit a greater conformational variability for the $\beta 5$ subunit (RMSD) when compared to the WT system. These significant differences are the result of side-chain rearrangements and small displacements of the protein backbone. Significant changes were observed in the distances between Thr1-Ala49 and Ala22-Ala49, indicating that the different amino acid substitutions are more susceptible to conformational changes in the region where Ala49 is placed. Moreover, the substitution of Cys52 for a more hydrophobic and larger residue such as phenylalanine, promotes changes in the shape and volume of the pocket, leading to significant structural changes in the closest protein regions such as the CT binding pocket. Furthermore, MD simulations showed that the volume of the catalytic pocket also changes with the analyzed mutations. This suggests that future drug design efforts should account for these conformational changes to ensure effective

binding. Additionally, in the Ala50Val system, a similar number of hydrogen bonds is established between the $\beta 5$ and $\beta 6$ subunits, while in the Ala49Thr mutation, the interaction between these subunits is affected (two major conformations are predominant: one with an average number of hydrogen bonds around 4 to 6, and another one with 9–12 hydrogen bonds), since a higher packing/interaction between the two subunits is observed. These observations are probably related to an approximation of α -helix 1 of the $\beta 5$ subunit to the $\beta 6$ subunit. Regarding the Cys52Phe mutation, a higher variance of hydrogen bonds was observed confirming the higher conformational variability in the Cys52Phe simulations. Changes in hydrogen bonding patterns, particularly in the Ala49Thr mutation, indicate altered interactions between the $\beta 5$ and $\beta 6$ subunits. This highlights the need for inhibitors that can adapt to these new interaction patterns.

Molecular docking calculations showed that the three mutations affect the binding to the CT-L active site, namely, through changes that occur in the S1 pocket and, consequently, modify the interaction pattern of bortezomib with the CT-L active site residues. Bulkier side chains leading to steric hindrance, fewer hydrogen bonds, fewer interactions with relevant residues, and thus the possibility of rotation of bortezomib, lead to a different position at the active site. Considering all these results, one can conclude that the Ala49Thr, Ala50Val, and Cys52Phe mutations change the conformational structure of the 20S proteasome $\beta 5$ subunit pocket, suggesting a significant influence on the resistance mechanisms associated with the therapeutic use of bortezomib. The insights gained can guide the development of more potent and selective drugs, capable of overcoming resistance mechanisms like those seen with bortezomib, thereby enhancing therapeutic efficacy in treating conditions like MM and other cancers where proteasome inhibitors are employed.

Data availability statement

The datasets presented in this study can be found in online repositories. The names of the repository/repositories and accession number(s) can be found in the article/[Supplementary Material](#).

Author contributions

PF: Data curation, Formal Analysis, Investigation, Validation, Visualization, Writing—original draft. RaG: Data curation, Visualization, Writing—original draft. BV: Formal Analysis, Validation, Visualization, Writing—original draft. JS: Funding acquisition, Project administration, Supervision, Writing—review and editing. RcG: Conceptualization, Data curation, Formal Analysis, Funding acquisition, Investigation, Methodology, Project administration, Resources, Software, Supervision, Validation, Visualization, Writing—original draft, Writing—review and editing.

Funding

The author(s) declare financial support was received for the research, authorship, and/or publication of this article. The authors

acknowledge Fundação para a Ciência e a Tecnologia (FCT) for financial support through projects PTDC/QEQ-MED/7042/2014, EXPL/UI-OUT/1288/2021, CPCA/A2/6972/2020, UIDB/04138/2020, UIDP/04138/2020, UIDB/04046/2020, and UIDP/04046/2020, and the European Union, (TWIN2PIPSA GA 101079147). Views and opinions expressed are however those of the author(s) only and do not necessarily reflect those of the European Union or the European Research Executive Agency (REA). Neither the European Union nor the granting authority can be held responsible for them. PD/BD/143158/2019 and Programa Lisboa 2020—area of Technological Infrastructures—within the scope of the “FFUL Computing Innovation Centre—Learn-Teach-Innovate-Transfer”.

Conflict of interest

The authors declare that the research was conducted in the absence of any commercial or financial relationships that could be construed as a potential conflict of interest.

References

- Abraham, M. J., Murtola, T., Schulz, R., Páll, S., Smith, J. C., Hess, B., et al. (2015). Gromacs: high performance molecular simulations through multi-level parallelism from laptops to supercomputers. *SoftwareX* 1 (2), 19–25. doi:10.1016/j.softx.2015.06.001
- Adasme, M. F., Linnemann, K. L., Bolz, S. N., Kaiser, F., Salentin, S., Haupt, V. J., et al. (2021). PLIP 2021: expanding the scope of the protein–ligand interaction profiler to DNA and RNA. *Nucleic Acids Res.* 49, W530–W534. doi:10.1093/nar/gkab294
- Basse, N., Montes, M., Maréchal, X., Qin, L., Bouvier-Durand, M., Genin, E., et al. (2010). Novel organic proteasome inhibitors identified by virtual and *in vitro* screening. *J. Med. Chem.* 53, 509–513. doi:10.1021/jm9011092
- Beck, P., Dubiella, C., and Groll, M. (2012). Covalent and non-covalent reversible proteasome inhibition. *biochem* 393, 1101–1120. doi:10.1515/hsz-2012-0212
- Berendsen, H. J. C., Postma, J. P. M., van Gunsteren, W. F., and Hermans, J. (1981). “Interaction models for water in relation to protein hydration,” in *Intermolecular forces: proceedings of the fourteenth Jerusalem symposium on quantum Chemistry and biochemistry held in Jerusalem, Israel, april 13–16, 1981*. Editor B. Pullman (Dordrecht: Springer Netherlands), 331–342. doi:10.1007/978-94-015-7658-1_21
- Berendsen, H. J. C., van der Spoel, D., and van Drunen, R. (1995). GROMACS: a message-passing parallel molecular dynamics implementation. *Comput. Phys. Commun.* 91, 43–56. doi:10.1016/0010-4655(95)00042-E
- Blackburn, C., Gigstad, K. M., Hales, P., Garcia, K., Jones, M., Bruzzese, F. J., et al. (2010). Characterization of a new series of non-covalent proteasome inhibitors with exquisite potency and selectivity for the 20S $\beta 5$ -subunit. *Biochem. J.* 430, 461–476. doi:10.1042/BJ20100383
- Borissenko, L., and Groll, M. (2007). 20S proteasome and its inhibitors: crystallographic knowledge for drug development. *Chem. Rev.* 107, 687–717. doi:10.1021/cr0502504
- Bussi, G., Donadio, D., and Parrinello, M. (2007). Canonical sampling through velocity rescaling. *J. Chem. Phys.* 126, 014101. doi:10.1063/1.2408420
- Chauhan, D., Catley, L., Li, G., Podar, K., Hideshima, T., Velankar, M., et al. (2005). A novel orally active proteasome inhibitor induces apoptosis in multiple myeloma cells with mechanisms distinct from bortezomib. *Cancer Cell* 8, 407–419. doi:10.1016/j.ccr.2005.10.013
- Chemical Computing group ULC (2023). *Molecular operating environment (MOE)*.
- Chondrogianni, N., Voutetakis, K., Kapetanou, M., Delitsikou, V., Papaevgeniou, N., Sakellari, M., et al. (2015). Proteasome activation: an innovative promising approach for delaying aging and retarding age-related diseases. *Ageing Res. Rev.* 23, 37–55. doi:10.1016/j.arr.2014.12.003
- Ciechanover, A. (2007). Intracellular protein degradation from a vague idea through the lysosome and the ubiquitin-proteasome system and on to human diseases and drug targeting: nobel lecture, december 8, 2004. *Ann. N. Y. Acad. Sci.* 1116, 1–28. doi:10.1196/annals.1402.078
- Da Fonseca, P. C. A., He, J., and Morris, E. P. (2012). Molecular model of the human 26S proteasome. *Mol. Cell* 46, 54–66. doi:10.1016/j.molcel.2012.03.026
- The author(s) declared that they were an editorial board member of Frontiers, at the time of submission. This had no impact on the peer review process and the final decision.
- Publisher’s note**
- All claims expressed in this article are solely those of the authors and do not necessarily represent those of their affiliated organizations, or those of the publisher, the editors and the reviewers. Any product that may be evaluated in this article, or claim that may be made by its manufacturer, is not guaranteed or endorsed by the publisher.
- Supplementary material**
- The Supplementary Material for this article can be found online at: <https://www.frontiersin.org/articles/10.3389/fchem.2023.1322628/full#supplementary-material>
- Da Fonseca, P. C. A., and Morris, E. P. (2008). Structure of the human 26S proteasome: subunit radial displacements open the gate into the proteolytic core. *J. Biol. Chem.* 283, 23305–23314. doi:10.1074/jbc.M802716200
- Darden, T., York, D., and Pedersen, L. (1993). Particle mesh Ewald: an $N \cdot \log(N)$ method for Ewald sums in large systems. *J. Chem. Phys.* 98, 10089–10092. doi:10.1063/1.464397
- de Bettignies, G., and Coux, O. (2010). Proteasome inhibitors: dozens of molecules and still counting. *Biochimie* 92, 1530–1545. doi:10.1016/j.biochi.2010.06.023
- Demo, S. D., Kirk, C. J., Aujay, M. a., Buchholz, T. J., Dajee, M., Ho, M. N., et al. (2007). Antitumor activity of PR-171, a novel irreversible inhibitor of the proteasome. *Cancer Res.* 67, 6383–6391. doi:10.1158/0008-5472.CAN-06-4086
- Diez-Rivero, C. M., Lafuente, E. M., and Reche, P. a. (2010). Computational analysis and modeling of cleavage by the immunoproteasome and the constitutive proteasome. *BMC Bioinforma.* 11, 479. doi:10.1186/1471-2105-11-479
- Durrant, J. D., de Oliveira, C. A. F., and McCammon, J. A. (2011). POVME: an algorithm for measuring binding-pocket volumes. *J. Mol. Graph. Model.* 29, 773–776. doi:10.1016/j.jmkgm.2010.10.007
- Durrant, J. D., Votapka, L., Sørensen, J., and Amaro, R. E. (2014). POVME 2.0: an enhanced tool for determining pocket shape and volume characteristics. *J. Chem. Theory Comput.* 10, 5047–5056. doi:10.1021/ct500381c
- Essmann, U., Perera, L., Berkowitz, M. L., Darden, T., Lee, H., and Pedersen, L. G. (1995). A smooth particle mesh Ewald method. *J. Chem. Phys.* 103, 8577–8593. doi:10.1063/1.470117
- European Medicines Agency (2023). EPAR—product information. Available at: https://www.ema.europa.eu/en/documents/product%20information/kyprolis%20%80%90epar%20%80%90product%20%80%90information_en.pdf. (Accessed April 5, 2023).
- FDA (2023). FDA highlights of prescribing information Kyprolis® (carfilzomib). Available at: https://www.accessdata.fda.gov/drugsatfda_docs/label/2020/202714s030lbl.pdf (Accessed April 5, 2023).
- Finley, D. (2009). Recognition and processing of ubiquitin-protein conjugates by the proteasome. *Annu. Rev. Biochem.* 78, 477–513. doi:10.1146/annurev.biochem.78.081507.101607
- Franke, N. E., Niewerth, D., Assaraf, Y. G., van Meerloo, J., Vojtekova, K., van Zantwijk, C. H., et al. (2012). Impaired bortezomib binding to mutant $\beta 5$ subunit of the proteasome is the underlying basis for bortezomib resistance in leukemia cells. *Leukemia* 26, 757–768. doi:10.1038/leu.2011.256
- Groll, M., Berkers, C. R., Ploegh, H. L., and Ova, H. (2006). Crystal structure of the boronic acid-based proteasome inhibitor bortezomib in complex with the yeast 20S proteasome. *Structure* 14, 451–456. doi:10.1016/j.str.2005.11.019
- Groll, M., Ditzel, L., Löwe, J., Stock, D., Bochtler, M., Bartunik, H. D., et al. (1997). Structure of 20S proteasome from yeast at 2.4 Å resolution. *Nature* 386, 463–471. doi:10.1038/386463a0

- Groll, M., Heinemeyer, W., Jäger, S., Ullrich, T., Bochtler, M., Wolf, D. H., et al. (1999). The catalytic sites of 20S proteasomes and their role in subunit maturation: a mutational and crystallographic study. *Proc. Natl. Acad. Sci. U. S. A.* 96, 10976–10983. doi:10.1073/pnas.96.20.10976
- Groll, M., and Huber, R. (2003). Substrate access and processing by the 20S proteasome core particle. *Int. J. Biochem. Cell Biol.* 35, 606–616. doi:10.1016/S1357-2725(02)00390-4
- Guedes, R. A., Aniceto, N., Andrade, M. A. P., Salvador, J. A. R., and Guedes, R. C. (2019). Chemical patterns of proteasome inhibitors: lessons learned from two decades of drug design. *Int. J. Mol. Sci.* 20, 5326–26. doi:10.3390/ijms20215326
- Guedes, R. A., Grilo, J. H., Carvalho, A. N., Fernandes, P. M. P., Ressurreição, A. S., Brito, V., et al. (2023). New scaffolds of proteasome inhibitors: boosting anticancer potential by exploiting the synergy of *in silico* and *in vitro* methodologies. *Pharmaceuticals* 16, 1096. doi:10.3390/ph16081096
- Guedes, R. A., Serra, P., Salvador, J. A. R., and Guedes, R. C. (2016). Computational approaches for the discovery of human proteasome inhibitors: an overview. *Molecules* 21, 927–27. doi:10.3390/molecules21070927
- Harshbarger, W., Miller, C., Diedrich, C., Sacchettini, J., Correspondence, J. S., and Sacchettini, J. (2015). Crystal structure of the human 20S proteasome in complex with carfilzomib. *Structure* 23, 418–424. doi:10.1016/j.str.2014.11.017
- Hess, B., Kutzner, C., van der Spoel, D., and Lindahl, E. (2008). GROMACS 4: algorithms for highly efficient, load-balanced, and scalable molecular simulation. *J. Chem. Theory Comput.* 4, 435–447. doi:10.1021/ct700301q
- Hochstrasser, M. (1995). Ubiquitin, proteasomes, and the regulation of intracellular protein degradation. *Curr. Opin. Cell Biol.* 7, 215–223. doi:10.1016/0955-0674(95)80031-X
- Huber, E. M., Basler, M., Schwab, R., Heinemeyer, W., Kirk, C. J., Groettrup, M., et al. (2012). Immuno- and constitutive proteasome crystal structures reveal differences in substrate and inhibitor specificity. *Cell* 148, 727–738. doi:10.1016/j.cell.2011.12.030
- Hunter, J. D. (2007). Matplotlib: a 2D graphics environment. *Comput. Sci. Eng.* 9, 90–95. doi:10.1109/MCSE.2007.55
- Jones, G., Willett, P., Glen, R. C., Leach, A. R., and Taylor, R. (1997). Development and validation of a genetic algorithm for flexible docking 1 Edited by F. E. Cohen. *J. Mol. Biol.* 267, 727–748. doi:10.1006/jmbi.1996.0897
- Jung, T., and Grune, T. (2012). “Structure of the proteasome,” in *Progress in molecular Biology and translational science* (Amsterdam, Netherlands: Elsevier Inc), 1–39. doi:10.1016/B978-0-12-397863-9.00001-8
- Kabsch, W., and Sander, C. (1983). Dictionary of protein secondary structure: pattern recognition of hydrogen-bonded and geometrical features. *Biopolymers* 22, 2577–2637. doi:10.1002/bip.360221211
- Kale, A. J., and Moore, B. S. (2012). Molecular mechanisms of acquired proteasome inhibitor resistance. *J. Med. Chem.* 55, 10317–10327. doi:10.1021/jm300434z
- Kisselev, A. F., Akopian, T. N., Woo, K. M., and Goldberg, A. L. (1999). The sizes of peptides generated from protein by mammalian 26 and 20 S proteasomes. *J. Biol. Chem.* 274, 3363–3371. doi:10.1074/jbc.274.6.3363
- Kisselev, A. F., Callard, A., and Goldberg, A. L. (2006). Importance of the different proteolytic sites of the proteasome and the efficacy of inhibitors varies with the protein substrate. *J. Biol. Chem.* 281, 8582–8590. doi:10.1074/jbc.M509043200
- Kisselev, A. F., Garcia-Calvo, M., Overkleeft, H. S., Peterson, E., Pennington, M. W., Ploegh, H. L., et al. (2003). The caspase-like sites of proteasomes, their substrate specificity, new inhibitors and substrates, and allosteric interactions with the trypsin-like sites. *J. Biol. Chem.* 278, 35869–35877. doi:10.1074/jbc.M303725200
- Kisselev, A. F., and Groettrup, M. (2014). Subunit specific inhibitors of proteasomes and their potential for immunomodulation. *Curr. Opin. Chem. Biol.* 23, 16–22. doi:10.1016/j.cbpa.2014.08.012
- Kisselev, A. F., van der Linden, W. A., and Overkleeft, H. S. (2012). Proteasome inhibitors: an expanding army attacking a unique target. *Chem. Biol.* 19, 99–115. doi:10.1016/j.chembiol.2012.01.003
- Kluyver, T., Ragan-Kelley, B., Pérez, F., Granger, B., Bussonnier, M., Frederic, J., et al. (2016). “Jupyter Notebooks - a publishing format for reproducible computational workflows,” in *Positioning and power in academic publishing: players, agents and agendas*. Editors F. Loizides and B. Schmidt (Amsterdam: IOS Press), 87–90. doi:10.3233/978-1-61499-649-1-87
- Korb, O., Stutzle, T., and Exner, T. E. (2009). Empirical scoring functions for advanced Protein–Ligand docking with PLANTS. *J. Chem. Inf. Model.* 49, 84–96. doi:10.1021/ci800298z
- Kortuem, K. M., and Stewart, A. K. (2013). *Carfilzomib*. *Blood* 121, 893–897. doi:10.1182/blood-2012-10-459883
- Kupperman, E., Lee, E. C., Cao, Y., Bannerman, B., Fitzgerald, M., Berger, A., et al. (2010). Evaluation of the proteasome inhibitor MLN9708 in preclinical models of human cancer. *Cancer Res.* 70, 1970–1980. doi:10.1158/0008-5472.CAN-09-2766
- Leonardo-Sousa, C., Carvalho, A. N., Guedes, R. A., Fernandes, P. M. P., Aniceto, N., Salvador, J. A. R., et al. (2022). Revisiting proteasome inhibitors: molecular underpinnings of their development, mechanisms of resistance and strategies to overcome anti-cancer drug resistance. *Molecules* 27, 2201. doi:10.3390/molecules27072201
- Lichter, D. I., Danaee, H., Pickard, M. D., Tayber, O., Sintchak, M., Shi, H., et al. (2012). Sequence analysis of β -subunit genes of the 20S proteasome in patients with relapsed multiple myeloma treated with bortezomib or dexamethasone. *Blood* 120, 4513–4516. doi:10.1182/blood-2012-05-426924
- Lindahl, E., Hess, B., and van der Spoel, D. (2001). GROMACS 3.0: a package for molecular simulation and trajectory analysis. *J. Mol. Model.* 7, 306–317. doi:10.1007/s008940100045
- Loizidou, E. Z., and Zeinalipour-Yazdi, C. D. (2014). Computational inhibition studies of the human proteasome by argyran-based analogues with subunit specificity. *Chem. Biol. Drug Des.* 84, 99–107. doi:10.1111/cbdd.12298
- Lü, S., Chen, Z., Yang, J., Chen, L., Gong, S., Zhou, H., et al. (2008a). Overexpression of the PSMB5 gene contributes to bortezomib resistance in T-lymphoblastic lymphoma/leukemia cells derived from Jurkat line. *Exp. Hematol.* 36, 1278–1284. doi:10.1016/j.exphem.2008.04.013
- Lü, S., Yang, J., Chen, Z., Gong, S., Zhou, H., Xu, X., et al. (2009). Different mutants of PSMB5 confer varying bortezomib resistance in T lymphoblastic lymphoma/leukemia cells derived from the Jurkat cell line. *Exp. Hematol.* 37, 831–837. doi:10.1016/j.exphem.2009.04.001
- Lü, S., Yang, J., Song, X., Gong, S., Zhou, H., Guo, L., et al. (2008b). Point mutation of the proteasome β 5 subunit gene is an important mechanism of bortezomib resistance in bortezomib-selected variants of Jurkat T cell lymphoblastic lymphoma/leukemia line. *J. Pharmacol. Exp. Ther.* 326, 423–431. doi:10.1124/jpet.108.138131
- Manasanch, E. E., Korde, N., Zingone, A., Tageja, N., Fernandez de Larrea, C., Bhutani, M., et al. (2014). The proteasome: mechanisms of biology and markers of activity and response to treatment in multiple myeloma. *Leuk. Lymphoma* 55, 1707–1714. doi:10.3109/10428194.2013.828351
- Manasanch, E. E., and Orlowski, R. Z. (2017). Proteasome inhibitors in cancer therapy. *Nat. Rev. Clin. Oncol.* 14, 417–433. doi:10.1038/nrclinonc.2016.206
- Merin, N., and Kelly, K. (2015). Clinical use of proteasome inhibitors in the treatment of multiple myeloma. *Pharmaceuticals* 8, 1–20. doi:10.3390/ph8010001
- Micale, N., Scarbaci, K., Troiano, V., Ettari, R., Grasso, S., and Zappalà, M. (2014). Peptide-based proteasome inhibitors in anticancer drug design. *Med. Res. Rev.* 34, 1001–1069. doi:10.1002/med.21312
- Niewerth, D., Jansen, G., Assaraf, Y. G., Zweegman, S., Kaspers, G. J. L., and Cloos, J. (2015). Molecular basis of resistance to proteasome inhibitors in hematological malignancies. *Drug resist. updat.* 18, 18–35. doi:10.1016/j.drug.2014.12.001
- Nosé, S., and Klein, M. L. (1983). Constant pressure molecular dynamics for molecular systems. *Mol. Phys.* 50, 1055–1076. doi:10.1080/00268978300102851
- Nussbaum, A. K., Dick, T. P., Keilholz, W., Schirle, M., Stevanović, S., Dietz, K., et al. (1998). Cleavage motifs of the yeast 20S proteasome β subunits deduced from digests of enolase. *Proc. Natl. Acad. Sci. U. S. A.* 95, 12504–12509. doi:10.1073/pnas.95.21.12504
- Oerlemans, R., Franke, N. E., Assaraf, Y. G., Cloos, J., van Zantwijk, I., Berkers, C. R., et al. (2008). Molecular basis of bortezomib resistance: proteasome subunit β 5 (PSMB5) gene mutation and overexpression of PSMB5 protein. *Blood* 112, 2489–2499. doi:10.1182/blood-2007-08-104950
- Páll, S., Abraham, M. J., Kutzner, C., Hess, B., and Lindahl, E. (2015). “Tackling exascale software challenges in molecular dynamics simulations with GROMACS,” in *Lecture notes in computer science (including subseries lecture notes in artificial intelligence and lecture notes in bioinformatics)* (Cham: Springer), 3–27. doi:10.1007/978-3-319-15976-8_1
- Parrinello, M., and Rahman, A. (1981). Polymorphic transitions in single crystals: a new molecular dynamics method. *J. Appl. Phys.* 52, 7182–7190. doi:10.1063/1.328693
- Petrucchi, M. T., Giraldo, P., Corradini, P., Teixeira, A., Dimopoulos, M. A., Blau, I. W., et al. (2013). A prospective, international phase 2 study of bortezomib retreatment in patients with relapsed multiple myeloma. *Br. J. Haematol.* 160, 649–659. doi:10.1111/bjh.12198
- Pronk, S., Páll, S., Schulz, R., Larsson, P., Bjelkmar, P., Apostolov, R., et al. (2013). GROMACS 4.5: a high-throughput and highly parallel open source molecular simulation toolkit. *Bioinformatics* 29, 845–854. doi:10.1093/bioinformatics/btt055
- Ri, M., Iida, S., Nakashima, T., Miyazaki, H., Mori, F., Ito, A., et al. (2010). Bortezomib-resistant myeloma cell lines: a role for mutated PSMB5 in preventing the accumulation of unfolded proteins and fatal ER stress. *Leukemia* 24, 1506–1512. doi:10.1038/leu.2010.137
- Schmid, N., Eichenberger, A. P., Choutko, A., Riniker, S., Winger, M., Mark, A. E., et al. (2011). Definition and testing of the GROMOS force-field versions 54A7 and 54B7. *Eur. Biophys. J.* 40, 843–856. doi:10.1007/s00249-011-0700-9
- Schmitt, S. M., Deshmukh, R. R., and Dou, Q. P. (2014). “Proteasome inhibitors and lessons learned from their mechanisms of action and resistance in human cancer,” in *Resistance to proteasome inhibitors in cancer* (Cham: Springer), 1–46. doi:10.1007/978-3-319-06752-0_1
- Schrader, J., Henneberg, F., Mata, R. A., Tittmann, K., Schneider, T. R., Stark, H., et al. (2016). The inhibition mechanism of human 20S proteasomes enables next-generation inhibitor design. *Science* 353, 594–598. doi:10.1126/science.aaf8993
- Schrödinger, L. (2023). *The PyMOL molecular graphics system*. Version 2.2.

- Schweitzer, A., Aufderheide, A., Rudack, T., Beck, F., Pfeifer, G., Plitzko, J. M., et al. (2016). Structure of the human 26S proteasome at a resolution of 3.9 Å. *Proc. Natl. Acad. Sci. U. S. A.* 113, 7816–7821. doi:10.1073/pnas.1608050113
- Shirley, M. (2016). Ixazomib: first global approval. *Drugs* 76, 405–411. doi:10.1007/s40265-016-0548-5
- Teicher, B. a., and Tomaszewski, J. E. (2015). Proteasome inhibitors. *Biochem. Pharmacol.* 96, 1–9. doi:10.1016/j.bcp.2015.04.008
- Touw, W. G., Baakman, C., Black, J., te Beek, T. A. H., Krieger, E., Joosten, R. P., et al. (2015). A series of PDB-related databanks for everyday needs. *Nucleic Acids Res.* 43, D364–D368. doi:10.1093/nar/gku1028
- Trivella, D. B. B., Pereira, A. R., Stein, M. L., Kasai, Y., Byrum, T., Valeriote, F. A., et al. (2014). Enzyme inhibition by hydroamination: design and mechanism of a hybrid carmaphycin-syringolin enone proteasome inhibitor. *Chem. Biol.* 21, 782–791. doi:10.1016/j.chembiol.2014.04.010
- Unno, M., Mizushima, T., Morimoto, Y., Tomisugi, Y., Tanaka, K., Yasuoka, N., et al. (2002). The structure of the mammalian 20S proteasome at 2.75 Å resolution. *Structure* 10, 609–618. doi:10.1016/S0969-2126(02)00748-7
- Van Der Spoel, D., Lindahl, E., Hess, B., Groenhof, G., Mark, A. E., and Berendsen, H. J. C. (2005). GROMACS: fast, flexible, and free. *J. Comput. Chem.* 26, 1701–1718. doi:10.1002/jcc.20291
- Verbrugge, S., Scheper, R. J., Lems, W. F., de Gruijl, T. D., and Jansen, G. (2015). Proteasome inhibitors as experimental therapeutics of autoimmune diseases. *Arthritis Res. Ther.* 17, 17. doi:10.1186/s13075-015-0529-1
- Verbrugge, S. E., Assaraf, Y. G., Dijkmans, B. A. C., Scheffer, G. L., Al, M., den Uyl, D., et al. (2012). Inactivating PSMβ5 Mutations and P-glycoprotein (multidrug resistance-associated protein/ATP-binding cassette B1) mediate resistance to proteasome inhibitors: *ex vivo* efficacy of (Immuno)Proteasome inhibitors in mononuclear blood cells from patients with rheumatoid arthritis. *J. Pharmacol. Exp. Ther.* 341, 174–182. doi:10.1124/jpet.111.187542
- Wagner, J. R., Sørensen, J., Hensley, N., Wong, C., Zhu, C., Perison, T., et al. (2017). POVME 3.0: software for mapping binding pocket flexibility. *J. Chem. Theory Comput.* 13, 4584–4592. doi:10.1021/acs.jctc.7b00500
- Waskom, M. (2021). seaborn: statistical data visualization. *J. Open Source Softw.* 6, 3021. doi:10.21105/joss.03021
- Williams, T., Kelley, C., Broker, H. B., John Campbell, R., Cunningham, D., Denholm, G., et al. (2019). *Gnuplot 5.2. 8: an interactive plotting program*.
- Zhu, Y., Zhao, X., Zhu, X., Wu, G., Li, Y., Ma, Y., et al. (2009). Design, synthesis, biological evaluation, and Structure–Activity relationship (SAR) discussion of dipeptidyl boronate proteasome inhibitors, Part I: comprehensive understanding of the SAR of α-amino acid boronates. *J. Med. Chem.* 52, 4192–4199. doi:10.1021/jm9005093



OPEN ACCESS

EDITED BY

Maria Manuel Marques,
Universidade Nova de Lisboa, Portugal

REVIEWED BY

Abbul Bashar Khan,
Jamia Millia Islamia, India
Giorgio Tofani,
National Institute of Chemistry, Slovenia

*CORRESPONDENCE

Paola R. Campodónico,
✉ pcampodonico@udd.cl

RECEIVED 05 September 2023

ACCEPTED 15 December 2023

PUBLISHED 10 January 2024

CITATION

Campodónico PR, Calderón C, Alcázar JJ,
Olivares B, Jaldin L and Suárez-Rozas C (2024),
Exploring the behavior of *Candida antarctica*
lipase B in aqueous mixtures of an imidazolium
ionic liquid and its surfactant analogue.
Front. Chem. 11:1289398.
doi: 10.3389/fchem.2023.1289398

COPYRIGHT

© 2024 Campodónico, Calderón, Alcázar,
Olivares, Jaldin and Suárez-Rozas. This is an
open-access article distributed under the terms
of the [Creative Commons Attribution License](#)
(CC BY). The use, distribution or reproduction in
other forums is permitted, provided the original
author(s) and the copyright owner(s) are
credited and that the original publication in this
journal is cited, in accordance with accepted
academic practice. No use, distribution or
reproduction is permitted which does not
comply with these terms.

Exploring the behavior of *Candida antarctica* lipase B in aqueous mixtures of an imidazolium ionic liquid and its surfactant analogue

Paola R. Campodónico^{1*}, Cristian Calderón², Jackson J. Alcázar¹,
Belén Olivares¹, Limberg Jaldin¹ and Cristian Suárez-Rozas¹

¹Centro de Química Médica, Instituto de Ciencias e Innovación en Medicina, Facultad de Medicina, Clínica Alemana Universidad del Desarrollo, Santiago, Chile, ²Facultad de Química y Biología, Universidad de Santiago de Chile, USACH, Santiago, Chile

The performance of *Candida antarctica* lipase B (CALB) has been evaluated in 1-butyl-3-methylimidazolium tetrafluoroborate (BMIMBF₄)/water mixtures in a wide range of molar fractions (χ_{BMIMBF_4}) with and without 1-dodecyl-3-methylimidazolium tetrafluoroborate (C₁₂-MIMBF₄), a surfactant derived from BMIMBF₄. The main aim of this work is to evaluate the influence of χ_{BMIMBF_4} over micellar aggregates to assess the activity of enzymatic reactions. The investigated reaction corresponds to the hydrolysis of the substrate *p*-nitrophenyl laureate in each χ_{BMIMBF_4} . The kinetic study for χ_{BMIMBF_4} at around 0.2 proved to be a border point in enzymatic activity. At $\chi_{\text{BMIMBF}_4} = 0.1$, the lipase activity increases in the presence of C₁₂-MIMBF₄. However, at higher concentrations, BMIMBF₄ has a negligible effect over the lipase activity. These results suggest specific interactions between water and BMIMBF₄ molecules in relation to CALB. This research highlights the superactivity phenomenon driven by the reaction media and the micelle interface. In this interfacial interaction, BMIMBF₄ acts directly on the changes induced on the enzyme upon its interaction with the micellar interface. This study opens a green perspective toward the biocatalysis field.

KEYWORDS

ionic liquids, enzyme, surfactant, catalysis, superactivity

1 Introduction

Natural resources facilitate reactions under gentle conditions. Enzymes, derived from readily available sources, serve as biodegradable, non-hazardous, and non-toxic catalysts. Typically, enzymatic reactions occur under mild conditions, such as physiological pH, room temperature, and atmospheric pressure. Leveraging enzymes in processes proves to be environmentally appealing, cost-effective, and sustainable.

In addition, biocatalysis considers at least 10 of the 12 principles of green chemistry (GC) (Sheldon and Woodley, 2018). GC, also known as sustainable chemistry, is not a particular set of technologies, but rather an area of study that emphasizes on the design of chemical products and processes with the aim of strongly reducing or eliminating chemicals that may become hazardous when transferred to the environment as waste (Sheldon, 2000). Catalysis is involved in i) highly selective and short synthesis and ii) products of high purity from a process that is efficient in energy with less waste compared to non-GC processes (Sheldon, 2016). Therefore, catalysts play a meaningful role in GC: i) decreasing energy

requirements; ii) increasing selectivity; iii) diminishing hazardous conditions; and iv) minimizing side products (Sheldon, 1997; Sheldon et al., 2007; Vekariya, 2017).

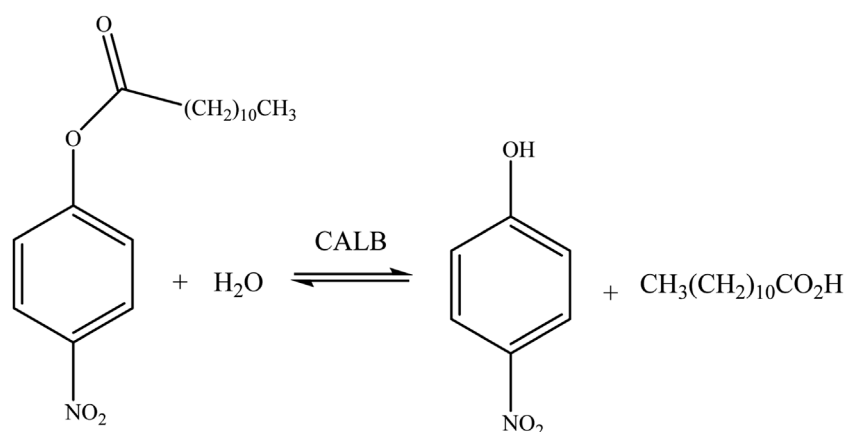
Lipases are a sub-class of enzymes within the esterase family whose natural function is to hydrolyze long chains of oils and fats (Schomburg et al., 1991; Fojan et al., 2000). Hydrolytic enzymes have found widespread application in organic synthesis as ecofriendly catalysts with versatile substrate specificities. They exhibit high stereoselectivity, operate under mild reaction conditions, are readily available commercially, and do not require cofactors (Dolman et al., 1997; Ventura et al., 2012). Among these enzymes, *Candida antarctica* lipase B (CALB) stands out as one of the most effective catalysts, recognized for its exceptional stability compared to other lipases. CALB, a monomeric protein composed of 317 amino acids, belongs to the α/β -hydrolase fold family. Its active site comprises serine, asparagine/glutamate, and histamine. Notably, CALB distinguishes itself from most lipases by lacking a lid covering the entrance to its active site. Demonstrating efficiency, CALB is a catalyst for hydrolysis in water and esterification in certain organic solvents (Wu et al., 2013; Rabbani et al., 2015).

Water is considered the greenest solvent based on its chemical nature and quantity. However, some enzymatic reactions that contain hydrophobic substrates cannot take place in aqueous media (Xu et al., 2017). On the other hand, the removal of water from catalytic processes that proceed in aqueous media is extremely expensive due to its high boiling point (Sheldon and Woodley, 2018), which creates the need for water replacement toward conventional organic solvents (COSs). Hence, COSs have been used in biocatalysis to increase enzyme stability, improve the solubility of hydrophobic reagents, and to prevent unwanted side reactions (Zaks and Klibanov, 1984). However, COSs are highly volatile due to their significant vapor pressure, flammability, and toxicity. Moreover, the inhibitory activity rates related to the enzyme are much lower in COSs than in water (Zaks and Klibanov, 1984; Carrea and Riva, 2008; Sheldon, 2016; Xu et al., 2017). Khmelnitsky et al. (1994) reported that the enzymatic activity in COSs can be increased by lyophilization with large amounts of salt (KCl). An alternative to the COS are ionic liquids (ILs). Further studies of enzymatic catalysis in room-temperature ionic liquids (RTILs) have shown increases in their rate coefficients compared with COSs (Itoh, 2017). RTILs are molten salts composed entirely of cations and anions that melt below 100°C (Welton, 1999; Weingärtner, 2008) with remarkable physicochemical properties, i.e., being non-flammable, non-corrosive, and non-volatile and bulk physical constant, which can be tuned by combining different cations and anions (Freemantle, 1998; Chiappe et al., 2007). High combinatorial flexibility has converted these materials into “designer solvents” or “task-specific” solvents (Freemantle, 1998; Chiappe et al., 2007) whose properties can be specified to suit the requirements of a particular reaction (Reichardt and Welton, 2011). For these reasons, RTILs have gained importance in the biocatalysis field, being recognized as a very promising reaction medium. RTILs have shown that enzymes have the same catalytic behavior compared to water and COSs, improving enzyme selectivity, activity, and stability and preventing unwanted side reactions (Xanthakis et al., 2006; de Gonzalo et al., 2007; Sheldon, 2016). Previous studies have shown that RTILs with hydrophobic anions are less denaturing than COSs displaying high catalytic activities, while

hydrophilic RTILs depend on the anion/cation moieties and alkyl chains, displaying harmful effects on enzyme activity/stability (Khmelnitsky et al., 1994; Sheldon et al., 2007; Van Rantwijk and Sheldon, 2007).

Since the 1990s, several types of enzymatic reactions in non-aqueous media have been studied, searching for alternative reaction media with an impact on GC (Gupta, 1992; Ballesteros et al., 1995; Cheong et al., 2022; Xue et al., 2022; Migowski et al., 2023). These have mainly considered proteases and lipases (Gupta, 1992; Ballesteros et al., 1995). The results based on the rate of the enzymatic reactions highlight the key role of hydrophobicity and polarity of the environment (Laszlo and Compton, 2001). Studies in solvent effects in enzymatic catalysis are a complex process as differences in enzyme hydration (Halling, 1994) and solvation of the enzyme and substrate must be considered. So, the key role of solvent effects focuses on the enzymatic activity for each solvent studied (Halling, 1994; Klibanov, 1997; Eckstein et al., 2002), and there is great scope within this field yet to be explored. Sheldon et al. (2002) published a second article on enzymes in RTILs and first on CALB in 1-butyl-3-methyl imidazolium hexafluorophosphate (BMIMPF₆) and 1-butyl-3-methyl imidazolium tetrafluoroborate (BMIMBF₄) comparing those RTILs with some COSs (Lau et al., 2000). Currently, a great number of publications show that RTILs based on hydrophobic anions, such as BF₄⁻, PF₆⁻, and bis(trifluoromethylsulfonyl)imide (NTF₂⁻) are less denaturing than some COSs, and they are responsible for higher catalytic activities (Van Rantwijk and Sheldon, 2007; Abe et al., 2008). However, hydrophilic anions, such as nitrate, acetate, or lactate anions, have a deleterious effect on the enzyme activity/stability by the formation of a strong hydrogen bond (HB) or Coulombic interactions (Sheldon et al., 2002; Lau et al., 2004). Therefore, anion studies based on RTILs have suggested that employing less polar RTILs may maintain a protective water layer around the enzyme, thereby contributing to its stabilization (Micaelo and Soares, 2008; Attri et al., 2011). Perhaps, this first shell of solvation might play a key role in enzyme activity through the HB established between the enzyme and anion(RTIL) (Sheldon et al., 2002). So, the anions should be able to accept the HB in order to maintain the structural conformation of the enzyme, discarding small and charged anions able to penetrate the protein matrix, reducing the flexibility or mobility of the enzyme active site (Anderson et al., 2002; Sheldon et al., 2002). On the other hand, increasing the alkyl chain in the cation leads to an increase in the hydrophobicity and van der Waals interactions responsible for the partial or total obstruction of the active site of the enzyme hindering the substrate–enzyme interaction and reducing the lipase activity (Fan et al., 2016).

Three approaches to working with non-conventional solvents in biocatalysis are i) pure solvent; ii) co-solvent in aqueous systems, and iii) biphasic systems (Kragl et al., 2002). In general, the solvent effect over the catalytic performance is described as i) stripping off the water layer around the enzyme interface; ii) penetrating the micro-aqueous phase to interact with the enzyme in order to change the conformation and/or active site; and iii) interacting directly with substrates and products or modifying their partitioning between hydrophilic and hydrophobic phases (Yang, 2009; Ventura et al., 2012). In summary, the influence of the reaction media over the enzymatic reaction is studied in terms of improving selectivity, activity, and stability. This influence depends on the catalyzed reaction and nature of the enzyme under study. Therefore, it is significant to elucidate under what circumstances and how the



SCHEME 1

General picture of the hydrolysis reaction of the substrate *p*-nitrophenyl laureate (*p*-NPL) mediated by CALB.

biocatalyst preserves its biological function and stability in these solvents. Currently, the research on relationships between solvents and enzyme functions is a large field to explore in order to identify suitable solvents that ensure enzyme stability/activity.

Despite the green features of the ILs, it is worth highlighting their potential damage to the environment (Pernak et al., 2001; Amde et al., 2015). Gonzalves et al. (2021) evidenced that the effect of these non-conventional solvents exerts an action over different organisms, suggesting that a critical role is centered over the cation based on their lipophilicity feature compared to the minor role of the anion (Gonzalves et al., 2021).

More recently, ionic liquids have been used as a surfactant in order to improve the lipase activity. In fact, surfactants immersed in ILs are a promising reaction medium because the interactions established (surfactant–water–IL) are minimized due to i) the nature of the surfactant headgroup and counterions (Calderón et al., 2019) and ii) solvation effects (Wijaya et al., 2016; Vicent-Luna et al., 2017). Then, this work uses BMIMBF₄ as a reference solvent and its long chain derivative, i.e., 1-dodecyl-3-methylimidazolium tetrafluoroborate (C₁₂-MIMBF₄), and our main aim is to evaluate the influence of molar fractions of BMIMBF₄/water mixtures over micellar aggregates in order to assess the activity of the enzymatic reaction. The investigated reaction corresponds to the hydrolysis of the substrate *p*-nitrophenyl laureate (*p*-NPL) in each reaction medium (see Scheme 1 below). This work shows a comparative study of the activity of CALB in pure and solvent mixtures at different molar fractions of BMIMBF₄/potassium phosphate buffer solution (considered water) and the same molar fractions with C₁₂-MIMBF₄, respectively.

2 Experimental section

2.1 Materials and methods

2.1.1 Materials

BMIMBF₄ and C₁₂-MIMBF₄ were purchased from Merck and IoLiTec, respectively. The specifications for BMIMBF₄ were purity

(HPLC) >98% and water (KF) < 0.1%. C₁₂-MIMBF₄ was not fully tested based on regulation (EC) 1272/2008. CALB, *p*-NPL (purity ≥98% by gas chromatography [GC]) 1, *p*-nitrophenol (*p*-NP, purity (DSC assay) > 99.5%), and dimethyl sulfoxide (DMSO, purity (GC) > 99.9%) were acquired from Sigma. The salts KH₂PO₄ and K₂HPO₄ were acquired from Merck (purities (alkalimetric assay) > 99.5%). All reagents were used as soon as delivered. Ultrapure water was used for the preparation of the aqueous solutions used (Merck Millipore Simplicity™ UV water purification system).

2.1.2 Lipase activity assays

This study uses pure BMIMBF₄ and phosphate buffer as the aqueous media, 50 mM and pH = 7.0, and BMIMBF₄/buffer mixtures in a wide range of molar fractions (χ) with/without the presence of a surfactant derived from the same ionic liquid, C₁₂-MIMBF₄ (10 mM). Each mixture was prepared by weighting the proper amount of the IL and buffer in a screw-capped vial. To favor mixing, each mixture was shaken and sonicated for 1 min and then left to equilibrate overnight before use. In all cases, the mixtures appeared homogeneous after this treatment. In those mixtures with C₁₂-BMIMBF₄, it was added after to be shaken and sonicated.

The substrate solution (*p*-NPL) was prepared in DMSO at 58 mM, and it was directly injected (10 μ L) in each reaction medium. Lipase activity was measured by UV–Vis spectrophotometry using an Agilent 8453 UV–Vis spectrometer. Aliquots from a stock solution (50 μ L) of lipase were added to 2.5 mL of each reaction medium containing the *p*-NPL. The release of *p*-NP was recorded by following the increase in absorbance at 410 nm. The concentration of *p*-NP was determined from absorbance data using a calibration curve. The initial reaction rates were calculated during the first 150 s of the initial segment of the reaction profiles. The enzymatic solution was prepared by adding 10 mg by 1 mL of potassium phosphate buffer solution. From the plots of *p*-NP release vs. time obtained at different *p*-NPL concentrations while keeping the amount of CALB added to each kinetic experiment constant, the dependence of the initial reaction rates with *p*-NPL was established. The determination of the Michaelis–Menten kinetic parameters (k_{cat} and K_M) was performed according to the following equation:

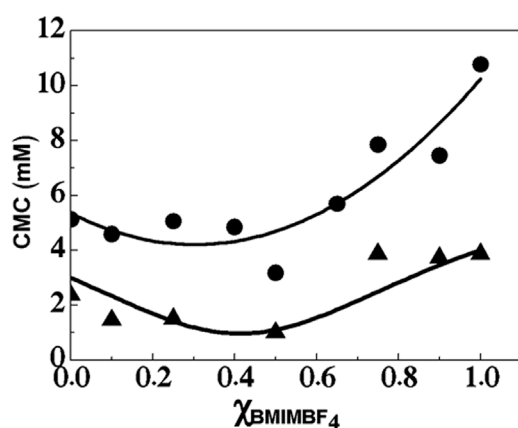


FIGURE 1
Variation in the critical micelle concentration (CMC) of C_{12} -MIMBF₄ with the molar fraction of BMIMBF₄ in an aqueous solution, without p -NPL (●) and 0.58 mM p -NPL (▲).

$$v = \frac{k_{cat} [E_0] [S]}{K_M + [S]}, \quad (1)$$

where v corresponds to the rates of CALB-catalyzed hydrolysis of p -NPL. $[E_0]$ is the enzyme concentration used in the hydrolysis experiments, and $[S]$ corresponds to the substrate concentration at which the associated reaction rate was determined (Calderón et al., 2019).

2.1.3 Critical micelle concentration determination

Conductivity measurements were used to evaluate the critical micelle concentration (CMC) of C_{12} -MIMBF₄ using an Adwa AD3000 conductometer provided with a 4-pole conductivity probe. The conductivity of water (buffer phosphate), BMIMBF₄, and BMIMBF₄/water mixtures was briefly measured upon adding some stock solution (c.a. 50–200 μ L) of C_{12} -MIMBF₄ (100 mM), prepared in the corresponding solvent mixture. CMC values were determined at the breaking point observed in the plots of conductivity, expressed in mS/cm vs. $[C_{12}\text{-MIMBF}_4]$ in all the ranges of molar fraction with respect to BMIMBF₄ (see Supplementary Figures S1, S2 in electronic Supplementary Material) (Evans, 1956).

3 Results and discussion

In order to obtain useful kinetic information that can be compared with the data obtained in pure media and solvent mixtures, special emphasis was placed on the evaluation of the extent of the influence of the micellar aggregates at a fixed molar concentration of surfactant (10 mM). This concentration was used in order to ensure that the surfactant concentration is beyond the CMC, where the presence of micellar aggregates acquires relevance. Figure 1 shows the relationships between the variation in the CMC of C_{12} -MIMBF₄ and the molar fraction to respect to BMIMBF₄ (χ_{BMIMBF_4}). All the χ_{BMIMBF_4} solutions were prepared in 50 mM buffer phosphate, pH = 7.0, and pure BMIMBF₄. The CMC is in the range 4–10 mM of the

surfactant without p -NPL (full circles in Figure 1). On the other hand, with p -NPL, the range is between 1 and 5 mM of the surfactant (full triangles in Figure 1).

Figure 1 shows two trends related to the variation in the CMC vs. IL content (in the presence and absence of the substrate), expressed as χ_{BMIMBF_4} . For the first trend (full circles, without p -NPL), there is a decrease with the initial addition of the IL ($\chi_{BMIMBF_4} = 0.1$); however, the CMC remains relatively constant until close to $\chi_{BMIMBF_4} = 0.4$. Past this point, the CMC values steadily increase, with a value close to 10 mM without p -NPL and a much lower value in the presence of p -NPL (close to 4 mM). Overall, the CMC is lower in the presence of p -NPL throughout the whole χ_{BMIMBF_4} range. The same fact was reported by Ventura et al. (2012); Łuczak et al. (2015). This observation is particularly interesting, given the fact that the significant change in CMC is attributable to the cosurfactant behavior displayed by the substrate (up to a concentration of 0.58 mM), which is readily incorporated into the micellar moiety. On the other hand, this is also relevant as a consideration for the substrate concentrations used in the enzymatic assays (10^{-5} – 10^{-4} M) because this concentration ensures no significant changes are introduced in the micellar moiety due to the incorporation of the substrate.

Figure 2 shows the variation in the lipase-catalyzed reaction rate at different χ_{BMIMBF_4} in the presence (10 mM of C_{12} -MIMBF₄, red color in Figure 2) and absence of the surfactant (black color, in Figure 2). These results suggest that in the enzymatic reaction, i) in pure solvents (buffer phosphate, $\chi_{BMIMBF_4} = 0.0$ and BMIMBF₄, $\chi_{BMIMBF_4} = 1.0$, respectively), the rate coefficients are negligible; ii) at $\chi_{BMIMBF_4} = 0.1$, the activity of lipase is increased with the presence of C_{12} -MIMBF₄ by 50% compared with the same reaction without the surfactant, reaching the highest value obtained (superactivity phenomena); iii) in the order $0.1 \leq \chi_{BMIMBF_4} \leq 0.4$, their rate coefficients decrease close to 25% and 80%, respectively, with respect to the lipase-catalyzed rate reaction obtained at $\chi_{BMIMBF_4} = 0.1$. In the cited range of molar fractions, the rate coefficient values are overturned, being they improved without the surfactant; and iv) at $\chi_{BMIMBF_4} > 0.4$, the enzyme activity decreases systematically (see inset in Figure 2).

Figure 1 agrees with Figure 2 because the range of χ_{BMIMBF_4} , where the CMC is almost constant ($0.1 \leq \chi_{BMIMBF_4} < 0.4$), recorded the highest enzyme activity. So, the best activity is recorded in the presence of C_{12} -MIMBF₄ compared to pure BMIMBF₄ or any mixture of it. The formation of micelles is being promoted by the self-aggregation of C_{12} -MIMBF₄, which is responsible for the increase in the anion–water interactions and the IL–water interface. Stamatis et al. (1999) reported that the presence of micelles provides a large increase in the interfacial area, increasing the interaction between the substrate and the enzyme active site. This significant increase in enzyme activity is known as superactivity (Spreti et al., 1999; Ventura et al., 2012; Sintra et al., 2014; Matteis et al., 2016; Calderón et al., 2019). This result is attributable to the reaction media because in water (buffer phosphate) and pure BMIMBF₄, there are no significant responses. In mixtures of IL/water, the enzymatic activity increases, but the same mixtures in the presence of C_{12} -MIMBF₄ showed increased superactivity phenomena, suggesting a preferential solvation process (Ben-Naim, 1990; Klahn et al., 2011; Alarcón-Espósito et al., 2016; Alarcón-Espósito et al., 2017).

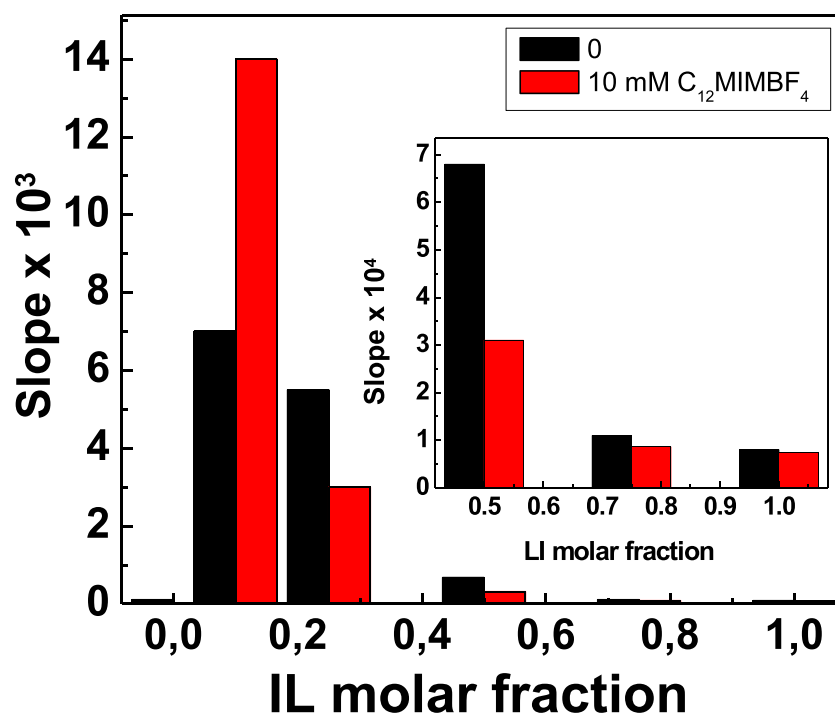


FIGURE 2

Reaction rate for the lipase-catalyzed decomposition of *p*-NPL as a function of the molar fraction of BMIMBF₄ in an aqueous solution, without C₁₂-MIMBF₄ (■) and 10 mM C₁₂-MIMBF₄ (■). Inset: zoom of the data in the region of BMIMBF₄ displaying lower CALB activity (region at $\chi_{\text{BMIMBF}_4} > 0.4$).

Furthermore, Figure 2 shows two environments close to $\chi_{\text{BMIMBF}_4} = 0.2$, being it value the border line, which is rich in water composition. For this reason, it is significant to elucidate how enzyme superactivity effects are induced by C₁₂-MIMBF₄ in IL/water mixtures. Previous studies on IL/water mixtures have demonstrated that the presence of water in the IL modifies their physical and chemical properties, for instance, viscosity, density, electrical conductivity, solvation, and solubility properties (Seddon et al., 2000; Cammarata et al., 2001; Alarcón-Espósito et al., 2015; Sánchez et al., 2018a; Sánchez et al., 2018b; Danna and Harper, 2019). Seddon et al. (2000) reported on the relevance of the HB in mixtures and their incidence in structural changes (Elaiwi et al., 1995). On the other hand, Sánchez et al. (2018c) suggested two strongly demarcated zones in BMIMBF₄/water mixtures. One of them was rich in water, which showed strong preferential solvent effects by the aqueous phase, while the other zone predominantly shows the “anion” solvent effects displayed by the IL composition (Alarcón-Espósito et al., 2016; Sánchez et al., 2018c). The authors established a relationship between the β parameter of Kamlet–Taft (β_{KT}) with χ_{BMIMBF_4} , where the β_{KT} value was related to the ability of the solvent to accept the HB (Kamlet and Taft, 1976; Kamlet et al., 1977; Kamlet et al., 1983). Then, while χ_{BMIMBF_4} increases until 0.2, the β_{KT} values increase at the same time, but since $\chi_{\text{BMIMBF}_4} > 0.2$, the β_{KT} parameter is shown to be high but constant and close to pure BMIMBF₄. This result agrees with that obtained by Fazio et al. (2008), who reported that high quantities of water in a mixture (IL/water) can weaken the structural network of the IL by increasing water–anion and water–water interactions, with a gradual loss of cation–anion interaction in the IL and displacing the cationic

moiety. For the enzymatic reaction investigated in this study, this suggests that it takes place at low compositions of BMIMBF₄ and the presence of large concentrations of micellar aggregates. Our results suggest that the presence of this critical composition of BMIMBF₄ has a direct influence on the enzyme and surfactant. This environment increases the catalytic rate constant (k_{cat}), being less efficient in pure media and other mixtures characterized by a high composition of BMIMBF₄. In our study, a significant decrease in lipase activity is observed at BMIMBF₄ concentrations greater than $\chi_{\text{BMIMBF}_4} > 0.4$. Ventura et al. (2012) reported that enzyme inhibition is related to strong interactions of the cation with the non-polar residues of the enzyme-active site (Constantinescu et al., 2007; Bekhouche et al., 2011), and such interactions could lead to an obstruction of the active site. Fluorescent measurements related to pyrene were reported by Sánchez et al. (2018c) for all mixtures at different molar fractions, showing that at $\chi_{\text{BMIMBF}_4} \leq 0.2$, the polarity of the mixtures diminishes dramatically with the addition of BMIMBF₄, as the water content in the mixture decreases. The authors suggest that $\chi_{\text{BMIMBF}_4} \leq 0.2$ is attributable to a reaction medium with high degrees of freedom and more susceptible to establish an HB.

Figure 3 shows the Michaelis–Menten kinetic parameters derived from the Lineweaver–Burk data analysis from the lipase activity assays (Viparelli et al., 1999; Biasutti et al., 2008; De Martino et al., 2018). The analyzed χ_{BMIMBF_4} in Figure 3 corresponds to those mixtures where the lipase activity shows its higher activities (see Figure 2). In Figure 3, the plot between k_{cat} vs. χ_{BMIMBF_4} shows that the maximum value of k_{cat} is displaced toward a lower χ_{BMIMBF_4} with a maximum value at $\chi_{\text{BMIMBF}_4} = 0.15$ in the absence of the

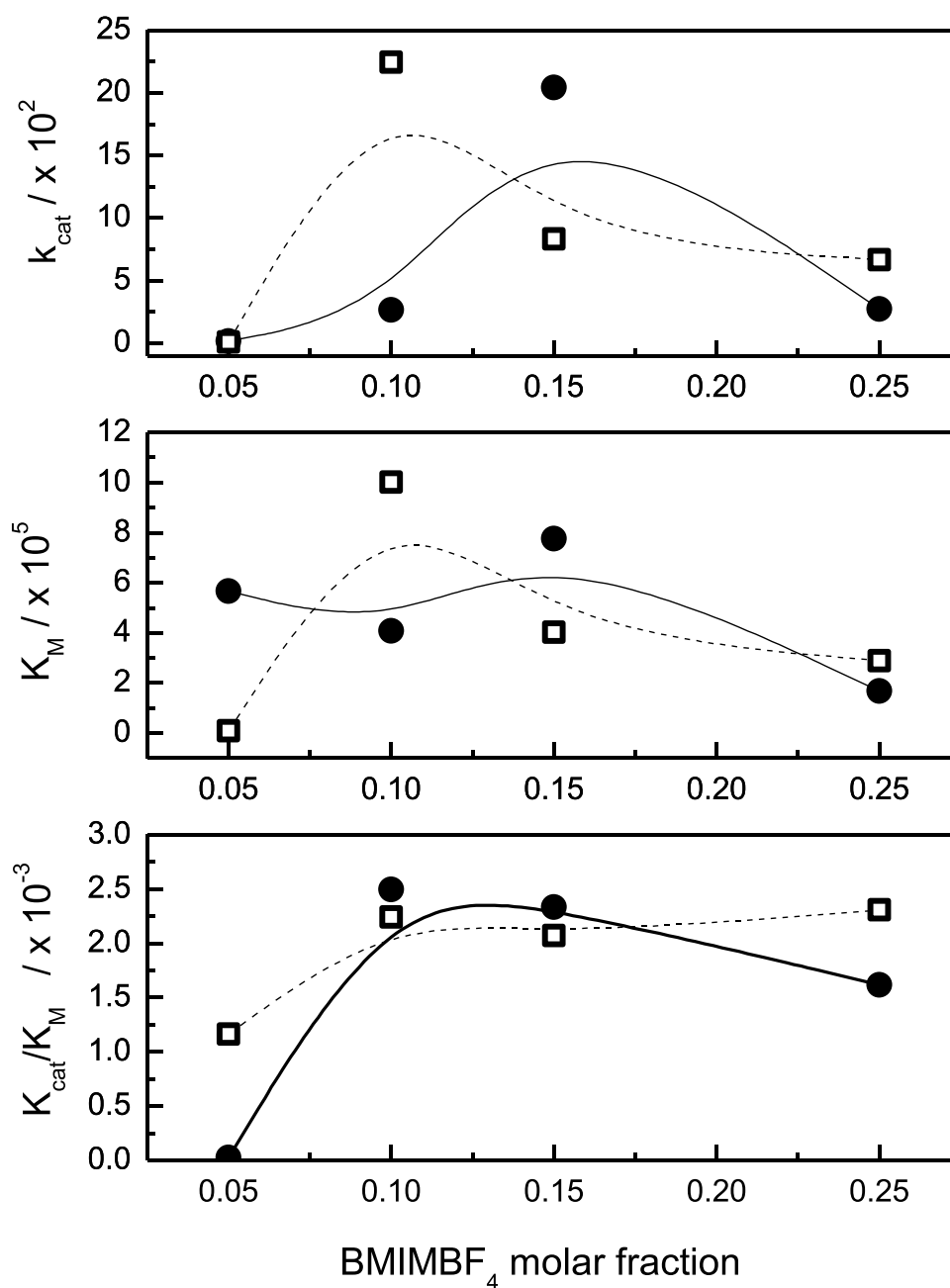


FIGURE 3
Michaelis–Menten parameters for the lipase-catalyzed solvolysis of *p*-NPL and its dependence on the molar fraction of BMIMBF₄. Parameter calculated based on the data obtained in the presence and absence of the surfactant: no surfactant (●) and 10 mM C₁₂-MIMBF₄ (□).

surfactant (full circles), and at 10 mM of C₁₂-MIMBF₄, the maximum value of k_{cat} is located at $\chi_{BMIMBF_4} = 0.1$ (empty squares). In Figure 3, the relationship between the affinity constant, denoted by K_M vs. χ_{BMIMBF_4} , displays more variability at lower χ_{BMIMBF_4} in the absence (full circles) and presence of C₁₂-MIMBF₄ (empty squares). Particularly, K_M decreases at $\chi_{BMIMBF_4} > 0.15$. Interestingly, K_M at $\chi_{BMIMBF_4} = 0.1$ shows a peak in the presence of C₁₂-MIMBF₄ and at $\chi_{BMIMBF_4} = 0.15$ in the absence of the surfactant. Finally, in Figure 3, the plot between k_{cat}/K_M vs. χ_{BMIMBF_4} shows the catalytic efficiency in mixtures of BMIMBF₄

with and without C₁₂-MIMBF₄. The magnitude of k_{cat}/K_M determined with (empty squares) and without C₁₂-MIMBF₄ (full circles) is higher in the range of χ_{BMIMBF_4} between 0.1 and 0.25, with a maximum value at $\chi_{BMIMBF_4} = 0.1$ for both trends. However, at $\chi_{BMIMBF_4} = 0.05$ without C₁₂-MIMBF₄ (full circles), a decrease in catalytic efficiency is observed.

Further inspection of the Michaelis–Menten catalytic parameters shows that there is a synergistic effect between BMIMBF₄ and the imidazolium-based surfactant. All experimental conditions considered, a complete incorporation of

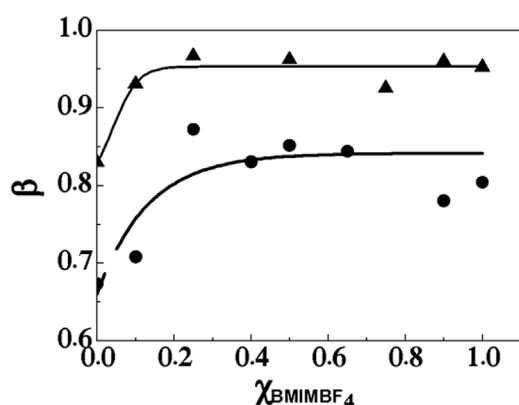


FIGURE 4
Counterion binding fraction (β) for micelles of C_{12} -MIMBF₄ as a function χ_{BMIMBF_4} in aqueous solutions. Full circles correspond to micelles without p -NPL, and full triangles correspond to micelles with 0.58 mM p -NPL.

the substrate into the micellar moiety can be expected, with the interfacial reaction taking place at the micelle/water interface, which appears to be enhanced by the presence of BMIMBF₄. This is particularly interesting, considering that the influence of BMIMBF₄ in the absence of the surfactant is regarded to have a moderate/high impact on the enzyme activity. Given that, in the presence of C_{12} -MIMBF₄, the studied lipase-catalyzed reaction requires the interaction of the enzyme with the micellar surface

to have access to the substrate, there are at least three possible effects responsible for the observed phenomenon:

- High substrate concentration and its incorporation into the micelles: The enzymatic reactions can take place in micellar environments; however, the occupation of the substrate and enzyme in the micelles is lower under the experimental condition considered. Moreover, BMIMBF₄ can influence changes in the surfactant CMC values measured, which leads to changes in the concentration of micelles in the system (assuming a constant surfactant aggregation number), but these changes do not fully correlate with the observed catalytic behavior.
- Increased enzymatic activity due to enhanced micellar partition of the enzyme: Similar to i), an increase in the local concentration of the enzyme on the micellar surface might lead to increased activity. However, considering a low micellar occupancy of the substrate molecules, the impact of the increased enzyme concentration should be minimal.
- Enhanced lipase activity due to changes in the intrinsic nature of the micellar interface: According to the available data in the present work, particularly the determination of the counterion occupancy at the micellar interface, it can be proposed that the interaction between the enzyme and the micelles, taking place at the water/micelle interface, leads to a modification of the enzyme activity attributed to conformational changes of the enzyme. This is further enhanced by the presence of BMIMBF₄, more specifically, by the BF₄[−] anion, which is largely incorporated at the water/micelle interface.

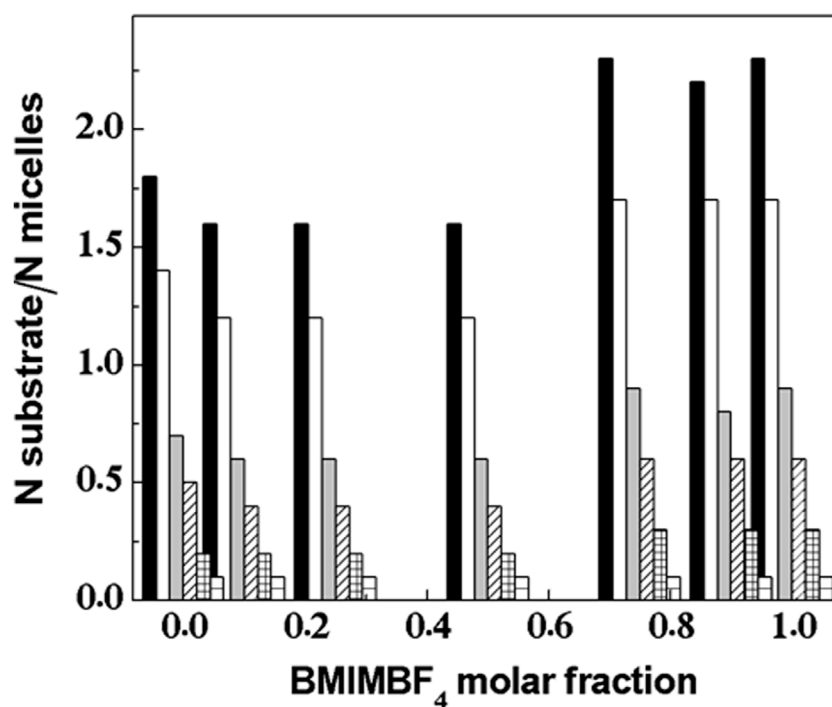
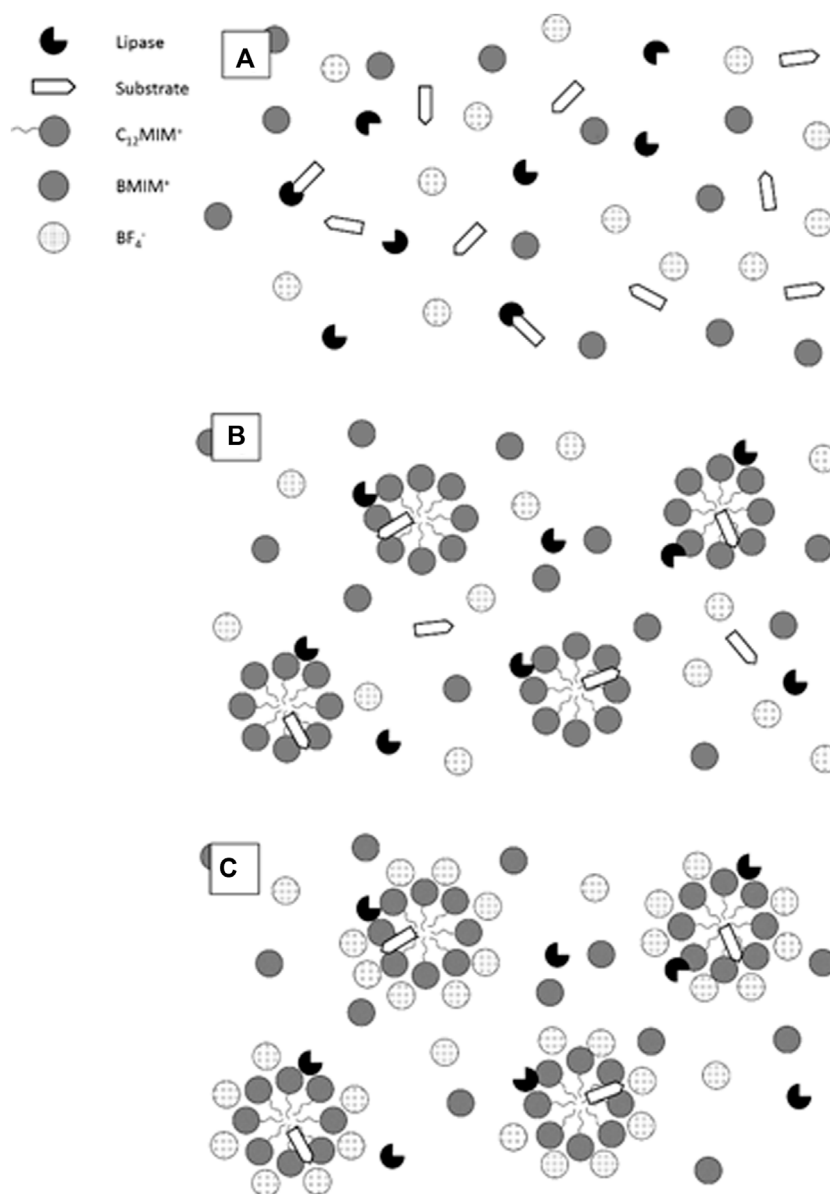


FIGURE 5
Estimated number of substrate molecules per micelle ratio as a function of BMIMBF₄ content in the studied aqueous mixtures. Bars correspond to different substrate concentrations (left to right): 2.0×10^{-4} M; 1.5×10^{-4} M; 7.5×10^{-5} M; 5.0×10^{-5} M; 2.5×10^{-5} M; and 1.0×10^{-5} M (data are given in Supplementary Material).



SCHEME 2

Depiction of the microenvironment for the lipase-catalyzed degradation of *p*-NPL. (A) Water/BMIMBF₄ mixtures; (B) 10 mM C₁₂-MIMBF₄ in low-IL content water/BMIMBF₄ mixtures; and (C) 10 mM C₁₂-MIMBF₄ in high-IL content water/BMIMBF₄ mixtures.

In order to address these possible effects, particularly those related with interfacial changes (point *iii*) in the previous paragraph) taking place in the micellar moiety, i.e., the zone delimited by the interaction between the solvent and the headgroups of C₁₂-MIMBF₄, the counterion binding to the micellar surface was determined (Khalid et al., 2017). Figure 4 shows the counterion binding fraction (β) for micelles of C₁₂-MIMBF₄ as a function of χ_{BMIMBF_4} in aqueous solutions. The degree of β was calculated according to the following equation:

$$\beta = (1 - \alpha), \quad (2)$$

where α corresponds to the ratio between the slopes of the post- and pre-CMC segments of conductivity vs. χ_{BMIMBF_4} plots (please refer

to Supplementary Figures S1, S2 in electronic Supplementary Material). Figure 4 shows two zones strongly demarcated. The first zone, rich in water at the range $0 \leq \chi_{\text{BMIMBF}_4} 0.2$, is characterized by strong variations in β -values. This parameter suggests an increase in counterions binding to the micelle. The second zone, at $\chi_{\text{BMIMBF}_4} > 0.2$, corresponds to a plateau, suggesting that the β -values are independent of χ_{BMIMBF_4} .

Figure 4 shows differences in the micellar environment in the presence of the substrate (0.58 mM, full triangles). The β -values are at least 20% higher than without the presence of the substrate. This fact suggests that the substrate operates as a cosurfactant in the micellar environment. Then, the number of available adsorption sites for the incorporation of the surfactant counterions (BF₄[−]) is

improved. At $\chi_{BMIMBF_4} > 0.2$, the β -value is close to unity (full triangles), suggesting that the interaction of the enzyme with the solvent/headgroup interface takes place in a surface saturated with BF_4^- anions, diminishing the catalytic activity (see Figure 2) with the increase in χ_{BMIMBF_4} .

Some reports have associated the interfacial phenomenon influencing the interaction between the micelle-bound substrate and lipase with the potential distribution of substrate molecules among the population of micelles present under a given experimental condition (Huang et al., 2008; Wu et al., 2008). Figure 5 shows the estimated number of substrate molecules per micelles with respect to χ_{BMIMBF_4} . Equation 3 allows us to estimate the concentration of micelles calculated by means of an approximate aggregation number (N), which is determined by geometrical considerations (surfactant hydrophobic chain length and headgroup approximate size), as well as hydrodynamic radius data determined by dynamic light scattering measurements,

$$N = 4\pi \frac{(L_c + r)^2}{a_0}, \quad (3)$$

where L_c corresponds to the surfactant chain length and r and a_0 are the radii and surface area of the surfactant headgroup, respectively.

Figure 5 shows an ideal scenario, where the substrate molecules are distributed as evenly as possible among the total number of micelles. Hence, the system is always dealing with low substrate occupancy in the micelles in the complete range of substrate concentrations considered. This indicates that the high efficiency achieved by the catalytic process takes place at the solvent/micelle interface, especially under the influence of $BMIMBF_4$. On the other hand, the loss of activity observed with the increase in χ_{BMIMBF_4} and its effect over the micellar solutions are not greatly affected by changes in the population of substrate molecules. This fact agrees with Figures 1, 4. Figure 1 (full triangles) shows the decreases in micelle concentration with the increase in CMC observed with the increase in χ_{BMIMBF_4} . Figure 4 (full triangles) shows changes in the enzyme–micelle interaction, which might lead to loss of activity due to the inability of lipase to interact with the micellized substrate molecules, being only able to interact with substrate molecules solubilized in χ_{BMIMBF_4} -rich aqueous media.

As a plausible description of the aforementioned phenomena, Scheme 2 shows the effect of the micelles on the studied enzymatic reaction. Scheme 2 is a general picture that describes more easily the effect of the micelles on the enzymatic reaction. Scheme 2A shows the enzymatic reaction in water– $BMIMBF_4$ mixtures. Schemes 2B shows the enzymatic reaction in micelles of C_{12} - $MIMBF_4$ in the presence of water– $BMIMBF_4$ mixtures (low χ_{BMIMBF_4}). Both schemes (A and B) show the substrate molecules available for the enzyme. However, Scheme 2B shows the interfacial interaction that leads to enhanced lipase activity. $BMIMBF_4$ operates directly on the changes induced in the enzyme upon its interaction with the micellar interface. Scheme 2C shows the enzymatic reaction in micelles of C_{12} - $MIMBF_4$ in the presence of water– $BMIMBF_4$ mixtures at high χ_{BMIMBF_4} . $BMIMBF_4$ and C_{12} - $MIMBF_4$ share the imidazolium moiety and the BF_4^- counterion. Then, the presence of either of these species should

be responsible for the modification of the micelle-induced enzymatic activity changes. Scheme 2C shows large counterion binding to the micellar moiety, which might indicate that the changes in lipase activity derive from the large local negative charge density directly influencing the enzyme conformation. This conformational change lead to the observed activity changes, with no relevant changes in the extent and/or mechanism of interaction of the enzyme with the water/micelle interface. A pertinent alternative will be integrated to a reliable molecular dynamics study in order to support the proposed explanation to the phenomenon described for the surfactant/ionic liquid/enzyme system under study.

Finally, one of the major limitations to the specific contributions made by the surfactant molecules in micellar aggregates lies in the fact that the concentration of micelles cannot be further increased without losing a significant amount of activity, attributable mainly to amounts of the enzyme that ends up adsorbed in micelles devoid of substrate molecules, hence lowering the effective concentration of the active enzyme in the system. Additionally, large micellar concentrations lead to changes in the aggregation number and geometry of the micelles, introducing further considerations to the overall phenomenon.

4 Conclusion

$BMIMBF_4$ can increase the catalytic rate of CALB in the hydrolysis of the p -NPL reaction at low χ_{BMIMBF_4} , particularly in the presence of C_{12} - $MIMBF_4$. The significant influence of low χ_{BMIMBF_4} over lipase activity suggests that specific interactions occur between $BMIMBF_4$ and lipase. Fluorescence analysis reveals this zone to be rich in water with strong preferential solvent effects mediated by the aqueous phase, showing a predominant “anion” solvent effect by the IL composition. These experimental conditions suggest a complete incorporation of the substrate into the micellar moiety. Hence, the interfacial reaction takes place at the micelle/water interface, enhanced by the presence of $BMIMBF_4$, attributable to conformational changes in the enzyme, and the possibility to incorporate the BF_4^- anion at the water/micelle interface, thus influencing directly the interfacial catalytic performance of the enzyme.

Data availability statement

The original contributions presented in the study are included in the article/Supplementary Material; further inquiries can be directed to the corresponding author.

Author contributions

PC: conceptualization, data curation, formal analysis, funding acquisition, investigation, methodology, project administration, resources, supervision, validation, writing–original draft, and writing–review and editing. CC: conceptualization, data curation, formal analysis, investigation, methodology, validation, and writing–review and editing. JA: formal analysis, investigation,

methodology, and writing–review and editing. BO: formal analysis, investigation, methodology, and writing–review and editing. LJ: formal analysis, investigation, methodology, and writing–review and editing. CS-R: formal analysis, investigation, methodology, and writing–review and editing.

Funding

The authors declare that no financial support was received for the research, authorship, and/or publication of this article.

Acknowledgments

PC acknowledges the Instituto de Ciencias e Innovación en Medicina (ICIM), Facultad de Medicina, Universidad del Desarrollo (UDD). LJ acknowledges the Doctorado en Ciencias e Innovación en Medicina, ICIM-UDD. JA acknowledges the Vicerectoría de Investigación y Doctorado (VRID) from ICIM-UDD.

REFERENCES

- Abe, Y., Kude, K., Hayase, S., Kawatsura, M., Tsunashima, K., and Itoh, T. (2008). Design of phosphonium ionic liquids for lipase-catalyzed transesterification. *J. Mol. Catal. B Enzym.* 51, 81–85. doi:10.1016/j.molcatb.2007.11.010
- Alarcón-Espósito, J., Contreras, R., and Campodónico, P. R. (2017). Iso-solvation effects in mixtures of ionic liquids on the kinetics of a model S_NAr reaction. *New J. Chem.* 41, 13435–13441. doi:10.1039/c7nj03246c
- Alarcón-Espósito, J., Contreras, R., Tapia, R. A., and Campodónico, P. R. (2016). Gutmann's donor numbers correctly assess the effect of the solvent on the kinetics of S_NAr reactions in ionic liquids. *Chem. Eur. J.* 22, 13347–13351. doi:10.1002/chem.201602237
- Alarcón-Espósito, J., Tapia, R. A., Contreras, R., and Campodónico, P. R. (2015). Changes in the S_NAr reaction mechanism brought about by preferential solvation. *RSC Adv.* 5, 99322–99328. doi:10.1039/c5ra20779g
- Amde, M., Liu, J.-F., and Pang, P. (2015). Environmental application, fate, effects, and concerns of ionic liquids. A review. *Environ. Sci. Technol.* 49, 12611–12627. doi:10.1021/acs.est.5b03123
- Anderson, J. L., Ding, J., Welton, T., and Armstrong, D. W. (2002). Characterizing ionic liquids on the basis of multiple solvation interactions. *J. Am. Chem. Soc.* 124 (47), 14247–14254. doi:10.1021/ja028156h
- Attri, P., Venkatesu, P., Kumar, A., and Byrne, N. (2011). A protic ionic liquid attenuates the deleterious actions of urea on α -chymotrypsin. *Phys. Chem. Chem. Phys.* 13, 17023–17026. doi:10.1039/c1cp22195g
- Ballesteros, A., Bornscheuer, U., Capewell, A., Combes, D., Condoret, J.-S., Koenig, K., et al. (1995). Review article enzymes in non-conventional phases. *Biotransformation* 13, 1–42. doi:10.3109/10242429509040103
- Bekhouche, M., Blum, L. J., and Doumèche, B. (2011). Ionic liquid-inspired cations covalently bound to formate dehydrogenase improve its stability and activity in ionic liquids. *ChemCatChem* 3, 875–882. doi:10.1002/cctc.201000390
- Ben-Naim, A. (1990). Preferential solvation in two- and in three-component systems. *Pure Appl. Chem.* 62, 25–34. doi:10.1351/pac199062010025
- Biasutti, M. A., Abuin, E. B., Silber, J. J., Correa, N. M., and Lissi, E. A. (2008). Kinetics of reactions catalyzed by enzymes in solutions of surfactants. *Adv. Colloid Interface Sci.* 136, 1–24. doi:10.1016/j.cis.2007.07.001
- Calderón, C., Contreras, R., and Campodónico, R. (2019). Surfactant-mediated enzymatic superactivity in water/ionic liquid mixtures, evaluated on a model hydrolytic reaction catalyzed by α -chymotrypsin. *J. Mol. Liq.* 283, 522–531. doi:10.1016/j.molliq.2019.03.106
- Cammarata, L., Kazarian, S. G., Salter, P. A., and Welton, T. (2001). Molecular states of water in room temperature ionic liquids. Electronic Supplementary Information available. *Phys. Chem. Chem. Phys.* 3, 5192–5200. doi:10.1039/B106900D
- Carrea, G., and Riva, S. (2008). *Organic synthesis with enzymes in non-aqueous media*. Jhon Wiley&Sons.
- Cheong, L.-Z., Mou, B., Wei, W., Hongli, Y., Hai, Z., Gege, Z., et al. (2022). "Ionic liquid as a green solvent for lipid processing." in *Recent advances in edible fats and oils Technology* Y. Lee, T. K. Tang, Phuah, and O. M. Lai (Singapore: Springer). doi:10.1007/978-981-16-5113-7_7
- Chiappe, C., Pieraccini, D., and Pomelli, C. S. (2007). The interactions affecting organic reactivity and selectivity in ionic liquids. *ACS Symp. Ser.* 1, 1–15. doi:10.1021/bk-2007-0950.ch001
- Constantinescu, D., Weingärtner, H., and Herrmann, C. (2007). Protein denaturation by ionic liquids and the Hofmeister series: a case study of aqueous solutions of ribonuclease A. *Angew. Chem. Int. Ed. Engl.* 46, 8887–8889. doi:10.1002/anie.200702295
- Danna, F., and Harper, J. (2019). Ionic liquids: properties and applications. *Frontiers Media SA*. Available at: <https://play.google.com/store/books/details?id=xzi3DwAAQBAJ>.
- de Gonzalo, G., Lavandera, I., Durchschein, K., Wurm, D., Faber, K., and Kroutil, W. (2007). Asymmetric biocatalytic reduction of ketones using hydroxy-functionalised water-miscible ionic liquids as solvents. *Tetrahedron Asymmetry* 18, 2541–2546. doi:10.1016/j.tetasy.2007.10.010
- De Martino, M. T., Abdelmohsen, L. K. E. A., Rutjes, F. P. J. T., and van Hest, J. C. M. (2018). Nanoreactors for green catalysis. *Beilstein J. Org. Chem.* 14, 716–733. doi:10.3762/bjoc.14.61
- Dolman, M., Halling, P. J., Moore, B. D., and Waldron, S. (1997). How dry are anhydrous enzymes? Measurement of residual and buried 18O-labeled water molecules using mass spectrometry. *Biopolymers* 41, 313–321. doi:10.1002/(sici)1097-0282(199703)41:3<313::aid-bip6>3.0.co;2-v
- Eckstein, M., Sesing, M., Kragl, U., and Adlercreutz, P. (2002). At low water activity α -chymotrypsin is more active in an ionic liquid than in non-ionic organic solvents. *Biotechnol. Lett.* 24, 867–872. doi:10.1023/A:1015564608261
- Elaiwi, A., Hitchcock, P. B., Seddon, K. R., Srinivasan, N., Tan, Y.-M., Welton, T., et al. (1995). Hydrogen bonding in imidazolium salts and its implications for ambient-temperature halogenoaluminate(III) ionic liquids. *J. Chem. Soc. Dalton Trans.* 3467, 3467. doi:10.1039/dt9950003467
- Evans, H. C. (1956). 117. Alkyl sulphates. Part I. Critical micelle concentrations of the sodium salts. *J. Chem. Soc.*, 579–586. doi:10.1039/JR9560000579
- Fan, Y., Dong, X., Li, X., Zhong, Y., Kong, J., Hua, S., et al. (2016). Spectroscopic studies on the inhibitory effects of ionic liquids on lipase activity. *Spectrochimica Acta Part A Mol. Biomol. Spectrosc.* 159, 128–133. doi:10.1016/j.saa.2016.01.047
- Fazio, B., Triolo, A., and Di Marco, G. (2008). Local organization of water and its effect on the structural heterogeneities in room-temperature ionic liquid/H₂O mixtures. *J. Raman Spectrosc.* 39, 233–237. doi:10.1002/jrs.1825
- Fojan, P., Jonson, P. H., Petersen, M. T. N., and Petersen, S. B. (2000). What distinguishes an esterase from a lipase: a novel structural approach. *Biochimie* 82, 1033–1041. doi:10.1016/S0300-9084(00)01188-3

Conflict of interest

The authors declare that the research was conducted in the absence of any commercial or financial relationships that could be construed as a potential conflict of interest.

Publisher's note

All claims expressed in this article are solely those of the authors and do not necessarily represent those of their affiliated organizations, or those of the publisher, the editors, and the reviewers. Any product that may be evaluated in this article, or claim that may be made by its manufacturer, is not guaranteed or endorsed by the publisher.

Supplementary material

The Supplementary Material for this article can be found online at: <https://www.frontiersin.org/articles/10.3389/fchem.2023.1289398/full#supplementary-material>

- Freemantle, M. (1998). DESIGNER SOLVENTS: ionic liquids may boost clean technology development. *Chem. Eng. News*. 76 (13), 32–37. doi:10.1021/cen-v076n013.p032
- Gonzalves, A. R. P., Paredes, X., Cristino, A. F., Santos, F. J. V., and Queirós, C. S. G. P. (2021). Ionic-liquids-a review of their toxicity to living organism. *Int. J. Mol. Sci.* 22, 5612–5662. doi:10.3390/ijms22115612
- Gupta, M. N. (1992). Enzyme function in organic solvents. *Eur. J. Biochem.* 203, 25–32. doi:10.1111/j.1432-1033.1992.tb19823.x
- Halling, P. J. (1994). Thermodynamic predictions for biocatalysis in nonconventional media: theory, tests, and recommendations for experimental design and analysis. *Enzyme Microb. Technol.* 16, 178–206. doi:10.1016/0141-0229(94)90043-4
- Huang, H., Han, Y., Wang, Y., Cao, M., and Wang, Y. (2008). Aggregation properties of cationic gemini surfactants with dihydroxyethylamino headgroups in aqueous solution. *Colloids and Surfaces A Physicochem. Eng. Asp.* 325, 26–32. doi:10.1016/j.colsurfa.2008.04.028
- Itoh, T. (2017). Ionic Liquids as tool to improve enzymatic organic synthesis. *Chem. Rev.* 117, 10567–10607. doi:10.1021/acs.chemrev.7b00158
- Kamlet, M. J., Abboud, J. L., and Taft, R. W. (1977). The solvatochromic comparison method. 6. The π^* scale of solvent polarities. *J. Am. Chem. Soc.* 99, 6027–6038. doi:10.1021/ja00460a031
- Kamlet, M. J., Abboud, J. L. M., Abraham, M. H., and Taft, R. W. (1983). Linear solvation energy relationships. 23. A comprehensive collection of the solvatochromic parameters, π^* , α , and β , and some methods for simplifying the generalized solvatochromic equation. *J. Org. Chem.* 48, 2877–2887. doi:10.1021/jo00165a018
- Kamlet, M. J., and Taft, R. W. (1976). The solvatochromic comparison method. I. The β -scale of solvent hydrogen-bond acceptor (HBA) basicities. *J. Am. Chem. Soc.* 98, 377–383. doi:10.1021/ja00418a009
- Khalid, K., Noh, M. A. M., Zain, S. M., and Khan, M. N. (2017). Determination of relative counterion binding constant to cationic micelles. *Top. Curr. Chem. (Z)* 375, 45. doi:10.1007/s41061-017-0132-9
- Khmelnitsky, Y. L., Welch, S. H., Clark, D. S., and Dordick, J. S. (1994). Salts dramatically enhance activity of enzymes suspended in organic solvents. *J. Am. Chem. Soc.* 116, 2647–2648. doi:10.1021/ja00085a066
- Klahn, M., Lim, G. S., Seduraman, A., and Wu, P. (2011). On the different roles of anions and cations in the solvation of enzymes in ionic liquids. *Phys. Chem. Chem. Phys.* 13, 1649–1662. doi:10.1039/C0CP01509A
- Klibanov, A. M. (1997). Why are enzymes less active in organic solvents than in water? *TIBTECH* 15, 97–101. doi:10.1016/S0167-7799(97)01013-5
- Kragl, U., Eckstein, M., and Kaftzik, N. (2002). Enzyme catalysis in ionic liquids. *Curr. Opin. Biotechnol.* 13, 565–571. doi:10.1016/S0958-1669(02)00353-1
- Laszlo, J. A., and Compton, D. L. (2001). α -Chymotrypsin catalysis in imidazolium-based ionic liquids. *Bioeng.* 75, 181–186. doi:10.1002/bit.1177
- Lau, R. M., Sorgedraeger, M. J., Carrea, G., van Rantwijk, F., Secundo, F., and Sheldon, R. A. (2004). Dissolution of *Candida Antarctica* lipase B in ionic liquids: effects on structure and activity. *Green Chem.* 6, 483–487. doi:10.1039/B405693K
- Lau, R. M., Van, R. F., Seddon, K. R., and Sheldon, R. A. (2000). Lipase-catalyzed reactions in ionic liquids. *Org. Lett.* 2 (26), 4189–4191. doi:10.1021/ol006732d
- Łuczak, J., Latowska, A., and Hupka, J. (2015). Micelle formation of Tween 20 nonionic surfactant in imidazolium ionic liquids. *Colloids Surfaces A Physicochem. Eng. Aspects* 471, 26–37. doi:10.1016/j.colsurfa.2015.02.008
- Matteis, L. D., De Matteis, L., Di Renzo, F., Germani, R., Goracci, L., Spredi, N., et al. (2016). α -Chymotrypsin superactivity in quaternary ammonium salt solution: kinetic and computational studies. *RSC Adv.* 6, 46202–46211. doi:10.1039/c6ra07425a
- Micaelo, N. M., and Soares, C. M. (2008). Protein structure and dynamics in ionic liquids. Insights from molecular dynamics simulation studies. *J. Phys. Chem. B* 112, 2566–2572. doi:10.1021/jp0766050
- Migowski, P., Lozano, P., and Dupont, J. (2023). Imidazolium based ionic liquid-phase green catalytic reactions. *Green Chem.* 25, 1237–1260. doi:10.1039/D2GC04749G
- Pernak, J., Rogoza, J., and Mirska, I. (2001). Synthesis and antimicrobial activities of new pyridinium and benzimidazolium chlorides. *J. Med. Chem.* 36, 313–320. doi:10.1016/S0223-5234(01)01226-0
- Rabbani, G., Ahmad, E., Khan, M. V., Ashraf, M. T., Bhat, R., and Khan, R. H. (2015). Impact of structural stability of cold adapted *Candida Antarctica* lipase B (CaLB): in relation to pH, chemical and thermal denaturation. *RSC Adv.* 5, 20115–20131. doi:10.1039/C4RA17093H
- Reichardt, C., and Welton, T. (2011). *Solvents and solvent effects in organic chemistry*. Wiley-VCH Verlag GmbH & Co. KGaA.
- Sánchez, B., Calderón, C., Garrido, C., Contreras, R., and Campodónico, P. R. (2018a). Solvent effect on a model SNAr reaction in ionic liquid/water mixtures at different compositions. *New J. Chem.* 42, 9645–9650. doi:10.1039/c7nj04820c
- Sánchez, B., Calderón, C., Garrido, C., Contreras, R., and Campodónico, P. R. (2018c). Solvent effect on a model SNAr reaction in ionic liquid/water mixtures at different compositions. *New J. Chem.* 42, 9645–9650. doi:10.1039/C7NJ04820C
- Sánchez, B., Calderón, C., Tapia, R. A., Contreras, R., and Campodónico, P. R. (2018b). Activation of electrophile/nucleophile pair by a nucleophilic and electrophilic solvation in a SNAr reaction. *Front. Chem.* 6, 509. doi:10.3389/fchem.2018.00509
- Schomburg, D., and Salzmann, M. (1991). “Oligonucleotidase,” in *Enzyme handbook 3: class 3: hydrolases*. Editors D. Schomburg and M. Salzmann (Berlin, Heidelberg: Springer Berlin Heidelberg), 765–768. doi:10.1007/978-3-642-76463-9_162
- Seddon, K. R., Torres, M. J., and Annegret, S. (2000). Influence of chloride, water, and organic solvents on the physical properties of ionic liquids. *Pure Appl. Chem.* 72, 2275–2287. doi:10.1351/pac200072122275
- Sheldon, R. A. (1997). Catalysis: the key to waste minimization. *J. Chem. Technol. Biotechnol.* 68, 381–388. doi:10.1002/(sici)1097-4660(199704)68:4<381::aid-jctb620>3.0.co;2-3
- Sheldon, R. A. (2000). Atom utilisation, E factors and the catalytic solution. *Comptes Rendus l'Académie Sci. - Series IIC - Chemistry* 3, 541–551. doi:10.1016/S1387-1609(00)01174-9
- Sheldon, R. A. (2016). Biocatalysis and biomass conversion in alternative reaction media. *Chemistry* 22, 12984–12999. doi:10.1002/chem.201601940
- Sheldon, R. A., Arends, I., and Hanefeld, U. (2007). *Green chemistry and catalysis*. John Wiley & Sons. Verlag GmbH & Co. KGaA. doi:10.1002/9783527611003
- Sheldon, R. A., Lau, R. M., Sorgedraeger, M. J., van Rantwijk, F., and Seddon, K. R. (2002). Biocatalysis in ionic liquids. *Green Chem.* 4, 147–151. doi:10.1039/B110008B
- Sheldon, R. A., and Woodley, J. M. (2018). Role of biocatalysis in sustainable chemistry. *Chem. Rev.* 118, 801–838. doi:10.1021/acs.chemrev.7b00203
- Sintra, T. E., Ventura, S. P. M., and Coutinho, J. A. P. (2014). Superactivity induced by micellar systems as the key for boosting the yield of enzymatic reactions. *J. Mol. Catal. B Enzym.* 107, 140–151. doi:10.1016/j.molcatb.2014.06.001
- Spredi, N., Alfani, F., Cantarella, M., D'Amico, F., Germani, R., and Savelli, G. (1999). α -Chymotrypsin superactivity in aqueous solutions of cationic surfactants. *J. Mol. Catal. B Enzym.* 6, 99–110. doi:10.1016/S1381-1177(98)00139-8
- Stamatis, H., Xenakis, A., and Kolisis, F. N. (1999). Bioorganic reactions in microemulsions: the case of lipases. *Biotechnol. Adv.* 17, 293–318. doi:10.1016/S0734-9750(99)00007-5
- Van Rantwijk, F., and Sheldon, R. A. (2007). Biocatalysis in ionic liquids. *Chem. Rev.* 107, 2757–2785. doi:10.1021/cr050946x
- Vekariya, R. L. (2017). A review of ionic liquids: applications towards catalytic organic transformations. *J. Mol. Liq.* 227, 44–60. doi:10.1016/j.molliq.2016.11.123
- Ventura, S. P. M., Santos, L. D. F., Saraiva, J. A., and Coutinho, J. A. P. (2012). Ionic liquids microemulsions: the key to *Candida Antarctica* lipase B superactivity. *Green Chem.* 14, 1620–1625. doi:10.1039/C2GC35197H
- Vicent-Luna, J. M., Romero-Enrique, J. M., Calero, S., and Anta, J. A. (2017). Micelle Formation in aqueous solutions of room temperature ionic liquids: a molecular dynamics study. *J. Phys. Chem. B* 121, 8348–8358. doi:10.1021/acs.jpcc.7b05552
- Viparelli, P., Alfani, F., and Cantarella, M. (1999). Models for enzyme superactivity in aqueous solutions of surfactants. *Biochem. J.* 344 (3), 765–773. doi:10.1042/bj3440765
- Weingärtner, H. (2008). Understanding ionic liquids at the molecular level: facts, problems, and controversies. *Angew. Chem. Int. Ed. Engl.* 47, 654–670. doi:10.1002/anie.200604951
- Welton, T. (1999). Room-temperature ionic liquids. Solvents for synthesis and catalysis. *Chem. Rev.* 99, 2071–2084. doi:10.1021/cr980032t
- Wijaya, E. C., Separovic, F., Drummond, C. J., and Greaves, T. L. (2016). Micelle formation of a non-ionic surfactant in non-aqueous molecular solvents and protic ionic liquids (PILs). *Phys. Chem. Chem. Phys.* 18, 24377–24386. doi:10.1039/c6cp03332f
- Wu, J., Li, N., Zheng, L., Li, X., Gao, Y., and Inoue, T. (2008). Aggregation behavior of polyoxyethylene (20) sorbitan monolaurate (tween 20) in imidazolium based ionic liquids. *Langmuir* 24, 9314–9322. doi:10.1021/la801358z
- Wu, Q., Soni, P., and Reetz, M. T. (2013). Laboratory evolution of enantiocomplementary *Candida Antarctica* lipase B mutants with broad substrate scope. *J. Am. Chem. Soc.* 135, 1872–1881. doi:10.1021/ja310455t
- Xanthakis, E., Zarevúcka, M., Šaman, D., Wimmerová, M., Kolisis, F. N., and Wimmer, Z. (2006). Application of ionic liquids in enzymic resolution by hydrolysis of cycloalkyl acetates. *Tetrahedron Asymmetry* 17, 2987–2992. doi:10.1016/j.tetasy.2006.10.045
- Xu, P., Zheng, G.-W., Zong, M.-H., Li, N., and Lou, W.-Y. (2017). Recent progress on deep eutectic solvents in biocatalysis. *Bioresour. Bioprocess* 4, 34. doi:10.1186/s40643-017-0165-5
- Xue, Y., Zhang, X.-G., Lu, Z.-P., Xu, C., Xu, H.-J., and Hu, Y. (2022). Enhancing the catalytic performance of *Candida Antarctica* lipase B by chemical modification with alkylated betaine ionic liquids. *Front. Bioeng. Biotechnol.* 10, 850890. doi:10.3389/fbioe.2022.850890
- Yang, Z. (2009). Hofmeister effects: an explanation for the impact of ionic liquids on biocatalysis. *J. Biotechnol.* 144, 12–22. doi:10.1016/j.jbiotec.2009.04.011
- Zaks, A., and Klibanov, A. M. (1984). Enzymatic catalysis in organic media at 100°C. *Science* 224, 1249–1251. doi:10.1126/science.6729453



OPEN ACCESS

EDITED BY

Maria Manuel Marques,
Universidade Nova de Lisboa, Portugal

REVIEWED BY

Satyajit Roy,
The University of Texas at Dallas, United States
Gourav Kumar,
Oregon Health and Science University,
United States
Angela Stefanachi,
Xxx, Italy

*CORRESPONDENCE

Laura Ielo,
✉ laura.ieleo@unito.it
Christian Dank,
✉ christian.dank@univie.ac.at

[†]These authors have contributed equally to this work and share first authorship

RECEIVED 29 December 2023

ACCEPTED 05 February 2024

PUBLISHED 19 February 2024

CITATION

Citarella A, Vittorio S, Dank C and Ielo L (2024),
Syntheses, reactivity, and biological applications
of coumarins.
Front. Chem. 12:1362992.
doi: 10.3389/fchem.2024.1362992

COPYRIGHT

© 2024 Citarella, Vittorio, Dank and Ielo. This is an open-access article distributed under the terms of the [Creative Commons Attribution License \(CC BY\)](#). The use, distribution or reproduction in other forums is permitted, provided the original author(s) and the copyright owner(s) are credited and that the original publication in this journal is cited, in accordance with accepted academic practice. No use, distribution or reproduction is permitted which does not comply with these terms.

Syntheses, reactivity, and biological applications of coumarins

Andrea Citarella^{1†}, Serena Vittorio^{2†}, Christian Dank^{3*} and Laura Ielo^{4*}

¹Dipartimento di Chimica, Università degli Studi di Milano, Milano, Italy, ²Dipartimento di Scienze Farmaceutiche, Università degli Studi di Milano, Milano, Italy, ³Institute of Organic Chemistry, University of Vienna, Vienna, Austria, ⁴Department of Chemistry, University of Turin, Turin, Italy

This comprehensive review, covering 2021–2023, explores the multifaceted chemical and pharmacological potential of coumarins, emphasizing their significance as versatile natural derivatives in medicinal chemistry. The synthesis and functionalization of coumarins have advanced with innovative strategies. This enabled the incorporation of diverse functional fragments or the construction of supplementary cyclic architectures, thereby the biological and physico-chemical properties of the compounds obtained were enhanced. The unique chemical structure of coumarine facilitates binding to various targets through hydrophobic interactions pi-stacking, hydrogen bonding, and dipole-dipole interactions. Therefore, this important scaffold exhibits promising applications in uncountable fields of medicinal chemistry (e.g., neurodegenerative diseases, cancer, inflammation).

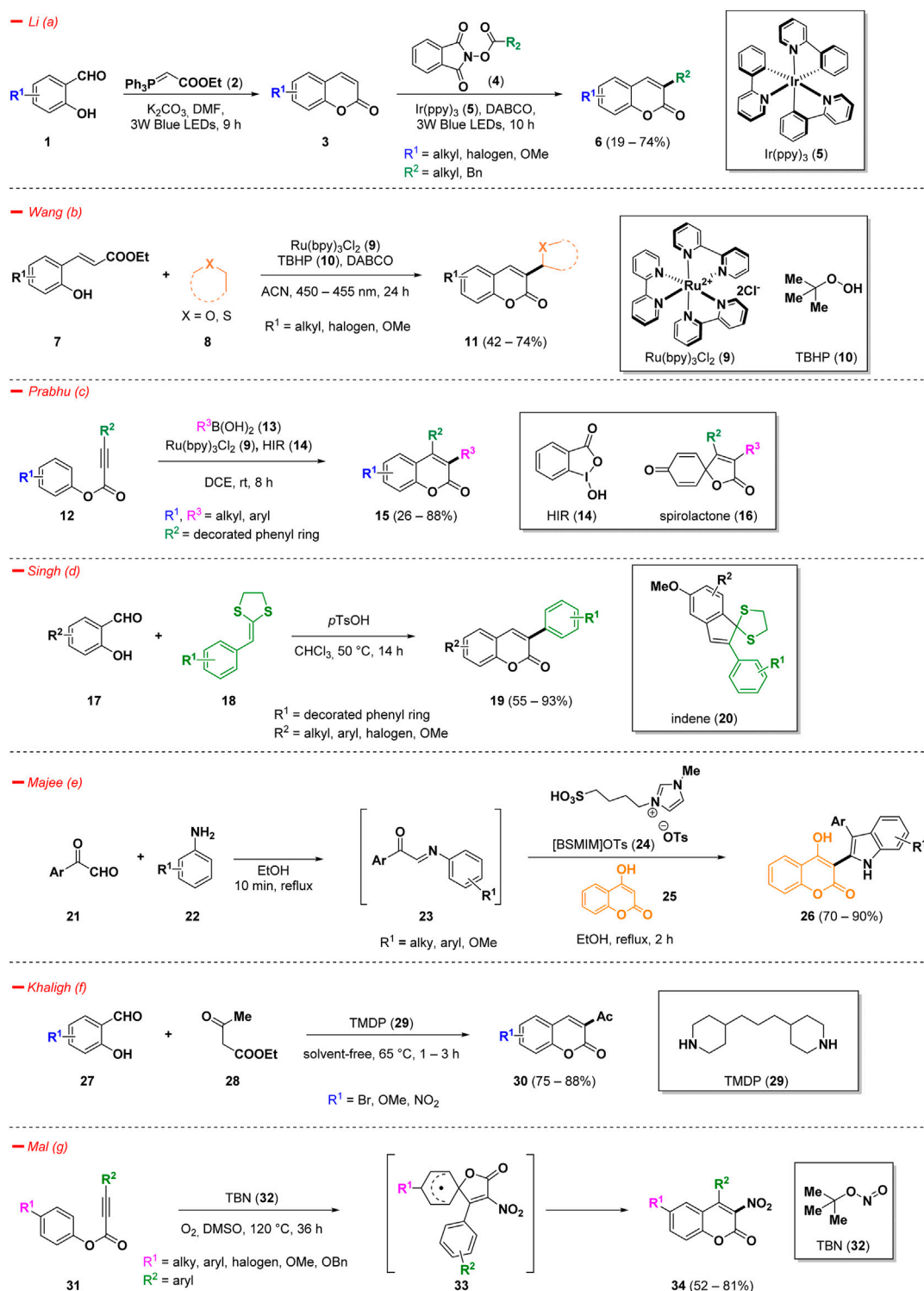
KEYWORDS

coumarins, synthesis, reactivity, biological applications, inhibitory activities

1 Introduction

Coumarins represent one of the foremost privileged scaffolds, frequently existing in a huge variety of natural products and bioactive molecules (Stefanachi et al., 2018). The diverse array of biological characteristics (Srikrishna et al., 2018) has rendered this notable category of heterocyclic compounds appealing to medicinal chemists throughout the years. These properties encompass antioxidant (Stanchev et al., 2009), anticonvulsant (Keri et al., 2022), antitumor (Wu et al., 2020), anti-inflammatory (Grover and Jachak, 2015), and antimicrobial (Al-Majedy et al., 2017) activities. Several coumarin derivatives have been approved by FDA for clinical usage. These include anticoagulant drugs such as warfarin (Ansell et al., 2004), acenocoumarol (Cesar et al., 2004), dicoumarol (Duxbury and Poller, 2001) and phenprocoumon (Warkentin et al., 2022), trioxsalen (Sehgal, 1974) which is employed for the treatment of vitiligo, and esculin (Smith and Moodie, 1988) which is used in combination against hemorrhoids.

The ready availability and the low price of the starting materials required for synthesizing coumarins have enabled the development of a wide range of methodologies. Furthermore, the distinct reactivities associated with the C-3 and C-4 positions of the coumarin system have paved the way for selective modifications, introducing pertinent functional groups (such as fluorinated moieties) for medicinal chemistry scopes and facilitating the construction of cyclic systems. This broadens the potential of coumarins as a valuable starting point for the synthesis of more intricate chemical architectures. Classical methods used for the synthesis of coumarins include



SCHEME 1
Synthesis of 3-substituted coumarins.

Knoevenagel (Bigi et al., 1999), Perkin (Johnson, 2004), Pechmann, (Pechmann, 1884; Yavari et al., 1998), Wittig (Yang et al., 2018), Claisen (Cairns et al., 1994), and Reformatsky (Shriner, 2004) reactions. The purpose of this discussion is to provide a comprehensive overview of the latest progress in the synthesis of

3-substituted, 4-substituted, and decorated or bicyclic coumarins, spanning from 2021 to the present. Moreover, a subsequent section presents the most relevant functionalization reactions of coumarins, for the selective introduction of diverse type of functional groups or for the construction of more complex cyclic derivatives. Finally, the

various biological activities specific to coumarin derivatives are illustrated. The focus of this review was on the last 3 years, aiming to delineate the most significant advancements that have emerged since the publication of other reviews encompassing this field (Bouhaoui et al., 2021; Patil, 2022).

2 Syntheses

2.1 3-Substituted coumarin derivatives

Increased interest on 3-substituted coumarins was observed, due to their biologically relevant applications in medicine and chemical biology (Vina et al., 2012; Stefanachi et al., 2018; Sokol et al., 2021). Therefore, the development of efficient and straightforward approaches for the synthesis of such scaffolds has garnered considerable attention (Xia et al., 2022). Recently, innovative strategies to access 3-alkyl, 3-heteroaryl, 3-acetyl, and 3-nitro coumarins have been developed, including green syntheses, photo- and metal-catalyzed reactions, and multi-component approaches, *inter alia* (Scheme 1).

Li et al. developed a structured one-pot method for the synthesis of 3-alkyl coumarins (**6**) using simple and cheap commercially available salicylaldehydes (**1**) (Kim et al., 2023). The reaction mechanism presumably involves a classical Wittig reaction to afford the coumarin ring (**3**), that *in situ* reacts with the proper alkyl donating reagents *N*-hydroxyphthalimide esters (**4**). The process smoothly occurs in presence of Ir(ppy)₃ photocatalyst (**5**) under blue LEDs irradiation at room temperature and DABCO (1,4-diazabicyclo [2.2.2]octane), providing variously 3-substituted coumarin derivatives (**6**) based on the *N*-hydroxyphthalimide ester (**4**) chosen with a wide reaction scope (Scheme 1—*path a*). The selected catalytic system exhibited a good functional group tolerance and DMF resulted to be the most efficient solvent for the conversion.

In the context of photocatalytic strategies for the innovative synthesis of 3-functionalized coumarins, Wang et al. came across a direct and regioselective C(sp²)–C(sp³) coupling reaction of hydroxy cinnamic esters (**7**) with (thio)ethers (**8**) under the presence of Ru(bpy)₃Cl₂ (**9**) as a photocatalyst and TBHP (**10**, *tert*-butyl hydroperoxide) as an oxidant (Scheme 1—*path b*) (Zhang et al., 2021). Overall, the process could be described as a cascade reaction consisting of a first alkenylation of α -C(sp³)H bond of ethers/thioethers and a subsequent lactonization. Novelty of such a methodology could be found in its broad substrate scope, mild reaction conditions, and the possibility to realize a one-pot procedure from commercially available salicylaldehyde, under *in situ*-Wittig olefination.

Prabhu and collaborators have developed a visible-light-mediated functionalization of activated alkynes (**12**) for the synthesis of coumarin derivatives (**15**) (Scheme 1—*path c*) (Manna and Prabhu, 2023). Within radical-induced reactions, the notable reactivity of aryl alkynoates has garnered substantial interest, largely attributed to their ease of accessibility and distinctive ability to readily accept radicals. They exploited the capacity of boronic acids (**13**) to be effective alkyl sources in the presence of hypervalent iodine reagent **14** (HIR) and photocatalyst **9**. Using this methodology, it was possible to access several simple chain-alkylated 3-substituted coumarins (**15**) with broad functional

group tolerance and good yields. Interestingly, the process demonstrated to be adaptable to the formation of a spiro lactone compound (**16**) instead of coumarin whenever alkynoate starting material bearing a *p*-methoxy substituent was used.

In the context of 3-aryl substituted coumarins, an interesting advance has been found in the work of Singh and co-workers (Scheme 1—*path d*) (Arora et al., 2022). The authors described a simple, high yielding and metal-free Brønsted acid-catalyzed methodology to afford 3-aryl coumarins (**19**) starting from commercially available salicylaldehydes (**17**). The best condition to perform the process was the employment of *p*-toluenesulfonic acid (*p*TsOH) as catalyst in refluxing chloroform, revealing excellent yields and broad substrate scope. Moreover, switching the starting material and modifying the reaction conditions, the methodology diverged to a facile synthesis method for indene derivatives (**20**).

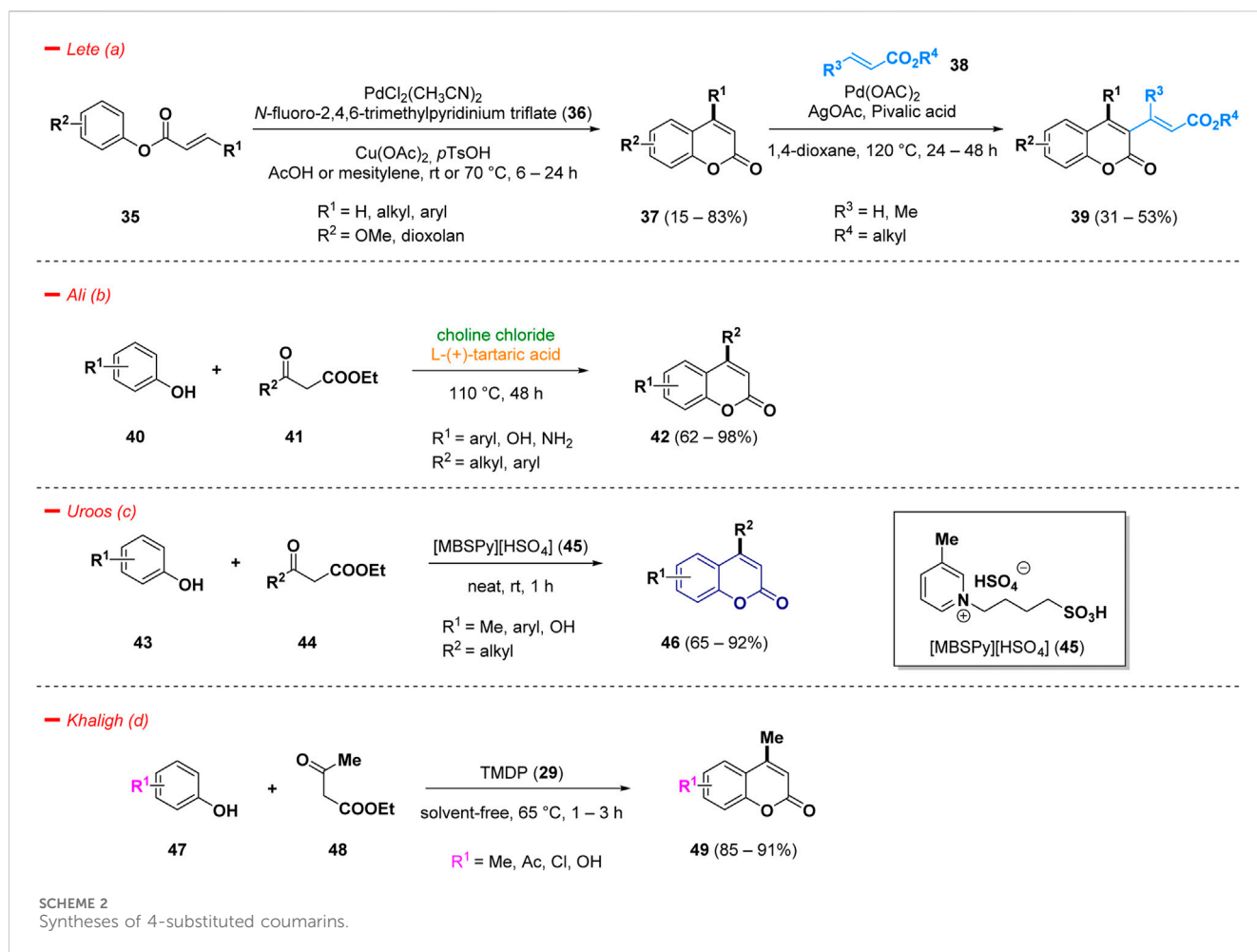
Majee et al. reported a metal-free and eco-friendly procedure for an easy access of coumarin derivatives (**26**) functionalized in position 3 with an indole scaffold (Scheme 1—*path e*) (Samanta et al., 2022). The process proceeded via a tandem cyclization reaction of phenylglyoxal derivatives (**21**) and several substituted anilines (**22**) in a multicomponent approach in the presence of the Brønsted acidic ionic liquid [BSMIM]OTf (**24**, 1-butane sulfonic acid-3-methylimidazolium tosylate) as a green catalyst in refluxing ethanol. Considering the emerging importance of indole scaffold endowed with antitumor, antiviral and antifungal effects (Citarella et al., 2023; Jagadeesan and Karpagam, 2023; Kudličková et al., 2023), the authors decided to screen the library of 3-indole coumarins (**26**) *in silico* for their ability to bind key proteins in tumorigenesis revealing interesting outcomes, which was confirmed also by a preliminary bioactivity evaluation.

Khaligh and others conducted a green Knoevenagel condensation using 4,4'-trimethylenedipiperidine (**29**, TMDP) in solvent-free conditions affording 3-substituted coumarins (**30**) starting from variously decorated salicylaldehydes (**27**) (Scheme 1—*path f*) (Gorjian and Khaligh, 2022).

Aryl alkynoates (**31**) readily underwent cascade-type cyclization reactions with *tert*-butyl nitrite (**32**, TBN) to provide 3-nitro coumarins (**34**) in good yield, following a 5-*exo-trig* pathway (Sau and Mal, 2021). The use of TBN (**32**) in nitration and nitrative cyclization reactions showed interesting eco-friendly and less-toxic advantages. The process discovered by Mal et al. is characterized by the formation of an intermediate spiro-compound (**33**) that after ester migration affords the desired 3-nitrocoumarins (**34**) (Scheme 1—*path g*). The presented robust methodology displayed high regioselectivity and good functional group tolerance. Control experiments conducted in the presence of the radical scavenger TEMPO (4-hydroxy-2,2,6,6-tetramethylpiperidin-1-oxyl) demonstrated that the reaction followed a radical pathway. Moreover, a conventional nitro-group reduction was conducted on a selected example and this approach represents an easy process to access biologically relevant 3-aminocoumarins.

2.2 4-Substituted coumarin derivatives

Examples of C-H functionalizations for the synthesis of diversified 4-substituted coumarins (**37**) were reported by Lete et al. and consisted in a Pd(II)-catalyzed direct C-H alkenylation (Fujiwara-Moritani reaction) (Ortiz-de-Elguea et al., 2021). The



substrate scope analyzed by the author highlighted the facility to afford 4-substituted coumarins (37), bearing several types of aliphatic and (hetero)aromatic fragments in good yields, in acetic acid or mesitylene, the presence of copper as additive, and *N*-fluoro-2,4,6-trimethylpyridinium triflate (36) as oxidant. The obtained 4-functionalized skeleton (37) can be further modified *via* C3 intermolecular alkenylation to easily afford highly substituted coumarins (39) (Scheme 2—path a).

The acid-catalyzed Pechmann condensation is the classic and easiest method to access 4-functionalized coumarins and, in the most simple case, involves the reaction of substituted phenols and β -ketoesters/acids (Lončarić et al., 2020). Many of the reported procedures require the use of stoichiometric amounts of costly catalysts, producing of acidic wastes without any possibility of recycling, with dangerous environmental impacts. Therefore, the search for greener procedure for the synthesis of substituted coumarins represents a challenging task and, in this context, the use of deep eutectic solvents (DES), acting simultaneously as solvents and catalysts, represents a valuable way to achieve this goal. Ali and collaborator carried out a Pechmann condensation under green conditions, via the use of choline chloride and L-(+)-tartaric acid (1:2) at 110°C to achieve 4-functionalized coumarin derivatives (42) (Scheme 2—path b) (Rather and Ali, 2022).

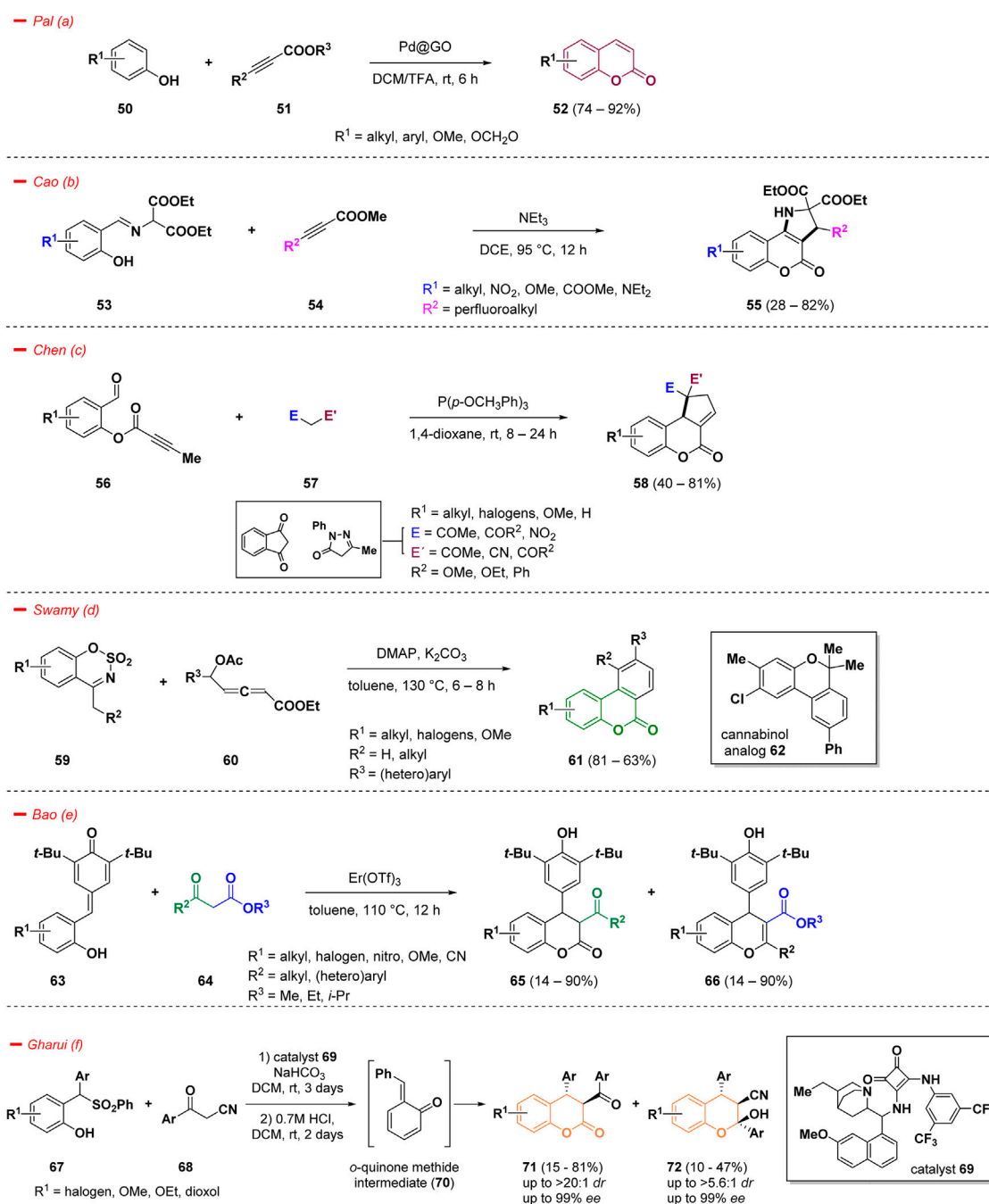
Pechmann reaction was also investigated using an eco-friendly doubly Brønsted acidic task specific ionic liquid

[MBSPy][HSO₄] (45, 1-butylsulfonic-3-methylpyridinium hydrogen sulfate) as catalyst. Under a solvent-free process at room temperature it was possible to obtain substituted coumarin derivatives (46) in good yields, starting from phenols (43) and β -ketoesters (44) (Scheme 2—path c) (Uroos et al., 2022). Moreover, the ionic liquid catalyst 45 could be reusable in accordance with green chemistry principles. The synthesized compounds were additionally assessed for their antifungal properties against *Macrophomina phaseolina*, a fungus that impacts over 500 plant species globally and lacks any specific commercially available fungicide, unrevealing novel potential applications for the mentioned scaffold (Marquez et al., 2021).

Another interesting green approach of the Pechmann reaction was discovered by Khaligh and others. They implemented the use of TMDP (29) as safe and greener catalyst for a facile synthesis of coumarin derivatives (49), functionalized in position 4 with a methyl group (Scheme 2—path d) (Gorjian and Khaligh, 2022).

2.3 Coumarins functionalized on the phenyl ring; polycyclic, and dihydrocoumarin derivatives

An effective strategy to access coumarins decorated in the phenyl ring relies on C–H functionalization. However, this



SCHEME 3
Synthesis of decorated coumarins.

approach holds several limitations, especially concerning the use of non-recyclable homogenous catalytic systems. Pal *et al.* developed a stereo- and regio-selective C–H bond functionalization strategy to access in high yields decorated biologically relevant coumarins (52) starting from different substituted phenols (50) and alkynes (51), catalyzed by palladium nanoparticles supported on graphite oxide (Pd@GO) at room temperature (Kyndiah *et al.*, 2023). The methodology showed improved catalytic efficiency and a good substrate scope with a low loading of the catalyst (Scheme 3— path a).

The recognition of heterocyclic fused rings has grown significantly, attributed to the improved pharmacological properties they offer, especially in nitrogen-containing architectures (Dank and Ielo, 2023). In particular, pyrrolidine-fused coumarins have been considered attractive targets in drug design, thanks to the biochemical relevance of both combined scaffolds (Ren *et al.*, 2021). In this context, Cao and collaborators reported an efficient strategy for the synthesis of pyrrolidine-fused coumarins with perfluorinated side chains (55), utilizing several imines derived from aromatic aldehydes (53) and methyl β -

perfluoroalkylpropiolates (**54**) as starting materials (Ren et al., 2021). The reaction comprises a tandem [3 + 2] cycloaddition and a subsequent intramolecular transesterification which afforded in a single step operation the fluoroalkylated final compounds (**55**) (Scheme 3—path b). The driving force of the entire process is represented by the strong electron withdrawing effect exerted by the perfluoroalkyl functionality. Moreover, the formation of such hyperfluorinated constructs can often ameliorate specific chemical-physical characteristics such as lipophilicity, binding selectivity, and metabolic stability, leading to a consistent improvement from the medicinal point of view (Swallow, 2015).

Regarding the development of efficient synthetic approaches to construct polycyclic ring systems, an interesting work from Chen and others introduced a novel phosphine-catalyzed, one-pot domino strategy for the annulation of 2-formylphenyl alkynoates (**56**) with activated methylene compounds (**57**) for the construction of several cyclopentene-fused dihydrocoumarins (**58**) (Chen et al., 2021). The authors intuitively designed an intramolecular cyclization strategy based on the reactivity of alkynoates (**56**) on the way to structurally diversified coumarins (**58**). Specifically, the process smoothly merged the reactivity of substituted 2-formylphenyl butynoates (**56**) and different 1,3-dicarbonyl compounds (**57**) in a tandem Knoevenagel condensation/[3 + 2] annulation leading to the target molecules under phosphine catalysis at room temperature in good yields (Scheme 3—path c).

A straightforward strategy for the synthesis of benzocoumarins (**61**) has been published by Swamy and co-workers (Chauhan et al., 2023). The authors highlighted a one-pot procedure taking advantage of the reactivity of cyclic sulfamidate imines (**59**) towards δ -acetoxy allenates (**60**), herein investigated as a 5C-synthon for the construction of a π -extended coumarin skeleton under the simple catalysis of DMAP (Scheme 3—path d). The mechanism proceeds through a domino reaction, featuring sequential benzannulation and lactonization, to give the target benzocoumarins (**61**) in high yields. Moreover, the synthetic utility of the process was demonstrated by the conversion of one derivative into a cannabinol analogue (**62**).

4-Aryl-3,4-dihydrocoumarin and 4-aryl-4H-chromene are important structural derivatives of coumarins endowed with improved biological and pharmacological activities. In the work of Bao and others, a straightforward cyclization of *para*-quinone methide derivatives (**63**) with 1,3-dicarbonyls (**64**) was highlighted for the first time and the proposed strategy allowed the formation of a series of versatile 4-aryl-3,4-dihydrocoumarins (**65**) and 4-aryl-4H-chromenes (**66**) (Scheme 3—path e) (Bao et al., 2023). The reaction proceeded under the catalysis of $\text{Er}(\text{OTf})_3$ and represents an interesting approach for an easy access to structurally diversified coumarins and chromenes. The divergent approach was realized modulating the starting materials and maintaining the reaction conditions: the use of malonates afforded the exclusive synthesis of 4-aryl-3,4-dihydrocoumarins (**65**), while switching to beta-diketones provided exclusively the chromene derivatives (**66**).

Considering the importance of 3,4-dihydrocoumarins and tetrasubstituted chromans, another interesting approach to access such functionalized scaffolds was reported by Gharui et al. following an *in situ* generation of *o*-quinone methide intermediate (**70**) from sulfones (**67**) and a subsequent addition of aromatic α -cyanoketones (**68**). The methodology gave access to 3,4-dihydrocoumarins (**71**)

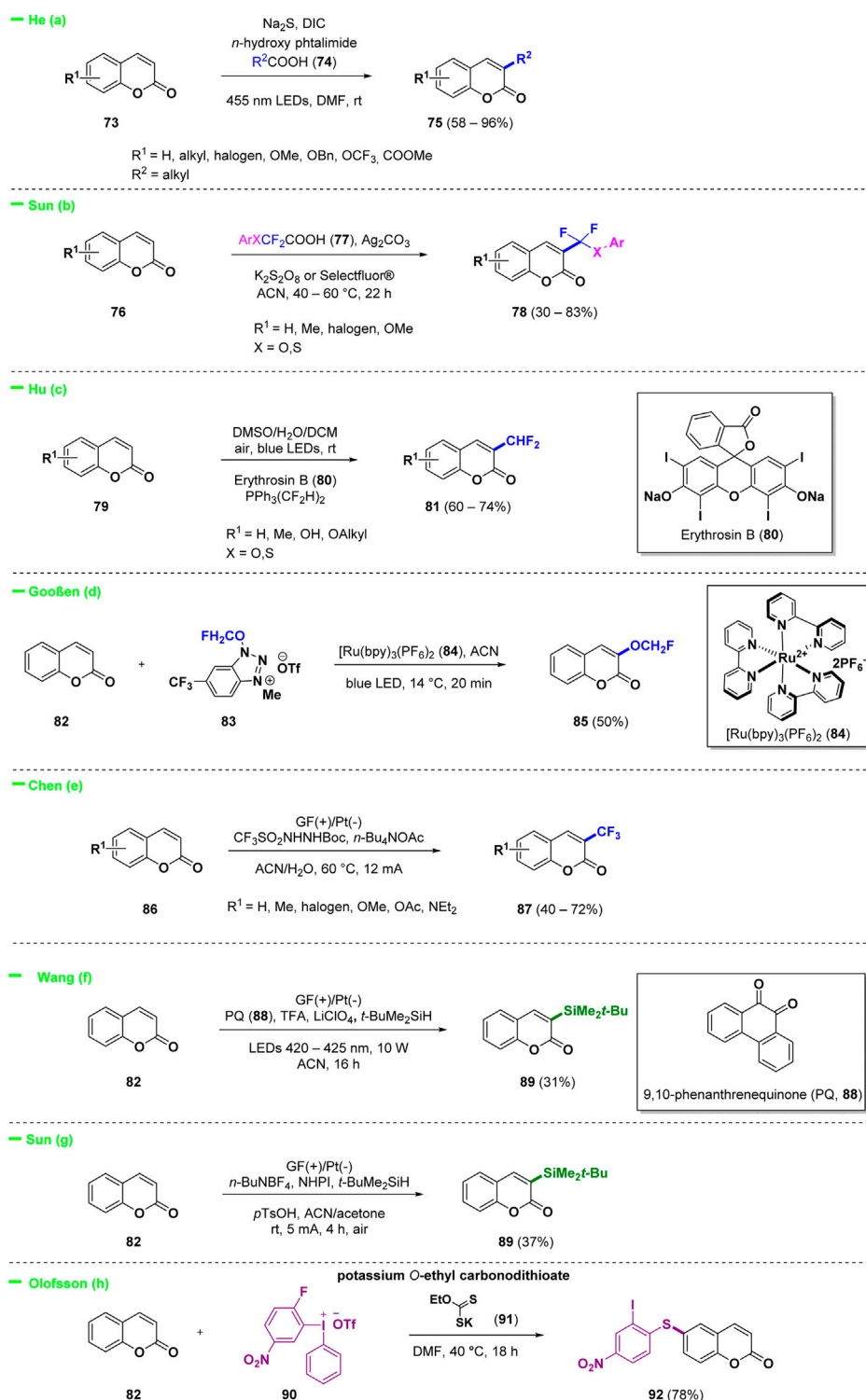
and tetrasubstituted chromans (**72**) in high enantio- and diastereoselectivities (Scheme 3—path f) (Gharui et al., 2021). The process proceeds under organocatalysis in good yields, however with prolonged reaction times.

3 Reactivity of coumarins

Structurally diverse coumarin derivatives have been synthesized by organic and medicinal chemists (Bouhaoui et al., 2021). The following discussion concerns the reactivity of the coumarin core, which was mainly investigated at the level of C-3 and C-4 of the pyranone ring. The following section is divided into a) general reactivity of coumarins, involving mainly the reactivity of C-3 whenever C-4 is unsubstituted, b) reactivity of 3-substituted coumarins, c) reactivity of 4-substituted coumarins, and d) reactivity of 3,4-disubstituted coumarins.

3.1 General reactivity of coumarins

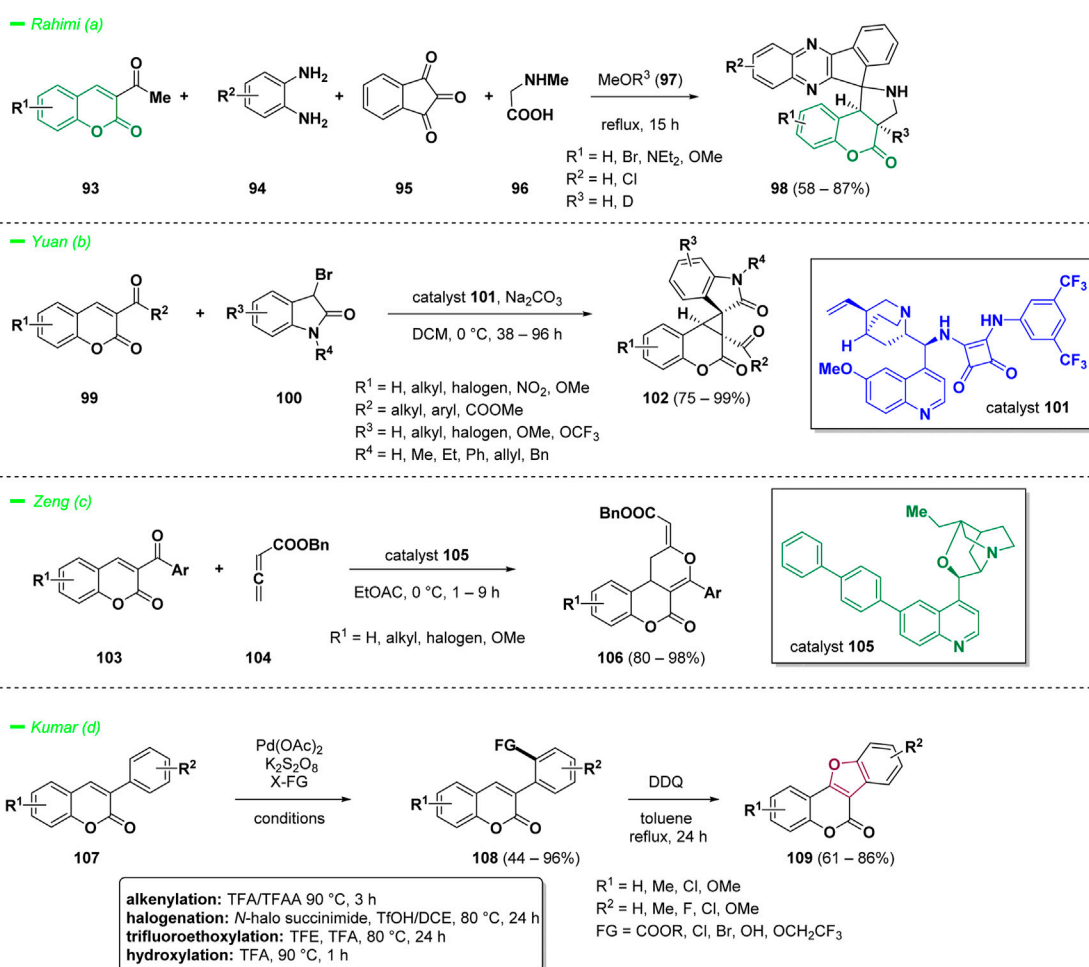
Recently, C-3 modification of coumarins was the most investigated approach to access a variety of interesting derivatives. A general scheme for the reactivity of C-3 substituted coumarins obtained under various conditions is reported below and describes the introduction of alkyl, silyl, CF_3 , CHF_2 , and OCH_2F groups to afford biologically relevant scaffolds (Scheme 4). 3-Alkylated coumarins (**75**) were successfully synthesized by He and collaborators using a simple and practical electron donor-acceptor photochemical strategy (Scheme 4—path a) (Song et al., 2023). The protocol involved carboxylic acids (**74**) as starting materials, *in situ* activated by NHPI (*N*-hydroxyphthalimide) using Na_2S as catalyst. Radical and photochemical approaches were also investigated *en route* to the introduction of fluorinated functionalities in position 3 of the coumarin system. Difluoromethylation today represents a straightforward manner to tune physico-chemical properties of pharmaceuticals and several research groups attempted to selectively incorporate this relevant functional group into bioactive compounds (Swallow, 2015; Miele et al., 2019; Citarella et al., 2022). Sun and collaborators realized a simple silver-catalyzed oxidative decarboxylation of arylthiodifluoroacetic acids or aryloxydifluoroacetics (**77**) for the selective C-3 functionalization of coumarins (**76**) with a difluoromethyl group (Scheme 4—path b) (Sun et al., 2022). Hu et al. proposed a selective photoredox catalysis-induced direct C-3 difluoromethylation of coumarins (**79**) by using bis(difluoromethyl) pentacoordinate phosphorane ($\text{PPh}_3(\text{CF}_2\text{H})_2$) and Erythrosin B (**80**) (Scheme 4—path c) (Song et al., 2023). Among fluorinated derivatives, also monofluoromethylation and trifluoromethylation recently gained a considerable attention among medicinal chemists. Goßen and others proposed a photocatalytic C-3 functionalization of coumarin (**82**) under $\text{Ru}(\text{II})$ catalysis in the presence of 1-(OCH_2F)-3-Me-6-(CF_3)benzotriazolium triflate (**83**) as source of monofluoromethyl units (Scheme 4—path d) (Bertoli et al., 2023). On the other hand Chen and collaborators described an efficient eco-friendly electrochemical trifluoromethylation of C-3 position of coumarins (**86**), catalyst free, using $\text{CF}_3\text{SO}_2\text{NHNHBoc}$ as the CF_3 source (Scheme 4—path e) (Cen et al., 2023). Other



SCHEME 4
General reactivity of coumarins.

interesting electrochemical approaches were described for the selective introduction of silyl group at C-3 position. Wang and others proposed an organoelectrophotocatalytic strategy for C-3 silylation of coumarin **82** using 9,10-phenanthrenequinone (**88**, PQ) both as an organocatalyst and as a hydrogen atom transfer (HAT)

reagent (Wan et al., 2023) (Scheme 4—path f). A Minisci-type reaction under electrochemical conditions was discovered by Sun et al. (Jiang et al., 2023) for the synthesis of several silylated heterocycles including coumarin **89**, employing NHPI as the hydrogen atom transfer (HAT) catalyst (Scheme 4—path g).



SCHEME 5
Reactivity of 3-acyl and 3-aryl coumarins.

Finally, selective modification of C-6 of the coumarin scaffold with carbonodithioate salt **91** was achieved in the work of Olofsson *et al.* by using iodonium salt **90** as reactive arylation and vinylation reagent (Scheme 4—path h) (Mondal *et al.*, 2023).

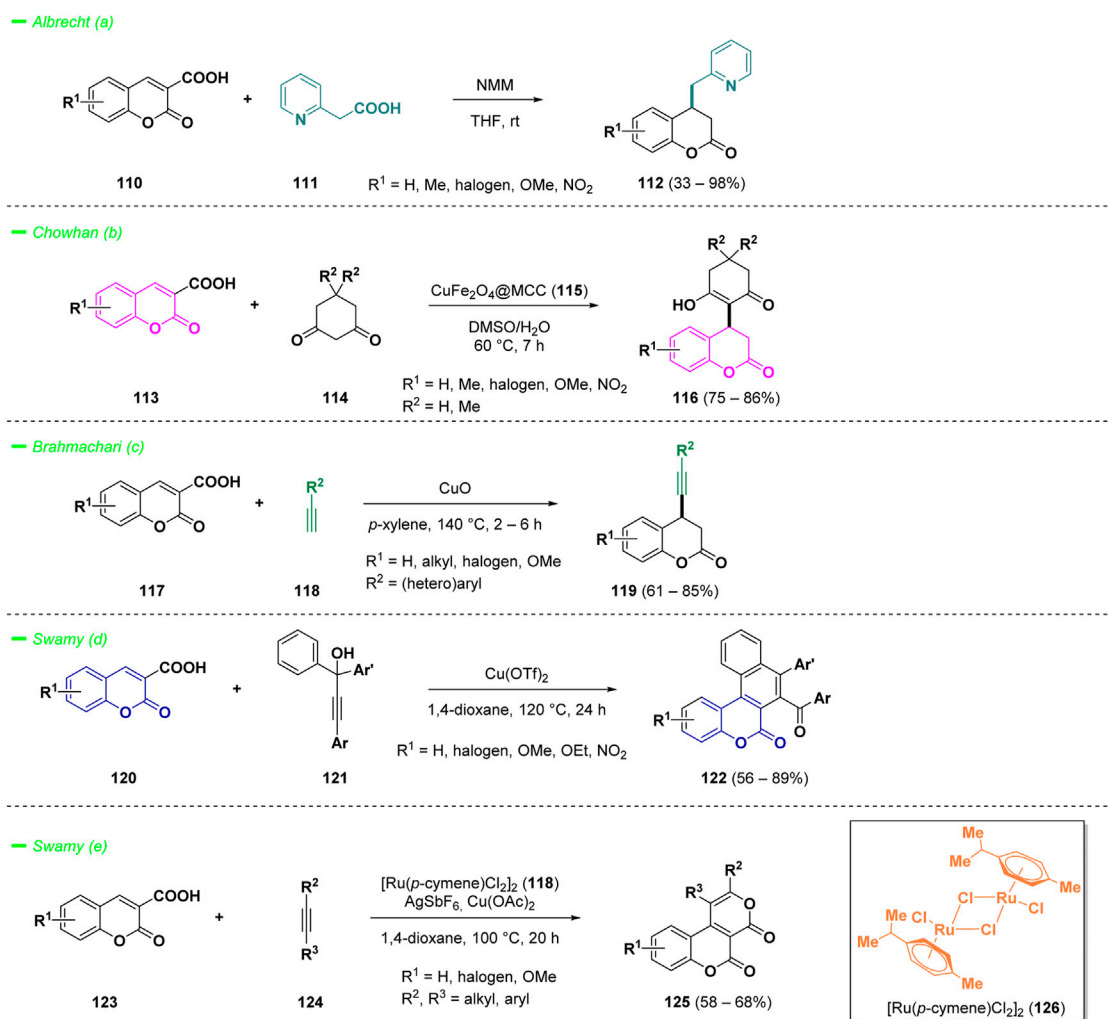
3.2 Reactivity of 3-substituted coumarins

3.2.1 3-Acyl and 3-aryl coumarins

The reactivity of 3-acetyl coumarins (**93**) in a multi-component reaction was investigated by Rahimi and others (Rahimi *et al.*, 2023). The authors decided to merge the concept of multi-component reactions, an important approach today in medicinal chemistry for the synthesis of bioactive heterocyclic compounds, with a 1,3-dipolar cycloaddition strategy taking advantage of the reactivity of azomethine ylides with olefinic dipolarophiles. The methodology was employed to convert 3-acetyl coumarins (**93**) into novel chromeno [3,4-*c*]spiropyrrolidine-indenoquinoxalines (**98**), in a four-component 1,3-dipolar cycloaddition reaction with 1,2-phenylenediamines (**94**), ninhydrin (**95**), and sarcosine (**96**) (Scheme 5—path a). The best solvent for the process was found to be refluxing MeOH and in reaction times of 15 h, a wide panel of

final compounds (**98**) were afforded with high regio- and stereoselectivity in moderate yields.

Another fascinating reactivity of 3-acyl or 3-aryl coumarins (**100**) was discovered by Yuan and co-workers. The authors provided a valuable easy strategy for the synthesis of spirooxindole-cyclopropa [c]coumarins (**103**), merging two important pharmacophores such as cyclopropa [c]coumarins, an important member of the group of coumarin derivatives that include a cyclopropane unit, and spirooxindole derivatives, endowed with interesting biological applications (Scheme 5—path b) (Yuan *et al.*, 2021). The reaction proceeds *via* a cyclopropanation reaction of the 3-acylcoumarin scaffold (**100**) with 3-haloindole (**101**) catalyzed by a squaramide-based organocatalyst (**102**) through a [2 + 1] Michael/intramolecular cyclization. The methodology was optimized for 3-benzoyl coumarins, and the best reaction conditions were observed whenever the process was conducted using the squaramide catalyst (**102**) in DCM at 0 °C. The scope of the reaction included a variegated series of spirooxindole-cyclopropa [c]coumarin compounds (**103**) bearing three continuous stereocenters, including two vicinal quaternary carbon stereocenters, obtained with high yields.



SCHEME 6
Reactivity of 3-carboxylic acid coumarins.

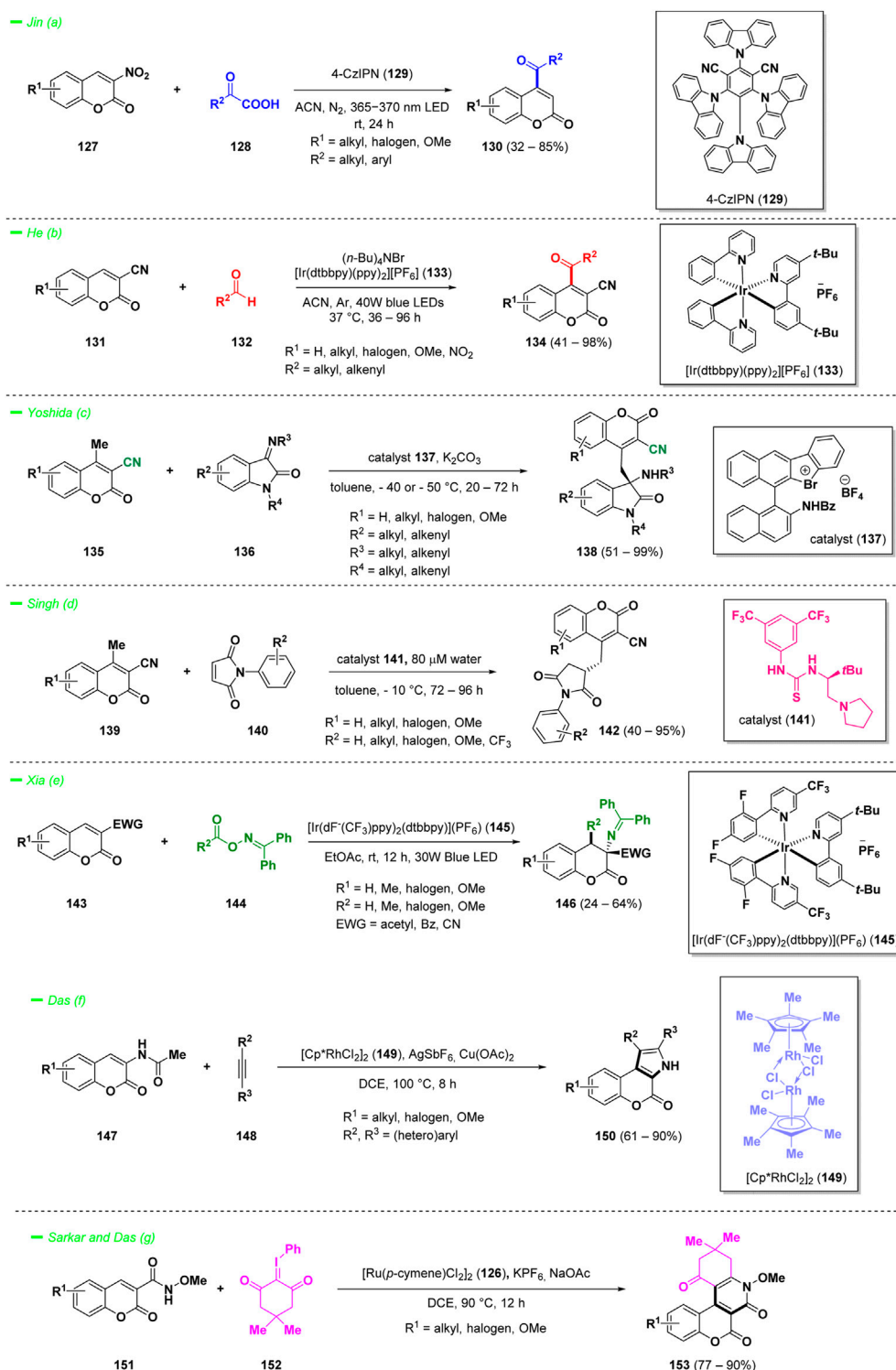
Zeng *et al.* reported the synthesis of dihydrocoumarin-fused dihydropyranones (**106**) via a tertiary amine (**105**) catalyzed [4 + 2] cyclization of 3-aryl coumarins (**103**) with benzyl 2,3-butadienoate (**104**) (Scheme 5—path c) (Li *et al.*, 2021). Pyran moieties have been incorporated into numerous bioactive compounds, so that the synthesis of such structures attracted considerable interest during the last years. The scope of the reaction was explored by synthesizing a series of chiral dihydrocoumarin-fused dihydropyranones (**106**) using 6'-(4-biphenyl)- β -iso-cinchonine as catalyst (**105**) with optimal yields.

The work of Kumar and others offered a captivating example of *ortho* C–H bond activation for the synthesis of functionalized coumarins (**108**) that employs the lactone ring as weak coordinating group to direct a selective modification of 3-aryl coumarins (**107**) (Shinde *et al.*, 2021). The methodology benefits from the cooperation of the catalyst Pd(OAc)₂ and the oxidant K₂S₂O₈ for the versatile alkenylation, halogenation, fluoroalkoxylation, and hydroxylation of variously decorated 3-aryl coumarins (**107**) (Scheme 5—path d). A broad scope of the reaction was examined, and a big variety of final products (**108**) were

obtained with high yields. As an application, the so generated *o*-hydroxy derivatives were converted into bioactive coumestan (**109**) in a cyclization reaction mediated by DDQ (2,3-dichloro-5,6-dicyano-1,4-benzoquinone).

3.2.2 3-Carboxy coumarins

The synthesis of chromanones and bicyclic compounds primarily relies on harnessing the reactivity of 3-carboxylic acid coumarins, which is governed by their intrinsic decarboxylation potential. Albrecht *et al.* reported a doubly decarboxylative Michael type addition of pyridyl acetic acids (**111**) to coumarin 3-carboxylic acids (**110**), providing access to interesting 4-(pyridylmethyl) chroman-2-ones derivatives (**112**), bearing two bioactive heterocyclic scaffolds (Bojanowski and Albrecht, 2021). The process has been conducted under Brønsted base catalysis, specifically *N*-methyl morpholine (NMM), in THF at room temperature and many substituents were well-tolerated during the transformation, including electron-withdrawing groups, electron-donating groups, and bulky aromatic rings (Scheme 6—path a).



SCHEME 7
Reactivity of 3-nitro, 3-cyano, 3-acetamido, and *N*-methoxy-3-carboxamide coumarins.

Merging the reactivity of Michael acceptors with decarboxylation of 3-COOH coumarins was also investigated in the eco-friendly approach published by Chowhan and others (Kumar et al., 2022). The authors synthesized a composite of copper ferrite oxide nanoparticles immobilized on

microcrystalline cellulose (**115**, CuFe₂O₄@MCC) and studied its catalytic properties for the reactivity of 3-COOH coumarins (**113**) against cyclic 1,3-diketones (**114**) to construct 3,4-dihydrocoumarin frameworks (**116**) (Scheme 6—path b). The protocol demonstrated a wide substrate scope, affording the final products (**116**) with good

yields. Additionally, the easily separable non-toxic catalyst enhances the efficiency of the work-up operation. An illustrative example on gram-scale of the mild process further underscored its applicability.

Brahmachari and co-workers reported a straightforward methodology for the efficient synthesis of functionalized 4-(aryl-/heteroaryl-ethynyl)chroman-2-ones (**119**) starting from coumarin-3-carboxylic acids (**117**) and terminal alkynes (**118**) (Bhowmick and Brahmachari, 2023). The formation of C (sp)–C (sp³) bonds was catalyzed by copper (II) oxide via a direct cross-coupling followed by decarboxylation. The protocol afforded a panel of 4-substituted coumarins (**119**) with high yields, without the use of any additional ligands or bases, showing a wide tolerance of diverse functional groups (Scheme 6—path c).

The reactivity of coumarins with carboxylic acid group in 3-position (**120**) with alkynes (**121**) was also investigated in the work of Swamy and others (Shankar and Swamy, 2023). The authors employed a decarboxylative annulation strategy for the construction of polycyclic heteroaromatic architectures such as naphthochromenones (**122**) (Scheme 6—path d). The process involved the reaction of coumarin-3-carboxylic acids (**120**) with *t*-Bu propargylic alcohols (**121**), following a Meyer-Schuster fashion *via in situ* generated α,β -unsaturated carbonyl compounds. The decarboxylation process, mediated by copper (II) catalysis, afforded a panel of novel naphthochromenones (**122**) with good yields. The same researchers reported also that ruthenium (II)-catalyst (**126**) could afford oxidative [4 + 2] annulation of coumarin-3-carboxylic acids (**123**) with alkynes (**124**) via the C–H activation to provide novel coumarin-fused pyranones (**125**) (Scheme 6—path e). (Shankar and Kumara Swamy, 2022)

3.2.3 3-Nitro, 3-cyano, 3-acetamido, and *N*-methoxy-3-carboxamide coumarins

3-Nitrocoumarins represent an intriguing class of compounds, and their versatility in organic synthesis stems from the ability to produce diverse derivatives of coumarins, particularly those with 4-acyl substitutions. Jin *et al.* discovered a novel green approach for the synthesis of C-4-acylated coumarins (**130**) starting from 3-nitrocoumarins (**127**) in the presence of α -keto acids (**128**) (Sun *et al.*, 2023). The protocol demonstrated to efficiently work under mild conditions using photocatalysis, mediated by 4-CzIPN (**129**, 1,2,3,5-tetrakis (carbazol-9-yl)-4,6-dicyanobenzene) when the light source was a 365–370 nm LED (Scheme 7—path a). The main advantages of this methodology are the good yields and the wide tolerance of functional groups, moreover the process demonstrated to be oxidant-free and scalable.

Another straightforward example of C-4 acylation of 3-functionalized coumarins is represented by the visible light-induced cross-dehydrocoupling observed for 3-cyanocoumarin derivatives (**131**) during the reaction with aldehydes (**132**), discovered by He and others (Qian *et al.*, 2023). The process took advantage of the inexpensive reagent (*n*-Bu)₄NBr and the photocatalyst [Ir(ppy)₂(dtbbpy)][PF₆] (**133**) to functionalize the C-4 position of the coumarin with a large panel of acyl substituents derived from aliphatic and α,β -unsaturated aliphatic aldehydes (**132**), in good to excellent yields (Scheme 7—path b).

Among 3-nitrile substituted coumarins, the derivatives bearing a supplementary methyl group in position 4 are endowed with different types of vinylogous reactivity. Yoshida *et al.* in

2021 proposed an enantioselective Mannich-type reaction of 3-cyano-4-methyl coumarins (**135**) with iminoisatins (**136**) under the catalysis of a chiral bromonium salt (**137**) (Scheme 7—path c) (Yoshida *et al.*, 2021). The same vinylogous-type reactivity was explored by Singh and collaborators studying the reactivity of similar 3-cyano-4-methyl coumarins (**139**) towards maleimides (**140**), as acceptors (Scheme 7—path d) (Singh *et al.*, 2022). The process represented the first non-covalent organocatalytic enantioselective vinylogous Michael-type addition of 3-cyano-4-methylcoumarins (**139**) with maleimides (**140**) and demonstrated to be versatile affording a panel of final products (**142**) with yields up to 95%.

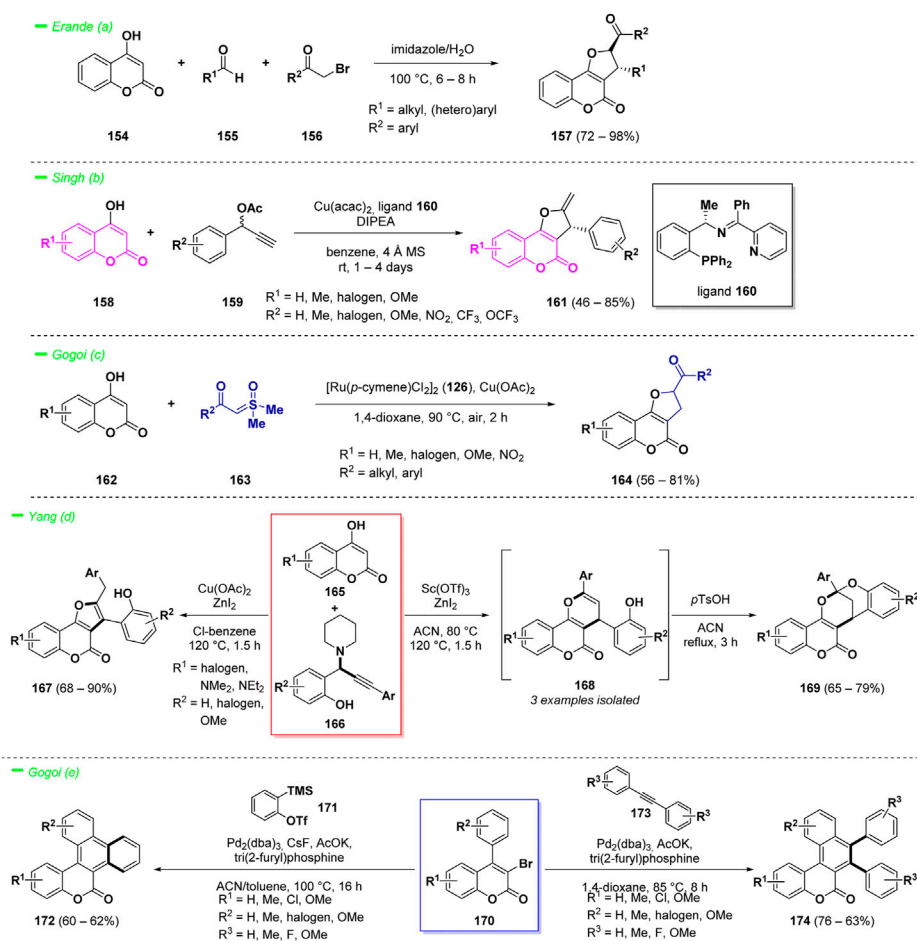
It is worth to mention another photocatalytic approach employed for the synthesis of variously substituted dihydrocoumarins (**146**) starting from coumarins substituted with an EWG at position 3 (**143**, Scheme 7—path e). The protocol reported by Xia and collaborators employed 3-CN, 3-acetyl, or 3-Bz substituted coumarins (as **143**) that were subsequently transformed into 4-amino dihydrocoumarins (**146**) via an alkylation reaction at room temperature in EtOAc using [Ir(dF-(CF₃)ppy)₂(dtbbpy)](PF₆) (**145**) as the photosensitizer (Jiang Y. S. *et al.*, 2023).

Transition-metal-catalyzed annulation reactions of coumarin derivatives are important tools for the construction of coumarin-fused polycyclic heteroaromatic frameworks. Specifically, Das *et al.* had reported a valid two-step protocol to construct pi-extended *N*-heterocycles involving Rh(III)-catalyzed C–H activation starting from 3-acetamidocoumarins (**147**) and internal alkynes (**148**), whereas the acetyl group is involved as a traceless directing functional group to synthesize pyrrolo-coumarin complex heterocycles (**150**) (Scheme 7—path f) (Das and Das, 2022). The same research group reported the formation of privileged pi-extended coumarin-fused pyridone scaffolds (**153**), starting from 3-*N*-methoxy carboxamide coumarin compounds (**151**) in a [4 + 2] annulation reaction (Scheme 7—path g). In this case, a ruthenium (II) catalyst (**126**) has been employed for the process with optimal reaction yields (Sarkar *et al.*, 2023).

3.3 Reactivity of 4-substituted and 3,4-disubstituted coumarins

Many biologically active pharmaceuticals endowed with therapeutic effects, such as warfarin, dicumarol, coumafuryl, contain a 4-hydroxy coumarin core scaffold (Jung and Park, 2009). Moreover, tricyclic frameworks such as *trans*-2,3-dihydrofuro [3,2-*c*]coumarins (DHFCs) acquired enhanced interest during the last years as therapeutics and could be considered complex derivatives of 4-hydroxy coumarins, easily accessible from the latter through various reactions (Jang *et al.*, 2012). Therefore, great efforts have been devoted to the construction of such heterocyclic architecture and lately the most elegant approaches have found to be multicomponent reactions and metal-catalyzed cycloadditions.

Erande *et al.* reported an eco-friendly and efficient one-pot multi-component reaction to access such complex structures (Mali *et al.*, 2022). The process involved the one pot reaction of 4-hydroxy coumarin derivatives (**154**) with aldehydes (**155**) and α -halo ketones



SCHEME 8
Reactivity of 4-hydroxy coumarins and 3,4-disubstituted coumarins.

(156) in a green solvent mixture of water and imidazole, affording the target compounds (157) in high yields. In this case the solvent mixture acted also as catalyst (Scheme 8—path a).

Another interesting approach for the synthesis of chiral dihydrofurocoumarins (161) was proposed by Singh and others (Rohilla et al., 2023). This protocol took advantage of the reactivity of 4-hydroxy coumarins (158) as C,O-bis-nucleophiles in [3 + 2] cycloaddition reactions with propargylic esters (159) under copper catalysis. The proposed strategy led to the synthesis of optically active dihydrofuro [3,2-c]coumarin analogues (161) in moderate to good yields and high enantioselectivities (Scheme 8—path b).

Another example with focus on metal-catalyzed synthesis of dihydrocoumarins relies on the reactivity of 3-hydroxy coumarins (162) for the preparation of dihydrofuran-fused compounds (164) was reported by Gogoi et al. (Phukon et al., 2023). The key point of the transformation is the three-component annulation reaction of hydroxycoumarins (162) with sulfoxonium ylides (163) mediated by the 1,4-dioxane acting simultaneously as methylene source and solvent, under ruthenium (II) catalysis (Scheme 8—path c).

Yang and collaborators described a versatile synthesis of complex furano [3,2-c]coumarins (167) and pyrano [3,2-c]coumarins (168)

exploiting the reactivity of 3-hydroxy coumarins (165) in a Lewis acid-catalyzed cascade annulation with *o*-hydroxyphenyl propargyl amines (166) (Sorabad and Yang, 2023). The methodology demonstrated to be regioselective and afforded the target compounds in good yields. Moreover, the pyrano-derivatives (168) could be easily converted into the more stable dioxabicyclic saturated heterocycles (169) via an acid-mediated cyclization (Scheme 8—path d).

π -Extended coumarins possess widespread applications in materials science, in particular they are endowed with photophysical properties (Christie et al., 2008). Such complex polycyclic structures could be obtained starting from 3,4-disubstituted coumarins via annulation reactions following C–H activation strategies. Gogoi et al. proposed a palladium-catalyzed alkyne and aryne annulation protocol for the synthesis of a wide range of π -extended coumarin derivatives (172) in good yields with good functional groups tolerance (Hazarik et al., 2023). The process is driven by C–H activation and the formation of two new C–C bonds represented the key to build up the ring system (Scheme 8—path e). The starting material of the reaction contains a 3-bromo group and a 4-aryl substituent and, by switching the employed conditions, it was possible to obtain variously substituted π -extended coumarins (174).

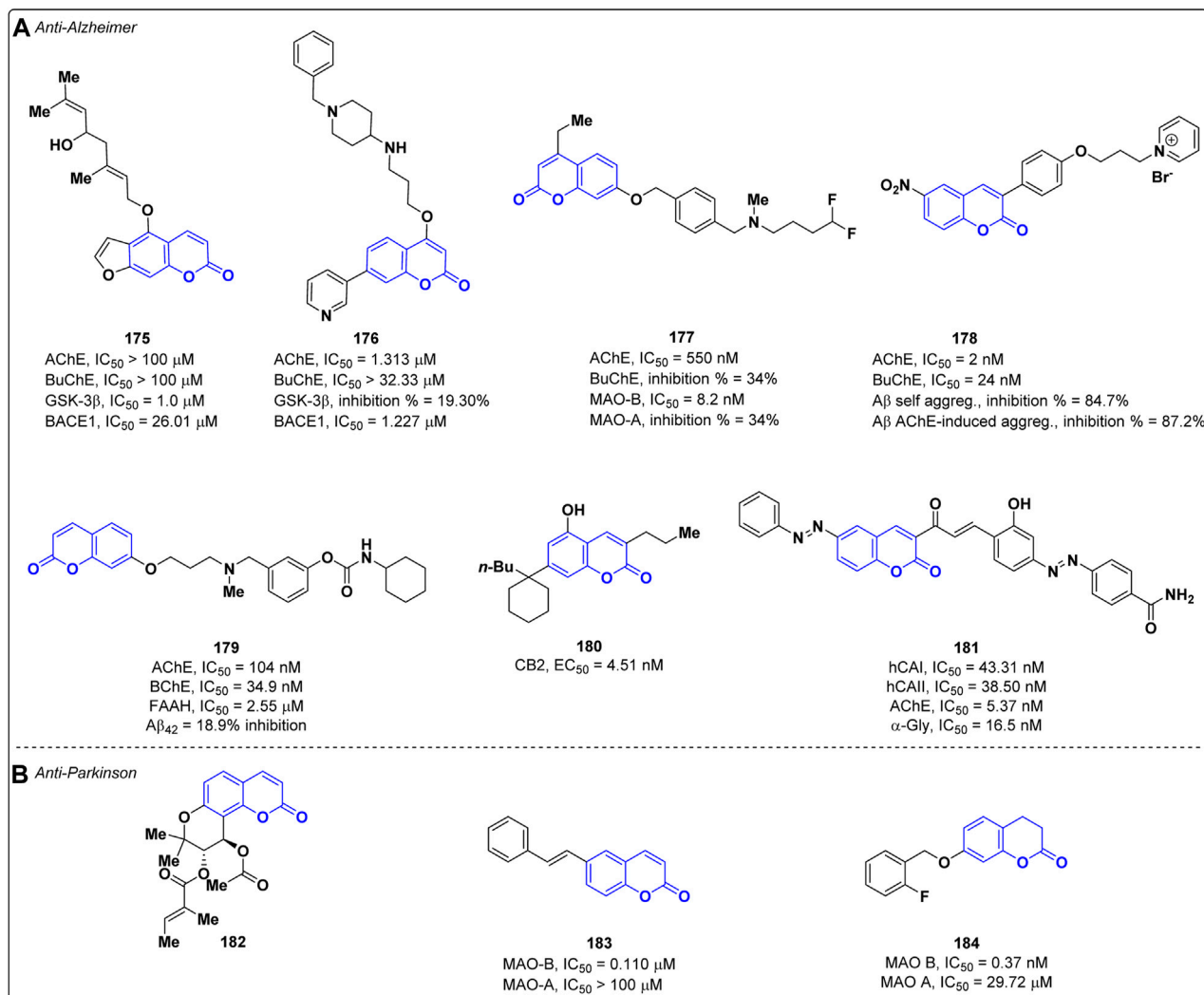


FIGURE 1
Coumarin-based compounds as anti-Alzheimer (A) and anti-Parkinson (B) agents.

4 Biological applications of coumarin derivatives

4.1 Neurodegenerative diseases

4.1.1 Anti-Alzheimer

Alzheimer's disease (AD) is the most common type of dementia in elderly age, characterized by the progressive loss of cognitive functions. Despite the physio-pathological mechanisms responsible for AD have been not fully clarified, some key factors related to the neurodegeneration process have been identified, such as the loss of cholinergic neurons (cholinergic hypothesis), accumulation of A β amyloid fibrils (amyloid hypothesis) and τ -protein, oxidative stress and neuroinflammation (Breijyeh and Karaman, 2020). The therapies currently available for the cure of AD are mainly addressed to reduce the symptoms and, therefore, the search for more effective treatments represents an active research area. In recent years, multi-target directed ligands (MTDLs) have been envisaged as valuable strategy to develop new therapeutic agents

for the cure of AD, and coumarin represents an appealing scaffold to address this task. In 2022, Zhao and co-workers adopted this approach by designing new coumarin derivatives that were tested against multiple targets relevant for AD, such as acetylcholinesterase (AChE), butyrylcholinesterase (BuChE), glycogen synthase kinase-3 beta (GSK-3 β) and Beta-secretase 1 (BACE1) (Liu et al., 2022). AChE is an enzyme involved in the degradation of the neurotransmitter acetylcholine (ACh) whose inhibition increases the level of ACh prolonging its effects (Rees and Brimijoin, 2003). BuChE is an enzyme implicated in the hydrolysis of ACh and other choline derivatives, and it is mainly distributed in the peripheral nervous system. Most of the ChE inhibitors (ChEIs) employed in the therapy of AD blocks both AChE and BuChE; however, experimental studies highlighted that compounds selectively targeting AChE have a higher therapeutic index as BuChE inhibition can cause adverse effects to the peripheral nervous system (Li et al., 2016). On the other hand, GSK-3 β is a kinase implicated in the phosphorylation and accumulation of τ -protein (Zhou et al., 2022) while BACE1 plays a pivotal role in the formation

of A β fibrils (Hampel et al., 2021). To achieve the multi-target activity, the authors exploited the natural furanocoumarin notopterol **175**, known to inhibit both BACE1 (IC_{50} = 26.01 μ M) and GSK-3 β (IC_{50} = 1.00 μ M), as lead compound. Among the synthesized derivatives, compound **176** (Figure 1A) displayed the highest affinity towards a) AChE (IC_{50} = 1.313 μ M), with a selectivity index over BuChE (IC_{50} = 32.33 μ M) of 24.623, and b) BACE1 (IC_{50} = 1.227 μ M), thus showing better potencies than the lead compound notopterol on both targets. However, most of the designed derivatives exhibited a poor inhibition against GSK-3 β without any improvement in respect to the lead, notopterol **175**. Kinetic studies highlighted that compound **176** acts as competitive inhibitor of AChE. Interestingly, derivative **176** proved to be able to cross the blood-brain barrier (BBB) in the parallel artificial membrane permeation assay for BBB (PAMPA-BBB) and to be safe at doses up to 1,000 mg/kg as demonstrated by *in vivo* toxicity studies performed on mice (Liu et al., 2022). In the same year, Pisani et al. developed a new series of coumarins endowed with multi-target activity against AChE and monoamine oxidase B (MAO-B) (Rullo et al., 2022). The latter is an enzyme implicated in the oxidation of monoamine neurotransmitters in the brain and its activity increases in AD patients (Schedin-Weiss et al., 2017). The best inhibitory profile on both targets was yielded by derivative **177** (Figure 1A) which showed IC_{50} values of 0.550 μ M and 0.0082 μ M against AChE and MAO-B, respectively. In addition, compound **177** revealed to be selective for MAO-B over MAO-A, displaying a selectivity index superior to 1,250. Preliminary ADME investigations highlighted that the dual inhibitor **177** possesses a balanced lipophilic/hydrophilic profile, a high permeation through both the intestinal epithelial barrier and the BBB, and a high metabolic stability. According to kinetic studies, compound **177** is a competitive inhibitor of MAO-B, while it displayed a mixed-mode inhibition on AChE. In addition, no significant cytotoxic effects were observed for **177** in SH-SY5Y and HepG2 cell lines and a neuroprotective effect against both A β_{1-42} and H $_2$ O $_2$ induced neuronal damage was exerted (Rullo et al., 2022). Khoobi et al. exploited the capability of pyridinium salt to interact with the catalytic anionic site of AChE developing a new class of coumarin derivatives cross-linked with pyridinium salt (Babaei et al., 2022). The most active compound **178** was able to inhibit both AChE and BuChE with IC_{50} values of 2.0 nM and 24.0 nM (Figure 1A), respectively, showing higher potency than donepezil (IC_{50} = 14.0 nM on AChE, IC_{50} = 2750 nM on BuChE; Structure not shown) used as reference. Moreover, derivative **178** was able to reduce the neuronal damage induced by H $_2$ O $_2$ in PC12 cells and by A β_{1-42} in SH-SY5Y cells. It decreased both the A β self- (84.7% inhibition) and AChE-induced (87.2% inhibition) aggregation at 100 μ M being more effective than the reference drug donepezil (30.8% inhibition on self- A β and 71.9% on AChE-induced aggregation).

In recent times, a newfound understanding of the relationship between the endocannabinoid system (ECS) and neuroprotection has emerged. The available evidence suggests that ECS signaling is implicated in the regulation of cognitive processes and plays a role in the pathophysiology of Alzheimer's disease (AD). For this reason, pharmacotherapy targeting ECS could represent a valuable contribution, opening a new perspective for the development of active agents with multitarget potential. Rampa et al. reported a

series of coumarin-based carbamic and amide derivatives as multipotent compounds acting on cholinergic system and ECS-related targets (Montanari et al., 2021). Their activity was evaluated on AChE and BChE, on fatty acid amide hydrolase (FAAH), and as cannabinoid receptor (CB1 and CB2) ligands. Moreover, their ability to reduce the A β_{42} self-aggregation was assessed. The most interesting profile was obtained for compound **179**, showing IC_{50} values of 104 nM on AChE, 34.9 nM on BuChE, 2.55 μ M on FAAH, and only 18.9% of inhibition on A β_{42} (Figure 1A). Even if a significant activity of these compound against the CB1/CB2 receptors was not observed, this can be a starting point for further developments. Due to the involvement of ECS in numerous essential physiological and pathological processes, Bräse and co-workers evaluated the activity of different modified coumarins as cannabinoid receptor ligands (Mohr et al., 2021). The most active compound, **180**, showed a CB2 selective agonistic profile (K_i = 6.5 nM, EC_{50} = 4.51 nM, see Figure 1A).

A multitarget approach was also chosen by Onar et al. for the design of new AD drugs (Çelik Onar et al., 2023). Twelve coumarin-chalcone derivatives were synthesized, and their biological activity was evaluated against AChE, human carbonic anhydrases (hCAs) I and II, and α -glycosidase (α -Gly). Derivative **181** showed promising results with IC_{50} values of 43.31 nM on hCA I, 38.50 nM on hCAII, 5.37 nM on AChE, and 16.5 nM on α -Gly, higher in comparison to the reference standards (Figure 1A). All the synthesized compounds showed acceptable physicochemical and pharmacokinetic properties.

4.1.2 Anti-Parkinson

Parkinson's disease (PD) is a progressive neurological disorder that mainly affects movement, causing tremors, stiffness, and difficulty with coordination and balance. The condition is characterized by the degeneration of dopamine-producing neurons in the brain, leading to a shortage of dopamine, a neurotransmitter essential for smooth and controlled muscle movements (Vittorio et al., 2020). The hallmark of PD consists of the presence of neuronal inclusions, called Lewi bodies, composed by phosphorylated and misfolded α -synuclein (α -syn) (Gitto et al., 2022). The inhibition of α -syn aggregation represents a promising disease-modifying strategy to halt or slow PD-related neurodegeneration (De Luca et al., 2022). In 2022, Kim and others reported the prevention of α -synuclein aggregation activity and the neuroprotective effect of the synthetic coumarin derivative PCiv (**182**) (Figure 1B) (Kim et al., 2022). This compound was able to inhibit α -syn aggregation *in vitro* and mitigated PFF-induced α -synucleinopathy in primary cortical neuron cultures. Preclinical investigations in a PD animal model revealed that PCiv (**182**) prevented the motor dysfunctions in the treated PD mouse model. *In vivo* studies confirmed the ability of PCiv (**182**) to permeate the BBB, despite a low bioavailability was observed in rats.

Another common strategy adopted in PD therapy is the use of selective inhibitors of MAO-B which is implicated in dopamine catabolism. In 2022, Matos and co-workers identified trans-6-styrylcoumarin **183** (Figure 1B) as selective inhibitor of human MAO-B with an IC_{50} values of 0.110 μ M and a selectivity index over MAO-A (IC_{50} > 100 μ M) greater than 900 (Mellado et al., 2022).

In 2023, Zhang and co-workers designed and synthesized novel 3,4-dihydrocoumarins as potent and selective MAO-B inhibitors (Liu et al., 2021). The best derivative is **184** with an IC_{50} value of

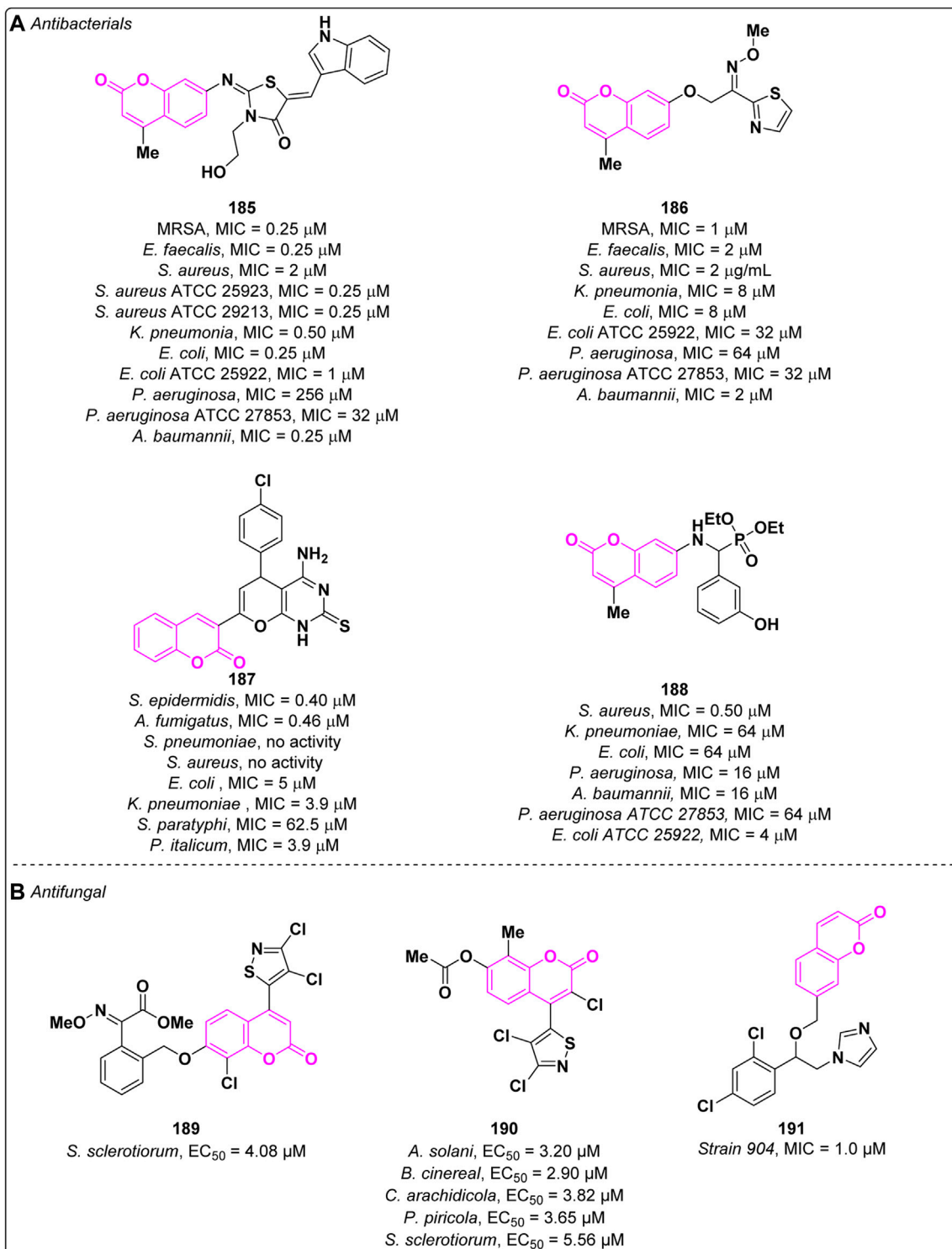


FIGURE 2
Antibacterial (A) and antifungal (B) activities of coumarin-based compounds.

0.37 nM (reference iproniazid, IC₅₀ = 7.69 nM) with a high selectivity towards MAO B (SI>270, MAO A IC₅₀ = 29.72 μ M) (Figure 1B). **184** acts as a competitive reversible inhibitor, effectively mitigating motor deficits in the MPTP-induced Parkinson's disease model.

4.2 Antimicrobial

4.2.1 Antibacterial derivatives

Multidrug-resistant (MDR) bacterial infections represent a global emergency leading to the increase of the mortality rate

due to the inefficacy of currently used antibiotics for the treatment of common infections (Serpi et al., 2023). In the last decade, several efforts have been made towards the discovery of broad spectrum antibacterials (Douglas et al., 2023). In this context, the coumarin moiety emerged as a promising scaffold for the design of potential antibacterial agents. The planar nature associated with the bicyclic ring facilitates interaction with vital biomacromolecules, such as DNA, making it an attractive choice for the development of intercalary agents. In 2022, Zhou and collaborators described the antibacterial activity of new thiazolidinone-conjugated coumarins which were tested against a panel of both Gram-positive and Gram-negative bacteria (Yang et al., 2022b). The most promising compound **185** displayed excellent activities on the tested bacteria, except for *P. aeruginosa* and *P. aeruginosa* ATCC 27853, at low concentrations (MICs = 0.25–2 μ M) (Figure 2A). Additional experiments demonstrated that derivative **185** possesses the ability to disrupt the integrity of bacterial membranes and effectively reduces the formation of bacterial biofilms, without any significant cytotoxicity in mammalian cells. Compound **185** is less prone to drug resistance in comparison to the reference norfloxacin and does not show hemolytic activity. According to experimental and *in silico* studies, derivative **185** intercalates into DNA base pairs and interacts with DNA gyrase B, hampering its function. In the same year, the same research group also reported a new series of coumarin thiazoles endowed with antibacterial activity (Yang et al., 2022a). Among the tested derivatives, compound **186** (Figure 2A) exhibited a strong inhibition on methicillin-resistant *Staphylococcus aureus* (MRSA) showing a MIC value of 1 μ M thus being more potent than norfloxacin and ciprofloxacin on the same strain (MICs = 8 μ M). In addition, derivative **186** displayed a broad spectrum being able to inhibit different bacterial strains exhibiting good to moderate activity (MICs = 2–64 μ M). Derivative **186** displayed no haemolytic effect along with the ability to eradicate MRSA biofilm. Moreover, it was also able to induce membrane damages leading to the leakage of intracellular material, to promote intracellular oxidative stress and to interact with DNA. Further studies highlighted a lower tendency of resistance of **186** against MRSA in comparison to norfloxacin.

In 2023, El-Kalyoubi et al. evaluated the antimicrobial activity of several nitrogen-containing coumarin derivatives (Fayed et al., 2022). Both Gram-positive (*S. Pneumoniae*, *S. Epidermidis*, *S. Aureus*, and *E. coli*) and Gram-negative (*K. Pneumoniae* and *S. Paratyphi*) bacteria were considered. Among the most promising derivatives **187** merits mention, which showed a MIC value of 0.40 μ M on *Sclerotinia epidermidis*, in comparison to the standard (MIC = 15.6 μ M) (Figure 2A). It also showed fungicidal activity against *A. fumigatus* (MIC = 0.46 μ M; standard MIC = 15.6 μ M).

Coumarin aminophosphonates (Koszelewski et al., 2023) are considered new antibacterial agents, able to combat bacterial resistance, as reported by Zhou and co-workers (Yang et al., 2023). Derivative **188** exhibited excellent inhibition potency against *S. aureus* (MIC = 0.5 μ M; standard MIC = 16 μ M) *in vitro* and showed considerable antibacterial potency *in vivo* (Figure 2A). It can eradicate the *S. aureus* biofilm, thus diminishing the development of *S. aureus* resistance. Furthermore, its combination with norfloxacin can enhance the antibacterial efficacy. Mechanistic explorations revealed that **188**

was able to destroy the integrity of cell membrane, which resulted in the leakage of protein and metabolism inhibition.

4.2.2 Antifungal derivatives

Similar to antibacterials, most of the antifungal agents currently employed present MDR along with the frequent occurrence of side effects. This prompted research to find more effective drugs (Prusty and Kumar, 2020).

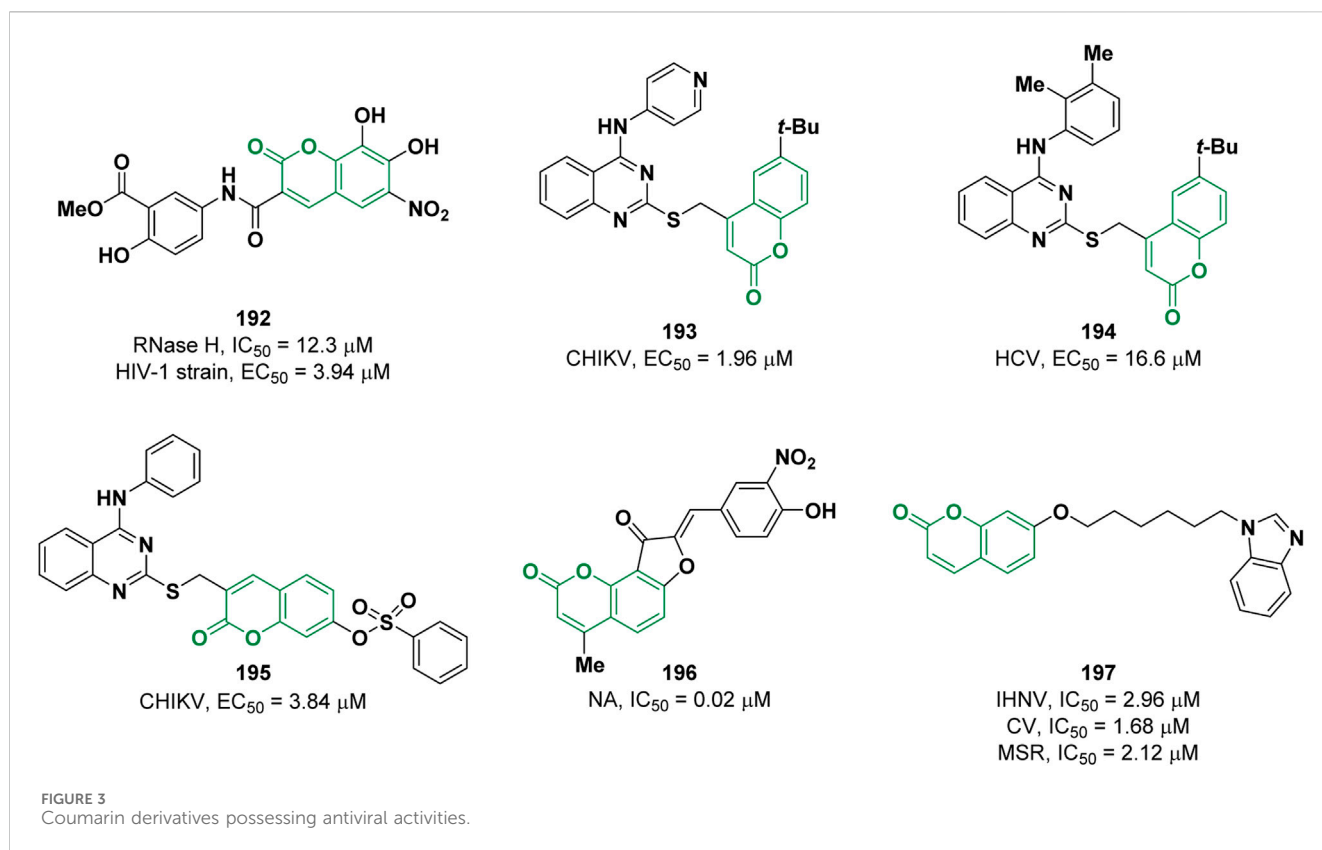
A series of 21 novel 3,4-dichloroisothiazolocoumarin-containing strobilurins were rationally designed and synthesized by Fan and co-workers (Lv et al., 2022). Derivative **189** exhibited good antifungal activity against *Sclerotinia sclerotiorum* with a EC_{50} of 4.08 μ M, (coumoxystrobin was used as reference, EC_{50} = 1.0 μ M) (Figure 2B). The same research group reported in 2023 the fungicidal activity of 4-(3,4-dichloroisothiazole)-7-hydroxy coumarins ester derivatives (Song et al., 2023). Compound **190** displayed good efficacy against *Alternaria solani* (EC_{50} = 3.20 μ M), *Botrytis cinerea* (EC_{50} = 2.90 μ M), *Cercospora arachidicola* (EC_{50} = 3.82 μ M), *Physalospora piricola* (EC_{50} = 3.65 μ M), and *S. sclerotiorum* (EC_{50} = 5.56 μ M), see Figure 2B.

In 2023, Gou et al. employed an alternative approach to avoid resistance (Yan et al., 2023). Specifically, certain coumarin derivatives endowed with antibiofilm activity were combined with CYP51 inhibitors to synthesize novel compounds with robust antifungal capabilities and reduced susceptibility to resistance. Compound **191** exhibited fungicidal effects against fluconazole-resistant strain 904 (MIC = 1 μ M) (Figure 2B). Most importantly, **191** showed to be potent as *in vivo* antifungal activity against pathogenic fungi and fluconazole-resistant strains was observed. Preliminary pharmacokinetic and toxicity tests demonstrated the drug-like properties of this compound.

4.2.3 Antivirals

Viral infections constitute an important global health problem. For most of the pathogenic viruses like severe acute respiratory syndrome (SARS), Ebola, Zika, Chikungunya (CHIKV) no effective therapeutic treatments and/or vaccines are available. Therefore, there is an urgent need to find new and effective anti-viral drugs (Yoshida et al., 2021). Over the years, coumarin derivatives have been widely explored as promising antiviral agents (Li et al., 2022). In 2021, Zhan and co-workers discovered some coumarin derivatives as human immunodeficiency virus type 1 (HIV-1) inhibitors (Kang et al., 2021). After the screening, compound **192** was found to be the most active with an IC_{50} of 12.3 μ M (DW-4, IC_{50} = 20.8 μ M), in an enzymatic assay against the viral RNase H (Figure 3). **192** showed increased potency in comparison to the reference compound (DW-4, EC_{50} = 101 μ M) against wild-type HIV-1 strain (EC_{50} = 3.94 μ M) and retained activity against a panel of mutant strains.

In 2022, the antiviral activity of a series of quinazolin-4-amine -SCH₂- coumarin conjugated compounds was determined by Neyts et al. against chikungunya (CHIKV) and hepatitis C (HCV) viruses (Hwu et al., 2022). Derivative **193** exhibited an EC_{50} value of 1.96 μ M on CHIKV while derivative **194** an EC_{50} value of 16.6 μ M on HCV (Figure 3). In the same year, the same research group reported the activity of a further series of functionalized quinazoline-coumarin hybrids carrying an arylsulfonate moiety against CHIKV (Hwu et al., 2022). Through a computational



approach the authors designed compound **195** (Figure 3) which proved to be the most effective among the tested molecules with an EC_{50} value of 3.84 μ M. The authors speculated that derivative **195** might interact with the nsP3 enzyme of CHIKV forming a covalent adduct with nucleophilic residues of the pocket through a Michael addition involving the coumarin moiety.

Pang and co-workers described a series of dihydrofurocoumarin derivatives as neuraminidase (NA) inhibitors, a promising target for the development of anti-influenza drugs (Zhong et al., 2021). The most potent inhibitor **196** possesses an IC_{50} value of 0.02 μ M, lower in comparison to the reference oseltamivir carboxylate (IC_{50} = 0.04 μ M) (Figure 3).

Chen et al. evaluated the activity of 35 new coumarin derivatives against infectious hematopoietic necrosis virus (IHNV) (Hu et al., 2021). The inhibitor with the best activity is **197** with an IC_{50} value of 2.96 μ M. Furthermore, **197** showed IC_{50} values of 1.68 and 2.12 μ M for two other rhabdoviruses, spring viremia of carp virus (CV) and *Micropterus salmoides* rhabdovirus (MSR), respectively (Figure 3). *In vivo* studies showed that **197** exhibited an anti-rhabdovirus effect in virus-infected fish by substantially enhancing the survival rate.

4.3 Anti-inflammatory

Inflammation can be defined as a complex response of the immune system triggered by harmful stimuli such as pathogens, damaged cells, irradiation, or toxic compounds (Chen et al., 2018). There are two discernible types of inflammation: acute and chronic. The former starts rapidly upon infections and last for a few days,

while the latter is a slow and long-term process involved in some pathologies such as diabetes, cardiovascular disease, allergies, arthritis, and chronic obstructive pulmonary disease (Zotova et al., 2023). The inflammatory reaction is mediated by the release of several molecules including pro-inflammatory cytokines, nitric oxide (NO), prostaglandin E_2 (PGE_2), that are involved in different biological pathways regulating the inflammatory response (Matthay et al., 2003). Despite several anti-inflammatory agents are currently used in therapy, they possess different side effects; therefore, the development of safer anti-inflammatory drugs is still an attractive research field (Almasirad et al., 2022). In 2021, Kang and others described the anti-inflammatory activity of four coumarins among which the 4-hydroxy-6-methylcoumarin **198** (Figure 4) resulted to be the most active (Kang et al., 2021). Coumarin **198** was able to reduce the levels of the pro-inflammatory cytokines IL-1 β , IL-6, TNF α , and PGE_2 by 80.6%, 73.1%, 32.8%, and 53.2%, respectively, in LPS stimulated RAW 264.7 cells in a dose-dependent manner at a concentration of 500 μ M. Western blot analysis confirmed the capability of **198** to downregulate the expression of iNOS and COX-2, two proteins implicated in the regulation of NO and PGE_2 levels, respectively. In addition, it was demonstrated that **198** inhibits both MAPK and NF- κ B signalling pathways.

Wang and co-workers reported a series of novel 3-(4-aminophenyl) coumarins as anti-inflammatory drugs for the treatment of rheumatoid arthritis (RA) (Miao et al., 2021). Preliminary results showed that compound **199** possesses the strongest inhibitory activity, among the tested compounds, on the proliferation of fibroid synovial cells (RA-FLSs, IC_{50} = 1.78 μ M) compared to the reference methotrexate (IC_{50} =

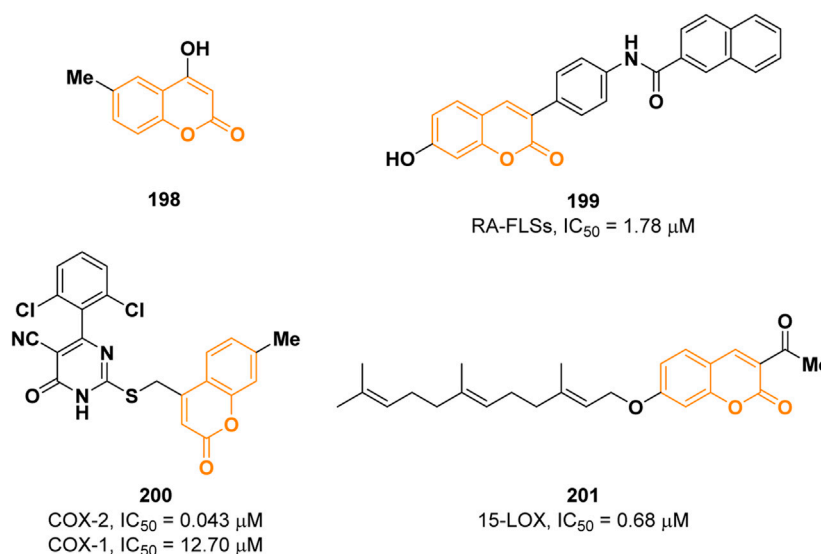


FIGURE 4
Coumarin derivatives with anti-inflammatory properties.

5.0 μM), and it also has inhibitory effect on RA related cytokines IL-1, IL-6, and TNF- α (Figure 4). Mechanistic studies showed that **199** could inhibit the activation of NF- κ B and MAPKs signal pathway. The anti-inflammatory activity was further determined *in vivo* in the rat joint inflammation model.

Non-steroidal anti-inflammatory drugs (NSAIDs) are among the most widely used medications to alleviate inflammation. They exhibit their effects *via* cyclooxygenase enzymes (COX) inhibition. COX enzymes exist in two distinct isoforms: COX-1 which is responsible for maintenance of physiological functions such as gastrointestinal integrity; COX-2 is responsible for proinflammatory conditions. Traditional NSAIDs with higher selectivity for COX-1 cause greater gastrointestinal bleeding, ulcer, and renal toxicity than those selectively targeting COX-2. Consequently, several studies led to the development of selective inhibitors of COX-2 isoform (coxibs) (Citarella et al., 2022). A new series of pyrimidine-5-carbonitrile-based coumarin derivatives was synthesized by Alfayomy et al. and their inhibitory activity was evaluated on both COX-1 and COX-2 (Alfayomy et al., 2021). Among them, derivative **200**, shown in Figure 4, showed the most promising potency with an IC_{50} value of 0.043 μM on COX-2 (reference celecoxib, $IC_{50} = 0.045 \mu M$) presenting a selectivity index of 295.35 (IC_{50} COX-1 = 12.70 μM). **200** displayed superior anti-inflammatory activity *in vivo* in comparison to celecoxib and during ulcerogenic liability testing, the compound was associated with mild lesions, comparable to celecoxib.

Concerning inflammations, lipoxygenases (LOXs) are well known to play an important role. They are nonheme iron-containing proteins that contribute to a new eicosanoid pathway by acting as biocatalysts in arachidonic acid's peroxidation at positions 5, 8, 12, and 15 to the corresponding hydroperoxide derivatives. In this context, Seyedi and co-workers reported a novel array of geranyloxy and farnesiloxy 3-acetylcoumarins as potent soybean 15-lipoxygenase inhibitors (Zerangnasrabad et al.,

2021). 7-Farnesiloxy-3-acetylcoumarin (**201**) was found to be the best inhibitor with an IC_{50} value of 0.68 μM (reference 4-MMPB, $IC_{50} = 18 \mu M$) (Figure 4). Docking studies revealed that the farnesyl moiety is well inserted in the hydrophobic cavity of the enzyme.

4.4 Anti-diabetes

Type-2 diabetes mellitus is a chronic metabolic disorder characterized by insulin resistance and impaired insulin secretion, associated with an enhancement of blood glucose levels. Lifestyle factors such as poor diet, sedentary behavior or obesity significantly contribute to its development. If left untreated, type-2 diabetes can result in serious complications, including cardiovascular diseases, kidney damage and brain dysfunctions (Munana, 1995). In skeletal muscle, accounting for the absorption of more than 80% of insulin-stimulated glucose, glucose uptake is mediated by protein carriers, namely, GLUT1 and GLUT4, whose function is impaired in T2DM. Therefore, the modulation of GLUT activity can be exploited for T2DM therapy. In 2023, Kamble et al. adopted a hybridization approach to design new anti-diabetic agents by combining three different pharmacophores: coumarin, 1,2,3-triazole, and thiazolidine-2,4-diones (Metre et al., 2023). The GLUT4 glucose uptake activity of the resulting compounds was evaluated on a yeast model leading to the identification of compound **202** (Figure 5) as the most effective with 93% glucose uptake at 200 μM , which is comparable to that of the reference pioglitazone (94%) at the same concentration. No significant cytotoxicity was detected by MTT assay for derivative **202**.

Coumarin and thiazolidinedione scaffolds were also employed by Pasala and co-workers to design new potential antidiabetics targeting aldose reductase-II (ALR2), an enzyme implicated in the conversion of glucose to sorbitol overactivated in diabetes (Kumar Pasala et al., 2021). Among the derivatives, the best activity was shown by **203** ($IC_{50} = 0.012 \mu M$) which proved to be

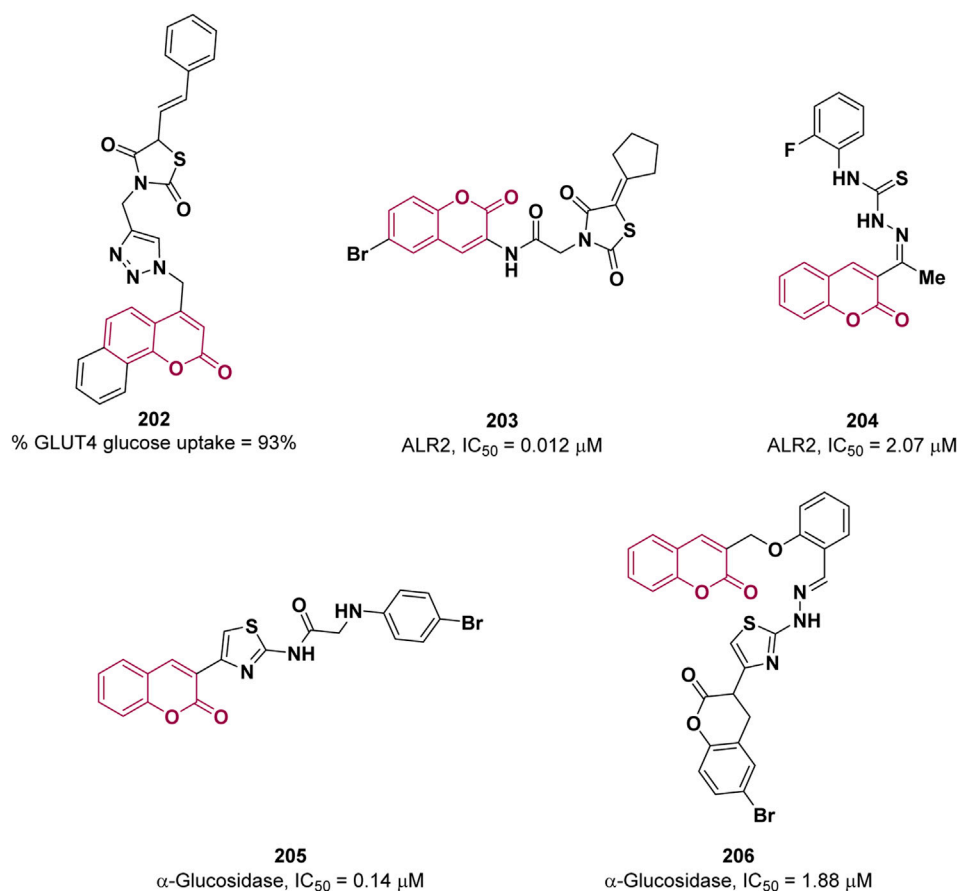


FIGURE 5
Coumarin derivatives having anti-diabetic potential.

selective towards ALR2 (selectivity index of 324.166), a forty-fold superiority over sorbinil (IC_{50} = 0.47 μ M) (Figure 5). *In vivo* experiments suggested that **203** delays the progression of cataract in rats in a dose-dependent manner warranting its further development as potential agent to treat the diabetic secondary complications, especially cataract.

Iqbal et al. reported coumarin-thiosemicarbazone hybrids as ALR2 inhibitors (Imran et al., 2021). Compound **204** proved to be the most promising inhibitor with an IC_{50} = 2.07 μ M (reference sorbinil, IC_{50} = 2.745 μ M) and high selectivity, relative to ALR1 (Figure 5). The X-ray crystal structure of **204** in complex with ALR2 revealed the most important interactions and partially explain the strong binding affinity towards ALR2. A common strategy, used to reduce post prandial glycemia, consists of the inhibition of α -glucosidase, an enzyme involved in the digestion of carbohydrates, whose inhibition delayed the absorption of glucose. In an attempt to find novel, safe and effective α -glucosidase inhibitors, Vora et al., proposed coumarin linked thiazole derivatives as potential scaffold on the basis of their interactions with the active site of α -glucosidase studied *in silico* (Ichale et al., 2023). The most active compound, **205**, showed an IC_{50} value of 0.14 μ M, in comparison to acarbose (IC_{50} = 6.32 μ M), shown in Figure 5.

The coumarin based azomethine-clubbed thiazoles synthesis was documented by Al-Harrasi and co-workers in 2023 (Ul Ain et al., 2023). The authors evaluated the *in vitro* activity of the

obtained compounds against α -glucosidase for the plausible treatment of diabetes mellitus (T2DM). The highest inhibition was observed for **206** with an IC_{50} value of 1.88 μ M, in comparison to the reference acarbose (IC_{50} = 873.34 μ M) (Figure 5). Docking studies were employed to predict the binding mode of the synthesized derivatives, revealing the significance of the interactions established by the azomethine moiety. This observation helps to explain the enhanced efficacy of the inhibitor.

4.5 Anticancers

The term “cancer” refers to a broad range of diseases characterized by an abnormal cell proliferation promoted by the mutations of genes implicated in the regulation of cell division and growth. These mutations can be induced by several factors such as irradiations, viruses, bacteria, smoking, and chemical compounds. Despite several progresses have been achieved in the anticancer therapy field, most cancers are still incurable. This prompted researchers to deeply study the cellular mechanisms involved in tumors, allowing the discovery of druggable targets that can be addressed for the development of novel therapeutic agents (Hassanpour and Dehghani, 2017).

Coumarins showed anticancer activity targeting different proteins implicated in cancer-related pathways. Recent advances

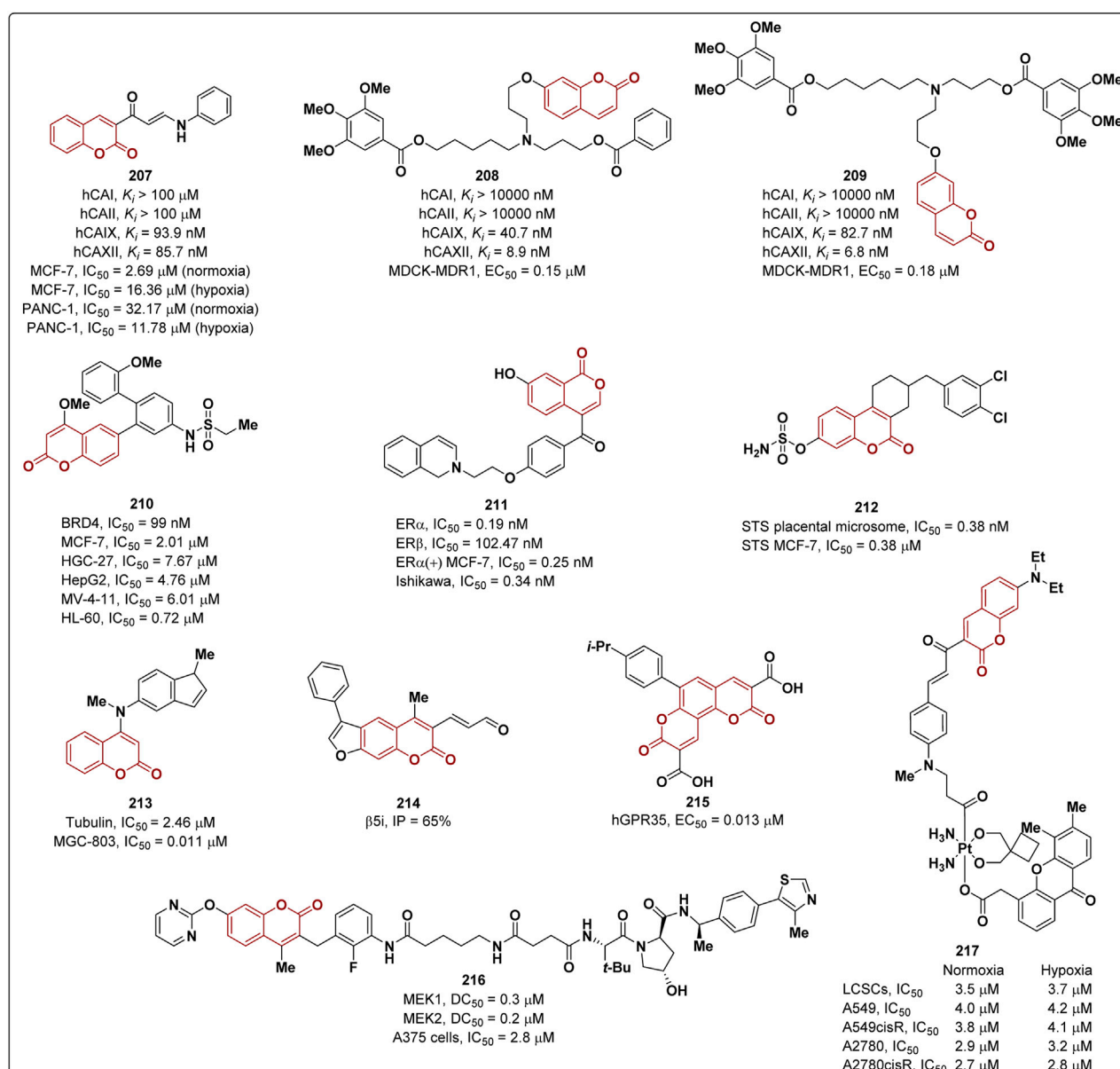


FIGURE 6
Coumarins with anticancer properties.

concerning the identification of coumarin-based compounds endowed with anticancer activity are reported in the following sections (Figure 6).

4.5.1 Coumarins as inhibitors of carbonic anhydrase IX and XII

Human carbonic anhydrases (hCAs) are zinc containing enzymes catalyzing the reversible hydration of carbon dioxide to bicarbonate ions and protons. Among the 15 different isoforms of hCA identified so far, hCA IX and XII are implicated in tumor progression and have been widely recognized as pharmacological targets for anticancer therapy (Moi et al., 2022). In the last years, coumarins have emerged as selective hCA IX and XII inhibitors. Within this scenario, Eldehna et al. described the hCA inhibitory activity of novel coumarin-based aryl enaminone derivatives

(Ibrahim et al., 2022). As results compound **207** (Figure 6) showed the highest selectivity towards the tumor associated isoforms hCA IX ($K_i = 93.9 \text{ nM}$) and hCA XII ($K_i = 85.7 \text{ nM}$) with selectivity ratios over the two ubiquitous isoforms hCA I and hCA II higher than 1,000, being more active than the reference compound acetazolamide (selectivity ratios between 0.5 and 43.9). The antiproliferative activity of **207** was evaluated on breast cancer MCF-7 and pancreatic cancer PANC-1 cell lines under both normoxic and hypoxic conditions. In the first case **207** displayed a more potent antiproliferative activity on MCF-7 cells ($\text{IC}_{50} = 2.69 \mu\text{M}$) than PANC-1 cells ($\text{IC}_{50} = 32.17 \mu\text{M}$). Under hypoxic conditions, a moderate inhibition was observed on both MCF-7 ($\text{IC}_{50} = 16.36 \mu\text{M}$) and PANC-1 cell lines ($\text{IC}_{50} = 11.78 \mu\text{M}$). Moreover, compound **207** delayed the cell cycle and induced apoptosis in MCF-7 cells.

A recent study revealed that hCA XII regulates the activity of P-glycoprotein (P-gp), a transporter protein associated with MDR involved in the active transport of chemotherapeutic drugs in the extracellular milieu reducing their cytotoxic effect. More specifically, the inhibition of hCA XII leads to a reduction of the intracellular pH which decreases Pgp activity (Kopecka et al., 2015). Therefore, the dual inhibition of hCA XII and P-gp represents an appealing strategy to overcome P-gp mediated MDR. Dei and others adopted a hybridization strategy to design novel hCA XII and P-gp dual inhibitors (Braconi et al., 2022). In particular, the authors combined the *N,N*-bis(alkanol)amine diester moiety, which is known to interact with P-gp, with the coumarin scaffold. The best inhibitory profile was shown by compounds **208** and **209** (Figure 6) which inhibited hCA XII with K_i values of 8.9 and 6.8 nM, respectively, and P-gp activity in MDCK transfected cells with EC_{50} values of 0.15 and 0.18 μ M, respectively. Both compounds were able to restore doxorubicin antineoplastic activity in HT29/DOX and A549/DOX cells which overexpress both proteins thus revealing to be promising P-gp mediated MDR reversers.

4.5.2 Coumarins as BRD4 inhibitors

BRD4 belongs to the bromodomain and extra-terminal (BET) protein family which comprises epigenetic proteins involved in the regulation of gene expression. In 2022, Cui et al. identified new BRD4 inhibitors bearing a coumarin scaffold (Cui et al., 2022). Among the synthesized derivatives, inhibitor **210** was identified as most promising anticancer agent. Compound **210** (Figure 6) inhibited BRD4 activity with an IC_{50} value of 99 nM and it was found to exert an antiproliferative activity in MCF-7 (IC_{50} = 2.01 μ M), HGC-27 (IC_{50} = 7.67 μ M), HepG2 (IC_{50} = 4.76 μ M), MV-4-11 (IC_{50} = 6.01 μ M) and HL-60 (IC_{50} = 0.72 μ M) cell lines, without significantly affecting normal cells. In addition, the coumarin derivative **210** determined the arrest of cell cycle at G0/G1 phase and induced apoptosis in MCF-7 cells. Interestingly, compound **210** was also able to reduce the expression and transcription of c-Myc protein.

4.5.3 Coumarins as antagonist of human estrogen receptor α

Human estrogen receptor α (ER α) is a nuclear transcription function whose activation by estrogens is responsible for an increment of cellular proliferation in breast cancer (Paterni et al., 2014). Therefore, the selective inhibition of ER α constitutes an approach for pharmacological intervention in breast cancer therapy. In 2022, Kurtanović et al. reported a new set of coumarin derivatives as selective ER α antagonists (Kurtanović et al., 2022). The most potent compound (**211**, see Figure 6, IC_{50} = 0.19 nM) displayed not only a good selectivity over ER β (IC_{50} = 102.47 nM) but also a higher inhibitory activity than the reference raloxifene (IC_{50} = 0.74 nM). Furthermore, derivative **211** exerted antiproliferative activity on ER α (+) MCF-7 cells (IC_{50} = 0.25 nM) and also on Ishikawa endometrial adenocarcinoma cell lines (IC_{50} = 0.34 nM) being more effective than raloxifene (IC_{50} of 0.89 and 0.94 nM on MCF-7 and Ishikawa cells, respectively). Compound **211** affected Raf-1/MAPK/ERK signal transduction pathway causing the arrest MCF-7 cell cycle at G₀/G₁ phase. The antitumoral activity of **211** was confirmed by *in vivo* experiments performed on a female Wistar rat breast cancer tumor model.

4.5.4 Coumarins as steroid sulfatase inhibitors

Steroid sulfatase (STS) is an enzyme implicated in the hydrolysis of aryl and alkyl steroids sulfates thus playing a crucial role in the production of biologically active steroids. STS is overexpressed in breast cancer and its inhibition reduces estrogen formation, hindering tumor proliferation thus paving the way towards the development of anticancer agents (Foster, 2021). Within this context, Chang and others designed novel coumarin-7-O-sulfamate derivatives as STS inhibitors (Chang et al., 2022). The most promising compound **212** (Figure 6) disrupted STS activity from human placenta and MCF-7 cells with IC_{50} values of 0.38 and 0.38 μ M, respectively, showing comparable potency to irosustat, which was used as reference and also has a coumarin core (IC_{50} of 0.20 and 0.16 μ M, respectively). Prior studies pointed out that the sulfamate moiety covalently binds to STS and therefore irreversibly inhibits its function. Considering this, kinetic studies were conducted to evaluate the K_i/k_{inact} ratio, which indicates the efficacy of covalent inhibition. Molecules with high K_i/k_{inact} values might exert their biological activity at low doses showing a longer half-life. As result, derivative **212** provided a K_i/k_{inact} value of 17.5 which is higher than that of irosustat (16.1). It is worth noting that compound **212** elicited antiproliferative effects on STS overexpressed cancer lines while being safe on normal cell lines.

4.5.5 Coumarins as tubulin polymerization inhibitors

Microtubules, formed by α and β -tubulin heterodimers, are essential components of the cytoskeleton. Compounds affecting tubulin polymerization targeting the colchicine binding site exert a remarkable antitumor activity by interfering with tumor cell division (Lu et al., 2012). Within this context, Song and co-workers reported a new series of tubulin polymerization inhibitors obtained by combining the indole and coumarin moieties as both scaffolds proved to affect tubulin polymerization (Song et al., 2022). The most potent compound **213** (Figure 6) was able to inhibit tubulin polymerization by interacting with colchicine binding site with an IC_{50} value of 2.46 μ M, showing a higher activity than colchicine (IC_{50} = 6.70 μ M). Derivative **213** displayed a significant antiproliferative activity on gastric cancer cell line MGC-803 with an IC_{50} of 0.011 μ M. Moreover, it promoted cell apoptosis, inhibited cell cycle at G₂/M phase and cell migration in MGC-803 and HGC-27 gastric cancer cell lines. Finally, compound **213** exhibited antitumoral effects *in vivo*.

4.5.6 Coumarins as proteasome inhibitors

The ubiquitin-proteasome system is responsible for the maintenance of protein homeostasis and the regulation of various cellular processes. Proteasome inhibition is a strategy employed in the anti-cancer therapy (Ielo et al., 2022; Ielo et al., 2023). Sosić and co-workers reported a series of coumarin derivatives as selective (immuno) proteasome inhibitors (Schiffrer et al., 2021). The most promising derivative resulted to be **214** with an inhibition percentage (IP) of 65% on the chymotrypsin-like (β 5i) subunit (Figure 6).

4.5.7 Coumarins as hGPR35 inhibitors

A series of coumarin-like diacid derivatives were designed and synthesized by Liang et al. as novel agonists of human G protein-coupled receptor 35 (hGPR35) which is implicated in a variety of

pathologies including cancer (Wei et al., 2021). An EC_{50} value of $0.013\ \mu\text{M}$ was determined for compound **215**, which proved to be one of the most active of the series (Figure 6).

4.5.8 Coumarins as MEK1/2 inhibitors

The RAF/MEK/ERK pathway is a fundamental signal path associated with the proliferation, differentiation, and apoptosis of tumors. MEK1/2 is a key kinase target in the pathway and ERK1/2 is its main substrate. Even if several MEK1/2 inhibitors were reported, acquired resistance remains a significant problem. Xu and co-workers designed and synthesized a series of coumarin-based MEK1/2 PROTAC MEK1/2 degraders based on a coumarin derivative which was a potent non-diarylamine allosteric MEK1/2 inhibitor effective in human cancer cells (Wang et al., 2023). **216** is the most promising derivative showing a DC_{50} values of 0.3 and $0.2\ \mu\text{M}$ in MEK1 and MEK2 degradation, respectively. Furthermore, it significantly inhibits the growth of A375 cells ($IC_{50} = 2.8\ \mu\text{M}$) (Figure 6).

4.5.9 Coumarins in light-driven cancer therapy

Light-driven cancer therapy including photodynamic therapy (PDT) represents an appealing strategy to cure tumors. This approach presents several advantages if compared to conventional chemotherapy, such as low invasiveness, the lack of cross-resistance, as well as spatially and temporally controllable activation. PDT usually relies on photosensitizers able to induce biomolecules damages by ROSs (Reactive Oxygen Species) production, thus requiring oxygen to exert the cytotoxic effects. However, tumoral cells are characterized by a hypoxic environment which limits the efficacy of PDT. To overcome this limitation, intracellular pH (pHi) homeostasis can be modulated to achieve anticancer effects. In 2023, Deng and collaborators described the development of a near-infrared (NIR) activated platinum (IV) complex **217** (Figure 6) carrying a coumarin-based photosensitizer as first example of Pt (IV) complex activatable in a two-photon excitation (TPE) manner, which allows a deeper IR tissue penetration (Deng et al., 2023). Complex **217**, localized in the endoplasmic reticulum, displayed low toxicity in the dark while exerting a significant antiproliferative effect on different cancer cell lines under both normoxic and hypoxic conditions ($IC_{50} = 2.7\text{--}4.2\ \mu\text{M}$), shown in Figure 6 thus suggesting an oxygen-independent photocytotoxic effect. Indeed, **217** interfered with pHi and was able to trigger the immune system and reduce tumor growth and metastasis formation.

4.6 Miscellaneous

4.6.1 Anti-leishmanial

Leishmaniasis is one of the most common parasite infections worldwide and has restricted therapeutic options. Novel coumarin-isatin hybrids were synthesized by Naseer and co-workers in order to evaluate their activity as anti-leishmanial agents (Khattoon et al., 2021). Docking studies suggested which of the prepared derivatives installed profitable interactions with the target, leading to the identification, via *in vitro* assays, of the best derivative, **218**, with an IC_{50} value $0.10\ \mu\text{M}$ and $0.87\ \mu\text{M}$ against *L. tropica* promastigote (LTP) and axenic amastigote (LTAA) forms, respectively (references tartar emetic $IC_{50} = 7.28\ \mu\text{M}$ and Amphotericin B $IC_{50} = 1.86\ \mu\text{M}$, respectively) (Figure 7).

4.6.2 Anti-thrombosis

Pochet et al. reported coumarins as inhibitors of factor XIIa (FXIIa), a promising target for artificial surface-induced thrombosis and different inflammatory diseases (Davoine et al., 2023). By using a fragment-based drug discovery approach, they designed a new class of coumarin derivatives. The most potent compound **219** possesses a K_i of $62.2\ \text{nM}$ on FXIIa and it was tested in plasma to evaluate its stability and efficacy on coagulation assays (Figure 7). It showed a plasmatic half-life of 1.9 h and a good selectivity for the intrinsic coagulation pathway over the extrinsic one.

4.6.3 Anti-tyrosinase

Tyrosinase (Tyr) is a key enzyme in the biosynthesis of melanin pigments (Mirabile et al., 2021). An excessive production of melanin can cause hyperpigmentation disorders such as melanoma (Vittorio et al., 2023). Kim and co-workers described a new series of thiophenyl-pyrazolylthiazole-coumarin hybrids as tyrosinase inhibitors (Nasab et al., 2023). The best activity was observed for derivative **220**, with an IC_{50} value of $0.043\ \mu\text{M}$ (reference kojic acid, $IC_{50} = 18.521\ \mu\text{M}$), which is a non-competitive inhibitor (Figure 7). It also demonstrated excellent antioxidant activity against DPPH and no cytotoxicity on B16F10 melanoma cells.

4.6.4 Vasorelaxant

Coumarins can act as NO donor drugs thus exerting a vasorelaxant effect. In 2022, Toimil and collaborators reported a new series of nitrate-coumarins that were tested in contraction-relaxation studies on rat aorta precontracted with phenylephrine (Matos et al., 2022). The most active compound **221** (Figure 7) showed an IC_{50} value of $1.92\ \text{nM}$ displaying superior potency than nitroglycerin ($IC_{50} = 12.73\ \text{nM}$) and sodium nitroprusside ($IC_{50} = 4.32\ \text{nM}$) used as reference.

4.6.5 Anti-tuberculosis

Coumarin-based compounds exert anti-tubercular activity targeting the thioesterase (TE) domain of Pks13 enzyme implicated in the biosynthesis of mycolic acids which constitute the major components of *Mycobacterium tuberculosis* (Mtb) cell wall (North et al., 2014). Within this scenario, Yu and co-workers reported the design of a new series of coumarin derivatives endowed with anti-tubercular activity (Zhang et al., 2022). The most active derivative **222** (Figure 7) displayed a MIC value of $0.0039\ \mu\text{M}$ proving to be more potent than the reference drugs isoniazid (MIC = $0.04\ \mu\text{M}$), rifampin (MIC = $0.125\ \mu\text{M}$) and ethambutol (MIC = $1\ \mu\text{M}$). Compound **222** inhibited Pks13-TE activity with an IC_{50} value of $1.30\ \mu\text{M}$ and resulted to be effective also on clinical resistant strains of Mtb, namely, DS-TB (V4207), MDR-TB (KZN494 and V2475), and XDR-TB (TF274 and R506), showing MIC values between 0.0039 and $0.0078\ \mu\text{M}$ (Figure 7). Interestingly, derivative **222** exhibited a good human microsomal stability and oral bioavailability in mice.

4.6.6 Antioxidant

Coumarins can elicit antioxidant effects by acting as Nrf2 (nuclear factor erythroid 2-related factor 2) agonists. Indeed, the Keap1-Nrf2 pathway represents the main protective response to oxidative stress. In physiological conditions, Keap1 regulates the

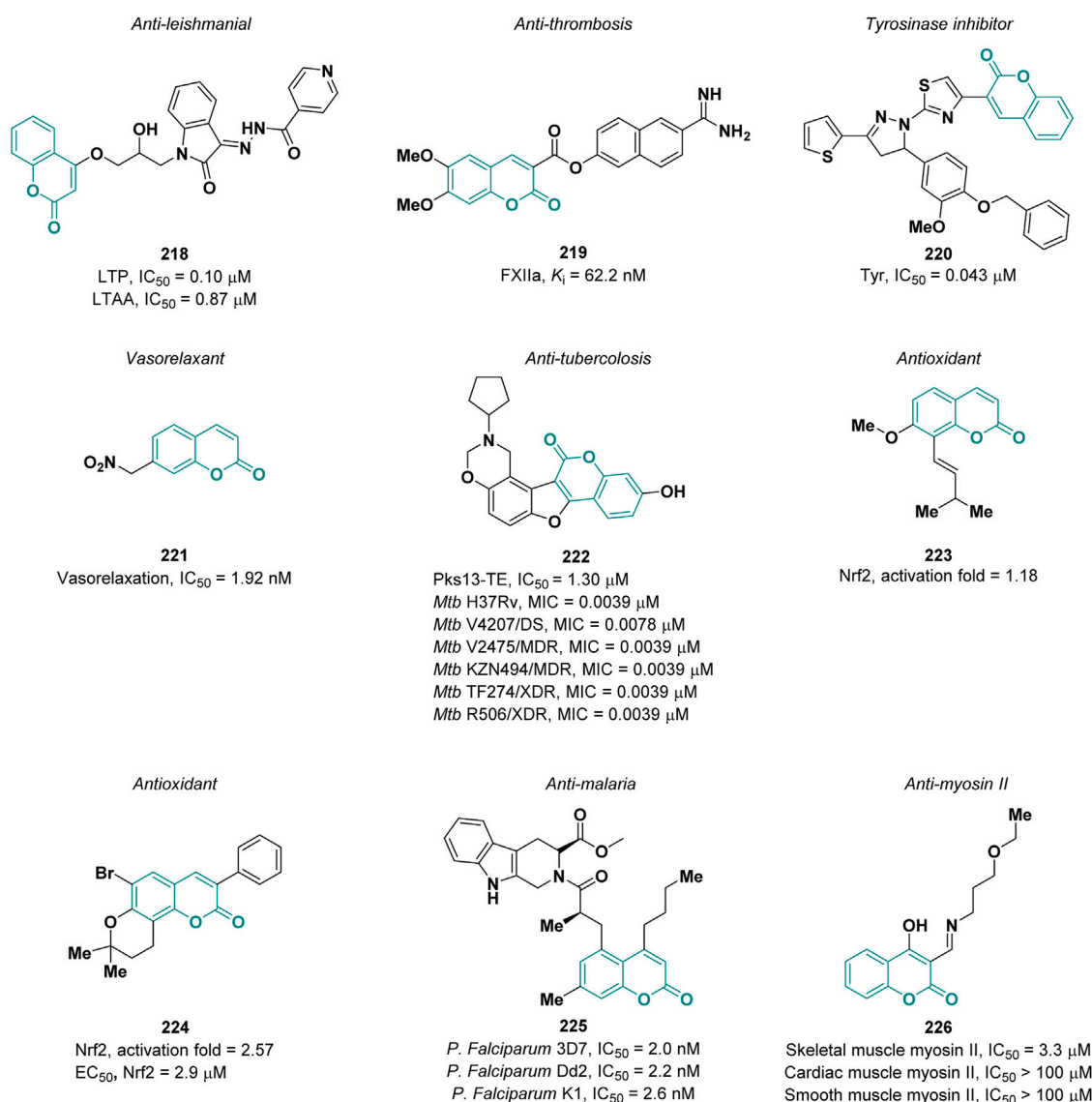


FIGURE 7
Coumarin derivatives endowed with miscellaneous pharmacological properties.

ubiquitination of Nrf2, while under oxidative stress conditions Keap1 dissociates from Nrf2 which in turn translocate into the nucleus promoting the transcription of cytoprotective genes (Buendia et al., 2016). In 2022, Ma and others described the Nrf2 agonistic activity of a new series of coumarin derivatives designed from osthole **223** (Figure 7), a naturally occurring coumarin able to increase the expression levels of Nrf2 (Huang et al., 2022). The most active compound **223** (Figure 7) showed an activation fold of 2.57 at a concentration of 20 μ M, proving to be more effective than osthole (activation fold of 1.18). The EC_{50} value of **224** was measured on 293T cells yielding a value of 2.9 μ M. Cellular thermal shift assay (CETSA) confirmed KEAP1 engagement by **224** in cellular environment.

4.6.7 Anti-malaria

Coumarins were also investigated as therapeutics for the treatment of malaria which represents still today a global

emergency due to the inefficacy of the currently employed chemotherapeutic agents against resistant *P. falciparum* strains. To find new and more effective antimalarial agents, Cho and collaborators designed a series of coumarin derivatives bearing a tetrahydro- β -carboline moiety (Cho et al., 2022). A phenotypic approach was employed to assess the ability of the synthesized derivatives to inhibit the malaria parasite growth. As result, compound **225** (Figure 7) was identified as the most potent antimalarial agents with an IC_{50} value of 2.0 nM against the wild-type *P. falciparum* strain 3D7, showing a higher activity than chloroquine (IC_{50} = 14 nM) used as reference. Moreover, **225** displayed a comparable inhibitory activity also against the chloroquine resistant strains Dd2 and K1 with IC_{50} values of 2.2 and 2.6 nM, respectively. Finally, derivative **225** decreased parasite growth in *P. berghei* ANKA-infected ICR mouse models, despite a short plasma half-life was observed.

4.6.8 Anti-myosin II

The inhibition of muscle myosin is of interest to develop therapeutic agents for the treatment of hypercontractile states. On this ground, Bell and others designed novel 4-hydroxycoumarin imines as muscle myosin II inhibitors (Smith et al., 2023). Among the synthesized derivatives, compound **226** (Figure 7) showed the highest selectivity towards skeletal myosin ($IC_{50} = 3.3 \mu M$) over the cardiac and smooth muscle isoforms ($IC_{50} > 100 \mu M$). Interestingly, derivative **226** did not affect non-muscle myosin in cytokinesis assay and did not exhibit significant cytotoxicity.

5 Discussion

Natural compounds constitute an invaluable source of biologically active molecules. Coumarins are an excellent example of natural products presenting multiple pharmacological properties thus representing a privileged scaffold in medicinal chemistry.

Over the years, advances in synthetic organic chemistry went hand in hand with development of new strategies for the synthesis and functionalization of coumarins. Straightforward selective functionalization approaches permitted the incorporation into the coumarin system of several fragments, such as biologically relevant fluorinated moieties, alkyl/aryl substituents, or rigidified cyclic architectures, endowing the resulting scaffold with enhanced biological or physico-chemical properties. Relevant applications mostly occurred at the level of C-3 and C-4 positions of the coumarin scaffold, which constitute two important sites of functionalization, characterized by a unique type of reactivity. Considering the numerous applications of coumarins among chemical and biological sciences, there is still an urgent need for innovative strategies to expand the synthetic accessibility and the functionalization of such compelling scaffold.

From a medicinal chemistry point of view, the peculiar structure of coumarin, characterized by its planarity and lipophilicity, feature mostly impaired by the presence of a cyclic lactone moiety, enables the binding to diverse targets through hydrophobic, *pi*-stacking, hydrogen bonding, and dipole-dipole interactions.

Concerning the pharmacological applications, coumarins were investigated as potential drugs in a wide array of pathologies, with a special mention to neurodegenerative diseases and cancer. Indeed, coumarins have shown very promising activity in the treatment of neurological disorders, like AD and PD, for their ability to selectively target enzymes involved in neurotransmitter metabolisms, such as AChE and MAO-B, at nanomolar concentrations. It is noteworthy that some of these derivatives such as **176** or **177** can cross the BBB maintaining a good hydrophilic/lipophilic balance which is essential to obtain a drug-like molecule. Furthermore, coumarins modulate many biological targets implicated in cancer, displaying antiproliferative activity in various cancer cell lines without affecting normal cells. Importantly, *in vivo* antitumoral effects were also observed for some derivatives like **211** or **213**. Since coumarins have favorable photophysical characteristics, they can be also utilized as photosensitizers in PDT which is gaining a growing attention in the recent years as minimally invasive therapy for the treatment of cancer.

It is worth to note that the coumarin scaffold is a valuable template for the development of MTDLs. Indeed, the concept “one drug one disease” has been overcome as several pathologies, such as

cancer and neurodegenerative diseases, involve multifactorial events and, therefore, the modulation of a single target often does not result in adequate efficacy. Coumarins have been successfully used in this sense especially in the search of MTDLs for AD (compounds **176** and **177**) and therapeutics for tumors (compounds **208** and **209**).

Besides their activity on neurodegenerative diseases and cancer, coumarins can also be engineered towards antimicrobial, antiparasitic, antidiabetic, anti-inflammatory, skin-lightening, and antioxidant activities. For examples, coumarins carrying a thiazole or thiazolidinones are potential antityrosinase and antidiabetic drugs as well as excellent antibacterial agents characterized by less tendency to resistance respect to some antibacterials currently used in therapy. However, coumarin-isothiazole hybrids showed good antifungal effects, while coumarins carrying a quinazoline moiety are endowed with promising antiviral properties.

Despite the satisfactory results achieved, more investigations are needed to assess the metabolic stability and toxicity of coumarins. In animal-based studies, coumarins resulted to be carcinogenic at very high doses and the carcinogenic mechanism appears to be metabolism-mediated (Lake, 1999). However, these considerations are true for natural coumarins and cannot be applied to synthetic derivatives whose toxicity and metabolic pathways strongly rely on the substitution pattern, and therefore, require additional investigations.

Author contributions

AC: Writing—original draft. SV: Writing—original draft. CD: Conceptualization, Writing—review and editing. LI: Conceptualization, Writing—review and editing.

Funding

The author(s) declare financial support was received for the research, authorship, and/or publication of this article. The authors thank the University of Turin and the University of Vienna for financial support. The authors acknowledge support from Project CH4.0 under the MUR (Italian Ministry for the University) program “Dipartimenti di Eccellenza 2023–2027” (CUP: D13C22003520001).

Conflict of interest

The authors declare that the research was conducted in the absence of any commercial or financial relationships that could be construed as a potential conflict of interest.

Publisher's note

All claims expressed in this article are solely those of the authors and do not necessarily represent those of their affiliated organizations, or those of the publisher, the editors and the reviewers. Any product that may be evaluated in this article, or claim that may be made by its manufacturer, is not guaranteed or endorsed by the publisher.

References

- Alfayomy, A. M., Abdel-Aziz, S. A., Marzouk, A. A., Shaykoon, M. S. A., Narumi, A., Konno, H., et al. (2021). Design and synthesis of pyrimidine-5-carbonitrile hybrids as COX-2 inhibitors: anti-inflammatory activity, ulcerogenic liability, histopathological and docking studies. *Bioorg. Chem.* 108, 104555. doi:10.1016/j.bioorg.2020.104555
- Al-Majedy, Y. K., Kadhumi, A. A. H., Al-Amieri, A. A., and Mohamad, A. B. (2017). Coumarins: the antimicrobial agents. *Syst. Rev. Pharm.* 8, 62–70. doi:10.5530/srp.2017.1.11
- Almasirad, A., Sani, P. S. V., Mousavi, Z., Fard, G. B., Anvari, T., Farhadi, M., et al. (2022). Novel thiazolotriazolone derivatives: design, synthesis, *in silico* investigation, analgesic and anti-inflammatory activity. *ChemistrySelect* 7, e20210322. doi:10.1002/slct.202103228
- Ansell, J., Hirsh, J., Poller, L., Bussey, H., Jacobson, A., and Hylek, E. (2004). The pharmacology and management of the vitamin K antagonists: the seventh ACCP conference on antithrombotic and thrombolytic therapy. *Chest* 126, 204S–233S. doi:10.1378/chest.126.3_suppl.204S
- Arora, S., Singh, S. P., Sharma, P., and Singh, A. (2022). Bronsted acid catalyzed annulations of ketene dithioacetals: synthesis of 3-aryl coumarins and indenones. *Org. Biomol. Chem.* 20, 8907–8911. doi:10.1039/d2ob01558g
- Babaei, E., Kucukkilinc, T. T., Jalili-Baleh, L., Nadri, H., Oz, E., Forootanfar, H., et al. (2022). Novel coumarin-pyridine hybrids as potent multi-target directed ligands aiming at symptoms of Alzheimer's disease. *Front. Chem.* 10, 895483. doi:10.3389/fchem.2022.895483
- Bao, X., Yu, W., Wang, L., Dong, X., Wang, G., Chen, W., et al. (2023). Synthesis of 4-aryl-3,4-dihydrocoumarins and 4-aryl-4H-chromenes via Er(OTf)(3)-catalyzed cascade reactions of p-quinone methides with 1,3-dicarbonyl compounds. *RSC Adv.* 13, 15942–15946. doi:10.1039/d3ra02267f
- Bertoli, G., Martínez Á, M., Goebel, J. F., Belmonte, D., Sivendran, N., and Gooßen, L. J. (2023). C-H fluoromethoxylation of arenes by photoredox catalysis. *Angew. Chem. Int. Ed.* 62, e202215920. doi:10.1002/anie.202215920
- Bhowmick, A., and Brahmachari, G. (2023). C(sp)-C(sp(3)) bond formation through ligand- and additive-free CuO-mediated decarboxylative direct cross-coupling of coumarin-/chromone-3-carboxylic acids and terminal alkynes. *Org. Lett.* 25, 7095–7099. doi:10.1021/acs.orglett.3c02369
- Bigi, F., Chesini, L., Maggi, R., and Sartori, G. (1999). Montmorillonite KSF as an inorganic, water stable, and reusable catalyst for the Knoevenagel synthesis of coumarin-3-carboxylic acids. *J. Org. Chem.* 64, 1033–1035. doi:10.1021/jo981794r
- Bojanowski, J., and Albrecht, A. (2021). Doubly decarboxylative synthesis of 4-(Pyridylmethyl)chroman-2-ones and 2-(Pyridylmethyl)chroman-4-ones under mild reaction conditions. *Molecules* 26, 4689. doi:10.3390/molecules26154689
- Bouhaoui, A., Eddahmi, M., Dib, M., Khoulil, M., Aires, A., Catto, M., et al. (2021). Synthesis and biological properties of coumarin derivatives. A review. *ChemistrySelect* 6, 5848–5870. doi:10.1002/slct.202101346
- Braconi, L., Teodori, E., Riganti, C., Coronello, M., Nocentini, A., Bartolucci, G., et al. (2022). New dual P-glycoprotein (P-gp) and human carbonic anhydrase XII (hCA XII) inhibitors as multidrug resistance (MDR) reversers in cancer cells. *J. Med. Chem.* 65, 14655–14672. doi:10.1021/acs.jmedchem.2c01175
- Breijyeh, Z., and Karaman, R. (2020). Comprehensive review on Alzheimer's disease: causes and treatment. *Molecules* 25, 5789. doi:10.3390/molecules25245789
- Buendia, I., Michalska, P., Navarro, E., Gameiro, I., Egea, J., and Leon, R. (2016). Nrf2-ARE pathway: an emerging target against oxidative stress and neuroinflammation in neurodegenerative diseases. *Pharmacol. Ther.* 157, 84–104. doi:10.1016/j.pharmthera.2015.11.003
- Cairns, N., Harwood, L. M., and Astles, D. P. (1994). Tandem thermal Claisen–Cope rearrangements of coumarate derivatives. Total syntheses of the naturally occurring coumarins: suberosin, demethylsuberosin, ostruthin, balsamiferone and gravelliferone. *J. Chem. Soc. Perkin Trans. 1*, 3101–3107. doi:10.1039/P19940003101
- Çelik Onar, H., Özden, E. M., Taslak, H. D., Gülçin, İ., Ece, A., and Erçağ, E. (2023). Novel coumarin-chalcone derivatives: synthesis, characterization, antioxidant, cyclic voltammetry, molecular modelling and biological evaluation studies as acetylcholinesterase, α-glycosidase, and carbonic anhydrase inhibitors. *Chem. Biol. Interact.* 383, 110655. doi:10.1016/j.cbi.2023.110655
- Cen, N., Wang, H., Zhou, Y., Gong, R., Sui, D., and Chen, W. (2023). Catalyst-free electrochemical trifluoromethylation of coumarins using CF(3)SO(2)NHNH(Boc) as the CF(3) source. *Org. Biomol. Chem.* 21, 1883–1887. doi:10.1039/d2ob01925f
- Cesar, J. M., García-Avello, A., Navarro, J. L., and Herraiz, M. V. (2004). Aging and oral anticoagulant therapy using acenocoumarol. *Blood Coagul. Fibrinolysis* 15, 673–676. doi:10.1097/00001721-200412000-00007
- Chang, C. N., Lin, I. C., Lin, T. S., Chiu, P. F., Lu, Y. L., Narwane, M., et al. (2022). The Design, Structure-Activity, and kinetic studies of 3-Benzyl-5-oxa-1,2,3,4-Tetrahydro-2H-chromeno-(3,4-c)pyridin-8-yl sulfamates as Steroid sulfatase inhibitors. *Bioorg. Chem.* 129, 106148. doi:10.1016/j.bioorg.2022.106148
- Chauhan, S., Kumar, A. S., and Swamy, K. K. K. (2023). δ-Acetoxy allenolate as a 5C-synthon in domino-annulation with sulfamidate imines: ready access to coumarins. *J. Org. Chem.* 88, 12432–12444. doi:10.1021/acs.joc.3c01183
- Chen, L., Deng, H., Cui, H., Fang, J., Zuo, Z., Deng, J., et al. (2018). Inflammatory responses and inflammation-associated diseases in organs. *Oncotarget* 9, 7204–7218. doi:10.18632/oncotarget.23208
- Chen, Y. S., Zheng, Y., Chen, Z. J., Xie, Z. Z., He, X. C., Xiao, J. A., et al. (2021). A phosphine-catalysed one-pot domino sequence to access cyclopentene-fused coumarins. *Org. Biomol. Chem.* 19, 7074–7080. doi:10.1039/d1ob01143j
- Cho, N., Kikuzato, K., Futamura, Y., Shimizu, T., Hayase, H., Kamisaka, K., et al. (2022). New antimalarials identified by a cell-based phenotypic approach: structure–activity relationships of 2,3,4,9-tetrahydro-1H-β-carboline derivatives possessing a 2-((coumarin-5-yl)oxy)alkanoyl moiety. *Bioorg. Med. Chem.* 66, 116830. doi:10.1016/j.bmc.2022.116830
- Christie, R. M., Morgan, K. M., and Islam, M. S. (2008). Molecular design and synthesis of N-arylsulfonated coumarin fluorescent dyes and their application to textiles. *Dyes Pig* 76, 741–747. doi:10.1016/j.dyepig.2007.01.018
- Citarella, A., Ielo, L., Stagno, C., Cristani, M., Muscarà, C., Pace, V., et al. (2022a). Synthesis, computational investigation and biological evaluation of α,α-difluoromethyl ketones embodying pyrazole and isoxazole nuclei as COX inhibitors. *Org. Biomol. Chem.* 20, 8293–8304. doi:10.1039/D2OB01382G
- Citarella, A., Moi, D., Pedrini, M., Pérez-Peña, H., Pieraccini, S., Dimasi, A., et al. (2023). Synthesis of SARS-CoV-2 M pro inhibitors bearing a cinnamic ester warhead with *in vitro* activity against human coronaviruses. *Org. Biomol. Chem.* 21, 3811–3824. doi:10.1039/D3OB00381G
- Cui, Q. H., Li, W. B., Wang, Z. Y., Xu, K. Y., Wang, S., Shi, J. T., et al. (2022). Design, synthesis and biological evaluation of coumarin derivatives as potential BRD4 inhibitors. *Bioorg. Chem.* 128, 106117. doi:10.1016/j.bioorg.2022.106117
- Dank, C., and Ielo, L. (2023). Recent advances in the accessibility, synthetic utility, and biological applications of aziridines. *Org. Biomol. Chem.* 21, 4553–4573. doi:10.1039/D3OB00424D
- Das, D., and Das, A. R. (2022). Access to π-extended heterocycles containing pyrrolo-coumarin cores involving -COCH(3) as a traceless directing group and materializing two successive sp(2)C-H/sp(3)N-H and sp(2)C-H/sp(2)N-H activations. *J. Org. Chem.* 87, 11443–11456. doi:10.1021/acs.joc.2c00958
- Davoine, C., Traina, A., Evrard, J., Lanners, S., Fillet, M., and Pochet, L. (2023). Coumarins as factor XIIIa inhibitors: potency and selectivity improvements using a fragment-based strategy. *Eur. J. Med. Chem.* 259, 115636. doi:10.1016/j.ejmech.2023.115636
- De Luca, L., Vittorio, S., Pena-Diaz, S., Pitasi, G., Fornt-Sune, M., Bucolo, F., et al. (2022). Ligand-based discovery of a small molecule as inhibitor of α-synuclein amyloid formation. *Int. J. Mol. Sci.* 23, 14844. doi:10.3390/ijms232314844
- Deng, Z., Li, H., Chen, S., Wang, N., Liu, G., Liu, D., et al. (2023). Near-infrared-activated anticancer platinum(IV) complexes directly photooxidize biomolecules in an oxygen-independent manner. *Nat. Chem.* 15, 930–939. doi:10.1038/s41557-023-01242-w
- Douglas, E. J. A., Marshall, B., Alghamadi, A., Joseph, E. A., Duggan, S., Vittorio, S., et al. (2023). Improved antibacterial activity of 1,3,4-oxadiazole-based compounds that restrict *Staphylococcus aureus* growth independent of LtaS function. *ACS Infect. Dis.* 9, 2141–2159. doi:10.1021/acsinfectdis.3c00250
- Duxbury, B. M., and Poller, L. (2001). State-of-the-art review: the oral anticoagulant Saga: past, present, and future. *Clin. Appl. Thromb. Hemost.* 7, 269–275. doi:10.1177/107602960100700403
- Fayed, E. A., Nosseir, E. S., Atef, A., and El-Kalyoubi, S. A. (2022). *In vitro* antimicrobial evaluation and *in silico* studies of coumarin derivatives tagged with pyranopyridine and pyranopyrimidine moieties as DNA gyrase inhibitors. *Mol. Divers* 26, 341–363. doi:10.1007/s11030-021-10224-4
- Foster, P. A. (2021). Steroid sulphatase and its inhibitors: past, present, and future. *Molecules* 26, 2852. doi:10.3390/molecules26102852
- Gharui, C., Parida, C., and Pan, S. C. (2021). Organocatalytic asymmetric addition of aromatic α-cyanoketones to o-quinone methides: synthesis of 3,4-dihydrocoumarins and tetrasubstituted chromans. *J. Org. Chem.* 86, 13071–13081. doi:10.1021/acs.joc.1c00435
- Gitto, R., Vittorio, S., Bucolo, F., Pena-Diaz, S., Siracusa, R., Cuzzocrea, S., et al. (2022). Discovery of neuroprotective agents based on a 5-(4-Pyridinyl)-1,2,4-triazole scaffold. *ACS Chem. Neurosci.* 13, 581–586. doi:10.1021/acscchemneuro.1c00849
- Gorjian, H., and Khaligh, N. G. (2022). The liquid phase of 4,4'-trimethylenedipiperidine: a safe and greener dual-task agent for clean and facile synthesis of coumarin derivatives. *Mol. Divers.* 26, 3047–3055. doi:10.1007/s11030-021-10364-7
- Grover, J., and Jachak, S. M. (2015). Coumarins as privileged scaffold for anti-inflammatory drug development. *RSC Adv.* 5, 38892–38905. doi:10.1039/C5RA05643H
- Hampel, H., Vassar, R., De Strooper, B., Hardy, J., Willem, M., Singh, N., et al. (2021). The β-secretase BACE1 in alzheimer's disease. *Biol. Psychiatry* 89, 745–756. doi:10.1016/j.biopsych.2020.02.001
- Hassanpour, S. H., and Dehghani, M. (2017). Review of cancer from perspective of molecular. *J. Cancer Res. Pract.* 4, 127–129. doi:10.1016/j.jcrpr.2017.07.001

- Hazarika, H., Dutta, D., Brahma, S., Das, B., and Gogoi, P. (2023). Pd-catalyzed alkyne and arylene annulations: synthesis and photophysical properties of π -extended coumarins. *J. Org. Chem.* 88, 12168–12182. doi:10.1021/acs.joc.2c01187
- Hu, Y., Shan, L., Qiu, T., Liu, L., and Chen, J. (2021). Synthesis and biological evaluation of novel coumarin derivatives in rhadoviral clearance. *Eur. J. Med. Chem.* 223, 113739. doi:10.1016/j.ejmech.2021.113739
- Huang, W., Huang, Y., Cui, J., Wu, Y., Zhu, F., Huang, J., et al. (2022). Design and synthesis of Osthole-based compounds as potential Nrf2 agonists. *Bioorg. Med. Chem. Lett.* 61, 128547. doi:10.1016/j.bmcl.2022.128547
- Hwu, J. R., Kapoor, M., Gupta, N. K., Tsay, S.-C., Huang, W.-C., Tan, K.-T., et al. (2022). Synthesis and antiviral activities of quinazolinamine–coumarin conjugates toward chikungunya and hepatitis C viruses. *Eur. J. Med. Chem.* 232, 114164. doi:10.1016/j.ejmech.2022.114164
- Ibrahim, H. S., Abdelrahman, M. A., Nocentini, A., Bua, S., Abdel-Aziz, H. A., Supuran, C. T., et al. (2022). Insights into the effect of elaborating coumarin-based aryl enamines with sulfonamide or carboxylic acid functionality on carbonic anhydrase inhibitory potency and selectivity. *Bioorg. Chem.* 126, 105888. doi:10.1016/j.bioorg.2022.105888
- Ichale, R., Kanhed, A. M., and Vora, A. (2023). Coumarin linked thiazole derivatives as potential α -glucosidase inhibitors to treat diabetes mellitus. *Mol. Divers.* doi:10.1007/s11030-023-10652-4
- Ielo, L., Patamia, V., Citarella, A., Efferth, T., Shahhamzehei, N., Schirmeister, T., et al. (2022). Novel class of proteasome inhibitors: *in silico* and *in vitro* evaluation of diverse chloro (trifluoromethyl) aziridines. *Int. J. Mol. Sci.* 23, 12363. doi:10.3390/ijms232012363
- Ielo, L., Patamia, V., Citarella, A., Schirmeister, T., Stagno, C., Rescifina, A., et al. (2023). Selective noncovalent proteasome inhibiting activity of trifluoromethyl-containing gem-quaternary aziridines. *Arch. Pharm.* 356, e2300174. doi:10.1002/ardp.202300174
- Imran, A., Tariq Shehzad, M., Al Adhami, T., Miraz Rahman, K., Hussain, D., Alharthy, R. D., et al. (2021). Development of coumarin-thiosemicarbazone hybrids as aldose reductase inhibitors: biological assays, molecular docking, simulation studies and ADME evaluation. *Bioorg. Chem.* 115, 105164. doi:10.1016/j.bioorg.2021.105164
- Jagadeesan, S., and Karpagam, S. (2023). Novel series of N-acyl substituted indole based piperazine, thiazole and tetrazoles as potential antibacterial, antifungal, antioxidant and cytotoxic agents, and their docking investigation as potential Mcl-1 inhibitors. *J. Mol. Struct.* 1271, 134013. doi:10.1016/j.molstruc.2022.134013
- Jang, Y.-J., Syu, S.-E., Chen, Y.-J., Yang, M.-C., and Lin, W. (2012). Syntheses of furo [3, 4-c] coumarins and related furyl coumarin derivatives via intramolecular Wittig reactions. *Org. Biol. Chem.* 10, 843–847. doi:10.1039/C1OB06571H
- Jiang, C., Liao, Y., Li, H., Zhang, S., Liu, P., and Sun, P. (2023a). Electrochemical silylation of electron-deficient heterocycles using N-hydroxyphthalimide as HAT catalyst. *Adv. Syn. Cat.* 365, 1205–1210. doi:10.1002/adsc.202300112
- Jiang, Y. S., Liang, F., Chen, A. M., Li, S. S., Luo, X. L., and Xia, P. J. (2023b). Photocatalytic regio- and site-selective alkylation of coumarins: access to 3-Amino and 4-Amino dihydrocoumarins. *Adv. Syn. Cat.* 365, 997–1001. doi:10.1002/adsc.202201391
- Johnson, J. R. (2004). The Perkin reaction and related reactions. *Org. React.* 1, 210–265. doi:10.1002/0471264180.or001.08
- Jung, J.-C., and Park, O.-S. (2009). Synthetic approaches and biological activities of 4-hydroxycoumarin derivatives. *Molecules* 14, 4790–4803. doi:10.3390/molecules14114790
- Kang, D., Urhan, C., Wei, F., Frutos-Beltrán, E., Sun, L., Álvarez, M., et al. (2021a). Discovery, optimization, and target identification of novel coumarin derivatives as HIV-1 reverse transcriptase-associated ribonuclease H inhibitors. *Eur. J. Med. Chem.* 225, 113769. doi:10.1016/j.ejmech.2021.113769
- Kang, J. K., Chung, Y. C., and Hyun, C. G. (2021b). Anti-inflammatory effects of 6-methylcoumarin in LPS-stimulated RAW 264.7 macrophages via regulation of MAPK and NF- κ B signaling pathways. *Molecules* 26, 5351. doi:10.3390/molecules26175351
- Keri, R. S., Budagumpi, S., and Balappa Somappa, S. (2022). Synthetic and natural coumarins as potent anticonvulsant agents: a review with structure–activity relationship. *J. Clin. Pharm. Ther.* 47, 915–931. doi:10.1111/jcpt.13644
- Khatoun, S., Aroosh, A., Islam, A., Kalsoom, S., Ahmad, F., Hameed, S., et al. (2021). Novel coumarin-isatin hybrids as potent antileishmanial agents: synthesis, *in silico* and *in vitro* evaluations. *Bioorg. Chem.* 110, 104816. doi:10.1016/j.bioorg.2021.104816
- Kim, H., Maeng, H. J., Kim, J. H., Yoon, J. H., Oh, Y., Paek, S. M., et al. (2022). Synthetic peucedanocoumarin IV prevents α -synuclein neurotoxicity in an animal model of Parkinson's disease. *Int. J. Mol. Sci.* 23, 8618. doi:10.3390/ijms23158618
- Kim, J. K., Liu, Y., Gong, M., Li, Y., Huang, M., and Wu, Y. (2023). A facile visible-light-induced one-pot synthesis of 3-alkyl coumarins from simple salicylaldehydes. *Tetrahedron* 132, 133249. doi:10.1016/j.tet.2023.133249
- Kopecka, J., Campia, I., Jacobs, A., Frei, A. P., Ghigo, D., Wollscheid, B., et al. (2015). Carbonic anhydrase XII is a new therapeutic target to overcome chemoresistance in cancer cells. *Oncotarget* 6, 6776–6793. doi:10.18632/oncotarget.2882
- Koszelewski, D., Kowalczyk, P., Brodzka, A., Hrunyk, A., Kramkowski, K., and Ostaszewski, R. (2023). Enzymatic synthesis of a novel coumarin aminophosphonates: antibacterial effects and oxidative stress modulation on selected *E. coli* strains. *Int. J. Mol. Sci.* 24, 7609. doi:10.3390/ijms24087609
- Kudličková, Z., Michalková, R., Salayová, A., Ksiažek, M., Vilková, M., Bekešová, S., et al. (2023). Design, synthesis, and evaluation of novel indole hybrid chalcones and their antiproliferative and antioxidant activity. *Molecules* 28, 6583. doi:10.3390/molecules28186583
- Kumar, B., Borah, B., Babu, J. N., and Chowhan, L. R. (2022). Direct Michael addition/decarboxylation reaction catalyzed by a composite of copper ferrite nanoparticles immobilized on microcrystalline cellulose: an eco-friendly approach for constructing 3,4-dihydrocoumarin frameworks. *RSC Adv.* 12, 30704–30711. doi:10.1039/d2ra05994k
- Kumar Pasala, V., Gudipudi, G., Sankeshi, V., Basude, M., Gundla, R., Singh Jadav, S., et al. (2021). Design, synthesis and biological evaluation of selective hybrid coumarin-thiazolidinedione aldose reductase-II inhibitors as potential antidiabetics. *Bioorg. Chem.* 114, 104970. doi:10.1016/j.bioorg.2021.104970
- Kurtanovic, N., Tomasevic, N., Matic, S., Mitrovic, M. M., Kostic, D. A., Sabatino, M., et al. (2022). Human estrogen receptor α antagonists, part 2: synthesis driven by rational design, *in vitro* antiproliferative, and *in vivo* anticancer evaluation of innovative coumarin-related antiestrogens as breast cancer suppressants. *Eur. J. Med. Chem.* 227, 113869. doi:10.1016/j.ejmech.2021.113869
- Kyndiah, L., Sarkar, F. K., Gajurel, S., Sarkar, R., Anal, J. M. H., and Pal, A. K. (2023). Pd@GO catalyzed stereo- and regio-selective addition of arenes to alkynes and synthesis of coumarins via C-H functionalization. *Org. Biomol. Chem.* 21, 7928–7934. doi:10.1039/d3ob01237a
- Lake, B. G. (1999). Coumarin metabolism, toxicity and carcinogenicity: relevance for human risk assessment. *Food Chem. Toxicol.* 37, 423–453. doi:10.1016/s0278-6915(99)00010-1
- Li, J. L., Wang, X. H., Sun, J. C., Peng, Y. Y., Ji, C. B., and Zeng, X. P. (2021). Chiral tertiary amine catalyzed asymmetric [4 + 2] cyclization of 3-aryl coumarins with 2,3-butadienoate. *Molecules* 26, 489. doi:10.3390/molecules26020489
- Li, Z., Kong, D., Liu, Y., and Li, M. (2022). Pharmacological perspectives and molecular mechanisms of coumarin derivatives against virus disease. *Genes Dis.* 9, 80–94. doi:10.1016/j.gendis.2021.03.007
- Li, Z., Mu, C., Wang, B., and Jin, J. (2016). Graveoline analogs exhibiting selective acetylcholinesterase inhibitory activity as potential lead compounds for the treatment of Alzheimer's disease. *Molecules* 21, 132. doi:10.3390/molecules21020132
- Liu, L., Chen, Y., Zeng, R.-F., Liu, Y., Xie, S.-S., Lan, J.-S., et al. (2021). Design and synthesis of novel 3,4-dihydrocoumarins as potent and selective monoamine oxidase-B inhibitors with the neuroprotection against Parkinson's disease. *Bioorg. Chem.* 109, 104685. doi:10.1016/j.bioorg.2021.104685
- Liu, W., Wu, L., Liu, W., Tian, L., Chen, H., Wu, Z., et al. (2022). Design, synthesis and biological evaluation of novel coumarin derivatives as multifunctional ligands for the treatment of Alzheimer's disease. *Eur. J. Med. Chem.* 242, 114689. doi:10.1016/j.ejmech.2022.114689
- Lončarić, M., Gašo-Sokač, D., Jokić, S., and Molnar, M. (2020). Recent advances in the synthesis of coumarin derivatives from different starting materials. *Biomolecules* 10, 151. doi:10.3390/biom10010151
- Lu, Y., Chen, J., Xiao, M., Li, W., and Miller, D. D. (2012). An overview of tubulin inhibitors that interact with the colchicine binding site. *Pharm. Res.* 29, 2943–2971. doi:10.1007/s11095-012-0828-z
- Ly, Y., Li, K., Gao, W., Hao, Z., Wang, W., Liu, X., et al. (2022). Design, synthesis and fungicidal activity of 3,4-dichloroisothiazolocoumarin-containing strobilurins. *Mol. Divers.* 26, 951–961. doi:10.1007/s11030-021-10207-5
- Mali, G., Maji, S., Chavan, K. A., Shukla, M., Kumar, M., Bhattacharyya, S., et al. (2022). Effective synthesis and biological evaluation of functionalized 2,3-Dihydrofuro [3,2-c]coumarins via an imidazole-catalyzed green multicomponent approach. *ACS Omega* 7, 36028–36036. doi:10.1021/acsomega.2c05361
- Manna, S., and Prabhu, K. R. (2023). Visible-light-mediated vicinal difunctionalization of activated alkynes with boronic acids: substrate-controlled rapid access to 3-alkylated coumarins and unsaturated spirocycles. *Org. Lett.* 25, 810–815. doi:10.1021/acs.orglett.2c04333
- Marquez, N., Giachero, M. L., Declerck, S., and Ducasse, D. A. (2021). *Macrophomina phaseolina*: general characteristics of pathogenicity and methods of control. *Front. Plant. Sci.* 12, 634397. doi:10.3389/fpls.2021.634397
- Matos, M. J., Uriarte, E., Seoane, N., Picos, A., Gil-Longo, J., and Campos-Toimil, M. (2022). Synthesis and vasorelaxant activity of nitrate-coumarin derivatives. *ChemMedChem* 17, e202200476. doi:10.1002/cmdc.202200476
- Matthay, M. A., Zimmerman, G. A., Esmon, C., Bhattacharya, J., Coller, B., Doerschuk, C. M., et al. (2003). Future research directions in acute lung injury: summary of a National Heart, Lung, and Blood Institute working group. *Am. J. Respir. Crit. Care Med.* 167, 1027–1035. doi:10.1164/rccm.200208-966WS
- Mellado, M., Gonzalez, C., Mella, J., Aguilar, L. F., Celik, I., Borges, F., et al. (2022). Coumarin-resveratrol-inspired hybrids as monoamine oxidase B inhibitors: 3-

phenylcoumarin versus trans-6-styrylcoumarin. *Molecules* 27, 928. doi:10.3390/molecules27030928

Metre, T. V., Kodasi, B., Bayannavar, P. K., Bheemayya, L., Nadoni, V. B., Hoolageri, S. R., et al. (2023). Coumarin-4-yl-1,2,3-triazol-4-yl-methyl-thiazolidine-2,4-diones: synthesis, glucose uptake activity and cytotoxic evaluation. *Bioorg. Chem.* 130, 106235. doi:10.1016/j.bioorg.2022.106235

Miao, Y., Yang, J., Yun, Y., Sun, J., and Wang, X. (2021). Synthesis and anti-rheumatoid arthritis activities of 3-(4-aminophenyl)-coumarin derivatives. *J. Enzyme Inhib. Med. Chem.* 36, 450–461. doi:10.1080/14756366.2021.1873978

Miele, M., Citarella, A., Micale, N., Holzer, W., and Pace, V. (2019). Direct and chemoselective synthesis of tertiary difluoroketones via weinreb amide homologation with a CHF(2)-carbene equivalent. *Org. Lett.* 21, 8261–8265. doi:10.1021/acs.orglett.9b03024

Mirabile, S., Vittorio, S., Paola Germano, M., Adornato, I., Ielo, L., Rapisarda, A., et al. (2021). Evaluation of 4-(4-Fluorobenzyl)piperazin-1-yl-Based compounds as competitive tyrosinase inhibitors endowed with antimelanogenic effects. *ChemMedChem* 16, 3083–3093. doi:10.1002/cmdc.202100396

Mohr, F., Hurrle, T., Burggraaff, L., Langer, L., Bemelmans, M. P., Knab, M., et al. (2021). Synthesis and SAR evaluation of coumarin derivatives as potent cannabinoid receptor agonists. *Eur. J. Med. Chem.* 220, 113354. doi:10.1016/j.ejmech.2021.113354

Moi, D., Vittorio, S., Angeli, A., Balboni, G., Supuran, C. T., and Onnis, V. (2022). Investigation on hydrazonobenzenesulfonamides as human carbonic anhydrase I, II, IX and XII inhibitors. *Molecules* 28, 91. doi:10.3390/molecules28010091

Mondal, S., Di Tommaso, E. M., and Olofsson, B. (2023). Transition-metal-free difunctionalization of sulfur nucleophiles. *Angew. Chem. Int. Ed.* 62, e202216296. doi:10.1002/anie.202216296

Montanari, S., Allarà, M., Scalvini, L., Kostrzewa, M., Belluti, F., Gobbi, S., et al. (2021). New coumarin derivatives as cholinergic and cannabinoid system modulators. *Molecules* 26, 3254. doi:10.3390/molecules26113254

Munana, K. R. (1995). Long-term complications of diabetes mellitus, Part I: retinopathy, nephropathy, neuropathy. *Vet. Clin. North Am. Small Anim. Pract.* 25, 715–730. doi:10.1016/s0195-5616(95)50064-6

Nasab, N. H., Raza, H., Eom, Y. S., Hassan, M., Kloczkowski, A., and Kim, S. J. (2023). Synthesis and discovery of potential tyrosinase inhibitor of new coumarin-based thiophenyl-pyrazolylthiazole nuclei: *in-vitro* evaluation, cytotoxicity, kinetic and computational studies. *Chem. Biol. Drug Des.* 101, 1262–1272. doi:10.1111/cbdd.14209

North, E. J., Jackson, M., and Lee, R. E. (2014). New approaches to target the mycolic acid biosynthesis pathway for the development of tuberculosis therapeutics. *Curr. Pharm. Des.* 20, 4357–4378. doi:10.2174/1381612819666131118203641

Ortiz-De-Elguea, V., Carral-Menoyo, A., Simón-Vidal, L., Martínez-Nunes, M., Barbolla, I., Lete, M. G., et al. (2021). Pd(II)-Catalyzed fujiwara-moritani reactions for the synthesis and functionalization of substituted coumarins. *ACS Omega* 6, 29483–29494. doi:10.1021/acsomega.1c03469

Paterni, I., Granchi, C., Katzenellenbogen, J. A., and Minutolo, F. (2014). Estrogen receptors alpha (ERα) and beta (ERβ): subtype-selective ligands and clinical potential. *Steroids* 90, 13–29. doi:10.1016/j.steroids.2014.06.012

Patil, S. B. (2022). Medicinal significance of novel coumarin analogs: recent studies. *Results Chem.* 4, 100313. doi:10.1016/j.rechem.2022.100313

Pechmann, V. H. (1884). Neue bildungsweise der cumarine. Synthese des daphnetins. I. *Berichte Dtsch. Chem. Ges.* 17, 929–936. doi:10.1002/cber.188401701248

Phukon, J., Bhorali, P., Changmai, S., and Gogoi, S. (2023). Hydroxyl-directed Ru (II)-Catalyzed synthesis of fused dihydrofurans using 1, 4-dioxane and sulfoxonium ylides as annulating agents. *Org. Lett.* 25, 215–219. doi:10.1021/acs.orglett.2c04068

Prusty, J. S., and Kumar, A. (2020). Coumarins: antifungal effectiveness and future therapeutic scope. *Mol. Divers.* 24, 1367–1383. doi:10.1007/s11030-019-09992-x

Qian, Z. M., Guan, Z., and He, Y. H. (2023). Visible light-induced cross-dehydrocoupling of 3-cyanocoumarins with unactivated aliphatic aldehydes enables access to 4-acylated coumarins. *J. Org. Chem.* 88, 6465–6475. doi:10.1021/acs.joc.2c02928

Rahimi, S., Ghandi, M., Fallahnezhad, M., and Abbasi, A. (2023). A facile synthesis of chromeno[3,4-c]spiro[pyrrolidine indenoquininoxalines] via 1,3-dipolar cycloadditions. *Mol. Divers.* doi:10.1007/s11030-023-10629-3

Rather, I. A., and Ali, R. (2022). An efficient and versatile deep eutectic solvent-mediated green method for the synthesis of functionalized coumarins. *ACS Omega* 7, 10649–10659. doi:10.1021/acsomega.2c00293

Rees, T. M., and Brimijoin, S. (2003). The role of acetylcholinesterase in the pathogenesis of Alzheimer's disease. *Drugs Today (Barc)* 39, 75–83. doi:10.1358/dot.2003.39.1.740206

Ren, N., Zhang, L., Hu, Y., Wang, X., Deng, Z., Chen, J., et al. (2021). Perfluoroalkyl-promoted synthesis of perfluoroalkylated pyrrolidine-fused coumarins with methyl β-perfluoroalkylpropionates. *J. Org. Chem.* 86, 15717–15725. doi:10.1021/acs.joc.1c01538

Rohilla, S., Shah, S., and Singh, V. K. (2023). Copper-catalyzed asymmetric propargylic [3+ 2] cycloaddition: synthesis of enantioenriched dihydrofuro [3, 2-c] coumarins and its quinolinone and thiocoumarin analogues. *Org. Lett.* 25, 3733–3738. doi:10.1021/acs.orglett.3c01198

Rullo, M., Cipolloni, M., Catto, M., Colliva, C., Miniero, D. V., Latronico, T., et al. (2022). Probing fluorinated motifs onto dual AChE-MAO B inhibitors: rational design, synthesis, biological evaluation, and early-ADME studies. *J. Med. Chem.* 65, 3962–3977. doi:10.1021/acs.jmedchem.1c01784

Samanta, S., Chatterjee, R., Sarkar, S., Pal, S., Mukherjee, A., Butorin, I. I., et al. (2022). Brønsted acidic ionic liquid-catalyzed tandem reaction: an efficient and sustainable approach towards the regioselective synthesis and molecular docking studies of 4-hydroxycoumarin-substituted indoles bearing lower E-factors. *Org. Biomol. Chem.* 20, 9161–9171. doi:10.1039/D2OB01431A

Sarkar, A., Saha, M., and Das, A. R. (2023). Ru(II) catalyzed chelation assisted C(sp²)-H bond functionalization along with concomitant (4 + 2) annulation. *Org. Biomol. Chem.* 21, 5567–5586. doi:10.1039/d3ob00828b

Sau, S., and Mal, P. (2021). 3-Nitro-coumarin synthesis via nitrative cyclization of aryl alkynoates using tert-butyl nitrite. *Chem. Commun.* 57, 9228–9231. doi:10.1039/d1cc03415d

Schedin-Weiss, S., Inoue, M., Hromadkova, L., Teranishi, Y., Yamamoto, N. G., Wiehager, B., et al. (2017). Monoamine oxidase B is elevated in Alzheimer disease neurons, is associated with γ-secretase and regulates neuronal amyloid β-peptide levels. *Alzheimers Res. Ther.* 9, 57. doi:10.1186/s13195-017-0279-1

Schiffner, E. S., Proj, M., Gobec, M., Rejc, L., Šterman, A., Mravljak, J., et al. (2021). Synthesis and biochemical evaluation of warhead-decorated psoralens as (Immuno) Proteasome inhibitors. *Molecules* 26, 356. doi:10.3390/molecules26020356

Sehgal, V. N. (1974). Trioxsalen therapy for vitiligo. *Arch. Dermatol.* 109, 578. doi:10.1001/archderm.1974.01630040082039

Serpi, M., Pertusati, F., Morozzi, C., Novelli, G., Giannantonio, D., Duggan, K., et al. (2023). Synthesis, molecular docking and antibacterial activity of an oxadiazole-based lipoteichoic acid inhibitor and its metabolites. *J. Mol. Struct.* 1278, 134977. doi:10.1016/j.molstruc.2023.134977

Shankar, M., and Kumara Swamy, K. C. (2022). Ru(II)-catalysed oxidative (4 + 2) annulation of chromene and coumarin carboxylic acids with alkynes/propargylic alcohols: isolation of Ru(0) complexes. *Org. Biomol. Chem.* 21, 195–208. doi:10.1039/d2ob01890j

Shankar, M., and Swamy, K. C. K. (2023). Cu(II)-Catalyzed decarboxylative (4 + 2) annulation of coumarin-3-carboxylic acids with *in situ* generated α,β-unsaturated carbonyl compounds from *tert*-propargylic alcohols. *Org. Lett.* 25, 3397–3401. doi:10.1021/acs.orglett.3c00925

Shinde, V. N., Rangan, K., Kumar, D., and Kumar, A. (2021). Palladium-catalyzed weakly coordinating lactone-directed C-H bond functionalization of 3-arylcoumarins: synthesis of bioactive coumestan derivatives. *J. Org. Chem.* 86, 9755–9770. doi:10.1021/acs.joc.1c01097

Shriner, R. L. (2004). The Reformatsky reaction. *Org. React.* 1, 1–37. doi:10.1002/0471264180.or001.01

Singh, S., Saini, R., and Singh, R. P. (2022). Enantioselective distal functionalization of 3-Cyano-4-methylcoumarins through direct vinylogous conjugate addition to maleimides. *J. Org. Chem.* 88, 7712–7723. doi:10.1021/acs.joc.2c02142

Smith, J. D., Brawley, J., Bordenave, K. C., Olsen, R. K., Intasiri, A., Cremo, C. R., et al. (2023). Isoform selectivities of novel 4-hydroxycoumarin imines as inhibitors of myosin II. *Eur. J. Med. Chem.* 247, 115008. doi:10.1016/j.ejmech.2022.115008

Smith, R., and Moodie, J. (1988). Comparative efficacy and tolerability of two ointment and suppository preparations ('Uniroid' and 'Proctosedyl') in the treatment of second degree haemorrhoids in general practice. *Curr. Med. Res. Opin.* 11, 34–40. doi:10.1185/03007998809111128

Sokol, I., Toma, M., Krnić, M., Macan, A. M., Drenjančević, D., Liekens, S., et al. (2021). Transition metal-catalyzed synthesis of new 3-substituted coumarin derivatives as antibacterial and cytostatic agents. *Future Med. Chem.* 13, 1865–1884. doi:10.4155/fmc-2021-0161

Song, H., Li, J., Zhang, Y., Chen, K., Liu, L., Zhang, J., et al. (2023a). Photoredox catalysis-enabled C-H difluoromethylation of heteroarenes with pentacoordinate phosphorane as the reagent. *J. Org. Chem.* 88, 12013–12023. doi:10.1021/acs.joc.3c01336

Song, H. Y., Liu, M. Y., Huang, J., Wang, D., Jiang, J., Chen, J. Y., et al. (2023b). Photosynthesis of 3-alkylated coumarins from carboxylic acids catalyzed by a Na(2)S-based electron donor-acceptor complex. *J. Org. Chem.* 88, 2288–2295. doi:10.1021/acs.joc.2c02679

Song, J., Guan, Y. F., Liu, W. B., Song, C. H., Tian, X. Y., Zhu, T., et al. (2022). Discovery of novel coumarin-indole derivatives as tubulin polymerization inhibitors with potent anti-gastric cancer activities. *Eur. J. Med. Chem.* 238, 114467. doi:10.1016/j.ejmech.2022.114467

Sorabad, G. S., and Yang, D.-Y. (2023). Lewis acid-catalyzed 1, 4-addition and annulation of 4-Hydroxy-coumarins with o-hydroxyphenyl propargyl amines: entry to regio-selective synthesis of furano [3, 2-c] coumarins and pyrano [3, 2-c] coumarins. *J. Org. Chem.* 88, 4730–4742. doi:10.1021/acs.joc.3c00213

Srikrishna, D., Godugu, C., and Dubey, P. K. (2018). A review on pharmacological properties of coumarins. *Mini-Rev Med. Chem.* 18, 113–141. doi:10.2174/1389557516666160801094919

Stanchev, S., Hadjimitova, V., Traykov, T., Boyanov, T., and Manolov, I. (2009). Investigation of the antioxidant properties of some new 4-hydroxycoumarin derivatives. *Eur. J. Med. Chem.* 44, 3077–3082. doi:10.1016/j.ejmech.2008.07.007

- Stefanachi, A., Leonetti, F., Pisani, L., Catto, M., and Carotti, A. (2018). Coumarin: a natural, privileged and versatile scaffold for bioactive compounds. *Molecules* 23, 250. doi:10.3390/molecules23020250
- Sun, B., Wang, Y., Wang, J., Chen, M., Zhong, Z., Wang, J., et al. (2023). Photoredox-catalyzed redox-neutral decarboxylative C-H acylations of coumarins with α -keto acid. *Org. Lett.* 25, 2466–2470. doi:10.1021/acs.orglett.3c00632
- Sun, J., Li, Z., Huang, X., Ke, Z., and Chen, Z. (2022). Silver-catalyzed C-3 arylthiodifluoromethylation and aryloxydifluoromethylation of coumarins. *Org. Biomol. Chem.* 20, 4421–4426. doi:10.1039/d2ob00568a
- Swallow, S. (2015). Fluorine in medicinal chemistry. *Prog. Med. Chem.* 54, 65–133. doi:10.1016/bs.pmc.2014.11.001
- Ul Ain, Q., Saeed, A., Khan, A., Ahmed, A., Ullah, S., Ahsan Halim, S., et al. (2023). Synthesis of new phenoxymethylcoumarin clubbed 4-arylthiazolylhydrazines as α -glucosidase inhibitors and their kinetics and molecular docking studies. *Bioorg. Chem.* 131, 106302. doi:10.1016/j.bioorg.2022.106302
- Uroos, M., Javaid, A., Bashir, A., Tariq, J., Khan, I. H., Naz, S., et al. (2022). Green synthesis of coumarin derivatives using Brønsted acidic pyridinium based ionic liquid [MBSPy] [HSO₄] to control an opportunistic human and a devastating plant pathogenic fungus *Macrophomina phaseolina*. *RSC Adv.* 12, 23963–23972. doi:10.1039/d2ra03774b
- Vina, D., Matos, M. J., Yanez, M., Santana, L., and Uriarte, E. (2012). 3-Substituted coumarins as dual inhibitors of AChE and MAO for the treatment of Alzheimer's disease. *MedChemComm* 3, 213–218. doi:10.1039/C1MD00221J
- Vittorio, S., Adornato, I., Gitto, R., Pena-Diaz, S., Ventura, S., and De Luca, L. (2020). Rational design of small molecules able to inhibit α -synuclein amyloid aggregation for the treatment of Parkinson's disease. *J. Enzyme Inhib. Med. Chem.* 35, 1727–1735. doi:10.1080/14756366.2020.1816999
- Vittorio, S., Dank, C., and Ielo, L. (2023). Heterocyclic compounds as synthetic tyrosinase inhibitors: recent advances. *Int. J. Mol. Sci.* 24, 9097. doi:10.3390/ijms24109097
- Wan, Q., Hou, Z. W., Zhao, X. R., Xie, X., and Wang, L. (2023). Organoelectrophotocatalytic C-H silylation of heteroarenes. *Org. Lett.* 25, 1008–1013. doi:10.1021/acs.orglett.3c00144
- Wang, C., Wang, H., Zheng, C., Li, B., Liu, Z., Zhang, L., et al. (2023). Discovery of coumarin-based MEK1/2 PROTAC effective in human cancer cells. *ACS Med. Chem. Lett.* 14, 92–102. doi:10.1021/acsmedchemlett.2c00446
- Warkentin, L., Hueber, S., Deiters, B., Klohn, F., and Kühlein, T. (2022). Vitamin-K-antagonist phenprocoumon versus low-dose direct oral anticoagulants (DOACs) in patients with atrial fibrillation: a real-world analysis of German claims data. *Thromb. J.* 20, 31. doi:10.1186/s12959-022-00389-9
- Wei, L., Hou, T., Li, J., Zhang, X., Zhou, H., Wang, Z., et al. (2021). Structure–activity relationship studies of coumarin-like diacid derivatives as human G protein-coupled receptor-35 (hGPR35) agonists and a consequent new design principle. *J. Med. Chem.* 64, 2634–2647. doi:10.1021/acs.jmedchem.0c01624
- Wu, Y., Xu, J., Liu, Y., Zeng, Y., and Wu, G. (2020). A review on anti-tumor mechanisms of coumarins. *Front. Oncol.* 10, 592853. doi:10.3389/fonc.2020.592853
- Xia, D., Liu, H., Cheng, X., Maraswami, M., Chen, Y., and Lv, X. (2022). Recent developments of coumarin-based hybrids in drug discovery. *Curr. Top. Med. Chem.* 22, 269–283. doi:10.2174/1568026622666220105105450
- Yan, Z., Huang, Y., Zhao, D., Li, Z., Wang, X., Guo, M., et al. (2023). Developing novel coumarin-containing azoles antifungal agents by the scaffold merging strategy for treating azole-resistant candidiasis. *J. Med. Chem.* 66, 13247–13265. doi:10.1021/acs.jmedchem.3c01254
- Yang, S.-M., Wang, C.-Y., Lin, C.-K., Karanam, P., Reddy, G. M., Tsai, Y.-L., et al. (2018). Diversity-oriented synthesis of furo[3,2-c]coumarins and benzofuranyl chromenones through chemoselective acylation/wittig reaction. *Angew. Chem. Int. Ed.* 57, 1668–1672. doi:10.1002/anie.201711524
- Yang, X. C., Hu, C. F., Zhang, P. L., Li, S., Hu, C. S., Geng, R. X., et al. (2022a). Coumarin thiazoles as unique structural skeleton of potential antimicrobial agents. *Bioorg. Chem.* 124, 105855. doi:10.1016/j.bioorg.2022.105855
- Yang, X.-C., Zeng, C.-M., Avula, S. R., Peng, X.-M., Geng, R.-X., and Zhou, C.-H. (2023). Novel coumarin aminophosphonates as potential multitargeting antibacterial agents against *Staphylococcus aureus*. *Eur. J. Med. Chem.* 245, 114891. doi:10.1016/j.ejmech.2022.114891
- Yang, X. C., Zhang, P. L., Kumar, K. V., Li, S., Geng, R. X., and Zhou, C. H. (2022b). Discovery of unique thiazolidinone-conjugated coumarins as novel broad spectrum antibacterial agents. *Eur. J. Med. Chem.* 232, 114192. doi:10.1016/j.ejmech.2022.114192
- Yavari, I., Hekmat-Shoar, R., and Zonouzi, A. (1998). A new and efficient route to 4-carboxymethylcoumarins mediated by vinyltriphenylphosphonium salt. *Tetrahedron Lett.* 39, 2391–2392. doi:10.1016/S0040-4039(98)00206-8
- Yoshida, Y., Mino, T., and Sakamoto, M. (2021). Chiral hypervalent bromine(III) (bromonium salt): hydrogen- and halogen-bonding bifunctional asymmetric catalysis by diaryl- λ^3 -bromanes. *ACS Cat.* 11, 13028–13033. doi:10.1021/acscatal.1c04070
- Yuan, W. C., Lei, C. W., Zhao, J. Q., Wang, Z. H., and You, Y. (2021). Organocatalytic asymmetric cyclopropanation of 3-acylcoumarins with 3-haloindoles: access to spiroindole-cyclopropa[c]coumarin compounds. *J. Org. Chem.* 86, 2534–2544. doi:10.1021/acs.joc.0c02653
- Zerangue, S., Jabbari, A., Khavari Moghadam, E., Sadeghian, H., and Seyedi, S. M. (2021). Design, synthesis, and structure–activity relationship study of O-prenylated 3-acetylcoumarins as potent inhibitors of soybean 15-lipoxygenase. *Drug Dev. Res.* 82, 826–834. doi:10.1002/ddr.21787
- Zhang, K., Qiao, L., Xie, J., Lin, Z., Li, H., Lu, P., et al. (2021). Visible-light-induced C(sp²)–C(sp³) coupling reaction for the regioselective synthesis of 3-functionalized coumarins. *J. Org. Chem.* 86, 9552–9562. doi:10.1021/acs.joc.1c00848
- Zhang, W., Lun, S., Wang, S. S., Cai, Y. P., Yang, F., Tang, J., et al. (2022). Structure-based optimization of coumestan derivatives as polyketide synthase 13-thioesterase(pks13-TE) inhibitors with improved hERG profiles for *Mycobacterium tuberculosis* treatment. *J. Med. Chem.* 65, 13240–13252. doi:10.1021/acs.jmedchem.2c01064
- Zhong, Z. J., Cheng, L. P., Pang, W., Zheng, X. S., and Fu, S. K. (2021). Design, synthesis and biological evaluation of dihydrofurocoumarin derivatives as potent neuraminidase inhibitors. *Bioorg. Med. Chem. Lett.* 37, 127839. doi:10.1016/j.bmcl.2021.127839
- Zhou, Q., Li, S., Li, M., Ke, D., Wang, Q., Yang, Y., et al. (2022). Human tau accumulation promotes glycogen synthase kinase-3 β acetylation and thus upregulates the kinase: a vicious cycle in Alzheimer neurodegeneration. *EBioMedicine* 78, 103970. doi:10.1016/j.ebiom.2022.103970
- Zotova, N., Zhuravleva, Y., Cheresnev, V., and Gusev, E. (2023). Acute and chronic systemic inflammation: features and differences in the pathogenesis, and integral criteria for verification and differentiation. *Int. J. Mol. Sci.* 24, 1144. doi:10.3390/ijms24021144



OPEN ACCESS

EDITED BY

Maria Manuel Marques,
Universidade Nova de Lisboa, Portugal

REVIEWED BY

Ramesh Mamidala,
A pharmaceutical company, United States
Tanmay Pati,
Rensselaer Polytechnic Institute, United States

*CORRESPONDENCE

Berit Olofsson,
✉ berit.oloofsson@su.se

RECEIVED 26 January 2024

ACCEPTED 19 February 2024

PUBLISHED 29 February 2024

CITATION

Doobary S, Di Tommaso EM, Postole A, Inge AK
and Olofsson B (2024), Structure-reactivity
analysis of novel hypervalent iodine reagents in
S-vinylation of thiols.
Front. Chem. 12:1376948.
doi: 10.3389/fchem.2024.1376948

COPYRIGHT

© 2024 Doobary, Di Tommaso, Postole, Inge
and Olofsson. This is an open-access article
distributed under the terms of the [Creative
Commons Attribution License \(CC BY\)](#). The use,
distribution or reproduction in other forums is
permitted, provided the original author(s) and
the copyright owner(s) are credited and that the
original publication in this journal is cited, in
accordance with accepted academic practice.
No use, distribution or reproduction is
permitted which does not comply with these
terms.

Structure-reactivity analysis of novel hypervalent iodine reagents in *S*-vinylation of thiols

Sayad Doobary¹, Ester Maria Di Tommaso¹, Alexandru Postole¹,
A. Ken Inge² and Berit Olofsson^{1*}

¹Department of Organic Chemistry, Stockholm University, Stockholm, Sweden, ²Department of Materials and Environmental Chemistry, Stockholm University, Stockholm, Sweden

The transition-metal free *S*-vinylation of thiophenols by vinylbenziodoxolones (VBX) constituted an important step forward in hypervalent iodine-mediated vinylations, highlighting the difference to vinylodonium salts and that the reaction outcome was influenced by the substitution pattern of the benziodoxolone core. In this study, we report several new classes of hypervalent iodine vinylation reagents; vinylbenziodazolones, vinylbenziodoxolonimine and vinyliodoxathiole dioxides. Their synthesis, structural and electronic properties are described and correlated to the *S*-vinylation outcome, shedding light on some interesting facets of these reagents.

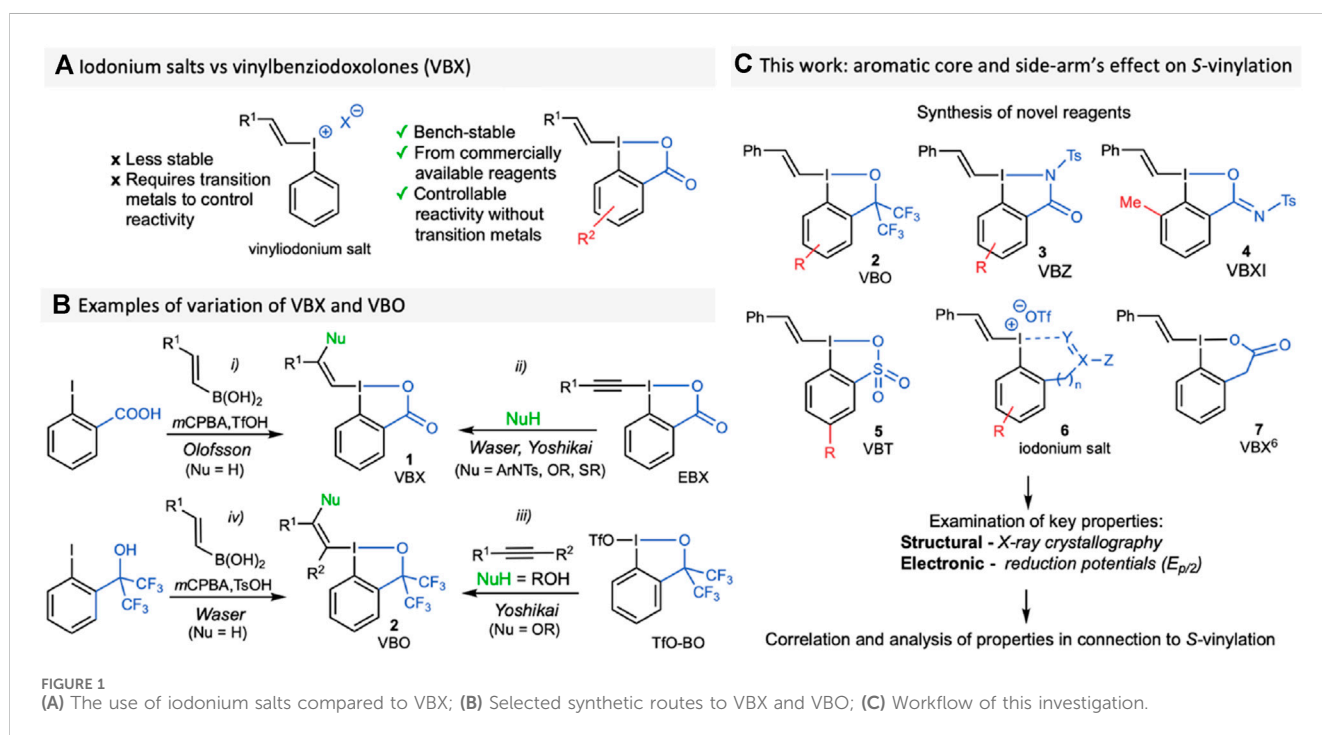
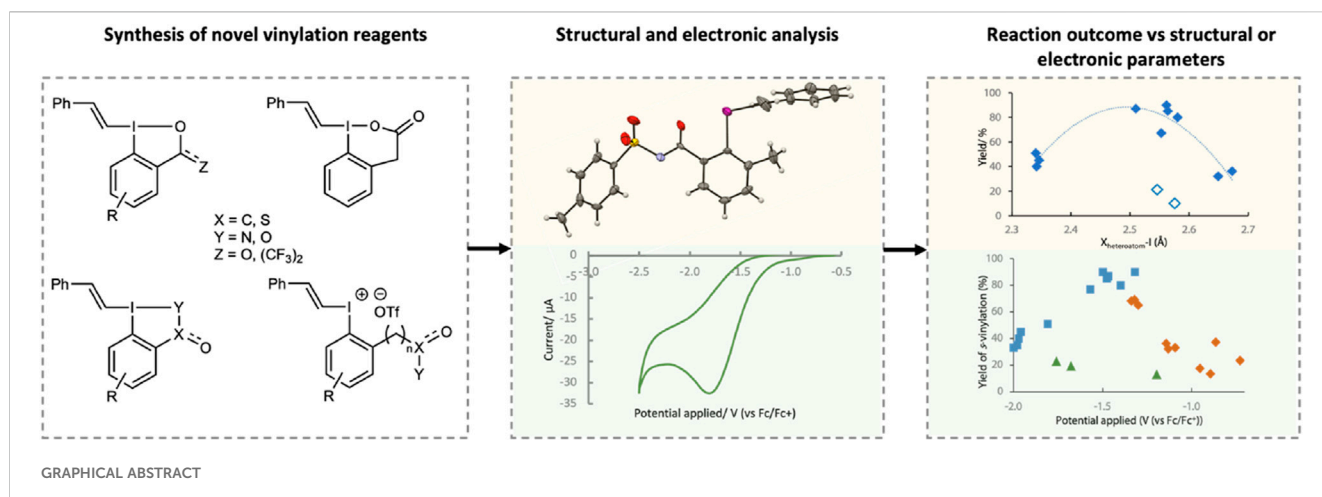
KEYWORDS

alkenes, benziodoxolones, hypervalency, reduction potential, X-ray crystallography, structure-reactivity analysis, VBX

1 Introduction

Hypervalent iodine reagents have been shown to be powerful reagents for chemoselective transformations under both transition metal-catalyzed and metal-free conditions. (Wirth, 2016; Yoshimura and Zhdankin, 2016; Flores et al., 2019; Olofsson et al., 2019). The use of iodonium salts has enabled transfer of aryl, alkynyl and vinyl groups to a variety of nucleophiles. (Merritt and Olofsson, 2009; Charpentier et al., 2015; Li et al., 2016; Rajkiewicz and Kalek, 2018; Villo et al., 2019; Declas et al., 2020; Dahiya et al., 2022; Le Du and Waser, 2023; Mironova et al., 2023; Yoshimura et al., 2023). New classes of alkenes have been accessed through the combination of vinylodonium salts with metal catalysts, (Skucas and MacMillan, 2012; Holt and Gaunt, 2015; Sheng et al., 2017; Yuan et al., 2019), whereas metal-free applications with those reagents remain scarce due to difficulties in controlling the reaction outcome. (Ochiai et al., 2001; Hara et al., 2006; Kepski et al., 2019). Recent developments in the field have shown that benziodoxolones (BX), which are iodine (III) compounds with a cyclic core, possess improved stability and often have more easily controlled reactivity. (Yoshimura et al., 2023). Indeed, the utility of trifluoromethyl-BX (Togni's reagent) and ethynyl-BX (EBX) have been efficiently demonstrated in the last decades. (Charpentier et al., 2015; Hari et al., 2019; Le Du and Waser, 2023).

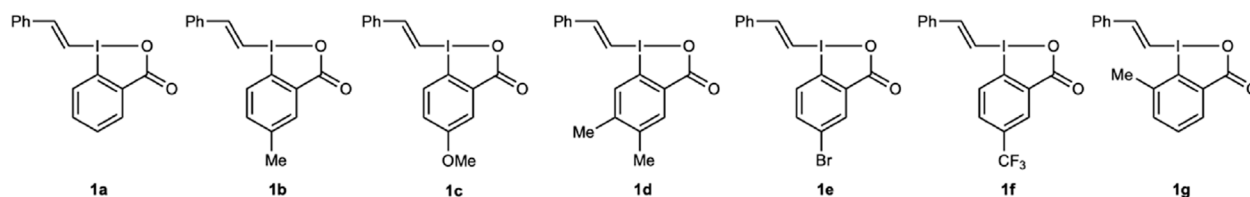
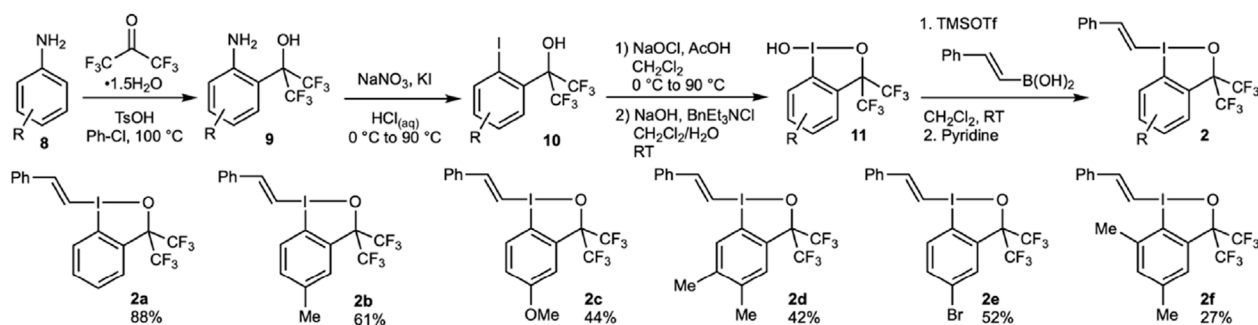
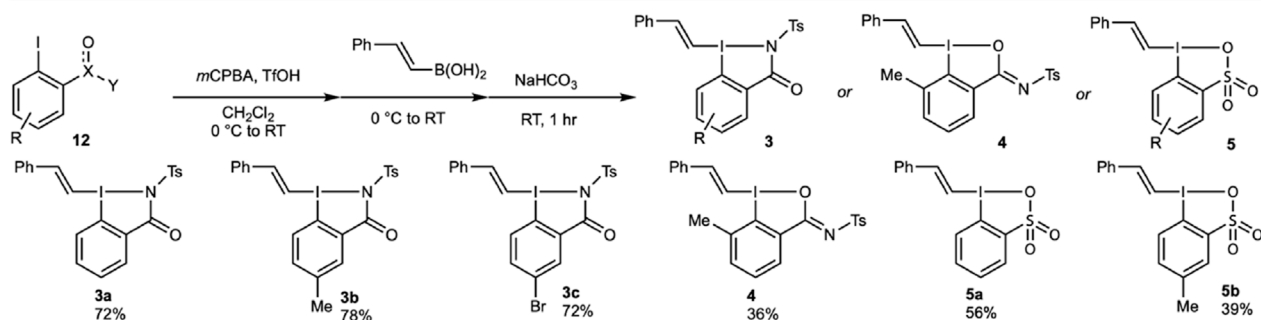
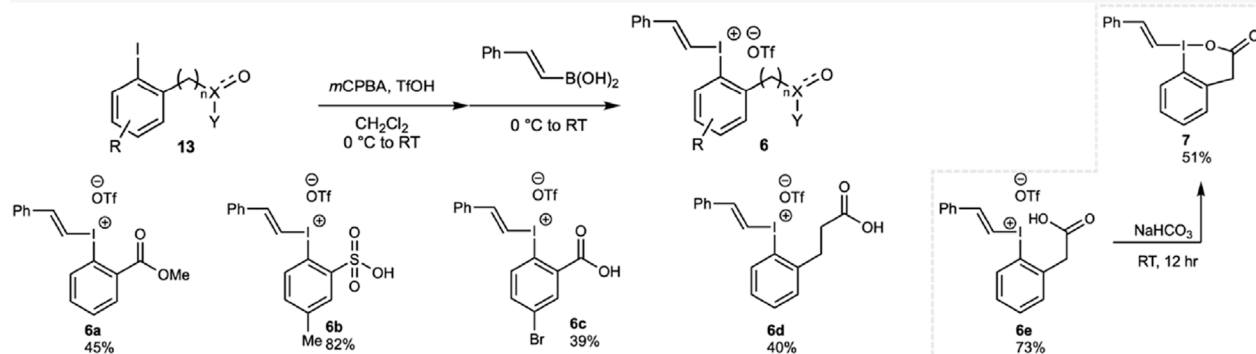
In 2016, our group reported the synthesis and first applications of vinyl-BX (VBX, 1) (Stridfeldt et al., 2016), which showed enhanced reactivity and selectivity compared to vinylodonium salts. (Figure 1A), (Stridfeldt et al., 2016; Declas et al., 2020). Transition metal-free applications include *S*- and *P*-vinylation methodologies, (Castoldi et al., 2020a; Castoldi et al., 2020b; Di Tommaso et al., 2022), as well as photocatalytic *C*-vinylations with



redox active compounds (Pal et al., 2023) and others. (Davies et al., 2017; Le Vaillant et al., 2018; Liu et al., 2018; Jiang and Studer, 2019; Li et al., 2019; Liu et al., 2020). Our one-pot synthesis of VBX is shown in Figure 1B i, and the scope was later expanded to include β -heteroatom-functionalized VBX through addition of a nucleophile and a proton over EBX (Figure 1B ii). (Frei et al., 2014; Caramenti et al., 2019; Shimbo et al., 2019; Tessier et al., 2019; Wu et al., 2019; Liu et al., 2020; Declas et al., 2022) In parallel, the corresponding vinylbenziodoxoles with a bis(CF₃)alkoxy moiety (VBO) were introduced by Yoshikai and coworkers, and have proved superior in some applications. (Wu et al., 2016; Wu J. et al., 2017; Shimbo et al., 2019; Wu et al., 2019; Chai et al., 2021; Wang et al., 2022). VBO can be synthesized from TfO-BO and mono- or di-substituted alkynes (Figure 1B iii). (Wu B. et al., 2017; Ding et al., 2020; Ura

et al., 2020; Chai et al., 2021; Declas et al., 2022; Kikuchi et al., 2022; Wang et al., 2022) Recently, Waser presented a one-pot synthesis of ethynyl bis(trifluoromethyl)iodoxole (EBO) directly from the corresponding iodoarene. (Milzarek et al., 2023). This method also included the synthesis of a VBO reagent, simplifying the access to such targets (Figure 1B iv).

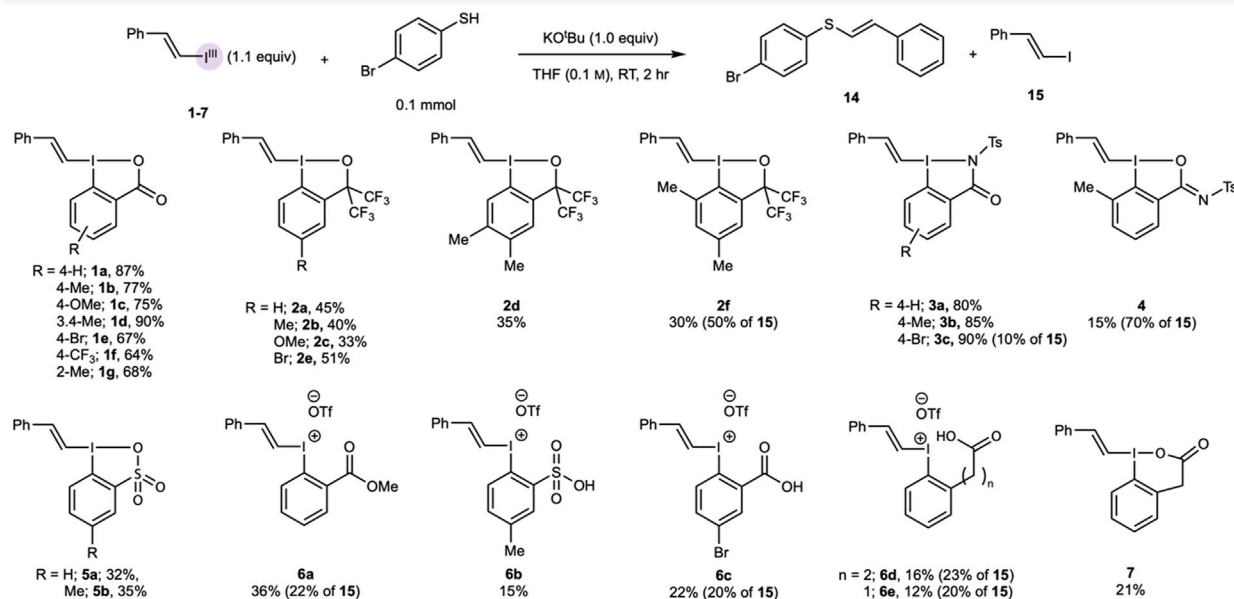
The reactivity of hypervalent alkynylating reagents with substituted aromatic ring cores, as well as variations of the “side-arm”, which binds to the iodine centre, have been explored. (Fernández González et al., 2013; Shimbo et al., 2019). While we evaluated the influence of core-substituents on VBX in the S-vinylation of thiols, (Castoldi et al., 2020b), there are no broad studies investigating the structural and electronic effects of varying these groups on vinylating reagents. (Mironova et al., 2023). Herein,

A VBX 1 used in this study**B Synthesis of novel VBO 2****C One-pot synthesis of novel VBZ 3, VBXI 4 and VBT 5****D One-pot synthesis of novel iodonium salts 6 and VBX₆ 7**

SCHEME 1
Synthesis of hypervalent vinylation reagents. (A) VBX reagents 1; (B) VBO reagents 2 (2a already reported), yields from 10 given; (C) VBZ reagents 3, VBXI reagent 4 and VBT reagents 5; (D) Acyclic iodonium salts 6 and VBX₆ 7.

we report the synthesis of several new VBO 2, as well as the synthesis of novel compound classes vinylbenziodazolones (VBZ, 3), vinylbenziodoxolonimine (VBXI, 4), and vinylidoxathiole dioxides (VBT, 5) (Figure 1C). It should be noted that the benziodazolone (Le Du et al., 2021) and benziodoxathiole (Koser et al., 1993; Kuposov et al., 2006) cores have been reported in other hypervalent iodine reagents, whereas the benziodoxolonimine is a novel side-arm. Additionally, we have

synthesised several novel *ortho*-functionalized iodonium salts 6, which serve as good comparisons in the studies. Finally, a vinylbenziodoxolone-type reagent with a six-membered side-arm (VBX₆ 7) was synthesized to evaluate the effect of the side-arm length and conjugation with the core. We have determined their crystal structures, as well as their reduction potentials, and correlated these parameters with the reagents' reactivity under the reported S-vinylation conditions.

Application of vinylation reagents to *S*-vinylation of 4-bromothiophenol

SCHEME 2

Comparison of vinylation reagents 1-7 in the *S*-vinylation of 4-bromothiophenol. Yields are NMR yields, which were calculated by using 1,3,5 trimethoxybenzene as internal standard.

2 Results and discussion

2.1 Synthesis of novel vinylation reagents

Several core-substituted VBX reagents **1** were synthesised according to literature methods (Stridfeldt et al., 2016; Boelke et al., 2017), Scheme 1A). The synthesis of novel VBO reagents **2** started from anilines **8**, which underwent a Friedel-Crafts reaction to access the amino benzyl alcohols **9** (Scheme 1B). A subsequent Sandmeyer reaction produced the required iodoarenes **10** in good yields. (Amey and Martin, 1979). The benziodoxole core was formed through oxidative chlorination and hydrolysis, without isolation in between the steps, to form hydroxy-BO **11**. The vinyl moiety was introduced from the corresponding boronic acid using TMSOTf and pyridine (Boelke et al., 2017) to form VBO **2** (yields from **10** given in Scheme 1B). It should be noted that *ortho*-substituted compound **2f** was incredibly unstable, making isolation and analysis difficult (See the Supplementary Material for details).

Variations of the side-arm were next investigated to obtain novel compound classes for vinylation. The synthesis of VBZ **3** proceeded in good yields from 2-iodophenyl *N*-tosylbenzamides **12a-c**, using our one-pot method developed for VBX (Stridfeldt et al., 2016) with *m*CPBA/triflic acid and (*E*)-styrylboronic acid (Scheme 1C). To our surprise, reactions with the *ortho*-methyl-substituted substrate **12d** behaved differently, and resulted in the formation of the novel compound class VBXI **4**, which has an I-O hypervalent bond instead of the expected I-N bond. It appears that the steric congestion caused by the *ortho*-methyl group promotes formation of the BXI core as opposed to the BZ core. Products **5** were obtained from 2-iodophenyl sulfonic acids **12d-e** in moderate yields due to incomplete conversion of the starting material.

For the sake of comparison to their cyclic counterparts, a series of vinylodonium salts **6** with *ortho* functionalities were also synthesised from the iodoarenes **13** (Scheme 1D). Our one-step method (Stridfeldt et al., 2016) without the basic workup was used to obtain these compounds in good to high yields. Interestingly, when the one-pot synthesis of VBX⁶ **7** was attempted, product formation alongside an inseparable impurity was observed. (See the Supplementary Material for details) However, when isolated compound **6e** was treated with an aqueous basic solution, **7** could be isolated in good yields with high purity. This strategy was also attempted for the synthesis of VBX⁷ from **6d**, but was unsuccessful (See the Supplementary Material for details).

2.2 Reactivity investigation in *S*-vinylation of thiols

The *S*-vinylation protocol developed by our group was used to evaluate the vinylation reagents, as this reaction had already proved sensitive to the VBX core structure. (Castoldi et al., 2020b). 4-Bromothiophenol was thus vinylation with reagents **1-7** to provide thioether **14** with vinyl iodide **15** sometimes formed as side-product (Scheme 2). The result obtained with the novel VBX reagent **1f** followed the trend in the original work, (Castoldi et al., 2020b), in which reagents with electron-donating groups (EDG) gave higher yields than those with electron-withdrawing groups (EWG). VBO reagents **2** performed markedly worse, with yields of **14** ranging from 25% to 51%. VBZ **3** behaved similarly to VBX, with **3c** providing the highest yield of 90%, whereas VBXI **4** and VBT **5** gave significantly lower yields, which could be due to solubility problems. *E/Z* ratios were recorded in of each of these reactions, but

Crystal structures of vinylating reagents

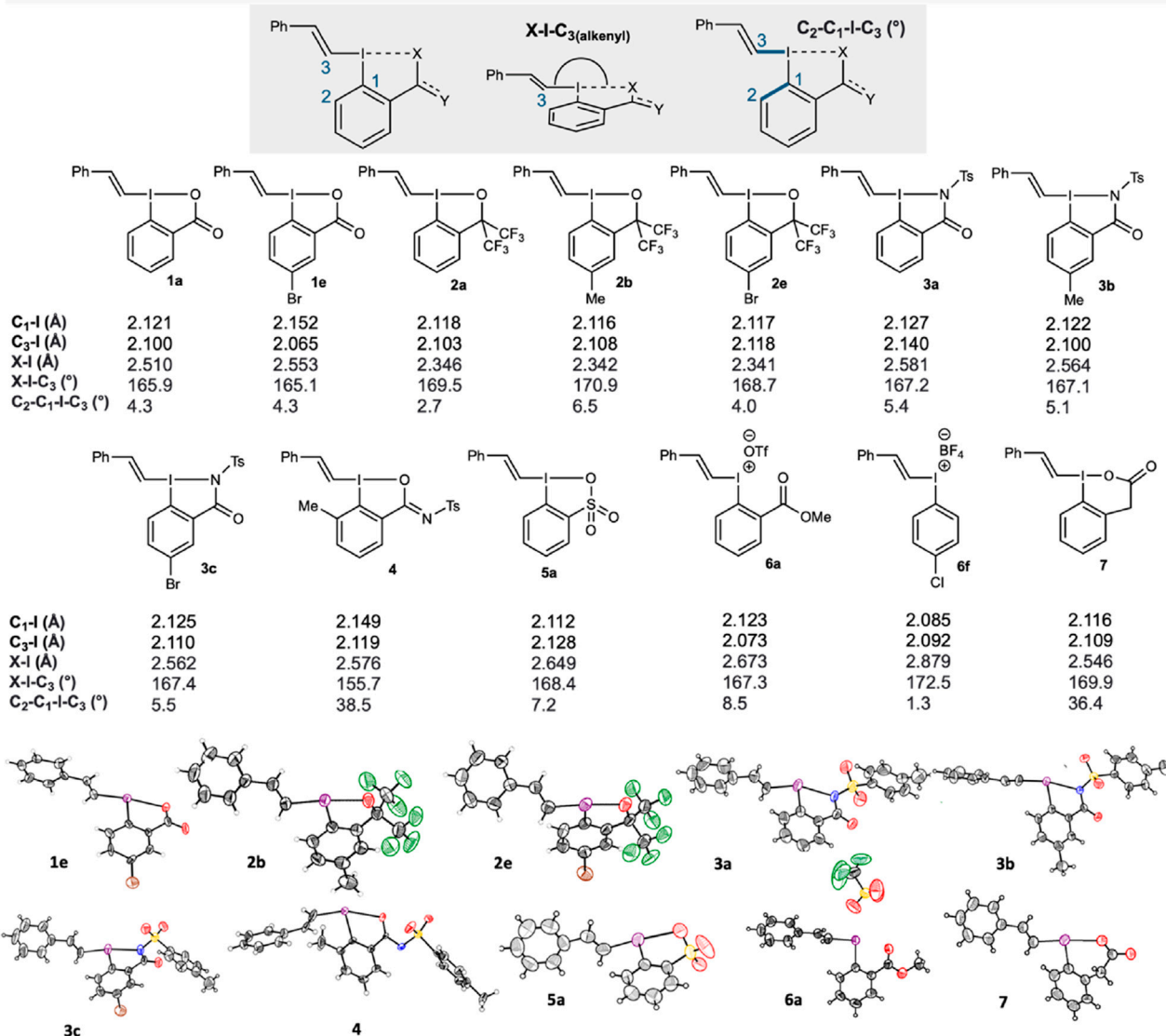


FIGURE 2 Novel crystal structures of reagents 1-7 compared to structures in the literature (1a (Stridfeldt et al., 2016), 2a (Pisella et al., 2020) and 6f (Clegg and Harrington, 1999)).

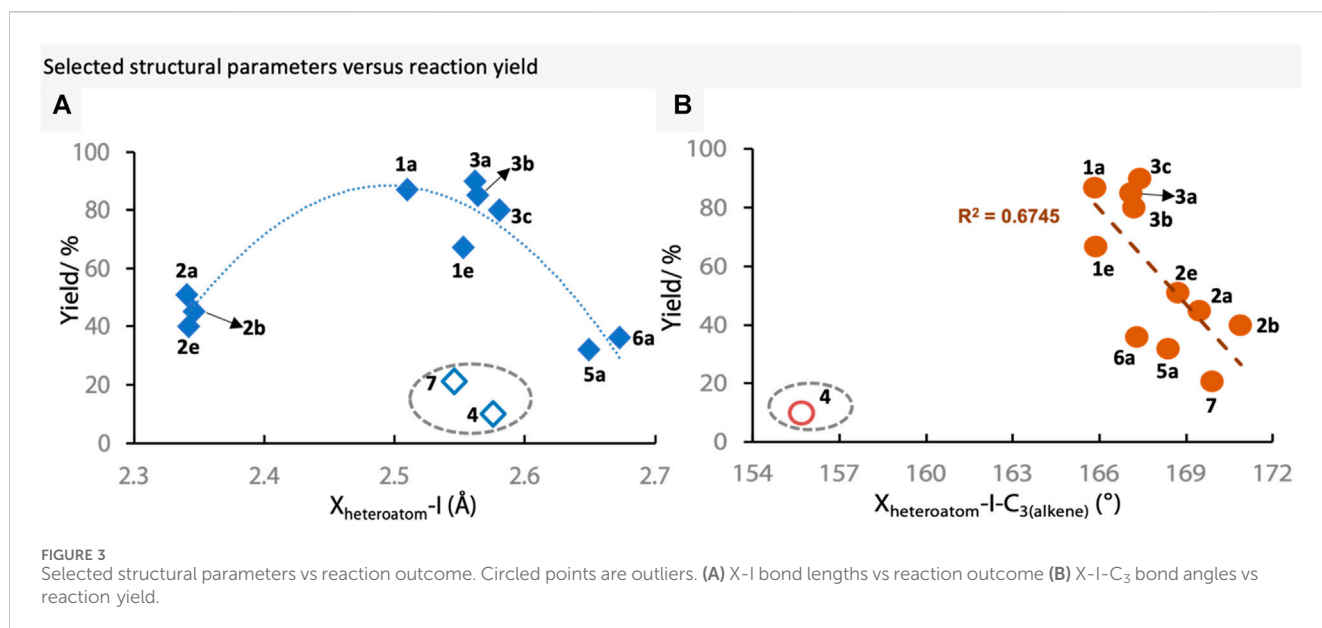
there was no observed trend with regards to the reagent used (See the [Supplementary Material](#) for details).

Additionally, the compounds with *ortho*-substituents performed worse than their counterparts (1a vs 1g, 2a vs 2f). Due to the rapid decomposition of those reagents during isolation and analysis, we hypothesise that the *ortho*-substituents increase the reactivity of these compounds, especially since the majority of product in these reactions were the vinyl iodide 15. Indeed, *ortho*-substitution in hypervalent iodine compounds has earlier been reported to cause considerable reactivity changes. (Guilbault and Legault, 2012; Malmgren et al., 2013; Abazid and Nachtsheim, 2020). Additionally, VBXI 4 produced a very poor yield of 14 in comparison to its analogues VBZ 3, possibly due to its BXI core. Similar to what was reported with acyclic vinylodonium salts in the

original S-vinylation paper, (Castoldi et al., 2020b), reagents 6 provided little product, with 15 again being the major product in these reactions. VBX⁶ provided a much lower yield than VBX, indicating the importance of the 5-membered ring for the application of this reagent.

2.3 X-ray crystallography analysis

To evaluate how the core substituents and side-arms influenced the structure, we collected single crystal X-ray diffraction data on selected compounds (Figure 2). Much of the crystal structure data in the literature focusses on vinylodonium salts, (Hinkle and McDonald, 2002; Ochiai et al., 2007; Yoshimura et al., 2021), and



varied substitution patterns on the vinyl groups of VBO (Wu et al., 2016; Wu J. et al., 2017; Wu et al., 2019; Ding et al., 2020; Pisella et al., 2020; Chai et al., 2021; Laskar et al., 2021; Wu et al., 2023) and VBX. (Stridfelt et al., 2016; Caramenti et al., 2019; Tessier et al., 2019). On the other hand, there appears to be no crystal structure investigations on the effect of cyclic vinylation reagents with different side-arms and core-substituents, as well as non-covalent interactions in *ortho*-substituted iodonium salts, on reaction outcome.

We evaluated the effect of the side-arm by comparison of core-unsubstituted VBX **1a**, VBO **2a**, VBZ **3a** and VBT **5a**, which showed very similar C₁-I bond lengths, 2.127, 2.118, 2.127 and 2.112 Å respectively. The same is also true for C₃-I bond lengths, as they measured at 2.100, 2.103, 2.140 and 2.128 Å respectively. However, X-I bond lengths were drastically different. **1a** and **3a** were somewhat similar with bond lengths of 2.510 and 2.581 Å respectively, whilst **2a** had a shorter bond length (2.346 Å) and **5a** has a longer bond length (2.649 Å). This is perhaps indicative of the increased *trans* effect caused by this functional group. (Ochiai et al., 2006). Additionally, measured X-I-C₃ bond angles showed that all compounds expressed a T-shaped conformation with **1a** having the smallest angle, 165.9°, and VBO **2b** the largest, 170.9°. The X-ray crystal structure of VBX **7** showed a strained 6-membered ring in the side-arm, with similar bond lengths and hypervalent bond angle with VBX **1a**. However, **7** has a C₂-C₁-I-C₃ bond angle of 36.4°, which is far higher than that of **1a** (4.3°).

To ascertain whether core-substituents made a measurable difference on any structural properties, several analogues of each class of vinylation reagent were also crystallised. Generally, the same trends followed within each class of compounds. Interestingly, the crystallographic data of *ortho*-substituted VBXI **4** showed a markedly lower X-I-C₃ bond angle of 155.7°, which is the lowest angle of any hypervalent iodine vinylation reagent in the literature. Additionally, **4** has a C₂-C₁-I-C₃ bond angle of 38.5°, which is far from the more idealised angle of 1°–8°

for the other compounds. These two measurements show that the *ortho*-methyl substituent induces sufficient steric strain to disrupt the hypervalent bond and ultimately leads to the formation of an I-O bond, as opposed to the I-N bond found in VBZ **3**. We hypothesise that this key difference contributes to the reagent's poor reactivity under the S-vinylation conditions. Furthermore, this characteristic likely contributes to their unstable and over-reactive nature as seen in Scheme 2. Interestingly, iodonium salt **6a** had similar C₁-I (2.123 Å) and C₃-I (2.073 Å) bond lengths to other compounds. Though, it has a much longer X-I bond length (2.673 Å), which is unsurprising considering the methyl ester ligand is not covalently bound, but it is markedly smaller than the X-I bond length of **6f** (The crystal structure data of **6f** is included as comparison to **6a**; we did not use **6f** in other parts of the study) (2.879 Å). This shows that whilst not having a covalently bound group will affect the structural properties, a much more significant effect will be observed when non-ligating substituents are used in the *ortho* position to the iodine.

Next, the possible correlation between structural parameters and reaction outcome was investigated (Figure 3). Firstly, the X-I bond lengths were plotted against the yield of S-vinylation, showing an upward slope from 2.341 Å (**2e**) to 2.581 Å (**3a**), which was proceeded by a downward slope towards 2.673 Å of **6a** (ester-bound iodonium) (Figure 3A). Interestingly, **4** and **7** were outliers to this trend (circled, hollow diamond). Thus, reagents with X-I bond lengths of ~2.55 Å represent a “sweet-spot” under these reaction conditions. Then the hypervalent bond angles (X-I-C₃) were plotted against reaction yields (Figure 3B). Within this parameter, it was observed that the higher the angle, and thus closer to the idealised 180°, the worse the reagent performed, with a peak of ~165°. Again, reagent **4** was an outlier in this trend. These results show that there is indeed a link between these two structural parameters and the reaction yield, and that both electronic and steric factors influence the reaction outcome.

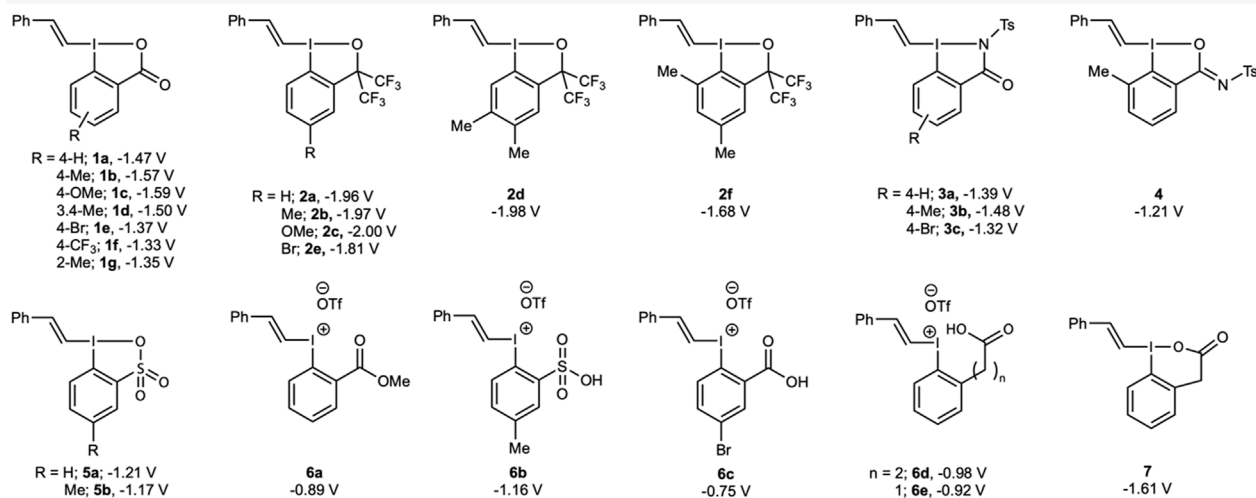
Reduction potentials of vinylation reagents (V vs Fc/Fc⁺)

FIGURE 4
Recorded reduction potentials (V vs Fc/Fc⁺) of reagents used in this study.

Reduction potentials of vinylation reagents vs yield of S-vinylation

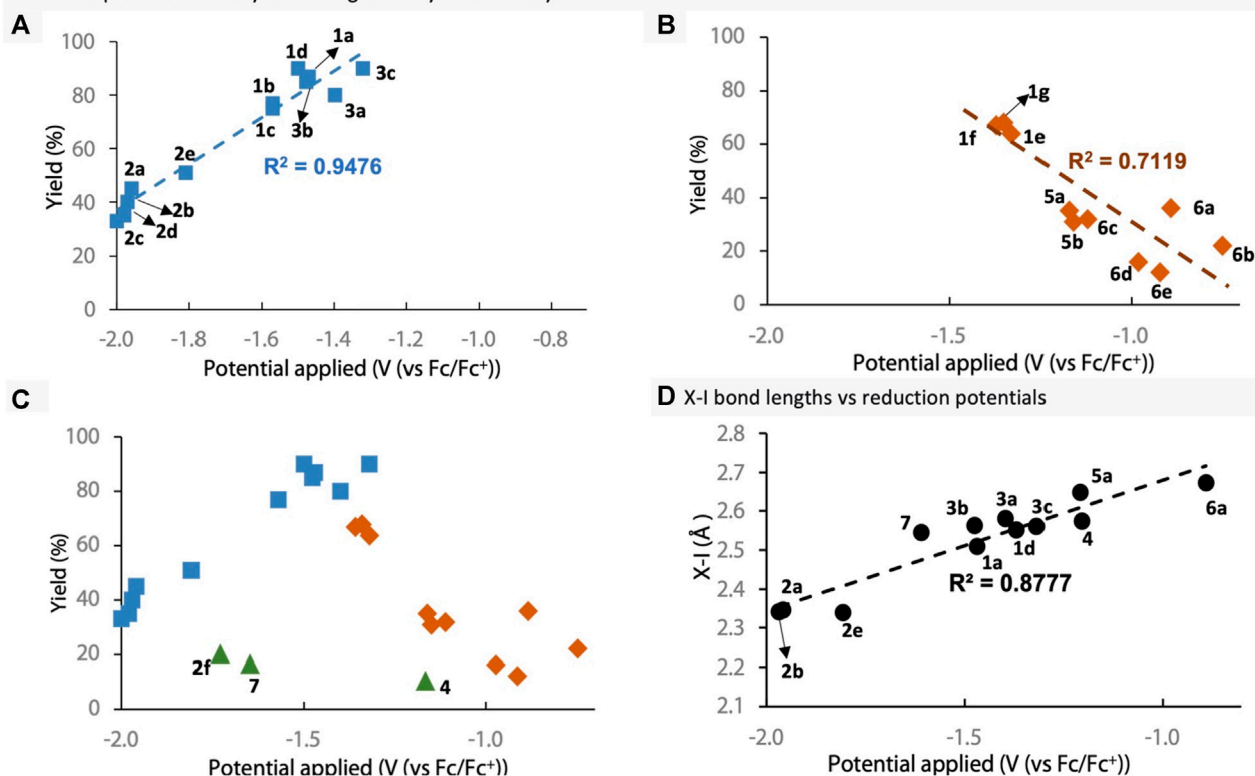


FIGURE 5
Reduction potentials of selected reagents plotted against S-vinylation. (A) Plot of 1a–1d, 2a–2e and 3. (B) Plot of 1e–1g, 5 and 6. (C) Overlay of plots (A, B), including the outlier compounds 2f, 4 and 7. (D) Plot of X–I bond lengths vs reduction potentials.

2.4 Reduction potential analysis

We also wanted to investigate how the reduction potentials of the reagents were affected by substituents of the aromatic ring core and the side-arm (Figure 4). Whilst there have been some reports of redox potentials of hypervalent iodine reagents in the literature, (Kokkinidis et al., 1989; Kokkinidis et al., 1991; Choi et al., 2015; Le Vaillant and Waser, 2017; De et al., 2019; Ramkumar et al., 2023), and even a computational study, (Radzhabov et al., 2020), there is currently no data on vinylation reagents and certainly no quantitative studies linking this parameter to reaction outcome.

To begin, we measured the potentials of each of the reagent used in this study. The higher the reduction potential (closer the value to 0 V (vs Fc/Fc⁺)), the more easily the reagent can be reduced. It was found that there was a tight range of reduction potentials within each class of reagent. VBX ranged from −1.33 V (**1f**) to −1.59 V (**1c**), which matches that EWG should make the reagent easier to reduce. Considering its strong likeness to **1a**, VBX⁶ **7** had a very different potential of −1.61 V. Whilst VBZ **3a-c** had slightly higher potentials between −1.32 and −1.48 V, VBXI **4** (−1.21 V) and VBT **5** (−1.21 and −1.17 V) had lower potentials. The lowest reduction potentials were measured for VBO **2**, ranging from **2c** (−1.98 V) to **2f** (−1.68 V). As controls, the potentials of some vinylidonium salts **6** were measured. Direct comparison of the uncyclized and cyclized analogues (**6c** vs **1e** and **6e** vs **6**) showed that the iodonium salts were indeed much easier to reduce. This was, however, not the case for **6b** (−1.16 V), which was very similar to its cyclized VBT counterpart **5b** (−1.17 V).

Next, to ascertain whether there is a relationship between reduction potentials of the vinylation reagents and their yield in *S*-vinylation, the two were plotted against each other (Figure 5). Firstly, we plotted the VBO, VBZ and only the EDG-substituted VBX reagents, as EWG-substituted VBX performed poorly in *S*-vinylation (Figure 5A). Reagents with lower reduction potentials were found to have a positive effect on the reaction yield. Secondly, we plotted the EWG-substituted VBX reagents, VBT reagents and iodonium salts (Figure 5B). In this case, lower reduction potential resulted in lowered reaction yield together with increased levels of vinyl iodide (see data in Scheme 2). This is interesting because the less reactive reagents (e.g., VBO) provided lower reaction yields, whereas the more reactive reagents (e.g., iodonium salts) gave low yields and more vinyl iodide. Furthermore, the results suggest that a reagent with a reduction potential between −1.3 and −1.5 V, represents the peak of this reaction, with potentials on either side being ultimately detrimental for the reagents. However, this could be due to the reaction itself being optimised on VBX **1a**. Curiously however, if both plots are overlaid with the previously excluded reagents, it becomes clear that there are some outliers to this trend (green triangles, Figure 5C). These are VBX⁶ **7** and *ortho*-substituted VBO **2f** and VBXI **4**, and the results might reflect the lack of idealised T-shaped conformation or conjugation in those structures. Clearly the reduction potential does not account for the change in T-shaped conformation and steric factors very well. Overall, it appears that the reduction potentials can be a good signifier for the efficiency of the vinylation reagent in the *S*-vinylation under these reaction conditions, but further reaction optimisation could potentially alter the outcome. Finally, a fine correlation was observed between X-I bond lengths and reduction potentials (Figure 5D),

signifying that X-I bond lengths could affect the reduction potentials greatly.

3 Materials and methods

For general experimental and instrumental methods, synthetic procedures, and full compound characterization, see the [Supplementary Material](#).

4 Conclusion

In conclusion, the synthesis of novel hypervalent iodine-based vinylation reagents has been reported, including the new compound classes VBZ, VBXI, VBT and VBX⁶. These reagents were evaluated in the *S*-vinylation of 4-bromothiophenol and VBZ performed similarly to VBX, whilst VBO, VBXI, VBT and iodonium salts proved inferior. Crystal structures of selected reagents were measured, as well as electronic potentials of all the reagents. Crystal structure data showed that there was a correlation between certain parameters and reaction outcome, and *ortho*-substituents were found to perturb the reagent's structure and hence destabilise it. Additionally, reduction potentials were plotted against reaction outcome, which showed a sweet spot of about −1.4 V, when ignoring certain outliers in the study. Additionally, there was a correlation between reduction potentials and X-I bond length. We believe that further investigations of properties vs reaction outcome could result in a method for predicting reaction outcome with hypervalent iodine reagents.

Data availability statement

The original contributions presented in the study are included in the article/[Supplementary Material](#), further inquiries can be directed to the corresponding author.

Author contributions

SD: Conceptualization, Validation, Writing—original draft, Writing—review and editing, Investigation, Methodology, Visualization. ED: Conceptualization, Investigation, Methodology, Validation, Supervision, Writing—review and editing. AP: Investigation, Writing—review and editing. AI: Investigation, Writing—review and editing, Validation, Visualization. BO: Conceptualization, Funding acquisition, Resources, Supervision, Validation, Writing—original draft, Writing—review and editing, Project administration, Visualization.

Funding

The author(s) declare financial support was received for the research, authorship, and/or publication of this article. Carl Trygger Foundation (20:316), the Swedish Research Council (2019-04232) and the Swedish Foundation for Strategic Research (SSF) are kindly acknowledged for financial support.

Conflict of interest

The authors declare that the research was conducted in the absence of any commercial or financial relationships that could be construed as a potential conflict of interest.

Publisher's note

All claims expressed in this article are solely those of the authors and do not necessarily represent those of their affiliated

organizations, or those of the publisher, the editors and the reviewers. Any product that may be evaluated in this article, or claim that may be made by its manufacturer, is not guaranteed or endorsed by the publisher.

Supplementary material

The Supplementary Material for this article can be found online at: <https://www.frontiersin.org/articles/10.3389/fchem.2024.1376948/full#supplementary-material>

References

- Abazid, A. H., and Nachtsheim, B. J. (2020). A triazole-substituted aryl iodide with omnipotent reactivity in enantioselective oxidations. *Angew. Chem. Int. Ed.* 59, 1479–1484. doi:10.1002/anie.201912023
- Amey, R. L., and Martin, J. C. (1979). Synthesis and reaction of substituted arylalkoxyiodinanes: formation of stable bromoarylalkoxy and arylalkoxy heterocyclic derivatives of tricoordinate organoiodine(III). *J. Org. Chem.* 44, 1779–1784. doi:10.1021/jo01325a007
- Bhaskar Pal, K., Di Tommaso, E. M., Inge, A. K., and Olofsson, B. (2023). Stereospecific photoredox-catalyzed vinylations to functionalized alkenes and C-glycosides**. *Angew. Chem. Int. Ed.* 62, e202301368. doi:10.1002/anie.202301368
- Boelke, A., Caspers, L. D., and Nachtsheim, B. J. (2017). NH₂-Directed C-H alkenylation of 2-vinylanilines with vinylbenziodoxolones. *Org. Lett.* 19, 5344–5347. doi:10.1021/acs.orglett.7b02630
- Caramenti, P., Declas, N., Tessier, R., Wodrich, M. D., and Waser, J. (2019). Stereoselective synthesis of alkyl-aryl-vinyl- and alkynyl-substituted Z-enamides and enol ethers. *Chem. Sci.* 10, 3223–3230. doi:10.1039/c8sc05573d
- Castoldi, L., Di Tommaso, E. M., Reitti, M., Gräfen, B., and Olofsson, B. (2020b). Electrophilic vinylation of thiols under mild and transition metal-free conditions. *Angew. Chem. Int. Ed.* 59, 15512–15516. doi:10.1002/anie.202002936
- Castoldi, L., Rajkiewicz, A. A., and Olofsson, B. (2020a). Transition metal-free and regioselective vinylation of phosphine oxides and H-phosphinates with VBX reagents. *Chem. Commun.* 56, 14389–14392. doi:10.1039/d0cc05992g
- Chai, J., Ding, W., Wang, C., Ito, S., Wu, J., and Yoshikai, N. (2021). Ritter-type iodo(III)amidation of unactivated alkynes for the stereoselective synthesis of multisubstituted enamides. *Chem. Sci.* 12, 15128–15133. doi:10.1039/d1sc05240c
- Charpentier, J., Fröh, N., and Togni, A. (2015). Electrophilic trifluoromethylation by use of hypervalent iodine reagents. *Chem. Rev.* 115, 650–682. doi:10.1021/cr500223h
- Choi, W. J., Choi, S., Ohkubo, K., Fukuzumi, S., Cho, E. J., and You, Y. (2015). Mechanisms and applications of cyclometalated Pt(II) complexes in photoredox catalytic trifluoromethylation. *Chem. Sci.* 6, 1454–1464. doi:10.1039/c4sc02537g
- Clegg, W., and Harrington, R. (1999). *Private communication to CSD*. CCDC Number. 1989094.
- Dahiya, A., Sahoo, A. K., Chakraborty, N., Das, B., and Patel, B. K. (2022). Updates on hypervalent-iodine reagents: metal-free functionalisation of alkenes, alkynes and heterocycles. *Org. Biomol. Chem.* 20, 2005–2027. doi:10.1039/d1ob02233d
- Davies, J., Sheikh, N. S., and Leonori, D. (2017). Photoredox imino functionalizations of olefins. *Angew. Chem. Int. Ed.* 56, 13361–13365. doi:10.1002/anie.201708497
- De, A., Santra, S., Hajra, A., Zyryanov, G. V., and Majee, A. (2019). Visible-light-induced regioselective C(sp³)-H acyloxylation of aryl-2H-azirines with (Diacetoxy) iodobenzene. *J. Org. Chem.* 84, 11735–11740. doi:10.1021/acs.joc.9b01625
- Declas, N., Maynard, J. R. J., Menin, L., Gasilova, N., Götze, S., Sprague, J. L., et al. (2022). *Chem. Sci.* 20, 12808–12817. doi:10.1039/d2sc04558c
- Declas, N., Pisella, G., and Waser, J. (2020). Vinylbenziodoxol(on)es: synthetic methods and applications. *Helv. Chim. Acta* 103, e2000191. doi:10.1002/hlca.202000191
- Ding, W., Chai, J., Wang, C., Wu, J., and Yoshikai, N. (2020). Stereoselective access to highly substituted vinyl ethers via *trans*-difunctionalization of alkynes with alcohols and iodine(III) electrophile. *J. Am. Chem. Soc.* 142, 8619–8624. doi:10.1021/jacs.0c04140
- Di Tommaso, E. M., Norrby, P., and Olofsson, B. (2022). Explaining regiodivergent vinylations with vinylbenziodoxolones**. *Angew. Chem. Int. Ed.* 61, e202206347. doi:10.1002/anie.202206347
- Fernández González, D., Brand, J. P., Mondière, R., and Waser, J. (2013). Ethynylbenziodoxolones (EBX) as reagents for the ethynylation of stabilized enolates. *Adv. Synth. Catal.* 355, 1631–1639. doi:10.1002/adsc.201300266
- Flores, A., Cots, E., Bergès, J., and Muñoz, K. (2019). Enantioselective iodine(I/III) catalysis in organic synthesis. *Adv. Synth. Catal.* 361, 2–25. doi:10.1002/adsc.201800521
- Frei, R., Wodrich, M. D., Hari, D. P., Borin, P. A., Chauvier, C., and Waser, J. (2014). Fast and highly chemoselective alkynylation of thiols with hypervalent iodine reagents enabled through a low energy barrier concerted mechanism. *J. Am. Chem. Soc.* 136, 16563–16573. doi:10.1021/ja5083014
- Guilbault, A. A., and Legault, C. Y. (2012). Drastic enhancement of activity in iodane-based α -silyloxylation of ketones: iodine(III) does the hypervalent twist. *ACS Catal.* 2, 219–222. doi:10.1021/cs200612s
- Hara, S., Guan, T., and Yoshida, M. (2006). Stereoselective generation of (E)- and (Z)-2-Fluoroalkylidene-Type carbenoids from (2-fluoro-1-alkenyl)iodonium salts and their application for stereoselective synthesis of fluoroalkenes. *Org. Lett.* 8, 2639–2641. doi:10.1021/ol0608707
- Hari, D. P., Nicolai, S., and Waser, J. (2019). in *Patai's Chemistry of functional groups*. Editors B. Olofsson, I. Marek, and Z. Rapoport (United States: Wiley Online Library), 523–580.
- Hinkle, R. J., and McDonald, R. (2002). (Z)-2-Methylbuten-1-yl(aryl)iodonium trifluoromethanesulfonates containing electron-withdrawing groups on the aryl moiety. *Acta Crystallogr. Sect. C Cryst. Struct. Commun.* 58, o117–o121. doi:10.1107/s0108270101019084
- Holt, D., and Gaunt, M. J. (2015). Copper-catalyzed oxy-alkenylation of homoallylic alcohols to generate functional *syn*-1,3-diol derivatives. *Angew. Chem. Int. Ed.* 54, 7857–7861. doi:10.1002/anie.201501995
- Jiang, H., and Studer, A. (2019). Transition-metal-free three-component radical 1,2-amidoalkynylation of unactivated alkenes. *Chem. Eur. J.* 25, 516–520. doi:10.1002/chem.201805490
- Kepski, K., Rice, C. R., and Moran, W. J. (2019). Cyclic vinyl(aryl)iodonium salts: synthesis and reactivity. *Org. Lett.* 21, 6936–6939. doi:10.1021/acs.orglett.9b02540
- Kikuchi, J., Maesaki, K., Sasaki, S., Wang, W., Ito, S., and Yoshikai, N. (2022). Stereoselective synthesis of β -alkoxy- β -amido vinylbenziodoxoles via iodo(III) etherification of ynamides. *Org. Lett.* 24, 6914–6918. doi:10.1021/acs.orglett.2c02570
- Kokkinidis, G., Hatzigrigoriou, E., Sazou, D., and Varvoglis, A. (1991). Electrochemical reduction of some hypervalent iodine compounds. *Electrochim. Acta* 36, 1391–1395. doi:10.1016/0013-4686(91)85324-z
- Kokkinidis, G., Papadopoulou, M., and Varvoglis, A. (1989). Electrochemical reduction of [bis(acyloxy)iodo]arenes. *Electrochim. Acta* 34, 133–139. doi:10.1016/0013-4686(89)87078-1
- Koposov, A. Y., Litvinov, D. N., Zhdankin, V. V., Ferguson, M. J., McDonald, R., and Tykwinski, R. R. (2006). *Eur. J. Org. Chem.* 21, 4791–4795. doi:10.1002/ejoc.200600683
- Koser, G. F., Sun, G., Porter, C. W., and Youngs, W. J. (1993). Synthesis of 1H-1-(1-alkynyl)-5-methyl-1,2,3-benziodoxathiole 3,3-dioxides: alkynyl(aryl)iodonium sulfonates with heterocyclic iodine. *J. Org. Chem.* 58, 7310–7312. doi:10.1021/jo00077a071
- Laskar, R. A., Ding, W., and Yoshikai, N. (2021). Iodo(III)-Meyer-Schuster rearrangement of propargylic alcohols promoted by benziodoxole triflate. *Org. Lett.* 23, 1113–1117. doi:10.1021/acs.orglett.1c00039
- Le Du, E., Duhal, T., Wodrich, M. D., Scopelliti, R., Fadaei-Tirani, F., Anselmi, E., et al. (2021). Structure and reactivity of N-heterocyclic alkynyl hypervalent iodine reagents. *Chem. Eur. J.* 27, 10979–10986. doi:10.1002/chem.202101475
- Le Du, E., and Waser, J. (2023). Recent progress in alkynylation with hypervalent iodine reagents. *Chem. Commun.* 59, 1589–1604. doi:10.1039/d2cc06168f
- Le Vaillant, F., Garreau, M., Nicolai, S., Gryn'ova, G., Corminboeuf, C., and Waser, J. (2018). Fine-tuned organic photoredox catalysts for fragmentation-alkynylation cascades of cyclic oxime ethers. *Chem. Sci.* 9, 5883–5889. doi:10.1039/c8sc01818a

- Le Vaillant, F., and Waser, J. (2017). Decarboxylative alkylation and cyanation of carboxylic acids using photoredox catalysis and hypervalent iodine reagents. *Chimia* 71, 226–230. doi:10.2533/chimia.2017.226
- Li, M., Li, W., Lin, C. D., Wang, J. H., and Wen, L. R. (2019). One base for two shots: metal-free substituent-controlled synthesis of two kinds of oxadiazine derivatives from alkynylbenziodoxolones and amidoximes. *J. Org. Chem.* 84, 6904–6915. doi:10.1021/acs.joc.9b00659
- Li, Y., Hari, D. P., Vita, M. V., and Waser, J. (2016). Cyclic hypervalent iodine reagents for atom-transfer reactions: beyond trifluoromethylation. *Angew. Chem. Int. Ed.* 55, 4436–4454. doi:10.1002/anie.201509073
- Liu, B., Alegre-Requena, J. V., Paton, R. S., and Miyake, G. M. (2020). Unconventional reactivity of ethynylbenziodoxolone reagents and thiols: scope and mechanism. *Chem. Eur. J.* 26, 2386–2394. doi:10.1002/chem.201904520
- Liu, B., Lim, C.-H., and Miyake, G. M. (2018). Light-Driven Intermolecular Charge Transfer Induced Reactivity of Ethynylbenziodoxol(on)e and Phenols. *J. Am. Chem. Soc.* 140, 12829–12835. doi:10.1021/jacs.8b05870
- Malmgren, J., Santoro, S., Jalalian, N., Himo, F., and Olofsson, B. (2013). Arylation with unsymmetrical diaryliodonium salts: a chemoselectivity study. *Chem. Eur. J.* 19, 10334–10342. doi:10.1002/chem.201300860
- Merritt, E. A., and Olofsson, B. (2009). Diaryliodonium salts: a journey from obscurity to fame. *Angew. Chem. Int. Ed.* 48, 9052–9070. doi:10.1002/anie.200904689
- Milzarek, T. M., Ramirez, N. P., Liu, X. Y., and Waser, J. (2023). One-pot synthesis of functionalized bis(trifluoromethylated)benziodoxoles from iodine(i) precursors. *Chem. Commun.* 59, 12637–12640. doi:10.1039/d3cc04525k
- Mironova, I. A., Noskov, D. M., Yoshimura, A., Yusubov, M. S., and Zhdankin, V. V. (2023). Aryl-Akynyl- and alkenylbenziodoxoles: synthesis and synthetic applications. *Molecules* 28, 2136–2179. doi:10.3390/molecules28052136
- Ochiai, M., Hirobe, M., Yoshimura, A., Nishi, Y., Miyamoto, K., and Shiro, M. (2007). Internal delivery of soft chlorine and bromine atoms: stereoselective synthesis of (*E*)- β -Halogenovinyl(aryl)- λ^3 -iodanes through domino λ^3 -iodanation–1,4-halogen Shift–Fluorination of alkynes. *Org. Lett.* 9, 3335–3338. doi:10.1021/ol071345q
- Ochiai, M., Sueda, T., Miyamoto, K., Kiprof, P., and Zhdankin, V. V. (2006). *Trans* influences on hypervalent bonding of aryl λ^3 -iodanes: their stabilities and isodesmic reactions of benziodoxolones and benziodazolonones. *Angew. Chem. Int. Ed.* 45, 8203–8206. doi:10.1002/anie.200603055
- Ochiai, M., Yamamoto, S., Suefuji, T., and Chen, D.-W. (2001). Stereoselective synthesis of (*Z*)-Enethiols and their Derivatives: vinylic S_N2 reaction of (*E*)-Alkenyl(phenyl)- λ^3 -iodanes with thioamides. *Org. Lett.* 3, 2753–2756. doi:10.1021/ol016356c
- B. Olofsson, I. Marek, and Z. Rappoport (2019). “The Chemistry of hypervalent halogen compounds,” *Patai's Chemistry of functional groups* (United States: Wiley Online Library).
- Pisella, G., Gagnebin, A., and Waser, J. (2020). Copper-catalyzed oxyvinilation of diazo compounds. *Org. Lett.* 22, 3884–3889. doi:10.1021/acs.orglett.0c01150
- Radzhabov, M. R., Sheremetev, A. B., and Pivina, T. S. (2020). Oxidative ability of organic iodine(iii) reagents: a theoretical assessment. *New J. Chem.* 44, 7051–7057. doi:10.1039/d0nj00837k
- Rajkiewicz, A. A., and Kalek, M. (2018). *N*-heterocyclic carbene-catalyzed olefination of aldehydes with vinylodonium salts to generate α,β -unsaturated ketones. *Org. Lett.* 20, 1906–1909. doi:10.1021/acs.orglett.8b00447
- Ramkumar, N., Baumann, L., Zacs, D., and Veliks, J. (2023). Merging copper(I) photoredox catalysis and iodine(III) Chemistry for the oxy-monofluoromethylation of alkenes. *Angew. Chem. Int. Ed.* 62, e202219027. doi:10.1002/anie.202219027
- Sheng, J., Wang, Y., Su, X., He, R., and Chen, C. (2017). Copper-catalyzed [2+2+2] modular synthesis of multisubstituted pyridines: alkenylation of nitriles with vinylodonium salts. *Angew. Chem. Int. Ed.* 56, 4824–4828. doi:10.1002/anie.201700696
- Shimbo, D., Shibata, A., Yudasaka, M., Maruyama, T., Tada, N., Uno, B., et al. (2019). Synthesis of *cis*- β -Amidevinyl benziodoxolones from the ethynyl benziodoxolone–chloroform complex and sulfonamides. *Org. Lett.* 21, 9769–9773. doi:10.1021/acs.orglett.9b03990
- Skucas, E., and MacMillan, D. W. C. (2012). Enantioselective α -vinylation of aldehydes via the synergistic combination of copper and amine catalysis. *J. Am. Chem. Soc.* 134, 9090–9093. doi:10.1021/ja303116v
- Stridfeldt, E., Seemann, A., Bouma, M. J., Dey, C., Ertan, A., and Olofsson, B. (2016). Synthesis, characterization and unusual reactivity of vinylbenziodoxolones—novel hypervalent iodine reagents. *Chem. Eur. J.* 22, 16066–16070. doi:10.1002/chem.201603955
- Tessier, R., Ceballos, J., Guidotti, N., Simonet-Davin, R., Fierz, B., and Waser, J. (2019). “Doubly orthogonal” labeling of peptides and proteins. *Chem* 5, 2243–2263. doi:10.1016/j.chempr.2019.06.022
- Ura, T., Shimbo, D., Yudasaka, M., Tada, N., and Itoh, A. (2020). Synthesis of phenol-derived *cis*-vinyl ethers using ethynyl benziodoxolone. *Chem. Asian J.* 15, 4000–4004. doi:10.1002/asia.202001102
- Villo, P., and Olofsson, B. (2019). in *Patai's Chemistry of functional groups*. Editors B. Olofsson, I. Marek, and Z. Rappoport (Cham: Hypervalent Halogen Compd), 461–522.
- Wang, C. S., Tan, P. S. L., Ding, W., Ito, S., and Yoshikai, N. (2022). Regio- and stereoselective synthesis of enol carboxylate, phosphate, and sulfonate esters via iodo(III) functionalization of alkynes. *Org. Lett.* 24, 430–434. doi:10.1021/acs.orglett.1c04123
- Wirth, T. (2016). *Hypervalent iodine Chemistry*. Cham: Springer International Publishing.
- Wu, B., Wu, J., and Yoshikai, N. (2017b). Benziodoxole triflate as a versatile reagent for iodo(III)cyclization of alkynes. *Chem. Asian J.* 12, 3123–3127. doi:10.1002/asia.201701530
- Wu, J., Deng, X., Hirao, H., and Yoshikai, N. (2016). Pd-catalyzed conversion of alkynyl- λ^3 -iodanes to alkenyl- λ^3 -iodanes via stereoselective 1,2-iodine(III) shift/1,1-hydrocarboxylation. *J. Am. Chem. Soc.* 138, 9105–9108. doi:10.1021/jacs.6b06247
- Wu, J., Deng, X., and Yoshikai, N. (2019). Stereocontrolled synthesis of halovinylbenziodoxoles by hydro- and iodochlorination of ethynylbenziodoxoles. *Chem. Eur. J.* 25, 7839–7842. doi:10.1002/chem.201901543
- Wu, J., Xu, K., Hirao, H., and Yoshikai, N. (2017a). Pd-Catalyzed, ligand-enabled stereoselective 1,2-iodine(III) shift/1,1-carboxyalkynylation of alkynylbenziodoxoles. *Chem. A Eur. J.* 23, 1521–1525. doi:10.1002/chem.201605772
- Wu, J., Xu, K., Hirao, H., and Yoshikai, N. (2023). *Private communication to CSD*. CCDC Number. 1498944.
- Yoshimura, A., Huss, C. D., Liebl, M., Rohde, G. T., Larson, S. M., Frahm, G. B., et al. (2021). Preparation, structure, and reactivity of pseudocyclic β -trifluorosulfonyloxy vinylbenziodoxolone derivatives. *Adv. Synth. Catal.* 363, 3365–3371. doi:10.1002/adsc.202100341
- Yoshimura, A., Saito, A., and Zhdankin, V. V. (2023). Recent progress in synthetic applications of cyclic hypervalent iodine(III) reagents. *Adv. Synth. Catal.* 365, 2653–2675. doi:10.1002/adsc.202300275
- Yoshimura, A., and Zhdankin, V. V. (2016). Advances in synthetic applications of hypervalent iodine compounds. *Chem. Rev.* 116, 3328–3435. doi:10.1021/acs.chemrev.5b00547
- Yuan, H., Guo, L., Liu, F., Miao, Z., Feng, L., and Gao, H. (2019). Copper-catalyzed tandem *O*-vinylation of arylhydroxylamines/[3,3]-rearrangement/cyclization: synthesis of highly substituted indoles and benzindoles. *ACS Catal.* 9, 3906–3912. doi:10.1021/acscatal.9b00470



OPEN ACCESS

EDITED BY

Maria Rosaria Plutino,
National Research Council (CNR), Italy

REVIEWED BY

Wei Lyu,
Donghua University, China
Lei Yu,
Yangzhou University, China

*CORRESPONDENCE

Maria Camilla Baratto,
✉ mariacamilla.baratto@unisi.it

RECEIVED 04 April 2024

ACCEPTED 28 June 2024

PUBLISHED 25 July 2024

CITATION

Fabrizi de Biani F, Corsini M, Pogni R and Baratto MC (2024), Practical applications of copper-based enzymes: synthesis of sulfonated polyaniline through laccase-catalyzed oxidation.
Front. Chem. 12:1412242.
doi: 10.3389/fchem.2024.1412242

COPYRIGHT

© 2024 Fabrizio de Biani, Corsini, Pogni and Baratto. This is an open-access article distributed under the terms of the [Creative Commons Attribution License \(CC BY\)](#). The use, distribution or reproduction in other forums is permitted, provided the original author(s) and the copyright owner(s) are credited and that the original publication in this journal is cited, in accordance with accepted academic practice. No use, distribution or reproduction is permitted which does not comply with these terms.

Practical applications of copper-based enzymes: synthesis of sulfonated polyaniline through laccase-catalyzed oxidation

Fabrizia Fabrizi de Biani^{1,2}, Maddalena Corsini¹, Rebecca Pogni^{1,3} and Maria Camilla Baratto^{1,3*}

¹Dipartimento di Biotecnologie, Chimica e Farmacia, Università di Siena Via Aldo Moro, Siena, Italy,

²INSTM, Research Unit of Siena, Siena, Italy, ³Centre for Colloid and Surface Science (CSGI), Firenze, Italy

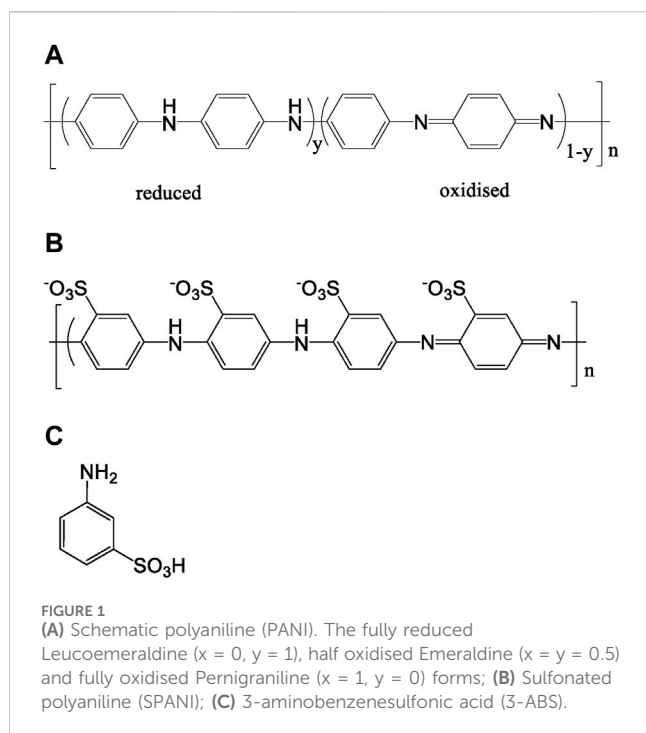
Known for its tunable conductivity and stability, Polyaniline (PANI) is a valuable polymer for electronics and sensing devices. Challenges in solubility have been addressed by creating sulfonated PANI (SPANI), enhancing its practical use. Synthesizing SPANI from sulfonated aniline is intricate, but laccase biocatalysis offers an eco-conscious solution, effective even against high redox potential obstacles. This research monitored the *Trametes versicolor* laccase-induced oxidation of 3-ABSa via UV-vis spectroscopy, with a notable peak at 565 nm signifying SPANI synthesis, effective even at suboptimal pH. Mediators further boost this process. Moreover, NMR and spectroelectrochemistry confirm the green synthesis of SPANI by laccase, hinting that pH fine-tuning could improve yields, alongside the concurrent creation of azobenzene derivatives.

KEYWORDS

laccase, sulfonated polyaniline, 3-aminobenzenesulfonic acid, cyclic voltammetry, spectroelectrochemistry, conducting polymers

1 Introduction

Polyaniline (PANI) is a conducting polymer that has been of interest since the 1980s due to its unique properties. It is one of the most studied conducting polymers due to its ease of synthesis, low cost, stability, and wide range of conductivity upon doping (Bhadra et al., 2020; Majeed et al., 2022). Polyaniline and similar oligomers/polymers serve as highly functional materials across various domains. Recent instances highlight the potential application of PANI composite materials in designing wearable electronics (Lyu et al., 2020; Zheng et al., 2023; Chen et al., 2023), for environment remediation (Lyu et al., 2021; Lyu et al., 2022) and for seawater desalination (Han et al., 2022), furthermore PANI-supported nano metal particles have been broadly applied as catalyst in coupling reactions (Zeng et al., 2023). The base form of PANI has a generalized composition as in Figure 1A. Leucoemeraldine is the fully reduced state of the polymer, it exists in the colorless base form. Emeraldine is the half-oxidized state of the polymer, it can be found in both the base form (blue) and the protonated “salt” form (green). Pernigraniline is the fully oxidized form of the polymer, it can also exist in both the base form (violet) and the salt forms (blue). One of the key properties of PANI is its adjustable electrical conductivity: the conductivity of PANI depends on its oxidation state, furthermore, it can be increased by up to ten orders of magnitude when treated with acids (Majeed et al., 2022). Since PANI also exhibits color changes associated with different oxidation states, it can be also used in sensors and



electrochromic devices (Majeed et al., 2022). Furthermore, PANI has excellent environmental stability, making it suitable for use in various conditions. In summary, PANI is a versatile conducting polymer with unique properties that make it suitable for a wide range of applications, however, limitations such as its poor solubility in common solvents and its high melting point have impeded its incorporation into industrial applications. To overcome these limitations, design strategies to enhance the solubility of PANI in an aqueous solution without adversely impacting conductivity and electroactivity have been developed over the years and various approaches have been pursued to enhance the solubility by the introduction of substituents on the PANI backbone. In 1990, Jiang et al. and Dao et al. reported the first water-soluble conducting derivatives of PANI, i.e. sulfonated polyaniline (SPANI) (Jiang and Epstein, 1990; Bergeron et al., 1990, Figure 1B). The process of sulfonating PANI using fuming sulfuric acid involves dealing with hazardous and corrosive chemicals, which makes it suboptimal and challenging to expand on a larger scale. Furthermore, the gradual dissolution of PANI in concentrated sulfuric acid is manifest. This is likely due to a simultaneous reaction with SO_3 , resulting in complicated reaction patterns including partial sulfonation of the polymer and multiple sulfonation on the same ring (Yue et al., 1992). Despite the difficulties, sulfonated polyanilines initially have been typically synthesized through post-polymerization treatment of PANI. Several research groups have attempted to homopolymerize sulfonated aniline, but this has proven to be a non-trivial task and initial efforts to directly polymerize ring-sulfonated aniline were unsuccessful. This outcome has been attributed to the combination of the steric inhibition and the electron-withdrawing nature of the sulfonic acid group, which reduces the monomer's susceptibility to oxidation (Yue et al., 1991). The first chemical homopolymerization of 3-aminobenzenesulfonic acid (3-ABSa, Figure 1C) was accomplished (in low yield) by conducting the reaction under high pressure (Chan

et al., 1998). Subsequently, polymerization of 3-ABSa was carried out under ambient pressure using $\text{FeCl}_3 \cdot 6(\text{H}_2\text{O})$ as both a binary oxidant and dopant agent. This reaction occurred in a solvent-free condition at temperatures ranging from 40°C to 45°C . Under these conditions, the fully oxidized pernigraniline form was successfully obtained (Modarresi-Alam et al., 2019). In their study, Mav et al. found that 3-ABSa does not homopolymerize through chemical oxidative polymerization in water at low pH (Mav et al., 1999). Also, when they prepared a series of copolymers using aniline and 3-ABSa with varying ratios of comonomers, they noticed a decrease in yield as the proportion of the less reactive sulfonated monomer increased in the reaction mixture. This observation aligned with the previously reported expectation that sulfonated aromatic rings should be isolated by at least one non-sulfonated aromatic ring in the structure of PANI (Yue et al., 1991). Despite these obstacles, electrochemical polymerization of 3-ABSa has eventually been performed either by the controlled current (Kitani et al., 1995) or by controlled potential (Márquez et al., 2007) conditions or by cycling voltammetry in a solvent mixture $\text{CH}_3\text{CN}/\text{H}_2\text{O}$ (Krishnamoorthy et al., 2002). In summary, even if there have been some fruitful attempts, the homopolymerization of ortho-, meta- and para-aminobenzenesulfonic acid (2,3,4-ABS) remains a challenging endeavor (Freund and Bhavana, 2007). On the other side, biocatalysis has emerged as an environmentally friendly alternative for synthesizing PANI (Karamyshev et al., 2003; Walde et al., 2019; De Salas et al., 2016). Biocatalysis offers advantages such as milder processing conditions (neutral pH and lower temperature) and reduced waste and toxicity, aligning with the principles of green chemistry (Clark, 1999). Laccase, a multicopper oxidoreductase, can catalyze the oxidation of many substrates, with atmospheric oxygen as the oxidizing agent. In the following, we illustrate the uncomplicated process for obtaining SPANI through the polymerization of the monomeric unit 3-ABSa facilitated by the catalytic activity of laccase. The redox potential of the laccases is in the range of $+0.40$ to $+0.80$ mV (vs NHE) and specifically *Trametes versicolor* laccase has a redox potential of $+0.78$ mV (Reinhammar, 1972; Xu et al., 1996). The pH-dependent redox potential of 3-ABSa is expected to be remarkably elevated, posing a challenge for laccase in its oxidation process. It has been previously reported (Polak and Jarosz-Wilkolazka, 2010) that at pH 4.5 the redox potential of 3-ABSa is $+1.18$ V (vs NHE) and therefore it should be not oxidized by *Trametes versicolor* laccase. Anyway, there are evidence that laccases can indeed oxidize compounds with a higher redox potential than their own, although the precise mechanism behind this phenomenon remains unclear (Amann, 1997; Bourbonnais et al., 1998). In our experimental observations, we encountered a similar outcome: *Trametes versicolor* laccase catalyzed the formation of a red-purple-colored polymer from 3-ABSa within a pH 4.6 buffered solution. Although not entirely surprising, this fascinating result is entangled by the inherent nature of the substrate, which opens the way to an array of diverse potential oxidation products.

2 Materials and methods

3-Aminobenzenesulphonic acid (3-ABS, 97%), laccase from *T. versicolor* (≥ 0.5 U/mg), 2,2'-azino-bis(3-ethylbenzothiazoline-6-sulphonic acid (ABTS, 98%), methylsyringate (98%) and

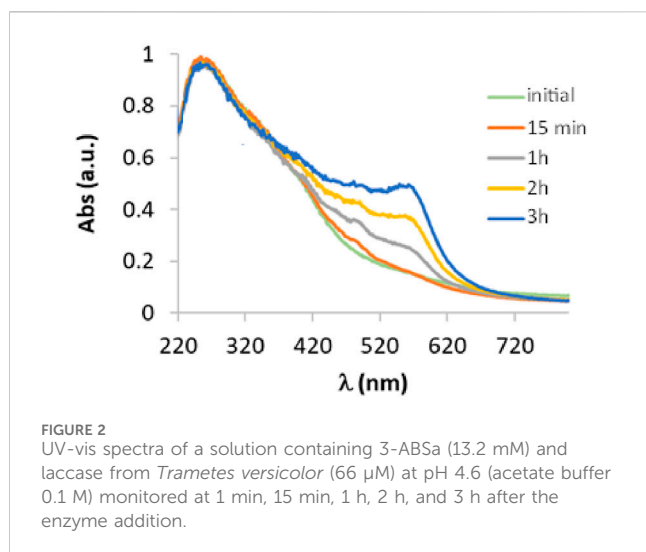


FIGURE 2
UV-vis spectra of a solution containing 3-ABSA (13.2 mM) and laccase from *Trametes versicolor* (66 μ M) at pH 4.6 (acetate buffer 0.1 M) monitored at 1 min, 15 min, 1 h, 2 h, and 3 h after the enzyme addition.

acetylacetone (98%) were purchased by Sigma-Aldrich. All solutions were prepared in deionized H₂O and in acetate buffer 0.1 M at pH = 4.6. The UV-Vis spectrophotometric measurements were conducted using a Perkin Elmer Lambda 900 instrument within the wavelength range of 200–900 nm. A Helma Certified quartz suprasil 10 mm cuvette was employed for the measurements. The reaction was monitored every 15 min for 3 h and then after 24 h. To achieve high-quality spectra, the solutions needed to be diluted fivefold due to the high extinction coefficient of the emerging absorption. Lyophilization and Chromatographic Separation: to determine the yield of the dye formation after 3 h and after 24 h and to perform the IR study of the dried product, the dye solution was lyophilized using a Lio5P freeze dryer. The solutions were lyophilized for 24 h. IR spectra of the lyophilized samples were recorded using an Agilent Cary 630 FTIR Instrument. ¹H NMR spectra were recorded at 400 MHz with a Bruker Advance DPX400. Cyclic voltammetry was conducted using a BAS 100 W potentiostat. The experiment employed a low-volume electrochemical cell equipped with an Ag/AgCl (3 M) Reference electrode, a Pt wire Counter electrode and a glassy carbon Working electrode. All the potential values have been converted to use NHE as a reference potential. Spectroelectrochemistry was performed using a quartz cuvette with an optical path length of 1 mm and using a Pt mesh as working electrode.

3 Results and discussion

3.1 UV-vis spectroscopy

To evaluate the catalytic activity of laccase in the oxidation of 3-ABSA, we have mixed a solution of 3-ABSA (13.2 mM) in a 0.1 M acetate buffer at pH 4.6 with a solution of laccase (66 μ M) at the same pH. The molar ratio of laccase to precursor was therefore 1:200. Throughout the experiment, we continuously monitored the reaction using UV-vis spectroscopy at regular 15-minute intervals over 3 h, followed by a final assessment after 24 h. The initial spectra (up to 3 h of reaction) are depicted in Figure 2. Clearly, the most prominent feature is the emergence of a band at 565 nm, which steadily intensifies. Additionally, there is a visible band at 300 nm with a broad

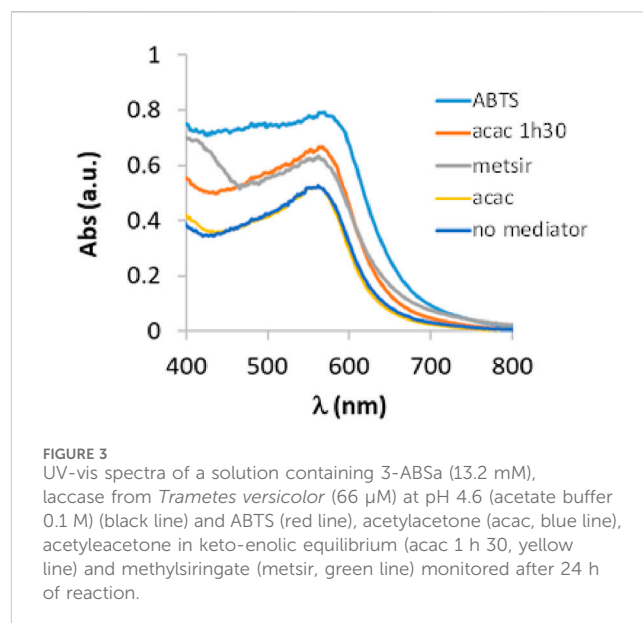
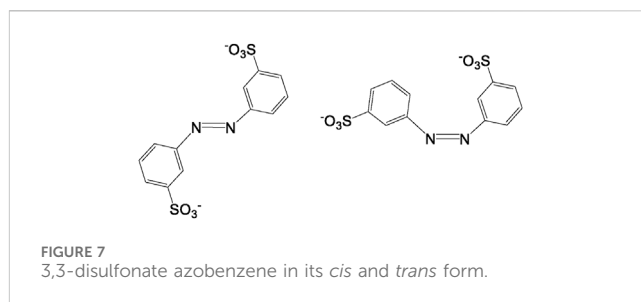
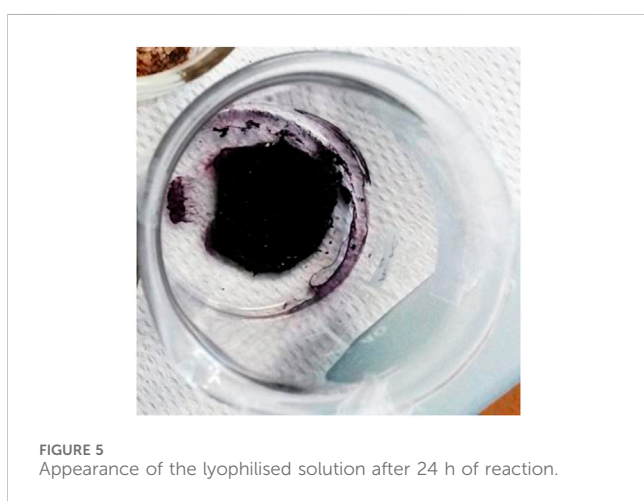
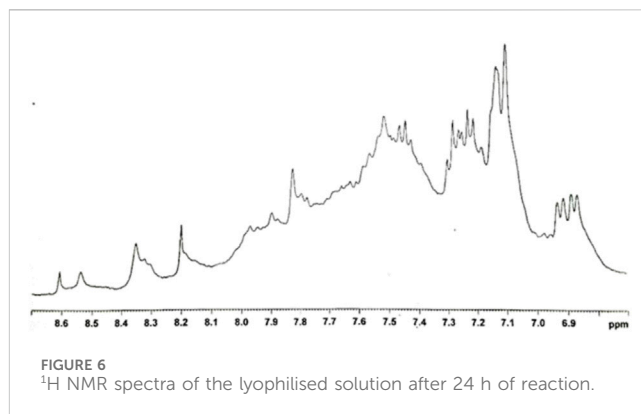
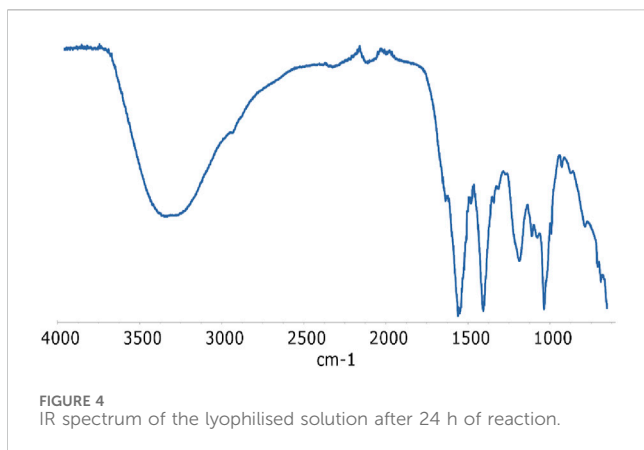


FIGURE 3
UV-vis spectra of a solution containing 3-ABSA (13.2 mM), laccase from *Trametes versicolor* (66 μ M) at pH 4.6 (acetate buffer 0.1 M) (black line) and ABTS (red line), acetylacetone (acac, blue line), acetylacetone in keto-enolic equilibrium (acac 1 h 30, yellow line) and methylsyringate (metsir, green line) monitored after 24 h of reaction.

shoulder at ~380 nm, and its intensity remains relatively constant. Furthermore, there is a shoulder around 410 nm that gradually increases. Since it is well-established that the catalytic activity of laccase can be expanded to a broader range of substrates by employing mediators, we also investigated the influence of the presence of three possible mediators: ABTS, acetylacetone, and methylsyringate, on the oxidation process. Moreover, in the case of acetylacetone we repeated the experiment using a solution that had been previously allowed to rest for 1 h and 30 min to reach the keto-enolic equilibrium. This allowed us to observe the impact of the keto-enolic equilibrium on the mediator efficiency. In all cases, the mediators were present at a concentration of 0.66 mM, resulting in a laccase: mediator:substrate ratio of 1:10:200. In Figure 3, we compare the UV-vis spectra of reactions in the presence of these mediators. Specifically, we examine the spectra obtained in the presence of the laccase-mediator (mediators: ABTS, acetylacetone, methylsyringate) with the reaction run solely in the presence of the precursor without any mediator. The high energy region of the spectra shows slight differences for each of the experiments, primarily because this is the region where the mediators have their own absorptions. However, after 24 h, all the spectra consistently display a prominent band at 565 nm, suggesting that the product formed remains consistent across all cases. Except when non-equilibrated acetylacetone was used, the presence of mediators results in a higher intensity of this band, indicating a certain level of efficiency for the mediators. Although the impact of mediators on the reaction yield is apparent, it is important to recognize that the reaction still occurs even in their absence. Consequently, to streamline the product characterization process and prevent interference from mediators, we exclusively investigated the laccase-precursor reaction for the remainder of our study.

3.2 FTIR spectroscopy

Regrettably, infrared spectroscopy did not prove very useful in identifying all the relevant functional groups within the lyophilized product for characterization. The IR spectrum (Figure 4) is largely

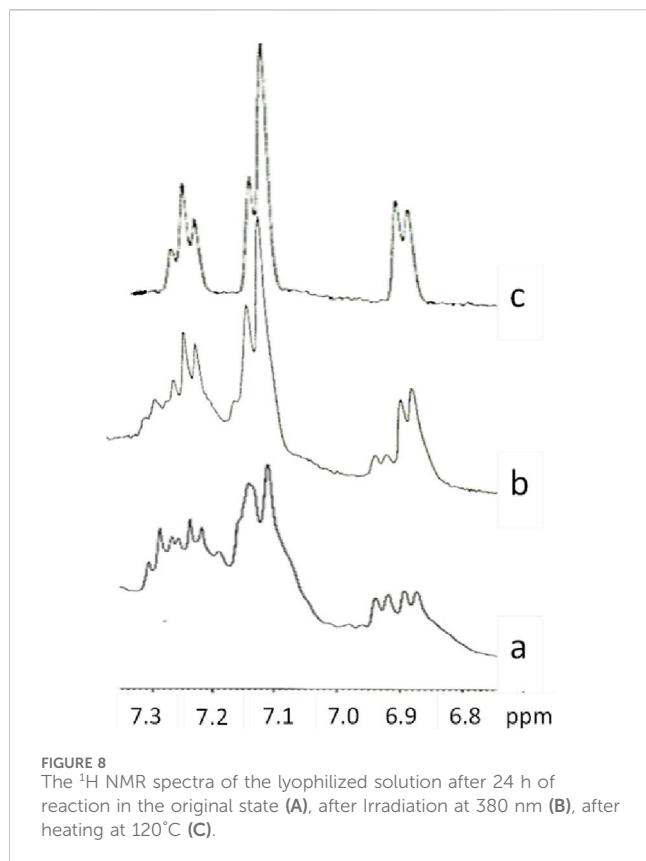


influenced by signals arising from sodium acetate, which originates from the acetate buffer. Therefore, the stretching vibrations associated with the carboxylic group of sodium acetate (at 1,554 and 1,403 cm^{-1}) dominate a critical region of interest for characterizing PANI compounds and somehow obscure the bands of quinonoid $\nu(\text{C}=\text{C})_{\text{Q}}$ and benzenoid $\nu(\text{C}=\text{C})_{\text{B}}$ ring stretching vibrations expected at $\sim 1,560$ and $1,490 \text{ cm}^{-1}$, respectively. The aromatic region (typically characterized by intense and sharp signals) in the $600\text{--}900 \text{ cm}^{-1}$ range also appears ambiguous. Anyway, the presence of the SO_3^- group is revealed by the peaks at 1,185 and $1,034 \text{ cm}^{-1}$, which may be assigned to symmetric and asymmetric stretching of the $\text{S}=\text{O}$ group (Krishnamoorthy et al., 2002). $\nu(\text{N-H})$ stretching modes are also visible around $3,350 \text{ cm}^{-1}$ and give a relevant indication on the oxidation state of the compound, since these modes are consistent with the partially oxidized (emeraldine) form of the polymer, while they are not present in the fully oxidized (pernigriline) form.

3.3 ^1H -NMR measurements

To get dry samples appropriate for the preparation of solutions in deuterated water, the purple solution has been lyophilized

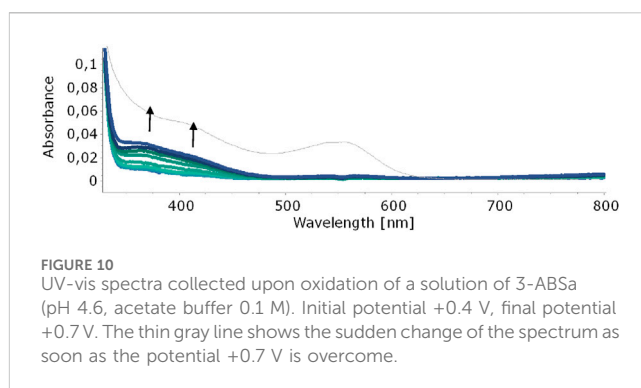
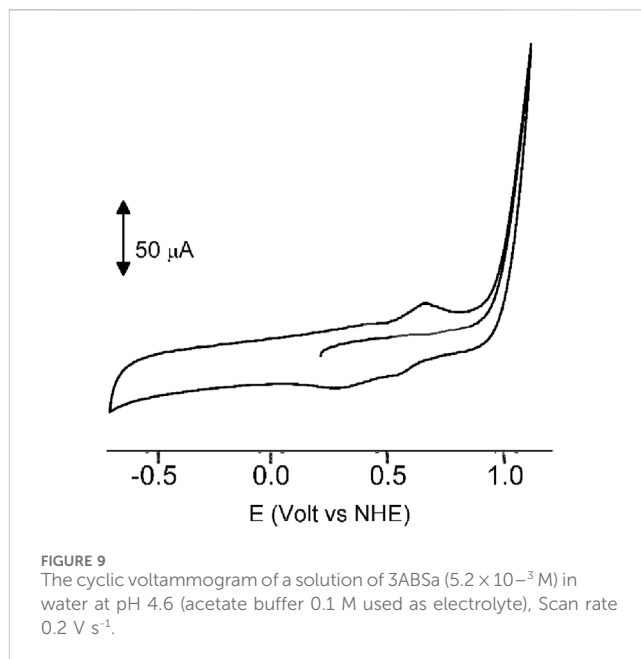
(Figure 5) and subsequently heated. The heating temperature was decided after having checked the behavior of the compound upon heating. Thus, samples obtained after different reaction times were tested to define a melting point. We observed that all the samples, however obtained, darken at around 200°C and it is not possible to detect a precise melting point. Given these considerations, to prevent samples decomposition, we opted to desiccate them by heating at 120°C (for 15 h). However, heating to this temperature also produced a change in the color of the samples. It is noteworthy that when the reaction between 3-ABSA and laccase was interrupted after 3 h, heating induced a significant color alteration in the resulting sample, which shifted from purple to brown-yellow. However, when the reaction had continued for 24 h, the color variation upon heating was less pronounced, transitioning from purple to brownish-violet. Therefore, we have further investigated the NMR analysis of the most stable product, obtained after 24 h of reaction. In Figure 6, we present the ^1H NMR spectrum of the purple sample obtained after 24 h of reaction, lyophilized, but not heated. The presence of two evident doublets at 6.87–6.91 ppm is highly suggestive of the presence of two isomeric forms. In a more precise interpretation, the region from 6.8 to 7.4 ppm can be interpreted as due to overlapping patterns arising from the signals of two isomers, both featuring a meta-aromatic substitution. Each of these overlapping patterns consists of the following components: a doublet, a singlet overlapping a doublet and a triplet. These features strongly suggest the presence of 3,3'-bis(sulfonate) azobenzene in its *cis* and *trans* forms (Figure 7). The remaining portion of the NMR spectrum consists of irregular peaks that are challenging to characterize, as is typical of polymers. To further investigate the presence of azobenzene isomers, which often exhibit



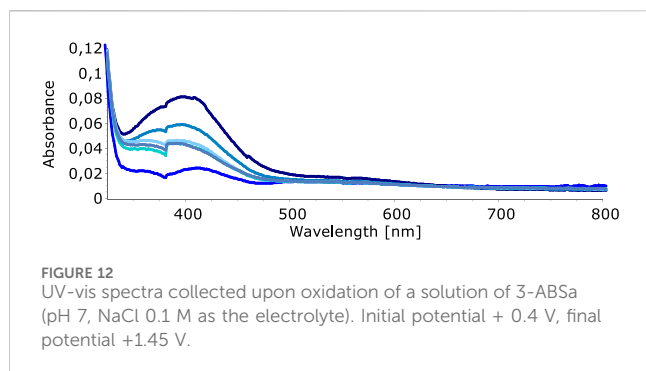
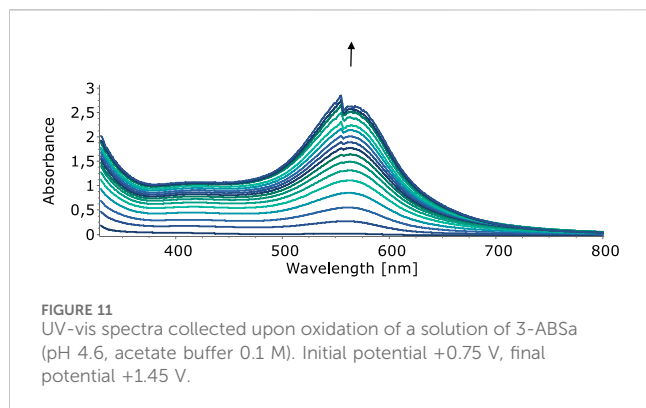
photoisomerization capabilities, we irradiated this sample with two different wavelengths, selected from those corresponding to the maximum absorption in the UV spectrum. We observed that while irradiation with a wavelength of 550 nm has no effect, irradiation at 380 nm leads to the gradual increase of the doublet signal at 6.87 ppm, at the expense of the signal at 6.91 ppm, which decreases (Figure 8). Furthermore, the spectral region between 7.0 ppm and 7.4 ppm reveals a significantly simplified structure, with the distinctive pattern of a meta-substituted aromatic compound (two doublets, one singlet and one triplet) becoming distinctly apparent. When heating the sample at 120°C, we observe a similar effect, as depicted in Figure 8C and the ^1H NMR spectrum confirms the existence of only one isomer. It is important to note that only the discussed region of the ^1H NMR spectrum exhibits alterations, while the remaining part of the spectrum remains unchanged. This behavior suggests that in the sample obtained through the oxidation of 3-ABSA catalyzed by laccase over 24 h, there is the simultaneous presence of two compounds, one of which is photoisomerizable. It is reasonable to assume that these compounds are 3,3'-bis(sulfonate) azobenzene (in both *cis* and *trans* forms) and a polymer of sulfonated aniline, SPANI.

3.4 Electrochemistry and spectroelectrochemistry

In our quest to understand the oxidation mechanism of 3-ABSA and to characterize the resulting species, we conducted electrochemical and spectroelectrochemical measurements.



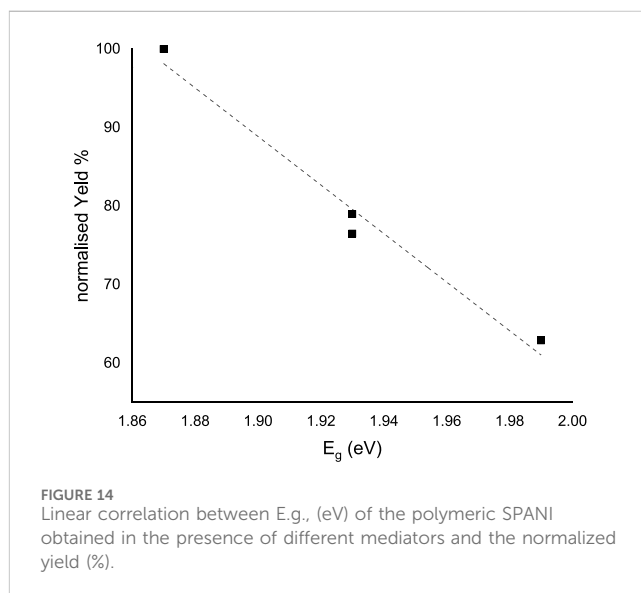
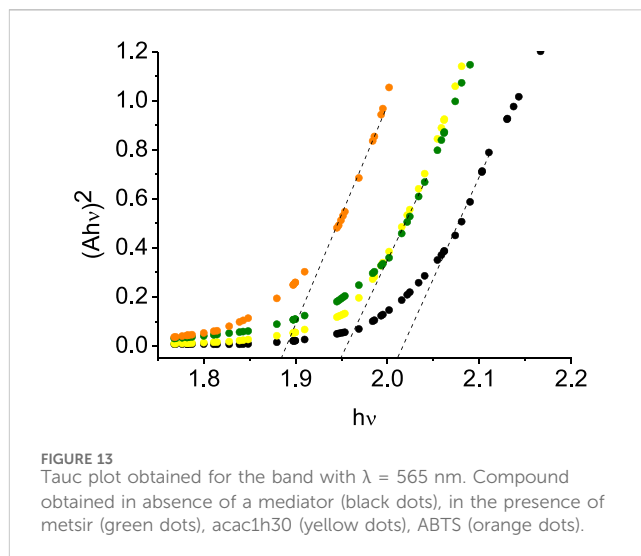
During these experiments, we induced the oxidation of 3-ABSA without laccase, keeping all other experimental conditions constant. Figure 9 shows the cyclic voltammogram of an aqueous solution of 3-ABSA (pH = 4.6, acetate buffer as electrolyte). During the initial anodic potential scan, we observed an irreversible oxidation process near the point of solvent discharge. This phenomenon appears as an offset at +0.9 V. Interestingly, immediately after surpassing this potential and initiating the oxidation of 3-ABSA, a purple coloration became visible near the electrode. As the positive potential scan continued, the species diffused into the bulk solution, eventually causing the entire solution to turn purple. On the back scan, around +0.55 V, we observed a cathodic peak, likely corresponding to the reduction of the recently formed and transient radical cation 3-ABSA $^{\bullet+}$. On the other hand, the cathodic current peak observed at +0.35 V is attributed to the reduction of the oligomeric or polymeric chains of sulfonated polyaniline, which then undergo an oxidation at +0.65 V. During potential cycling, the redox peaks associated to the redox change of SPANI oligomers/polymers exhibited only a slight increase and we did not observe the electrodeposition of a film on the electrode surface. Instead, colored soluble oligomeric/polymeric products were observed streaming away from the electrode surface.



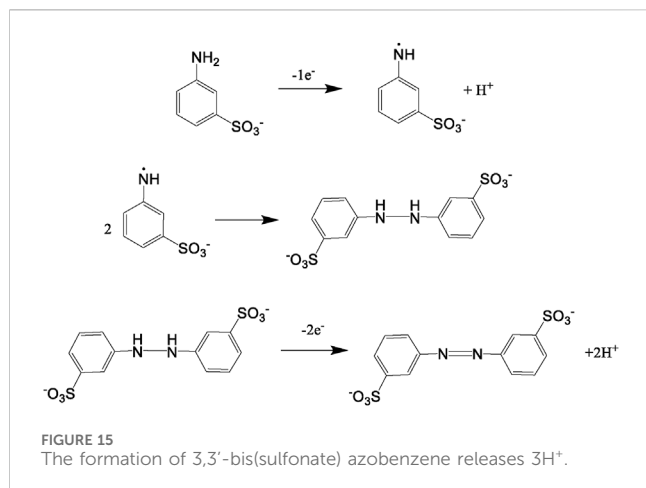
In **Figures 10, 11**, we show the UV-vis spectra obtained during the spectroelectrochemical analysis of 3-ABSa at pH 4.6. This analysis involved collecting spectra while varying the potential from +0.4 V to +1.45 V. As the potential approaches +0.7 V, we clearly observe two overlapping bands at 370 nm and 410 nm, which exhibit slight growth (see **Figure 10**). However, when the potential reaches +0.9 V, a broad and extremely intense band centered at 565 nm suddenly appears and dominates the spectral aspect (see **Figure 11**). When the experiment is repeated at pH = 7 with NaCl as the electrolyte, we observe the following spectral behavior upon oxidation: the bands at 370 nm and 410 nm appear, while the band expected at 565 nm is dramatically diminished and is almost never visible (**Figure 12**). This intriguing behavior can be elucidated by considering that the species formed during the oxidation of 3-ABSa at pH = 7 may also be the same species that forms in the initial phase of oxidation at pH = 4.6. This species likely corresponds to sulfonated azobenzene. On the other hand, during more vigorous oxidation at pH = 4.6, the resulting species likely consists of purple-colored SPANI oligomers.

4 Discussion

When 3-ABSa undergoes oxidation, whether through enzymatic processes or electrochemistry, it produces a purple product characterized by a broad peak around 565 nm. Previous studies have associated this absorption band with an exciton-like transition occurring in the quinoid diimino units of the conducting semioxidized (emeraldine) form (**Krishnamoorthy et al., 2002**;



Madhurima et al., 2019). Additionally, there is another absorption band observed at ~300 nm, which is attributed to a $\pi-\pi^*$ transition in benzenoid units. Remarkably, during spectroelectrochemical experiments, we observe spectra that reveal additional bands at 370 nm and 410 nm. These bands are typically not present in previous studies on SPANI, especially those conducted in strongly acidic media. Later, we will delve into more detail, but it is reasonable to associate these two bands with the presence of 3,3'-bis(sulfonated) azobenzene. Focusing specifically on the absorption band at 565 nm, it is noteworthy that in the presence of mediators, this band experiences a slight blue shift following the order: λ_{max} (no-mediator) \approx acac < metsyn \leq acac1h30 < ABTS. This shift could be attributed to the improved orientation and an associated increase in the conjugation length of the SPANI chain. To determine the optical absorption band gap ($E_{g, \text{opt}}$) of the polymer obtained under different experimental conditions, we employed the



Tauc relation, assuming a direct and allowed electronic transition (Tauc, 1972):

$$(Ah\nu)^2 = k(h\nu - E_g)$$

where A is the Absorption (in arbitrary units) and k is a constant. Figure 13 shows the plot of $(Ah\nu)^2$ vs. $h\nu$. The estimated band gap values range from 2.00 eV (SPANI obtained without a mediator or with acac) to 1.87 eV (SPANI obtained in the presence of ABTS). The reduction in the band gap implies that the presence of a mediator promotes the aligned arrangement of SPANI chains. This phenomenon appears to be linked to the efficiency of the SPANI formation process. As depicted in Figure 14, the optical band gap values ($E_{g, \text{opt}}$) exhibit a positive correlation with the SPANI yield obtained under various conditions (normalized with respect to the maximum yield, achieved in the reaction with ABTS). Although the precise reason behind this correlation remains undisclosed, it is highly plausible that a well-organized and highly conjugated polymer would yield superior outcomes. Having confirmed the presence of SPANI, spectroelectrochemistry has proven to be particularly useful in revealing the formation of 3,3'-bis(sulfonated) azobenzene as a byproduct. Notably, the spectra collected during oxidation at pH 4.6 exhibit an initial evolution that differs from what is observed as the potential becomes more positive. According to the literature (Desideri et al., 1973), when the pH is only moderately acidic, the oxidation of aminobenzenesulfonic acids predominantly leads to the formation of sulfonated azobenzene compounds. This occurs via a radical intermediate, as depicted in Figure 15. Therefore, a plausible interpretation of the behavior observed through spectroelectrochemistry is that at the outset, the reaction begins under mildly acidic conditions and 3,3'-bis(sulfonated) azobenzene (bands at 370 and 410 nm) initially forms as a byproduct of the oxidation of 3-ABSa. However, as the process unfolds, the release of 3 H⁺ ions from the oxidation of 3-ABSa lowers the local pH into the high acidity region, and 3-ABSa oligomers (band at 565 nm) emerge in the advanced stage, when the local acidity reaches a critical level. This hypothesis is confirmed by the spectroelectrochemical experiment conducted at pH = 7, which reveals the appearance of only the bands around 380 nm and 410 nm. This gives indication that at this specific pH value, only the azobenzene derivative forms. Finally, the

presence of 3,3'-bis(sulfonated) azobenzene in its two isomers, which forms alongside SPANI, is confirmed by NMR experiments and irradiation experiments. These experiments demonstrate a selective variation in one part of the spectrum due to irradiation, while another part remains unchanged. This behavior aligns with what one would expect from a mixture of SPANI and azobenzene derivatives.

5 Conclusion

In conclusion, we have demonstrated that sulfonated polyaniline polymer SPANI can be easily obtained through the oxidation of 3-ABSa, catalyzed by laccase from *T. versicolor*. This process can be carried out under environmentally friendly conditions, using water at moderate pH values, room temperature and without the need for additional reagents. However, SPANI is not obtained as a sole product; rather, its formation is accompanied by 3,3'-bis(sulfonated) azobenzene. It is reasonable to think that achieving a higher production of SPANI could be possible by operating at a lower pH. However, excessively low pH values are incompatible with laccase enzymes: even fungal laccases, which typically perform better in acidic conditions, have their optimal pH value around 4 (Arregui et al., 2019). In the future, investigating optimal pH values to maximize SPANI production and exploring how these pH values impact the length of polymer chains could yield valuable insights.

Data availability statement

The original contributions presented in the study are included in the article/Supplementary Material, further inquiries can be directed to the corresponding author.

Author contributions

FF: Conceptualization, Data curation, Formal Analysis, Investigation, Methodology, Visualization, Writing—original draft, Writing—review and editing. MC: Formal Analysis, Investigation, Methodology, Writing—review and editing. RP: Validation, Writing—review and editing. MB: Conceptualization, Data curation, Methodology, Writing—review and editing.

Funding

The author(s) declare that financial support was received for the research, authorship, and/or publication of this article. The University of Siena is acknowledged for its contribution to the publication fee.

Conflict of interest

The authors declare that the research was conducted in the absence of any commercial or financial relationships that could be construed as a potential conflict of interest.

Publisher's note

All claims expressed in this article are solely those of the authors and do not necessarily represent those of their affiliated

organizations, or those of the publisher, the editors and the reviewers. Any product that may be evaluated in this article, or claim that may be made by its manufacturer, is not guaranteed or endorsed by the publisher.

References

- Amann, M. (1997). "The lignozym[®] process coming closer to the mill," in 9th International Symposium on Wood and Pulp Chemistry, Montreal, Quebec, Canada, June 9–12, 1997, 1–5.
- Arregui, L., Ayala, M., Gómez-Gil, X., Gutiérrez-Soto, G., Hernández-Luna, C. E., Herrera de los Santos, M., et al. (2019). Laccases: structure, function, and potential application in water bioremediation. *Microb. Cell Fact.* 18, 200. doi:10.1186/s12934-019-1248-0
- Bergeron, J. Y., Chevalier, J. W., and Dao, L. H. (1990). Water-soluble conducting poly (aniline) polymer. *Chem. Comm.*, 180–183. doi:10.1039/c39900000180
- Bhadra, J., Alkareem, A., and Al-Thani, N. (2020). A review of advances in the preparation and application of polyaniline based thermoset blends and composites. *J. Polym. Res.* 27, 122. doi:10.1007/s10965-020-02052-1
- Bourbonnais, R., Leech, D., and Paice, M. G. (1998). Electrochemical analysis of the interactions of laccase mediators with lignin model compounds. *Biochim. Biophys. Acta* 1379, 381–390. doi:10.1016/s0304-4165(97)00117-7
- Chan, H. S. O., Ng, S. C., Wong, P. M. L., Neuendorf, A. J., and Young, D. J. (1998). Synthesis of fully sulfonated polyaniline: a novel approach using oxidative polymerisation under high pressure in the liquid phase. *Chem. Commun.* 1327, 1327–1338. doi:10.1039/a802970i
- Chen, Z., Liu, H., Lin, X., Mei, X., Lyu, W., and Liao, Y. (2023). Competitive proton-trapping strategy enhanced anti-freezing organohydrogel fibers for high-strain-sensitivity wearable sensors. *Mat. Horiz.* 10, 3569–3581. doi:10.1039/d3mh00459g
- Clark, J. H. (1999). Green chemistry: challenges and opportunities. *Green Chem.* 1, 1–8. doi:10.1039/a807961g
- Desideri, P. G., Lepri, L., and Heimler, D. (1973). Electrochemical behavior of the aminobenzenesulfonic acids in aqueous solutions. *Electroanal. Chem. Interf. Electrochem.* 43, 387–396. doi:10.1016/s0022-0728(73)80279-7
- Freund, M. S., and Bhavana, A. D. (2007). "Self-Doped derivatives of polyaniline," in *Self-doped conducting polymers* (John Wiley and Sons, Ltd), 75–155.
- Han, J., Xing, W., Yan, J., Wen, J., Liu, Y., Wang, Y., et al. (2022). Stretchable and superhydrophilic polyaniline/halloysite decorated nanofiber composite evaporator for high efficiency seawater desalination. *Adv. Fiber Mat.* 4, 1233–1245. doi:10.1007/s42765-022-00172-5
- Jiang, Y., and Epstein, A. J. (1990). Synthesis of self-doped conducting polyaniline. *J. Am. Chem. Soc.* 112, 2800–2801. doi:10.1021/ja00163a051
- Karamyshev, A. V., Shleev, S. V., Koroleva, O. V., Yaropolov, A. I., and Sacharov, I. Y. (2003). Laccase-catalyzed synthesis of conducting polyaniline. *Enz. Microb. Techn.* 33, 556–564. doi:10.1016/s0141-0229(03)00163-7
- Kitani, A., Satoguchi, K., Tang, H.-Q., Ito, S., and Sasaki, K. (1995). Eletrosynthesis and properties of self-doped polyaniline. *Synth. Metall.* 69, 129–130. doi:10.1016/0379-6779(94)02387-e
- Krishnamoorthy, K., Contractor, A. Q., and Kumar, A. (2002). Electrochemical synthesis of fully sulfonated n-dopable polyaniline: poly (metanillic acid). *Chem. Commun.*, 240–241. doi:10.1039/b110157a
- Lyu, W., Li, J., Trchová, M., Wang, G., Liao, Y., Bober, P., et al. (2022). Fabrication of polyaniline/poly(vinyl alcohol)/montmorillonite hybrid aerogels toward efficient adsorption of organic dye pollutants. *J. Hazard. Mat.* 435, 129004–129007. doi:10.1016/j.jhazmat.2022.129004
- Lyu, W., Li, J., Zheng, L., Liu, H., Chen, J., Zhang, W., et al. (2021). Fabrication of 3D compressible polyaniline/cellulose nanofiber aerogel for highly efficient removal of organic pollutants and its environmental-friendly regeneration by peroxydisulfate process. *Chem. Eng. J.* 414, 128931–128933. doi:10.1016/j.cej.2021.128931
- Lyu, W., Zhang, W., Liu, H., Liu, Y., Zuo, H., Yan, C., et al. (2020). Conjugated microporous polymer network grafted carbon nanotube fibers with tunable redox activity for efficient flexible wearable energy storage. *Chem. Mat.* 32, 8276–8285. doi:10.1021/acs.chemmater.0c02089
- Madhurima, D., Siddhartha, S. B., and Somenath, R. (2019). Poly(m-amino benzene sulfonic acid)-based composites on plastic substrates: a simple and cost effective approach towards low ppm ammonia detection at room temperature and kinetic analysis. *Synth. Metall.* 248, 1–13. doi:10.1016/j.synthmet.2018.12.019
- Majeed, A. H., Mohammed, L. A., Hammoodi, O. G., Sehgal, S., Alheety, M. A., Saxena, K. K., et al. (2022). A review on polyaniline: synthesis, properties, nanocomposites, and electrochemical applications. *Int. J. Pol. Sci.* 2022, 1–19. doi:10.1155/2022/9047554
- Márquez, A. G. C., Rodríguez, L. M. T., and Rojas, A. M. (2007). Synthesis of fully and partially sulfonated polyanilines derived from ortanilic acid: an electrochemical and electromicrogravimetric study. *Electrochim. Acta* 52, 5294–5303. doi:10.1016/j.electacta.2007.02.048
- Mav, I., Zigon, M., and Sebenik, A. (1999). Sulfonated polyaniline. *Synth. Met.* 101, 717–718. doi:10.1016/s0379-6779(98)01166-7
- Modarresi-Alam, A. R., Zeraatkar, V., Tabatabaei, F. A., Bazrafkan, M., Dastgerdi, A. S., and Malekmakan, R. (2019). A solid-state synthesis, mechanism, and characterization of high molecular weight poly (3-aminobenzenesulfonic acid) with FeCl₃·6H₂O as a binary oxidant and dopant. *J. Polym. Res.* 26, 22. doi:10.1007/s10965-018-1674-4
- Polak, J., and Jarosz-Wilkolazka, A. (2010). Whole-cell fungal transformation of precursors into dyes. *Microb. Cell Fact.* 9, 51. doi:10.1186/1475-2859-9-51
- Reinhammar, B. R. M. (1972). Oxidation–reduction potentials of the electron acceptors in laccases and stellacyanin. *Biochim. Biophys. Acta* 275, 245–259. doi:10.1016/0005-2728(72)90045-x
- Walde, P., Kashima, K., and Čirić-Marjanović, G. (2019). Synthesizing polyaniline with laccase/O₂ as catalyst. *Front. Bioeng. Biotech.* 7, 165. doi:10.3389/fbioe.2019.00165
- Xu, F., Shin, W., Brown, S. H., Wahleithner, J. A., Sundaram, U. M., and Solomon, E. I. (1996). A study of a series of recombinant fungal laccases and bilirubin oxidase that exhibit significant differences in redox potential, substrate specificity, and stability. *Biochim. Biophys. Acta* 1292, 303–311. doi:10.1016/0167-4838(95)00210-3
- Yano, J., Hata, C., and Yamasaki, S. (1999). Cation immobilizing ability of an aramid resin film fixing metanilic acid oligomer. *Electrochem. Solid-State Lett.* 11, 564–566. doi:10.1149/1.1390905
- Yue, J., Gordon, G., and Epstein, A. J. (1992). Comparison of different synthetic routes for sulphonation of polyaniline. *Polymer* 33, 4410–4418. doi:10.1016/0032-3861(92)90288-8
- Yue, J., Wang, Z. H., Cromack, K. R., Epstein, A. J., and MacDiarmid, A. G. (1991). Effect of sulfonic acid group on polyaniline backbone. *J. Am. Chem. Soc.* 113, 2665–2671. doi:10.1021/ja00007a046
- Zeng, Z., Chen, Y., Zhu, X., and Yu, L. (2023). Polyaniline-supported nano metal-catalyzed coupling reactions: opportunities and challenges. *Chem. Lett.* 34, 107728–107731. doi:10.1016/j.ccl.2022.08.008
- Zhang, L., Jiang, X., Niu, L., and Dong, S. (2006). Syntheses of fully sulfonated polyaniline nano-networks and its application to the direct electrochemistry of cytochrome c. *Biosens. Bioelectr.* 21, 1107–1115. doi:10.1016/j.bios.2005.04.004
- Zheng, Y., Man, Z., Zhang, Y., Wu, G., Lu, W., and Chen, W. (2023). High-performance stretchable supercapacitors based on centrifugal electrospinning-directed hetero-structured graphene–polyaniline hierarchical fabric. *Adv. Fiber Mat.* 5, 1759–1772. doi:10.1007/s42765-023-00304-5
- Tauc, J. (1972). in *Optical properties of solids* (North Holland, Amsterdam: Abeles).



OPEN ACCESS

EDITED BY

Claudia Espro,
University of Messina, Italy

REVIEWED BY

Srajan Kapoor,
University at Buffalo, United States
Dharmendra Kumar Yadav,
Gachon University, Republic of Korea

*CORRESPONDENCE

Teresa Santos-Silva,
✉ tsss@fct.unl.pt

†PRESENT ADDRESSES

Filipe Freire, iBET, Instituto de Biologia
Experimental e Tecnológica, Oeiras, Portugal,
Instituto de Tecnologia Química e Biológica
António Xavier, Universidade Nova de Lisboa,
Oeiras, Portugal
Jayaraman Muthukumar, Department of Biotechnology, Sharda School
of Engineering and Technology, Sharda
University, Greater Noida, India
João Ramos, Department of Molecular Biology and Genetics,
Aarhus University, Aarhus, Denmark
Dmitri Svergun, BIOSAXS GmbH, Hamburg, Germany
Henrique S. Fernandes, Sérgio F. Sousa, LAQV/
REQUIMTE, Departamento de Biomedicina,
BioSIM—Faculdade de Medicina da
Universidade do Porto, Porto, Portugal

RECEIVED 31 January 2024

ACCEPTED 28 June 2024

PUBLISHED 06 August 2024

CITATION

Paquete-Ferreira J, Freire F, Fernandes HS,
Muthukumar J, Ramos J, Bryton J,
Panjkovich A, Svergun D, Santos MFA,
Correia MAS, Fernandes AR, Romão MJ,
Sousa SF and Santos-Silva T (2024), Structural
insights of an LCP protein—LytR—from
Streptococcus dysgalactiae subs. *dysgalactiae*
through biophysical and *in silico* methods.
Front. Chem. 12:1379914.
doi: 10.3389/fchem.2024.1379914

COPYRIGHT

© 2024 Paquete-Ferreira, Freire, Fernandes,
Muthukumar, Ramos, Bryton, Panjkovich,
Svergun, Santos, Correia, Fernandes, Romão,
Sousa and Santos-Silva. This is an open-access
article distributed under the terms of the
Creative Commons Attribution License (CC BY).
The use, distribution or reproduction in other
forums is permitted, provided the original
author(s) and the copyright owner(s) are
credited and that the original publication in this
journal is cited, in accordance with accepted
academic practice. No use, distribution or
reproduction is permitted which does not
comply with these terms.

Structural insights of an LCP protein—LytR—from *Streptococcus dysgalactiae* subs. *dysgalactiae* through biophysical and *in silico* methods

João Paquete-Ferreira^{1,2}, Filipe Freire^{2†},
Henrique S. Fernandes^{3,4†}, Jayaraman Muthukumar^{2†},
João Ramos^{2†}, Joana Bryton^{1,2}, Alejandro Panjkovich⁵,
Dmitri Svergun^{5†}, Marino F. A. Santos^{1,2}, Márcia A. S. Correia^{1,2},
Alexandra R. Fernandes^{1,6}, Maria João Romão^{1,2},
Sérgio F. Sousa^{3,4†} and Teresa Santos-Silva^{1,2*}

¹Associate Laboratory i4HB—Institute for Health and Bioeconomy, NOVA School of Science and Technology, Universidade NOVA de Lisboa, Caparica, Portugal, ²UCIBIO—Applied Molecular Biosciences Unit, Department of Chemistry, NOVA School of Science and Technology, Universidade NOVA de Lisboa, Caparica, Portugal, ³Associate Laboratory i4HB—Institute for Health and Bioeconomy, University of Porto, Porto, Portugal, ⁴UCIBIO—Applied Molecular Biosciences Unit, Faculty of Medicine, University of Porto, Porto, Portugal, ⁵European Molecular Biology Laboratory, Hamburg Unit, Deutsches Elektronen-Synchrotron, Hamburg, Germany, ⁶UCIBIO—Applied Molecular Biosciences Unit, Department of Life Sciences, NOVA School of Science and Technology, Universidade NOVA de Lisboa, Caparica, Portugal

The rise of antibiotic-resistant bacterial strains has become a critical health concern. According to the World Health Organization, the market introduction of new antibiotics is alarmingly sparse, underscoring the need for novel therapeutic targets. The LytR-CpsA-Psr (LCP) family of proteins, which facilitate the insertion of cell wall glycopolymers (CWGPs) like teichoic acids into peptidoglycan, has emerged as a promising target for antibiotic development. LCP proteins are crucial in bacterial adhesion and biofilm formation, making them attractive for disrupting these processes. This study investigated the structural and functional characteristics of the LCP domain of LytR from *Streptococcus dysgalactiae* subsp. *dysgalactiae*. The protein structure was solved by X-ray Crystallography at 2.80 Å resolution. Small-angle X-ray scattering (SAXS) data were collected to examine potential conformational differences between the free and ligand-bound forms of the LytR LCP domain. Additionally, docking and molecular dynamics (MD) simulations were used to predict the interactions and conversion of ATP to ADP and AMP. Experimental validation of these predictions was performed using malachite green activity assays. The determined structure of the LCP domain revealed a fold highly similar to those of homologous proteins while SAXS data indicated potential conformational differences between the ligand-free and ligand-bound forms, suggesting a more compact conformation during catalysis, upon ligand binding. Docking and MD simulations predicted that the LytR LCP domain could interact with ADP and ATP and catalyze their conversion to AMP. These predictions were experimentally validated by malachite green activity assays, confirming the protein's functional versatility. The study provides significant insights into the

structural features and functional capabilities of the LCP domain of LytR from *S. dysgalactiae* subsp. *dysgalactiae*. These findings pave the way for designing targeted therapies against antibiotic-resistant bacteria and offer strategies to disrupt bacterial biofilm formation.

KEYWORDS
LytR-CpsA-Psr, X-ray diffraction, SAXS, molecular dynamics, docking, wall teichoic acids, pyrophosphatase

1 Introduction

The bacterial cell wall is the first line of contact for the cell with the environment. It is responsible for functions related to protection and communication with the surroundings, but it also plays a very important structural role in preserving the cell’s shape and increasing resistance to mechanical stress (Cabeen and Jacobs-Wagner, 2005).

In Gram-positive bacteria, the cell wall is constituted of a thick layer of peptidoglycan decorated with polymers and glycopolymers (Siegel et al., 2016). These modifications confer different properties to the cell wall, affecting porosity, charge, communication, and protection. In fact, some of these polymers are essential for cell viability and pathogenesis (Weidenmaier and Peschel, 2008).

The wall teichoic acids (WTAs) are among these polymers. They make up most of the polymers present in the cell wall, representing up to 60% of its total mass. Unlike their counterpart, lipoteichoic acids (LTAs), WTAs are not anchored to the cell membrane but are covalently attached to the peptidoglycan through a phosphodiester bond between the WTAs and the C6 hydroxyl group of the N-Acetylmuramic acid (MurNAc) residues of the peptidoglycan (Brown et al., 2013). Nevertheless, both types of teichoic acids, WTAs and LTAs, share a general structure consisting of a linkage unit and a long main chain. In the case of the WTAs, the linkage unit holds an N-Acetylmannosamine (ManNAc) (β1→4) N-Acetylglucosamine (GlnNAc)-1-phosphate and a small chain of glycerol 3-phosphate, whereas the LTAs linkage unit consists of a glycolipid that varies among the different types of LTAs. The main chain of both glycopolymers contains different repeating units, generally glycerol 3-phosphate or ribitol 5-phosphate, that can be further decorated (Brown et al., 2013; Chapot-Chartier and Kulakauskas, 2014; Schneewind and Missiakas, 2014).

The structural similarity between WTAs and LTAs leads to some overlapping roles, even if other features are specific to the WTA (Swoboda et al., 2010). One of the important functions of WTAs is the binding of positively charged ions (e.g., Ca²⁺ and Mg²⁺). Since WTAs are more exposed than LTAs, there are numerous negatively charged phosphate groups available for ionic interactions, allowing the cell to keep a storage of metals near the surface. This also creates localized pH changes through modulation of the proton binding capacity (Biswas et al., 2012; Brown et al., 2013). Another important function of the WTAs is related to the cross-linking of the peptidoglycan which occurs after WTAs attachment. It has been suggested that their presence guides the cross-linking process, either by playing scaffolding roles or contributing to stereochemical hindrances (Campbell et al., 2011). This same scaffolding role of the WTAs seems to be important in cell division and morphology (Biswas et al., 2012). Schaefer and

colleagues showed that non-cross-linked peptidoglycan is a suitable substrate for WTAs modification and that WTAs transfer prior to cross-linking suggests that these molecules might have a regulatory role in the cell wall maturation process (Schaefer et al., 2018). However, this is still a debatable topic and further research is necessary (Brown et al., 2013). WTAs have also been considered important for the pathogenesis of some bacteria,

TABLE 1 X-ray Data collection and Refinement statistics of LytR LCP domain from *Streptococcus dysgalactiae* subsp. *dysgalactiae*.

PDB ID	8QTY
Space Group	I 4 2 2
Unit Cell	
(a, b, c), Å	141.27 141.27 133.74
Molecules per Asymmetric Unit	1
Matthews Coefficient	4.98
Solvent Content, %	75
Data Collection	
Distance to detector, cm	34.091
Wavelength, Å	0.966
Collected Images	747
Processed Images	747
Resolution Range, Å	48.56–2.80 (2.95–2.80)
R _{pim}	0.049 (0.885)
Completeness, %	99.9 (99.9)
<I/σ(I)>	15.5 (1.9)
Half-set correlation coefficient, CC _{1/2}	0.999 (0.666)
Observed Reflections	136,196 (20,406)
Unique Reflections	16,955 (2,436)
Multiplicity	8.0 (8.4)
Refinement	
R _{work} /R _{free} %	27.13/29.27
R.M.S.D. Bond Lengths, Å	0.017
R.M.S.D. Bond Angles, °	1.968
Ramachandran Plot	
Favored/Disallowed, %	90.6/0.0

TABLE 2 SAXS sample and analysis for LytR LCP domain.

(a) Sample details		
Organism	<i>Streptococcus dysgalactiae</i> subsp. <i>dysgalactiae</i>	
Source	LytR protein, <i>E. coli</i> (BL21) recombinant expression	
Scattering particle composition	S1 (SASDTH2)	S2 (SASDTG2)
Protein	LytR LCP domain	
Ligand		Geranylgeranyl pyrophosphate
Stoichiometry of components		1:2
Solvent composition	50 mM HEPES pH 8.0, 150 mM NaCl and 5 mM MgCl ₂	
Sample concentration (mg/mL)	3.05	2.19
(b) SAS data collection		
	DESY P12	ESRF BM29
Data-acquisition/reduction software	BECQUEREL	BSXCuBE
Source/instrument description	PETRA III U29 undulator, Pilatus 6M	2 Pole Wiggler, Pilatus3 2M in-vac
Mesaured q-range (q _{min} - q _{max}) (Å ⁻¹)	0.0022–0.482	0.0042–0.522
Exposure time (s), No. of exposures	0.045, 15 frames	10 frames
(c) SAS-derived structural parameters		
Method(s)/software	S1 (SASDTH2)	S2 (SASDTG2)
Guinier analysis		
I (0) ± ? (cm ⁻¹)	11.42 ± 0.069	7.41 ± 0.063
R _g ± ?(nm)	2.3 ± 0.02	2.45 ± 0.03
qRg range (datapoint range)	0.31–1.13 (16–97)	0.36–1.28 (12–94)
Linear fit assessment (AUTORG fidelity)	0.55	0.99
PDDF/P(r) analysis		
I (0) ± ? (cm ⁻¹)	9.17 ± 0.14	7.37 ± 0.054
R _g ± ?(nm)	2.42 ± 0.0068	2.43 ± 0.017
d _{max} (nm)	9.0	8.0
q-range (nm ⁻¹)	0.19–3.37	0.014–0.326
p(r) reciprocal-space fit	0.78	0.69

especially when these polymers are further modified by D-alanylation, as they allow for overcoming the host-defense mechanisms or modulating the host-tissue adhesion during biofilm formation. (Gross et al., 2001), Despite the crucial role of WTAs, they are not considered virulence factors. This is because their absence leads to non-viable or highly defective cells, establishing their biosynthetic pathway as very interesting drug targets for the development of new antibiotics (Brown et al., 2013). Several studies suggest that WTAs depletion is an effective strategy for eliminating bacteria and inhibiting biofilm formation. Brown and colleagues showed that methicillin-resistant *Staphylococcus aureus* (MRSA) mutated strains regain their susceptibility towards methicillin (Campbell et al., 2011; Brown et al., 2012).

Several antibiotics target the cell wall biosynthesis pathway in bacteria, namely, by inhibiting peptidoglycan biosynthesis. However, the increasing number of bacterial strains resistant to common antibiotics urges finding new targets (Årdal et al., 2019; Miethke et al., 2021; Varela et al., 2021). The LytR-CpsA-Psr (LCP) (LytR - autolysin regulator; CpsA-capsule-associated protein A and Psr-penicillin-binding protein regulator) is a family of enzymes responsible for the last step of the assembly of WTA and other cell wall glycopolymers. It has been considered as important drug targets, but so far, no efficient inhibitors have been described (Kawai et al., 2011).

In this work, we studied the LytR protein from the Gram-positive bacterium *Streptococcus dysgalactiae* subsp. *dysgalactiae*

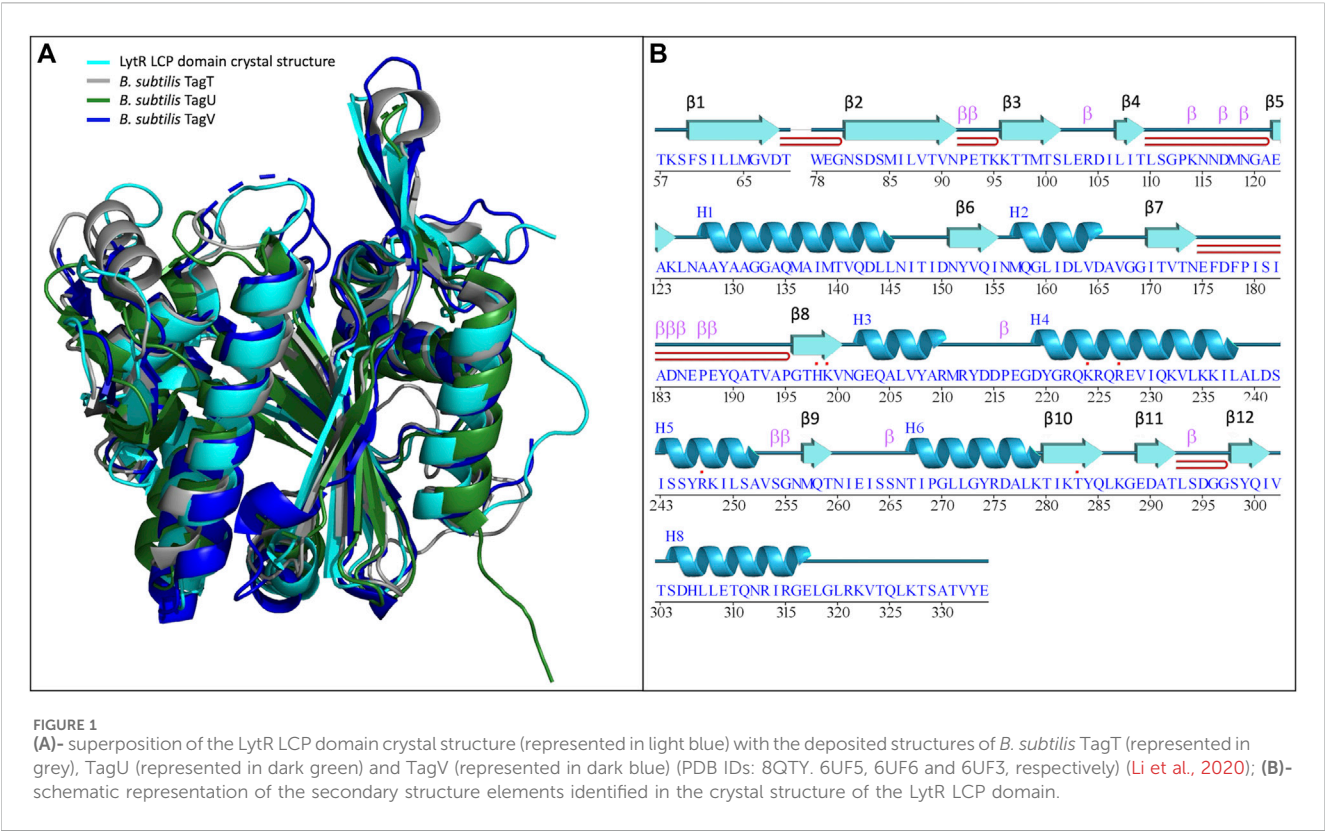


TABLE 3 Comparison of sequence identity and root mean square deviation (R.M.S.D.) values of LytR LCP domain with other deposited models.

Protein	PDB ID	Sequence identity (with LytR)	R.M.S.D. free form vs. ligand bound (aligned C _α)	R.M.S.D. towards LytR (aligned C _α)
TagT from <i>B. subtilis</i>	6UF5 (free form) (Li et al., 2020)	25.6%	-	1.12 Å (168/223)
	6MPS (bound to LIIa-WTA) (Schaefer et al., 2018)		0.44 Å (228/245)	1.06 Å (171/252)
	6MPT (bound to LI-WTA) (Schaefer et al., 2018)		0.27 Å (210/245)	1.16 Å (177/230)
	4DE9 (bound to octaprenyl phosphate) (Eberhardt et al., 2012)		0.30 Å (217/217)	1.15 Å (164/269)
TagU from <i>B. subtilis</i>	6UF6 (Li et al., 2020)	29.7%	-	2.67 Å (169/201)
TagV from <i>B. subtilis</i>	6UF3 (Li et al., 2020)	29.0%	-	1.65 Å (178/216)
Wzg from <i>S. pneumoniae</i>	2XXP (bound to octaprenyl phosphate) (Kawai et al., 2011)	21.7%	-	1.20 Å (149/202)
	4DE8 (R267A) (bound to octaprenyl phosphate) (Eberhardt et al., 2012)		-	1.23 Å (149/202)
	3TFL (bound to octaprenyl diphosphate) (Kawai et al., 2011)		-	1.25 Å (149/202)
	2XXQ (R267A) (bound to octaprenyl diphosphate) (Kawai et al., 2011)		-	1.28 Å (149/202)
LcpA from <i>S. aureus</i>	6UEX (bound to octaprenyl-pyrophosphate-GlcNAc) (Li et al., 2020)	30.4%	-	1.71 Å (169/219)

(SDSD), a known animal pathogen and one of the leading causes of bovine mastitis and fish streptococcosis (Nomoto et al., 2004; Alves-Barroco et al., 2019a). These diseases lead to serious consequences and losses for the dairy and aquaculture industries (Abdelsalam et al., 2013). Besides, SSDS can form biofilms making it very difficult to eliminate, since in that

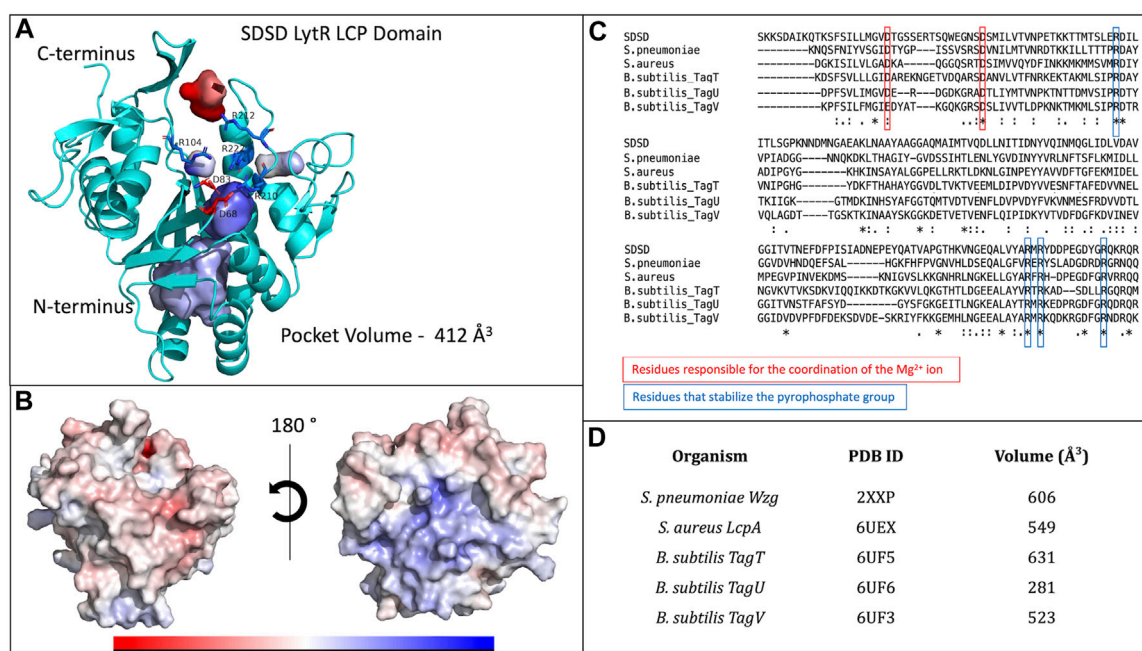


FIGURE 2
(A) - representation of the LytR LCP domain crystal structure determined at 2.8 Å resolution (PDB ID 8QTY). The surface of the pocket is shown in purple and in red. The arginine residues (dark blue) that stabilize the pyrophosphate group and the aspartate residues (red), that coordinate the Mg²⁺ ion (not present in the structure), are represented as stick; **(B)** - electrostatic surface of the LytR LCP domain in two orientations; **(C)** - alignment of some LCP sequences from deposited structures in the PDB. The conserved residues present in the catalytic site are represented: in red, for the residues responsible for coordination of the Mg²⁺ ion, and in dark blue, for the arginine residues that stabilize the pyrophosphate group; **(D)** - pocket volumes of the LCP proteins present in the alignment and their respective PDB IDs (Kawai et al., 2011; Li et al., 2020).

growth phenotype, bacterial are a lot less susceptible to antimicrobial agents. SDSD was shown to also infect humans (Park et al., 2012; Roma-Rodrigues et al., 2016; Alves-Barroco et al., 2019b; Alves-Barroco et al., 2022).

LytR and other members of the LCP family have been described as pyrophosphatases. They cleave the pyrophosphate bond in glycopolymer precursors. These precursors contain several undecaprenyl units, the pyrophosphate group and the glycopolymer that is going to be transferred to the peptidoglycan, usually to the MurNAc residues. This process occurs in the outer layer of the cell wall. Besides very complex and large polymers, these enzymes can also bind shorter molecules containing only the hydrophobic undecaprenyl units (decaprenyl, octaprenyl and geranylgeranyl) and phosphate/pyrophosphate groups (Kawai et al., 2011; Eberhardt et al., 2012). In fact, these simpler substrates are commonly used in activity assays although their low solubility in aqueous solutions is a great challenge.

LCPs can be found in virtually all Gram-positive bacteria, and commonly, with several enzymes per organism (up to 11 as in *Streptococcus coelicor*) (Hübscher et al., 2008). The presence of these different members is relevant for functional redundancy purposes and usually, only the knock-out of all the LCP proteins will lead to non-viable cells (Kawai et al., 2011).

The LCP proteins have a quite variable topology. Besides the LCP domain, that is extracellular and structurally very conserved, these proteins often possess accessory domains of unknown function. Accessory domains can be present both in the N- or C-terminus relative to the LCP domain and can be intracellular or extracellular.

For example, the Wzg protein from *Streptococcus pneumoniae* has an extracellular accessory domain in the N-terminus, while LytR from SDSD has a similar extracellular domain but in the C-terminus and Lcp2 from SDSD has the accessory domain in the N-terminus, intracellularly (Kawai et al., 2011). Since these enzymes operate on the outer side of the cell wall, they possess anchoring helices that attach the LCP domain to the membrane, connecting it to the auxiliary domain when this is present. According to available data, LCP proteins commonly have one transmembrane helix, but these can go up to three as in the CpsA proteins (Hübscher et al., 2008).

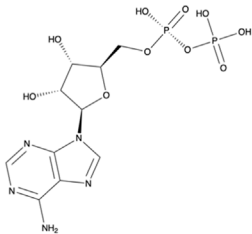
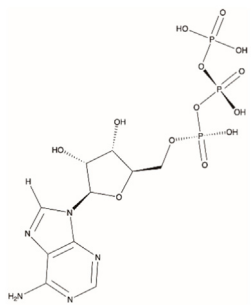
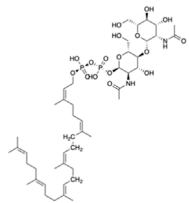
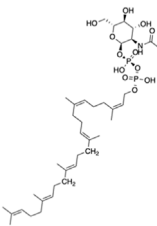
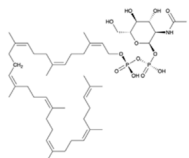
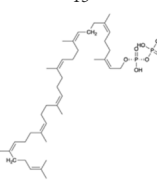
In this study, our goal is to investigate the structure and function of the LytR protein from *Streptococcus dysgalactiae* subsp. *dysgalactiae* (SDSD) and its implications in the biosynthesis of wall teichoic acids. Through a combination of crystallography, X-ray scattering, molecular dynamics simulations, docking, and activity assays, we aim to elucidate the molecular mechanisms underlying the enzymatic activity of LytR and its potential as a target for novel antibiotics.

2 Materials and methods

2.1 Plasmid construction

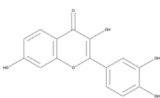
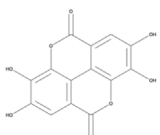
To produce the LytR protein from *S. dysgalactiae* subs. *dysgalactiae*, a DNA fragment coding the amino acid residues 48–342 was amplified from genomic DNA (VSD9 strain). The amplified fragment was then cloned into a pET21c (+) vector (Novagene) into the NdeI and XhoI restriction sites. The primers

TABLE 4 Results of the different scoring functions available in GOLD.

Molecule	Structure	Score				Score normalized			
		PLP	ASP	Chemscore	Goldscore	PLP	ASP	Chemscore	Goldscore
ADP	<div>9</div>	94.54	43.15	16.42	90.10	3.50	1.60	0.61	3.34
ATP	<div>10</div>	106.68	51.19	17.69	98.11	3.44	1.65	0.57	3.16
LIa-WTA	<div>2</div>	152.52	55.57	45.67	114.53	2.28	0.83	0.68	1.71
LI-WTA	<div>11</div>	144.34	47.99	48.84	127.26	2.72	0.91	0.92	2.40
Octaprenyl-pyrophosphate-GlcNAc	<div>12</div>	145.61	43.38	50.19	110.80	2.31	0.69	0.80	1.76
Octaprenyl diphosphate	<div>13</div>	133.59	41.61	49.27	124.18	2.73	0.85	1.01	2.53

(Continued on following page)

TABLE 4 (Continued) Results of the different scoring functions available in GOLD.

Molecule	Structure	Score				Score normalized			
		PLP	ASP	Chemscore	Goldscore	PLP	ASP	Chemscore	Goldscore
Fisetin		63.41	30.05	27.44	59.46	3.02	1.43	1.31	2.83
Ellagic acid		44.83	22.65	22.14	53.83	2.04	1.03	1.01	2.45

used can be found in Table 1 of Supplementary Material. The region comprising residues 1–47 corresponds to the protein's signal peptide and was not included, as well as residues 342–422 which are predicted to be highly flexible and disordered.

2.2 Protein expression and purification

E. coli BL21 (DE3) cells were transformed with the plasmid DNA and the cells were grown in LB medium supplemented with ampicillin (100 µg/mL), at 37°C. Once the optical density reached 0.5–0.8, protein expression was induced with 1 mM isopropyl β-D-1-thiogalactopyranoside (IPTG), for 5 h, at 30°C. Cells were collected through centrifugation (7477 x g, 15 min at 4°C), resuspended in the lysis buffer (10 mM Na₂PO₄ pH 7.2, 100 mM NaCl, 5 mM MgCl₂, 10 mM imidazole) and lysed by sonication using 10 × 1 min cycles (80% amplitude, 0.5 cycles) (UP100H MS7, Hielscher Ultrasonics). The lysate was clarified through centrifugation (12,857 x g, 60 min at 4°C). LCP domain was purified using an immobilized metal-affinity chromatography (IMAC) column HisTrap HP 5 mL (Cytiva). The protein was eluted using a 30–500 mM linear imidazole gradient. Fractions containing the protein of interest were pooled together, and the buffer was exchanged using HiTrap desalting columns (Cytiva) to 10 mM Na₂PO₄ pH 7.2, 500 mM NaCl, and 5 mM MgCl₂, which allowed increasing NaCl concentration and removing the imidazole. The sample was later concentrated and loaded into a size exclusion chromatography (SEC) column Superdex 75 10/300 GL (Cytiva) equilibrated with the desalting buffer. The fractions containing pure LytR LCP domain were pooled together, concentrated, and stored at –20°C.

2.3 Crystallization and structure determination

Protein crystals were obtained by sparse-matrix screening (JBScreen Classic 1 to 4 and JBScreen Classic 5 to 8) using an Oryx 8 crystallization robot and two protein concentrations (100 and 200 mg/mL). Crystals appeared in different conditions using the sitting drop vapor diffusion technique, but the best diffracting ones were found with 2.2 M ammonium sulphate and 20% (v/v) glycerol. The crystals grew at a

maximum size of 0.06 × 0.06 × 0.06 mm in 4 days, were cryo-protected in parathone and flash-frozen in liquid N₂. Diffraction data were collected at the European Synchrotron Radiation Facility (ESRF, Grenoble, MASSIF-1 beamline) up to 2.80 Å resolution, processed with XDS, and merged and scaled with AIMLESS (Kabsch, 2010; Evans and Murshudov, 2013). The structure was solved by molecular replacement with MR BUMP (from the CCP4 package) (Keegan and Winn, 2008), using 3OKZ as search model. The refinement was performed with REFMAC5 (from the CCP4 package) (Murshudov et al., 2011). The manual construction and visual inspection of the model were done with COOT (data collection and refinement statistics in Table 1). (Emsley et al., 2010; Kovalevskiy et al., 2016) The resulting model was deposited in the Protein Data Bank (PDB) with the accession code 8QTY.

2.4 Small angle X-ray scattering (SAXS)

SAXS experiments were performed at the ESRF, beamline BM29. Two samples of protein at 7.2 mg/mL in 50 mM HEPES pH 8.0, 150 mM NaCl, 5 mM MgCl₂ and 40% ethylene glycol were prepared in the absence (S1) and in the presence (S2) of 540 µM geranylgeranyl pyrophosphate. Scattering data was collected as intensity $I(s)$ versus s , where $s = 4\pi\sin\theta/\lambda$ nm^{–1}, 2θ is the scattering angle, and λ is the X-ray wavelength, 0.124 nm. Data processing, reduction and primary analysis were performed with the program PRIMUS (Konarev et al., 2003). This allowed us to obtain the overall parameters (radius of gyration, R_g , forward scattering, I_0) and to compute the distance distribution function $p(r)$ using GNOM (Svergun, 1992). The overall parameters of the data collection and analysis are summarized in Table 2. The scattering from the crystal structure and from the models was computed and compared with the experimental data using the program CRY SOL (Svergun et al., 1995). The high resolution models with added flexible chains were refined against the scattering data by SREFLEX (Panjkovich and Svergun, 2016).

2.5 Molecular dynamics

A preparation step of the crystal structure was required prior to the Molecular Dynamics (MD) simulations. In this step, it was

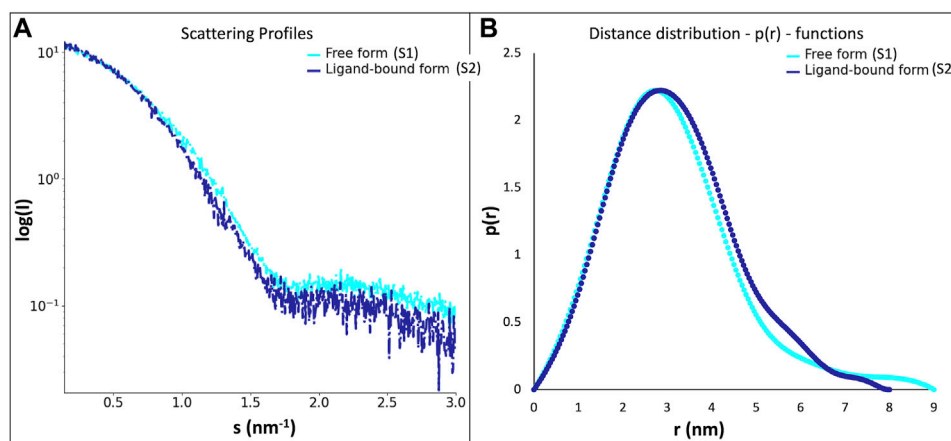


FIGURE 3 (A)- scattering profiles of the LytR LCP domain free form (S1, in light blue) and ligand-bound form (S2, in dark blue); (B)- distance distribution functions $p(r)$ of the LytR LCP domain free form (S1, in light blue) and ligand-bound form (S2, in dark blue).

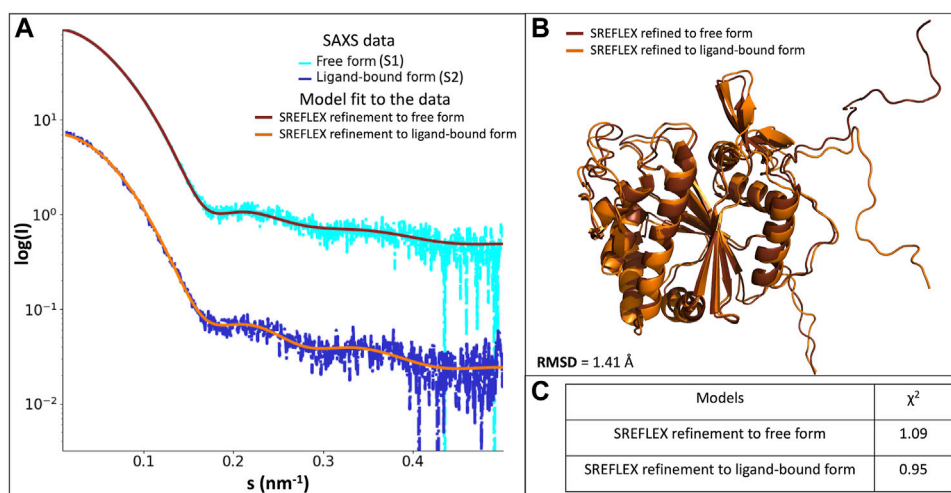


FIGURE 4 (A)- scattering profiles of the scattering profiles of the LytR LCP domain free form (S1, in light blue) fitted with the SREFLEX refined model (brown), and ligand-bound form (S2, in dark blue) fitted with the SREFLEX refined model (orange). (B)- superposition of the SREFLEX refined models to the S1 (brown) and to S2 (orange). (C)- χ^2 values of the fitted SREFLEX models.

necessary to add the missing loop (G70 to Q77) with Modeler (version 9.23) (Fiser et al., 2000). The protonation state of all residues at the physiological pH of 7.4 was estimated in the PlayMolecule ProteinPrepare web server (Martínez-Rosell et al., 2017). The addition of an Mg²⁺ ion was performed using VMD and the molUP plugin, available through the VMD Store. (S. Fernandes et al., 2018; 2019). The ligand LIIa-WTA was added to the protein by superposition with the deposited protein structure 6MPS and the remaining ligands were obtained based on this one, using also VMD (Humphrey et al., 1996). MD simulations were performed with the Amber software (version 20) using forcefield amber14sb (recommended forcefield for protein simulations within the amber forcefield family), in a 12 Å cubic box that was filled with TIP3P water molecules (Maier et al., 2015; Case et al., 2020). The

utilization of TIP3P water molecules reduces the required computational power and is a regular choice when using the forcefield amber14sb. Parametrization of the several used ligands (LIIa-WTA, prenyl-11-g3p-20, prenyl-11-g3p-5, prenyl-6-g3p-5, prenyl-3-g3p-5, prenyl-2-g3p-5 and prenyl-1-g3p-5—Figure 6) was done with Antechamber using the second generation of the General Amber Force Field (GAFF2) (Wang et al., 2004). To obtain the partial atomic charges for these ligands, the Restrained ElectroStatic Potential (RESP) charge derivation protocol was used (Sun et al., 1992). These charges were calculated from the respective optimized structure at the Hartree-Fock level of theory with the 6–31G(d) basis set (i.e., HF/6–31G(d)). The geometry optimization was performed using Gaussian09. For ADP, the parameters were obtained from the Bryce parameters database (Meagher et al., 2003).

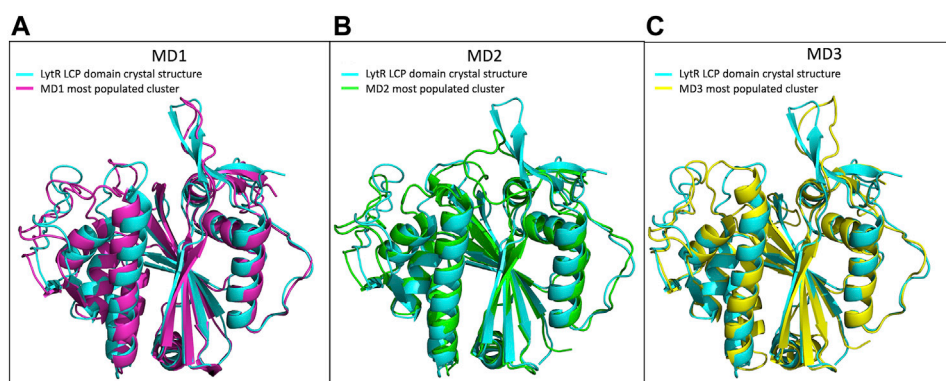


FIGURE 5

Superposition of the LytR LCP domain crystal structure (PDB ID 8QTY) with the structures representing the most populated clusters of MD1, MD2 and MD3. (A)- Superposition of the LytR LCP domain crystal structure (light blue) with the structure representing the most populated cluster of MD1 (pink); (B)- superposition of the LytR LCP domain crystal structure (light blue) with the structure representing the most populated cluster of MD2 (green); (C)- superposition of the LytR LCP domain crystal structure (light blue) with the structure representing the most populated cluster of MD3 (yellow).

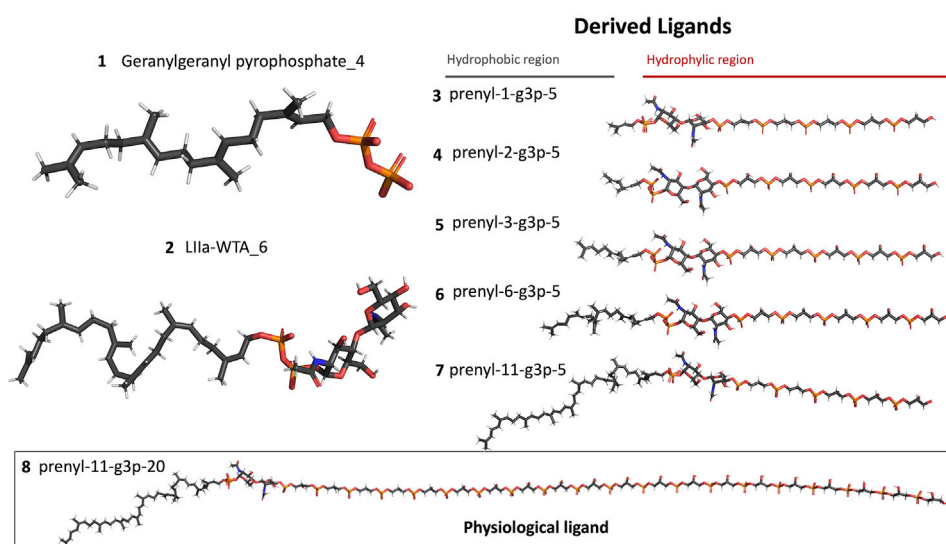


FIGURE 6

Representation of the different ligands used in the molecular dynamic's simulations. The ligand in the box, prenyl-11-g3p-20, represents the ligand that more resembles the native substrate of the LCP proteins (MD data not included for this ligand).

Four minimization steps were applied to remove clashes, followed by two equilibration steps and a final production run. The minimization procedure consisted of four stages. In each minimization stage, the first half of the total steps use the steepest descent method, changing thereafter to the conjugate gradient method. Firstly, only the water molecules were minimized (5,000 steps), with Cartesian positional restraints with a weight of $50 \text{ kcal mol}^{-1} \cdot \text{\AA}^2$ applied on all other atoms. Secondly, all hydrogen atoms were minimized (5,000 steps), with the same restraint weight applied to all non-hydrogen atoms. Thirdly, all non-backbone atoms in the system were minimized (5,000 steps), and the same restraint weight was applied to all protein backbone atoms. Lastly, all system atoms were minimized with no restraints (10,000 steps).

The two 50 ps equilibration steps consisted of: heating the system to 310 K using a Langevin thermostat at constant volume (NVT ensemble); and equilibration of the density of the system at 310 K. Lastly, the 1,000 ns production run was performed in an NPT ensemble with a temperature of 310 K and 1 bar pressure. A time step of 2 fs was used, and the SHAKE algorithm was applied to constrain the bonds involving hydrogen atoms. Analysis of the molecular dynamics was performed using cpptraj and molecular visualisation and inspection were done with VMD (Roe and Cheatham, 2013).

The K-means clustering method was used to analyze the trajectory, group, and characterize the different intermediate states into 3 main clusters of conformations based on the Root

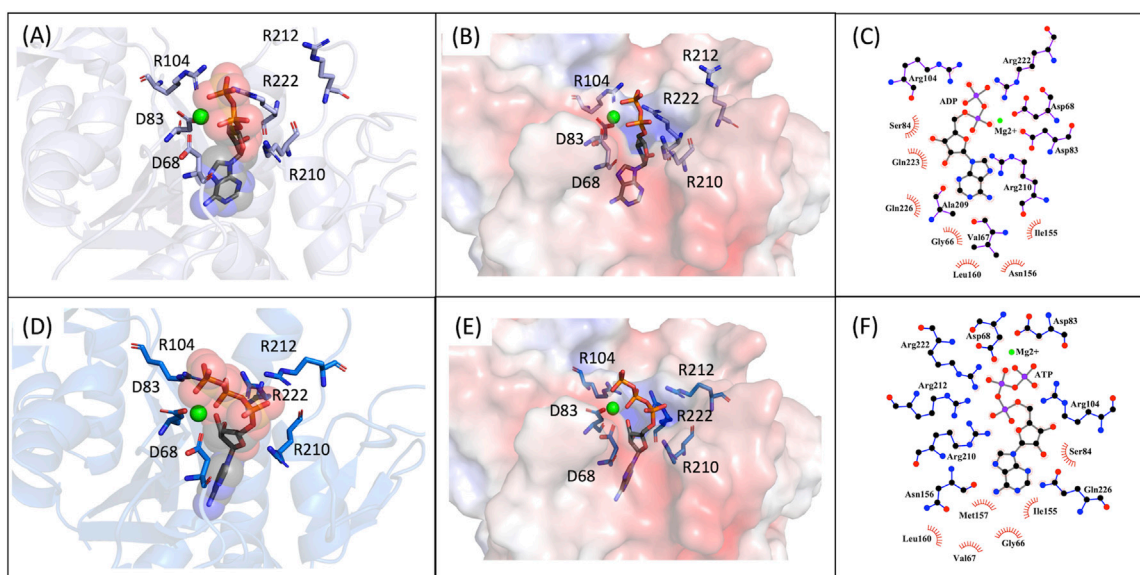


FIGURE 7
MD9 and MD10 representative structures of the most populated clusters. **(A)**- Cartoon representation of the MD9 representative structure of the most populated cluster, the conserved aspartate and arginine residues are represented as sticks (in purple), the ADP is represented as sticks and spheres with transparency (in grey), and the Mg^{2+} ion is represented as a sphere (in green). **(B)**- Electrostatic surface of the MD9 representative structure of the most populated cluster, the conserved aspartate and arginine residues and the ADP are represented as sticks (in purple and in grey, respectively), and the Mg^{2+} ion is represented as a sphere (in green). **(C)**- 2D representation of the interacting residues with ADP. The ADP (in grey) and the residues performing hydrogen bonds (in purple) are represented as ball and stick and the ones performing hydrophobic interactions represented by the label and red mark. **(D)**- Cartoon representation of the MD10 representative structure of the most populated cluster, the conserved aspartate and arginine residues are represented as sticks (in purple), the ATP is represented as sticks and spheres with transparency (in grey), and the Mg^{2+} ion is represented as a sphere (in green). **(E)**- Electrostatic surface of the MD10 representative structure of the most populated cluster, the conserved aspartate and arginine residues and the ATP are represented as sticks (in purple and in grey, respectively), and the Mg^{2+} ion is represented as a sphere (in green). **(F)**- 2D representation of the interacting residues with ATP. The ATP (in grey) and the residues performing hydrogen bonds (in blue) are represented as ball and stick and the ones performing hydrophobic interactions represented by the label and red mark.

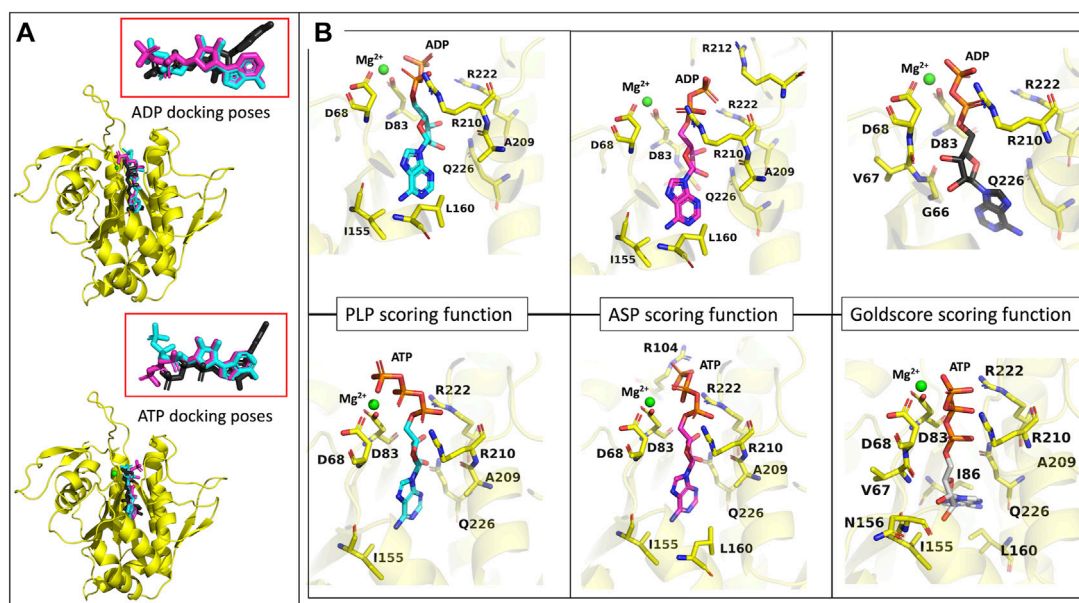
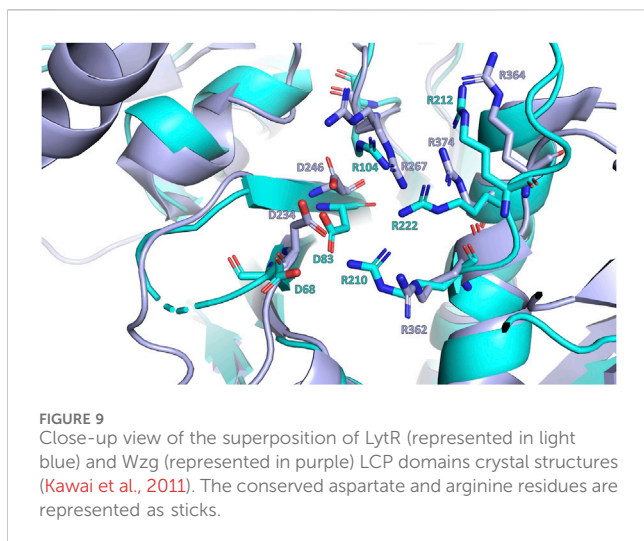


FIGURE 8
ADP and ATP binding modes predicted by the GOLD three best scoring functions. **(A)**- representation of the model representing the most populated cluster of MD3 (yellow), in the presence of a Mg^{2+} ion (green), with the superposition of the binding modes of ADP and ATP, predicted by PLP (light blue), ASP (pink) and Goldscore (black) scoring functions. Ampliation of the binding modes alone for both molecules. **(B)**- representation of the binding modes predicted by the three best scoring functions, for ADP and ATP, the Mg^{2+} ion (green) and the amino acids important for interaction.



Mean Square Deviation (R.M.S.D.) of all non-hydrogen atoms as a measure of similarity. Representative average structures for each of these 3 clusters were determined.

Simulations were repeated with a simple neutralized simulation box in the presence of specific ionic strength, with 500 mM of NaCl, and in the absence of a Mg^{2+} bound to the protein. Besides, simulations were also repeated in the presence of Mg^{2+} and LipidII-WTA (a truncated precursor of the WTA bound to the lipidic precursor) and later extended to several ligands with different numbers of prenyl units in the hydrophobic chain. Additionally, simulations in the presence of a Mg^{2+} ion and ADP or ATP were also performed. In [Table 2](#) from [Supplementary Material](#) there is a description of the conditions for all the MD simulations performed.

2.6 Docking

The target for the docking was obtained from the major cluster of the molecular dynamics in the presence of LIIa-WTA, and a Mg^{2+} ion. The ligand was removed, and a version with the hydrophobic region trimmed, the 2 prenyl units, was used to define the binding region; the Mg^{2+} was kept in. The structures of ADP, ATP and the other validation molecules (LIIa-WTA, LI-WTA, octaprenyl-pyrophosphate-GlcNAc and octaprenyl diphosphate) were obtained from the Protein Data Bank (PDB) in sdf format, and using OpenBabel, the protonation was defined. Datawarrior was used to determine some descriptors and chemical properties from the chemical structures, important later for the analysis (Sander et al., 2015). The GOLD (version 5.8) software was used to perform the docking, employing all available scoring functions in GOLD as all shown to represent well the binding of known substrates to these proteins (Jones and Willett, 1995; Jones et al., 1997). 100 GA runs were performed, with a binding region based on a radius of 10 Å from a cavity file, centered on the coordinates of the reference ligand. Visual inspection was performed in Pymol (Schrödinger, 2024). Further data processing was done in Datawarrior and Microsoft Excel datasheets.

2.7 Activity assay - malachite green

The malachite green assay was used to determine the amount of released P_i from the substrate, thus determining the pyrophosphatase activity of the protein. Protein at a concentration of 35.5 μM , in 50 mM HEPES pH 8.0, 150 mM NaCl, and 5 mM $MgCl_2$ and ADP and ATP at 750 μM , in the same buffer, were used. Two time-points were collected, the first one measured after mixing the protein with ADP or ATP and the second after incubating the mixture overnight, at 37°C. Before the assay, a calibration curve with serial dilutions of Na_2HPO_4 was done. The assay was adapted by Tom Duncan from (Lanzetta et al., 1979) as follows: 25 μL of the sample were mixed with 100 μL of a solution containing a mixture of 1 volume of 0.045% (w/v) malachite green oxalate, 3 volumes of 4.2% (w/v) sodium molybdate in 4 N HCl and 5 mL of 2% (w/v) Triton-X100 per each 0.1 mL of solution; after 2 min, 12.5 μL of a 34% (w/v) sodium citrate solution were added followed by another incubation at room temperature for 5 min before measuring the absorbance at 650 nm in a microplate reader. Triplicates were performed for the calibration curve and the protein-ADP assays.

3 Results

3.1 LytR overall structure

The structure of the LCP domain of LytR, comprising residues S48 to S342, was solved by molecular replacement using gbs0355 from *Streptococcus agalactiae* (PDB ID: 3OKZ) as a model (sequence identity 75.4%) at a resolution of 2.8 Å (Data collection and refinement statistics are available in [Table 1](#)). Analysis of the electron density maps suggests the presence of three sulphate ions at the surface of the protein. No electron density was observed at the active site that could correspond to bound substrates. The regions S48-Q56, G70-Q77, and N335-S342 are highly disordered, with no interpretable electron density in the 2Fo-Fc map. For this reason, these residues were not included in the final model.

The structure is composed of 8 α -helices alternated with 12 β -sheets in a 3-layer ($\alpha\beta\alpha$) sandwich architecture ([Figure 1](#)). The characteristic central six-stranded β -sheet is sandwiched between the α -helices and the double-stranded antiparallel β -sheets ($\beta 4$ - $\beta 5$, $\beta 7$ - $\beta 8$ and $\beta 11$ - $\beta 12$). The overall structure determined was compared with those of other LCP domains (sequence identity and RMSD of the superpositions are in [Table 3](#); [Figure 1](#)). The results of the comparison align with what is described in the literature and show that, despite the low sequence identity among the proteins of the LCP family, the structural similarities are striking.

LytR LCP domain contains a long and narrow pocket located between the central β -strand and the α -helices 3 to 7, near the N-terminus. This pocket is composed of several different hydrophobic residues (F60, V153, L160, A209, I261 and Y274), that point their side chains towards the pocket. Polar residues (M99, M157, M257, Q226, S84, T97, T259, and N156) are also present, with their side chains towards the pocket, except for N156. The pocket is highly accessible and has a solvent-accessible surface area of 547.75 Å² (values were calculated using Computed Atlas of Surface Topography of proteins - CASTp) (Tian et al., 2018).

The presence of this pocket is extremely conserved in the LCP family of proteins corresponding to the binding site of the undecaprenyl units - the hydrophobic section - of the physiological substrates. For LytR LCP domain, the pocket's volume is 412 Å³ (Figure 2).

The binding site of LCP proteins is composed of conserved positive and negatively charged residues: two aspartates (D68 and D83 for SDSD LytR) coordinate the Mg²⁺ cofactor and are present in all members of the family identified so far, except for just two cases. In the *B. subtilis* TagV protein (PDB IDs 3NXH and 6UF3) one of the aspartates is replaced by a glutamate, and in *E. siraeum* LCP protein (EUBSIR_01389–PDB ID 4OBM), only one of the aspartates is present with the other residue replaced by an alanine residue. The positive charges come from four conserved arginines (R154, R210, R212 and R222 for SDSD LytR) that are expected to interact with the pyrophosphate group present in the native substrates (Figure 2). In the case of the *Eubacterium siraeum* LCP protein, the four conserved arginines are replaced by three proline and one threonine residues.

Crystal structures of wildtype Wzg protein and its R267A mutant from *Streptococcus pneumoniae* show high isomorphism with an R.M.S.D. of 0.14 Å upon superposition of 321 aligned Ca out of 380 (Table 3, Supplementary Material), PDB codes are 3TFL and 2XXP for wildtype Wzg, and 2XXQ and 4DE8 for R267A Wzg (Kawai et al., 2011; Eberhardt et al., 2012). The presence of substrates sitting in the substrate pocket of R267A suggests that mutating this arginine does not impact the protein's binding ability. Further studies are necessary to understand whether catalysis is affected and if the same effect is observed when other or several arginine residues are mutated at the same time since activity was not measured by the authors.

With the wide range of available crystal structures of this family of proteins, we conducted a structural comparison between models obtained in the presence and absence of 5 ligands (Table 4): the substrate analogs octaprenyl-diphosphate, Lipid-II-WTA (LII-WTA), Lipid-I-WTA (LI-a-WTA) and octaprenyl-pyrophosphate-GlcNAc and the reaction product decaprenyl-pyrophosphate. The structural resemblance between free and ligand-bound forms (substrate or reaction product) is very high, as observed by the low R.M.S.D. values of the superpositions (Table 3). This suggests that the protein in the crystal forms deposited so far adopts the same conformation regardless of the presence of ligands in the active site. To study the protein structure in solution we used SAXS.

3.2 Small angle X-ray scattering

SAXS data (Table 2; Figure 3) was collected in batch mode, with protein in the absence (S1) and in the presence (S2) of geranylgeranyl pyrophosphate, a substrate analogue of this protein family that mimics the hydrophobic part of the physiological substrates. Data reduction and initial analysis revealed the presence of concentration effects on the value of R_g for all the experiments performed and allowed the determination of R_g and I_0 values. The pair-distance distribution functions ($p(r)$) were calculated using the scattering at high angles of the highest concentration curves merged with the scattering at low angles of the lowest concentration curves; the $p(r)$ functions (Figure 3B) yielded the D_{max} values.

The experiments performed in the absence and presence of geranylgeranyl pyrophosphate revealed some changes in the $p(r)$ profiles (Figure 3). The radius of gyration (about 2.4 nm) remained practically unchanged upon ligand addition. However, a decrease in the D_{max} value by about 0.9 nm was observed in the presence of geranylgeranyl pyrophosphate, suggesting that the protein in solution adopts a somewhat more closed conformation upon ligand interaction.

To obtain a more detailed assessment of the protein conformation and flexibility in solution, we generated a tentative model of full-length LytR LCP domain based on the crystal structure. We added the missing portions S48-Q56, G70-Q77, and N335-S342 using MODELER. This model yielded a good agreement with the experimental SAXS data in the presence of a ligand (discrepancy $\chi^2 = 1.12$), but a poor fit in the absence of a ligand (discrepancy $\chi^2 = 1.91$). Further refinement with SREFLEX provided models yielding an improved agreement to the experimental data. In the presence of ligand, the refined model (R.M.S.D. of 2.3 Å to the initial one) had a discrepancy of $\chi^2 = 0.95$ to the experimental curve with the ligand. The model in the absence of ligand had an RMSD of 4.8 Å to the initial model, providing a discrepancy of $\chi^2 = 1.09$ to the experimental data without ligand. The fits of the refined models to the SAXS data are very good as displayed in Figure 4. Figure 1, from Supplementary Material, shows the comparison between the SREFLEX derived models and the LCP domain full-length.

The SAXS analysis confirmed that the overall crystal structure of LytR is largely preserved in solution and the missing portions in the crystal display significant flexibility. Tentative conformations of these portions were visualized by fitting the SAXS data collected from the full-length domain. Likely, the differences between the native protein and the one with bound geranylgeranyl pyrophosphate can be largely attributed to the changes in the flexible portions of LytR.

3.3 Molecular dynamics

We performed molecular dynamics simulations for the LytR LCP domain in the absence of ionic strength and in the presence of an Mg²⁺ ion bound to the protein. We used the crystal structure described here as the initial model. The results allowed us to determine the main modes of vibration of the protein and their distribution in conditions that mimic the experimental ones. This helped identifying the most affected regions upon visual inspection. Overall, and accordingly with what was expected, loops were the regions with the highest movement. Cluster analysis allowed us to identify three main clusters, with a distribution of 87.8%, 10.6% and 1.6%, respectively. The overall conformation of the protein is the same in all clusters and the R.M.S.D. of the superpositions ranges from 0.758 to 1.491 Å (Table 4; Supplementary Material). To understand if the ionic strength alone could alter the conformation of the LytR LCP domain, we conducted another MD simulation of the LytR LCP domain in the presence of 500 mM NaCl and the absence of the Mg²⁺ ion bound to the protein. For this MD simulation, the cluster analysis revealed a distribution of 40.6%, 22.3% and 13.4% with the R.M.S.D. between the three determined clusters ranging from 0.941 to 1.278 Å (Table 4; Supplementary Material). The superposition of the

crystal structure with the different MD clusters shows there is a bad agreement when the MD simulations are performed in the presence of a Mg^{2+} ion and a better agreement when this is absent, and the ionic strength increases. (Table 4; Supplementary Material). In Figure 5, there is a comparison between the LytR LCP domain crystal structure and the models representing the most populated clusters for MD1, MD2 and MD3.

We also carried out MD simulations in the presence of a Mg^{2+} ion and different ligands (Figure 6, molecules 1 and 2), inspired by the physiological substrates of LCP proteins (Figure 6, molecule 8). The results obtained suggest that the length of the hydrophobic region does not impact the binding and that the determinant for the protein-ligand interaction is the presence of the pyrophosphate group. To test this hypothesis, we designed several other ligands with different numbers of prenyl units in the hydrophobic chain (corresponding to molecules 3 – 7 in Figure 6) with the smallest chain having only one prenyl unit. In all cases, the ligands kept bound to the protein during the entire simulation. As expected, the WTA part of the precursor stayed outside the pocket, with a wide range of movement of the glycerol-3-phosphate moieties, that interacted non-specifically with the protein. We also performed MD simulations in the presence of ADP presuming that this could be a putative hydrolysable substrate of the LCP domains. The results suggest that, not only the diphosphate group is responsible for keeping the ADP bound to the protein, allowing the molecule to remain in the active site during the entire simulation, but also that the binding mode is very different from the physiological substrates. According to the structures of TagT from *B. subtilis* (6MPS and 6MPT) and LcpA from *S. aureus* (6UEX), that was crystallized in the presence of glycopolymers, we were expecting to find the sugar moiety of the ligands sitting outside the pocket. However, in the case of ADP MD simulation, the sugar and purine moieties are held inside the pocket. Most likely, the lack of a long hydrophobic chain occupying the hydrophobic pocket can help explain this behavior. Additionally, an MD simulation was performed in the presence of a Mg^{2+} ion and ATP to evaluate if it would compete for the same binding site as ADP. Figure 7 shows the binding modes for the two molecules of the representative structures of the most populated cluster from each MD simulation. The results show a similar binding mode for both molecules, in the active site. However, ATP interacts with the Mg^{2+} ion through the β - and γ -phosphates, whereas the α -phosphate interacts only with R210 and R212. This suggests that LytR LCP domain can cleave the bond between the β - and γ -phosphates, converting ATP to ADP and subsequently ADP into AMP. These results support the hypothesis of competition of ADP and ATP for the active site, as well as the ability of the protein to hydrolyze both molecules.

The R.M.S.D. and R_g plots of the molecular dynamics simulations (MD1 - MD10) are shown in Supplementary Material, Figures 2–4.

3.4 Docking

Docking was employed to study the interaction of the LytR LCP domain with ADP and compare its binding affinity with known protein-binders (LIIa-WTA, LI-WTA, octaprenyl-pyrophosphate-GlcNAc and octaprenyl diphosphate) that were used as validation

molecules (Kawai et al., 2011; Schaefer et al., 2018). Fisetin and ellagic acid, although known anti-biofilm agents, were also used as validation molecules, but as negative controls, as a thermal shift assay (TSA) was conducted that showed no evidence of binding (data not included). Supplementary Figure S5 shows the binding modes predicted by the scoring functions PLP, ASP and Goldscore, for the validation molecules (binders and non-binders). All the scoring functions present in Gold were tested and the respective scores and normalized scores are present in Table 4.

All the scoring functions can correctly discriminate the known protein binders from the non-binders, both in terms of absolute scores and relative scores. For the known protein binders, the scores for PLP ranged from 133.59 to 152.52 and from 2.28 to 2.73, for ASP from 41.61 to 55.57 and from 0.69 to 0.91, for Chemscore from 45.67 to 50.19 and from 0.68 to 1.01, and for Goldscore from 110.80 to 127.26 and from 1.71 to 2.53, absolute and relative values, respectively. For the known non-binders, the scores for PLP ranged from 44.83 to 63.41 and from 2.04 to 3.02, for ASP from 22.63 to 30.05 and from 1.03 to 1.43, for Chemscore from 22.14 to 27.44 and from 1.01 to 1.31 and for Goldscore from 53.83 to 59.46 and from 2.45 to 2.83, absolute and relative values, respectively.

Apart from Chemscore, all scoring functions estimate an absolute score for ADP well above the negative controls, and close to the positive controls, even considering its much smaller molecular weight. When normalizing the score of ADP by the number of heavy atoms, and comparing with the positive controls, the resulting scores with PLP, ASP and Goldscore are significantly higher than those of the positive controls, suggesting the ADP exhibits a higher relative binding affinity than the positive controls taking its size into account.

In Table 4, we can observe that in all cases the scores for the known protein binders are higher than for the known non-binders. In the case of ASP, that difference is less pronounced, yet all the known binders have higher scores than the non-binders. Regarding the values normalized by heavy atoms, the non-binders always present higher scores than the known binders. As the non-binders are smaller molecules this explains the difference between the absolute and relative scores. Regarding ADP we see that, besides Chemscore, the normalized values are always close to the non-binders but slightly higher. As both non-binders and ADP have similar sizes, it is possible to directly compare realizing that ADP has a higher binding affinity than the non-binders, suggesting that ADP can interact with the LytR LCP domain. We used molecular docking to further evaluate and support the hypothesis of competition between ADP and ATP. The scores for ADP and ATP are very similar for all the scoring functions, with ATP having slightly higher scores, suggesting similar affinities from both molecules towards LytR LCP domain. This result supports the hypothesis of competition between the two molecules for the active site. It also suggests that the presence of a third phosphate does not seem to strongly increase the affinity towards the LytR LCP domain.

Figure 8 highlights the binding modes predicted by the three best scoring functions for ADP and ATP. The superposition of the models shows that the binding modes are very similar for the PLP and ASP scoring functions, with slight changes in the position of the diphosphate group and the sugar moiety. Regarding the Goldscore, the predicted binding mode presents

slight changes in the position of the diphosphate group and pronounced differences in the position of the purine moiety. Interestingly, in the case of ATP, despite the resemblance of the binding poses, PLP and ASP predict more exposed poses, when comparing with ADP, while Goldscore predicts a more buried one.

To analyze the specific interactions between the ligands and the protein amino acid residues, we divide them into three groups: the interactions with (i) the phosphates, (ii) the purine moiety, and (iii) the sugar moiety (See Figure 8). Regarding the first (i), the three best scoring functions predict the interaction between the Mg^{2+} ion and the α - and β -phosphates for ADP, and β - and γ -phosphates for ATP. The phosphates are also involved in salt bridges with and the arginine residues R210 and R222. The consistency of these two arginines in forming ionic interactions with the phosphates, irrespective of the number of phosphates or scoring function, highlights their significance. Additionally, ASP scoring function suggests further interactions with R212 for ADP, and R104 for ATP. The interactions between the protein active site and the purine moiety (ii) are hydrophobic and through hydrogen bonds. In the case of ADP, the different scoring functions predict hydrophobic interactions with I155, L160, and Q226. In the case of ATP, because this molecule is not as buried in the pocket as the diphosphate counterpart, the PLP scoring function does not predict any hydrophobic interactions, while the other scoring functions predict interaction with L160, I86, I230 and Q226. The interaction with I86 further elucidates the more buried pose predicted by Goldscore for ATP since this residue is located inside the substrate binding pocket. Regarding hydrogen bonds, the N6 of the purine moiety is hydrogen bonded to the protein, either to I155 in both ATP and ADP, or to L160 for ADP or Q226 for ATP. The interactions with the sugar moiety (iii) are done through hydrogen bonds with another set of residues. For ADP and ATP, the interacting residues that are common for most of the scoring functions are A209, R210 and Q226. G66 and V67 have also been predicted for ADP interaction, and V67, I155 and N156, for ATP.

The hydrophobic interactions and hydrogen bonds with the purine moiety and the hydrogen bonds with the sugar moiety help elucidate why the predicted binding modes of the two molecules position these parts of the ligands inside the pocket. In contrast, physiological substrates interact with the sugar moiety at the surface. These findings suggest the potential to design competitive inhibitors featuring two or three phosphate groups that interact with the catalytic residues, along with an amphipathic region occupying the elongated substrate pocket. Additionally, the protein's flexibility may facilitate the entry into the pocket of long hydrophobic tails, as in the physiological substrates, and bulkier ligands as in ADP/ATP.

3.5 Activity assays

We used the malachite green assay to determine if ADP and ATP could be hydrolysed by LytR LCP domain, by measuring the release of inorganic phosphate (Pi) and the formation of AMP or ADP. In the presence of ADP, the protein was able to release 110 μ M of Pi, corresponding to a conversion of 14.7% of the substrate, whereas in the presence of ATP it was able to release 435 μ M, corresponding to a conversion of 29%. This result indicates that, under these conditions, not only LytR LCP domain is properly folded and active but is also apt to hydrolyze ADP or ATP, corroborating the role of LCP proteins as

pyrophosphatases. Controls where only the ligands or the protein were present did not show an increase in the amount of Pi (Figure 6 from Supplementary Material).

4 Discussion

The proteins responsible for the transfer of WTA to the peptidoglycan have remained poorly studied for a long time. In recent years, it has been shown that the LCP family of proteins is involved in cell wall maturation (Kawai et al., 2011). The function of these proteins was confirmed when biochemical assays revealed their capability to transfer the disaccharide present in the linkage unit of the WTAs from lipid-linked precursors to the peptidoglycan (Gale et al., 2017).

In this study, the structure of the LCP domain of LytR protein from *S. dysgalactiae* subsp. *dysgalactiae* was determined at 2.80 Å, confirming that despite low sequence homology with other LCP-family members, the overall structure is highly conserved.

The presence of the negatively charged residues at the active site, typically two aspartic residues, is crucial for the protein's activity. In 2011, Kawai and collaborators showed that a D234 A mutation of the protein Wzg from *S. pneumoniae* significantly reduced the protein activity. The same result was obtained in the presence of a chelating agent (EDTA), suggesting that the Mg^{2+} ion is also required for catalysis (Kawai et al., 2011). More recently, studies by Gale et al. and Schaefer et al., using LCP proteins from *B. subtilis* and *S. aureus*, respectively, demonstrated that the transfer of WTAs to the peptidoglycan is performed by LCP proteins (Gale et al., 2017; Schaefer et al., 2018). As expected, the assays conducted in the presence of EDTA inhibited the transfer. The active site is also decorated with four conserved arginines, and to assess their role, the authors prepared the single mutant R267A and observed that the protein's ability to interact with a pyrophosphate-containing substrate was unaffected, compared to the wild-type (Kawai et al., 2011). This observation is further validated by deposited structures of this mutant with the ligand in the hydrophobic pocket. Schaefer and colleagues studied the impact of the mutations R118A, R219A and R227A on the TagT protein from *B. subtilis* for transferring the LIIa-WTA to the peptidoglycan. The authors observed that each single mutation in the arginine residue completely abolished the protein's transfer reaction. The results highlight the importance of the arginine(s) for activity but not so much for the interaction with the ligand. In the superposition of LytR and Wzg, these aspartates and arginine residues occupy the same positions in LytR, suggesting a similar role for the activity of this protein (Figure 9).

To the best of our knowledge, all deposited crystal structures, regardless of the presence or absence of ligands, show a compact conformation. This conformation is likely easier to crystallize. However, the ability of the protein to adopt different conformations should not be excluded as it might be associated with its physiological role. During catalysis, the protein accommodates long aliphatic chains inside the hydrophobic pocket which are released after delivering the WTA acid to the peptidoglycan. A more relaxed and open conformation might facilitate substrate binding and product release, with the protein adopting a more closed conformation during the cleavage of the diphosphate bond and the formation of the new phosphate bond. The SAXS experiments performed in the presence and absence of ligand support this hypothesis; the presence of

geranylgeranyl-pyrophosphate induces a closed conformation, whereas its absence promotes a relaxed form.

Molecular dynamics simulations were conducted with various ligands, including physiological substrates, ADP, and ATP, to explore their interactions with the protein. The findings highlighted the pivotal role of the pyrophosphate group in ligand binding, whereas the length of the hydrophobic region was less influential. Distinctive binding behaviors were observed for ADP and ATP compared to physiological substrates, with these nucleotides positioning their sugar and purine components within a lengthy and narrow pocket. These simulation results were corroborated by experimental evidence using the malachite green assay, which confirmed the protein's capacity to cleave the pyrophosphate bonds in ADP and ATP, releasing inorganic phosphate. Additionally, docking studies reinforced these observations, indicating that ADP and ATP could compete with physiological substrates for the active site in the LytR LCP domain. Although ADP and ATP showed lower absolute binding scores relative to known binders, their normalized scores indicated they are still competitively bound. Notably, the extra phosphate in ATP did not substantially enhance its affinity, with only the β - and γ -phosphate groups showing significant interactions. Given their hydrophilic properties and ease of handling in solutions, ADP and ATP are recommended as primary substrates in enzymatic assays for upcoming drug development initiatives. Furthermore, these results open new pathways for creating inhibitors targeting this protein family without requiring long hydrophobic tails.

Taken together, the structural and function data of the LCP domain of LytR protein from *S. dysgalactiae* subsp. *dysgalactiae* offer promising new directions for therapeutic strategies against bacterial infections.

Data availability statement

The datasets presented in this study can be found in online repositories. The names of the repository/repositories and accession number(s) can be found below: <https://www.rcsb.org/>, 8QTY; <https://www.sasbdb.org/>, SASDTH2; <https://www.sasbdb.org/>, SASDTG2.

Author contributions

JP-F: Writing—original draft, Writing—review and editing. FF: Writing—review and editing. HF: Writing—review and editing. JM: Writing—review and editing. JR: Writing—review and editing. JB: Writing—review and editing. AP: Writing—review and editing. DS: Writing—review and editing. MS: Writing—review and editing. MC: Writing—review and editing. AF: Writing—review and editing. MR: Writing—review and editing. SS: Writing—review and editing. TS-S: Writing—review and editing.

References

- Abdelsalam, M., Asheg, A., and Eissa, A. E. (2013). *Streptococcus dysgalactiae*: an emerging pathogen of fishes and mammals. *Int. J. Vet. Sci. Med.* 1, 1–6. doi:10.1016/j.ijvsm.2013.04.002
- Alves-Barroco, C., Botelho, A. M. N., Américo, M. A., Fracalanza, S. E. L., de Matos, A. P. A., Guimaraes, M. A., et al. (2022). Assessing *in vivo* and *in vitro* biofilm development by *Streptococcus dysgalactiae* subsp. *dysgalactiae* using a murine model of catheter-associated biofilm and human keratinocyte cell. *Front. Cell Infect. Microbiol.* 12, 874694. doi:10.3389/fcimb.2022.874694
- Alves-Barroco, C., Roma-Rodrigues, C., Balasubramanian, N., Guimarães, M. A., Ferreira-Carvalho, B. T., Muthukumaran, J., et al. (2019a). Biofilm development and

Funding

The author(s) declare financial support was received for the research, authorship, and/or publication of this article. This work is financed by national funds from FCT—Fundação para a Ciência e a Tecnologia, I.P., in the scope of the project UIDP/04378/2020 (DOI: 10.54499/UIDP/04378/2020) and UIDB/04378/2020 (DOI: 10.54499/UIDB/04378/2020) of the Research Unit on Applied Molecular Biosciences—UCIBIO and the project LA/P/0140/2020 (DOI: 10.54499/LA/P/0140/2020) of the Associate Laboratory Institute for Health and Bioeconomy—i4HB, and through the PhD fellowship 2020.08580.BD.

Acknowledgments

The authors would like to thank the staff of beamlines MASSIF-1 (ESRF), BM29 (ESRF) and P12 (DESY) for their assistance during the X-ray and SAXS data collection.

In memoriam

In memory of Ilda Santos-Sanches, an excellent and inspiring teacher.

Conflict of interest

The authors declare that the research was conducted in the absence of any commercial or financial relationships that could be construed as a potential conflict of interest.

Publisher's note

All claims expressed in this article are solely those of the authors and do not necessarily represent those of their affiliated organizations, or those of the publisher, the editors and the reviewers. Any product that may be evaluated in this article, or claim that may be made by its manufacturer, is not guaranteed or endorsed by the publisher.

Supplementary material

The Supplementary Material for this article can be found online at: <https://www.frontiersin.org/articles/10.3389/fchem.2024.1379914/full#supplementary-material>

computational screening for new putative inhibitors of a homolog of the regulatory protein BrpA in *Streptococcus dysgalactiae* subsp. *dysgalactiae*. *Int. J. Med. Microbiol.* 309, 169–181. doi:10.1016/j.jimm.2019.02.001

Alves-Barroco, C., Roma-Rodrigues, C., Raposo, L. R., Brás, C., Diniz, M., Caço, J., et al. (2019b). *Streptococcus dysgalactiae* subsp. *dysgalactiae* isolated from milk of the bovine udder as emerging pathogens: *in vitro* and *in vivo* infection of human cells and zebrafish as biological models. *Microbiologyopen* 8, 006233–e713. doi:10.1002/mbo3.623

Årdal, C., Balasegaram, M., Laxminarayan, R., McAdams, D., Outtersson, K., Rex, J. H., et al. (2019). Antibiotic development — economic, regulatory and societal challenges. *Nat. Rev. Microbiol.* 18, 267–274. doi:10.1038/s41579-019-0293-3

Biswas, R., Martinez, R. E., Göhring, N., Schlag, M., Josten, M., Xia, G., et al. (2012). Proton-binding capacity of *Staphylococcus aureus* wall teichoic acid and its role in controlling autolysin activity. *PLoS One* 7, e41415. doi:10.1371/journal.pone.0041415

Brown, S., Santa Maria, J. P., and Walker, S. (2013). Wall teichoic acids of gram-positive bacteria. *Annu. Rev. Microbiol.* 67, 313–336. doi:10.1146/annurev-micro-092412-155620

Brown, S., Xia, G., Luhachack, L. G., Campbell, J., Meredith, T. C., Chen, C., et al. (2012). Methicillin resistance in *Staphylococcus aureus* requires glycosylated wall teichoic acids. *Proc. Natl. Acad. Sci. U. S. A.* 109, 18909–18914. doi:10.1073/pnas.1209126109

Cabeen, M. T., and Jacobs-Wagner, C. (2005). Bacterial cell shape. *Nat. Rev. Microbiol.* 3, 601–610. doi:10.1038/nrmicro1205

Campbell, J., Singh, A. K., Santa Maria, J. P., Kim, Y., Brown, S., Swoboda, J. G., et al. (2011). Synthetic lethal compound combinations reveal a fundamental connection between wall teichoic acid and peptidoglycan biosyntheses in *Staphylococcus aureus*. *ACS Chem. Biol.* 6, 106–116. doi:10.1021/cb100269f

Case, D. A., Belfon, K., Ben-Shalom, S. R., Brozell, S. R., Cerutti, D. S., Cheatam, T. E., et al. (2020). *Amber 2020*.

Chapot-Chartier, M.-P., and Kulakauskas, S. (2014). Cell wall structure and function in lactic acid bacteria. *Microb. Cell Fact.* 13, S9. doi:10.1186/1475-2859-13-S1-S9

Eberhardt, A., Hoyland, C. N., Vollmer, D., Bisle, S., Cleverley, R. M., Johnsborg, O., et al. (2012). Attachment of capsular polysaccharide to the cell wall in *Streptococcus pneumoniae*. *Microb. Drug Resist.* 18, 240–255. doi:10.1089/mdr.2011.0232

Emsley, P., Lohkamp, B., Scott, W. G., and Cowtan, K. (2010). Features and development of coot. *Acta Crystallogr. D. Biol. Crystallogr.* 66, 486–501. doi:10.1107/S0907444910007493

Evans, P. R., and Murshudov, G. N. (2013). How good are my data and what is the resolution? *Acta Crystallogr. D. Biol. Crystallogr.* 69, 1204–1214. doi:10.1107/S0907444913000061

Fernandes, S., Ramos, M. J., and Cerqueira, N. M. F. S. A. (2018). molUP: a VMD plugin to handle QM and ONIOM calculations using the Gaussian software. *J. Comput. Chem.* 39, 1344–1353. doi:10.1002/jcc.25189

Fernandes, S., Sousa, S. F., and Cerqueira, N. M. F. S. A. (2019). VMD store—A VMD plugin to browse, discover, and install VMD extensions. *J. Chem. Inf. Model* 59, 4519–4523. doi:10.1021/acs.jcim.9b00739

Fiser, A., Do, R. K. G., and Šali, A. (2000). Modeling of loops in protein structures. *Protein Sci.* 9, 1753–1773. doi:10.1110/ps.9.9.1753

Gale, R. T., Li, F. K. K., Sun, T., Strynadka, N. C. J., and Brown, E. D. (2017). *B. subtilis* LytR-CpsA-psr enzymes transfer wall teichoic acids from authentic lipid-linked substrates to mature peptidoglycan *in vitro*. *Cell Chem. Biol.* 24, 1537–1546.e4. doi:10.1016/j.chembiol.2017.09.006

Gross, M., Cramton, S. E., Gotz, F., and Peschel, A. (2001). Key role of teichoic acid net charge in *Staphylococcus aureus* colonization of artificial surfaces. *Infect. Immun.* 69, 3423–3426. doi:10.1128/IAI.69.5.3423-3426.2001

Hübscher, J., Lüthy, L., Berger-Bächi, B., and Stutzmann Meier, P. (2008). Phylogenetic distribution and membrane topology of the LytR-CpsA-Psr protein family. *BMC Genomics* 9, 617. doi:10.1186/1471-2164-9-617

Humphrey, W., Dalke, A., and Schulten, K. (1996). VMD: visual molecular dynamics. *J. Mol. Graph.* 14, 33–38. doi:10.1016/0263-7855(96)00018-5

Jones, G., and Willett, P. (1995). Docking small-molecule ligands into active sites. *Curr. Opin. Biotechnol.* 6, 652–656. doi:10.1016/0958-1669(95)80107-3

Jones, G., Willett, P., Glen, R. C., Leach, A. R., and Taylor, R. (1997). Development and validation of a genetic algorithm for flexible docking 1 Edited by F. E. Cohen. *J. Mol. Biol.* 267, 727–748. doi:10.1006/JMBI.1996.0897

Kabsch, W. (2010). XDS. *Acta Crystallogr. Sect. D.* 66, 125–132. doi:10.1107/S0907444909047337

Kawai, Y., Marles-Wright, J., Cleverley, R. M., Emmins, R., Ishikawa, S., Kuwano, M., et al. (2011). A widespread family of bacterial cell wall assembly proteins. *EMBO J.* 30, 4931–4941. doi:10.1038/emboj.2011.358

Keegan, R. M., and Winn, M. D. (2008). MrBUMP: an automated pipeline for molecular replacement. *Acta Crystallogr. D. Biol. Crystallogr.* 64, 119–124. doi:10.1107/S0907444907037195

Konarev, P. V., Volkov, V. V., Sokolova, A. V., Koch, M. H. J., and Svergun, D. I. (2003). PRIMUS: a Windows PC-based system for small-angle scattering data analysis. *J. Appl. Crystallogr.* 36, 1277–1282. doi:10.1107/S0021889803012779

Kovalevskiy, O., Nicholls, R. A., and Murshudov, G. N. (2016). Automated refinement of macromolecular structures at low resolution using prior information. *Acta Crystallogr. D. Struct. Biol.* 72, 1149–1161. doi:10.1107/S2059798316014534

Lanzetta, P. A., Alvarez, L. J., Reinach, P. S., and Candia, O. A. (1979). An improved assay for nanomole amounts of inorganic phosphate. *Anal. Biochem.* 100, 95–97. doi:10.1016/0003-2697(79)90115-5

Li, F. K. K., Rosell, F. I., Gale, R. T., Simorre, J.-P., Brown, E. D., and Strynadka, N. C. J. (2020). Crystallographic analysis of *Staphylococcus aureus* LcpA, the primary wall teichoic acid ligase. *J. Biol. Chem.* 295, 2629–2639. doi:10.1074/jbc.RA119.011469

Maier, J. A., Martinez, C., Kasavajhala, K., Wickstrom, L., Hauser, K. E., and Simmerling, C. (2015). ff14SB: improving the accuracy of protein side chain and backbone parameters from ff99SB. *J. Chem. Theory Comput.* 11, 3696–3713. doi:10.1021/acs.jctc.5b00255

Martinez-Rosell, G., Giorgino, T., and De Fabritiis, G. (2017). PlayMolecule ProteinPrepare: a web application for protein preparation for molecular dynamics simulations. *J. Chem. Inf. Model* 57, 1511–1516. doi:10.1021/acs.jcim.7b00190

Meagher, K. L., Redman, L. T., and Carlson, H. A. (2003). Development of polyphosphate parameters for use with the AMBER force field. *J. Comput. Chem.* 24, 1016–1025. doi:10.1002/JCC.10262

Miethke, M., Pieroni, M., Weber, T., Brönstrup, M., Hammann, P., Halby, L., et al. (2021). Towards the sustainable discovery and development of new antibiotics. *Nat. Rev. Chem.* 5, 726–749. doi:10.1038/s41570-021-00313-1

Murshudov, G. N., Skubák, P., Lebedev, A. A., Pannu, N. S., Steiner, R. A., Nicholls, R. A., et al. (2011). REFMAC5 for the refinement of macromolecular crystal structures. *Acta Crystallogr. D. Biol. Crystallogr.* 67, 355–367. doi:10.1107/S0907444911001314

Nomoto, R., Munasinghe, L. L., Jin, D.-H., Shimahara, Y., Yasuda, H., Nakamura, A., et al. (2004). Lancefield group C *Streptococcus dysgalactiae* infection responsible for fish mortalities in Japan. *J. Fish. Dis.* 27, 679–686. doi:10.1111/j.1365-2761.2004.00591.x

Panjikovich, A., and Svergun, D. I. (2016). Deciphering conformational transitions of proteins by small angle X-ray scattering and normal mode analysis. *Phys. Chem. Chem. Phys.* 18, 5707–5719. doi:10.1039/C5CP04540A

Park, M. J., Eun, I.-S., Jung, C.-Y., Ko, Y.-C., Kim, Y.-J., Kim, C., et al. (2012). *Streptococcus dysgalactiae* subspecies *dysgalactiae* infection after total knee arthroplasty: a case report. *Knee Surg. Relat. Res.* 24, 120–123. doi:10.5792/ksrr.2012.24.120

Roe, D. R., and Cheatham, T. E. (2013). PTRAJ and CPPTRAJ: software for processing and analysis of molecular dynamics trajectory data. *J. Chem. Theory Comput.* 9, 3084–3095. doi:10.1021/ct400341p

Roma-Rodrigues, C., Alves-Barroco, C., Raposo, L. R., Costa, M. N., Fortunato, E., Baptista, P. V., et al. (2016). Infection of human keratinocytes by *Streptococcus dysgalactiae* subspecies *dysgalactiae* isolated from milk of the bovine udder. *Microbes Infect.* 18, 290–293. doi:10.1016/j.micinf.2015.11.005

Sander, T., Frey, J., von Korff, M., and Rufener, C. (2015). DataWarrior: an open-source program for chemistry aware data visualization and analysis. *J. Chem. Inf. Model* 55, 460–473. doi:10.1021/ci500588j

Schaefer, K., Owens, T. W., Kahne, D., and Walker, S. (2018). Substrate preferences establish the order of cell wall assembly in *Staphylococcus aureus*. *J. Am. Chem. Soc.* 140, 2442–2445. doi:10.1021/jacs.7b13551

Schneewind, O., and Missiakas, D. (2014). Lipoteichoic acids, phosphate-containing polymers in the envelope of gram-positive bacteria. *J. Bacteriol.* 196, 1133–1142. doi:10.1128/JB.01155-13

Schrödinger, L. L. C. (2024). *The PyMOL molecular graphics system*.

Siegel, S. D., Liu, J., and Ton-That, H. (2016). Biogenesis of the Gram-positive bacterial cell envelope. *Curr. Opin. Microbiol.* 34, 31–37. doi:10.1016/j.mib.2016.07.015

Sun, Y., Spellmeyer, D., Pearlman, D. A., and Kollman, P. (1992). Simulation of the solvation free energies for methane, ethane, and propane and corresponding amino acid dipeptides: a critical test of the bond-PMF correction, a new set of hydrocarbon parameters, and the gas phase-water hydrophobicity scale. *J. Am. Chem. Soc.* 114, 6798–6801. doi:10.1021/ja00043a027

Svergun, D., Barberato, C., and Koch, M. H. J. (1995). CRYSOLE – a program to evaluate X-ray solution scattering of biological macromolecules from atomic coordinates. *J. Appl. Crystallogr.* 28, 768–773. doi:10.1107/S0021889895007047

Svergun, D. I. (1992). Determination of the regularization parameter in indirect-transform methods using perceptual criteria. *J. Appl. Crystallogr.* 25, 495–503. doi:10.1107/S0021889892001663

Swoboda, J. G., Campbell, J., Meredith, T. C., and Walker, S. (2010). Wall teichoic acid function, biosynthesis, and inhibition. *ChemBioChem* 11, 35–45. doi:10.1002/cbic.200900557

Tian, W., Chen, C., Lei, X., Zhao, J., and Liang, J. (2018). CASTp 3.0: computed atlas of surface topography of proteins. *Nucleic Acids Res.* 46, W363–W367. doi:10.1093/nar/gky473

Varela, M. F., Stephen, J., Lekshmi, M., Ojha, M., Wenzel, N., Sanford, L. M., et al. (2021). Bacterial resistance to antimicrobial agents. *Antibiotics* 10, 593. doi:10.3390/antibiotics10050593

Wang, J., Wolf, R. M., Caldwell, J. W., Kollman, P. A., and Case, D. A. (2004). Development and testing of a general amber force field. *J. Comput. Chem.* 25, 1157–1174. doi:10.1002/JCC.20035

Weidenmaier, C., and Peschel, A. (2008). Teichoic acids and related cell-wall glycopolymers in Gram-positive physiology and host interactions. *Nat. Rev. Microbiol.* 6, 276–287. doi:10.1038/nrmicro1861

Frontiers in Chemistry

Explores all fields of chemical science across the periodic table

Advances our understanding of how atoms, ions, and molecules come together and come apart. It explores the role of chemistry in our everyday lives - from electronic devices to health and wellbeing.

Discover the latest Research Topics

[See more →](#)

Frontiers

Avenue du Tribunal-Fédéral 34
1005 Lausanne, Switzerland
frontiersin.org

Contact us

+41 (0)21 510 17 00
frontiersin.org/about/contact

